Probabilistic and deterministic models of Pb-Zn mineralisation and post-mineralisation megabreccia, in the Lawn Hill Region, Australia

Thesis submitted by

Leonardo Feltrin, B. Sc. (Hons.), M. Sc.

August 2006

For the degree of Doctor of Philosophy
in the School of Earth Sciences
James Cook University

ELECTRONIC COPY

I, the undersigned, the author of this work, declare that the electronic copy of this thesis provided to the James Cook University Library, is an accurate copy of the print thesis submitted, within the limits of the technology available.

_____   _____

Signature   Date

STATEMENT OF ACCESS

I, the undersigned, author of this work, understand that James Cook University will make this thesis available for use within the University Library and, via the Australian Digital Theses network, for use elsewhere.

All users consulting this thesis will have to sign the following statement: "In consulting this thesis I agree not to copy or closely paraphrase it in whole or in part without the written consent of the author; and to make proper public written acknowledgment for any assistance that I have obtained from it.

I understand that, as an unpublished work, a thesis has significant protection under the Copyright Act.

_____   _____

Signature   Date

STATEMENT OF SOURCES

DECLARATION

I declare that this thesis is my own work and has not been submitted in any form for another degree or diploma at any university or other institution of tertiary education. Information derived from the published or unpublished work of others has been acknowledged in the text and a list of references is given.

_____   _____

Signature   Date

STATEMENT OF CONTRIBUTIONS

General contributions towards this study included:

- International Postgraduate Research Scholarships (IPRS)
- James Cook University Postgraduate Research Scholarships (JCUPRS)
- Pmd*CRC Top-up Scholarship
- Pmd*CRC educational and training fund

Contributions from others towards this thesis are clearly stated at the forefront of each chapter where applicable. A summary of the major contributions is also provided here:

- **Chapter 4:** Dr. J. G. McLellan – 2D Numerical modelling of the Century deposit and text.

- **Chapter 5:** Dr. J. G. McLellan – 3D Numerical modelling of the Century deposit and text.

- Normal supervisory condition throughout the preparation of the thesis included discussions and proofreading by Prof. N.H.S. Oliver (all thesis), and Dr. J.G. McLellan (Chapters 4, 5).

Acknowledgements

I am grateful to dad Gianni, mum Isabella, Martina and Susanna for their patience and support.

Thesis abstract

Quantitative analysis with the aid of numerical and computational modelling has been used to address geological problems since the 1940s. The number of applications developed and used to solve geological problems has increased largely because of the advent of desktop microcomputers. However, despite the introduction of mathematical-computational methods, the observational, inductive approach of Hutton and Wegner remains deep in the geological science.

Qualitative rather than quantitative geology has won in the past because of the naturalistic inclination of geologists - "rather than sit on their desk typing and modelling natural phenomena, they were more interested in exploring the world with the naked eye, spending their time conceptualising models and integrating the data collected in the field".

With globalisation geologists have broadened their objectives as larger and numerous databases are available. Therefore, rather than collecting their own data, they now have new technologies to retrieve and process large databases. The drawback of this advantage is the lack of data quality verification, which can be a substantial problem. However, a statistical treatment of datasets can be a partial solution to this.

The author as a geologist felt the need of demonstrating that a quantitative-computer based description of a multivariate geological system could lead to a significant improvement of the understanding of such a system.

A line can be drawn to subdivide computational approaches that use inference networks based on physical laws (e.g. Geodynamic modelling) to bound variables, or empirical laws (e.g. Bayesian Probability Analysis) that are not characterised by the nature of the data (such as measures of spatial association). Alternative methods (e.g. Fuzzy Sets, Dempster-Shafer, Neural Networks) have been suggested to treat multivariate data less empirically.

A possible way to improve the quantitative analysis is the simulation of geological parameters (Chapter 4 – 5). The interaction between the geologist and the computer is iterative in this case – multiple simulation leads to a refinement of chosen approximation. Nevertheless, this methodology is often biased and arbitrary. The best approach perhaps remains the validation of computational models comparing therm against the experimental results and observations.

The objective of this thesis was then to apply quantitative/computational tools to different geological scenarios in the Lawn Hill Region, Mount Isa Inlier. Part of this study focused on one of the largest Pb-Zn mineral resources in Australia, the Century zinc deposit. The objective of the first section of this thesis was to discover possible new mineral resources similar to the Century orebody, and comprehend how the mineral deposit formed.

Two case study applications to the Lawn Hill Region at regional and mineral deposit scale (Century deposit) are presented. The first study reflects the need of data

integration in a multivariate system to obtain a statistical estimate of the likelihood of finding a mineral deposit. The concepts of Bayesian reasoning were reviewed and a computer program (coded in Visual Basic) was developed to perform Bayesian modelling. The results were then compared against an expert-driven model to obtain a predictive map for the Lawn Hill Region. The analysis suggested that most of the mineral deposits/prospects are located where knowledge driven models favour the occurrence of SEDEX mineralisation. The data driven model suggests that other Pb-Zn deposits more likely are proximal to the Termite Range fault. Integration of KD and DD models suggests prospectivity for SEDEX-style mineralisation north of the Edith cluster a vein style ore.

The second study involved the quantitative 3D spatial analysis of the Century deposit. The 3D model of the mineral deposit was also combined with a 2D-3D coupled deformational and fluid flow simulation for the mineral deposit. The integration of these modelling tools allowed a better conceptualisation of the variables controlling the spatial distribution of base metals within the mineral deposit. In this case the research effort was directed toward the use of computational tools to solve the classical problem of understanding how the ore deposit formed. The results obtained support (re) mobilisation and a broad scale metal zoning similar to what is observed at Lady Loretta and HYC. Results also illustrated how basin compartmentalisation can control (re)mobilisation, fluid-flow and therefore how a mineral deposit evolves in time. A comparison between the different scale of zoning observed coupled with numerical 2D-3D results outlined that more likely Century is an exhalative system that however experienced later epigenetic introduction of base metals. Modelling results have in

general outlined that classification of geological patterns can be an effective way of discriminating the genesis of an ore deposit. For instance, the textural evolution of a mineral deposit which is derived from a combination of mechanical and chemical processes (the mechano-chemical coupling modelled by Ortoleva, 1994) may represent non-linear behaviour and lead to patterning of the geological system. In this context, the relationships observed and modelled between the evolution of permeability structure and the spatial distribution of mineral grades represent an example of how understanding the dynamics of complex system provides improved interpretations.

The third study, focused on the post-mineralisation Lawn Hill Megabreccia, and explores the variety of patterning of sedimentary textures and deformational features, aimed at differentiating the timing and origin of this brecciation event. The research combined qualitative and quantitative analysis of structural, sedimentary and stable isotopic features at various scales. The results indicate a synsedimentary (Cambrian) origin for the brecciation. However, the study has emphasised that different causative processes (e.g. tectonic, meteorite impacts) may lead to similar patterning.

To conclude, quantitative modelling of the presented geological examples suggests that we need to improve accuracy and numerical descriptions of the system to reveal the timing of formation and how a certain geological process occurred. In other words the loss of data induced by generalisation and oversimplification (often required in computational and quantitative modelling) can reduce the reliability of a predicted answer. Self-organisation and chaos theories (Synergetics) may be a new way to approach and describe the observed patterning of geological events and could be used

to provide better mathematical models to understand ore genesis, discover a mineral

deposit or ascertain the origin of a catastrophic event.

Table of contents

Chapter 3

Predictive modelling of prospectivity for Pb-Zn deposits in the Lawn Hill Region,

Chapter 4

***Testing the structural and geomechanical processes in the formation of the
Century (Zn-Pb-Ag) Deposit*** _____ ***4-1***

Chapter 7

Complexity and self-organisation _____ *7-1*

List of figures

Chapter – 2

Chapter – 3

Chapter – 4

Chapter – 5

Chapter – 7

List of tables

Chapter – 3

Chapter – 4

Chapter – 5

Chapter – 6

Chapter 1

Introduction

1.1.   *General introduction*

This study is primarily focused on the understanding of geological systems by the aid of computers, the "intelligence amplifiers" (see Merriam, 2004). Three geological problems are discussed in the forthcoming chapters, focused on economic, structural and sedimentary geology related themes:

- Exploration for Pb-Zn mineral deposits of large tonnage (Lawn Hill Region),
- Understanding the genesis of the Century zinc deposit,
- Reconstruction of the processes that led to the formation of the Middle Cambrian Lawn Hill Megabreccia.

A primary objective is to obtain temporal and spatial reconstructions of the geological evolution of each component, or sub-system of the study area, the Lawn Hill Region in northern Queensland, Australia. The project was specifically aimed at using advanced computational tools to analyse geological variables, but it also involved the development of computer software to solve specific problems.

1.2. Application of computer science to geology

I have been always fascinated by computers therefore as a geologist I decided that I wanted to prove to myself that the computer "is worth a try in geology". When I started this project I had already gained experience with the use of computers in geology mainly developing geological models in 3D and producing animations of geological terrains, taking the audience across dynamic, virtual scenarios to observe structural characters with great detail. Most importantly the virtual experience was a way to deliver quickly the information to them at different scales (zooming up and down). This first attempt was driven by the understanding that computers extend our ability to represent multivariate systems. In the end it revealed also that frequently these methodologies are so fascinating that the science behind these models becomes of secondary importance for the unaware audience. This should not happen. Science has long been fascinating for its simplicity not for its technicality.

Stepping from the "glossy animations" I approached the real potential of such tools in addressing a classic topic of Economic Geology – ore genesis. Computer software such as GoCAD, FLAC, FLAC-3D and some programs I developed were used to reconstruct several mineral deposit scenarios. The results were integrated to offer a vision of ore genesis obtained from the different modelling perspectives.

The interrelationship among humans and machines is now so deep that it is becoming difficult to evaluate if the benefit is derived exclusively from the machine itself (hardware) (e.g. Merriam, 1999) or from the software developed by hundreds of developers. In other words computers are now not only huge databases, they also have

the ability to store and retrieve our intellect (correlating data and developing inferences) in the form of high level computer software (structured languages). This process is iterative, irreversible and gradually sees the transfer and upgrade of knowledge from humans to machines (e.g. the OpenSyc, Formalized Common Knowledge project; http://www.opencyc.org), until perhaps the computers will start to think autonomously. These perspectives were, in part, the reason for a second stage of the project devoted to the exploration of mineral deposits in the Lawn Hill Region using empirical modelling of probability. In this context the application of computers to geology assumes a role that is different from the previous, because computer programs are not exclusively a representation of a multivariate system and how its variables are related to one another. Boolean logic takes the place of partial differential equations (used in process modelling) to empirically explore interlocked variables in this case, but the main difference is that the computer software provides a final output that is derived from an automated inference mechanism- the Bayesian reasoning.

A geological problem can be addressed quantitatively in different manners; the same dataset can be fitted using several mathematical models (Krumbein, 1962). This raises the question of what technique is the best and which one should be used. However, there is no clear answer to this. More likely it is better to favour the fusion (integration involving rejection of poor models) of diverse mathematical models rather than limit the analysis (i.e. the search for mineral deposits as function of a single ore genetic model). The problem is how to define the goodness of fit of our models (e.g.

Fisher, 1925). This leads to a final stage in this thesis - the relationship of qualitative versus quantitative geology.

Computational modelling is certainly an improved methodology, which deals more adequately with geological complexity. Therefore it represents a valid alternative to more consolidated (conventional) methodologies of analysis, of geological problems. For example (see Chapter 3), modern digital mapping tools have effectively been valuable alternatives to conventional outcrop mapping, when exploring for mineral deposits. Nonetheless, the quality of field based studies retain its importance for obvious reasons. Similarly, when treating quantitatively and computationally the problem of genesis and timing of a geological event (Chapters 4-6) a multi-dimensional (space, time) perspective is available. Multi-dimensionality leads to better conceptualisation of a geological system. With computational modelling a more comprehensive vision is offered to the geologists, which are then able to test their hypothesis more elegantly. Quantitative modelling is therefore a natural step (required) to improve the qualitative methodology of the past, but it should never be considered as a way to avoid *a priori* qualitative assessment.

1.3. *Aims and objectives*

In summary this study had the following aims:

- Compile software that allows constructing predictive exploration GIS models that make use of Bayesian probability analysis, (Chapter 3);

- construct and run 3D models and simulations to understand the genesis of the Century zinc deposit, (Chapters 4 and 5);

- combine qualitative and quantitative analysis to understand the timing and origin of the Lawn Hill Megabreccia, (Chapter 6); and

- synthesis and conclusions (Chapter 7).

In addition to the application of commercial softwares in all chapters, additional computer code was developed in Visual Basic to address both small and large scale issues or to extend the functionalities of proprietary software such as GoCAD (see Appendix C).

1.4. Thesis outline

Chapter 1   Introduction

The first chapter is a general introduction to the thesis work, discussing how the work explores different types of computer applications to geology.

Chapter 2   Historic overview and modelling background

The second chapter discusses the historical background that has in part guided the author toward this study. Firstly the evolution of numerical geological science is examined, becoming progressively quantitative although the qualitative, observational side remains still rooted and essential. This mathematisation process is complemented by the introduction of computers and programs designed to solve geological problems.

The chapter then concludes with a general overview and theoretical background of the type of applications used in chapters 3-6.

Chapter 3   An integrated knowledge-based and data-driven modelling study of the Lawn Hill Region, Queensland, Australia

This chapter compares, at regional scale, a knowledge-driven model based on expert driven scores using common knowledge of SEDEX-type deposits and MVT-type deposits, and a data-driven model developed using Bayesian analysis with the Weights of Evidence method. Considerations are made concerning the validity of the two methodologies and of the benefit derived from their integration.

Chapter 4   Testing the structural and geomechanical processes in the formation of the Century Zn-Pb-Ag Deposit

The fourth chapter is a camp-scale to deposit-scale study focused on the Century deposit aiming at understanding and testing different ore genetic models for the Zn-Pb-Ag mineralisation. Camp-scale reconstructions focus on the understanding of the structural evolution and role of faulting in contributing to the spatial distribution of mineral grades. Numerical 2D simulations of deformation and fluid flow are also presented to test previously proposed genetic models.

Chapter 5   Modelling the giant, Zn-Pb-Ag Century deposit, Queensland, Australia

The fifth chapter is a deposit scale study. The interrelationship between faulting and mineralisation and the role of other controlling variables is evaluated, to understand the spatial patterning of mineralisation. Inferences derived from the integration of 3D structural and property modelling combined with 3D coupled fluid flow and deformation numerical simulations are considered in the context of basin history, emphasising the importance of basin compartmentalisation.

Chapter 6   Catastrophic mass failure of a Middle Cambrian platform margin, the Lawn Hill Megabreccia, Queensland, Australia

The sixth chapter is a deposit scale study of the Middle Cambrian limestones unconformably covering Century. The study represents an example of how quantitative geology can be combined with observational qualitative, field based studies to resolve complex geological scenarios (i.e. multiple phases of breccia development).

Chapter 7   Complexity and self-organisation

The seventh chapter proposes an alternative non-linear view of geological processes suggesting that complex patterning (e.g. mineral deposit formation, breccia development etc.) and randomness can be treated with an innovative approach that combines deterministic with probabilistic laws.

Chapter 8   Conclusions

This final chapter contains a brief summary of the conclusions, and a general conclusive statement.

Appendix A-B

Mathematical models (technical background).

Appendix C

Software developed.

Appendix D

Table of specimens used in the thesis.

Appendix E

- Digital copy of the thesis.

- PowerPoint animation of 3D structural and property model of the Century deposit.

- WofE-2D software.

- High resolution Figs 3.1 and 5.7

Chapter 2

Historic overview and modelling background

Acknowledgement of Contributions

N.H.S. Oliver – normal supervisory contributions

2.1 Introduction

This chapter considers a historic overview that focuses on the gradual shift from qualitative to quantitative geology looking also at the advances that the use of computer has brought into quantitative geology. Retracing this history underlies important connections of present applications with the past. These references clarify the derivation of the approaches adopted in the thesis and the theoretical paths used to explore the geological problems. The chapter concludes with a section that provides the theoretical background relative to the statistical and deterministic models applied later in this thesis.

The work treated in the core of the thesis considers "decision functions" in a mineral exploration case. 3D models are also constructed using interpolation algorithms derived from geostatistical methods (e.g. Mallet, 1989). These quantitative approaches are statistical and use software tools derived from advances in mathematical geology (Howarth, 2001). In addition to this, deterministic simulations (e.g. fluid flow and deformation in sedimentary basins, Bethke et al., 1988) were also generated with the aid of fast workstations to study the physical processes that involve migration of fluids in and around faults in sedimentary basins.

The historical perspective draws marked lines between these models. This division derives from the philosophical approach adopted to solve scientific problems that see two distinct methodologies: the *deterministic* based on sets of equations that fully

describe the system with a finite number of variables, and the *statistical* approach based on stochastic models with equations that fit a real system with infinite variables. In this regard Agterberg (1967) discusses some of the methodologies adopted to better understand stochastic processes, illustrating the evolution from Surface Trend Analysis to other more refined methods of regression including *geostatistical approaches* (e.g. moving average), *Poisson distribution*, the use of *Fourier-transform* and *Power Spectra analysis*. The counterpart to such statistical models is matched by the sophistication of *finite-difference* techniques in numerical simulations (e.g. Harbaugh and Bonham-Carter, 1970).

2.2 Historic overview

2.2.1 From qualitative to quantitative geology

The roots of quantitative geology are very deep (Merriam, 1981; Howarth, 2001; Merriam, 2004). For instance, Agricola made use of trigonometry in mining applications as he reports on his book the De Re Metallica (Merriam, 2004). However, even earlier is the estimation of the earth circumference based on astronomical observations of the sun by Eratosthenes (276-194 BC) in ancient Greece (Fig. 2.1).
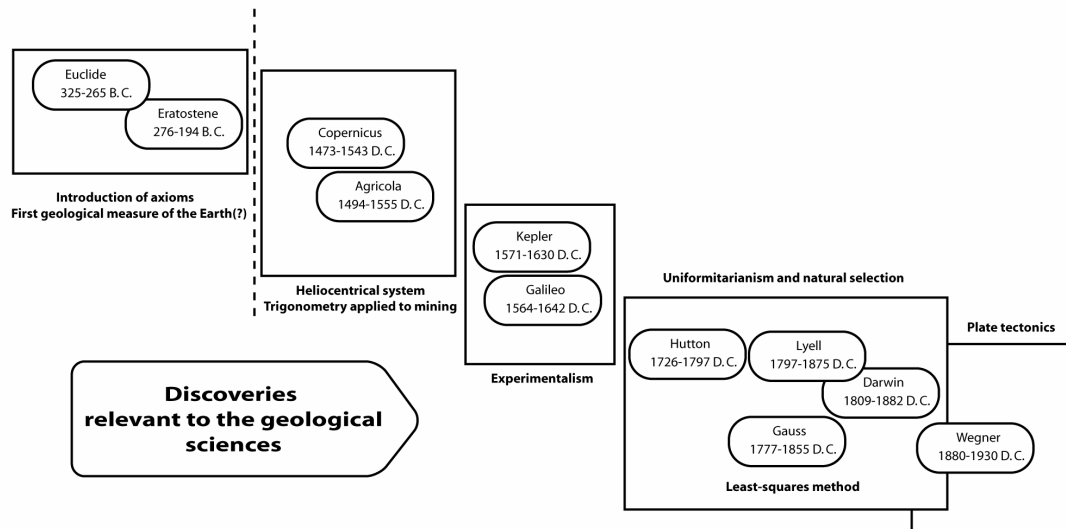
Fig. 2.1 Diagram showing a summary of the personalities that influenced the history of science and as a consequence contributed directly and indirectly to the advance in natural sciences including geology.

Unfortunately in the past, practitioners of quantitative methods were few, and the application of mathematical and statistical methods to geology required several scientific revolutions to gain consideration, including the advent of computers. At the beginning of the 17th Century, only after Galileo and Kepler "the experimentalists" (see Einstein, 1934), a quantitative approach to science became a necessary requirement to improve theoretical models. However, a considerable time after this philosophical advance was still necessary for a young discipline such as geology to become effectively numerated.

Early theories such as plutonism (Hutton, 1726-1797), uniformitarianism (Lyell, 1797-1875), and plate tectonics (Wegner, 1880-1930) were mostly the success of an observational science. Wegner, in fact, proposed his theory initially by noting a similarity among the margins of continents. Qualitative reasoning was therefore a primary tool that also became more refined later after Chamberlain introduced the method of "multiple working hypothesis" in 1897 (Krumbein, 1962). A qualitative approach could certainly grasp generalised laws of nature such as natural selection (Darwin 1809-1882). However, early scientific investigations have been turned to more rational and careful analysis of experience, leading to the present reductionism. Reductionism can be exemplified by modern experiments in particle physics. Understanding simple parts of a system at sub-atomic scale (non-observable) requires inevitably a quantitative approach. Qualitative holist science must therefore become reductionist quantitative science, reflecting the need of extending our scientific experiences. Reductionism remains also unavoidable as it is far easier to describe independently the element of a system rather than look at the whole, because this would require a full understanding of variable interactions (the variable interlocking of Krumbein) a task that is often impossible to fully achieve, hence the use of statistical methods. There seems to be then, a natural tendency towards quantitative geology as shown by Merriam (2004) in the exponential trend and relative stages of evolution of mathematical sciences (Fig. 2.2). The application of mathematics and

computer science to geology can also be understood by looking at the history of the

scientists that contributed to them (Fig. 2.3).

THIS IMAGE HAS BEEN REMOVED DUE TO COPYRIGHT RESTRICTIONS

Fig. 2.2 Diagram illustrating the different stages of development of quantitative geology. Modified from Merriam (2004). An additional stage is considered that forecasts the advent of intelligent systems.

THIS IMAGE HAS BEEN REMOVED DUE TO COPYRIGHT RESTRICTIONS

Fig.2.3 Tree of quantification portraying some names of eminent researchers involved with the interrelationships of physical and natural sciences. Some of these figures contributed to the mathematisation of the geological science. Adapted from Merriam (2004).

2.2.2 Regression

Howarth (2001) provides an excellent description of how regression and model-fitting methods have evolved in earth sciences. This section adapts then the historic reconstruction of Howarth showing the derivation of statistical and deterministic methods.

Howarth (2001) reports a historical study of magnetic declination, which probably was the first example of application of quadratic functions to predict the variation of the earth's magnetic field. This work was developed by a mathematical practitioner, Henry Bond (1600-1678), who predicted correctly the magnetic declination in London for the year 1657 and subsequently published a series of manuscripts with 30 years forecasts of magnetic declination. Other historical studies were more focused on astronomical observations and the measuring of the Earth's shape, which led to the development of new mathematical formulations, respectively developed by Mayer (1723-1762) and Boskovic (1711-1787), but also others (Howarth, 2001). However, only at the end of the 18th Century did the German mathematician Gauss (1777-1855) develop a new method to fit a generic mathematical equation to a finite number of data points. This was the famous least square method that he firstly applied to interpolate the elliptical orbit of an inferred planet (the planetoid Ceres). The least-squares method is mathematically expressed as the minimization of the sum of the squared residuals (e_i) that is the difference between

measured (y_i) and computed ($\hat{y}_i$) values derived from the mathematical model fitted to the data, where *n* refers to the number of measured values:

$$\sum_{i=n} e_i^2 = \sum_{i=n} \left(y_i - \hat{y}_i\right)^2 \mapsto 0 \qquad (2.1).$$

The first publication of the method is attributed to Legendre (1752-1833) in 1805 who published the method as a way to determine cometary orbits. From this stage, the least-squares method was progressively divulged by Gauss (e.g. models of the global magnetic field, see Fig. 2.4) and others (e.g. Airy, 1801-1892).

However, significant progress in regression analysis as it is known to modern scientists (e.g. Sahoo and Pandalai, 1999), had to wait until the beginning of the 20th century when the work of Pearson (1857-1936) and his collaborator Yule (1871-1951) elucidated the connection existing between least-squares and the regression line coefficients (β_0, β_1), which could be represented as the intersection of a line with the ordinate axis and angular coefficient of a linear function in *y* (*x*) of type:

$$y_i = \beta_o + \beta_1 x_i \qquad (2.2).$$

Equations (1) and (2) can be combined to derive the best coefficients for $y(x)$ that fit randomly collected data of a population:

$$\sum_{i=n} e_i^2 = \sum_{i=n} \left(y_i - \left(\beta_o + \beta_1 x_i \right) \right)^2 \mapsto 0 \qquad (2.3).$$

The least-squares method being coupled with the regression line became effectively a statistical tool for bi- and multivariate analysis. However, it was only after Fisher (1890-1962) that a firm theoretical basis was set in a definitive manner. Fisher (1925) introduced concepts such as the variance of a population (the residuals gained importance rather than being neglected) and formal tests for statistical significance of coefficients (β_0, β_1) in the regression equation (Howarth, 2001). In the second quarter of the 20th Century the efforts of Krumbein (1902-1979) (one of the fathers of mathematical geology) led to widespread application of mathematics and statistics to sedimentary geology problems, e.g. Manual of Sedimentary Petrography (Krumbein and Pettijohn, 1938). Krumbein was interested in discriminating between large trends in sedimentary facies distributions and local anomalies. His contribution led to the extension of the least-squares fitting method to the approximation of polynomial functions representing regional datasets that were approximated either by linear or non-linear surfaces. This

method was named Trend-Surface Analysis (Krumbein, 1959). The model consisted in combining the least-squares Gauss equation with a generic polynomial of type:

$$t = A_{00} + A_{10}\,U + A_{01}\,V + A_{20}U^2 + A_{11}\,UV + \ldots + A_{pq}U^{\,p}V^{\,q} \tag{2.4}$$

where t represents the trend component (e.g. a larger wavelength geophysical anomaly) of a variate X in $(U,\ V)$ space. A general relationship considers ε as an additional component of X:

$$X = t + \varepsilon \tag{2.5}$$

suggesting that the roughness of the real dataset is also controlled by an additional component of random error and smaller scale oscillations (ε). The polynomial (t) is then a smoothing function that is used to generalise the real distribution of data.

Among the applications of *Surface Trend Analysis* it is worth noting the compilation of tables to perform calculations of linear coefficients in (2.4) using orthogonal polynomials (e.g. Oldham and Sutherland, 1955; Grant, 1957). These were used to remove the regional anomalies from gravitational field data. Miller (1956) used also least-squares to fit linear surfaces, and the method of averages to fit piecewise quadratic surfaces. His work pointed out that methodologies attempting to fit internal

points of regular grids (not at vertices) were better for geological applications, a case also illustrated below in the discussion of the Discrete Smooth Interpolation (DSI) method.

The progress of these methodologies was relatively slow because of the tedious calculations. Howarth (2001) gives a curious comparison reporting that in the 19th Century scientists such as Sabine had the advantage of human 'computers'- a group of trained soldiers was used to perform the calculations required. But to gain similar and even more 'extraordinary' computational power the advent of computers had to wait until the 1950s. After World War II, a period that stimulated the diffusion of statistics and promoted the development of computers for military applications, computers represented the solution to such tedious calculations, leading geologists to also start looking into automatic data processes (Krumbein, 1962). After computers entered the scene, the inversion of a $10 \times 10 \left[U, V \right]$ matrix (Krumbein, 1959; Howarth, 2001) became an easy task therefore accelerating interpolation methods and favouring their diversification, that finally led to modern geostatistics (Krige and Ueckermann, 1963; Matheron, 1970).
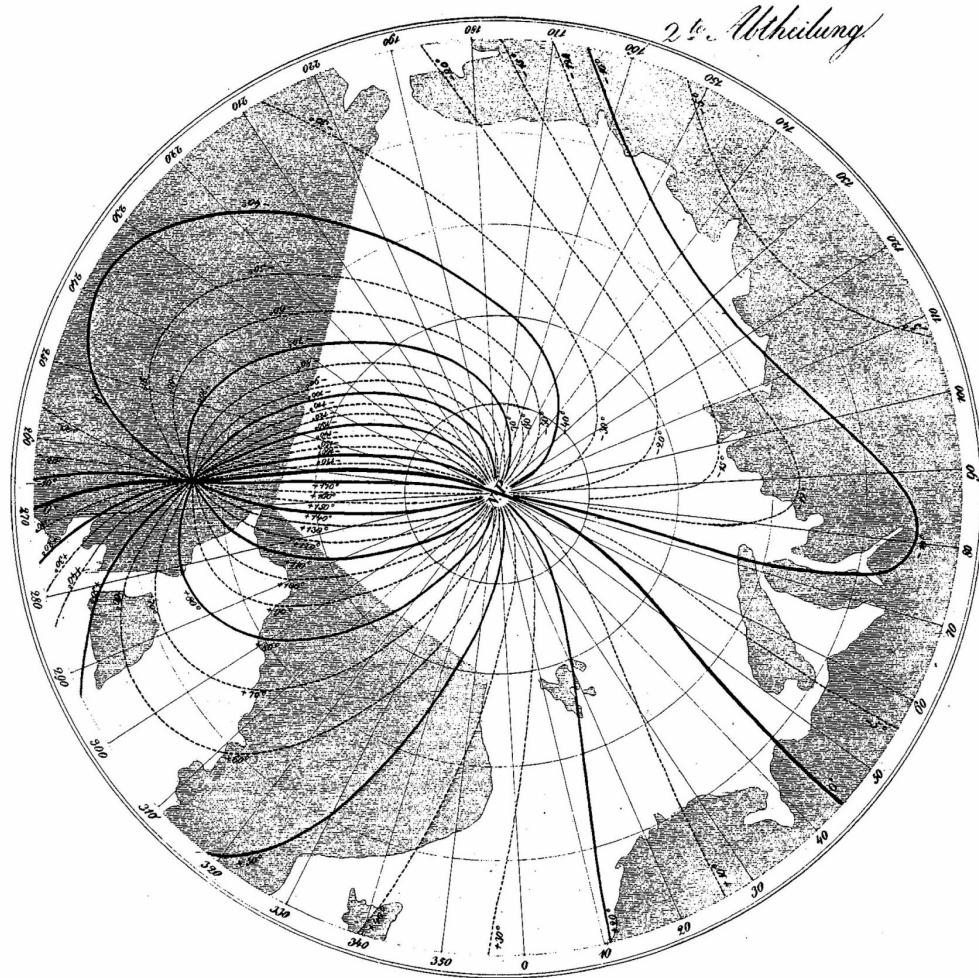
Fig. 2.4 Example of application of polynomial fitting to geophysical data. Isolines of magnetic declination of the Northern Hemisphere. Reproduced from Gauss and Weber (1839).

2.2.3 Geostatistics

The introduction of new methodologies was also due to the limitation encountered with polynomials, requiring more refined algorithms to resolve the excessive smoothness of this type of approximation. This led Griffin (1949), for example, to apply the method of moving averages to geophysical gravimetric data. The difference between this method and the use of polynomials lies in a generalisation based on averages of predefined neighbourhoods rather than a polynomial function that describes the whole spatial pattern. Howarth (2001) reports also an interesting application of these methodologies to Economic Geology problems such as gold estimation by a South African mining geologist (Krige, 1960). The most important discovery that this author reports is the autocorrelation function of gold assays - a spatial correlation among samples as a direct function of their distance from one another. This realisation led Krige to develop methodologies to correct grade estimations with the aid of regression analysis (Krige, 1951), also performing spatially weighted averages of ore blocks (Krige, 1966). Beside these early attempts to extend regression analysis at relatively small scales (e.g. mines, oil fields etc.), it was only after the substantial contribution of Matheron (e.g. Matheron, 1965) that the field of geostatistics found its independence as a modern, individual discipline in earth sciences. The work of Matheron was particularly important in mining applications although his contributions to geostatistics are largely accepted also outside

the geoscience world (Agterberg, 2001), reflecting the importance of his mathematical models. Matheron (1965) provides a theoretical framework for the early empirical models that accounted for both the interpolation of data, and more importantly for the uncertainty estimates associated with predictive models. Matheron was the first to use the term Kriging (in honour of Krige). Kriging is a type of interpolation based on two core algorithms. Firstly, a weighting algorithm aims to guess the value of a spatial point ($\hat{Z}_0$) on the basis of certain sphere of influence, similar to IDW (Inverse Distance Weighting) methods (see Bonham-Carter, 1994). Kriging equations contain a sample of the population of data with known variables (Z_i). Usually the sample can be represented as a cluster of points in space, occurring at variable distance. These need to be weighted accordingly. The relationship is then of the type:

$$\hat{Z}_0 = \sum_{i=1}^{n} w_i \, Z_i \qquad\qquad (2.6)$$

where w_i is a weighting coefficient that ranges from 0 to 1 (to avoid normalisation otherwise adopted in IDW methods);

Secondly an algorithm is needed to determine the level of uncertainty in the estimation of the w_i coefficients. This is because the calculation of these coefficients is function of the spatial variability of the dataset, relying on two types of covariance:

$$w_i = \frac{d}{C} \tag{2.7}.$$

Within this equation (d) is a linear vector that represents spatial 'covariances' between each Z_i and $\hat{Z}_0$ whereas (C) is a vector expressing the covariance among all the couples Z_i. These relationships can be expressed in compact form using the matrix notation as follows:

$$\begin{bmatrix} w_1 \\ \cdot \\ \cdot \\ w_n \\ \mu \end{bmatrix} = \begin{bmatrix} C_{10} \\ \cdot \\ \cdot \\ C_{n0} \\ 1 \end{bmatrix} \begin{bmatrix} C_{11} & C_{12} & \cdot & C_{1n} & 1 \\ \cdot & \cdot & \cdot & \cdot & \cdot \\ \cdot & \cdot & \cdot & \cdot & \cdot \\ C_{n1} & C_{n2} & \cdot & \cdot & 1 \\ 1 & 1 & \cdot & 1 & 0 \end{bmatrix}^{-1} \tag{2.8}.$$

The term μ is a dummy number (Lagrange multiplier) used to rescale the weights in the range (0,1). (d) and (C) represent a measure of the dispersion, distance and spatial autocorrelation of a selected variable. Note that kriging uses multiple parameters to compute the weights, but these are measured on 'internal properties' of the same dataset and do not rely on other 'external' parameters (e.g. the relationship to other variables). In general terms the covariance C is expressed as a measure of spatial association between two variables for a sample (n):

$$C = \frac{1}{n} \sum_{i=1}^{n} \left(X_i - \overline{X} \right) \left(Y_i - \overline{Y} \right) \tag{2.9}$$

with *X, Y* as spatial coordinates. An analogous relationship is more commonly adopted to construct semi-variograms that are the most widespread tool in mining applications (e.g. Houlding, 1994). Usually such plots consider the moment of inertia versus the distance between couples of points (lag). The moment of inertia (γ) is defined as:

$$\gamma(h) = \frac{1}{2n} \sum_{t=1}^{n} \left(Z_t - Z_{t+h} \right)^2 \tag{2.10}.$$

The mathematical relationship is similar to equation (2.9) except that in this case the lag (*h*) is externally chosen and is regularly spaced to obtain the variogram. This autocorrelation function is based on a single variable and provides the degree of correlation between a central point Z_t positioned in *t* and any other point in the chosen neighbourhood (*t* + *h*). Both *C*(*h*) and γ(*h*) can be used to construct an experimental variogram that can be fitted with a mathematical model. Commonly, spherical or exponential curves are used to characterise the signal (Isaaks and Srivastava, 1989; Houlding, 1994). These equations are represented by a linear system of equations as

shown for different mathematical fitting models in Figs. 2.5a, b, c. The equations contain a series of coefficients that are used to fit the shape of the variogram and are also meaningful to their interpretation. For instance, in Fig. 2.5a the *spherical* model (Matheron, 1965) is represented by four coefficients: (s) is the *lag* or sample distance; (a) represents a limit after which the correlation starts vanishing; (C) is the variogram *sill,* a range of spatial association $\gamma(s)$; (C_0) is the *nugget effect*, the noise or background signal. Once the model is representative of the region of interest it can be applied to neighbour domains where the experimental autocorrelation is unknown. The three coefficients (a, C, C_0) are used then to obtain the covariance for each point within the chosen region allowing the definition of the w_i and therefore leading to the solution of equation (2.6). The interpretation of the variogram is however complex because of its variability as a function of the orientation of the region of interest and also as a direct function of the overall trend of the dataset. Bonham-Carter (1994) remarks that the fluctuation in the data can be of different scales and it is convenient to distinguish the trend (regional fluctuations) from the signal (the parameter of interest) and the noise. This can be done using methods such as Trend-Surface analysis. Kriging works in agreement with Agterberg (2001) only for stationary conditions and also for normal distributions (Houlding, 1994). The data are commonly pre-processed to respect these statistical constraints. A recent development is *Universal Kriging* that is essentially a combination of the above mentioned methodologies. Other types of kriging are also used for particular

purposes. For instance *Indicator Kriging* shares analogies with Bayesian modelling (Chapter 3), because it is used to evaluate the probability of meeting a certain threshold parameter chosen *a priori*, and also has similar data processing (reduction to Boolean data format).
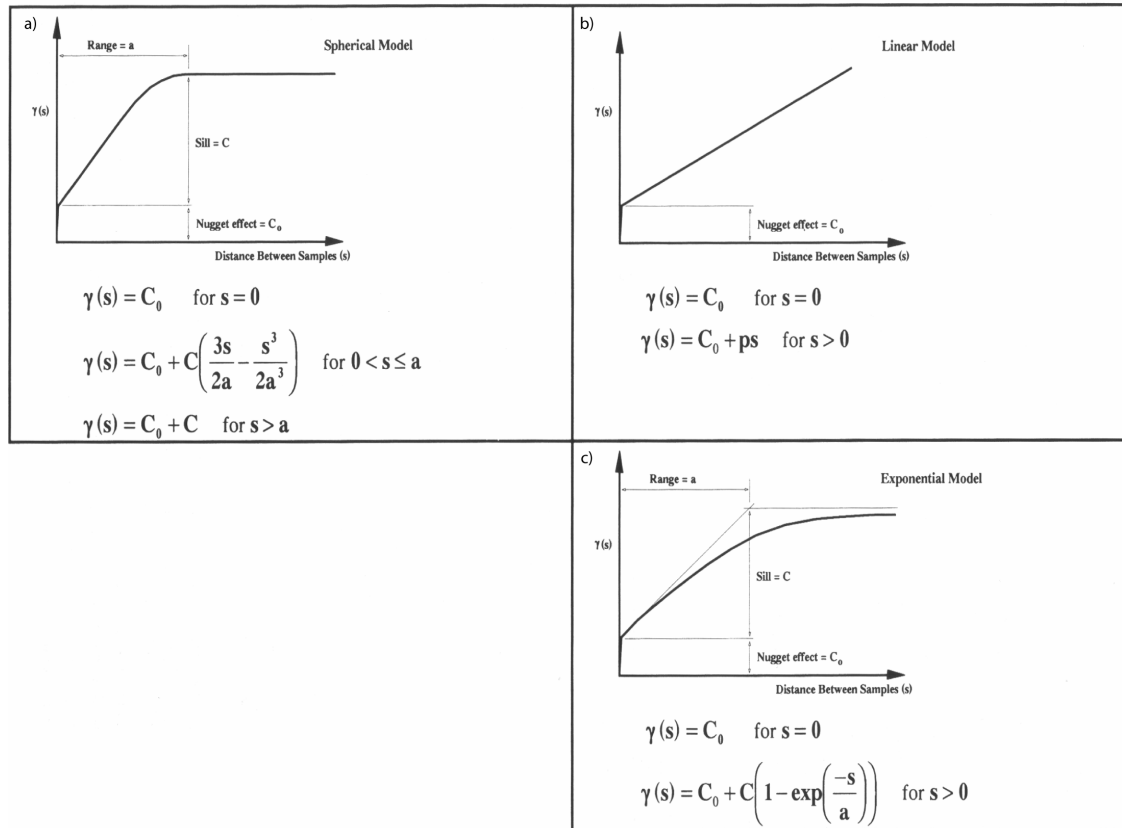
Fig. 2.5 Example of variogram plots showing respectively: (a) Spherical; (b) Linear; and (c) exponential model. Linear systems of equations of fitting curves are also included (see text for coefficients definitions), adapted from Houlding (1994).

Beside the diversification of kriging techniques, progress in geostatistics has also favoured the application of regression methods in alternative directions. One of the fields that gained progressive importance is the three-dimensional modelling used to simulate geological and biological objects. The need for a 3D representation of geologic themes has stimulated the development of specialised algorithms. For example Mallet (1989) proposed a discrete smoothing approach (DSI) to interpolate triangulated surfaces, which are often complex to handle with common tools such as spline based algorithms if datasets are geological. In a general sense the method provides a similar result to kriging interpolation (Mallet, 1989) although it is used to fit geometries rather than to predict ore grades. DSI and other algorithms were implemented in GoCAD, a software compiled in originally in C, but subsequently further developed in C++ language, at the University of Nancy (France).

Probabilistic regression models (Agterberg and Robinson, 1972; Tukey, 1972) were derived from mining and oil search applications. These more risk averse regression tools had the objective of answering the needs of exploration geologists when dealing with multivariate systems. The method consisted in rationalising the information in Boolean logic [0, 1] format that was particularly suited for digital computers, and allowed the combination of evidence. Data were organised in bi-dimensional format such as raster tables or grids representing the spatial distribution of a certain geological indicator (e.g. the geochemical distribution of an element). Regression curves were then fitted to each

variable and combined with a linear regression model. In an alternative to these early models Tukey (1972) suggested the use of logistic functions to ensure a range of probability (π) constrained in the [0, 1] interval (a definition of probability is given in the forthcoming section). The logistic function can be expressed in a general form as follows (Sahoo and Pandalai, 1999):

$$logit\,(\pi)=\beta_0+\beta_1\,x_1+\beta_2\,x_2+\ldots+\beta_p\,x_p \tag{2.11}$$

π is expressed as the sum of contributions of different linear coefficients that can be represented by a linear vector $X_i = [x_1,\ x_{2\ldots}\ x_p]$. The coefficients β_p reflect the slopes of each variate except for β_0 which represents the intercept of the regression line. The equation can be arranged in exponential fashion as follows to obtain the cell probability:

$$\pi_i=\frac{e^{X_i'\beta}}{1-e^{X_i'\beta}} \tag{2.12}$$

Logistic regression, in contrast to kriging, makes use of multiple 'independent' variables rather than relying on different properties of the same variable (covariances) to provide estimates in the unknown region. Logistic equations of probability are also used in Weights of Evidence modelling. Favourability mapping methods (including Predictive

Neural Networks) are tools that find their root in Bayesian reasoning (e.g. Harris and Pan, 1999). They work as "trained networks" in which pairwise correlation (mineral deposits against other evidential themes) is used to adjust the weights (like the neural reinforcement of synapses), performing predictions where the correlations are verified.

As seen the progress brought firstly by analogue and then digital computers has contributed to a wide diversification of regression techniques. In part this has contributed to the development of relatively new ways to deal with geological problems. Computer simulation is certainly one of them. Among the diversification of mathematical models discussed so far computer simulation is one of the most actual, and represents in a certain way also a philosophical advance in the scientific approach.

2.2.4 Computer simulations

The use of simulation in the scientific sense has a fairly recent origin. It was firstly implemented in the 1940's by John von Neumann, who applied Monte Carlo Analysis in dealing with problems related to the shielding of nuclear reactors (Harbaugh and Bonham-Carter, 1970). The experimental approach in this case was rejected in favour of simulation because of the expenses and hazard involved. However, it is after the advent of digital computers in the 1950s that simulation, as it is conceived in modern applications, became relative common practise among economists, mathematicians and

later also among geologists. Perhaps one of the first geological applications is the work of

Briggs and Pollack (1967), a digital simulation of evaporite sedimentation that solved

partial differential equations by the Gauss-Seidel point iterative method on a high speed

digital computer. The mathematical model allowed plotting of fluid flow vectors and also

definition and graphic visualisation of spatial variability of salt concentrations across a

bi-dimensional reconstruction of an epeiric basin in Michigan. The example is also part

of an instructive chapter of 'Computer Simulation in Geology' (Harbaugh and Bonham-

Carter, 1970), a book considered at least a decade ahead of its time (Merriam, 2004). The

work of Brigs and Pollack (1967) concludes that statistical approaches are useless when

dealing with a well known system modelled efficiently by deterministic methods (in this

case dynamic simulation based on partial differential equations). However, laws of

generalisation such as the Laplace equation (see below) have limited applicability- they

work diligently only if the model is simplistic and integrable. In this context Nicolis

(1995) reports that since the 1950s, physicists begun to realise (at least from a

mathematical perspective) that most natural systems are non integrable, leading to

Hamiltonian chaos. The evidence of a limit in the deterministic approach is also

remarked in the problem of the particle/wave dualism of Heisenberg. Only adopting the

concept of statistical distributions of Schrödinger was it then possible to define in a

probabilistic manner the position and energy of an electron revolving around the nucleus

of an atom. Physical experiences suggest therefore that deterministic models are

somehow confined to a partial solution. Probably a hybrid methodology may be more appropriate (i.e. chaos theory).

To summarise, the reviewed history of least-squares methods and the diversification of mathematical approaches (Fig. 2.6a, b, c) to model natural systems illustrates that scientific methodology had few major revolutions. Among them of notable importance are the establishment of experimental science and the advent of computers. The mathematical models adopted in this thesis offer some practical perspectives of the advantages that such revolution has brought to the geological world. Both statistical and deterministic applications are presented, and also they explore how the computer can be of use to the geologist at present. The meaning of usability can be evinced from Krumbein (1962) who foresaw computers as machines that *store* data, *integrate* data but also *think* as geologists do.

In this thesis then axiomatic logic and computer applications are implemented at different spatiotemporal scales, to solve geological problems in a similar manner to our scientific ancestors although in a more privileged technological age.

THESE IMAGES HAVE BEEN REMOVED DUE TO
COPYRIGHT RESTRICTIONS

Fig. 2.6 Diversification of quantitative applications to geology in the 60s. (a) applications to the various geological sub disciplines; (b) time of entry of computer application in stratigraphy; (c) application of Markov models. Adapted from Krumbein (1969).

2.3 Mathematical models and computer software used in the

Lawn Hill Region

The work presented here focuses on three major types of mathematical models:

(1) Bayesian modelling adapted to a mineral exploration case; (2) Discrete Smooth

Interpolation approach used to model geological objects; (3) Fast Lagrangian Analysis of Continua used to model the coupling of fluid flow and deformation in 2D and 3D space. The first two models represent a derivation of regression analysis, whereas the third involves computer simulation. Even though the core chapters will address more specific aspects of the background of computational applications, here some general theory is considered.

2.3.1 Elements of probability

As seen computers not only can store and process a large amount of information (e.g. Hayes, 2002), they can also make inferences and provide predictive outputs. Statistical theories simulating human intellect are also used to make estimates of the uncertainty in risk analysis. Therefore AI (Artificial Intelligence) applications can be used more confidently in the making-decision process. This type of software is usually based on probabilistic laws composed of logical axioms (Agterberg, 1974; Haken, 2004). Elements of probability introduced here serves as basic theory for the more advanced treatment of Weights of Evidence modelling theory (Chapter 3).

2.3.1.1   Definition of probability

One way of looking at the meaning of probability is to consider the simple example of coin tossing, the simplest example of a chance mechanism corresponding to a binomial distribution [1, 0] (e.g. Bernoulli, 1954). The experiment involves tossing of a coin for a certain number of times representing the sampling of a population (a certain number of heads or tails is counted). When sufficient knowledge is available it can be concluded that there is a 50% probability to obtain one of the two states considered, $P = \frac{1}{2}$. If multiple averaging during coin tossing is performed (considering head as one and tails as zero) it is realised that the mathematical average progressively moves towards $P = \frac{1}{2}$, reflecting the likelihood ratio of the two possible states of equilibrium (*A, B*). A similar experiment can be undertaken using a dice, but in this case the number of possible states is 6, hence $P = \frac{1}{6}$.

A formal definition of probability is given: *The probability of an event is an abstraction of the idea of the relative frequency by which this event occurs in a sequence of trial measurements during a given experiment* (Agterberg, 1974).

Comparing the two examples some additional considerations can be drawn: the frequency of distribution is inversely proportional to the number of states of equilibrium (equal likelihood) allowed by the system (Haken, 2004). The two experiments show that

the probability function has a random, oscillatory behaviour although the fluctuation is always positive $(P \geq 0)$ for each defined set A of the sample population of countable values, defined as ω.

2.3.1.2   Addition and multiplication of probability

The experiments and considerations made suggest that the sum of the probabilities is always equal to one, $P(\omega) = 1$, provided that each set is independent from one another, $A \cap B = 0$. The generalisation of these axioms suggests that the probability of a certain number of states is equal to the sum of the probabilities of each independent state. To verify this rule, the dice example can be used to calculate the probability of obtaining an odd number, which is $P = \dfrac{1}{2}$. As seen each state $(A, B \ldots)$ has a probability $P = \dfrac{1}{6}$. Knowing that, it can be easily verified that the probability is function of the number of degrees of freedom (Haken, 2004, see also example presented in Fig. 2.7a).

$$P\left(A \cup B\right) = P(A) + P(B). \tag{2.13}$$

Another fundamental operation (especially in Bayesian modelling) is the multiplication of probabilities defined also as *joint probability*, a concept useful to

describe the interrelationship among the probability functions of multiple variables. The simplest case is a bi-variate situation with $P(X)$ and $P(Y)$, with X and Y considered as random stets of variables (x_i, y_j). To verify that

$$P\left(X=x_i,\, Y=y_j\right)=P\left(X=x_i\right)P\left(Y=y_j\right) \qquad\qquad (2.14)$$

an example of two layers of data in binary format is considered (Fig. 2.7b). Each layer is subdivided in a series of parallel rows and columns holding a random distribution of binary pixels. Each pixel can be white or black [0, 1]. The layers have equal size and also same number of rows and columns therefore they perfectly overlap. A finite number $(k+1)$ of possible combinations (x_i, y_j) can be defined as a function of the k-layers. Using a Boolean operator "AND" each overlapping couple of pixels is multiplied to obtain a new layer. To assess the probability of finding a black pixel for each layer it can be demonstrated that for instance $P\left(X=x_b\right)=\dfrac{x_b}{x_{tot}}$; this is true also for all the other layers. It can be therefore proved that the probability of a black pixel in the third layer $P\left(Z=z_b\right)=\dfrac{z_b}{z_{tot}}$ is equal to the multiplication operation $\left[P\left(X=x_b\right)P\left(Y=y_b\right)\right]$. In other words calculating the $P(Z)$ by counting the black pixels on the Z layer or multiplying the probabilities of the two layers (X,Y) gives the same result.

Sum of Probability

$P(Xn) = (1/9)$

$P(Xw) = nw/nt = (2/3)$

$P(Xb) = nb/nt = (1/3)$

$P(X) = P(Xw) + P(Xb) = 1$

Joint Probability

$P(n1) = (2/9)$

$P(n2) = (1/9)$

$P(n3) = (1/9)$

$P(n3) = Xb / Xt$

$P(n3) = P(n1, n2) = P(n1)*P(n2) = (1/9)$
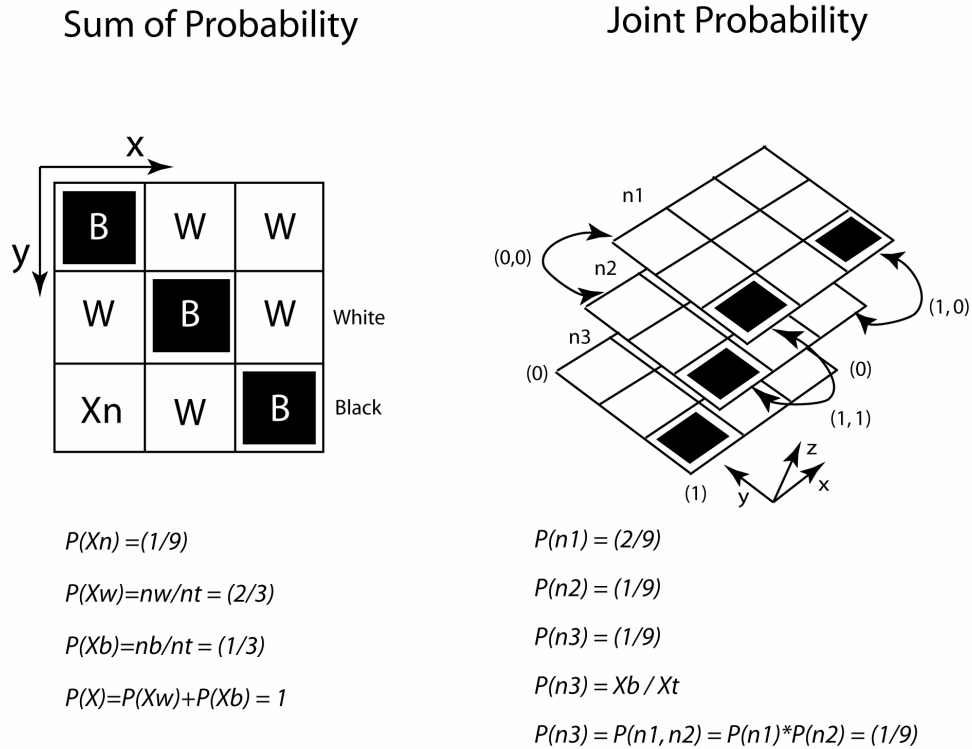
Fig. 2.7 Diagram presenting the concepts of addition and multiplication of probability (joint probability). (a) Nine cells model with black and white cells. Knowing that probability of each state is (1/9) it can be demonstrated that the sum of the probabilities for each individual state gives one. (b) Joint probability of multi-layer model considering the multiplication of two layers (n1, n2) giving n3 (see text for discussion).

2.3.1.3   Distribution, normal distribution and confidence interval

The probability distribution of a sample is a partial figure of the probability distribution of the population. To examine how the density of distribution varies it is convenient to explore a sampled population (ω) considering a number of well defined

subsets represented by equivalent intervals h_n of the random variable (X) as shown in the histogram of Fig. 2.8a. These subdivisions can also be considered as a series of probability intervals $P\left(h_k \leq X \leq h_{k+1}\right)$ because of the initial consideration. This axiom can be generalised for a subset A in the form:

$$P\left(X \in A\right) = \sum_{v_n \in A} P_n \tag{2.15}$$

where v_n are distinct values of the subset A belonging to $X(\omega)$ and P_n are their elementary probabilities $P\left(X = v_n\right)$ (Fig. 2.8b). An alternative approach to explore the density $P(X)$ variation for a discrete countable (ω) is also the definition of a cumulative probability function $F_X(X)$ (Fig. 2.8c) where the subset A simply represents and interval between $-\infty$ and x hence:

$$F_X\left(x\right) = P\left(X \leq x\right) = \sum_{v_n \leq x} P_n \tag{2.16}$$

The elementary probability (P_n) is clearly a discrete parameter in the histogram of Fig. 2.8a. However, it can be generalised to a piecewise continuous function $F_X(x)$ that is integrable in its interval of definition:

$$F_X(x) = \int_{-\infty}^{x} f(x)\, dx \tag{2.17}$$

The generalisation holds for a subset A leading to:

$$P(X \in A) = \int_A f(x)\, dx \tag{2.18}.$$
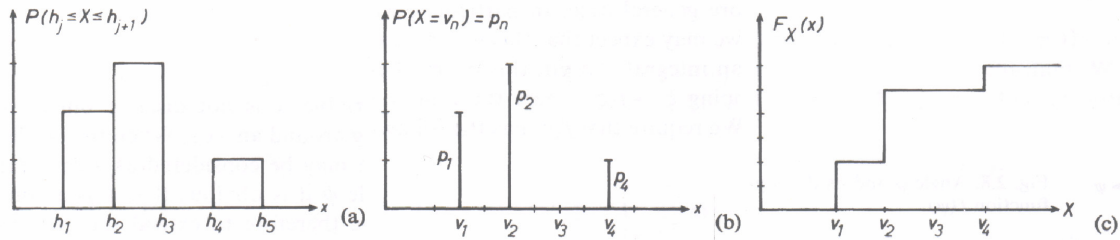
Fig. 2.8 Probability (P) of finding a set between h_j and h_j+1. (a) Histogram representing the distribution of samples. (b) Probability measure, the number of individuals v_i per each set A. (c) Distribution function $F_X(x)$ representing the cumulative proportions depending upon the number of sets considered (adapted from Haken, 2004).

The last two definitions (2.17, 2.18) suggest that a sampled population (ω) can be approximated by a mathematical function $f(x)$. One example that is the most common distribution type is the Gaussian normal distribution. Following Agterberg (1974) the probability distribution $f(x)$ and its cumulative function $F(x)$ can be defined as follows:

$$f(x) = \frac{1}{\sigma \sqrt{2\pi}} \exp \left\{ -\frac{1}{2} \left(\frac{x - \mu}{\sigma} \right)^2 \right\} \tag{2.19}$$

and

$$F(x) = \left(\frac{1}{\sigma \sqrt{2\pi}} \right) \int\limits_{-\infty}^{x} \exp \left\{ -\frac{1}{2} \left(\frac{x - \mu}{\sigma} \right)^2 \right\} dx \qquad (2.20)$$

where σ is the standard deviation from the mean (μ) and x is an ordinary variable of $f(x)$.

Commonly these equations can be simplified by defining a normal random variable z

equal to $\left(\frac{X - \mu}{\sigma} \right)$ with mean equal to zero and standard deviation of one. Then $f(z)$ and

$F(z)$ can be written as:

$$\phi(z) = \frac{1}{\sqrt{2\pi}} e^{-\frac{1}{2} z^2} \qquad (2.21)$$

and

$$\Phi(z) = \frac{1}{\sqrt{2\pi}} \int\limits_{-\infty}^{z} e^{-\frac{1}{2} z^2} dz \qquad (2.22)$$

This rescaling (2.21, 2.22) translates the population mean (μ) at zero and sets the inflection points of the Gaussian at σ (for a normal population). Combining equation (2.17) and (2.18), $P(X \leq z) = \Phi(z)$.

Choosing Z [-1, 1] an interval is defined in which a random sample X has $P(-1 < Z < 1) = \Phi(1) - \Phi(-1) = 0.841 - 0.159 = 0.682$,   considering   also   that $z = \left(\frac{X - \mu}{\sigma} \right)$ and rearranging $P(-\sigma + \mu < X < \sigma + \mu) = 0.682$. The solution suggests that there is a chance of 68% to sample within σ. The same formula can be extended to determine the probability to sample between 2σ or 3σ, respectively with a probability 0.954 and 0.997. Otherwise the use of a z value of 1.64 or 1.96 is widespread. Agterberg (1974) extends this approach suggesting that it is possible to use the concept of confidence interval to obtain a standard test (z-test of significance) for the measure of the normality of a population. To formulate the test it is necessary to follow three steps: (1) establish a null-hypothesis H_0; (2) define a significance limit and (3) compute the average $\bar{x}$ and compare it with the region of acceptance. The main distinction with the previous case is that a real population is sampled with mean (μ_0) that could be different or equal to the Gaussian mean (μ). The H_0 test proposes then to verify if $\mu_0 = \mu$, however commonly this condition is too restrictive. A range of acceptance firstly redefines the z value as:

$$z = \frac{\overline{x} - \mu}{\sigma \sqrt{n}}$$ (2.23).

In this case the average $\overline{x}$ is used because it is representative of the sampled real population. The relationship can be also expressed as modulus and a significance limit of 1.96, as follows:

$$|z| = \left| \frac{\overline{x} - \mu}{\sigma \sqrt{n}} \right| < 1.96$$ (2.24).

The condition (2.24) suggests that for large z, H_0 is rejected. Rearranging and considering that μ_0 may not be defined depending upon available sampling it is however possible to define a confidence interval for the average $\overline{x}$ with probability:

$$P\left(\overline{x} - 1.96 \frac{\sigma}{\sqrt{n}} < \mu < \overline{x} + 1.96 \frac{\sigma}{\sqrt{n}} \right) = 0.95$$ (2.25).

If the (2.25) is valid then the test is passed because the population has a mean value $\mu_0 \cong \mu$ and therefore approximates a normal distribution. However, with a level of significance $\alpha = 0.05$ there is still a 5% chance that the sample average will be rejected

because of the error limit considered. In other words firstly it is ensured that the sample resembles a normal distribution, but if the sample has several x_i that fall outside the error limit the hypothesis would be rejected even if the sample effectively relates to a normal population represented by a random variable X.

2.3.1.4   Mathematical expectation and variance

The two model parameters most commonly used in probabilistic approaches to estimation are the mean or "expected value" of the random variable and its variance (Isaaks and Srivastava, 1989). These are also defined as Moments, an integral form to express the mean and standard deviation of a piecewise continuous function. It is therefore convenient to start analysing the concept of expectation (mean) from a discrete perspective to then define it in integral form. It will be shown then how the standard deviation can be calculated, for similar reasons, from the mean.

Returning to the example of the dice, six states with equal probability of occurrence were observed. Performing the simple mathematical average $\overline{x}$ of a sample of several throws (n) of value v_i, this is given by:

$$\overline{x} = \frac{1}{n}\left(\sum_{i=1}^{n} v_i\right)$$ (2.26)

The probability of occurrence based on the total number of throws can be expressed as

$p_n = \dfrac{v_{in}}{n}$ where v_{in} is the number of outcomes for a certain state. Therefore, the mean can

also be expressed as the weighted average of the outcomes for each possible class

multiplied by the relative probability:

$$E(X) = \sum_n v_n \, p_n \tag{2.27}$$

where $E(X)$ is the expectation and v_n represents each possible class of outcomes (six for

the dice). The expectation can be evaluated also for continuous functions $f(x)$ of random

variables generalising as follows:

$$\mu_1 = EX = \int v f(v) \, dv \tag{2.28}$$

also defined as the first moment.

The second moment in contrast is used to define the variance (σ^2) of the mean of

a continuous function. The variance of a discrete random variable is expressed as:

$$\sigma^2 = \frac{1}{n} \sum_{i=n} \left(v_i - \bar{v} \right)^2 \qquad\qquad (2.29)$$

For similar reasons leading to (2.27) equation (2.29) can incorporate the elementary probabilities p_n as follows, however in this case it is convenient to refer to the definition of the moment about the mean (see Agterberg, 1974). The discrete equation follows:

$$\sigma^2 = \sum_n \left(v_n - \mu \right)^2 \times p_n \qquad\qquad (2.30)$$

In integral form for continuous functions the same considerations are valid and lead to:

$$\sigma^2 = \int \left(v - \mu \right)^2 f(v) \, dv \qquad\qquad (2.31)$$

Equation (2.30) can be imagined as a histogram with bins oscillating around a mean value weighted using the elementary probabilities.

2.3.2 GoCAD and the DSI algorithm

The mathematical models examined in this section are mostly used in geometrical modelling and were implemented to reconstruct regional and deposit scale 3D models of the Century deposit. To construct a 3D structural model of this mineralised body, the software package GoCAD was used. GoCAD is suited to model natural objects, whereas traditional CAD platforms are based on software engines that use polynomial algorithms (e.g. Bézier, 1974; Barnhill, 1985; Farin, 1988) created to answer the exigencies of industries that make manufactured objects. These two approaches are different in the sense that modelling geological objects has to respect the data imported during the preliminary phase of model construction. CAD applications have as a primary aim the creation of models with smooth and nice curves, surfaces, and volumes. As a consequence it is not easy to integrate geological datasets in common CAD software and the use of GoCAD becomes obvious. The software has been developed within a consortium which is widely open both to the industry and universities around the world. Several collaborative organisations (e.g. pmd*CRC - Predictive Mineral Discovery Cooperative Research Centre) are interested in the type of geomodelling proposed by GoCAD and want to use and/or contribute to the development of this new technology.

Mallet (2002) presents a comprehensive description of the mathematical algorithms behind GoCAD, in particular discussing the DSI (discrete smooth

interpolation algorithm) that represents the core of this application. Recently the software has become more a collection of several modules that allows import/export of a number of formats and also different types of interpolation functionalities. The GoCAD technology prefers to adopt a discrete method that is close to a "finite elements" approach, rather then use a parametric approach based on continuous polynomial functions. Discrete modelling methods are well known and represent an easier way to mathematically treat geological problems (Mallet, 2002).

2.3.2.1   Topology of an object

The topology represents the arrangement in which the nodes of a curve, surface or solid are connected to each other. Thus object topology can be described using a mathematical function of two variables $\xi(\Omega, N)$ where Ω is a set of nodes used to describe the object. Each node is identified by its rank order: $\Omega = \{1,2,\ldots., \alpha,\ldots.,M\}$. N is defined as an application from Ω into a subset of Ω such that

$$\{\beta \in N(\alpha)\} \quad \Leftrightarrow \quad \{\beta \text{ can be reached in at most } s(\alpha) \text{ steps from } \alpha\}.$$

This means that a generic node α is part of Ω and is surrounded by neighbours (β_n nodes),

and that the topological relationship existing between α and its neighbourhood can be

expressed as a function $N(\alpha)$, which is called neighbourhood operator (Fig. 2.9).

THIS IMAGE HAS BEEN REMOVED DUE TO
COPYRIGHT RESTRICTIONS

Fig. 2.9 Neighbourhood diagram $N(\alpha)$ from Mallet (2002), representing a discrete domain of a point in space with a central point (α) surrounded by a series of points (β) representing a local subset interconnected by a polygonal mesh. This set represents the minimum scale at which the DSI interpolation operates $s(\alpha) = 1$.

The notion of a discrete topological model can be used to approximate the topology of

any geological object. Some examples are: (1) *geological horizon* or fault (surface) as a

set of adjacent triangles; (2) *geological body* (solid) as a set of adjacent tetrahedrons; (3)

geological cross-section (curve) as a set of adjacent segments; (4) *geological layer*

(solid) as a regular curvilinear or rectilinear grid. The vertices of the triangles are equal to

the nodes of $\xi(\Omega, N)$, while the edges partly define the topology of these objects (Fig. 2.10).

THESE IMAGES HAVE BEEN REMOVED DUE TO COPYRIGHT RESTRICTIONS

Fig. 2.10 Examples of objects approximated by a discrete model. (a) Triangulated surface; (b) Tetrahedral solid filling a geological horizon; (c) Polygonal curves; (d) Faulted curvilinear grid (adapted from Mallet, 2002).

2.3.2.2   Concept of discrete model

The notion of a topological discrete model has to be further extended, because a discrete topological model does not take into account the properties of the represented geological objects and the possible constraints that might be applied to them. Hence, the

function $\xi(\Omega, N)$ has to be included in a generic function $M^n(\Omega, N, \varphi, C)$ where φ is a set of functions $\varphi(\alpha)$:

$$\varphi(\alpha) = \{\varphi^1(\alpha), \ldots, \varphi^v(\alpha), \ldots, \varphi^n(\alpha)\} \qquad \forall \ \alpha \in \Omega \qquad (2.32)$$

$\varphi(\alpha)$ represents a series of properties of an object node α. For example, the spatial location of a node is defined from the following components of $\varphi(\alpha)$:

$$\{ \varphi^x(\alpha), \varphi^y(\alpha), \varphi^z(\alpha) \} \qquad (2.33).$$

C is a set of constraints that can be split into three subsets:

$$C = C^{\widetilde{=}} \cup C^{=} \cup C^{>}; \qquad (2.34),$$

where $C^{\widetilde{=}}$ is the set of "soft" equality constraints that have to be honoured in a least square sense, $C^{=}$ is the set of "hard" equality constraints that have to be strictly honoured, and $C^{>}$ is the set of "hard" inequality constraints that have to be strictly honoured.

These subset functions represent three ways to impose a property $\varphi^v(\alpha)$ on an object and as a consequence these subsets have different control (e.g. on its topology). Constraints and properties, as seen below, are expressed by similar mathematical expressions. Applying a constraint to a generic model and subsequent interpolation usually forces the properties to adapt to the constraint. A simple example of constraint can be envisaged as a set of control points that are used to define the topology of a surface. Using the GoCAD GUI (Graphic User Interface) functionalities it is possible to fit a surface to the selected control points using them as a *control point* constraint.

2.3.2.3   Discrete Smooth Interpolation approach

The Discrete Smooth Interpolation method (DSI) has been designed specifically for interpolating the function φ of a discrete model $M^n(\Omega, N, \varphi, C)$, while respecting all the constraints $c \in C$. Here, only soft constraints $c \in C^{\cong}$ and a subset C^L of $C^=$ are implemented to give an easier introduction to this mathematical formulation. A scalar continuous function φ defined within the segment $\overline{\Omega} = [1, M]$ and letting Ω be the set of nodes corresponding to the regular sampling of $\overline{\Omega}$ with a step equal to 1: $\Omega = \{1, 2,...., \alpha,...., M\}$. In Fig. 2.11 the nodes $\alpha \in \Omega$ correspond to the white points, while the black points correspond to some given data points $\{l, \varphi(l) : l \in L\}$ to be interpolated and associated

with a given subset L of Ω. For this purpose, a classic method (Farin, 1988) consists in looking for a spline function φ, minimising the "global roughness" $\check{R}(\varphi)$ such that:

$$\breve{R}(\varphi) = \int_{\Omega} \mu(x) \cdot \breve{R}(\varphi|x)\, dx \qquad (2.36),$$

$$\text{with: } \breve{R}(\varphi|x) = \left| \frac{d^2\varphi}{dx^2} \right|^2 \qquad (2.37).$$

In this expression, $\mu(x) > 0$ is a given "stiffness" function (that can be taken constant and equal to 1), while $\breve{R}(\varphi|x)$ can be considered a measure of the "local roughness" of φ at each point $x \in \Omega$ considering that:

$$\overline{\varphi}(x) = \frac{\varphi(x-1) + \varphi(x+1)}{2} \qquad (2.38).$$

Then, as suggested in Fig. 2.11, it can be verified that a finite-difference approximation

of $\left| \dfrac{d^2\varphi}{dx^2} \right|$ is such that:

$$\left| \frac{d^2\varphi}{dx^2} \right| \approx 2 \cdot \left\{ \overline{\varphi}(x) - \varphi(x) \right\} = \left\{ 1 \cdot \varphi(x-1) + 1 \cdot \varphi(x+1) \right\} - 2\varphi(x) \tag{2.39}.$$

The next section on numerical simulation gives an explanation of how finite-difference

approximation works.
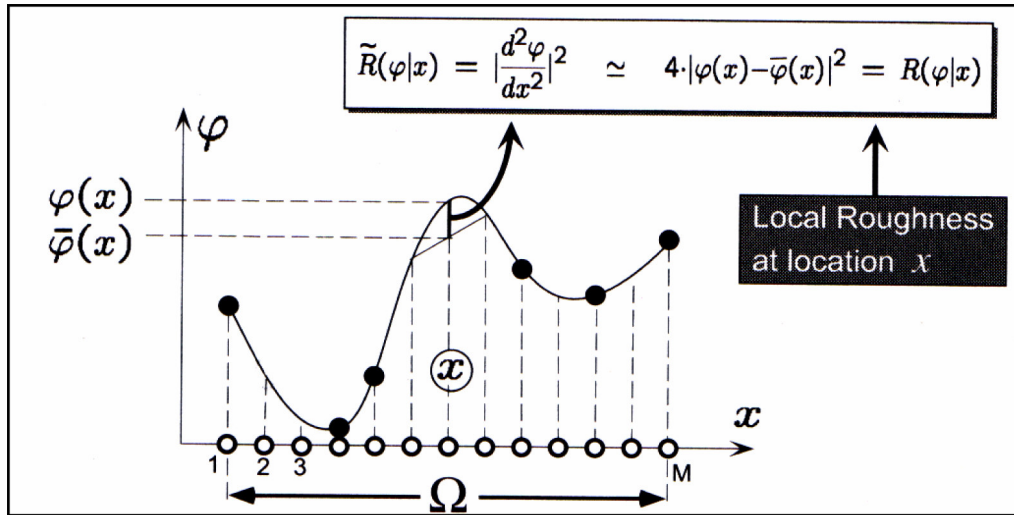
Fig. 2.11 Finite difference approximation using a spline function $\varphi(x)$ and relative local roughness/function $\tilde{R}(\varphi|x)$ representing the residual of $\overline{\varphi}(x)$ defined in a finite interval $\Omega[1, M]$. The objective of using a local roughness criterion is to minimise its value therefore reducing the residuals, similarly to the least square method, to obtain a better fit (adapted from Mallet, 2002).

If φ is a continuous periodic function with period equal to Ω the above approximation can be considered valid. Hence it follows that

$$\breve{R}\left(\varphi|x\right) \approx \left|\sum_{\beta \in N(\alpha)} v\left(\alpha,\beta\right)\cdot \varphi\left(\beta\right)\right|^{2} \tag{2.40},$$

where $v(\alpha, \beta)$ represents an arbitrary coefficient used to weight the magnitude of the variation of each component $\varphi^{v}(\alpha)$ of $\varphi(\alpha)$. For a detailed description on how to set the weighting coefficients refer to Mallet (2002) - here there is more concern with the result of this approximation. Thus defining $R(\varphi)$ as an approximation of $\breve{R}(\varphi)$ (global roughness), and

$$R(\varphi) = \sum_{\alpha \in \Omega} \mu\left(\alpha\right)\cdot R\left(\varphi|\alpha\right) \tag{2.41}$$

with:

$$R\left(\varphi|\alpha\right) = \left|\sum_{\beta \in N(\alpha)} v\left(\alpha,\beta\right)\cdot \varphi\left(\beta\right)\right|^{2} \tag{2.42},$$

it can be concluded that $\breve{R}(\varphi) \approx R(\varphi)$. Minimising $\breve{R}(\varphi)$ or $R(\varphi)$ therefore holds approximately equivalent results (Mallet, 1989; Mallet, 2000; Mallet, 2002).

2.3.2.4   Discrete Smooth Interpolation algorithm

A discrete model $M^I(\Omega, N, \varphi, C)$ is considered here. In this case, φ has only one component, thus no distinction will be made between φ and φ^1. L and H are also considered as two complementary subsets of Ω such that (1) L = set of nodes $l \in \Omega$ where $\varphi(l)$ is known and represents a constraint; (2) H = set of nodes $h \in \Omega$ where $\varphi(h)$ is unknown. The set L is called the set of "Control-Nodes" and is associated with a particular subset C^L of the set of hard constraints $C^=$. The aim is to compute the values $\{\varphi(h): h \in H\}$ in such a way that the resulting function φ is "as smooth as possible" on $\xi(\Omega, N)$. The "control values" $\{\varphi(l): l \in L\}$ should be strictly honoured, and each of the constraints $c \in C^\cong$ should be respected as much as possible. For this purpose, it is necessary to quantify the local roughness $R(\varphi|\alpha)$ of φ in the neighbourhood of each node $\alpha \in \Omega$ and evaluate the degree of violation $\rho(\varphi|c)$ of each constraint $c \in C^\cong$ by φ as follows:

$$R(\varphi : \alpha) = \left| \sum_{\beta \in N(\alpha)} v(\alpha,\beta) \cdot \varphi(\beta) \right|^2 \tag{2.43},$$

$$R(\varphi : c) = \left| \sum_{\alpha \in \Omega} A_c(\alpha) \cdot \varphi(\alpha) - b_c \right|^2 \tag{2.44},$$

where A_c and b_c are coefficients that define the type of constraint depending on their value (soft, hard).

The function φ must be chosen to minimise $R^*(\varphi)$, the "general roughness" criterion:

$$R^*(\varphi) = \sum_{\alpha \in \Omega} \mu(\alpha) \cdot R(\varphi|\alpha) + (\phi \cdot \overline{\omega}) \sum_{c \in C^=} \overline{\omega}_c \cdot \rho(\varphi|c) \tag{2.45}.$$

Equation (2.45) combines on its right side the local roughness and violation functions, but also considers the stiffness function $\mu(\alpha) > 0$ which modulates the importance of the local roughness $R(\varphi|\alpha)$ at node (α). $\overline{\omega}_c$ is a term that controls the relative weights of different constraints whereas $(\phi \cdot \overline{\omega})$ is used to define a balance between the two sets of functions:

$$\sum_{\alpha \in \Omega} \mu\left(\alpha\right) \cdot R\left(\varphi|\alpha\right) \ \ \text{and} \ \ \sum_{c \in C^{=}} \overline{\omega}_c \cdot \rho\left(\varphi|\, c\right) \tag{2.46}.$$

From the mathematical formulation of Mallet (2002) we can conclude that the DSI approach treats complex problems as a discrete subset of simpler linear problems. Thus a degree of simplification is induced in the first part of this method (discretization), whereas in a secondary step a "minimum energy" principle is applied, aiming to reduce the "global roughness", which can be seen as the difference between the applied constraints and the unconstrained functions that represent the properties of an object. The use of constraints during the modelling phases of the Century deposit represented an excellent tool to define an accurate shape for horizons and faults and interpolate the grades on both two-dimensional and three-dimensional grid based models.

2.3.3 FLAC (Fast Lagrangian Analysis of Continua)

This section briefly introduces the core algorithms behind the explicit Lagrangian formulation adopted in FLAC, a program designed to run geomechanical simulations that was firstly developed by Peter Cundall in 1986 (Itasca, 2003, and further enhanced by CSIRO Exploration and Mining) to handle a wider range of geological problems including application to mineral deposit exploration. The software was used in this thesis

to model coupled deformation and fluid flow within 2D-3D geological scenarios that resemble the Century mineral system.

2.3.3.1   General description of FLAC

FLAC simulates behaviours of geological materials that undergo plastic flow during yield and it has been applied in many geological situations (Ord, 1991b, a; Ord and Oliver, 1997; Oliver et al., 1999; 2001; Ord et al., 2002; McLellan et al., 2004; Miller and Wilson, 2004; Oliver et al., 2006). Materials are represented by polyhedral elements within a two- or three-dimensional grid that can be adjusted by the user to fit the shape of the geological bodies to be modelled. Two versions of the software were utilised to perform numerical simulations both in 2D and 3D. The simulated materials can yield and flow leading to permanent deformation of the grid. Two numerical approaches represent the basis of the FLAC environment: (1) the explicit, Lagrangian calculation scheme and (2) the mixed-discretization zoning technique (Itasca, 2003). These mathematical models are used to ensure that plastic collapse and flow are modelled accurately. They also require less computational effort compared to FEM (Finite Element Models) because they avoid utilization of a large stiffness matrix to reach a final stable solution (Itasca, 2003). Additionally problems such as small time-step limitation and dumping (e.g. dissipation of kinetic oscillatory energy) are handled respectively by inertia scaling and automatic

damping functions (Itasca, 2003). In addition to the core algorithms based on the use of finite-difference approximation, which is perhaps one of the oldest numerical techniques used for the solution of sets of differential equations (given initial values and/or boundary values; Desai and Christian 1977), the software offers ten different constitutive models to simulate mechanical deformation of various materials:

(a) the "null" model;

(b) three elasticity models (isotropic, transversely isotropic and orthotropic elasticity); and

(c) six plasticity models (Drucker-Prager, Mohr-Coulomb, strain hardening/softening, ubiquitous-joint, bilinear strain hardening/softening ubiquitous-joint, and modified Cam-clay).

Each zone in a FLAC grid may have a different material model or property and also gradients or statistical distributions can be specified as well. Additional anisotropies can be introduced such as interfaces or slip-planes between two ore more portions of the grid to simulate for example a fault/fracture or other parallel bedding anisotropies. FLAC also incorporates the facility to model confined fluid flow and pore-pressure dissipation, and the full coupling between deformable porous solid and a viscous fluid flowing within the pore space. The fluid is assumed to obey the isotropic form of the Darcy's law. Both

fluids and grains in the porous solid are deformable. All zones in a model are assumed to be fully saturated; therefore it is not possible to simulate phreatic surfaces in FLAC.

2.3.3.2   Basics of the finite-difference method to solve differential equations

To briefly illustrate the fundaments of finite-difference approximation methods, reference is made to the book of Harbaugh and Bonham-Carter (1970). The book was written from a geologist's perspective therefore its simple and applied approach to basic mathematical concepts such as differential computation, represents an attractive way to understand the finite difference method in a general manner. Finite difference is used, for instance in FLAC, to obtain solutions of partial differential equations relative to motion and also to solve the constitutive laws (discussed in more detail below) both in a spatial and temporal scenario. The approach is also appealing for computer based implementation, because although the finite-difference approximation is a relatively simple method, it requires an elevated number of calculations (on the order of thousands if not millions).

Considering a simple example of an algebraic equation such as:

$$3x + 4 = 0 \tag{2.47}$$

The equation can be solved by manipulation obtaining $x = -\dfrac{4}{3}$. This example

shows then that some equations can be easily solved without the need of any particular

method, but this approach fails in other cases. Harbaugh and Bonham-Carter (1970)

suggest for example that the only way to solve the equation that describes the wave

motion from deep to shallow water settings in a sedimentary basin, is to use an iterative

approach. The equation is the following:

$$l = L \tanh\left(\frac{2\pi h}{l}\right) \tag{2.48},$$

where l and L are the wavelengths respectively at shallow and deeper depths and h

is the water depth. Equation (2.48) cannot be solved with algebraic manipulation because

of the occurrence of the term (l) on both sides. However, rewriting the equation in this

form, introducing a new l_0 term:

$$l = L \tanh\left(\frac{2\pi h}{l_0}\right) \tag{2.49}$$

allows exploration in an experimental way of the field of solutions for l considering an

array of l_0 values that are selected trying to reach the condition $l = l_0$. Unfortunately this

approach is cumbersome when the field of solutions is characterised by multiple maximum values where $l=l_0$, because the equation may be satisfied by more than a single combination of independent variables. In this regard a number of mathematical approaches can be adopted to solve the problem, e.g. integration where possible or the finite-difference approximation examined here, or even more advanced tools such as genetic search based algorithms that look for the "fittest solution" in a search space (see Coley, 1999).

A differential equation can be ordinary or partial, depending on the number of variables and their relative derivatives. The order of a differential equation is defined by highest exponential derivation; here first and second order linear ordinary and partial differential equations are considered, as they are sufficient to introduce how the FLAC finite-difference approximation works.

Considering a simple example of ordinary differential equation of the first order:

$$\frac{dN}{dT} = rN \qquad\qquad\qquad (2.50)$$

it is instructive to note that the relationship considers a first order derivative in time (T) of N individuals in a generic population, which is equal to N individuals multiplied by a

constant of proportionality (r). The relationship can be easily solved with integration as follows:

$$\int \frac{1}{N}\, dN = r \int dT$$ (2.51).

Then solving algebraically the integration it is obtained: $\ln(N) = rT$. This equation can be also written for an interval of time [0, T] as follows:

$$N_t = N_o\, e^{rT}$$ (2.52),

where N_0 is an initial value for the population and N_t represents its growth at time (t). Graphically this relationship is represented by an exponential curve as illustrated in Fig. 2.12. As already mentioned it is not always possible to solve an equation using algebraic approaches therefore here the same example can be alternatively solved using the finite-different quotient approximation (Nystrom's method).
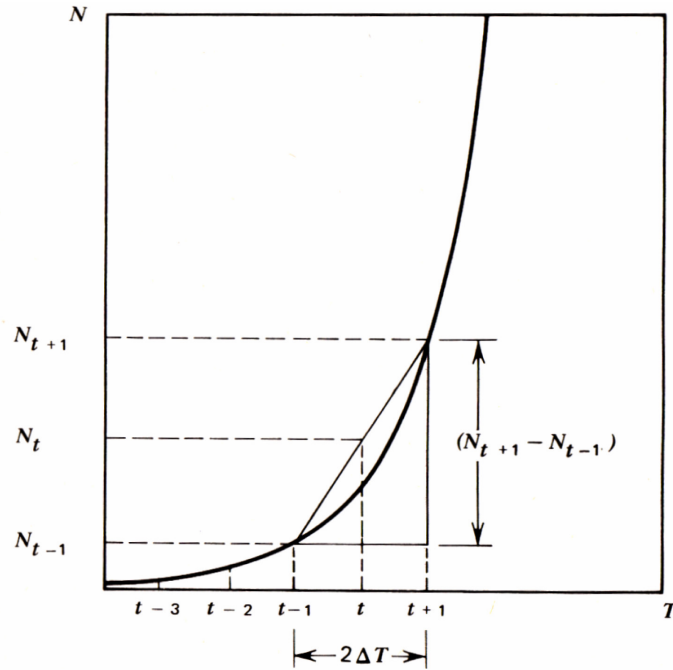
Fig. 2.12 Example of an exponential curve and relative intervals of discretization Δt illustrating the growth of a generic population (N). The growth value for an instantaneous time (t) can be estimated using the finite-difference quotient approximation (Nt+1-Nt-1)/2Δt. Adapted from Harbaugh and Bonham-Carter (1970).

The numerical solution of a differential equation can be obtained then transforming continuous derivatives into finite-difference quotients, hence:

$$\frac{dN}{dT} \cong \frac{\Delta N}{\Delta T}$$ (2.53).

This approximation improves for smaller finite-difference intervals of approximation ($\Delta T \rightarrow 0$). In this regard this concept can be clarified selecting a mid point (*t*) (see Fig. 2.12) which seats at *t+1* and *t-1* from two extremes at ΔT giving:

$$\frac{dN}{dT} = \frac{N_{t+1} - N_{t-1}}{2\Delta T}$$ (2.54).

Combining with (2.50) removes the differential term to provide an analytical solution to the differential equation of this type:

$$\frac{N_{t+1} - N_{t-1}}{2\Delta T} = rN_t$$ (2.55).

This can be also rearranged as follows:

$$N_{t+1} = 2\Delta T r N_t + N_{t-1}$$ (2.56).

Provided that an r = 0.5 is selected and also that ΔT = 1, this relationship can be further reduced to:

$$N_{t+1} = N_t + N_{t-1}$$ (2.57).

It is then possible to compute a point of intersection of the function knowing two points

at ΔT allowing then the construction of an approximate curve. If $\Delta T \mapsto 0$ the

approximation will be more accurate, because the guessed extreme, using (2.57), will be

closer to the known intersecting points. By analogy the same approximation holds if the

derivation describes the rapidity of variation of a space variable. Therefore for first- and

second-order derivations in bi-dimensional space (x, y) it is possible to write the

following formulas of approximation:

$$\left(\frac{dy}{dx}\right)_j \cong \frac{1}{2\Delta x}\left(y_{j+1} - y_{j-1}\right); \tag{2.58}$$

$$\left(\frac{d^2 y}{dx^2}\right)_j \cong \frac{1}{2\Delta x}\left(y_{j+1} - 2y_j + y_{j-1}\right); \tag{2.59}$$

where j represents a generic point on the curve. Once the finite-difference quotients have

been calculated, as seen, a number of linear equations can be compiled to represent the

field of solutions needed to describe the spatial variation of x and y. The coefficients

$y(x)$ will be obtained throughout an iterative process (e.g. Gauss-Seidel). However, the

field of solutions depends also on the boundary values assigned, guessed before starting

the iteration. These values remain constant and are not updated during the progressive

steps of iteration.

The finite-difference approach can be extended to more than a single variable

introducing multiple derivations (partial derivatives) of a variable in respect of others,

generalising then to a surface-based or volume-based space. Two examples of partial

differential equations are given:

$$\frac{\partial^2 z}{\partial x^2} + \frac{\partial^2 z}{dy^2} = 0; \tag{2.60},$$

$$\frac{\partial^2 \Phi}{\partial x^2} + \frac{\partial^2 \Phi}{dy^2} + \frac{\partial^2 \Phi}{dz^2} = 0; \tag{2.61}.$$

Equation (2.60) describes the spatial variation of a surface $z = f(x,y)$ in three-

dimensional space, whereas (2.61) represents the Laplace equation that define the spatial

variation of a generic function Φ in three-dimensional space $\Phi = f(x, y, z)$. The two

examples are illustrated in Fig. 2.13a, b, c and d. To represent this type of function in a

discrete manner, it is usually convenient to construct squared meshes projected in three-

dimensional space or cubic voxels in the case of (2.61). The solution of the differential

equations can be obtained in a similar manner replacing the partial differential terms with relative finite-difference approximation terms as follows:

$$\frac{1}{\Delta x^2}\left(z_{i,j+1} - 2z_{i,j} + z_{i,j-1}\right) + \frac{1}{\Delta y^2}\left(z_{i+1,j} - 2z_{i,j} + z_{i-1,j}\right) = 0 \qquad (2.62),$$

and for the Laplace equation considering $\Delta x = \Delta y = \Delta z$ leads to the following:

$$\frac{1}{\Delta x^2}\left(\Phi_{i,j-1,k} + \Phi_{i,j+1,k} + \Phi_{i-1,j,k} + \Phi_{i+1,j,k} + \Phi_{i,j,k-1} + \Phi_{i,j,k+1} - 6\Phi_{i,j,k}\right) = 0 \qquad (2.63),$$

the indexes [i, j, k] represent the direction in which the function Φ is approximated (see Fig. 2.13b, d). The (2.62, 2.63) can be used to derive a value of the functions z or Φ on a surface or in a volume represented by a finite number of cells identified by [i, j, k].

Similarly to the example of ordinary differential equations the search of the solution space is performed with an iterative approach. But this time the number of boundary values is represented by a neighbourhood of cells surrounding the space in which the search for a solution is required. Several solutions are possible suggesting that the constraint applied to the system of linear equations causes an internal adjustment of the solutions that depends not exclusively from the equations themselves (e.g. boundary values dependency). Beside these conditions that are functions of scale and location, the

computer based method works for all the classes of differential equations considered. Most of the differential equation can be therefore discretised using a finite-difference approach.
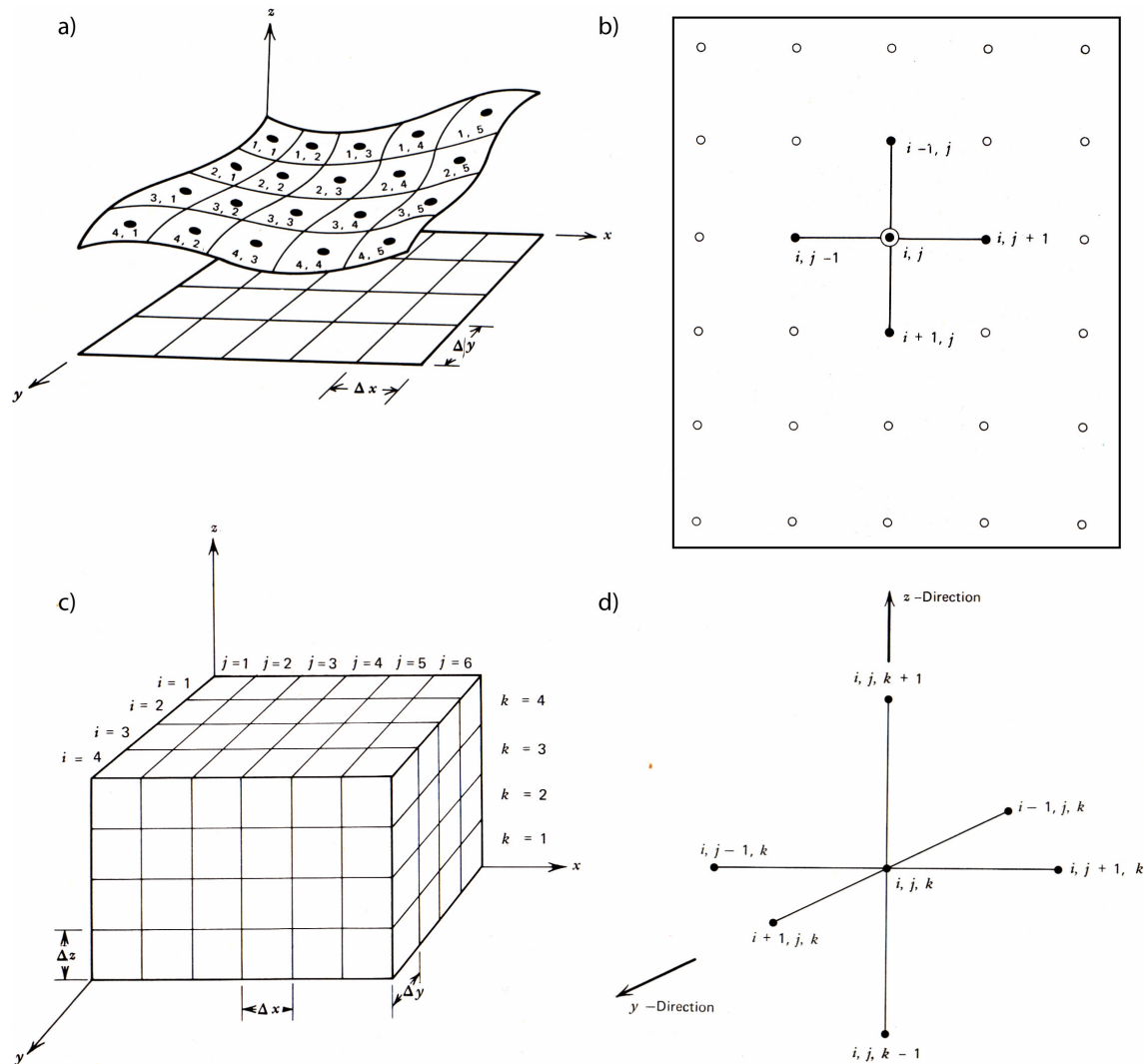
Fig. 2.13 Summary of two- and three-dimensional grids used to discretise the geological continuum. (a) Representation of a continuous function $f(x, y)$ in z with relative indexing used to refer to individual cells defined by intervals $\Delta x, \Delta y$ (b) Four point star method of indexing points implemented for the solution of

partial differential equations of type z = *f*(*x, y*). The star is moved iteratively to adjust the solution from node to node. Usually the partial differential equation is solved alternatively for the variables (*x, y*). (c) Three-dimensional meshwork and relative indexing [*i, j, k*]. (d) Six point star model adopted to solve partial differential equations representing the spatial variation of a generic property Φ as function of (*x, y, z*) coordinates. The finite-difference approximation method is equivalent to the four star model although the star is moved in 3D space. Adapted from Harbaugh and Bonham-Carter (1970).

2.3.3.3   The Lagrangian description

Finite-difference approximations simulating plastic deformation and fluid flow with the aid of a computer represent a reasonable way to handle continuum problems (e.g. using FLAC). This numerical simulation software is composed of different classes of differential equations that deal with specific tasks. For example, FLAC handles the spatial and temporal arrangement of tetrahedrons composing the chosen FLAC-grid during deformation, but also it computes the variation of their spatial organisation as a function of the constitutive relationships and assigned boundary conditions, commonly specified in the numerical model before attempting any kind of simulation. Finite-difference approximation is then used several times to discretise the continuum, both in space and time.

A description of the various classes of equations and their meaning thus follows. In Appendix A the "nodal formulation" is also reviewed for the Newtonian stress/strain relationships considered during deformation of a tetrahedral grid in FLAC (nodal means to reduce the equations to the individual nodes of each tetrahedron composing the FLAC

grid). The equations relative to the Mohr-Coulomb constitutive model and the fluid flow module are also discussed in the end.

2.3.3.3.1 *FLAC configuration (explicit finite difference model)*

The mathematical background required to understand the following discussion concerns elements of continuum mechanics. For a deeper understanding of some of the concepts presented the reader is referred to Coman (2004). This section outlines how the partial differential equations and mechanical models are organised in the FLAC environment. The structure of the FLAC program is explored looking at the different algorithms.

The Lagrangian dynamic picture of a continuum is the general model adopted in FLAC to describe a body of rock or other materials. The Lagrangian vision is more advanced than classical Newtonian mechanics although preserving the conservation of energy principles. In contrast to Newtonian laws the Lagrangian formulation describes the movement (deformation, fluid flow etc.) of a global system (e.g. a body of fluid or rock) aiming therefore at a generalisation of Newtonian laws to systems composed of multiple particles. (or grid nodes).

2.3.3.3.2 *Lagrangian and Eulerian representations (inertial systems)*

The Lagrangian description is however not the only formulation available to describe the body motion. The Eulerian description can be also used to account for the spatio/temporal variability of a scalar, vectorial or tensorial field in an even more global manner. This mathematical model differs from the Lagrangian because the same physical laws are constructed upon a different reference system that considers the position of the infinitesimal elements of volume in space. For example, the Lagrangian material description of the body motion (e.g. movement of a rock in space, or a time-dependent flow) is represented at a given position by a particle moving in space and time with velocity $\vec{v}_p(t)$ although no information is given of its position (see Stuart and Tabor, 1990), whereas in the Eulerian space a full description of all the positions of the particles is described $\vec{v}_p(\vec{x}, t)$. In other words if a Lagrangian particle moving in space has no certain information of the sort of velocity it will be assuming at a later position (local information only), when computing a partial derivation in time it is also necessary to know its spatial gradient $v_{p,p}$. Eulerian particles will assume an expected value represented by the measure of the spatial field, therefore the velocity is already known in space requiring only an ordinary derivation in time $\left(\dfrac{dv}{dt}\right)$ (see Barr, 2001). Note that the Einstein summation of indexes is used. This is a simple omission of the symbol $\sum$ when

dealing with indexes that sum over one another. For example a vector can be described

with three components $\left\{u_1\vec{e}_1, u_2\vec{e}_2, u_3\vec{e}_3\right\}$ such as $\vec{u} = \sum_{i=1}^{3} u_i\,e_i$ that becomes elegantly

simplified as $\vec{u} = u_i\,\vec{e}_i$. Note also that in continuum mechanics an index preceded by a

comma $\left(\sigma_{ij},_j\right)$ indicates a partial derivation in space of the variable, giving then in

more extended form:

$$\sigma_{ij},_j = \frac{\partial \sigma_{i,j}}{\partial x_j}$$ (2.64).

2.3.3.3.3 *Cauchy traction tensor and constitutive equations*

Equation 2.64 represents the spatial variation of a tensorial field. Here, vectors are

distinguished from tensors because a vector is sufficiently represented by three

components, whereas six components are necessary to define a tensor. Both objects share

an important property which is defined as the *invariance*. An invariant is independent of

its reference system. This is a really important point in relativistic theory because the

Newtonian Laws are essentially dependent on the considered inertial systems. Relativistic

adopting such invariant systems had a more generalized applicability (e.g. Einstein,

1934). Beside the importance in physics the Cauchy's formulae are implemented in

FLAC to define the state of stress and strain of a body. FLAC uses a finite element grid that is composed of tetrahedrons and it will be often necessary to refer to them. Moreover the material points representing the Lagrangian description correspond to the nodes of the tetrahedron subjected to deformation. When a stress is applied to tetrahedrons, these react accumulating stress and rearranging dynamically their shape, thus simulating a state of strain. To characterize this system it is useful then to define a traction vector $\vec{t}$ as follows:

$$t_i = \sigma_{ij} \, n_j \tag{2.65}.$$

In equation 2.65 the traction is equal to the stress tensor component (σ_{ij}) parallel to the normal (n_j) to each face of the tetrahedron. The distribution of tensions will then control the distribution of stresses in the elements of a whole body. Adding the time dimension leads to deformation as a function of stress- and relative strain-rate. These are quantities representing the ratio between the deformations within a finite interval of time. In particular, the strain-rate in a nodal formulation (Appendix A) can be described by the relative velocities of movement of the nodes of a tetrahedron in FLAC. Two components can be defined for the strain-rate, translational (ξ_{ij}) and rotational (ω_{ij}):

$$\xi_{ij} = \frac{1}{2}\left(v_{i,j} + v_{j,i}\right)$$
(2.66),

$$\omega_{ij} = \frac{1}{2}\left(v_{i,j} - v_{j,i}\right)$$
(2.67),

with vectorial components of velocity (v_i, v_j) derived respectively in x_j and x_i.

In addition to the basic concepts of stress and strain FLAC also considers two sets of equations in its representation of the plastic deformation: (1) the equations of motion and equilibrium; and (2) the constitutive relationships. The motion of a body is fully described in continuum mechanics with the conservation of momentum relationships (linear, angular and inertial terms of momentum are combined in the Cauchy 's equations of motion). In this regard the formulation in FLAC could be expressed as follows:

$$\sigma_{ij,j} + \rho b_i = \rho \, \frac{dv_i}{dt}$$
(2.68).

Equation 2.68 relates the partial differentiation of the stress tensor (σ_{ij}) to the body force (b_i), which is essentially a field force (e.g. the magnetic and gravitational fields that act indirectly on a body). In contrast, the stress tensor can be considered a contact force. For a unitary mass the action of body and contact forces result in a material derivation in time

of the velocity (an acceleration term). This multiplied by the density (ρ) becomes equivalent to a force. When forces equilibrate the material acceleration is zero.

The equations of motion and the rate of rotational and translational stress and strain can be reduced to a system of 9 linear equations in 15 unknowns therefore requiring the use of six additional equations to solve the deformation of a body. These are the constitutive relationships that are experimental laws for the materials considered in the numerical model (see Appendix A where the Mohr-Coulomb constitutive model is reviewed). The constitutive formulation aims at guessing the state of stress of a certain material in an interval of time in which the material velocities are considered constant inside a tetrahedron. This allows using the rate of strain as a measure of the co-rotational stress-rate tensor $\left[\breve{\sigma}\right]_{ij}$. The constitutive equations can be expressed then in a general form as functions (H) of the stress and strain tensors (σ_{ij}, ξ_{ij}) and also of the loading history considered (k):

$$\left[\breve{\sigma}\right]_{ij} = H_{ij}\left(\sigma_{ij}, \xi_{i,j}, k\right) \tag{2.69}.$$

Such functional relationship represents a constraint for the co-rotational stress-rate tensor that controls the nodal velocities within the model. For a more detailed discussion of the mathematical background behind FLAC refer to Appendix A.

What follows after this introductive section is a series of self-contained chapters intended for individual publications. They are ordered according to the scale of the data sets utilized, from regional scale targeting of mineral deposits through to deposit scale models used to address ore genesis, to even more complex scenarios involving the development of the Lawn Hill Megabreccia.

The flow of the thesis as introduced in Chapter 1 will provide the reader with tangible examples of the different quantitative models discussed. In the end (Chapter 6) this leads to an example of integration of qualitative and quantitative modelling showing that observational science is still important in complex geological problems, in order to obtain an appropriate conceptual model. It is also essential to validate the quantitative analysis.

Most of the thesis focuses on linear techniques to address the geological issues concerning the various studies. A non-linear alternative is also proposed to suggest that more refined mathematical approaches may better describe the deterministic and random components of a system. Chapter 7 proposes an application of these concepts to Pb-Zn mineral systems.

Chapter 3

Predictive modelling of prospectivity for Pb-Zn deposits in the Lawn Hill Region, Queensland, Australia

Acknowledgement of Contributions

N.H.S. Oliver – normal supervisory contributions

Abstract

Different approaches can be combined to explore for mineral deposits, involving a combination of geodynamic modelling, mineral potential mapping, and mineral deposit studies, aiming to provide a comprehensive understanding of ore systems at all scales. This chapter is focused on the mineral potential aspect, exploring the interrelationship between a knowledge-driven approach, which uses subjective evidence based on expert knowledge, and a data-driven model based on Bayesian probabilistic reasoning. The limitations and strengths of these approaches provide an example of how blending human interpretation with computational models can be an effective way to aid exploration and ore genesis interpretation. The study is focused on the Lawn Hill Platform, Mount Isa Inlier, situated in Northwestern Queensland, Australia. The models are used to predict the mineral potential in the area, focussing on SEDEX (Sedimentary Exhalative Deposits) and VS (Vein style) Pb-Zn mineralisation. The results of the comparison of Knowledge-Driven (KD) models versus Data-Driven models (DD) indicate that the Century zinc deposit (the largest Pb-Zn mineral resource found in this region) occurs in the area with highest mineral potential for SEDEX-type ore. The Lawn Hill Region shows good mineral potential close to the Termite Range Fault, within areas marginal to known prospects and vein/lode hosted deposits. However, there are lower favourability sites suggesting significant potential in the Kamarga Dome. Integration of the KD- and DD-models is considered a potential way to more reliably assess the favourability of locating a Century-type system. Use of this combined technique suggests that the highest favourability of locating a shale hosted mineralisation similar to Century is close to this

deposit along the Termite Range Fault zone. One particularly prospective site has been identified north of the Edith cluster.

Keywords: Weights of Evidence, Mineral potential mapping, Mount Isa Inlier, Bayesian Probability, Century zinc deposit.

3.1. Introduction

Before the construction of a predictive model, which can be defined as representing the favourability or probability for occurrence of a mineral deposit of the type/style sought, a schematic subdivision has to be drawn depending on the type of inference mechanism considered. The two model types are: (1) knowledge-driven; and (2) data-driven. Knowledge-driven models may show expert dependency, because the judgment of an expert is required during the weighting of evidential information, which depends directly on the expert-knowledge derived from wide and inhomogeneous experience. In contrast, data-driven models are more objective tools that should be considered independent from expert judgment (Carranza and Hale, 2003); however partial subjectivity is introduced when establishing the initial conditions in the data driven case (Agterberg, 1974). Particular care has to be taken then when choosing these subjective variables, to guarantee objectivity in the DD-model. In this study, a combination of these two approaches is presented (KD and DD), in which subjective and objective models are combined to help the predictive exploration process of a Pb-Zn mineral system. The knowledge-driven model is based upon geological information that defines structural and

lithological boundaries. Common knowledge related to Pb-Zn deposits is also considered during score assignment, to define favourability models for both VS and SEDEX-style mineralisation. This model is then compared with a data-driven model to further the understanding of how objective methods such as WofE (Weights of Evidence Modelling) effectively work within a Pb-Zn mineral district.

Knowledge-driven (KD) and data-driven (DD) modelling can be performed using different mathematical, computational approaches (e.g. Neural Networks, Genetic Algorithms, and Expert Systems). These are independent fields of computer science, born after the sharp decline of artificial intelligence (AI) investments, which occurred in the early 90s following the lack of significant progress in this field. Since then, a number of researchers contributed to the development of new applications based on such emerging areas, including data-driven models applied to mineral exploration (Singer and Kouda, 1996; Harris and Pan, 1999). These workers implemented neural-net algorithms to explore for Kuroko type deposits in the Hokuroku District, Japan. The application of Expert Systems based on probabilistic reasoning was also extensive. PROSPECTOR (Duda et al., 1978) is a good example of an expert agent capable of answering questions relative to the genesis of oil/mineral systems as a human would do. To clarify, an Expert System is a computer program that acts like an expert in a particular field of knowledge, usually a profession, such as geology or medicine. These novel methodologies became objects of criticism in the 90s. For instance, Wolf (1994) states that the rate of discovery in mineral exploration was not really benefiting from implementation of Expert Systems although a clear measure of their success rate was not possible at that time. If these systems were not successful as expected in practical applications, they did stimulate

debate, especially between AI researchers and statisticians. Criticism of the formalism required to treat uncertainty contributed to a series of philosophical outcomes, which prepared the ground for the development of present probabilistic inference approaches such as the example proposed here. Recently, more successful applications have been presented in the literature (Raines, 1999; Brown et al., 2000; Asadi and Hale, 2001; Carranza, 2004; Agterberg and Bonham-Carter, 2005; Carranza et al., 2005)**.**

To handle uncertainty the subjectivist or personalist Bayesian method was implemented (see Spiegelhalter, 1986). This method holds that probability statements may be made regarding any potentially verifiable proposition; whether a chance mechanism can be imagined or not. The only constraints are that probability statements should be coherent (Spiegelhalter, 1986). This approach appeared to be particularly suitable for expert systems as the representation of an inference mechanism was based on potentially verifiable propositions "hypotheses" that all had the same logical type (Spiegelhalter, 1986). The Bayes' rule is widely applied when dealing with different sources of uncertainty. These can be defined in terms of conditional probabilities, which are progressively updated as soon as new propositions with their own probabilities are added to the model.

Other probabilistic methods have been developed to address the problem of uncertainty and incompleteness of a database. For instance, a detailed discussion of the Dempster-Shafer belief functions (Shafer, 1976) is briefly revised in Spiegelhalter (1986) and more extensively discussed in Smets (1990) and Carranza and Hale (2003). The latter propose a stochastic model based on a combination of belief functions with the Weights of Evidence method firstly applied to mineral exploration by Agterberg (1989) (and also

Bonham-Carter et al., 1989; Bonham-Carter, 1994). This "hybrid" probabilistic model represents an alternative to exclusively knowledge- or data- driven models. Spiegelhalter (1986) argues in agreement with Smets (1990), that Dempsterian models are more appropriate when dealing with missing information. Smets (1990) proposes also a subdivision of probabilistic models based on the quality of the probabilistic measure available. With well known values the Bayesian model is considered to be the best representation of knowledge, whereas for more uncertain cases ULP (upper and lower probability) models, for example the Dempster's model, are proposed as an alternative.

In the data-driven model presented below, a Bayesian approach was used because of the good representation of knowledge (large number of mineral deposits/prospects, D = 82) and it was easier to implement propositional logic into an OO (Object Oriented) application developed using Microsoft Visual Basic Express (VBE) referring to the original FORTRAN programs presented in Bonham-Carter (1994). VBE is demonstrated to be a flexible environment, useful during sensitivity testing carried out to reduce and understand the control of known variables on uncertainty.

3.2. Geologic setting

The examined area is located south of the Gulf of Carpentaria in Northwestern Queensland, and covers approximately 4764.29 km^2 corresponding to the Lawn Hill Region 1:100.000 geological map published in 1982 by the Bureau of Mineral Resources (Fig. 3.1a). Exposed stratigraphic sequences are part of the Mount Isa Inlier, which is subdivided into three north-south trending structural belts (Carter et al., 1961; Blake, 1987): (1) Western Fold Belt, (2) Leichhardt-Kalkadoon Belt, (3) Eastern Fold Belt (Fig.

3.1b). These have distinctive geophysical signatures (Wellman, 1992) and are separated by regionally extensive transcurrent fault zones (Blake and Stewart, 1992). The Lawn Hill Region is part of the Lawn Hill Platform, which is included in the Western Fold Belt (e.g. Blake, 1987). The Mount Isa Inlier is well known for its mineral endowment, which hosts some of the largest Pb-Zn stratiform deposits in the world (e.g. Mount Isa, HYC, Century), and also several IOCG (Iron Oxide Copper Gold) deposits (e.g. Ernest Henry, Eloise, Starra). Common characters to this mineral endowment are the proximity of deposits and prospects to faults that were active during basin evolution (Neudert and McGeough, 1996; Betts and Lister, 2002), suggestive of a strong tectonic control of mineralising events (Betts et al., 2004), both synsedimentary and syntectonic.
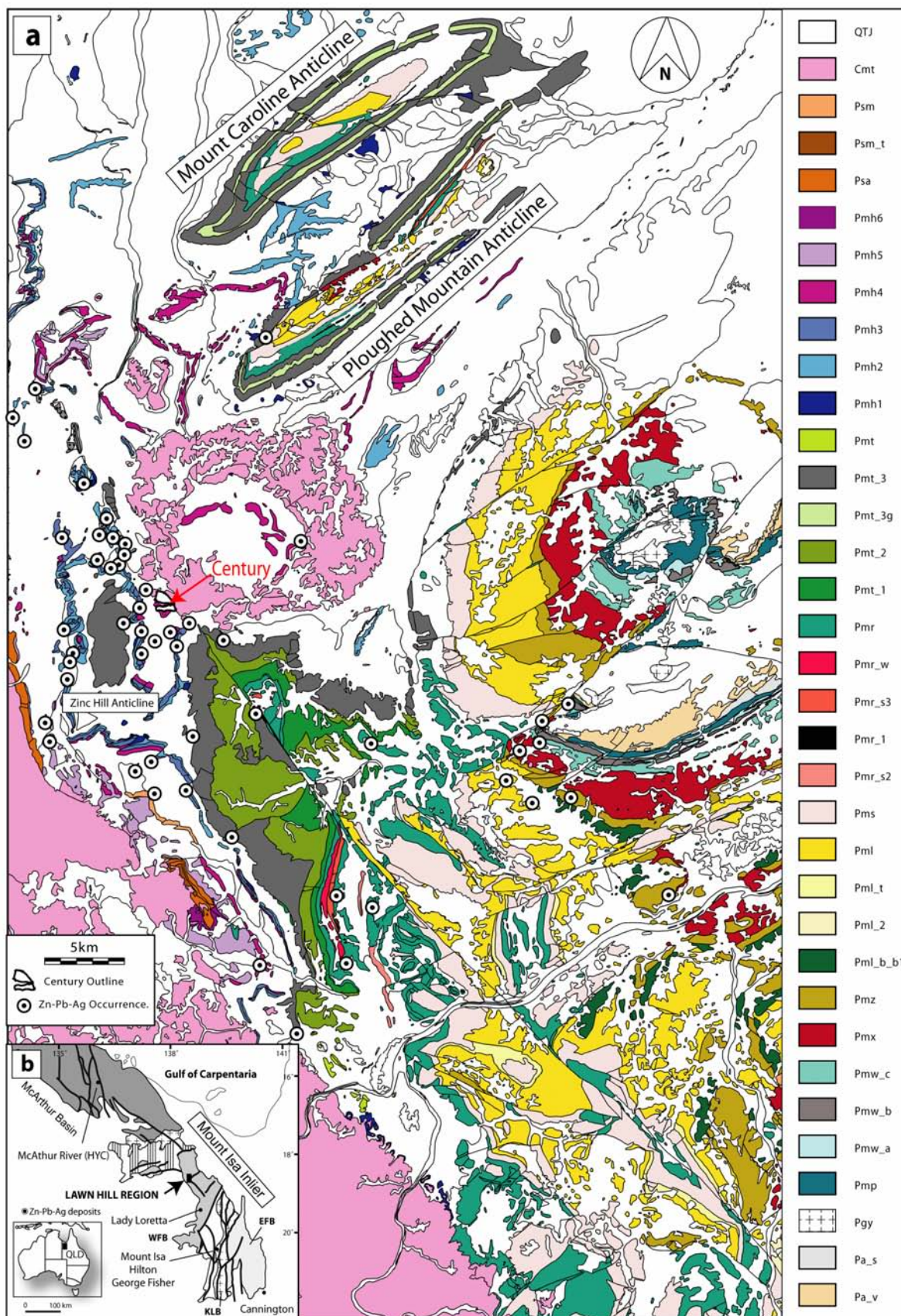
Fig. 3.1 Simplified geological map of the Lawn Hill Region (redrawn from the original 100:000 sheet). From youngest to oldest, (**QTJ**) Cainozoic and Mesozoic cover sediments. Quaternary (**Q**) sediments include alluvial clay, silt, sand, gravel. Tertiary (**T**) outcrops are mainly colluvium and residual soils, with variable degree of redbed oxidation. Alluvial sediments are also present with clay, silt and minor sand and travertine (Black clays). Sedimentary breccia and massive limestone close the basal part of the sequence. Jurassic rocks (**J**) are dominated by quartz-rich sandstones. Cherts, dolomites and phosphorites characterize the Cambrian period (**Cmt**). Mesoproterozoic South Nicholson Group lithotypes include siltstones and shales (Mullera Fm. – **Psm**) and hematitic, limonitic sandstones intercalated with shale beds (**Psm_t**). Conglomerate and sandstones represent the basal part of this group (**Psa**). Proterozoic Lawn Hill Fm. includes: (**Pmh6**) shale and flaggy siltstone-sandstone, (**Pmh5**) flaggy to blocky, micaceous and feldspatic sandstones; locally purple siltstones interbeds, (**Pmh4**) grey, fissile to flaggy siltstone and shale; flaggy tuff beds and minor dolomite, (**Pmh3**) flaggy to blocky, micaceous, lithic sandstones and conglomeratic sandstone, (**Pmh2**) fissile to flaggy tuff and tuffaceous siltstone, thinly interbedded siltstone, sandstone and shale, and (**Pmh1**) carbonaceous shale, flaggy siltstone interbeds and grey silty concretions; minor tuff. Termite Range Fm. includes: (**Pmt**) interbedded sandstone, quartzwacke, siltstone and shale, (**Pmt_3**) thick bedded, fine to coarse, poorly sorted sandstone and lithic greywacke interbedded with laminated siltstone, (**Pmt_3g**) medium to thick bedded, silicified quartzwacke interbedded with laminated siltstone and shale, (**Pmt_2**) thin to medium bedded, clayey siltstone and ferruginous sandstone, and (**Pmt_1**) thick-bedded, poorly-sorted sandstone and quartzwacke interbedded with siltstones. Riversleigh Siltstones Fm. includes: (**Pmr**) laminated and thin bedded, quartz-rich siltstones and shales, (**Pmr_w**) clayey siltstone and shale, (**Pmr_s3**) thin- to thick-bedded, quartz sandstone with clayey matrix; strongly cross-bedded, (**Pmr_l**) laminated quartz siltstone. (**Pmr_s2**) thick-bedded and silicified, dolomitic sandstones interbedded with siltstones. Shady Bore Quartzite (**Pms**) comprises orthoquartzites and sandstone with siltstone and dolomite interbeds. Lady Loretta Fm. includes: (**Pml**) thinly bedded to laminated intraclastic and stromatolitic dolomite with interbedded dolomitic siltstones and sandstones, (**Pml_t**) orthoquartzite, and (**Pml_b_b1**) breccia of chert and altered siltstones cemented by limonite; deeply weathered rocks. Esperanza Fm, (**Pmz**) consists of stromatolitic chert, siltstones, sandstones and dolomite. Paradise Creek Fm, (**Pmx**) is dominated by laminated and stromatolitic dolomites, dolomitic siltstone and sandstones; minor chert. The Gunpowder Creek Fm. includes: (**Pmw_c**) dolomite, dolomitic siltstone, oolitic dolomite, dolomitic sandstone, carbonaceous siltstone and sandstone, (**Pmw_b**) ferruginous arkosic sandstone, minor conglomerate, siltstone, stromatolitic dolomite, and (**Pmw_a**) micaceous siltstone, pyritic carbonaceous shale, siltstone and sandstone. Torpedo Creek Quartzite (**Pmp**) are predominantly massive sandstones, that becomes conglomeratic in the basal part. Yeldham Granite (**Pgy**) muscovite-rich leucogranite. Kamarga Volcanics includes: (**Pa_s**) feldspathic, conglomeratic and ferruginous sandstones, and (**Pa_v**) vesicular, amygdaloidal and massive basalt interbedded with feldspathic sandstones and conglomerates.

3.2.1. Tectonic evolution

Different tectonic models have been proposed to explain the geodynamic evolution of the Northern Australian Craton. Earlier models did not consider the structural implications of the intracratonic rifting history (Bell, 1983; Blake, 1987), explaining most of its structural features as a result of a major orogenic cycle (Mount Isa Orogeny, ca 1585-1500). Other workers developed geodynamic models based on detailed studies of fault architecture and basin history (e.g. Derrick, 1982; O'Dea et al., 1996; Betts et al., 1998; Scott et al., 1998b; Betts, 1999) providing new insights on the extensional characters of this terrain. The extensional evolution of the Mount Isa Inlier is best observed in the Western Fold Belt where the stratigraphic sequences are better preserved as regional shortening is less intense compared to the Eastern Fold Belt (Betts and Lister, 2002). Three extensional events were defined in chronological order: the Leichhardt Rift Event, the Myally Rift Event and the Mount Isa Rift Event (O'Dea et al., 1997; Lister et al., 1999; Betts, 2001). The Proterozoic extensional history was apparently terminated with the onset of the Isan Orogeny (ca. 1585-1500).

In the Western Fold Belt, the pre-existing basin architecture exerted strong control on the orientation of Isan Orogeny-related structures (O'Dea and Lister, 1995; Lister et al., 1999). Evidence of regional scale extension was derived from reconstructed stratal geometries of fault blocks; these are strongly asymmetric in cross-section exhibiting a pronounced rotational thickening and tilting, inferred to be related to listric faults. Interpreted unconformities cut down-section suggesting that differential uplift and rotation were responsible for their development (O'Dea et al., 1997). Other evidence of extensional tectonism was interpreted from the occurrence of doleritic intrusions along

some listric faults, and syn-kinematic granitic intrusions that contributed to thermal anomalies that produced low-pressure, high-temperature metamorphism and extensive metasomatism in the region (Blake, 1987; Rubenach, 1992). The resulting geodynamic model invoked two cycles of intracontinental rifting each followed by metamorphism and crustal shortening (Barramundi and Mount Isa Orogeny) (O'Dea et al., 1997; Betts and Lister, 2001).

Scott et al. (1998b; 2000) and Southgate et al. (2000) proposed an alternative tectonic model based on sequence stratigraphic reconstructions and detailed geochronological constraints (e.g. Page et al., 2000). Rather than a rift-sag model they argue that extensional features, observed in the Mount Isa Inlier, could be explained as a local response to shear stress variation across major strike-slip faults active in a convergent setting. Development of strike-slip sub-basins was interpreted from isopach distributions and sequence stratigraphic thickness correlations (e.g. Krassay et al., 2000). Sub-basins were interpreted as potentially derived from increased accommodation during strike-slip deformation. However, Betts and Lister (2001) argued that the scale and influence of such tectonic activity was secondary, and cannot explain the broad distribution of half-graben structures within the Isa Superbasin. The large spatial and temporal distribution of half-grabens might be compared to the spatial and temporal extent of the Basin and Range province (Betts and Lister, 2001, 2002). This consideration coupled, for example, with the complex distribution of mineral deposits across the Mount Isa Inlier (Betts et al., 2003) led these workers to reinterpret these features as a result of prolonged activity within a back-arc dominated setting rather than a pure intracontinental rifting scenario. Intraplate, extensional deformation at regional scale may have been linked to the

emplacement of a mantle plume (Oliver et al., 1991; Khain, 1992; Betts and Lister, 2001), promoting lithospheric thinning (Intracontinental rifting case) and steeper geothermal gradients. However, the evidence of a convergent margin preserved in the eroded remanents of the Strangways, Argilke and Chewings orogens (Collins and Shaw, 1995), and related arc magmatism (Zhao and McCulloch, 1995) led Betts et al. (2003) and Giles et al. (2004) to propose that basin development in Mount Isa was a consequence of far-field continental back-arc, extension. Subsequent basin inversion and tectonic reactivation occurred during local extensional relaxation of the lithosphere (Giles et al., 2004; Betts and Giles, 2006).

The controversy existing among these briefly introduced tectonic models is due to the often difficult interpretation of complex deformational features resulting from overprinting of extensional and compressional phases (e.g. Ploughed Mountain and Mount Caroline Anticlines, see Betts and Lister, 2002). Certain features (e.g. half-graben development) may also be diagnostic of either an extensional or compressional setting. In any case, within the Lawn Hill Platform the multiple styles of Pb-Zn mineralisation, likely reflect the interaction among the protracted reactivation history and concomitant hydrothermal events. The strong correlation of mineralisation with faulting hardly represents a pinpoint for the age of mineralisation in the Lawn Hill Platform, as faulting occurred throughout the entire structural evolution.

3.2.2. Style of faulting in the Lawn Hill Region

The Termite Range Fault (Fig. 3.1a, 3.2a) is the prominent structure in the study area, striking northwest for at least 70km in length (Hutton and Sweet, 1982). It was

interpreted as one of the major conduits for mineralising brines that led to the formation of the Century zinc deposit, which is the major mineral resource in the Lawn Hill Platform, and (Andrews, 1998; Broadbent et al., 1998; Ord et al., 2002). The last significant offset, recorded along this fault, is relatively small (a few hundred meters) and displays a sinistral component of shearing (King, 2002). Some of the brittle deformation is interpreted as acting after the north-south folding (local D2, see Broadbent, 1999) as these shallow plunging folds (e.g. Zinc Hill Anticline, see Fig. 3.1a) are offset by northeast trending faults (e.g. Bresser, 1992; Broadbent, 1999). Northeast faulting is interpreted as synchronous with repeated activity (reactivation) of the Termite Range Fault, as these structures do not crosscut, neither offset this major discontinuity. Northeast faults are steep dipping with a dextral, transpressional strike-slip component (Bresser, 1992). Often they are prone to dilational step-over (see Sibson and Scott, 1998) and host significant concentrations of vein-style Pb-Zn ± Ag-Cu mineralisation (e.g. Silver King, Watson's Lode, see Fig. 3.1a.). Most of these faults are sub-vertical suggesting that they may have, originally, formed as dip-slip structures developed during earlier stages of basin formation, within an extensional regime, and were contemporaneously active with the Termite Range Fault (e.g. Sibson, 1985a; Betts and Lister, 2002). This would explain their incompatible orientation if considered as Riedel shears of the Termite Range Fault (Hobbs et al., 1976).

E-W oriented faults are the third class of faults recognised in the region. Some of them (e.g. Pandora's Fault – intersecting Century) display a normal component of slip. E-W discontinuities are poorly represented across the Lawn Hill Region and mostly are localised in well-defined structural domains (e.g. positive or negative flowers along the

Termite Range Fault). Therefore, at least some of them formed in response to local near-field stress conditions related to this fault. E-W faults appear sealed by m- to km-scale quartz veins, which are interpreted as forming either during or after strike-slip transpressional step-over (Fig. 3.2b). A number of lines of evidence suggest that all described fault systems were active in several periods during and after basin development: (1) fault dips are suggestive of formation in extensional conditions, whereas strike-slip off-sets are clearly post-folding (e.g. Zinc Hill Anticline); (2) the existence of km-scale folds (Ploughed Mountain and Mount Caroline Anticlines, Fig. 3.1a), with orientations incompatible with the broad stress tensors inferred to be approximately east-west (e.g. Broadbent et al., 1998; Betts and Lister, 2002), might be attributed to the reactivation of older basement faults (Betts and Lister, 2002) that formed during early rifting; (3) seismic profiles intersecting regional scale faults in the Northern Lawn Hill Platform (e.g. Elisabeth creek fault zone, Scott et al., 1998b) show that thickening of strata proximal to fault discontinuities developed during syn-depositional fault movement. The likely reactivation of faults represents a substantial issue either in term of definition of the timing of different fault generations and also when attempting to attribute a certain age to the mineralisation.
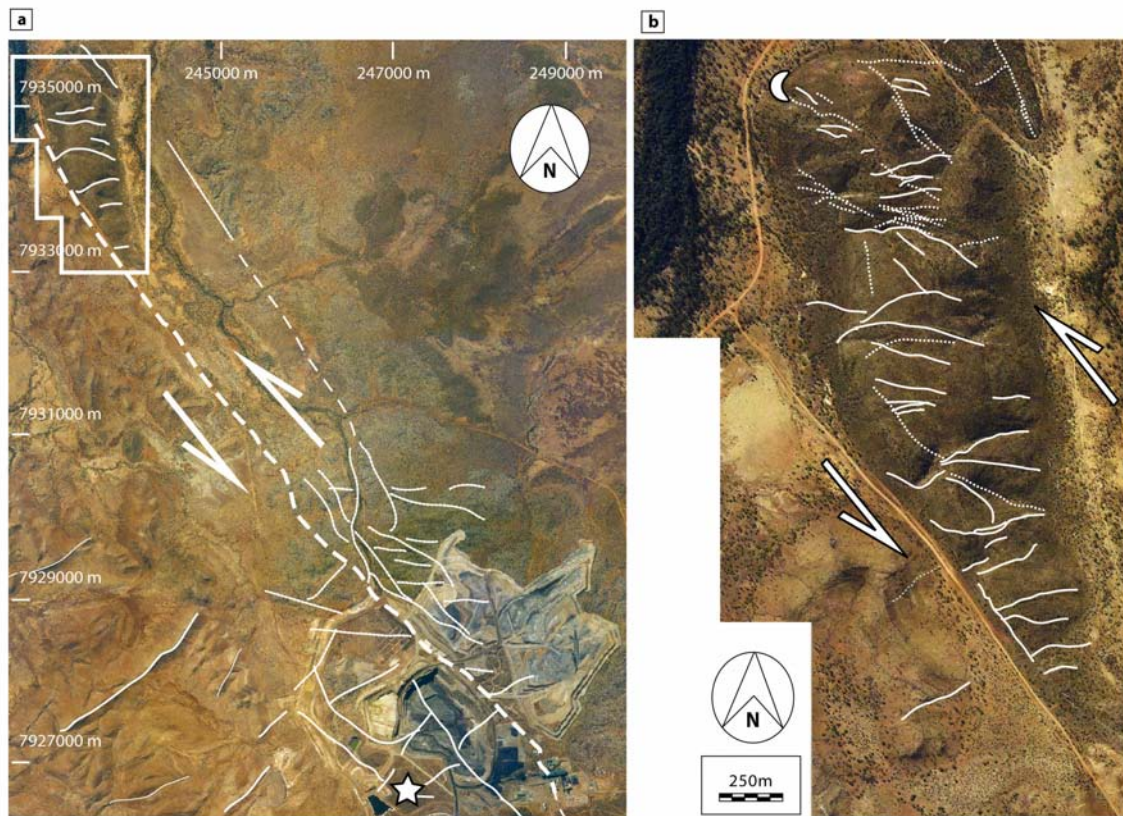
Fig. 3.2 Aerial photograph views illustrating the structural grain of the Century Area. (a) Prominent northwest and northeast striking faults in the study area. The Termite Range Fault (dashed lines) has anastomosed geometry indicative of its mature stage of reactivation. The fault displays sinistral shearing. Lateral splays of the fault apparently intersect the Century deposit (open cut). Local vein arrays are observed at the intersection of NW- and NE-faults south of Century (star symbol – see Fig. 3.6a and 3.6b). (b) Enlarged view of a contractional jog with interpreted faults. Outlined faults could be easily identified because of their quartz seals. A sinistral sense of shear is inferred considering the evidence of sinistral off-set in the Century pit area. A contractional scenario may also account for the presence of supra-lithostatic fluid pressures (jigsaw textures – moon site, see Fig. 3.6g).

3.2.3. Lawn Hill stratigraphy

Rocks exposed in the Lawn Hill Region comprise up to 8500 m of mildly deformed sediments that extend from the Murphy Tectonic Ridge in the north to the west of Mount Isa in the south (Hutton and Sweet, 1982). Bimodal suites of volcanic extrusives represent the basal part of these sedimentary packages and unconformably overlay older

granitic intrusions, for example, the Yeldham Granite, outcropping in the southeastern corner of the Lawn Hill Region, approx. 1820 Ma, and the Big Toby granite, 1800 Ma (Wyborn et al., 1988; Scott et al., 1998b). O'Dea et al. (1997) discuss the subdivision in cover sequences previously mentioned and outlined in Fig. 3.3. Kamarga and Eastern Creek Volcanics overlying the basement granites are now regarded as part of the Haslingden Group (included in the Myally Supersequence interval, ca. 1780–1765 Ma). All these units are synchronous with the Leichhardt- and Myally-rift events (Betts et al., 1999). Cover sequences 3 and 4 unconformably overlie these sub-groups and can be subdivided into three distinct formations within the Lawn Hill Platform: (1) the Bigie Formation and Fiery Creek Volcanics and their equivalents; (2) the Surprise Creek Formation; (3) the McNamara Group. The Bigie Formation is characterised by predominantly coarse clastic hematitic units, mainly conglomerates and sandstones that were interpreted by Hutton and Sweet (1982) as product of shallow depositional, sabhka or playa lake settings that would account for the intense redbed oxidation of detrital iron. The Fiery Creek Volcanics are a rift-related suite of bimodal volcanics (Wyborn et al., 1988), which are intercalated with the Bigie Formation. Dating of the Fiery Creek Volcanics yields a U–Pb zircon eruption age of 1708 ± 2 Ma (Scott et al., 1998a). The Surprise Creek Formation comprises basal conglomerates and a sandstone facies that were deposited after uplift and erosion of the Fiery Creek Volcanics (Derrick et al., 1980; Hutton and Sweet, 1982; Betts et al., 1999). The Surprise Creek Formation fines upward, becoming more distal as testified by sandy intervals containing well-rounded pebbles (Hutton and Sweet, 1982). In the top part, this formation becomes silty and sandstone dominated. The McNamara Group which hosts the major mineral resources in the Lawn

Hill Platform (e.g. Century Pb-Zn-Ag deposit) can be subdivided in an upper and lower unit (Andrews et al., 1996). The lower unit has in its basal part a clastic component partly derived form reworking of underlain intervals (Torpedo Creek Quartzite). Following this alluvial phase a deeper marine setting is inferred from evidence of euxinic conditions dominated by intercalated siltstone and shales becoming particularly enriched in carbonaceous material in the Kamarga Dome Area (see Fig. 3.1a); these lithotypes represent the Gunpowder Creek Formation. This formation underwent uplifting, erosion and lateritisation (redbeds), followed by deposition of dolomites and cherts. Shallow water dominated settings persisted until deposition of the Shady Bore Quartzite and includes the following formations: (1) Mount Oxide Chert Member, (2) the Paradise Creek Formation, (3) the Esperanza Formation and (4) the Lady Loretta Formation. All these formations are particularly enriched in carbonates - predominantly dolomites, their textural appearance and grain-size represent the result of deposition in subtidal (below wave base) to supratidal conditions (Hutton and Sweet, 1982). Stromatolites and cross-laminated sandstones with ripple-marks, and rare pseudomorphs of evaporitic anhydrite are indicative of intertital to supratidal settings. Periods of fine grained low-energy subtidal deposition were defined by crystalline dolomites, cherts, siltstones and shales, which formed laminated beds. Local euxinic facies are observed; their restricted nature may be indicative of lagoonal settings and was apparently a favourable trap for mineral deposits, for example, the Lady Loretta Pb-Zn-Ag deposit (e.g. Large and McGoldrick, 1998). Its small tonnage and rich grades (8.3 Mt at 18.4% Zn, 8.5% Pb, and 125 g/t Ag) may be a direct function of such a depositional environment.

The upper part of the McNamara Group is marked by its more transgressive nature (Andrews et al., 1996), and can be subdivided in four main formations: (1) the Shady Bore Quartzite, (2) the Riversleigh Siltstone (3) the Termite Range Formation (4) and the Lawn Hill formation, which hosts the Century deposit in its upper member (Andrews et al., 1996; Andrews, 1998; Krassay et al., 2000). The Shady Bore Quartzite has similar connotation to the Lady Loretta Formation with lithotypes typical of marginal to shallow water settings (e.g. quartzose sandstones and dolomitic siltstones). A phase of transgression is initiated with the deposition of the Riversleigh Siltstone that progressively leads to more mid- to outer-shelf settings dominated by finer lithotypes. The transgressive episode continued during deposition of the Termite Range Formation although it has a more distal connotation as shelfal depositional textures are lacking. Andrews (1998) interprets these members as high concentration turbidites, in which control of provenance of sediment supply and grain-size variation may have partly been influenced by synsedimentary growth faults. This latter consideration is supported by more recent regional tectonic interpretations for the northern part of the Lawn Hill Platform (see Scott et al., 1998b), which documents possible syn-depositional faulting. The Lawn Hill Formation represents the terminal formation of the McNamara Group, and was originally subdivided into six members by Hutton and Sweet (1982) (classification adopted for the mineral potential maps presented below – Fig. 3.3) and three other sub-units were defined by Andrews. The sedimentation of the Lawn Hill Formation occurred predominantly in outer-shelfal to deep-water settings (Andrews, 1998), and it is characterised by sandstone, siltstone, and carbonaceous shale deposition. This is confirmed by the widespread abundance of siltstone and shale dominated facies that

extends for several km- across the platform; therefore, being more typical of deep marine facies as Andrews (1998) interprets. Typical also is the intercalation of laminated shales and siltstones with volcaniclastic tuffaceous layers. Felsic activity may have been synchronous with episodes of tectonic extension of the Mount Isa Basin, which may have partly controlled depositional cycles. The initiation of the Isan Orogeny (approx. -1585 Ma) may have controlled uplifting during the later phases of deposition (e.g. Krassay et al., 2000). Fig. 3.3 presents a summary of these lithostratigraphic sequences.
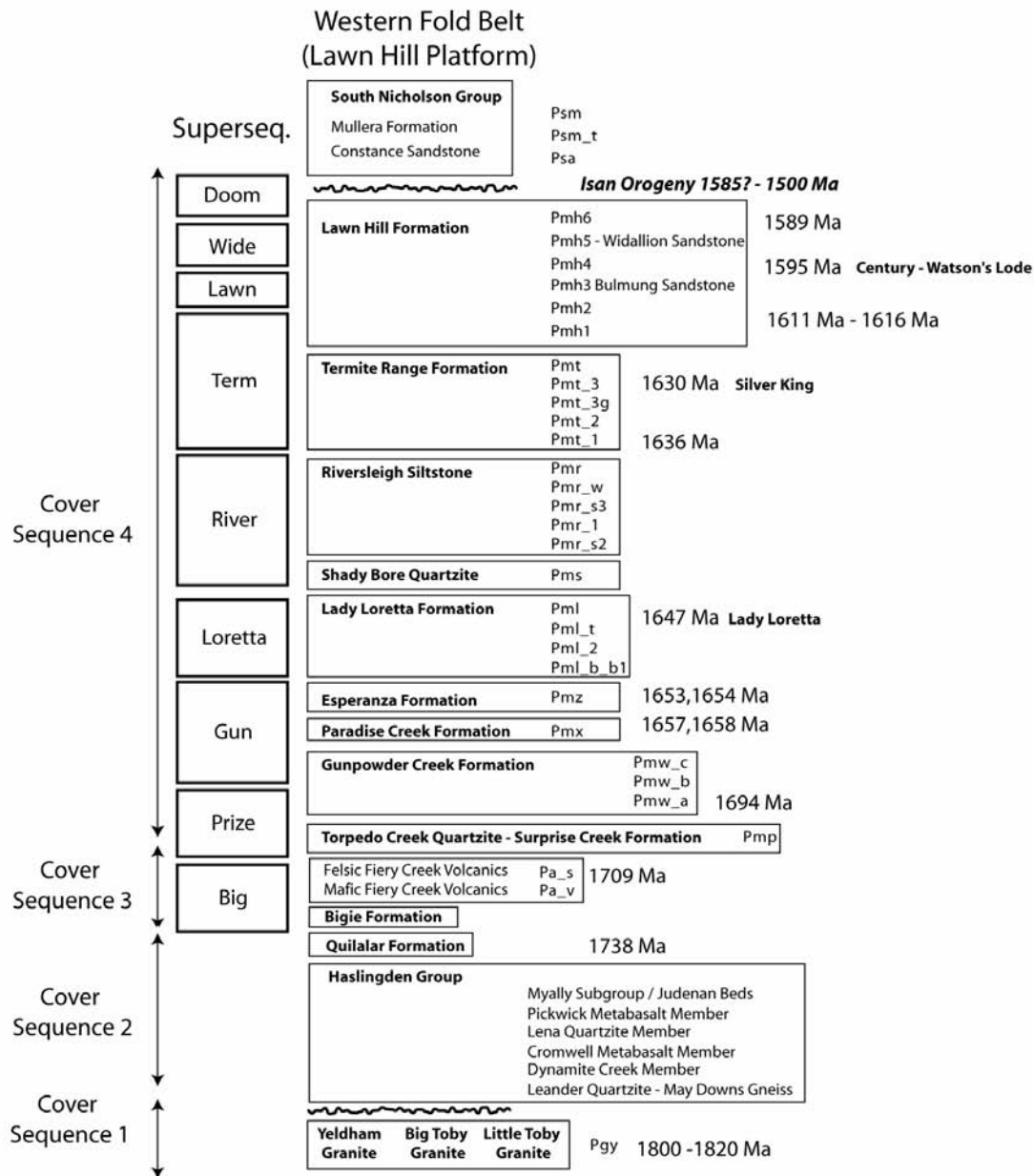
Fig. 3.3 Schematic diagram of the Lawn Hill Platform illustrating stratigraphic subdivisions of Hutton and Sweet (1982). This classification was adopted for both KD- and DD-models. For the DD- model, subunits were grouped accordingly with their formations (e.g. Pmh6 has been grouped as Pmh). The age of the Isan Orogeny is from Hand and Rubatto (2002). Sedimentary ages from Page et al. (2000). Supersequence classification from Krassay et al. (2000) and Southgate et al. (2000). Cover sequence subdivision from O'Dea et al. (1997).

Changes in the palaeogeographic conditions seem to exert a prominent control on the spatial distribution of Pb-Zn mineralisation in the Mount Isa Inlier. Pb-Zn massive sulphides appear spatially associated with organic rich lithotypes near supersequence boundaries. Therefore, even if Pb-Zn massive sulphides formed in different depositional settings or by different processes they share this commonality. Perhaps when comparing the spatial distribution of deep marine shales versus lagoonal type carbonaceous shales, the deeper settings may be more prospective because of their wider lateral extent. This could also account for the low tonnage occurrences found in restricted, shallower settings (e.g. Lady Loretta).

The deformational history (e.g. repeated activity of a fault system) needs also to be coupled with the sedimentary facies evolution to further constrain the search for Pb-Zn mineral deposits. In the next section a simple model is introduced that tries to answer the problem of integration of these parameters, in a 2D-GIS environment. The problem of investigating how tectonic and sedimentary components are uniquely associated with a certain style of mineralisation will also be discussed.

3.3. Mineral deposits characters and relative conceptual models

3.3.1. Deposit classification

This section provides a brief outline of the characters and ore genetic models typical of the different styles of Pb-Zn mineralisation observed in the Lawn Hill Region (Table. 3.1). Conceptual models are used to define the search criteria; this is followed by the

favourability modelling. Detailed descriptions of mineral deposit characters are abundant in literature (e.g. Gustafson and Williams, 1981). Many workers concerned with Pb-Zn deposits have attempted to draw well defined boundaries between the various styles of Pb-Zn ore observed. However, it is common belief that many examples of Pb-Zn ores are transitional to the three classes of mineral deposits discussed here:

- **SEDEX model**
- **MVT model**
- **IRISH model**

There are however some substantial differences among these styles of mineralisation, these are:

- the depositional setting: for example we notice that MVTs and IRISH-style mineralisation are more typical of the carbonatic platform and shallow water shelfal settings, whereas SEDEX occurs more in deeper parts of a basin usually within restricted half-grabens as illustrated in Table 3.1.

- Additional differences are also the type of textural appearance of the mineralisation which is more coarse grained in MVTs and many IRISH deposits. However, the latter have also examples (e.g. Navan deposit) that effectively could be comparable to the very fine textural relationships and morphologies of sulphide species observed in laminated SEDEX deposits.

- Another important distinction is also the size and form of the three categories illustrated below. Apparently, SEDEX are the most laterally extensive as they

can be more than 1 Km in length. MVT have more irregular shape and occur often in less continuous fashion (100s of metres), because of the irregular network of fluid flow paths developed in limestone cavities and collapse breccias. IRISH-style ores appear to be a compromise between these two extremes; however, they are usually smaller in size than SEDEX being also apparently more focused within fault controlled settings.

Illustrated characters may be interpretable as the direct product of specific metallogenic patterns. In other words, as Kesler (1997) proposes, there are a number of parameters that control the final outcome of a metallogenic event. Deep crustal or mantle features may exert the strongest control on the type of mineral deposits. However, the actual style of deposits is controlled by upper crustal features, particularly the relative abundance of carbonate and silicate in the country rock. Therefore, different typologies of deposits might be considered a direct example of upper crustal controls.

In addition to tectonic and petrologic factors, Kesler (1997) remarks that global forcing mechanisms such as global anoxia and plate reorganisations should also be considered. Certainly the role of global anoxia has produced deep water environments that favoured the formation of SEDEX mineralisation either on the seafloor (or subsurface, if the anoxic water recharged underlying aquifers). These rare events in the geological record may be responsible for the uniqueness of certain deposits. For example, we might consider an intracontinental back-arc system – the Okinawa trough in the Japan Sea. This hydrothermally active region is the only modern day example of an evolving back-arc scenario involving continental crust (Glasby and Notsu, 2003). Such a tectonic scenario could be compared with the early stages of extension and sagging observed in

the Mount Isa Inlier, although substantial differences may exist in term of tectonic organisation of the continental margin and also some of the features observed in the petrology and metal endowment in the Mount Isa Inlier may also be function of the later orogenic overprint. Nonetheless, the size of mineral deposits in the Jade field, Okinawa trough, appears to be smaller (the largest ore body in the Jade field is a few tens of metres in diameter and 15 m high and has a total area of 0.2 Km^2) compared to the Mesoproterozoic examples, such as Century, HYC or Mt. Isa (Century exceeds 3 Km^2). Global forcing mechanisms may then have been a requirement to obtain such giant ore bodies, as modern examples seem to be lacking.

Table 3.1. Summary of the broad characteristics of SEDEX, IRISH-style and MVT deposits.

	SEDEX - Sedimentary Exhalative Zn-Pb-Ag	*IRISH - Type, Carbonate hosted Zn-Pb*	*MVT - Mississippi Valley Type, Carbonate hosted Zn-Pb*
General description	*These deposits are stratiform in nature with beds and laminations of sphalerite, galena, pyrite, pyrrhotite and rare chalcopyrite, with or without barite, in euxinic clastic marine sedimentary strata. Deposits are typically tabular to lensoidal in shape and range from centimetres to tens of metres thick. They can also occur in multiple lenses at considerable distance from one another*	*Irish-type carbonate-hosted deposits are stratabound, massive sphalerite, galena, iron sulphide and barite lenses with associated calcite, dolomite and quartz gangue in dolomitised platformal limestones. Deposits are structurally controlled, commonly wedge shaped adjacent to normal faults. Deformed deposits are irregular in outline and commonly elongate parallel to the regional structural grain.*	*Mineral deposits are stratabound and have relatively simple mineralogy, with galena and sphalerite as the main ore minerals nearly always accompanied by pyrite and/or marcasite. Barite and fluorite are common in some districts. Chalcopyrite is a minor associate. Deposits commonly develop within breccias or palaeokarst topography in platformal carbonates. They are also found at the interface between carbonates and shales.*
Tectonic setting	*Intracratonic, or continental margin in fault controlled throughs. Troughs are typically half grabens developed by extension along continental margins or within back-arc basins*	*Platformal sequences on continental margins which commonly overlie deformed and metamorphosed continental crustal rocks.*	*Deposits tend to be found at or near the edges of basins as presently preserved or on arches between basins.*
Depositional environment	*The depositional environment varies from deep, starved marine to shallow water shelfal setting. There is often evidence of penecontemporaneous movement of faults bounding sites of sulphide deposition.*	*Adjacent to normal growth faults in transgressive, shallow marine platformal carbonates near basin margins.*	*They may occur in relatively undisturbed platformal carbonates or within foreland fold and thrust belts.*
Age of mineralization and host	*The major metallogenic events are Middle Proterozoic, Early Cambrian, Early Silurian and Middle to Late Devonian to Mississippian. The Middle Proterozoic and Devonian-Mississippian events are recognised worldwide.*	*Known deposits are believed to be of Palaeozoic age and younger their host rocks; Irish deposits are hosted by Lower Carboniferous rocks; Kootenay Arc deposits are in the Lower Cambrian.*	*Host rocks range in age from Proterozoic to Cretaceous, although many fewer deposits are known in the Proterozoic, Jurassic and Cretaceous than in the Cambro-Ordovician and Carboniferous.*

	SEDEX - Sedimentary Exhalative Zn-Pb-Ag	IRISH - Type, Carbonate hosted Zn-Pb	MVT - Mississippi Valley Type, Carbonate hosted Zn-Pb
Host/Associated rock types	The most common host-rocks are those found in euxinic, starved basins, namely carbonaceous black shale, siltstone, cherty argillite and chert. Thin interbeds of turbiditic sandstone, granule to pebble conglomerate, pelagic limestone and dolostone, although volumetrically minor are common. Evaporites, calcareous siltstone and mudstone are common in shelf settings. Slump breccia, fan conglomerates and similar deposits occur near synsedimentary growth faults. In some basins high-level mafic sills with minor dikes are important.	Hosted by thick, non-argillaceous carbonate rocks; these are commonly the lowest pure carbonates in the stratigraphic succession. They comprise micritic and oolitic beds, and fine-grained calcarenites in calcareous shale, sandstone, calcarenite succession. Underlying rocks include sandstones or argillaceous calcarenites and shales. Iron formations, comprising interlayered hematite, chert and limestone, may occur as distal facies to some deposits. Deformed Kootenay Arc deposits are enveloped by fine grained grey, siliceous dolomite that is generally massive or only poorly banded and locally brecciated.	Although early workers commonly suggested that deposits were located within carbonate reef masses, subsequent work as shown that only a few of them are found in this setting. MVT are closely controlled by the prior development of porosity, and thus may be located in platformal carbonates of biostromal character, back-reef or fore-reef settings are also preferential sites of mineralisation.
Deposit form	These deposits are stratiform but also stratabound, with tabular to lens shaped morphology. Sulphides and/or barite occur often in laminae that extend for several metres to 100s of metres. Usually lateral extent is more than the vertical extent.	Deposits are typically wedge shaped, ranging from over 30 m thick adjacent to, or along growth faults, to 1-2 cm bands of massive sulphides at the periphery of lenses. Economic mineralisation rarely extends more than 200 m from the faults. Large deposits comprise individual or staked sulphide lenses that are roughly concordant with bedding. In detail, however, most lenses cut host stratigraphy at low angles. Contacts are sharp to gradational. Deformed deposits are typically elongated within and parallel to the hinges of tight folds.	Highly irregular. May be peneconcordant as planar, braided or linear replacement bodies. May be discordant in roughly cylindrical collapse breccias. Individual ore bodies range from a few tens to a few hundreds of metres in the two dimensions parallel with bedding. Perpendicular to bedding, dimensions are usually a few tens of metres. Deposits tend to be interconnected thereby blurring deposit boundaries.

	SEDEX - Sedimentary Exhalative Zn-Pb-Ag	IRISH - Type, Carbonate hosted Zn-Pb	MVT - Mississippi Valley Type, Carbonate hosted Zn-Pb
Texture/Structure	Sulphide and barite laminae are usually very finely crystalline where deformation is minor. In intensely folded deposits, coarser grained, recrystallized zones are common. Sulphide laminae are typically monomineralic.	Sulphide lenses are massive to occasionally well layered. Typically massive sulphides adjacent to faults grade outward into veinlet-controlled or disseminated sulphides. Colloform sphalerite and pyrite textures occur locally. Breccias are common with sulphides forming the matrix to carbonate (or as clasts). Sphalerite-galena veins, locally brecciated, commonly cut massive sulphides. Rarely (Navan), thin laminated, graded and crossbedded sulphides, with framboidal pyrite, occur above more massive sulphide lenses. Strongly deformed sulphide lenses comprise interlaminated sulphides and carbonates which, in some cases, has been termed shear banding.	Most commonly as sulphide cement to chaotic collapse breccia. Sulphide minerals may be disseminated between breccia fragments, deposited as layers atop fragments ("snow-on-roof"), or completely filling the intra-fragment space. Sphalerite commonly displays banding, either as colloform cement or as detrital layers ("internal sediments") between host-rock fragments. Sulphide stalactites are abundant in some deposits. Both extremely fine-grained and extremely coarse-grained textured sulphides minerals may be found in the same deposit. Precipitation is usually in the order pyrite (marcasite) →sphalerite → galena.
Ore mineralogy	(Principal and subordinate): The principal sulphide minerals are pyrite, pyrrhotite, sphalerite and galena. Some deposits contain significant amounts of chalcopyrite, but most do not. Barite may or may not be a major component of the ore zone. Trace amounts of marcasite, arsenopyrite, bismuthinite, molybdenite, enargite, millerite, freibergite, cobaltite, cassiterite, valleriite and melnikovite have been reported from these deposits. These minerals are usually present in very minor amounts.	(Principal and subordinate): Sphalerite, galena; barite, chalcopyrite, pyrrhotite, tennantite, sulfosalts, tetrahedrite, chalcopyrite.	(Principal and subordinate): Galena, sphalerite, barite, fluorite. Some ores contain up to 30ppm Ag. Although some MVT districts display metal zoning, this is not a common feature. The Southeast Missouri district and small portions of the Upper Mississippi Valley district are unusual in containing significant amounts of Ni-, Co-, and Cu-sulphides.

3.3.2. Conceptual models

Several conceptual models have been proposed to explain the defined styles of Pb-Zn mineralisation. Beside the control exerted by the host rock, substantial debate among researchers concerns the source of metals, the type of fluids transferring metals, the structure of hydrothermal systems, and also the primary driving forces that caused fluids to move in the crust (in some districts for 100s of kilometres), and their relationship to the geothermal, salinity and hydraulic gradients. For instance, the role of mantle plumes, or upper crust melting with relative intrusive activity and volcanism have been proposed as possible causes of the large convection systems required to source and concentrate metals in the sites of deposition (Solomon and Groves, 1994). Also the role of topographic uplift in creating hydraulic gradients capable of transferring fluids for large distances was considered among the possible mechanism for driving fluids (e.g. Garven, 1985). Finally, for the Irish districts, it has been proposed and questioned that the fluids interacted with basement to extract Pb-Zn (Oliver et al., 2006). Classical models are then reviewed in following sections to explore some of these topics.

3.3.2.1. SEDEX and IRISH

Similar ore genetic models are commonly proposed for sediment hosted exhalative deposits and Irish-style ores:

(1) syngenetic seafloor deposition (e.g. Goodfellow et al., 1993): evidence for syngenesis includes stratiform geometry of some deposits, occurrence together of bedded

and clastic sulphides, sedimentary textures in sulphides, and, where determined, similar ages for mineralization and host rocks;

(2) diagenetic to epigenetic replacement: replacement and open-space filling textures, lack of laminated sulphides in most deposits, alteration and mineralization above sulphide lenses, and lack of seafloor oxidation.

In these models it is mainly the fluid mixing and interaction with the host rock that causes base metal fixation. Hydrothermal fluids may derive directly from seawater that, penetrating at depth, recharges aquifers and increases its temperature according to the geothermal gradient. The gradient can be anomalous if plumes or intrusive/extrusive activity is proximal or if large convection cells transfer laterally thermal energy away from magmatic sources. High salinities especially Cl^- facilitate the enrichment and transport of metals (Pb-Zn-Cu-Ag-Au etc.). Brines can travel for considerable distances until they encounter a major discontinuity that connects aquifers allowing fluids to ascend and encounter fresh sea-water and/or suitable host rocks that can interact with them causing ore deposition. In this context, essential parameters are an extensive network of aquifers, which are the primary source of metals, a major fault that act as a fluid flow driver focussing fluids, and finally a trap where by either mixing with other fluids and/or whole rock-reactions metals accumulate efficiently.

3.3.2.2. MVTs

Mississippi Valley Type deposits are epigenetic, having been emplaced after host rock lithification. Ore hosting breccias are considered to have resulted from dissolution of more soluble sedimentary units, followed by collapse of overlying beds. The major

mineralizing processes appear to have been open-space filling between breccia fragments, and replacement of fragments or wall rock. The relative importance of these two processes varies widely among, and within, deposits. Fluid inclusion data show that these deposits formed from warm (75°- 200°C), saline, aqueous solutions similar in composition to oil-field brines. Brine movement out of sedimentary basins, through aquifers or faults, to the hosting structures is the most widely accepted mode of formation (e.g. Garven and Freeze 1984a, b; Garven, 1985).

Two main processes have been proposed to move ore solutions out of basin clastics and into carbonates:

    A. compaction-driven fluid flow generated by over-pressuring of subsurface aquifers by rapid sedimentation, followed by rapid release of basinal fluids (see Jackson and Beales, 1967), and

    B. gravity-driven fluid flow which flushes subsurface brines by artesian groundwater flow from recharge areas in elevated regions of a foreland basin, to discharge areas in regions of lower elevation (e.g. Garven, 1985).

In addition to fluid transport, three geochemical mechanisms have been proposed to account for chemical transport and deposition of ore constituents:

    1. *Mixing* - Base metals are transported by fluids of low sulphur content. Precipitation is caused by mixing with fluids containing hydrogen sulphide, replacement of diagenetic iron sulphides, and/or reaction with sulphur released by thermal degradation of organic compounds.

2. *Sulphate reduction* - Base metals are transported together with sulphate in the same solution. Precipitation is the result of reduction of sulphate by reaction with organic matter or methane.

3. *Reduced sulphur* - Base metals are transported together with reduced sulphur. Precipitation is brought about by change in pH, dilution, and/or cooling.

In all models structure and reactive hosts are the main controlling parameters for the deposition of Pb-Zn ore bodies. These aspects formed the basis for the prospectivity modelling of the Lawn Hill Region. Individual deposit attributes listed in Tab. 3.1 are chosen and explained in their role in the prospectivity models (below).

3.4. Knowledge driven modelling

A knowledge-driven model can be considered a conceptual model that involves a component of generalisation, and uncertainty (Harbaugh and Bonham-Carter, 1970). Experienced geologists have to take in consideration these elements when drawing their conclusions. The conceptual model can be based entirely on human inferences and their testing, although also empirical testing can be carried out using computer-based simulation (e.g. numerical modelling, Ord and Oliver, 1997; Mair et al., 2000; Oliver et al., 2001; McLellan et al., 2004; Miller and Wilson, 2004).

A data structure (Bishop et al., 1975) was created to simplify the definition and organisation of parameters (n-variables) (Fig. 3.4). The source of information used for this KD-model can be subdivided into structural and lithological. The first includes field observations, structural information derived from available digital maps and 3D models, and knowledge of mineralisation and faulting in the region. Individual lithostratigraphic

intervals were derived from the geological map of the Lawn Hill Region and from selection and re-compilation of data collected within the NABRE project (Northern Australian Basin Research Evaluation project, Southgate, 2000).
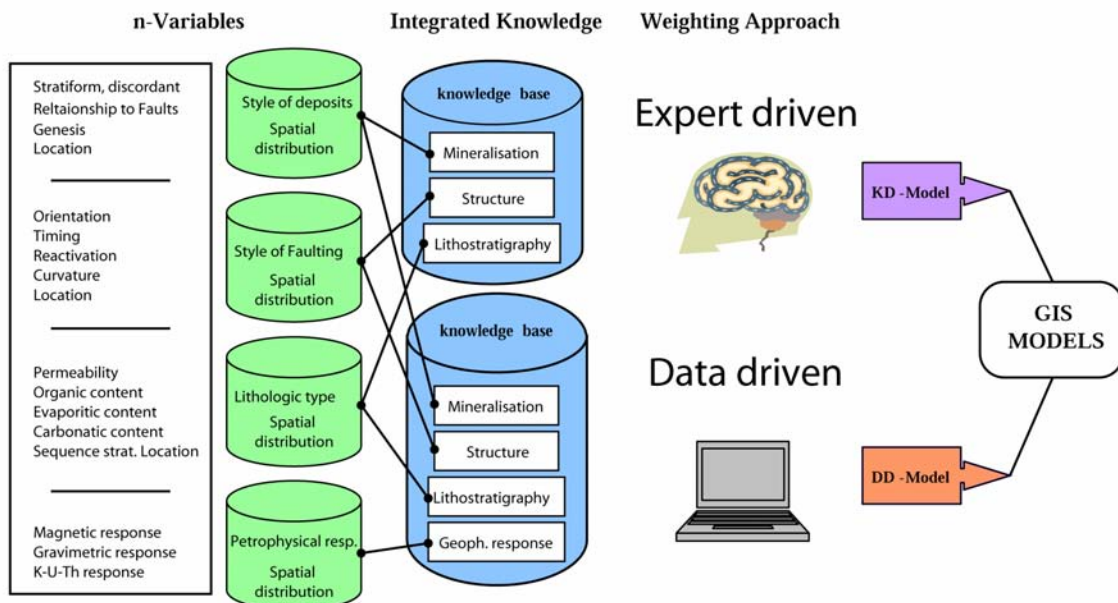
Fig. 3.4 Conceptual model used to generate a data structure to perform the KD- and DD-modelling of mineral potential. n-variables represent parameters inferred to be controlling features for the mineralisation. Each n-variable can be grouped in clusters of variables, which comprise a descriptive component and its spatial distribution. Components represent the knowledge-base that an expert or a computer program can use to develop inferences. These can be expressed as GIS models.

3.4.1. Deformational control on mineralisation

The structural component of the KD-model is examined here, focussing on the influence of faulting on mineralisation. To understand the role of faulting it is essential to firstly understand the style of mineralisation. The Lawn Hill Region hosts two main styles of mineral deposits containing extremely massive to sub-economic concentrations of Pb-Zn-Ag ore:

 (1) Laminated/banded massive sulphides (stratiform nature), the most outstanding example being the world class, shale hosted Century zinc deposit (138 Mt at 8.23% Zn, 1.16% Pb, and 29 g/t Ag; Kelso, personal communication, 2003) (Fig. 3.1a).

(2) Structurally controlled veins/lodes, often occurring as agglomerated clusters of occurrences with small tonnage (e.g. Silver King-type), with predominantly Pb-Zn ± Ag-Cu. The latter are found in the surroundings of Century, but also, elsewhere (e.g. Flat Tyre prospect). Ore styles are also distinct by age and paragenesis (Richards, 1975; Bresser, 1992; Broadbent, 1999; Feltrin et al., 2004; Feltrin and Oliver, 2004).

3.4.1.1. Stratiform mineralisation

Many mineral deposits containing zinc, lead, copper, barium and/or precious metals are stratiform in that their general morphology is similar to sedimentary strata (Stanton, 1972; Morganti, 1981). The Century zinc deposit as for other several Pb-Zn deposits in the Mount Isa Inlier (e.g. HYC, McArthur Basin) is stratiform according to this definition. The spatial distribution of ore with respect to its host has been used frequently to attribute certain timing to the mineralisation although the acceptance of evolutionary concepts such as remobilisation, which causes secondary redistribution of sulphides, precludes the use of these geometrical arguments. A summary of Century's features is provided here; see Broadbent (1999) for detailed description of petrographic relationships. The Century Zn-Pb-Ag deposit occurs within an approximately 45 m thick interlayered black shale and siltstone in the Upper Lawn Hill Formation, within unit Pmh4 of Hutton and Sweet (1982). Andrews (1998) reclassified these in two sub-members (H4s, r) now considered part of the Wide Supersequence (Krassay et al., 2000).

Century has relatively simple sulphide mineralogy (Waltho et al 1993, Broadbent et al. 1998) with sphalerite, galena and pyrite as main mineralogical phases (Fig. 3.5a-d). Sulphides occur in multiple generations (Broadbent, 1999). This is also indicated by multiple generations of carbonates that overprint and form contemporaneously with sulphides of different timing (Broadbent et al., 1998; Feltrin and Oliver, 2004). Sphalerite has exceptionally pure stoichiometric compositions (Broadbent, 1999), and is frequently finely bedded (mm-scale) and mixed with different proportions of organic carbon (porous, non-porous sphalerite, see Broadbent et al. 1998). Galena occurs as fine grained, disseminated, euhedral crystals that forms bedded laminae. It occurs also in veins associated with sphalerite, galena, siderite and quartz. Deformational textures are also observed and can be interpreted as examples of remobilisation. Galena is the easiest sulphide to be mechanically displaced and plastically deformed by shearing (Fig. 3.5a, d). Pyrite occurs in very fine-grained size from millimetres to micrometres, displaying framboidal aggregates. These characters are typical of a seafloor or early-diagenetic setting, as formation of framboidal pyrite has been documented in the first few meters of the seafloor (e.g. Bertolin et al., 1995). However, the development of other generations of pyrite (late-diagenetic to syntectonic) is evident, as pyrite also occurs in veins (e.g. Fig 3.5b-c). The deposit comprises two stratiform lenses of massive, laminated to disseminated sulphides (H4r sub-unit), which are proximal to the Termite Range Fault, although their relationship with this major fault is less obvious compared to other giant ore deposits. For example, at the HYC deposit, interlayered mineralised talus breccias host graded sulphides (Large et al., 1998). At Century, evidence of synsedimentary breccias interbedded with mineralised black shale and siltstones could be inferred from

reworked, tuffaceous layers hosting lobate to angular, autochthonous clasts of monomictic breccia. However, their origin is arguable as they could be due to syn- to post-depositional shearing along bedding planes (Fig. 3.5e).

Several sub-ordinate faults intersect Century. They have an orientation compatible with the Termite Range Fault, but also other regional-scale trends. They apparently postdate laminated mineralisation. Fault associated stringer zones are lacking at Century (e.g. Gecko Fault, Fig. 3.5f) although evidence of fracture controlled mineralised veins is documented in restricted portions of the mineral deposit (Fig. 3.5b, 5c and 5d). However, veins often appear unrelated to major faults at meso-scale. There is also lack of major reaction fronts which would be suggestive of a likely spatial association between stratiform mineralisation and faulting. Most of the mapped faults intersecting the mineral deposit appear to have formed well after its formation.
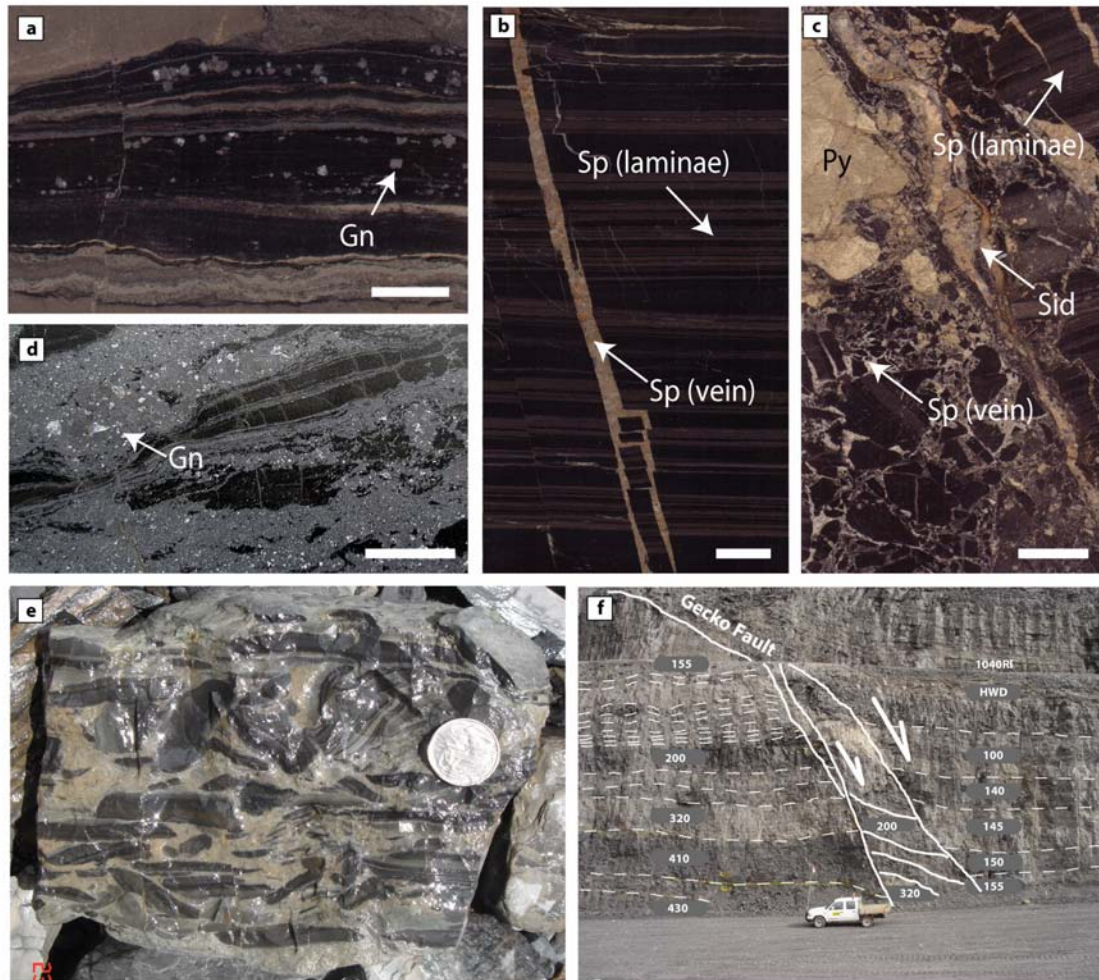
Fig. 3.5 Example of Century-style mineralisation and later deformational overprint. (a) Disseminated coarsen euhedral, cubic, galena (arrow, Gn). This was interpreted as the earliest phase of mineralisation at Century (e.g. Broadbent, 1999); however, at least part of the disseminated galena may have formed in a late syn- to post-diagenetic phase either postdating or being synchronous with discordant sphalerite (Sp- veins) (b), and also later pyritic (Py) phases (c). (d) Example of discordant galena (Gn) veins. (e) Example of siltstone/shale breccia with monomictic clasts floating in a tuffaceous sandstone, some clasts preserve earlier folding events, although glide folds may have formed relatively early during initial depositional phases. The specimen could be interpreted either as the product of synsedimentary brecciation or later tectonic related shearing originated from mechanical sliding localised in less cohesive tuff-intervals. (f) Open-pit exposure with highlighted mine stratigraphic intervals hosting the Century ore (e.g. unit 200). The deposit is intersected by later faults that apparently post-dates the mineralisation (scale bars in a, b, c, and d, 1 cm) (Appendix D for specimens spatial location).

3.4.1.2. Regional scale veins and lodes

Veins are one of the closest lines of evidence of the interplay between mineral species and fluids percolating a rock mass. They form in response to density imbalance, for example, induced by deformation. Vein-style mineralisation is widespread in the Lawn Hill Mineral Field, and has variable mineralogical composition (Fig. 3.6a-6g). This appears to reflect partly the variation of the host rock suggesting at least some local sources of infill (e.g. Bons, 2001; Oliver, 2001). For example, sandstone/siltstone-rich intervals (e.g. Termite Range Fm.) are frequently cross-cut by quartz-chlorite rich assemblages, whereas carbonaceous and carbonate-bearing shales appear to be more associated with quartz-rich, but also carbonate-rich infill (dolomitic to sideritic) (Fig. 3.6a, b). Siderite is found frequently associated with sulphides at Century, whereas quartz intermixed with sulphides are prominent in vein-hosted deposits. The paragenetic evolution of two major vein/lode Pb-Zn-Ag mineral occurrences (Silver King and Watson's Lode) is discussed in detail by Bresser (1992) who distinguish six paragenetic stages. The ore and alteration assemblage consists of quartz, carbonate (siderite, ankerite), sphalerite, galena, pyrite and minor chalcopyrite, either forming massive or fibrous vein intergrowths. Sulphides and gangue minerals form also colloform or comb (fine-grained layered) textures suggestive of mineral precipitation in open space, at shallow-depths of formation (Cox et al., 1987) (e.g. Fig. 3.6c, d, e). They also locally display crack-seal textures with infill of consistent mineralogy (Fig. 6f), suggesting a syn-deformational origin. In some cases vein fibres display also more complex patterns derived from syn-kinematic rotational components (King, 2002). Bresser (1992) reports 46 fluid inclusion analyses from main sphalerite phases at Silver King and also sphalerite

and quartz at Watson's lode. These yield homogenisation temperatures within a range of 110 to 130°C. The salinity range is from 6.3 wt% to 21.3 wt%, equiv. NaCl, which is consistent with other MVT-type Pb-Zn deposits (e.g. Red Dog, Alaska). Leach et al. (2004) provide a comparison between deposits from Red Dog (Brooks Range, Alaska) and these regional lodes proximal to Century. Using bulk extraction ion chromatography, fluid inclusions of Silver King and Watson's lode are remarkably similar to the Red Dog deposit, with elevated Cl/Br ratio indicating derivation from evaporated seawater (Leach et al., 2004). Cl/Br molar values for the Silver King deposit inclusions are suggestive of original seawater dominated brines with elevated salinities between 30-35%. Fluid inclusions salinity range of 6.3 wt% may indicate therefore dilution, probably occurring through mixing with other fluids as inferred by Bresser (1992). The vein/lode systems were strongly controlled by faults that remained open for sufficient time to allow mineralisation in response to vertical channelised flow (Sibson and Scott, 1998). The depth of formation of this mineralisation is probably shallow considering the seawater dominated signature of the brines and the evidence of colloform textures indicative of open space conditions. Dilational step-over operated likely during later compressional tectonics, mostly favouring the opening of northeast fault arrays located west of the Termite Range Fault where vein style prospects and small deposits are clustered. However, evidence of hydrothermal activity is also documented close to the Termite Range Fault and seems to be associated with this major fault. Vein style mineralisation also intersects the Century deposit on its northeastern side (Waltho and Andrews, 1993; Feltrin et al., 2004; Feltrin and Oliver, 2004). The complex series of stages of deformation along faulted corridors involved brittle fracturing of pre-existing veins that

resulted in complex patterning with formation of vein arrays (e.g. Fig. 3.6a and 3.6b).

Sealed, dilational jogs (Sibson, 1985b) and jigsaw breccias (Fig. 3.6f, g) suggest that

fluid pressures probably exceeded the tensile strength along fault margins, favouring

hydrofracturing in response supra-lithostatic pore pressure gradients.
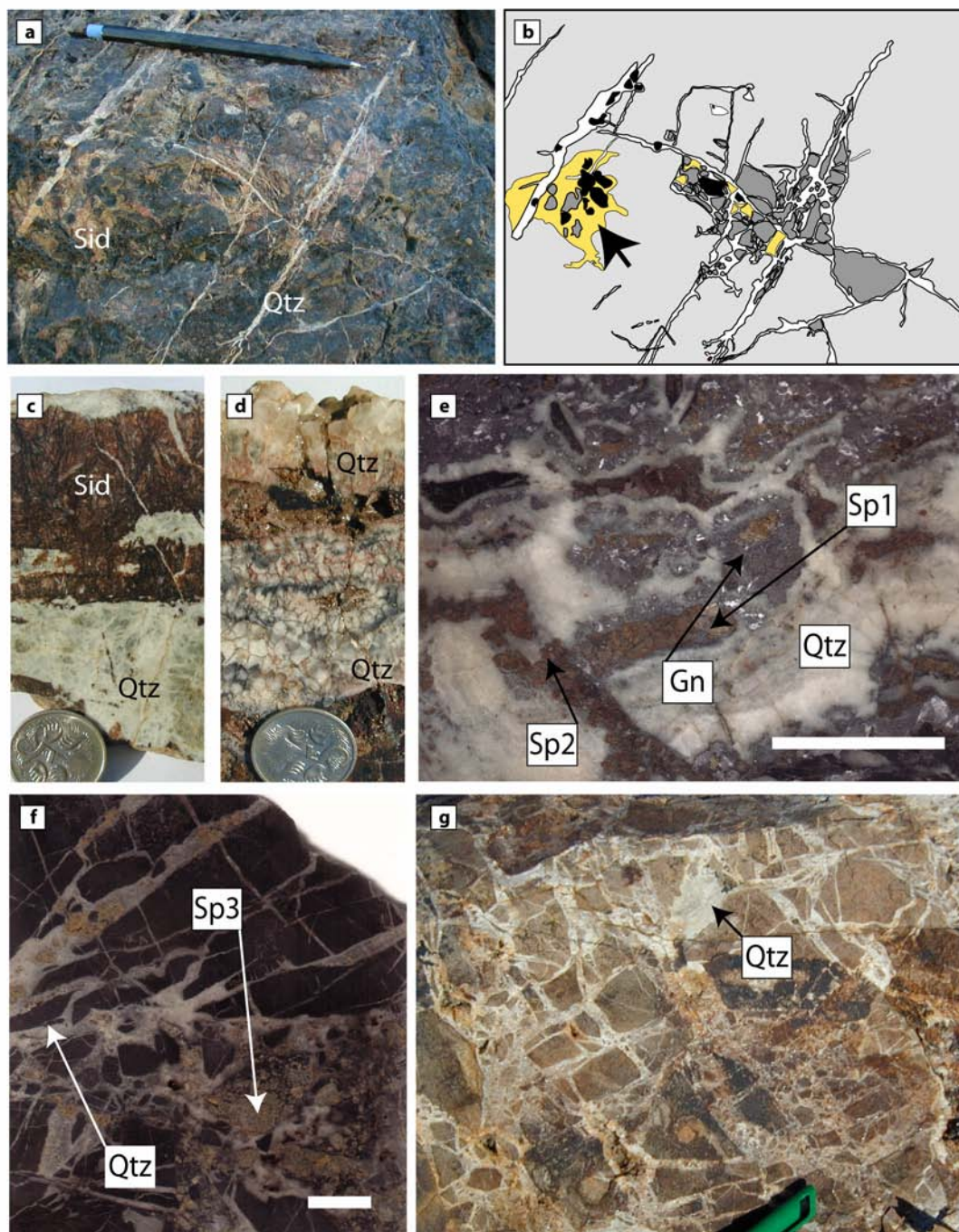
Fig. 3.6 Breccia-style mineralisation and hydrothermal alteration occurring regionally along the Termite Range Fault Zone. (a, b) example of a vein array found at the intersection of NW- and NE-faults and proximal to the Century deposit (star site in Fig. 3.2). Steep dipping quartz veins strikes N140 and are off-set by later parallel bedding shear veins. Vein arrays vary in size from hairline healed fractures to m-scale massive veins. Shear sense indicators suggest apparent sinistral sense of movement. Both quartz-rich vein-sets may be synchronous forming in the same tectonic cycle. However, they postdate an earlier stage of brecciation with more sideritic infill, see arrow in (b). Reddish sideritic cement includes rounded to angular polymictic clasts displaying different degree of REDOX alteration. (c) Paragenetic relationships of quartz

(Qtz) postdating massive crystalline siderite (Sid) at Watson's lode. (d) Comb quartz showing multiple quartz overgrowths, Watson's lode. (e) Colloidal microcrystalline quartz intergrown with sphalerite (Sp) and galena (Gn) (Silver King Mine). Variation in the availability of sulphur may have controlled alternating phases of quartz-carbonates vs. sulphides. Sulphides occur either as vein-infill or angular clasts, suggesting that their emplacement was synchronous with the brecciation. (f) Similar sequence of stages observed in (e) although quartz (Qtz) occurs in veins. (g) and (f), are both examples of hydraulic brecciation (jigsaw breccia in g from moon site, see Fig. 3.2b). This is inferred to have formed during contraction at depth, likely a tectonic component after burial have contributed to elevated pore-pressure values, exceeding the lithostatic stress. Samples (e , f) repolished from Bresser collection (1992) (scale bars in e, f respectively 3.5 and 1 cm).

3.4.1.3. End member relationship between stratiform mineralisation and fault related mineralisation

As seen the two styles of mineralisation recognised have different connotations. Century-style ore occurs predominantly in carbonaceous rocks and its relationship to faulting is somehow ambiguous; whereas, Silver King-style ores are clearly linked to faulting and may occur in a wider range of lithotypes. There is a component of trade-off between these end-members that depends on the genetic overlap existing between the two styles. Deformation and other factors such as diagenesis and metamorphism may cause mixing of the different generations of base metals (e.g. Feltrin and Oliver, 2004). Certain mineralogical textures may reflect a response to the rock's reorganisation due to deformation or other mechanisms involving density variations – remobilisation or mobilisation are then a driven process that follows the entropy laws (e.g. Ortoleva et al., 1993; Park and Ortoleva, 2003). The permeability of a rock mass is an important variable in this context that can be used to asses the degree of self-organisation of a mineral deposit and may help to discriminate its genesis (e.g. a protracted tectonic activity may reorganise mineralisation not previously related to faults).

In this context, the clustering of vein-style deposits observed around Century is considered a plausible indicator of a genetic relationship existing between SEDEX-style mineralisation and inferred later VS deposits. Intuitively, clusters of remobilised sulphide veins are more likely to form where a large reservoir of sulphides is available and proximal, if such a reservoir is accessible to hydrothermal fluids.

3.4.2. Lithological control on mineralisation

The host-rock composition may directly control the chemistry of hydrothermal fluids if the velocity of percolation is sufficiently slow to permit equilibration throughout host rock chemical reactions (Heinrich et al., 1996; Bons, 2001; Oliver, 2001). This section focuses then on the role of lithological variations across the Lawn Hill Region; these have a direct correlation with parameters such as primary and secondary permeability, and also organic, carbonatic (dolomitic) and evaporitic content. These factors influence the solubility of base metals in a solvent (the brine). Therefore, five variables were defined in the KD-probabilistic model to account for the lithological variation: (1) primary permeability, (2) secondary permeability, (3) organic content, (4) presence of maximum flooding surfaces and (5) occurrence of evaporites and dolomites. Model components were combined to generate two different mineral potential models depending upon the style of Pb-Zn mineralisation considered.

Vein style mineralisation (VS) might be interpreted, following Bresser (1992) and Broadbent (1999), as reminiscent of MVT-style mineralisation (Mississippi Valley Type), because most of the veins are inferred to form by hydrothermal solutions that were driven by the orogenic uplift similarly to the groundwater flow model proposed for the

Pine Point deposit in Canada (Garven, 1985). However, the majority of VS ore is not typically MVT-type as it does not occur in carbonates and dolomites within solution collapse breccia (e.g. Anderson, and Macqueen, 1982; Leach and Sangster, 1993). There are only some prospects localised in the Kamarga dome area that do occur in stromatolitic dolomites and might be therefore considered MVT-style or perhaps Irish-style examples (e.g. Kamarga deposits). Available data are however insufficient to confidently classify them. It is therefore used the term VS to avoid misclassification of epigenetic mineralisation. Beside their classification these ores are diverse form classical syngenetic mineralisation. Their strong tectonic imprint is more typical of Irish-style stratabound mineralisation whereas some of the colloform textures observed in fault associated cavities are also typical of MVTs. The five lithological parameters introduced above are briefly discussed emphasising the role they play depending upon the style of mineralisation considered. As discussed below two different KD models are presented and favourability indexes were developed considering also the different role played by the host rock.

3.4.2.1. Primary permeability

Primary permeability (effective porosity) is inferred to be of notable importance for SEDEX-type and early diagenetic mineralisation (e.g. Chen et al., 2003) allowing diffusion of fluids with reasonable transfer velocities, therefore, favouring the development of broad haloes, observed in some of the world class Mount Isa Pb-Zn occurrences (Large and McGoldrick, 1998; Large et al., 2000; Feltrin et al., 2006). Additionally, connected voids associated with primary permeability are the first pathways

used during expulsion of fluids due to compaction in a sedimentary basin. Consequently these are frequently filled with cements during diagenesis suggesting that primary permeability is only effective until early stages of burial and compaction. The primary permeability is function of grain size and composition of the host-rock. Grain size controls the initial volume of void space; the rock composition affects the 3D permeability variation and cementation processes. To account for the variation of these parameters the classification of different lithotypes provided by Krassay et al. (2000) and Southgate et al. (2000) was used. A pairwise comparison among the various lithotypes was then adopted to develop a series of expert based scores (see Appendix E) for each lithological unit included in the 100.000 km geological map of the Lawn Hill Region (Fig. 3.1a).

   For an early diagenetic, shallow depth system, the primary permeability provides access to extensive volumes of sediments favouring deposition or/and massive replacement of stratal geometries. The discovery of a copper-bearing sulphide replacement horizon of sandy turbidites at approximately 200 m depth in the Juan de Fuca spreading centre (Zierenberg et al., 1998) represent a good example of such early diagenetic replacement. During early stages of sediment deposition aspects such as osmotic pressure may be also particularly important controlling sub-seafloor (re)distribution of mineralisation (see Cheng et al., 2003 for an example of the role of carbonatic layers at the HYC deposit). Primary permeability when connectivity of micro-pores is sufficiently high is then interpreted here as a factor that controls the patterning of sulphides at shallow depths, in conjunction with seafloor deposition of sulphides. In some cases the role of sub-seafloor replacement may be limited in finer sediments leading to

patterns exclusively governed by sedimentary deposition of sulphides such as finely laminated bands.

3.4.2.2. Secondary permeability

As soon as the degree of cementation progresses the primary permeability is overcome by secondary permeability enhancement and fluid flow consequently will be focused preferentially along newly formed cavities, stylolites, hydro-fractures, and faults. Secondary permeability can be controlled by dissolution/precipitation processes involving a fluid phase and the host rock. For example, at the Pine Point deposit, Canada, a wide range of open filling, colloform, concretional textures are associated with dissolution cavities developed within a dolomitic host (Anderson and Macqueen, 1982). The worldwide association of Mississippi Valley Type and Irish Type deposits with dolomitic limestone and carbonate-enriched sandstones, in which secondary enhancement of permeability is favoured, was therefore considered one of the major controlling factors for the localisation of VS epigenetic mineralisation in the KD-model.

3.4.2.3. Organic content

There is worldwide evidence of a spatial association of organic matter or hydrocarbons to Pb-Zn mineralisation. For instance, the hydrothermal sites of the Guyamas Basin are present day examples where discharge of metalliferous brines occurs contemporaneously with the formation of petroleum, by cracking of organic matter in the sediments. This occurs in a high-temperature convective regime (Simoneit and Lonsdale,

1982; Rona, 1984). The interaction between sulphides and hydrocarbon occurs either at seafloor or at considerable depth when the maturation of organic compounds is a response to the normal geothermal gradient. A spatial association of sulphides with hydrocarbon is therefore not indicative of formation at certain depths (see also Coveney et al., 2004).

Other more ancient examples of spatial association might be the extensive Viburnum Trend in North America, which is localized at marginal sites within sedimentary basins where organic rich shales and hydrocarbons were abundant (Coveney, 2000). Also within the Northern Australian Craton, evidence of association between organic matter / hydrocarbon and mineralisation has been reported for giant shale-hosted systems such as HYC and Century. Recently, Chen et al. (2003) proposed an interesting analogy between fossil hydrocarbon found in ore and mudstone at HYC (McArthur River), and the previously mentioned oils of the Guyamas Basin, advocating that abundances and distributions of polycyclic aromatic hydrocarbons are linked to hydrothermal gradients formed during ore deposition. At Century, Broadbent et al. (1998) recognised the interaction between small veinlets of hydrocarbon, more likely derived from the organic rich shales (hosting the mineralisation during maturation), and sphalerite. He also proposed a model in which the textural appearance of sphalerite was controlled by the physical state of a hydrocarbon-reservoir (gaseous/liquid phase proportions). In Fig. 3.7a and 3.7b a plot of the stratigraphic variation of metal content across the stratigraphy at Century is presented, which outlines its possible linkage with the organic matter content. A fairly good correlation is apparent, although the multiple possible roles of organic matter and hydrocarbons as reducing agents and as possible sulphur suppliers at different

times are arguable. The spatial association observed might be the result of a favourable

condition of preservation of both sulphides and oil rich shales. The contemporaneous

accumulation of sulphides raining on to the seafloor, in presence of stratified waters with

euxinic conditions, does not imply a direct interaction of sulphide bearing brines with

organic components (see Goodfellow, 1987; Turner, 1992).
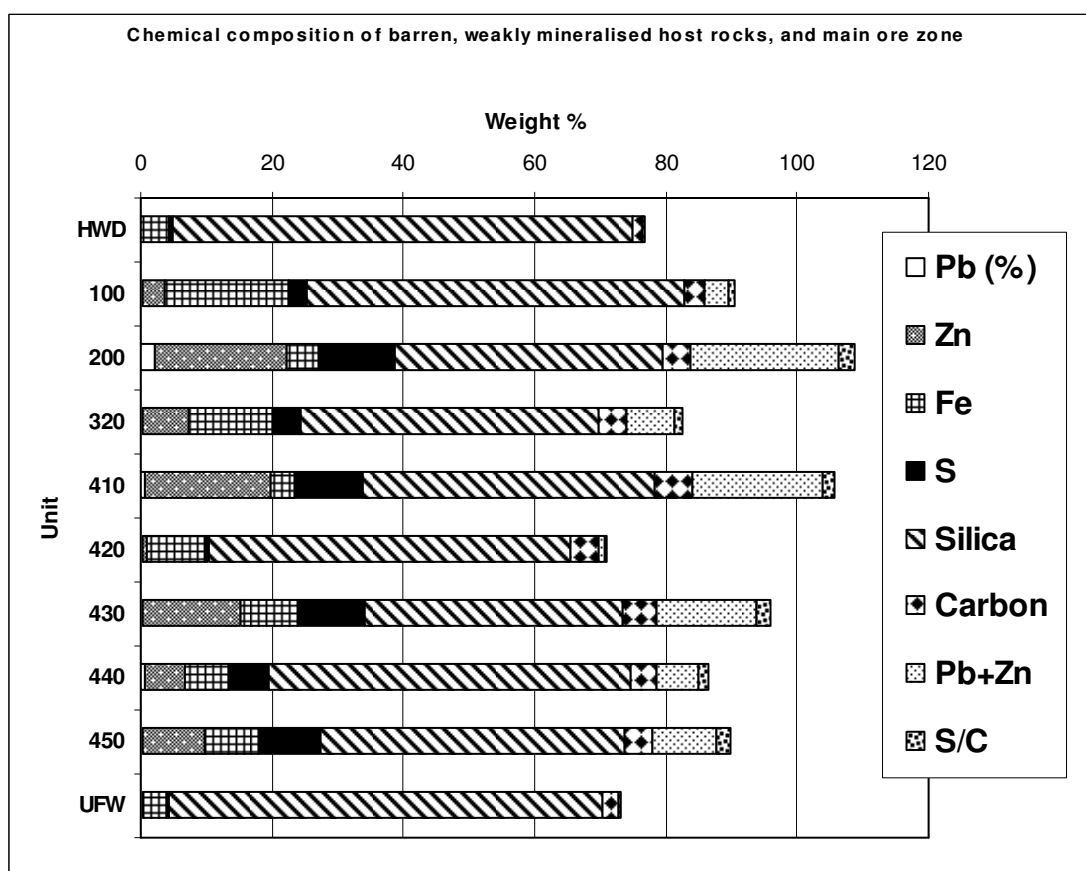
Fig. 3.7a Diagram illustrating the stratigraphic variation of Pb, Zn, Fe, S, Silica, Carbon, Pb + Zn contents, and Sulphur/Carbon ratio (drill core LH412, data from Johnson, 2000). Weight % of base metals (Pb, Zn) and C are covariant. Silica content shows inverse proportional relationship to mineralisation. The sulphur-carbon ratio is indicative either of a hydrothermal supply of exotic sulphur-rich fluids or might be indicative of oscillations from reductive through to oxidative seawater chemical conditions at the seafloor.
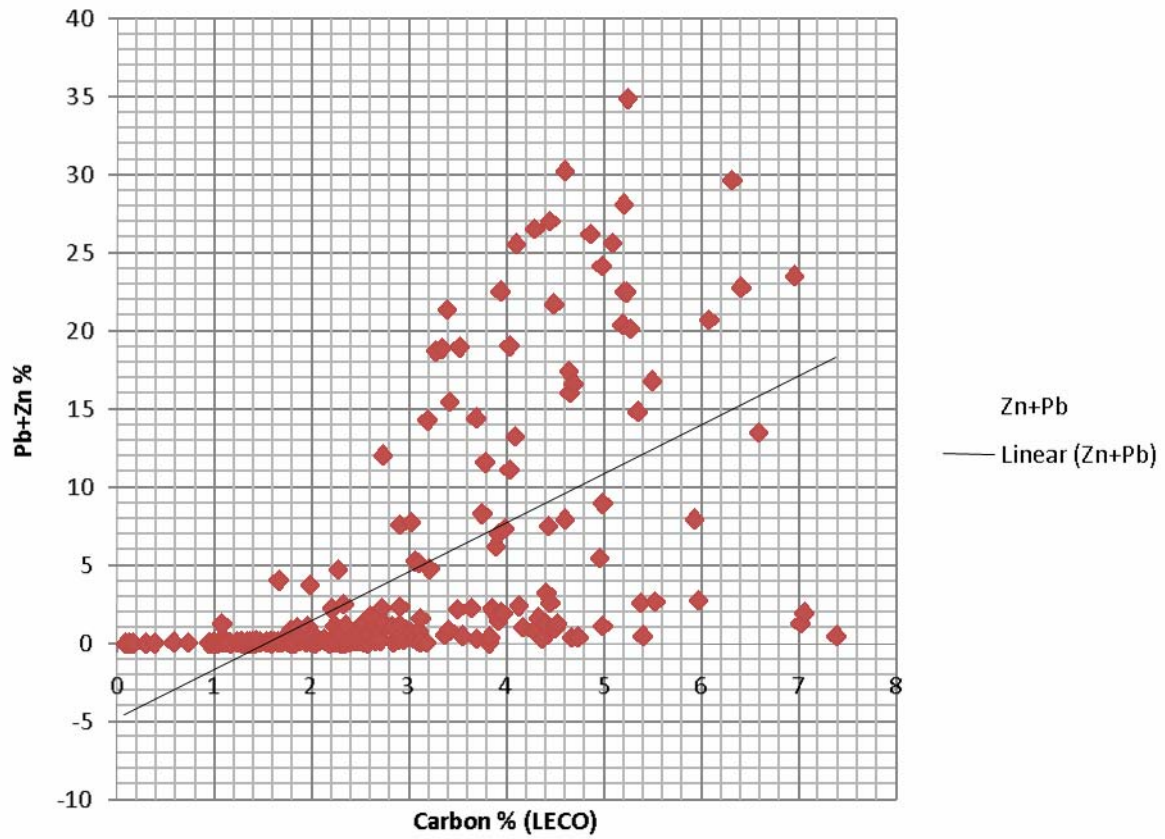
Fig. 3.7b Scatter plot illustrating the correlation between base metals and carbon content (drill-core LH412, data from Johnson, 2000). Despite the scattered distribution the diagram outlines a positive correlation with higher concentrations of Pb+Zn when carbon is above 5%. Low % Pb+Zn are also observed within the same interval; however, they might be interpreted as simple low % zones or outliers. Depletion in some layers may have occurred during diagenesis and local deformation (faults/fractures) lowering the base metal content.

3.4.2.4. Sequence stratigraphic boundaries

The lithostratigraphic formations were reclassified using sequence stratigraphic concepts (Southgate et al., 2000). The use of depositional sequences defines important depositional boundaries such as maximum flooding surfaces, which are sites where syngenetic mineralisation is deposited. Therefore, using the NABRE database composed of an extensive number of drill logs and stratigraphic sections a summary of the number of second and third order maximum flooding surfaces was compiled. Subsequently,

increments of expert based scores were applied accordingly to this parameter. Maximum

flooding surfaces also represent condensed sections of a sedimentary basin (Fig. 3.8)

where orthochemical deposition is favoured as clastic supply is virtually absent.

Synsedimentary, metalliferous shales may accumulate in condensed sections, remaining

preserved in these intervals (Large, 1988; Ruffell et al., 1998). Within starved basins the

slow rates of sedimentation can significantly affect the composition of siliciclastic layers.

For example, seasonal oscillations in the pycocline (surface separating oxidised from

anoxic seawater) favour the precipitation of Mn-oxides and carbonates as well as

controlling the percentage of organic matter preserved during sedimentation (e.g. Algeo

and Maynard, 2004).

Fig. 3.8 Schematic diagram of sequence stratigraphic facies variation in relationship to eustatic oscillations. SEDEX mineralisation is found more likely in condensed section at maximum flooding surfaces. Whereas, MVT-style or Irish-style mineralisation may form proximal to maximum flooding surfaces above and below them. These sites have more permeable carbonatic and sandstone-siltstones dominated packages (redrawn from Ruffell et al., 1998).

3.4.2.5. Presence of carbonates and evaporites

Both the end-members considered (SEDEX, MVT or IRISH) have possible genetic correlation with the occurrence of carbonatic and evaporitic sequences in a sedimentary basin. Carbonates and evaporites form in sabhka lake or epicontinental seas at relatively shallow water depths (e.g. Zechstein Basin of Central Europe). Such restricted conditions increases water salinities (including the concentration of SO_4^{2-}) and also contributes to water stratification that helps the preservation of organic matter at seawater/sediment interface. Within this context, there is a need to differentiate the type of correlation existing between the different styles of mineralisation and this particular association of lithofacies. SEDEX-type deposits are found associated with the organic rich part of these

sequences and it has been inferred that some of the sulphur co-precipitated with base metals might be derived directly from the proximal evaporitic sequences. Therefore, the spatial association is indirect, as SEDEX deposits simply share a favourable depositional environment, within which evaporites and dolomitic sequences form. SEDEX-type ore also forms in several other types of settings including deep water siliciclastic environments below wave base, in which dolomitic and evaporitic components are lacking (e.g. Century).

MVT or IRISH mineralisation as pointed out has stronger correlation with carbonatic-evaporitic hosts. Derivation of sulphur from base metal fixation can be inferred similarly to SEDEX although MVT or IRISH mineralisation displays a spatial association with these lithotypes that is of direct type and driven by secondary permeability enhancement. Dolomitic and evaporitic units are easier to dissolve by fluids interacting with them as they are more reactive than siliciclastic rocks.

3.4.3. KD model integration

The knowledge base presented in the previous sections has been utilised to develop numeric scores that helped the standardization of information as constraint for the development of favourability layers. These were subsequently converted to digital form within a 2D-GIS model using the software IDRISI (Clark University, Massachusetts). Two main evidential layers were developed: one based on the structural aspects of the studied region (e.g. scale of half-graben structures) and another based on the parameters discussed for the observed lithotypes. Integration was achieved using an Ordered Weights Average (OWA) approach that ranks the factors utilised to establish mineral potential

plausibility. This method allows more control on risk analysis and trade-off between the different lines of evidence considered within the model (Eastman, 1999; Yager, 1988).

Most problems approached with a GIS are multi-criteria in nature. Our concern lies with how to combine these criteria to arrive at a composite decision. As a consequence, the first major area of concern in GIS with regard to Decision Theory is Multi-Criteria Evaluation. In the case of Boolean criteria (constraints), the solution usually lies in the union (logical OR) or intersection (logical AND) of conditions. However, for continuous factors, a weighted linear combination (Voogd, 1983) is most commonly used. With a weighted linear combination, factors are combined by applying a weight to each followed by a summation of the results to yield a suitability map, i.e., $S = \sum w_i x_i$, where S = suitability, w_i = weight of factor i, x_i = criterion score of factor i. Because of the different scales upon which criteria are measured, it is necessary that factors be standardized before combination using the formula above, and that they be transformed, if necessary, such that all factors maps are positively correlated with suitability. Voogd (1983) reviews a variety of procedures for standardization, typically using the minimum and maximum values as scaling points. The simplest is a linear scaling such as: xi = (Ri-Rmin) / (Rmax-Rmin) * standardized range, where R = raw score. However, if we recognize that continuous factors are really fuzzy sets, we easily recognize this as just one of many possible set membership functions. In IDRISI, the module named FUZZY was used for the standardization of factors using a whole range of fuzzy set membership functions. The module provides the option of standardizing factors to either a 0-1 real number scale or a 0-255 byte scale. Once the standardisation is completed a wide variety of techniques exist for the development of weights that need to be assigned to the relative

factors (favourability layers). In very simple cases, assigning criteria weights may be accomplished by dividing 1.0 among the criteria. However, when the number of criteria is more than a few, and the considerations are many it becomes quite difficult to make weight evaluations on the set as a whole. Breaking the information down into simple pairwise comparisons in which only two criteria need to be considered at a time can greatly facilitate the weighting process, and will likely produce a more robust set of criteria weights. A pairwise comparison method has the added advantages of providing an organised structure.

Once the criteria maps have been developed, an evaluation (or aggregation) stage is undertaken to combine the information from the various factors and constraints. Three logics for the evaluation/ aggregation of multiple criteria are commonly applied: Boolean intersection, weighted linear combination (WLC – firstly developed by Saaty, 1977), and the ordered weighted average (OWA).

- The most simplistic type of aggregation is the Boolean intersection or logical AND. This method is used only when factor maps have been strictly classified into Boolean suitable/unsuitable images with values 1 and 0. The evaluation is simply the multiplication of all the images. The derivation of criterion (or factor) weights is described above.

- The weighted linear combination (WLC) aggregation method multiplies each standardized factor map (i.e., each raster cell within each map) by its factor weight and then sums the results. Since the set of factor weights for an evaluation must sum to one, the resulting suitability map will have the same range of values as the standardized factor maps that were used.

- In its use and implementation, the ordered weighted average approach is not unlike WLC. The OWA method is almost identical to that of WLC, with the exception that a second set of weights appears. This second set of weights, the *order weights*, controls the manner in which the weighted factors are aggregated (Eastman and Jiang, 1996; Yager, 1988). Indeed, WLC turns out to be just one variant of the OWA technique.

To better explain the OWA technique, it is instructive to firstly review WLC in terms of two new concepts: tradeoff and risk.

- **Tradeoff:** factor weights are weights that apply to specific factors, i.e., all the pixels of a particular factor image receive the same factor weight. They indicate the relative degree of importance each factor plays in determining the suitability for an objective. In the case of WLC the weight given to each factor also determines how it will tradeoff relative to other factors. For example, a factor with a high factor weight can tradeoff or compensate for poor scores on other factors, even if the unweighted suitability score for that highly-weighted factor is not particularly good. In contrast, a factor with a high suitability score but a small factor weight can only weakly compensate for poor scores on other factors. The factor weights determine how factors tradeoff but, as described below, order weights determine the *overall* level of tradeoff allowed.

- **Risk:** Boolean approaches are extreme functions that result either in very risk-averse solutions when the AND (multiplication of layers) operator is used or in

risk-taking solutions when the OR (addition) operator is used. In the former, a high aggregate suitability score for a given location (pixel) is only possible if *all* factors have high scores. In the latter, a high score in any factor will yield a high aggregate score, even if all the other factors have very low scores. The AND operation may be usefully described as the *minimum*, since the minimum score for any pixel determines the final aggregate score. Similarly, the OR operation may be called the *maximum*, since the maximum score for any pixel determines the final aggregate score. The AND solution is *risk-averse* because we can be sure that the score for every factor is at least as good as the final aggregate score. The OR solution is *risk-taking* because the final aggregate score only tells us about the suitability score for the single most suitable factor. The WLC approach is an averaging technique that softens the hard decisions of the Boolean approach and avoids the extremes. In fact, given a continuum of risk from minimum to maximum, WLC falls exactly in the middle; it is neither risk-averse nor risk-taking.

• **Order Weights, Tradeoff and Risk:** the use of order weights allows for aggregation solutions that fall anywhere along the risk continuum between AND and OR. Order weights are quite different from factor weights. They do not apply to any specific factor. Rather, they are applied on a pixel-by-pixel basis to factor scores as determined by their rank ordering across factors at each location (pixel). Thus, it is possible that a single order weight could be applied to pixels from any of the various factors depending upon their relative rank order. To examine how

order weights control levels of tradeoff and risk, let us consider the case where factor weights are equal for two factors A and B. For instance A = B = 10 gives a vector x = [10, 10]. If it is adopted the following set of order weights y = [1, 0] the final outcome of a combination would give a result in the final aggregation z = 10. If we consider another example in which y = [0.5, 0.5] we would obtain the same result. However, in this case this is due to the initial assumption of having equal factor weights. The main difference between these simple examples is that order weights in the first case are forcing the final result of a layers combination to be conditioned heavily by the first factor. In the second example order weights are essentially in full tradeoff. In other words, the degree of tradeoff is governed by the relative distribution of order weights between the ranked factors. Thus, if the sum of the order weights is evenly spread between the factors, there is strong tradeoff, whereas if all the weight is assigned to a single factor rank, there is no tradeoff. In addition to the tradeoff concept, favourability layers are combined using a compromise between Boolean OR/AND operations. Using OWA makes these rules less restrictive because the use of order weights allows to control the risk condition. For example, in case of full tradeoff (which means spread order weights across the different factors) the model is forced in the middle of the risk continuum, resembling a softer solution equivalent to a WLC approach.

Two probabilistic models are presented, one for SEDEX and one for VS deposits. The outcome is represented by plots of stratigraphic potential and maps of predictability for SEDEX type ore, and VS ore. There is an implicit overlap between these end-

members, although the end-member subdivision was valuable for exploring the relationship between geological complexity and spatial distribution of known mineral occurrences.

By analogy with the data-driven model (DD), an expert-driven model is a two-fold process that involves a preliminary phase of data standardization and subsequent phase of data assembly. Usually the criteria considered (evidential layers) are distinguished as constraints or factors. These are respectively considered hard and soft components of a KD-model. Structure and lithology were represented in a binary format (Boolean constraints), whereas continuous variation of favourability was approximated utilising fuzzy membership functions (see Bonham-Carter, 1994). These latter constitute a softer approach that allows a certain degree of trade-off depending on the function adopted and the type of aggregation method (see below).

Different assumptions were utilised for the SEDEX and VS models. The SEDEX model considered a fault database composed of three main groups (NE, NW, E-W). These were used to create independent evidential layers that were combined using an OWA (Ordered Weighted Average) with ranking coefficients of (0.4, 0.3 and 0.3) respectively for NE, NW, E-W faults. This assumption gives more weight to NE structures as they were considered normal dip-slip faults that are interpreted as older growth faults (Broadbent et al., 1998; Betts and Lister, 2002). Within a SEDEX context these structures may have contributed as sources for mineralising fluids during synsedimentary tectonic activation. However, the chosen weights are a full trade-off that reflects the level of uncertainty of this assumption. NW and E-W faults may have been important as well and other variables may have been conditioning the relationship

between structure and mineralisation (e.g., fault intersections in case of fluid mixing). SEDEX deposits do not necessarily form proximal to faults (e.g. Rona, 1984), e.g. brine pools may migrate towards deeper parts of starved basins away from faults although the range of mobility is restricted by the scale of half-graben developed during syn-rift activity or sagging. A buffer of 5km was used as the maximum distance from the faults to take into account these considerations. This assumption could be important, as identification of resources away from major faults may be a discriminator between SEDEX and VS ore. A different set of assumptions was considered valid for VS deposits: equal order weights were adopted for all the sub-groups of faults reducing the OWA to its full trade-off end-member, which is the equivalent of a weighted linear combination (WLC) model in which ranking coefficients are equal. A Boolean buffer of 1km, a risk-averse choice compared to the wider buffer previously adopted, was chosen because proximity to faults is more important for this style of mineralisation, as secondary permeability enhancement is the main spatial constraint.

3.4.3.1. Assumption for lithotype-based evidential layers

A similar procedure to the previous standardization of structural layers was utilised to develop the lithotypes based evidential layers. Two layers (SEDEX, VS) were developed. The number of variables considered was higher than in the previous model. To help the development of weighting coefficients, five independent criteria were defined: primary and secondary permeability, organic content, carbonate/evaporite content and number of maximum flooding surfaces. Initial pairwise comparison of lithotypes led to the definition of primary permeability scores; a subsequent phase involved the update of

these initial values. Fig. 3.9 summarises the assumptions made and presents the workflow

utilised (see also Appendix E - CD folder).

	Primary Permeab. Score (SEDEX)	Primary Permeab. Score (MVT)	Total Score (SEDEX)	Total Score (MVT)
Bre	0.5	17.5	5	26.5
C-Sh	15	3	24	7.5
Che	17.5	0.5	22	18.5
Cg	0.5	17.5	0.5	22
Cr-dol	17	1	21.5	14.5
D-mud-sts	11.5	6.5	16	20
D-mud-gra-str	9	9	13.5	27
San-Sts_str	5.5	12.5	10	30.5
Dololut	10.5	7.5	15	12
L-San	2.5	15.5	7	15.5
Carb-Qtz-San	8	10	12.5	28
Qtz-San	2.5	15.5	2.5	15.5
Qtz-San-Dolst	5	13	9.5	26.5
Dolosts-sh	12	6	21	15
Sh	15	3	24	7.5
Sts	7	11	11.5	11
Sts-San	5	13	9.5	13
Sts-Sh	12	6	21	6
T	14.5	3.5	14.5	3.5

Fig. 3.9 Schematic diagram portraying different phases of expert-driven weighting. Initial phases involved development of numerical scores based on pairwise comparison of primary permeability of different lithotypes. Incremental scoring is used in a second phase to account for the organic content, secondary permeability variation and relative content of evaporites and dolomites. Proportional scoring uses a qualitative estimate (average %) of the spatial distribution of lithofacies within each considered stratigraphic interval. The final models (SEDEX, VS) considers also additional scores for occurrence of maximum flooding surfaces and proximity to faults (see text).

Assumptions regarding the primary permeabilities considered impermeable rock

types more favourable to SEDEX-style ore, whereas permeable units were assumed to be

advantageous for VS ore. For the VS model, the role of secondary permeability

enhancement increased the scores as a consequence of the solubility of the

carbonate/evaporite content. The importance of organic content and the number of

maximum flooding surfaces were used to increment the weights in the SEDEX model,

because of the well-known spatial association between base metals and organic rich intervals as previously discussed. The outcome was a classification of all the lithotypes in term of mineral potential for SEDEX and VS deposits (Fig. 3.10). The lithostratigraphic classification of the Lawn Hill area was utilised as a reference for the spatial distribution of outcropping lithologies. Mapped geological intervals are composed of different predominant lithotypes; therefore, using available data (more than 80 sites among regional drill-holes and stratigraphic sections from Southgate et al. 2000 and Krassay et al. 2000) an averaged weight of mineral potential per unit was estimated, considering the relative abundance of each lithotype.

3.4.3.2. Aggregation of evidence

Standardized information relative to structure (spatial distribution of faults) and lithology was assembled performing pixel based algebra in GIS, firstly multiplying the raw-evidence layers by the developed weights and subsequently summing up the values of partial probabilities. An ordered weights average (OWA) was favoured as it allows ranking of criteria (evidence themes). Additional ranking based weights were developed during aggregation of the SEDEX lithostratigraphic model with the fault-layers. Lithological control was favoured rather than the spatial association to faults, assigning respectively ranking coefficients of 0.7 and 0.3 (Fig. 3.9), emphasising the role of lithological variations as SEDEX can be formed away from the faults. No ranking was utilised for the VS model as structure and lithology were considered equally important. The resulting models and enlargements of four subsets are shown in Fig. 3.11a, b, c, d and e.
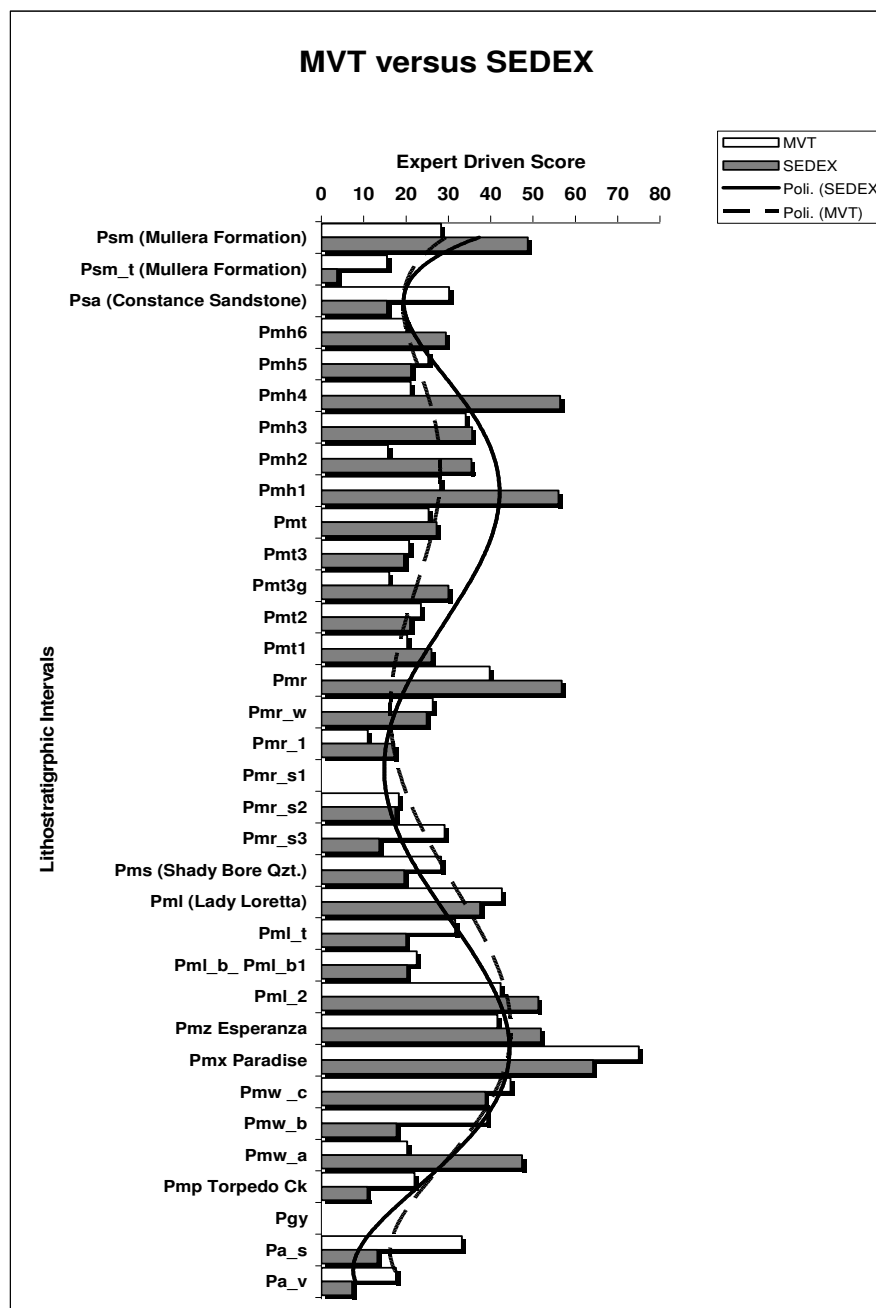
Fig. 3.10 Summary of lithostratigraphic mineral potential for the Lawn Hill Region. Comparing SEDEX potential with VS potential it is noted that the upper part of the sequence (Lawn Hill Fm – Riversleigh Fm.) is more favourable to SEDEX-style mineralisation. In the lower part of the sequence (in particular Lady Loretta, Esperanza and Paradise Creek Fm.) the comparison suggests that mineral potential is high for both styles of mineralisation.

3.4.3.3.Interpretation

The KD-model results can be used as multi-objective tools. The purpose was to evaluate the spatial distribution of the variables considered within the model against known distribution of deposits and prospects in the region to their relationships to prospects/deposits. The following interpretation is proposed based on the KD model.

SEDEX potential is widespread (see Fig. 3.11a) suggesting that suitable conditions for the formation and preservation of exhalative to early diagenetic deposits may occur in different depositional settings. More prospective units (favourability score above 35) were: Psm, Pmh4, Pmh3, Pmh2, Pmh1, Pmr, Pml, Pml_2, Pmz, Pmx, Pmw_c, Pmw_a (see Fig. 3.1a for location).

Comparing the SEDEX prospectivity map of Fig. 3.11a (notice that favourability scores have been rescaled within an interval [0, 256] in all maps) against known mineral deposits/prospects, there was evidence of good agreement of mineralised sites and highest score of favourability in the KD-model although in some cases occurrences intersecting low-favourability fields are recorded. Note that known mineral occurrences include only a single, discovered, shale-hosted giant system (Century deposit – arrow in Fig. 3.1a, b); therefore, most of the prospects and small mines are structurally controlled veins and lodes that however might be proximal to major stratiform deposits. For instance, Century is occurring within a cluster of vein style occurrences. This might indicate that correlation of clusters of VS systems within prospective units is a discriminating factor for SEDEX-type ore; therefore, prospective areas were restricted based on this criterion in two targets, the Century subset and the Kamarga subset (Fig. 3.11a and 3.11b).

The VS-KD model (Fig. 3.11b) indicates that VS occurrences should be preferentially hosted in stratigraphic units outcropping in the southeastern part of the Lawn Hill map. This is also evident on the histogram that outlines mineral potential (Fig. 3.10). Particularly prospective are the Lady Loretta, Esperanza, Paradise Creek Formations and part of the Gunpowder Creek Formation. There is a major peak occurring within the Paradise Creek Formation although this may be the result of a bias related to input data (see below). Localised peaks in mineral potential occur also within the Pmh3 and Pmr intervals, but overall the background appears to be lower compared to SEDEX prospectivity. Comparing the VS-KD model with known mineral occurrences it is noted that only 20 occurrences are localised within or proximal to units with a favourability higher than 0.75. This suggests that the likelihood of finding a VS deposit is higher in the Kamarga Dome area, and south of it. Most of the known deposits/prospects occur within the 1km fault buffer, confirming their structural control.

- Although both KD-models allow definition of favourability maps for distinct styles of mineralisation, there is a clear overlap existing between them. Therefore, with this approach it is possible to delineate the areas with high favourability for SEDEX-style mineralisation, but the result is only a likelihood estimate. Various limitations apply, for instance, the approximation relative to the classification of lithotypes- often too simplistic. A more detailed classification would be a requirement to increase the power of prediction. The analysis is also limited spatially to outcropping lithologies. Favourability scores are derived from assumptions made upon measured stratigraphic sections and available drill-holes. Therefore, the component of uncertainty involved is often difficult to quantify.

These issues can be partly overcome developing a Data-Driven model that uses additional information and permits quantification of the uncertainty related to the missing information. It should also be realised that in KD modelling, operator-bias in assignment of scores is subjective (i.e. no two experts will give the same scores to the same evidence), and uncertainty due to operator bias is also difficult to quantify (Carranza, pers. comm.).
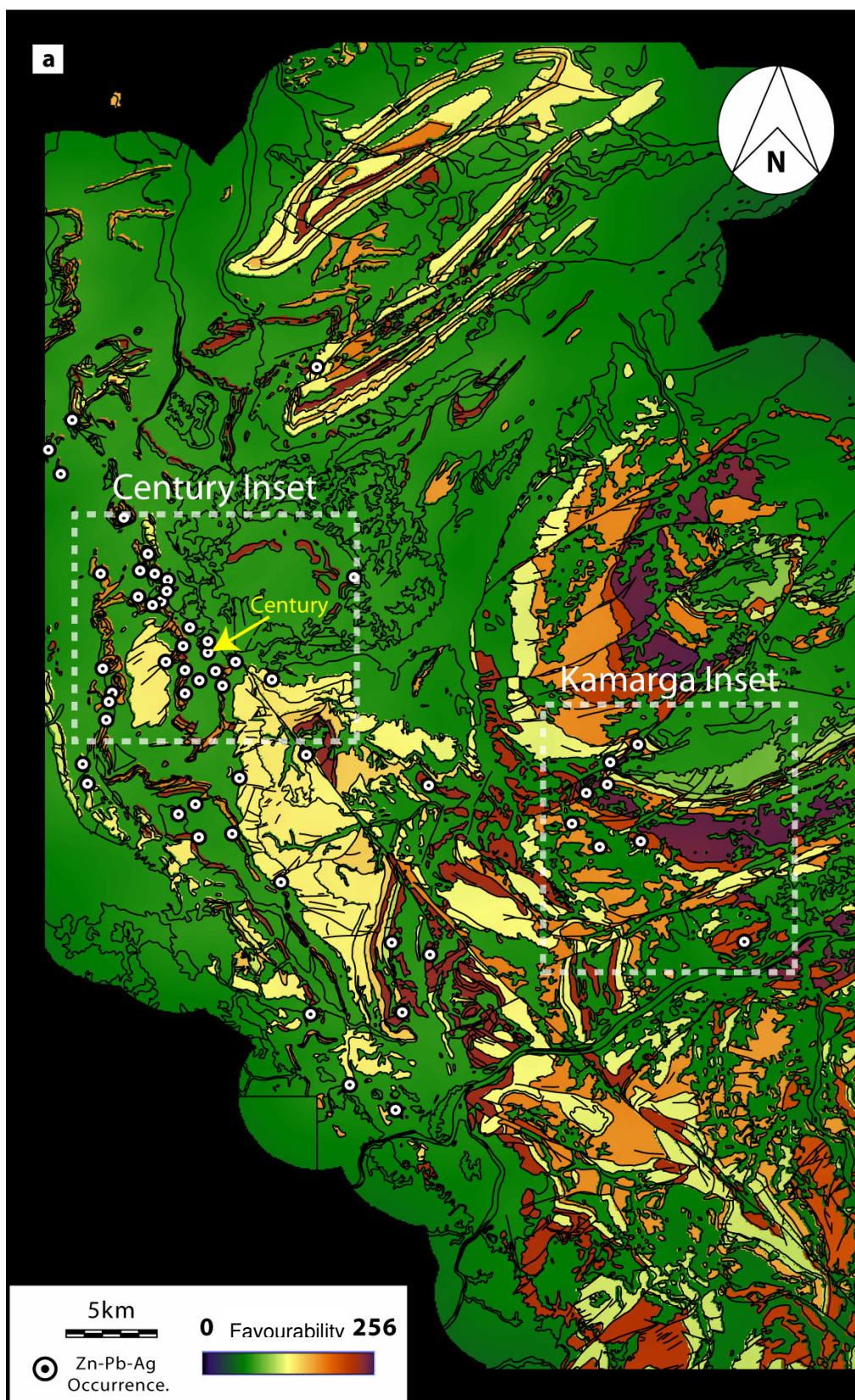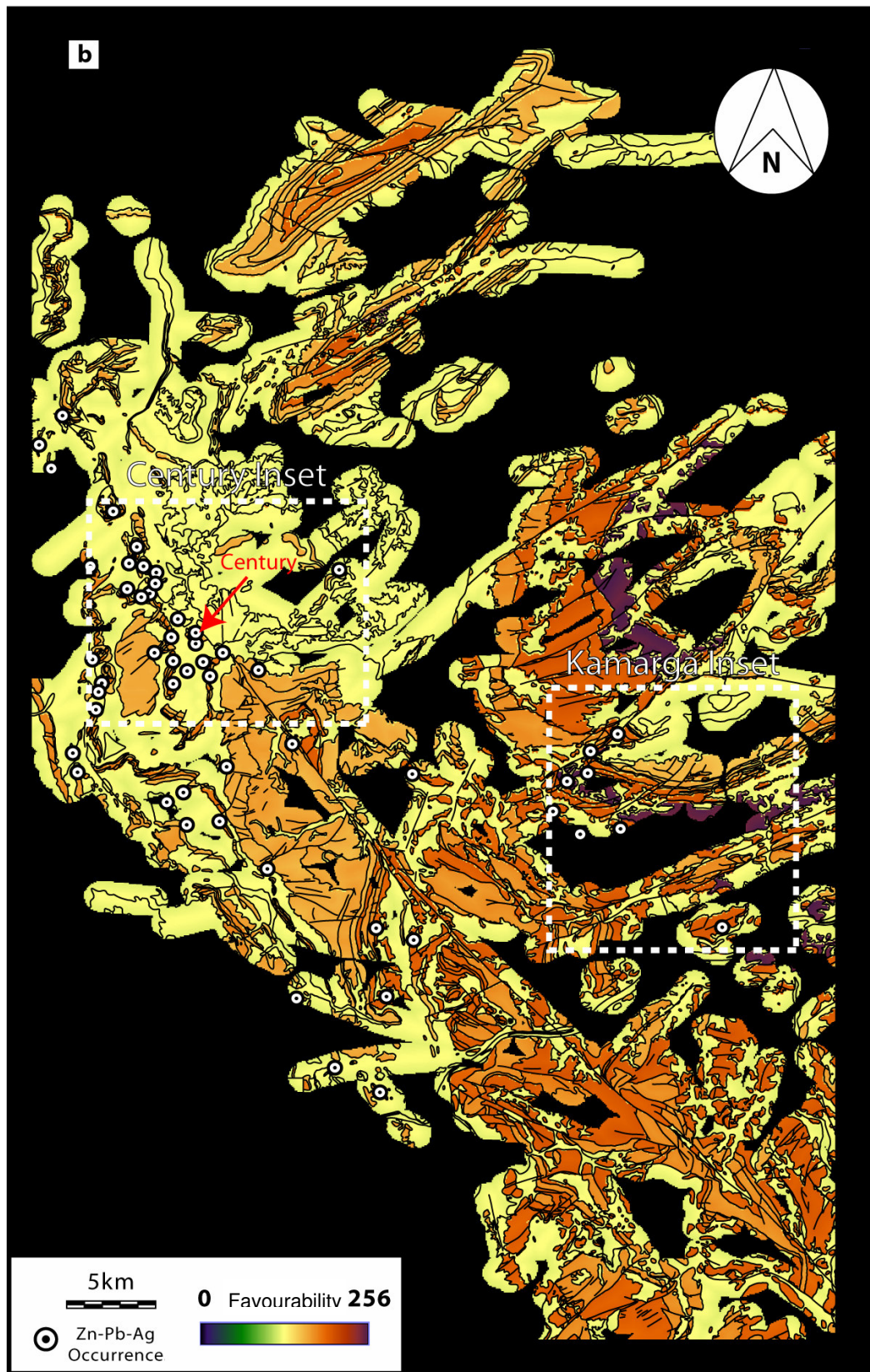
(c)
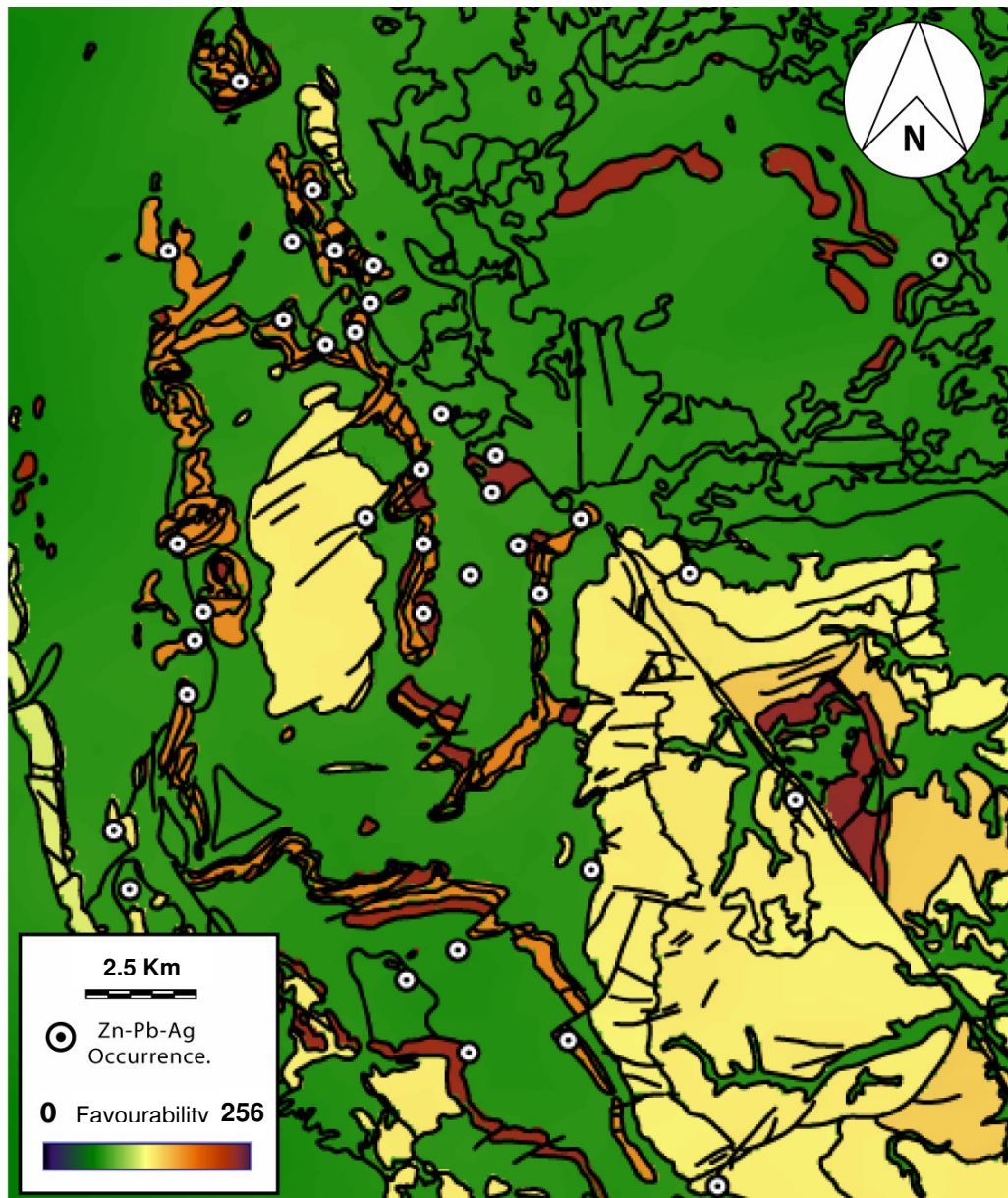
(d)
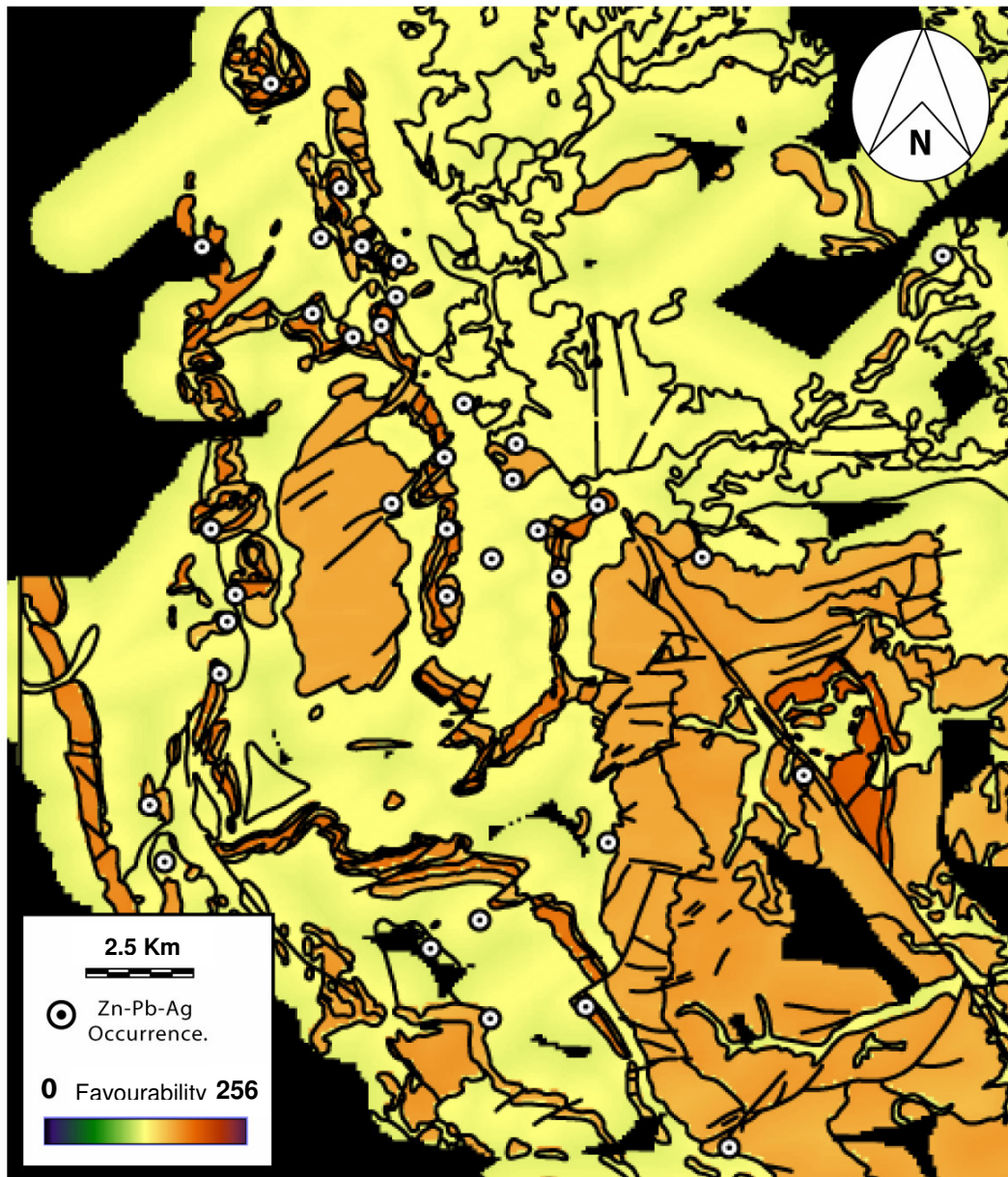
(e)
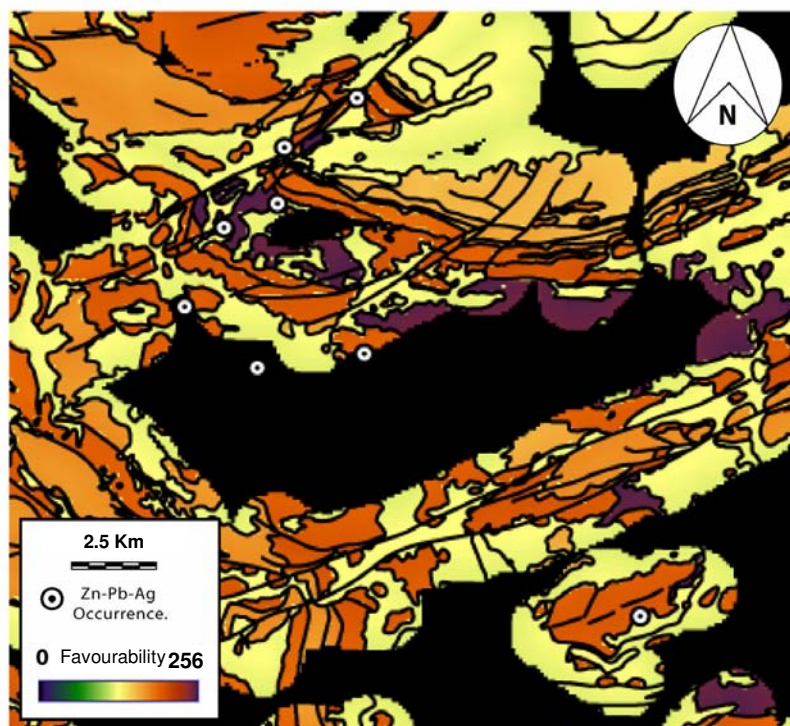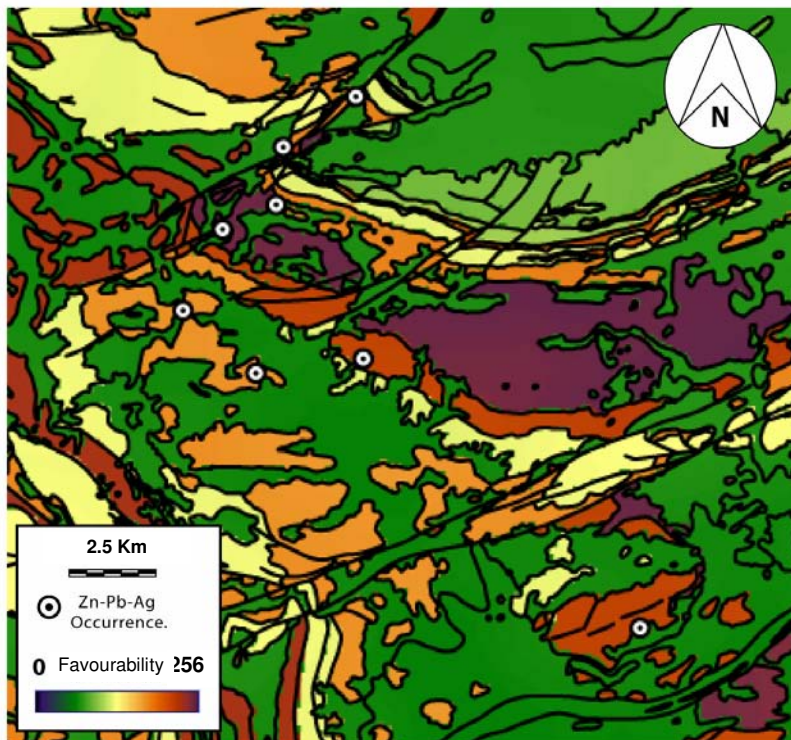
Fig. 3.11 Maps of mineral potential derived from KD-modelling compared against known distribution of mineral occurrences. (a) SEDEX model shows that known deposits are localised within areas where less-permeable units are present. Favourability is dominated by lithological variation rather than fault control (note large 5km fault buffering). The model is not restrictive therefore wide areas may have potential for SEDEX-type mineralisation in the region. However, if we consider the relationship to clusters of small tonnage deposits and Century, the prospectivity may be constrained to areas where a similar spatial association occurs (e.g. the Kamarga Dome Area). This area records also elevated lithostratigraphic potential. (b) VS model with equal weighting for faults and lithological control (1km buffer chosen for faults). Most of the prospect/deposits occur in the northwestern part of the Lawn Hill Region. In contrast, the KD-model output for VS ore predicts the occurrence of mineralisation in the southeastern part of the Lawn Hill Region. This may be explained either as due to relative undiscovered sites in the favourable intervals or to local redistribution of syngenetic mineralisation that would justify the linkage of VS deposits to Century-style mineralisation in less favourable areas. (c, d, e) Enlargements showing chosen subsets with relative clusters of deposits/prospects.

3.5. *Data driven modelling*

The Weights of Evidence approach (WofE) (reviewed in Spiegelhalter, 1986; Bonham-Carter, 1994) was utilised to develop a Data-Driven model for the Lawn Hill Region. An advantage derived from the objectivity of this method is its exploratory nature. As it will be demonstrated in the following sections, the spatial association between known deposits and other geological patterns can be explored in detail using the WofE approach. This method, rather than relying on expert knowledge, defines the probability distribution of each evidential layer by estimating a positive and a negative weight for the degree of spatial association existing between the area distribution of deposits/prospects, and the pattern considered.

3.5.1. Datasets considered within the model and integration with GIS software

An initial phase involves data integration, usually carried out in a GIS environment. The datasets include either geo-referenced, vectorial or raster files with predefined resolution. For this case study, the DD-model considered geophysical datasets in addition to the layers considered in the KD-model. Data were provided by Zinifex Pty Ltd (Formerly Pasminco Pty Ltd) and Xstrata Pty Ltd. These include gravimetric, magnetic (TMI), and Radiometric Airborne Surveys (K-Th-U). Gravimetric and magnetic data provide information relative to deeper structures of the basement and the spatial distribution of igneous rocks, and also may locally aid identification of sulphide mineralisation. The radiometric spectra yield qualitative information on the spatial distribution of certain lithotypes; for instance, the siliciclastic rocks occurring in the study area contain abundant phyllosilicates and feldspars, so their distribution is matched by elevated K and Th signatures. U being a relatively immobile element in its hexavalent state is commonly concentrated in carbonaceous shales that are one of the most prospective lithotypes in the region.

A number of *a priori* assumptions are necessary to construct the model. A unit cell area of 0.1 km^2 was chosen for prospects and deposits, which represents an average size between the super large Century deposit (approx 2.25 km^2) and the smaller veins/lodes (e.g. Silver King, Watson's Lode) (approx. 0.05 to 0.1 km^2). The Prior probability (P_{prior}) expressed as the ratio between the area of known deposits/prospects and the total study area was estimated considering 87 Pb-Zn-Cu mineral occurrences although selecting an area of 0.1 km^2 generated a degree of overlap between some prospects. Overlapping

occurrences were interpreted as coeval and therefore overlapping pixels were counted as being part of a single prospect. This caused a reduction to 82 occurrences to account for the approx. 5.75 % of overlap within the model. Note that unit cell size does not reflect the real pixels of integrated raster layers. Pixel rescaling is implemented, because of the mathematical assumption in the Bayes calculations that have to respect the criterion of 1unit cell = 1 deposit (Carranza, 2002).

3.5.2. Phases of Weights of Evidence modelling

Three phases are fundamental to the Weights of Evidence approach:

(1) Contrast analysis that involves mathematical computation of Weights of Evidence for all the evidence considered, and includes cut-off determinations for buffer selection;

(2) combination of layers using the Bayes rule (e.g. Bonham-Carter, 1994); and

(3) conditional independence (CI) evaluation using multivariate statistical testing (e.g. χ^2, OT and New OT tests).

After the data assembly and establishment of preliminary assumptions, criteria standardization is required. This involves the weighting of evidence layers, and also a ranking of their degree of spatial association with known deposits. These two steps were accomplished using the WofE modeller (software developed by the author at James Cook University). This application has been compiled using Visual Basic Express 2005

integrating Bayesian algorithms. Handling of data and probability calculations are simplified by the use of a GUI (graphic user interface) in a Windows platform (Fig. 3.12).
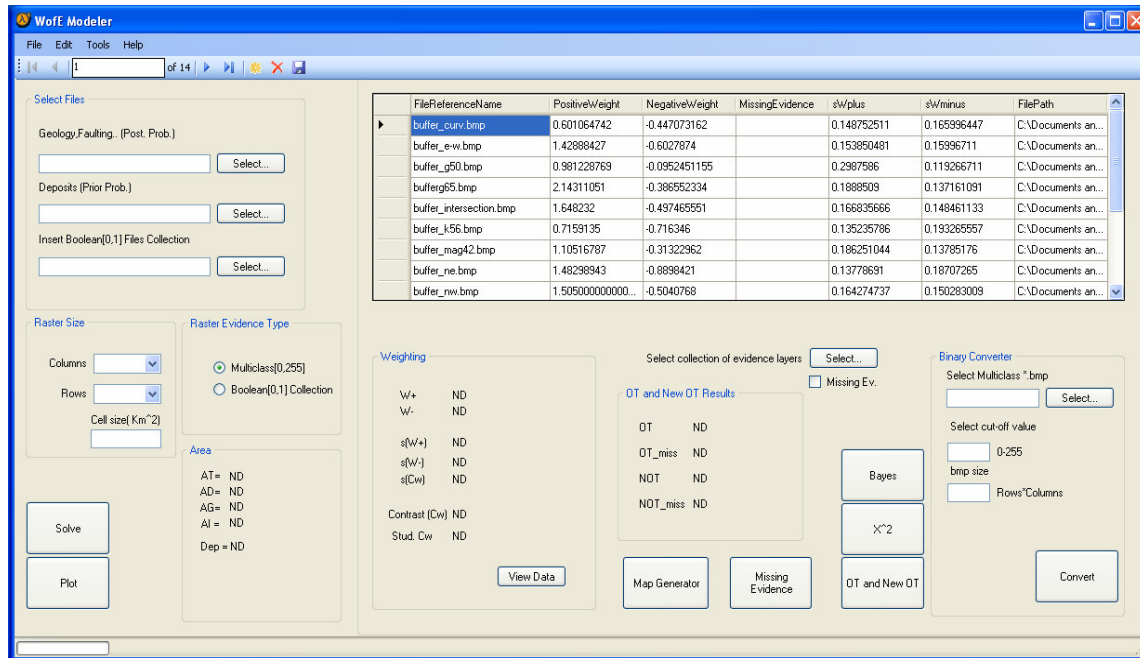
Fig. 3.12 Graphic User Interface (GUI) of the WofE modeller, which was used to perform Bayesian analysis and testing of CI assumptions (see text).

3.5.2.1. Standardization procedure

Algorithms and mathematical assumptions implemented in the WofE modeller are summarised in Appendix B. To measure spatial association the methodology suggested in Bonham-Carter (1994) was implemented, which is considered one of the most widely used for mineral potential mapping (Porwal et al., 2006).

3.5.2.2. Classification of spatial evidence

Three different approaches were utilised to evaluate the degree of correlation amongst geological features (e.g. faulting, lithotypes etc.) and mineralised areas. All of them are based on the Contrast (C) measure. The Contrast is expressed mathematically as the difference between positive and negative Weights of Evidence ($C = W_n^+ - W_n^-$, see Appendix B). It yields positive or negative values; suggesting correlation or inverse correlation. If the Contrast value is zero, there is no spatial association among geological features and deposits/prospects (see Bonham-Carter, 1994).

The methods adopted for the standardization of evidential layers were different, because of the different datasets utilised, and they can be distinguished as follows:

(1) Contrast analysis on multi-class layers obtained from simplification of pre-existing classes was applied to simplify the 32 lithostratigraphic subdivisions considered (see Fig. 3.3). Binary simplification was used before Bayesian analysis as it increases statistical robustness (Agterberg and Bonham-Carter, 2005). This procedure may involve discarding of classes displaying weaker correlation amongst patterns and known deposits (e.g. multiclass geophysical datasets, Paganelli et al., 2002);

(2) Contrast analysis based on cumulative buffers representing distance from geological features was considered for NW, NE, E-W faults, fault intersections, and points of maximum curvature (which represent a parameter similar to the measure of roughness; Blenkinsop et al., 2004). This approach progressively increases the area surrounding the geological pattern considered, providing multiple C values. Usually the maximum Contrast value is chosen. This variation

of Contrast is expressed as a function of distance in a graph (see Fig. 3.13). The Contrast (C) can be used to rank the importance of considered factors; for instance, to evaluate which fault orientations have greater mineral potential. One of the difficulties encountered in the definition of the best buffer was the presence of multiple maximum values for the Contrast (e.g. Fig. 3.13a and 3.13b). The presence of a multimodal distribution produces this type of output reflecting independent classes of spatial association. To improve the interpretation of Contrast curves it is convenient to plot the ratio between C and its standard deviation s(C), which is defined as studentised Contrast (Bonham-Carter, 1994). This parameter, being inversely proportional to error s(C), provides a better way to constrain spatial association and decide which maximum C has to be used for buffer standardization. Highest values of studentised Contrast reflect the best Contrast estimation although in some cases geological interpretation is required to select an appropriate buffer. Several buffer sizes are trialled to obtain the correct maximization of C. Here linear fuzzy membership functions were also used to increase the resolution of the Contrast's curves. This method provided better estimates for the C value and buffer size (conf. Fig. 3.14a with 3.14b). A correct representation of the Contrast is essential to avoid conditional dependences that violate the Bayes rule (see below); and

(3) Contrast analysis of multi-class data based on cumulative buffering, where the centre of each buffer is defined by plotting histograms representing the distribution of multiclass patterns intersecting deposit areas. When standardization is applied to geophysical datasets generally, a reclassification of

the original raster is required (Bonham-Carter et al., 1989; Paganelli et al., 2002). Property ranges are used for buffer definition. The reclassification procedure can be arbitrary, for example, visually the geologist can define certain classes of spatial association between property ranges and deposits. In contrast, a method was trialled in which the centre of the classes is determined by interpreting histogram plots of Boolean intersections of multiclass property layers with the deposit evidential layer. These provide a qualitative analysis of the distribution of peaks of correlation among certain pattern's classes and known mineral deposits (see Fig. 3.15). Both unimodal and multimodal distributions occur. Peak values of association were used for reclassification defining a new number of classes and their centre. The Contrast analysis based on cumulative buffers departing from these selected centres was implemented to define buffer size and Weights of Evidence. Multiclass data were then preserved reducing them to multiple binary files, representing both strong and weak trends of spatial correlation.

(a)

(b)
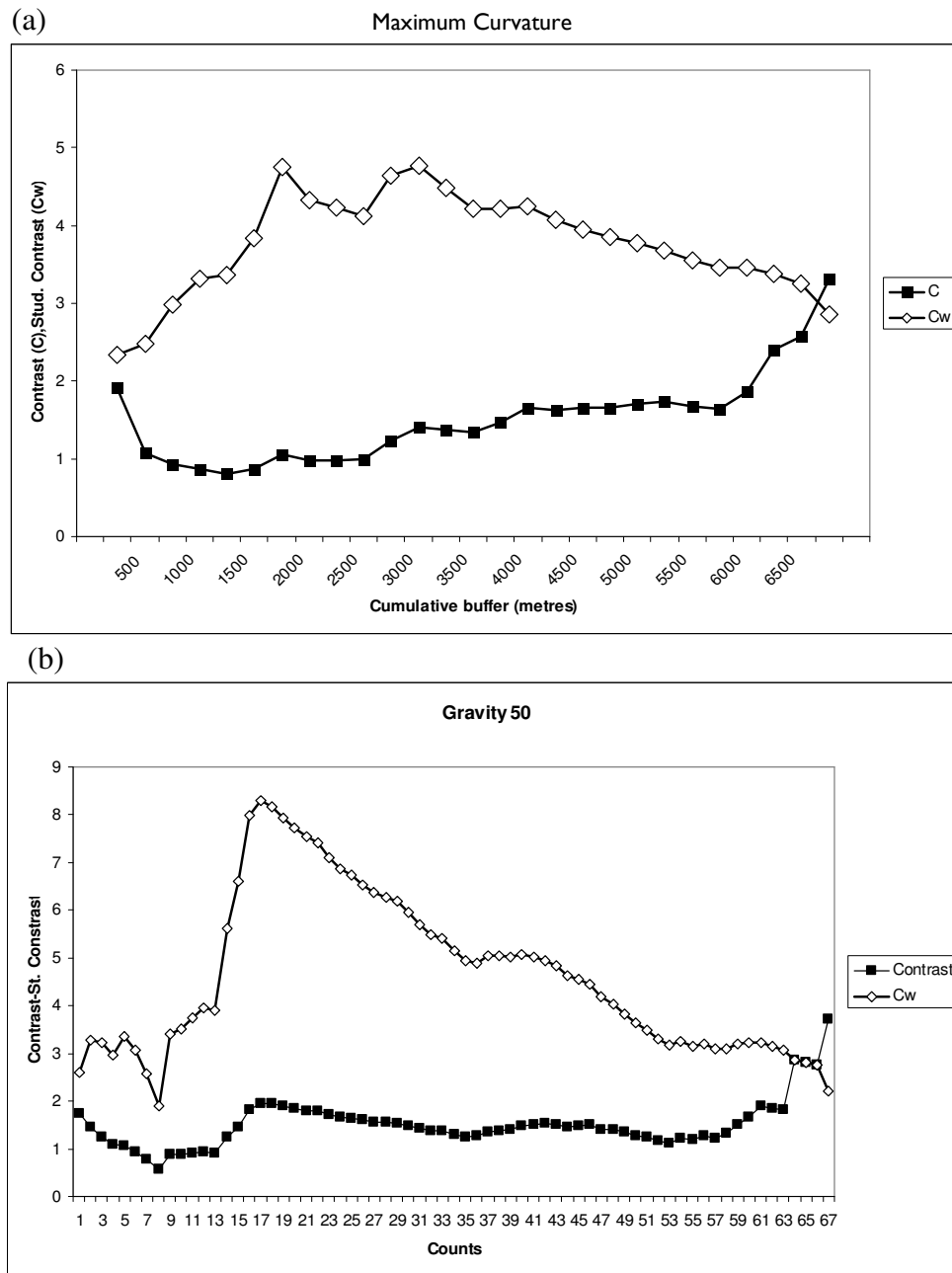
Fig. 3.13 Examples of output of contrast analysis and calculated studentised value (C_w) for the contrast measure (C). (a) Multiple maximum curvature values for C and C_w indicative of multiple spatial correlation of cluster of mineral deposits to certain buffers of the Maximum Curvature evidence layer. (b) Same type of correlation for the Gravity dataset suggesting a multimodal spatial association between certain gravimetric classes and the mineral deposit layer.

(a) NE faults 250 m buffer interval
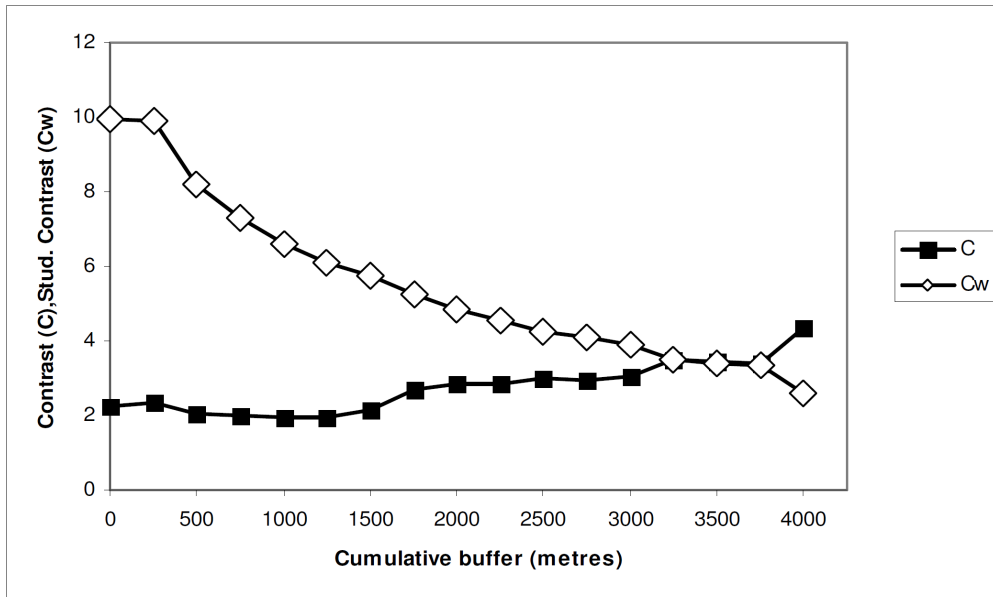
(b) NE faults fuzzy linear rescaling with 16.7 m buffer
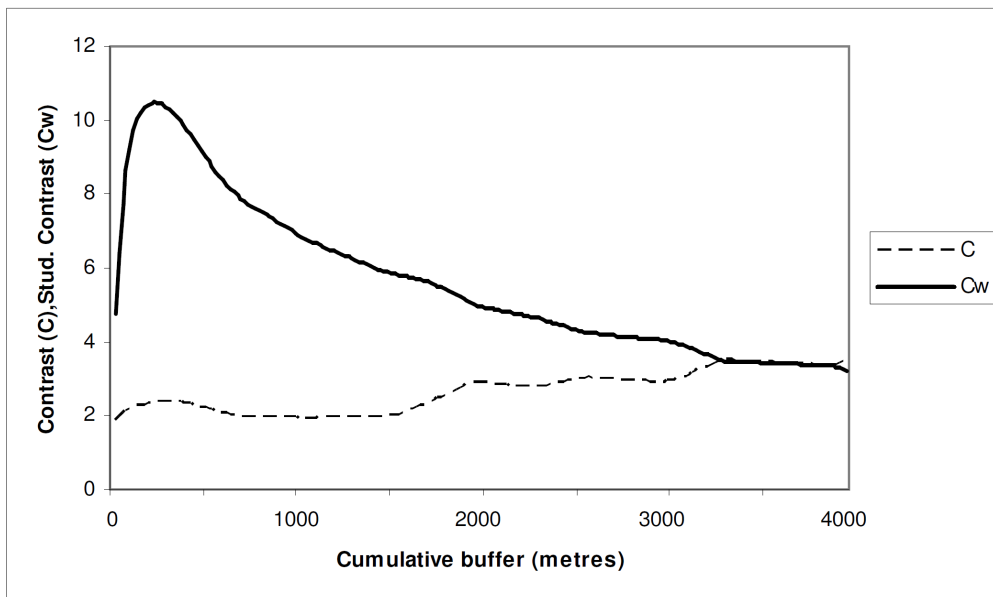
Fig. 3.14 Comparison of conventional contrast approach using constant buffers of 250 m interval with Contrast analysis performed using dynamic rescaling based on fuzzy linear functions. The smooth result allows better selection of the buffer, which reduces the possibility of overestimation of posterior probabilities.
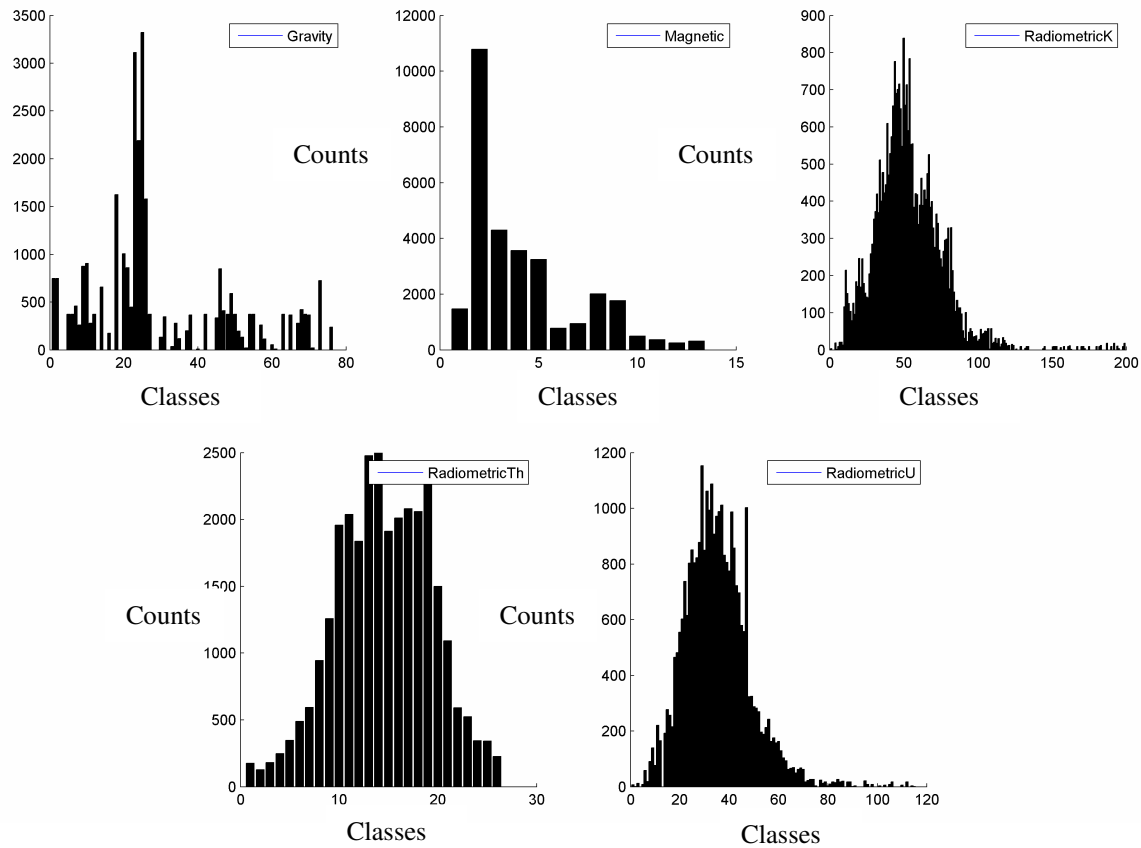
Fig. 3.15 Histograms obtained from Boolean intersection of multiclass geophysical layers. These were used to select the centre of each buffer. Buffer's centres correspond to peaks of correlation and were subsequently used as a starting point for contrast analysis based on cumulative buffering, which was used to select an appropriate buffer size. Gravity and Magnetics datasets have multimodal distributions; therefore, they were subdivided in multiple binary files before contrasting them against the mineral deposit layer.

3.5.2.3. Classification results and ranking

The results of the classification of evidential layers are summarised in Tables 3.2, 3.3, and 3.4. Contrast calculations for the geology were computed over binary layers representing 10 units out of the 36 considered in the previous KD model. This simplification was based on grouping of individual lithostratigraphic units into respective geological formations. Only four units have a studentised C above 1.5 (Pmh, Pa, Pmw, Pmp) and only 3 above 1.95 (Pmh, Pa, Pmw). 1.5 was considered as quality limit for the

Contrast estimation following the recommendation of Bonham-Charter (1994). Contrast results were interpreted considering the error involved in the estimation of the weights, which was calculated following the assumption of asymptotic theory of Bishop et al. (1975), for example Agterberg et al. (1990).

Table 3.2 Weights of evidence computed considering the intersection of deposit area $A(D)$ with each geological unit area $A(P)$ and relative variances s(W), Contrast (C), and studentised Contrast (Cw) for grouped, lithostratigraphic formations outcropping in the Lawn Hill Region.

Lithostrat.	A(D)	A(P)	A(D)/A(P)	W^+	W^-	$s(W^+)$	$s(W^-)$	C	C_w
pmh	17	1121	0.015	2.196	-0.211	0.244	0.124	2.407	8.784
pa	3	230	0.011	1.863	-0.027	0.634	0.112	1.890	2.936
pmw	3	429	0.006	1.270	-0.023	0.622	0.113	1.293	2.047
pmp	1	175	0.008	1.572	-0.014	0.838	0.112	1.586	1.877
pmz	2	763	0.003	0.535	-0.012	0.671	0.112	0.546	0.804
pmr	3	1554	0.002	0.148	-0.005	0.570	0.113	0.153	0.264
pmx	1	678	0.002	0.200	-0.003	0.840	0.112	0.204	0.240
pmt	3	2635	0.001	-0.497	0.023	0.603	0.113	-0.520	-0.847
pml	2	2331	0.001	-0.821	0.028	0.754	0.112	-0.850	-1.114
pms	1	1908	0.000	-1.374	0.031	1.099	0.111	-1.405	-1.272
Tot.	36	11847		0.555	-0.282	0.168	0.147	0.837	3.743
Miss. Ev.	46	35796		-0.282	0.555	0.147	0.168	-0.837	-3.743

   The highest number of occurrences is found in the Pmh formation. Other units have one order of magnitude less occurrences, between 1 and 3. Contrast values obtained are also reflected in the ratios of deposit area versus pattern's area ($A(D)/A(P)$, cfr. Tab. 3.2).

   The scale of variation of negative weights is indicative of the limited outcrop (small pattern areas compared to total regional area). Additionally, 36 occurrences of 82 are included in known Mesoproterozoic outcrop, whereas the remaining 46 occurrences are proximal to outcropping lithologies, but they are found under Palaeozoic cover sediments

unrelated to mineralisation. To address this issue the cover was considered as missing evidence (see below).

Table 3.3 illustrates the results relative to the Contrast analysis of the structural evidence layers. Contrast and studentised Contrast values were used to order the structural patterns as follow: (1) NE faults, which have the higher degree of spatial association with deposits, with a maximum of 45 deposits/prospects within a 500 m buffer. Then following patterns are; (2) NW faults; (3) fault intersections; (4) E-W faults; and (5) maximum-curvature (fault bends). Although fault intersections have higher Contrast compared to NE faults (C $_{intersections}$ = 2.513 vs. C $_{NE}$ = 2.253), the relative variation of C_w is indicative for the intersection layer of more robustness with a larger buffer of 1000 m. This reduces the C value to 2.121. Therefore, NE faults were considered more important than intersections. This consideration is based also on the total number of occurrences that for equal buffer size, appear to be greater in the NE layer with 55 deposits/prospects in the first 250 m. The fault intersections layer reach 53 deposits only at 1500 m buffer. Comparing the different orientations of faults, note that correlation for NE and NW faults is similar. In Contrast, E-W fault buffers contain markedly lower deposits and maximization of the C is reached at 1750 m instead of 500 m. Comparison of curvature versus intersections indicates that fault intersections have greater potential than bends - this is confirmed at all buffers by deposit number and a C value of 2.207 at highest C_w, against a C of 1.055 for the maximum-curvature. All the structural criteria considered demonstrated a strong positive degree of spatial association, suggesting that the structural component is a predominant variable in the Lawn Hill

Region. This would be expected if all the deposits/prospects are fault-hosted examples of vein/lode type.

Gravimetric and magnetic datasets display multimodal distributions - respectively, four and two classes of correlation were defined simplifying original multiclass rasters. Multimodal layers were subdivided in multiple binary rasters representing individual classes of positive correlation. Gravimetric data have the greatest spatial association with deposits/prospects among all geophysical layers. The class Gravity-65 (-892.7 milligals) has the highest value of Contrast and the top value for C and Cw is reached with a buffer between -936.4 and -849.0 milligals intersecting 30 occurrences (Tab. 3.4). Only class Gravity-50 (-1220.4 milligals) other than class Gravity-65 records a studentised Contrast above 1.95 with 12 deposits at maximum C and Cw values. Classes Gravity-86 (-433.8 milligals) and Gravity-113 (156.1 milligals) have lower degree of spatial correlation, and an increasing cumulative buffer results in negative values of Contrast, which indicates negative correlation. These latter two classes appear to be of negligible importance as they never exceed a C_w of 1.95 and buffering never includes more than 10 occurrences within considered ranges of maximization of C. Only initial spikes (see Tab. 3.4 - narrow buffers), are observed in the tabled values for C with relatively large s(C) suggesting inaccurate estimations.

Table 3.3 Weights (W), contrast (C) and relative studentised values (Cw) for cumulative distances from linear and point patterns (fault traces, fault intersections and maximum fault curvature). A(D) deposits area in unit cells, A(P) cumulative buffer areas.

Buffer Dist. (m)	A(D)	A(P)	A(D)/A(P)	W^+	W^-	$s(W^+)$	$s(W^-)$	C	C_w
NE faults:									
≤250	55	8045	0.007	1.801	-0.452	0.174	0.144	2.253	9.969
≤500	59	12296	0.005	1.397	-0.952	0.135	0.195	2.349	9.896
≤750	64	16125	0.004	1.040	-1.004	0.130	0.212	2.044	8.213
≤1000	68	19491	0.003	0.845	-1.131	0.125	0.239	1.976	7.315
≤1250	70	22375	0.003	0.706	-1.233	0.122	0.267	1.940	6.617
>1250	82	47643		0.000		0.111			
NW faults:									
≤250	38	5008	0.008	1.594	-0.187	0.246	0.124	1.780	6.469
≤500	45	7854	0.006	1.493	-0.515	0.163	0.151	2.008	9.031
≤750	52	10638	0.005	1.221	-0.634	0.149	0.166	1.854	8.313
≤1000	59	13268	0.004	1.050	-0.759	0.139	0.184	1.810	7.859
≤1250	60	15767	0.004	0.949	-0.939	0.131	0.208	1.888	7.675
≤1500	62	18024	0.003	0.804	-0.937	0.129	0.216	1.741	6.915
>1500	82	47643		0.000		0.111			
E-W faults:									
≤250	9	1258	0.007	1.822	-0.050	0.465	0.114	1.872	3.906
≤500	15	2125	0.007	1.384	-0.084	0.343	0.117	1.468	4.051
≤750	22	3051	0.007	1.412	-0.156	0.260	0.122	1.567	5.450
≤1000	27	4008	0.007	1.462	-0.255	0.212	0.130	1.717	6.906
≤1250	36	5012	0.007	1.383	-0.318	0.192	0.136	1.701	7.229
≤1500	43	6014	0.007	1.431	-0.465	0.168	0.148	1.896	8.480
≤1750	44	7026	0.006	1.426	-0.605	0.154	0.160	2.031	9.148
≤2000	47	8039	0.006	1.305	-0.620	0.151	0.163	1.925	8.653
≤2250	49	9056	0.005	1.234	-0.677	0.146	0.170	1.911	8.518
>2250	82	47643		0.000		0.111			
Fault intersections:									
≤250	18	1182	0.015	2.479	-0.033	0.592	0.113	2.513	4.169
≤500	29	2792	0.011	2.179	-0.219	0.240	0.125	2.398	8.871
≤750	39	4773	0.008	1.822	-0.385	0.186	0.138	2.207	9.534
≤1000	45	6973	0.006	1.573	-0.548	0.160	0.153	2.121	9.552
≤1250	48	9296	0.005	1.321	-0.631	0.150	0.164	1.952	8.768
≤1500	53	11624	0.005	1.115	-0.682	0.144	0.173	1.797	7.967
>1500	82	47643		0.000		0.111			

Buffer Dist. (m)	A(D)	A(P)	A(D)/A(P)	W^+	W^-	$s(W^+)$	$s(W^-)$	C	C_w
Fault max-curvature:									
≤250	6	1188	0.005	1.900	-0.016	0.813	0.112	1.917	2.336
≤500	12	3065	0.004	1.033	-0.047	0.420	0.115	1.080	2.481
≤750	19	5497	0.004	0.838	-0.094	0.288	0.120	0.933	2.992
≤1000	26	8224	0.003	0.718	-0.147	0.228	0.127	0.865	3.316
≤1250	34	11099	0.003	0.610	-0.192	0.197	0.134	0.802	3.368
≤1500	44	13942	0.003	0.586	-0.276	0.171	0.145	0.862	3.839
≤1750	48	16692	0.003	0.619	-0.437	0.150	0.164	1.055	4.746
≤2000	53	19300	0.003	0.519	-0.456	0.145	0.172	0.975	4.333
≤2250	57	21712	0.003	0.465	-0.515	0.138	0.186	0.980	4.237
≤2500	63	23898	0.003	0.418	-0.570	0.133	0.199	0.988	4.121
>2500	82	47643		0.000		0.111			

Table 3.4 Summary of contrast analyses for considered sub-classes of geophysical datasets.

Buffer Property	A(D)	A(P)	A(D)/A(P)	W^+	W^-	$s(W^+)$	$s(W^-)$	C	C_w
Gravity 50:	12	3056	0.004	0.981	-0.095	0.299	0.119	1.076	3.346
Gravity 65:	30	2653	0.011	2.143	-0.387	0.189	0.137	2.530	10.838
Gravity 86:	4	1917	0.002	0.617	-0.012	0.681	0.112	0.629	0.911
Gravity 113:	2	1063	0.002	1.158	-0.017	0.719	0.112	1.175	1.616
Potassium 56:	57	16513	0.003	0.716	-0.716	0.135	0.193	1.432	6.072
Thorium 17:	61	28001	0.002	0.201	-0.265	0.140	0.181	0.466	2.037
Uranium 48:	67	32416	0.002	0.205	-0.533	0.124	0.243	0.738	2.705
Magnetic 42:	45	17234	0.003	1.105	-0.313	0.186	0.138	1.418	6.121
Magnetic 48:	78	26348	0.003	0.316	-0.335	0.144	0.174	0.651	2.886

Magnetic classes demonstrate higher correlation to the number of deposits compared to Gravimetric classes; they are also represented by buffers that cover a more extensive area causing a substantial decrease of C, lowering therefore their overall impact on the mineral potential. Among Magnetic classes, Magnetic-42 (-777.1 nanoTesla) has stronger positive correlation, with a relatively narrow buffer. The maximum for C and Cw is respectively 1.418 and 6.121. Magnetic-48 (-452.9 nanoTesla) reaches a maximum value

for C of 0.404 within the first buffer, and then progressively decreases until it finds a strong positive correlation that is derived from the influence of class 42. This trend coupled with a lower Contrast value suggests that class 48 has lower degree of spatial correlation.

In contrast with magnetic and gravimetric datasets, radiometric layers (U-Th-K) are all unimodal and approximately of normal distributions. All classes have Contrast value C that never exceeds 1.5. The K class (1.5 cps) shows the highest positive association. A maximum for C of 1.432 is reached at C_w of 6.072. Despite the elevated number of deposits intersected by Th (11.0 cps) and U (22.6 cps) buffers at maximised C_w, these patterns show larger area compared to the K layer, and consequently lower Contrast. However, the U layer was considered in the Bayesian model due to its strong association to organic-rich lithologies and its value of maximum C_w of 2.705, which is above the 1.5 limit of robustness.

A summary of the evidential layers with C_w above a cut-off of 1.5 is presented in Table 3.5. This includes the Weights of Evidence (W^+, W^-) and relative variances $s(W^{\pm})$, the number of deposits/prospects A(D) in overlap with the considered pattern A(P), and relative ratio A(D)/A(P), the calculated Contrast (C), and its studentised value (C_w). Tabulated data were ranked by C to evaluate which layers display the strongest spatial relationship with deposits and prospects. C ranges from 2.530 to 0.738, with all layers demonstrating a positive spatial association. The highest value for the Contrast corresponds to the class Gravity-65 although the Pmh lithotype class has stronger positive correlation (W^+) and higher A(D)/A(P) ratio. The variance of positive weights exceeds 0.2 on the geological map layers; this is due to their size, as they have small areas

intersecting only a small number of occurrences (see Carranza, 2004). Grouping of lithological sub-units was adopted to minimise this type of error. Grouping layers increases the nominal area for a certain lithostratigraphic unit reducing the error on the estimation of the weights $s(W^k)$. Appendix B shows the equation utilised to calculate the standard deviation of the weights following asymptotic assumptions of Bishop et al. (1975). The final layers will be integrated using the Bayes methodology presented in the next section.

Table 3.5 Predictor binary patterns and relative Weights of Evidence, variances and area proportions ranked by contrast (C).

Buffer Class	A(D)	A(P)	A(D)/A(P)	W^+	W^-	$s(W^+)$	$s(W^-)$	C	C_w
Gravity 65	30	2653	0.011	2.143	-0.387	0.189	0.137	2.530	10.838
pmh	17	1121	0.015	2.196	-0.211	0.244	0.124	2.407	8.784
NE	54	7453	0.007	1.483	-0.890	0.138	0.187	2.373	10.213
Intersection	38	4593	0.008	1.648	-0.497	0.167	0.148	2.146	9.608
E-W	43	6221	0.007	1.429	-0.603	0.154	0.160	2.032	9.154
NW	38	5082	0.008	1.505	-0.504	0.164	0.150	2.009	9.024
pa	3	230	0.011	1.863	-0.027	0.634	0.112	1.890	2.936
pmp	1	175	0.008	1.572	-0.014	0.838	0.112	1.586	1.877
Potassium 56	57	16513	0.003	0.716	-0.716	0.135	0.193	1.432	6.072
Magnetic 42	45	17234	0.003	1.105	-0.313	0.186	0.138	1.418	6.121
pmw	3	429	0.006	1.270	-0.023	0.622	0.113	1.293	2.047
Gravity 50	12	3056	0.004	0.981	-0.095	0.299	0.119	1.076	3.346
max-curvature	46	15168	0.003	0.601	-0.447	0.149	0.166	1.048	4.702
Uranium 48	67	32416	0.002	0.205	-0.533	0.124	0.243	0.738	2.705

3.5.2.4. Bayesian analysis

The Bayesian rule of combination assumes a conditional independence (CI) between evidential layers (Bonham-Carter, 1994). This condition is posed to avoid the overestimation of posterior probabilities, which often requires rejection of some evidence.

3.5.2.4.1. *Set theory*

The most intuitive way to describe the Bayesian method of data aggregation is using the Venn notation (Bonham-Carter, 1994; Carranza and Hale, 2000). Fig. 3.16 portrays an example of Venn diagrams that describes the spatial associations between different variables. Areas of overlap of evidential layers within Venn diagrams define a series of positive and negative spatial associations. Intersections can be thought of as a graphical representation of the degree of spatial association between multiple datasets.
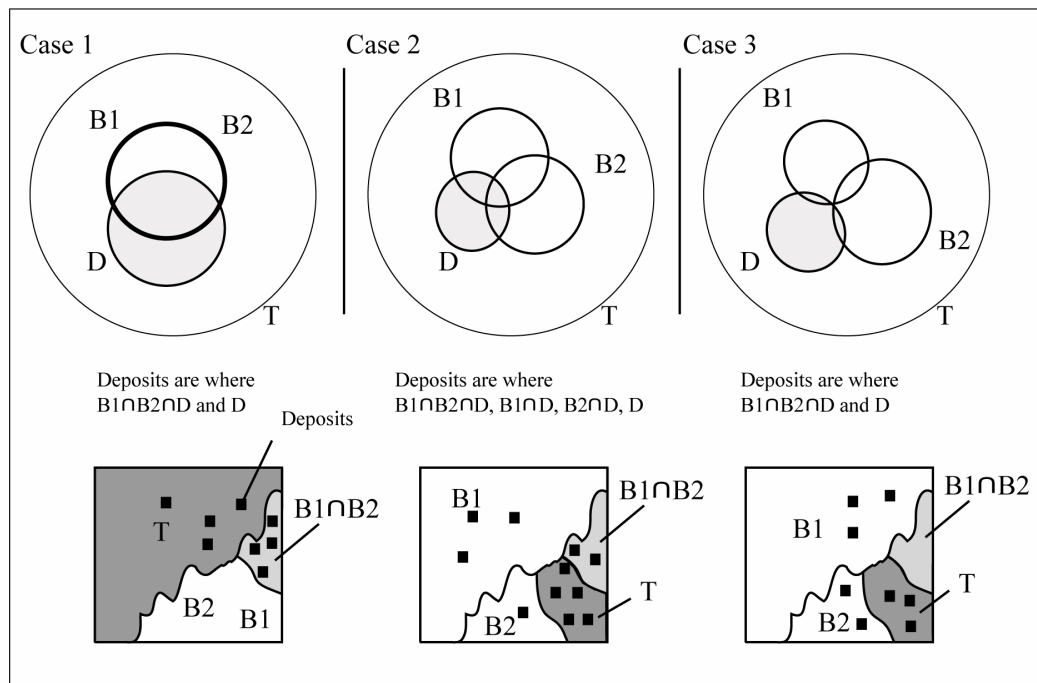
Fig. 3.16 Venn diagrams and schematic plan views representing different conditions of overlap among binary layers. Application of the Bayes rule can lead to overestimation as a function of the type of overlap among patterns and deposit areas. Case 1 shows that if B1=B2 then CI is always violated (see text). Case 2 is the most common example in which CI may be respected or not depending upon the area proportions. Case 3 always violates the conditional independence assumption as double intersection has always value equal to zero; whereas, single intersections are positive (area >0). However, this type of violation is unlikely as patterns are usually chosen maximising spatial correlation to mineral deposits.

3.5.2.4.2. *Definition of P_{prior} and P_{post}*

Usually in mineral potential mapping, a prior probability (P_{prior}) is defined dividing the total area of known mineral occurrences N(D) by the total area of a selected region N(T) containing the mineral deposits/prospects (both terms are expressed in unit cell), $P_{prior} = $ N(D)/N(T). P_{prior} represents the likelihood of finding a mineral deposit in the selected region, estimated using the spatial knowledge of known occurrences. Conventionally every known mineral deposit/prospect occupies a small unit cell area (pixel) (Agterberg et al., 1990), to minimise the errors of estimation s(W^k) respecting the asymptotic theory assumptions (see Appendix B). Consideration of additional themes, for example the NW faults which appear associated with an elevated number of prospects, is a bias for the P_{prior}. New deposits/prospects are expected to be discovered where other NW faults intersect the study area. However, other variables may have influenced the spatial distribution of known deposits. All evidential themes (B_1, B_2, $B_n...B_{n+1}$) are weighted against the mineral deposit layer (D). Positive and negative spatial association is expressed in 2D-GIS as a probability surface. Therefore, a posterior probability (P_{post}) can be defined as the product of P_{prior} with a series of factors representing updating functions, based on the new knowledge of spatial association.

Probability in WofE is represented as Odds (see Appendix B for equations). Odds are also expressed in logarithmic form obtaining a representation of the probability as pri- and postlogit that favours integration (see Appendix B), because simple addition of weights to the prilogit allows combination of evidence (Spiegelhalter, 1986; Bonham-Carter, 1994). This approach can be defined as the Bayes rule of combination.

3.5.2.5. Conditional independence testing

3.5.2.5.1.   Meaning of conditional independence

As previously introduced, a Bayesian model is based on the assumption that conditional independence (CI) between overlapping patterns is unviolated. The model assumes that calculated Weights of Evidence must be derived from patterns that are independent of one another. Thiart et al. (2003) remark that it is unlikely that such conditions will be fulfilled when overlapping multiple themes. It is natural then to raise questions regarding the extent of violation and also to define where such violations occur to understand where the probabilistic model is responding with overestimation. Therefore, to quantify and qualify CI, multivariate statistical tests commonly used to define the interval of confidence were adapted to mineral potential applications (e.g. G^2, see Agterberg et. al., 1989; χ^2, Bonham-carter, 1994; OT and New OT, Agterberg and Cheng, 2002, and Carranza, 2004). The CI assumption can be algebraically defined, for a two-layer model, as:

$$P\left(B1 \cap B2 | D\right) = P\left(B1 \cap D\right) P\left(B2 \cap D\right) \tag{3.1}$$

This equation states that the joint probability $P(B1 \cap B2 \mid D)$ of finding a mineral deposit (*D*) at the intersection of two patterns (*B1, B2*) must be equal to the product of the independent probabilities of finding occurrences within *B1* and *B2*. Areas of intersection

vary as a function of selected patterns and, as a consequence, the above relationship can be either satisfied or not.

3.5.2.5.2   *Graphic approach to understand CI*

To better define the significance of the CI assumption an example is proposed that considers two patterns that exactly coincide, i.e. *B1 = B2* (Fig. 3.16, case 1). Being equal patterns the two layers have analogous spatial association with the mineral deposits and therefore equal weights (W^k). Assuming that the mineral deposit areas are relatively small, then the posterior probability resulting from the doubling of patterns *B1* and *B2* will be e^2, which is 7.4 times larger than if the two layers are conditionally independent (Agterberg and Cheng, 2002). A comparison between different types of intersections is presented in Fig. 3.19. The previous example, adapted from Agterberg and Cheng (2002), represents an end-member condition (Case 1) in which CI is always violated as the double intersection *B1* ∩ *B2* ∩ *D* is equal to *B1* ∩ *D* and *B2* ∩ *D*. The Case 2, adapted from Bonham-Carter (1994), is a more generalised example of pattern overlap that can lead either to violation or non-violation of conditional independence. Case 3 represents the counterpart to Case 1 and has zero probability of finding a mineral occurrence where B1 and B2 intersect one another. However, both patterns show spatial association with mineral deposits. Case 3 leads to CI violation. This consideration suggests that violation of CI might occur also when patterns tend to overlap without having equal spatial association with mineral deposits. However, the latter example is rare as evidential layers are chosen and standardised aiming at maximizing correlation. The Illustrated examples suggest that CI will be violated more likely if proximal to end-member conditions (Case

1 and Case 3), which means when the areas of intersection $B1 \cap D$, $B2 \cap D$ and $B1 \cap B2$ $\cap D$ are equal or tend to zero.

3.5.2.5.3   CI tests

Overestimation of posterior probability due to CI violations is reduced in different ways; the simplest approach is to reject evidential themes that cause CI violation (e.g. Thiart et al., 2003). However, in some cases (e.g. considering geochemical patterns) it is convenient to merge problematic themes using logistic regression or principal component analysis (Agterberg, 1992; Carranza, 2004).

CI violation can be assessed using goodness of fit tests (e.g. Bishop et al. 1975), or alternatively using overall calculations of posterior probability. Both approaches can be used to identify which layers induce violation although the latter allows testing of multiple layers, reducing the number of iterations required to identify problematic patterns.

The first approach makes use of Pearsonian statistics (Chi-square) (see Bonham-Carter, 1994) or likelihood-ratio statistics (G^2 e.g. Bonham-Carter et al., 1989) that can be used for multinomial or Poisson distributions (Bishop et al., 1975). These tests are commonly pairwise and run on fourfold tables constructed to attribute a structure to the data. Tests for the goodness of fit are limited to areas intersecting deposits in mineral potential applications (Fig. 3.17). The probability of occurrence in a certain cell is indexed by two characteristic variables (i, j) that define its dependency from chosen parameters. In addition to internal probabilities, marginal unconditional probabilities are calculated to obtain maximum likelihood estimates. It is of particular interest to explore

the difference existing between internal and external (marginal) probabilities in a fourfold table, to evaluate spatial association. Two equations are commonly used to calculate respectively Chi- and *G*-square statistics:

$$\chi^2 = \sum_{i=n}^{n} \frac{\left(O_i - E_i\right)^2}{E_i} \tag{3.2}$$

$$G^2 = \sum_{i=n}^{n} x_i \ln\left(\frac{\hat{m}_i}{x_i}\right) \tag{3.3}$$

The first represents the summation of the squared differences between expected (*Ei*) and observed (*O_i*) frequencies of unit cells (*n*). *G*-square is distributed as χ^2 with 2 degrees of freedom (Bishop et al., 1975) with $\hat{m}$ representing the predicted area versus observed area in unit cells. If $\hat{m}$ differs strongly from *x,* the test fails. Both methods consider a centred sampling distribution to fulfil the null hypothesis (*H_0*); therefore, Chi- or *G*-square estimates tend to zero when there is no difference among patterns. Commonly a p-value (alpha) is defined choosing an interval of confidence (e.g. 95%). If the calculated p-value is less than the chosen value the test is rejected. The chosen p-value corresponds to the value limit for acceptance of Chi- or G-square results. Statistical tables are available for comparison. Tabulated values are ordered by chosen alpha, but also they vary as a function of the degree of freedom (*df*), which is the number of parameters that may be independently varied. *df* is then function of the number of evidential layers, but also the number of classes within a single theme contributes augmenting its value. For example, the *df* is calculated for a 2x2x2 table as follow:

$$df = (n - classes\ within\ theme\ B1 - 1) \times (n - classes\ within\ theme\ B2 - 1) \tag{3.4}$$

Results of Chi- or G-square statistics have to be carefully evaluated. Here I briefly discuss the problem relative to the Chi-square analysis as this approach was preferred and implemented in the WofE modeller considering the examples proposed in Bonham-Carter (1994). The software is capable of choosing automatically all the possible n-pairs of evidence and calculating multiple Chi-square values based on the fourfold table previously introduced (Fig. 3.17). Note that several limitations apply to this methodology and this test cannot be considered statistically robust (Bonham-Carter, 1994). Chi-square results should be considered in relationship to others and not in an absolute sense; this is due to their dependency from the area of study, and also from the resulting area of intersection among patterns and deposit layers. Area dependency for example means that having a limited number of deposits may induce erroneous results because of low expected frequencies in the contingency table (Snedecor and Cochran, 1967; Bonham-Carter, 1994; Carranza, 2002). This is mainly due to the limit conditions of the asymptotic result commonly used in case of finite random variables (Bishop et al., 1975). In a mineral potential example if the number of samples (deposits) is small and resulting prior probability is close to 0, the approximation is poor. It is possible then to apply the Yates correction (see following equation) inducing a reduction of the final Chi-square values; however, the correction cannot be applied if the absolute value of the difference between observed and expected counts is lower than 0.5 (Bonham-Carter, 1994). In any case if the expected value in any cell is less than 5, the Chi-square results are inaccurate.

More empirical estimations such as the Overall test (Bonham-Carter, 1994) and the New Omnibus Test (Agterberg and Cheng, 2002; Thiart et al., 2003; Carranza, 2004)

were integrated in the WofE modeller to offer an alternative to pairwise Chi-square tests. The main reason for relying on multiple tests is that they offer a comprehensive evaluation of conditional independence and help substantially when recombination or rejection of evidence is required. Overall tests can be applied after Bayesian combination, over multiple layers. Experimental results presented in the next session suggest that CI is not only a function of the overlapping conditions occurring among positive patterns (as assumed in pairwise Chi-square testing), leading in several cases to discrepancies between Chi-square results and overall tests. Therefore, assessment of CI with different methodologies is considered essential to the more complex cases involving a large number of evidential layers such as the application presented below, with a total of 14 themes. Two linear equations that reflect sums of post-probability summarise the methodology and logic of these tests:

$$N(D)_{Pred} = \sum_{k=n}^{n} \left(P_k \, N(k) \right) \tag{3.5}$$

$$NOT = \frac{N(D)_{Pred} - N(D)}{s\left(N(D)_{Pred}\right)} \tag{3.6}$$

These kernel algorithms simply compare the number of known deposits $N(D)$ in a certain region (P_{prior}) with the number of predicted mineral deposits or prospects $N(D)_{Pred}$ obtained from (P_{post}) overall values. A posterior probability map can be imagined in 3D as composed of columns of pixels (unit cells) that carry different weights depending upon their spatial location (Fig. 3.18). Each column is part of a certain class (i) of pixel columns with a total posterior probability (P_k). Each class (k) has a certain size defined

by the area of occupancy expressed as pixel number $N(k)$. The overall posterior probability (number of predicted deposits) can be estimated summing up the products of all known classes k_n for their respective n-pixels of occupancy. The total posterior probability can be converted back to a hypothetical number of deposits multiplying by the overall P_{post} for the total number of unit cells $N(T)$. Bonham-Carter (1994) firstly adopted this methodology suggesting that a cut-off of 10-15% (OT value of 0.85) has to be considered as a limit for violation. In other words, CI is violated when predicted deposits are 10-15% more than known occurrences, and OT results are lower than 0.85. There is however uncertainty regarding the imposed limit that is set purely on an empirical base and may be too conservative (Thiart et al., 2003). In fact, lower limits might still be acceptable if comparing results from WofE with Logistic Regression analysis (Thiart et al., 2003). Similar results are illustrated in the following application where excessive OT conservativity was revealed by comparing OT with NOT results.
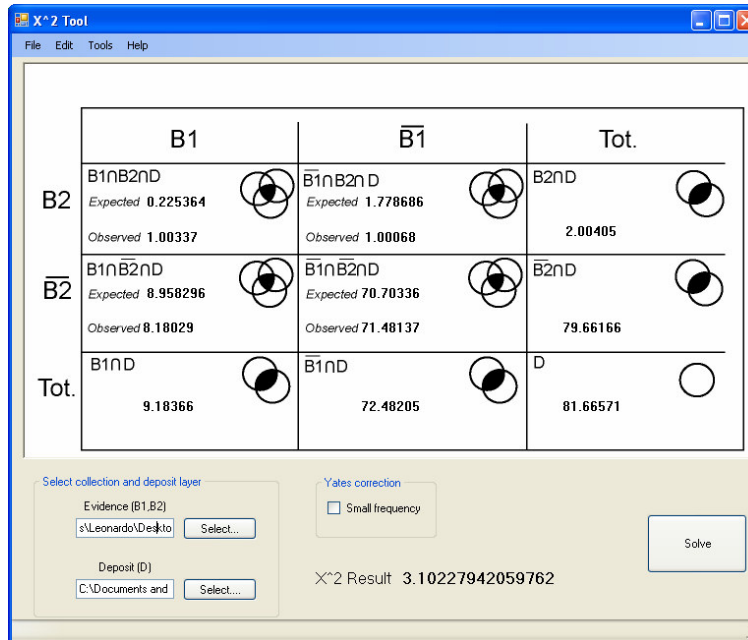
Fig. 3.17 Example of χ^2 output of the WofE modeller (Appendix E) showing a contingency table in which partial output of the χ^2 analysis can be assessed to allow application of Yates correction if required (see Bonham-Carter, 1994). The overall χ^2 value is also computed and displayed, additionally a *.txt file is saved if multiple layers are considered rather than just a binary couple (B1, B2).
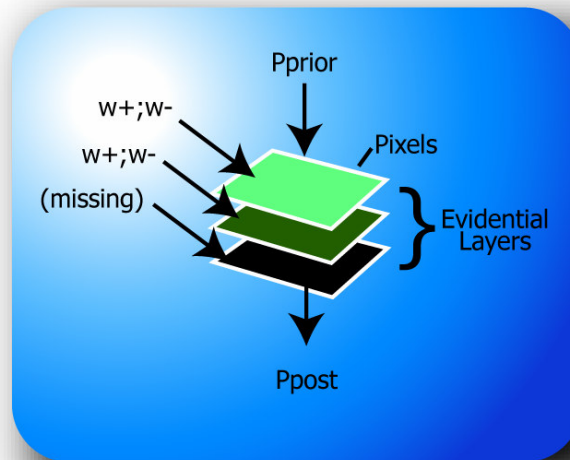
Fig. 3.18 Diagram portraying Bayesian combination of multiple evidential layers. Each evidential layer is composed of n-pixels. These can be imagined as part of columns of multiple n-pixels in case of multiple layers. n-columns correspond to n-combinations of n-weights and or missing information. Sum of evidence in each pixel column can be seen as an overlap relationship in which initial Pprior is updated to give a final Ppost.

To refine the results of the OT test Agterberg et al. (1993) has applied the Kolmogorov-Smirnov statistic for the goodness-of-fit assuming that the P_{post} distribution approximates normality. This test fits the observed P_{post} distribution to a cumulative curve representing a normal distribution. Usually P_{post} are firstly divided by the total number of known occurrences D, and afterwards are plotted within a confidence envelope. If observed P_{post} /D values exceed this interval the test fails (e.g. Agterberg and Cheng, 2002, Bonham-Carter et al., 1989). The validity of this test for mineral potential mapping applications is briefly discussed in Agterberg and Cheng (2002). Before applying the goodness-of-fit test it is preferable to evaluate the null hypothesis (number of predicted deposits equal to number of known deposits), which is equivalent to the CI hypothesis. In Weights of Evidence modelling the maximum difference is generally expressed as $(N(D)_{Pred}/N\{D\} - 1)$. Testing in advance the proposition $N(D)_{Pred}=N\{D\}$ would be reducing the maximum difference to zero allowing application of the Kolmogorov-Smirnov statistic. The proposition can be tested statistically as it is possible to calculate the s^2 $(N(D)_{Pred})$ see Appendix B. Briefly the error estimate of $N(D)_{Pred}$ is derived from the errors estimated for the Weights of Evidence.

In this context the NOT (New Omnibus Test) represents an improved formulation of the OT test, in which the uncertainty in the estimation of $N(D)_{Pred}$ is introduced as additional parameter (see equation 3.6). Note that the variance of the posterior probability $s^2(P_{post})$ inherits the asymptotic approximation assumptions as it is based on the variance of the weighs of evidence calculated using the formulas based on asymptotic approximation of Bishop et al. (1975). Therefore, this test is statistically more robust than the OT allowing a better qualification of probability estimates although it is more

effective on large populations. The effect of CI violation induces underestimation of the standard deviation of P_{post} incrementing the NOT result. Therefore, the NOT test is more sensible to CI violation. NOT results approximate a normal distribution that can be used to calculate p-values that are finally compared against a certain confidence interval alpha, as previously seen for the Chi-square tests, although in this latter case a normal distribution is fitted to the data.

3.5.3. Uncertainty from missing evidence

As mentioned an estimate of the error involved in the calculation of P_{post} is available $s(P_{post})$. This parameter depends upon the uncertainty of information gathered. When information is lacking, for certain areas, and in some if not all evidential layers, then uncertainty of P_{post} will be higher compared to unit cells where information is complete for all patterns. To account for missing patterns the methodology of Agterberg et al. (1990) was implemented in the WofE modeller. Mathematically, ignorance is expressed considering any P_{prior} as an expectation function (Ex) of P_{post}. In other words, P_{prior} may be closely matching P_{post} and the certainty regarding this hypothesis (expectation) is function of the amount of available evidence $P(x)$ that may support a prior estimate. This concept can be expressed as an iterative sum of evidence:

$$P_{prior} = \int P_{Post} \cdot P(x)\, dx = Ex\left[P_{Post}\right] \tag{3.7}$$

Considering two patterns *(B1, B2)* updating a $P_{prior} = P(D)$ the iteration becomes a finite sum of probabilities multiplied by a weighting coefficient that depends upon their respective area of occupancy expressed as $P(B_i, B_j...B_n)$ and relative intersection with known deposits *D*. The final equation becomes then:

$$P(D) = P(D|B1, B2) \cdot P(B1, B2) + P(D|\overline{B1}, B2) \cdot P(\overline{B1}, B2) +$$
$$+ P(D|B1, \overline{B2}) \cdot P(B1, \overline{B2}) + P(D|\overline{B1}, \overline{B2}) \cdot P(\overline{B1}, \overline{B2}) \tag{3.8}$$

All possible combinations of *B1* with *B2* update the P_{prior} in a different manner. The relative uncertainty involved in this calculation, in case of a single missing evidence layer, can be defined as the sum of the square difference between P_{post} calculated without missing evidence and P_{post} calculated for missing evidence. For one layer of missing information P_{post} becomes P_{prior}. The variance $s_m^2(P_{post})$ is obtained then by summing up these partial variances weighted by their relative area proportions, similarly to the expectation function:

$$s_m^2\left(P_{Post}\right) = \left[P\left(D|B1\right) - P(D)\right]^2 \cdot P(B1) + \left[P\left(D|\overline{B1}\right) - P(D)\right]^2 \cdot P\left(\overline{B1}\right) \tag{3.9}$$

A numerical example of its application is found in Carranza (2004). Missing patterns affect the calculation of P_{post}, not only its variance (Appendix B for equation). The results obtained can be used to map the spatial distribution of uncertainty across the study area; however, this tends to resemble the overall pattern of P_{post} (Agterberg et al. 1990).

Once the calculation of the error involved with missing patterns is completed, its value is simply added to the error derived from the calculation of weights (W^+, W^-). Both terms are calculated on a pixel (unit cell) base, and their overall sum is obtained and imputed in equation (3.6) for NOT calculation.

There is then a double component of error involved in the estimation of P_{post} that is a function of uncertainty in the value of P_{post} due to missing evidence and also an error due to the asymptotic approximation adopted. Limits of this methodology are remarked in Bishop et al. (1975, Chapter 14). A way to improve P_{post} calculation might be to consider, similarly to what Agterberg et al. (1989) suggest, a map that represents the ratio between P_{post} and $s(P_{post})$. The methodology of rejection could be then based on the rejection of pixel columns (rather than entire layers of information) tested in term of both uncertainty of estimation and also CI violation.

3.6. Pb-Zn mineral potential for the Lawn Hill Region

The final outcome of the posterior probability analysis is a map composed of evidential themes that passed CI tests for conditional independence. A reduction from fourteen to eleven layers was required to ensure CI acceptance under described statistical tests. However, to obtain such results a multiple testing procedure was established because the number of layers was large. With multiple layers, N^2 combinations are possible (N is the number of layers) although some simplification arise from the problem symmetry, reducing the number to ($N^2 - N/2$). Therefore, having an initial number of 14 layers, a total of 91 binary combinations were tested using χ^2 statistics for CI (Fig. 3.19).

One of the advantages of the WofE modeller is its internal algorithm for pairwise combination that automatically determines the N possible couples providing comprehensive Chi-square statistics. A summary of the results is presented in Fig. 3.19; the diagram illustrates the Chi-square output for each possible combination and is ordered as a function of the magnitude of Chi-square values, which is equivalent to the distance from the null hypothesis (H_0). Nine couples were selected for further comparison with OT and NOT tests. Selection criteria aimed to include values that violated CI for the following intervals of confidence: (1) a Chi-square of 5.4 at 98% and (2) a 3.8 value for a confidence interval chosen at 95% of the Chi-square distribution (see Bonham-Carter, 1994; Walker and Lev, 1953). Overall results and chosen couples revealed that:

(1)   Approximately 10% of combinations violate the Chi-square test;

(2)   only geophysical and structural patterns revealed a CI violation issue; and

(3)   multiple pairwise Chi-square comparison can be used to define how much a layer is contributing to CI violation throughout its interrelationship with other themes. Binary themes were ranked using this consideration showing that the intersection layer was the most troubled pattern followed then by northwest oriented faults, gravity-65, magnetic-42, gravity-50 and finally the east-west faults.

In several cases, the frequency for expected values of contingency tables were lower than five (reducing robustness). The Chi-square tests demonstrated a higher sensibility to CI violation if compared to the overall tests. This might be exclusive of the examined area, but more likely was linked to the different approach utilised by these latter methods in assessing CI. Chi-square analysis considers exclusively areas of patterns intersecting

the mineral occurrences layer (D), whereas Omnibus (Overall) tests consider all the unit cells in the model. To further understand this difference, OT and NOT were run on the same combinations identified as violating CI after Chi-square analysis, for comparison (see Tab. 3.6, comparison CHI OT NOT). Results suggest the following considerations: three combinations failed all tests; these include only structural layers (Intersection, NW, NE and E-W). All the other cases failed for Chi-square, but passed both OT and NOT. This discrepancy depends on area proportions and relative pattern overlap. For the Lawn Hill region, the area between any pattern and known occurrences do not exceed a maximum of 8.2 km^2, which is a relatively small area compared to the total area of 4764.2 km^2. Therefore, the number of pixels contributing with negative spatial association (W$^-$) is always greater than pixels having positive association. Described spatial interactions cause then a reduction of the overall estimation of posterior probability justifying the difference among tests and resulting estimates proximal to 1 for the OT, and 0 for the NOT tests (Tab. 3.7). Note also that failure of OT and NOT is occurring within layers that have the larger areas of positive spatial association (W$^+$).

Table 3.6 Comparison of CI results of chi-square pairwise evaluation against OT and NewOT tests.

Couples		$\chi2$	$\chi2$ *(Yates corr. applied)*	*OT*	*(OT)*	*NOT*	*(NOT)*
Gravity65	Magnetic42	33.290	30.198	1.075	passed	-0.557	passed
Gravity65	Fault intersections	27.267	24.575	0.950	passed	0.365	passed
Gravity65	Northwest faults	23.280	20.805	0.989	passed	0.082	passed
Magnetic42	Fault intersections	12.300	10.722	0.951	passed	0.432	passed
Northwest faults	Fault intersections	10.814	9.394	0.674	failed	2.038	failed
Northwest faults	Magnetic42	9.704	8.312	0.959	passed	0.327	passed
Northwest faults	Gravity50	7.977	6.053	1.041	passed	-0.277	passed
Northeast faults	Fault intersections	6.444	5.314	0.629	failed	2.226	failed
Fault intersections	East west faults	5.436	4.446	0.804	failed	1.421	failed
Magnetic42	Gravity50	5.207	3.621	1.040	passed	-0.263	passed

Table 3.7 Omnibus and New-Omnibus test results for multiple combinations of evidential themes.

Groups	n-layers	OT	(OT)	NOT	p(NOT)	(NOT)
Missing evidence absent						
Structure	5	0.209	Failed	4.957	0.000	Failed
Geology	4	1.005	Passed	-0.023	0.509	Passed
Geophysics	5	1.108	Passed	-0.920	0.821	Passed
Structure + Geophysics	10	0.174	Failed	11.970	0.000	Failed
Structure + Geology	9	0.192	Failed	5.723	0.000	Failed
Geology + Geophysics	9	0.898	Passed	0.909	0.182	Passed
Total Evidence	14	0.163	Failed	13.831	0.000	Failed
Optimised Evidence	11	0.481	Failed	5.798	0.000	Failed
Missing evidence present						
Geology	4	0.851	Passed	0.007	0.497	Passed
Structure + Geology	9	0.177	Failed	1.474	0.070	Failed
Geology + Geophysics	9	0.789	Passed	0.037	0.485	Passed
Total Evidence	14	0.153	Failed	6.101	0.000	Failed
Optimised Evidence	11	0.437	Failed	0.460	0.323	Passed
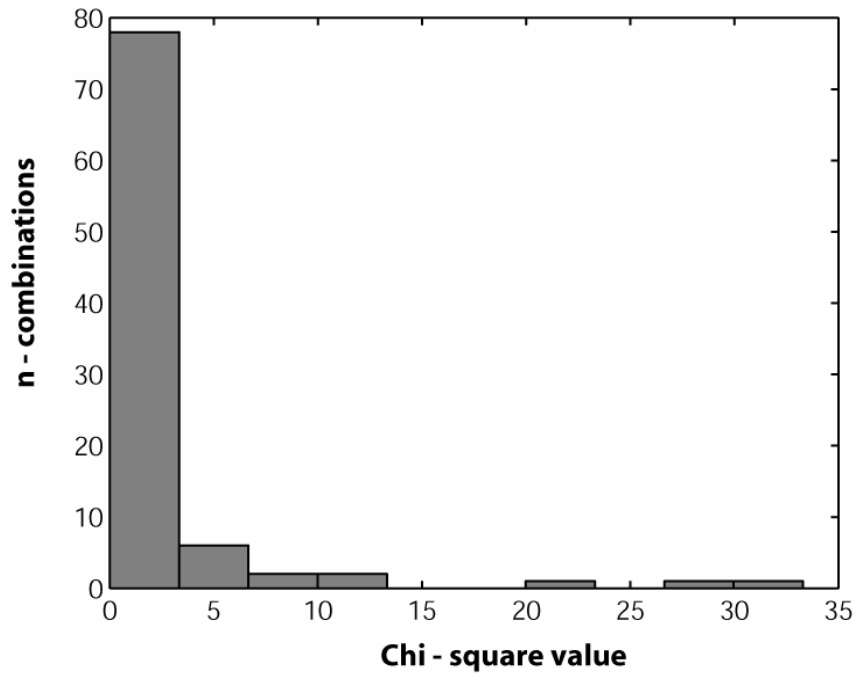
Fig. 3.19 Histogram of 91 pairwise combinations obtained using the WofE modeller (χ^2 tool). Most of the couples pass the χ^2 test at 95% confidence. Couples that violate the χ^2 test were considered in additional CI tests for comparison (see text).

To further validate the mineral potential model, the 14 layers were grouped distinguishing them by type (Structural, Geological, and Geophysical), and running multilayer OT and NOT tests either on separated groups or coupling them (see Tab. 3.7). Outcomes of this analysis include also OT, NOT tests for a full (14 layers) model, and a final optimal combination with 11 layers, rejecting the intersection, curvature and E-W layers to show P_{post} variation during rejection procedure.

Serial rejection tests were carried out firstly evaluating possible internal CI violations within selected groups. Among the 3 multiple sets only the Structure-set failed both overall tests. Geology- and Geophysics-sets passed all overall tests confirming that the Structure-set has the only internal violations of CI. In contrast, the geophysical pattern is showing underestimation of P_{post}, e.g. OT records a value of 1.1 (Tab. 3.7). The observed relation suggests that serial analysis may help revealing CI violation but also can be used to understand why certain combinations tend to smooth CI problems as they reveal underestimation cases in addition to troubled CI layers.

Coupling of groups suggested that CI violation was also occurring among them (e.g. Structure and Geology). In fact, all the combinations including the Structural-set failed both overall tests. When also the Geophysics-Geology combination passed OT and NOT tests, it was concluded that only the Structural group had CI violation issues. Therefore, a rejection of some of the structural layers based on the degree of violation assessed comparing the different tests (Tab. 3.7), led to an optimal model that passed CI tests in the case of missing evidence. As seen in the examples presented in Thiart et al. (2003) and Carranza (2004), consideration of missing patterns tends to increase the number of

predicted mineral deposits/prospects, favouring rejection of OT, but at the same time favouring acceptance of the NOT test (see equation in Appendix B).

The NOT results satisfy the condition imposed by the Weights of Evidence method with a value of 0.460 and p-value of 0.323, which is greater than an alpha of 0.05 at 95% confidence. This result was computed using the WofE modeller, which can treat uncertainty due to missing information during estimation of posterior probabilities and relative standard deviation induced by a missing pattern s_m (P_{post}). The software was also designed to handle multiple missing patterns, to improve multilayer OT and NOT tests. It allows loading one or more binary files representing a missing evidence pattern for each evidence theme considered in the P_{post} model. Integrated patterns are used to update the Weights of Evidence, converting the weights calculated with Contrast analysis to zero if they represent a missing pattern. Additionally, WofE computes the $s_m(P_{post})$ that is added to the error derived from the weights approximation s(W).

The results presented in Table 3. (including the final P_{post} model based on 11 layers), represent examples of OT and NOT variation considering missing patterns. Four missing evidence patterns were considered to account for additional uncertainty within geologic units that were obtained from recombination of twenty lithostratigraphic classes (same classification as KD model above, but simplified into formations, see Fig. 3.3). Areas counted as missing evidence represent Post-Proterozoic cover sediments that might be hiding undercover mineral deposits. This also is an obstacle to the correct assignment of Weights of Evidence and their calculation. Recalculation of post probabilities was then undertaken considering a common missing pattern representing the cover.

Values of OT and NOT (Tab. 3.7) are suggesting, in agreement with the observation of Agterberg and Cheng (2002) and Carranza (2004), that considering missing evidence generally improves the result of overall tests for conditional independence, as indicated by the relative increase of OT and decrease of NOT values. Equation 3.6 expresses dependency of CI violation from two parameters: (1) P_{post} values vary accordingly to weights variation depending on the proportion of pixels converted to zero when missing information is considered; and (2) Number and extent of missing patterns influence the estimation of $s_{Tot}(P_{post})$ as $s_{Tot}(P_{post}) = s(P_{post}) + s_m(P_{post})$. In the Lawn Hill region example, the missing patterns occur mostly where weights revealed negative-correlation to mineral deposits/prospects (W). If these areas are considered as missing patterns then an increase of the P_{post} is expected due to the omitted effect of negative correlation, which contributes to violation. The OT result fails the test with a higher value, confirming this hypothesis. Nonetheless, the increased uncertainty in the calculation of P_{post} plays an important role controlling the validity of NOT tests. The NOT result revealed that the missing information may be a determinant in reducing violation of CI, in particular for circumstances as shown previously with an 11 layer model. Even though the OT test fails, the model passes the NOT test. Indeed this result is consistent with remarks of Thiart et al. (2003) who compared OT and NOT results. In this regard the more statistical robustness of the NOT test was considered as a guideline to ascertain validity of the mineral potential model. The empirical violation limit of 0.85 for the OT test (Bonham-Carter, 1994) was then considered too conservative.

The eleven layer model is presented in Fig. 3.20a and 3.20b as a final P_{post} map. Probabilities were rescaled using a 256 colour gradient to display their variation; each

value above zero represents a posterior probability greater than the prior probability calculated from the mineral deposit layer. This map was created using a binary converter that creates a bitmap file from a binary array of posterior probabilities using windows GDI+ (Graphic Device Interface Library).

The probabilistic map shows that a limited area (approximately 14.85 %) records a ratio of P_{post} / P_{prior} greater than one, which is favourable for Pb-Zn mineralisation. The probabilistic map compared to known mineral occurrences (Fig. 3.20a) shows also that nearly 70% of the mineral deposits and prospects (57 out of 82) occur within the area considered as having probable potential for Pb-Zn ore. It is interesting to note that this data-driven model has highest values of probability (0.9441) corresponding to the Century zinc deposit. Similar potential is recorded northwest of Century where frequent clusters of mineral deposits and prospects are predominantly hosted in veins and lodes and proximal to northeast trending structures. However, the data-driven model does not discriminate any tonnage for the mineral deposits and it is not differentiating between vein-style mineralisation and stratiform ore deposits similar to Century. The range of probabilities observed can be grouped in low-probability domains (0 to 0.4721) and high-probability domains (0.4721 to 0.9441). Most of the highly predictive domains are focused around the Termite Range Fault and form a broad zone that, as expected, fits known occurrences although adding new potential targets proximal to them (see Fig. 3.20b). It is also interesting to note that intermediate to low-probability targets occur in other peripheral areas. For example, the Kamarga Dome area has small clusters of predictive pixels mostly where faults intersect the Pmx, Pmz and Pmp units. Low-probability domains may be regarded as possible sites of new discovery as the training

sites utilised in this data-driven model had most of the deposits occurring in the High-probability domains. The mineral potential model is also based on a large number of predictive themes; therefore, in some cases some of the low-probability values may be resulting from smoothing of themes that alone might have been suggesting significant mineral potential.

To further validate the mineral potential map a methodology similar to Carranza (2002) was adopted; firstly constructing a geochemical map representing interpolated anomalies of Zn for known stream sediment data and in a second step calculating the percentage of overlap existing among values of P_{post} higher than P_{prior} and Zn anomalies above 100 ppm (stream sediment data were provided by Zinifex Pty. Ltd. Century Mine) (Fig. 3.20b – white highlighted polylines). The outcome suggests a moderate agreement with mineral potential, with 47% overlap. This result could be justified considering that as previously discussed the extent of Post-Proterozoic cover may contribute to underestimation of covered sites. The same argument may be considered to explain also the occurrence of 46 deposits in areas proximal to predictive domains, but recorded outside them. Comparing the deposit theme with the cover theme approximately 50% of the prospects occur in cover sediments or Post-Proterozoic areas mostly proximal to the Mesoproterozoic mineralised outcrops, supporting this argument. In the conclusions, some of these limitations, due to incomplete data and scarce knowledge concerning the mineral deposits/prospects, is addressed integrating data-driven results with the KD-model. However, the constructed mineral potential map passed CI tests for violation of conditional independence and has demonstrated a reasonable agreement with known

deposits and stream sediment data; therefore, it is believed to be a valuable guide to establish new strategic exploration sites in the Lawn Hill Region.
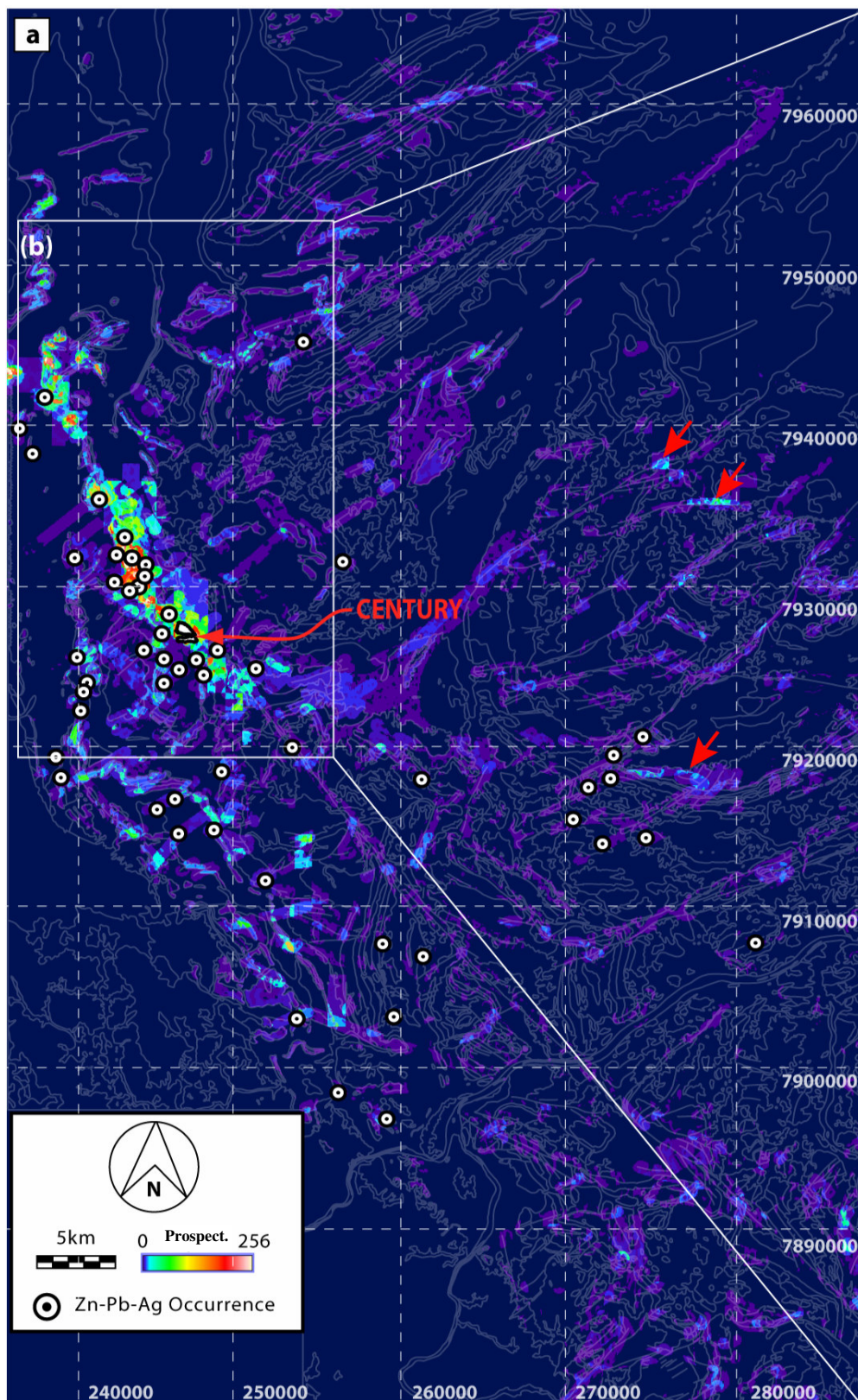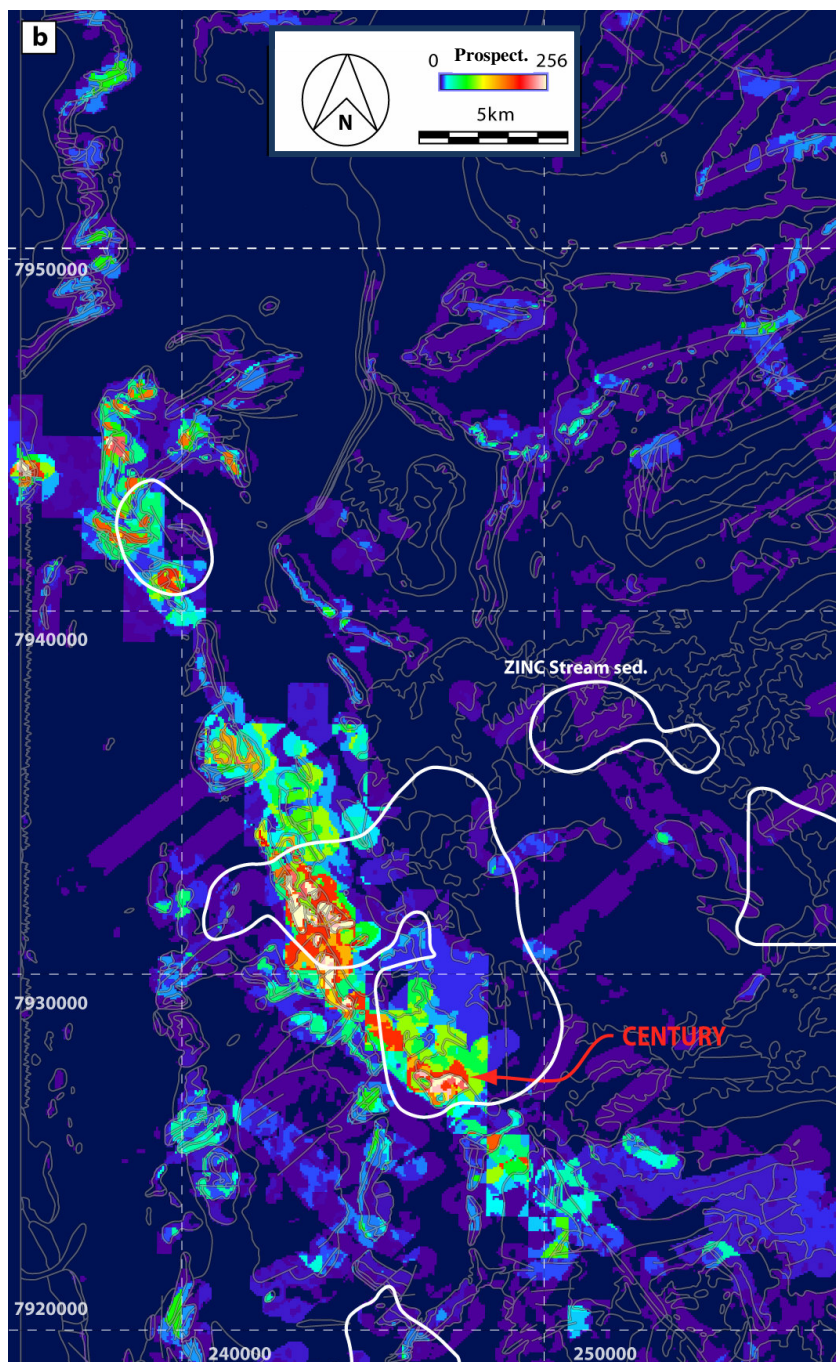
Fig. 3.20 Output of data driven modelling considering 11 layer (3 rejections) considering missing information related to cover sediments (QTJ – see Fig. 3.1a). (a) Data-driven model compared against known mineral deposits/prospects. Note the high potential along the Termite Range Fault, which was expected considering that clusters of known deposits are located in this area. However, local highs (although with lower values) are found in the Kamarga Dome area (see arrows). (b) Enlargement of Century area showing comparison of high-probability sites with geochemical stream sediment data (anomalies above 100 ppm of Zn content are indicated as closed polylines).

3.7. Conclusions

Constructed models were used to derive inferences relative to the two problems introduced in the first section of this chapter. These concern the definition of prospective areas for exploration and the possible "probabilistic" implications for the genesis of the different styles of mineralisation occurring in the Lawn Hill Region. The first point was addressed making use of pixel based algebra with a Boolean AND operation. Three final maps of favourability were constructed using this combination rule (Fig. 3.21a, b and c). Maps represent the integration of the KD- and DD-model for the SEDEX- and VS mineralisation. A third map was developed differentiating the integrated maps (KD + DD) for SEDEX and VS to obtain a final plot of the maximum likelihood of finding SEDEX-style or VS ore. The final model has constrained high favourability targets proximal to known occurrences. Other Century-style mineralisation might be located 7 km north of the "Edge" cluster (Fig. 3.21c). This apparently high P_{post} zone has similar values to Century, occurs in Pmh4, and is intersected by a NW fault which is parallel to and might be part of the Termite Range Fault termination.

This approach has limited application to ore genesis interpretations. It is however remarked that both KD-models and their integration show that the Century deposit is localised within a domain in which there is higher-favourability to locate SEDEX-style mineralisation, although VS ore could be present as well - meaning that the probabilistic approach is predicting both styles, but suggesting a higher proportion of SEDEX rather than VS ore.

Model results therefore partly reflect a previous study of this giant ore deposit (see Feltrin et al., 2006), which proposed that Century is more likely an exhalative to early-

diagenetic system with a component of later syntectonic mineralisation. It is also interesting to note that a comparison between the KD- and DD-probabilistic results provide an indication of scarce DD-mineral potential for areas where VS mineralisation would be favoured, based on KD-model results. This discrepancy might be due to undiscovered occurrences in VS-favourable domains or it could be interpreted as a lack of a major VS (syntectonic) fluid flow event in the region. In other words, if the later orogenic phase was only a minor "redistributing event", with only local circulation of fluids, then this would also explain the clustering of small VS occurrences observed around Century.
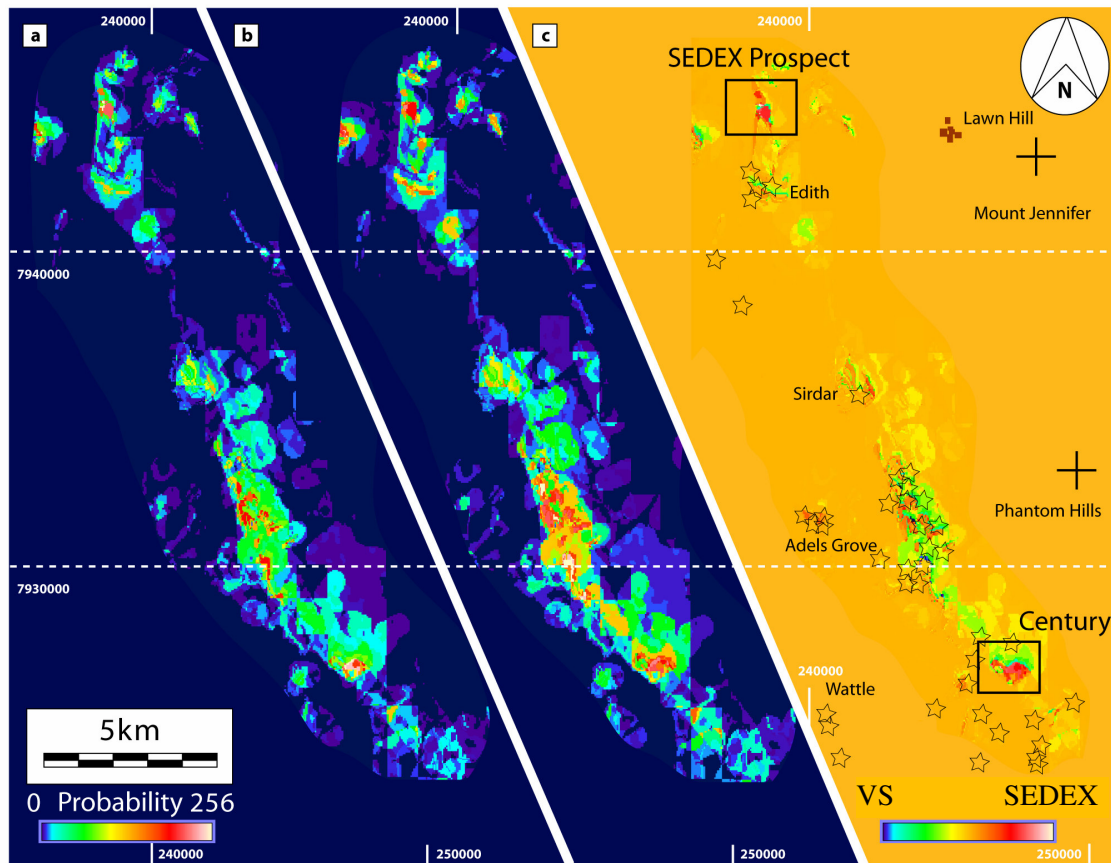
Fig. 3.21 Comparison of integrated KD-DD models. (a) SEDEX model. (b) VS model. Difference between the two total models is outlined in (c). The first two models offer similar results although local differences (km-scale) can be used to discriminate on a probabilistic ground between areas of elevated mineral potential for SEDEX or VS. A potential SEDEX target is outlined because of its similar favourability values to the Century deposit.

Chapter 4

Testing the structural and geomechanical processes in the formation of the Century (Zn-Pb-Ag) Deposit

Acknowledgement of Contributions

Contributions made to this chapter involved:

L. Feltrin – 3D Structural Modelling, Century data and review

Dr. J. G. McLellan – Geomechanical Modelling

Dr. D. R. W. Foster – Mount Isa Time Space Plot

L. Feltrin – 70% (p. 1-24), 90% (p.25-43), 10% (p. 44-76), 60% (p.77-80)

J. G. McLellan – 30% (p. 1-24), 10% (p. 25-43), 90% (p. 44-76), 40% (p. 77-80)

N.H.S. Oliver – normal supervisory contributions

Abstract

The Century zinc deposit is one of the giant Mesoproterozoic Zn-Pb-Ag deposits of the Northern Australian Zinc Belt. There is substantial controversy regarding the genesis of this deposit. Previous workers proposed a timing for the emplacement of the Century mineralisation as early diagenetic to syn-tectonic. In this work we present one of the first applications of 3D structural modelling combined with coupled mechanical and fluid flow modelling which aims to address ore genesis using computer simulation techniques. This approach has revealed the benefit of using software such as GoCAD as a data integration platform and FLAC as a process modelling tool. We have characterised the structural controls, ore distribution and thickness variations across the half-graben, which hosts the mineralisation. From this analysis we have been able to reconstruct the geometry and location of damage zones resulting from syn- to post-Isan Orogeny wrench style deformation, allowing also the distinction of early syn-sedimentary growth faults. 3D modelling has established overprinting relationships between temporally distinct hydrothermal events, and suggests a multistage evolution for this system. Fluid flow modelling using FLAC was aimed to test the control of permeability and deformation on subsurface fluid flow, i.e. a diagenetic or epigenetic model for fluid migration leading to mineralisation. However, this modelling shows that subsurface fluid flow through the mineralised shales was very unlikely to have occurred in preference to flow through faults and sandstones. Accordingly, both the spatial GoCAD and FLAC modelling suggests that a subsurface replacive origin for the mineralisation is less likely than a syngenetic model.

4.1.   Introduction

Plate tectonics has been recognised as a primary control on the nature and location of mineral deposits in the earth's crust. For example, Sawkins (1990) describes how different classes of metal deposits occur at specific locations of continental and oceanic margins. The relative abundance of metals and size of these occurrences depend on the tectonic context in which a mineral deposit forms as a direct function of the structural architecture, chemical composition of the crust, and type of mechanisms that allow the transfer of mineralising brines to produce economic grade mineralisation.

If we focus on shale-hosted Zn-Pb sulphide deposits (definition from Large 1980; Sangster 1983), we note that favourable present day sites for sulphide deposition are divergent plate boundary environments (e.g. median valley of the Red Sea; Degens and Ross 1969; Hackett and Bischoff 1973). This is represented by ore genetic models that invoke anomalous geothermal gradients as a key driving force for focussing metal bearing fluids along crustal discontinuities (e.g. SEDEX models), leading to ore deposition in rift dominated settings (Russell 1978; Goodfellow 1993). In contrast, not all Pb-Zn deposits occur in extensional setting, as several other varieties reportedly occur in compressional settings, during contraction (e.g., Garven 1985; Oliver 1986; Duane and de Wit, 1988; Bradley and Leach, 2003). Moreover, when giant accumulations of Zn-Pb are found in complexly deformed terrains (which record both extensional and compressional tectonic regimes), identifying the most favourable scenario for ore deposition becomes complicated. This issue is well known within the

Northern Australian Zinc Belt (Fig. 4.1), where many Zn-Pb occurrences (e.g.

McArthur River, Mount Isa, George Fisher, Lady Loretta, Walford Creek and Century)

are notable for their contentious genetic models.
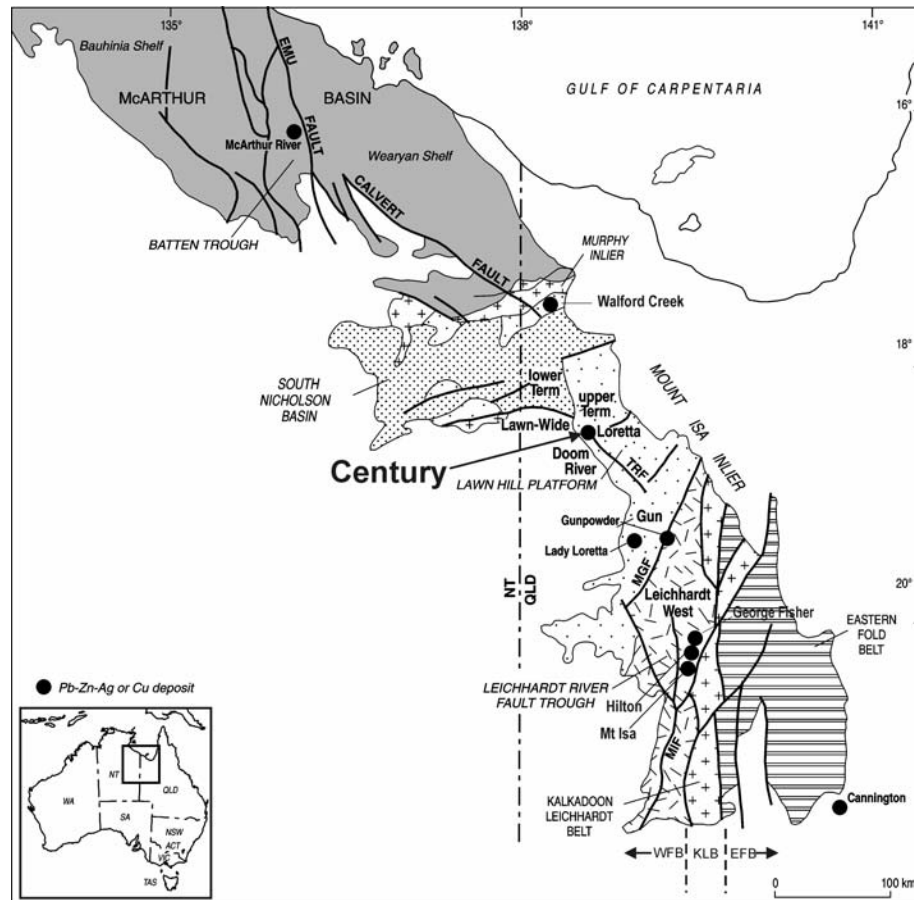
Fig. 4.1 Location map of the Century deposit and the major subdivisions of the Mount Isa Block and the Northern Australian Zinc Belt. The Mount Isa Block is subdivided into the main tectonic units of the Western Fold Belt (WFB), Kalkadoon Liechhardt Belt (KLB) and the Eastern Fold Belt (EFB). Major deposits (principally Zn-Pb-Ag) are shown and the Century deposit is highlighted in the Lawn Hill Platform (modified from Southgate et al., 2000).

A general method used to define the tectonic setting responsible for ore

deposition, in the Mt Isa Block Zn-Pb deposits, has been to attempt to identify the

relative timing of emplacement of massive sulphides with respect to the main stages of

Mesoproterozoic rifting, and to the Isan Orogeny (Fig. 4.2). Using paragenetic, structural, and geochemical constraints, previous authors have recently proposed different ore genetic models with syn-diagenetic timing for the George Fisher deposit (Chapman, 2004), syn-tectonic timing for the Mount Isa deposit (Davis, 2004), and syn-genetic timing for the McArthur River deposit (Ireland et al., 2003). It is clear that ore genetic controversies are still strong and may suggest:

a) That all these genetic models depict viable ore forming processes as Garven et al. (2001) proposes, and that a protracted hydrothermal evolution may have progressively accounted for the present metallogenic scenario within the Western Fold Belt (Sun et al., 1994), hence each deposit could have formed differently.

b) Only one of the above models (syn-sedimentary, syn-diagenetic, syn-tectonic) is valid for all these deposits.

c) Zn-Pb mineralisation is a result of a multi-stage hydrothermal evolution in which again all the models are viable scenarios, but all the deposits experienced a common hydrothermal history (i.e. remobilisation).

Some of the issues affecting these types of studies based on relative timing are:

1) Poor available constraints on the age of the Isan Orogeny (1585 - 1500 Ma) leading in some cases to possible overlap between depositional ages of sediments hosting the mineralisation (Page et al., 2000), and deformation ages (Connors and Lister, 1995; Connors and Page 1995). The Isan Orogeny itself has seen different deformational phases (e.g.

Bell, 1983, Bell and Hickey, 1996) and there is some possibility that the metamorphic peak and structural evolution may have been diachronous across the district (Table 4.1 also, compare Rubenach et al., 2001 and Giles and Nutman, 2003 with Oliver, 1995 and Bell and Hickey, 1996).

2) Presently accepted models fail to apply exclusively to specific tectonic scenarios, leading to confusion regarding the real ore genetic mechanism. For example, if we clearly identify the evidence for Mississippi Valley Type (MVT) mineralisation, in some cases it is not enough to sustain a contractional scenario for ore deposition. There are examples in the literature of rift-related Mississippi Valley Type Deposits; minor lead deposits found along the Red Sea coast of Egypt (Dadet et al., 1970; El Arif, 1984), and economic Pb-Zn MVT deposits that lie along the axis of the Benue Trough in Nigeria (Farrington 1952; Grant, 1971; Akande et al., 1988). After burial and subsequent metamorphism, it would be easy to interpret or misinterpret these mainly vein-hosted MVT ores as a syn-tectonic product.
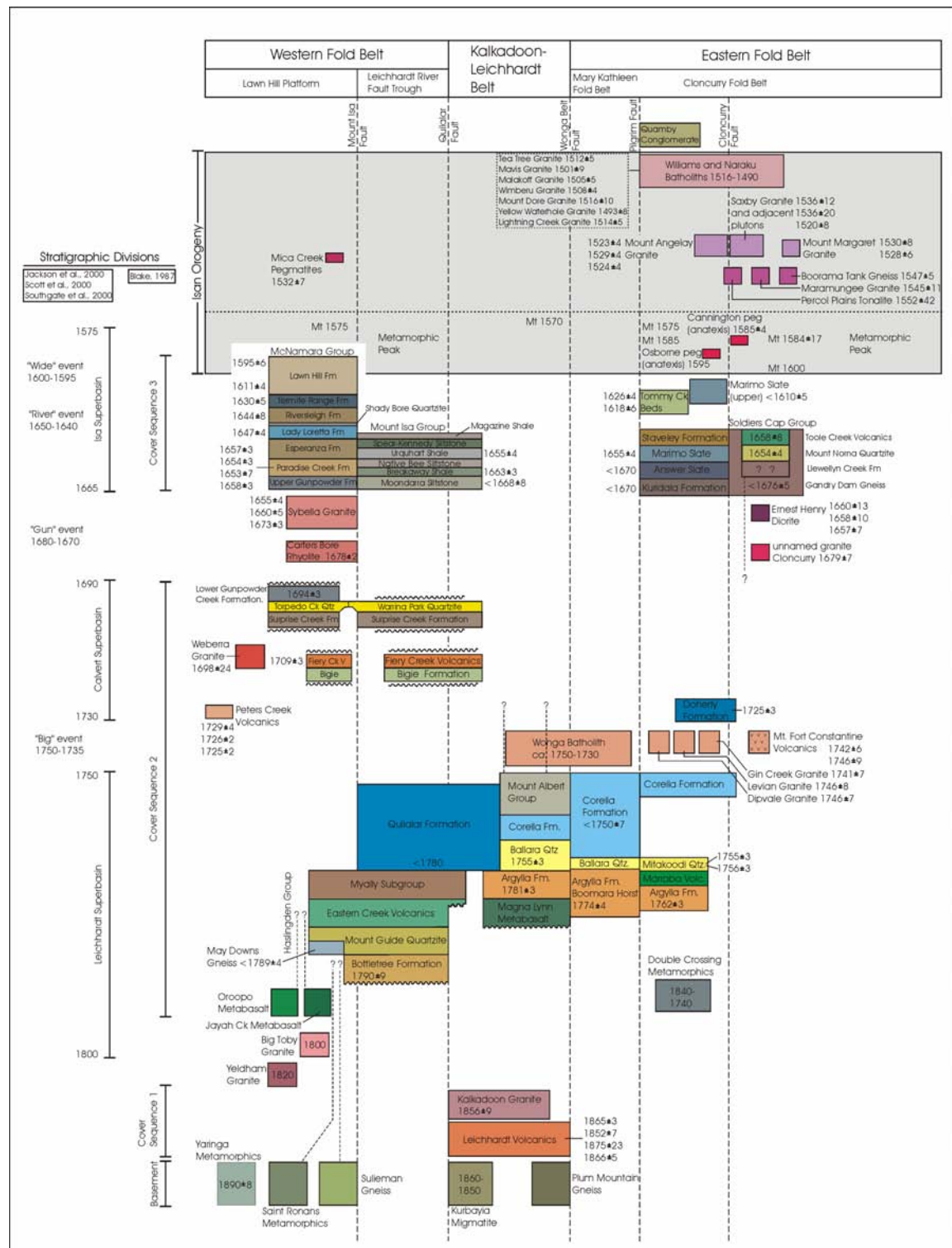
Fig. 4.2 (overleaf) Chronostratigraphy for the Mount Isa Block after Foster (2003). Modified from the compilations of Blake (1987), Blake and Stewart (1992), Page and Sun (1998), Page and Sweet (1998), and Page et al. (2000). Following Blake (1987), the stratigraphy is divided into 3 cover sequences, and divisions into the Leichhardt, Calvert and Isan supersequences. Delineation of the "Big", "Gun", "River" and "Wide" events are after Jackson et al. (2000), Scott et al. (2000), and Southgate et al. (2000). Age determinations for the stratigraphic units or intrusions are U-Pb zircon (mostly via SHRIMP) determinations, with exception of the pegmatites at Osborne (U-Pb titanite) and anatexis at Cannington (SHRIMP U-Pb monazite). Metamorphic ages (Mt) include U-Pb zircon and monazite (SHRIMP), and Sm-Nd garnet determinations. Detrital ages obtained from zircon constrain only the maximum possible age for the unit and are indicated by '<' at the front of the age.

Knowing these limitations we have attempted to use newly available computational tools to explore the problem of ore genesis from two new perspectives involving initially, 3D spatial/structural analysis (GoCAD), and subsequently, finite difference models of deformation and fluid flow (FLAC) that test one of the proposed ore genetic models for the Century Zn-Pb-Ag deposit.

Here, after a general introduction to the regional and local geology, we focus on the Century deposit considering the main features relevant to ore deposition. Revising and testing proposed ore genetic models, we re-interpret the genesis of Century based on the newly available data. However, the scope of this research also covers evaluation of the capacity of 3D modelling and FLAC modelling to answer ore genesis research questions.

4.2.   Tectonic evolution of the Mount Isa Block and

stratigraphic subdivisions

4.2.1.   The Mount Isa Block

The Mount Isa Block comprises three broad tectonic units; the Western Fold Belt (WFB), the Kalkadoon Leichhardt Belt (KLB), and the Eastern Fold Belt (EFB) (Fig. 4.1), which are predominantly north-south trending and separated by transcurrent fault zones (O'Dea et al. 1997; Blake and Stewart, 1992). Much of northern Australia underwent several periods of extension, leading to the development of intraplate sedimentary basins in which bimodal volcanic rocks and rift-sag sequences accumulated (Etheridge et al., 1987; O'Dea et al., 1997, Betts et al., 2003). The chronostratigraphic framework of the Mt Isa Block is outlined in Figure 4.2, and within the Mt Isa Block four major Proterozoic sequences are present (Blake, 1987). The oldest rocks, or basement, were first deformed and metamorphosed during the Barramundi Orogeny at approximately 1870 Ma (Etheridge et al., 1987). Following this orogeny, the Mount Isa terrain underwent a long and complex history of intermittent rifting and deposition, and several Palaeoproterozoic basins evolved between ca. 1800 and 1590 Ma (Carter et al., 1961; Smith, 1969; Plumb et al., 1980; Derrick, 1982; Blake, 1987; Page, 1988; Andrews, 1998; Page et al., 2000; Scott et al., 2000) in the North Australian Craton, which are best preserved and understood in the Mount Isa Block and McArthur Basin. Igneous and sedimentary rocks of this period were formed

or deposited during several superimposed intracontinental rifting episodes and associated post-rift subsidence, and designated Cover Sequences 1 to 3 (Blake, 1987) (see Fig. 4.2). Cover Sequence 1 (ca. 1870 – 1840 Ma) is restricted to a narrow central strip (Kalkadoon Leichhardt Belt) and consists predominantly of felsic meta-volcanic rocks. This belt acted as a 'high' and Cover Sequences 2 and 3 subsequently formed on the Eastern and Western sides (Eastern and Western Fold Belt Successions) during separate basin forming events.

Cover Sequence 2 was the result of a period of crustal extension from ca. 1790 – 1740 Ma, with early-syn-rift phase clastic sedimentary and bimodal volcanic rocks deposited in restricted fault controlled basins. These rocks were then overlain by clastic and carbonate sedimentation during a post-rift or sag phase, with termination of this cycle in the Eastern Fold Belt co-incident with the intrusion of the Wonga Batholith at around 1750 Ma (Stewart and Blake, 1992). Basement structures that developed during the deposition of Cover Sequence 2 appear to have had an influence on the depositional characteristics of Cover Sequence 3 (ca. 1670 -1595 Ma), which is best represented in the Western Fold Belt and unconformably overlies Cover Sequence 2. Cover Sequence 3 consists mainly of volcaniclastic rocks, conglomerates, sandstones, shales and carbonates, and is the host to Pb-Zn-Ag mineralisation in the Mount Isa Block. For a comparison between the Western, Kalkadoon-Leichhardt and Eastern Fold Belts, see Figure 4.2. Several attempts have been made to constrain the timing of the main deformational events in the Mount Isa Block during the Isan Orogeny, which vary substantially in relation to spatial aspects, isotopic dating and interpretation (e.g. cf. Page and Bell, 1986; Page and Sun, 1998; Bell and Hickey, 1996) (see Table 4.1). More

recently Giles and Nutman (2002) challenged the common perception of orogeny in the

Mt Isa Block in which 'peak metamorphism', and the deformation events associated

with it, can be correlated across the entire Mount Isa terrane.

Table 4.1. Correlation of deformational history in three locations of the Mount Isa Block, including a summary of age dates from several locations.

Deformation Event	Eastern Fold Belt Age	Western Fold Belt Age	Selwyn Region Adshead-Bell (1998)	Selwyn Region Jaques *et al.* (1982)	Selwyn Region Beardsmore (1988)
D_1 N/S Compression		D_1 - 1610 ± 13 Ma (Page and Bell, 1986)	D_1		D_1
D_2 E/W Compression	**U/Pb** 1584 ± 17 Ma (Page and Sun, 1998) **Ar/Ar** 1590 Ma (Perkins and Wyborn, 1998) 1580 -1600 Ma (Giles and Nutman, 2002)	D_2 - 1544 ± 12 Ma (Page and Bell, 1986) 1580 ± 5 Ma (Hand and Rubatto, 2002)	D_2	D_1	D_2
D_3 E/W Compression		$D_{2.5}$ (Bell and Hickey, 1986)	D_3		
D_4 E/W Compression	**U/Pb** 1493 – 1508 Ma (Page and Sun, 1998)	D_3 - 1510 ± 13 Ma (Page and Bell, 1986)	D_4	D_2	D_3
D_5 E/W Compression			D_5		
D_6 E/W Compression		D_4 (Bell and Hickey, 1986)	D_6		D_4

4.2.2.   The Western Fold Belt

In the Western Fold Belt three superbasins have been identified and delineated;

the Leichhardt Superbasin (ca. 1800 -1740 Ma), Calvert Superbasin (ca. 1730 – 1690

Ma) and Isa Superbasin (ca. 1665 – 1575 Ma) (Fig. 4.3). Preceding the development of

the Isa Superbasin, a complex history of extensional basin development, sedimentation and volcanism resulted in two superimposed and unconformity bounded basins; the Leichhardt Superbasin and the Calvert Superbasin. The Leichhardt Superbasin, which was controlled by half-graben bounding faults (O'Dea et al., 1997), is essentially comprised of shallow marine and fluvial sediments and bimodal igneous rocks and formed during the Leichhardt Rift Event (Betts and Lister, 2002) (Fig. 4.3). Basin inversion then followed, with localised shortening evident in the Leichhardt Superbasin (Betts et al., 1999). Following basin inversion extension was accompanied by shallow marine and fluvial sedimentation and bimodal volcanism in developing half-grabens (Betts et al., 1998; 1999; Southgate et al., 2000) in association with the development of the Calvert Superbasin (Jackson et al., 2000) and the Mount Isa Rift Event (O'Dea et al., 1997).

Reactivation of N-S rift bounding faults and E-W cross-rift faults during the Mount Isa Rift Event to some extent controlled the architecture of the Calvert Superbasin and subsequent sedimentation. Half-graben bounding faults were active in the Lawn Hill Platform and transverse faults, such as the Termite Range Fault, were considered active during deposition of the Isa Superbasin (Scott et al., 2000). The Isa Superbasin has been interpreted as the result of a sag phase or thermal subsidence (Betts et al., 1998). This subsidence appears to have been more extensive to the west/northwest of the Leichhardt River Fault Trough (Fig. 4.1), which resulted in extensive deposition of carbonaceous shale, sandstone and siltstone and formed the McNamara Group (ca. 1660 – 1595 Ma) which is the host to the major shale-hosted massive sulphide Pb-Zn- Ag deposits of the region (Fig. 4.4). Most deposit Pb-Pb or U-

Pb ages correspond well with their host successions, Century being the main apparent exception which is dated at around 1575 ± 6 Ma (Carr, 1996), 20 Ma younger than the 1595 ± 6 Ma host sediments. However, the Pb isotopic ratios could have been potentially influenced by later more radiogenic fluids. Moreover, the 1595 ± 6 Ma age for the H4s re-sedimented tuff-beds are maximum ages that do not necessarily coincide with the sedimentation age, and could be younger, overlapping with mineralisation timing in analogy to e.g. Mount Isa, McArthur River (HYC) and Broken Hill.

This extensional history and overall basin development was interrupted by compression, basin inversion and regional wrenching during the Isan Orogeny ca. 1585-1500 Ma (O'Dea et al., 1997, Betts et al., 1999; Betts et al., 2006). The subdivisions of the Mt Isa Block display contrasting responses to deformation in the region, with associated strain less intense in the Western Fold belt than that of the Eastern Fold Belt due to strain accommodation by underlying basin fault architecture (Betts, 2001). In the Eastern Fold Belt thin-skinned tectonics dominate with shallow dipping faults, whereas in the Western Fold Belt, brittle deformation affected much of the upper crust. The Kalkadoon-Leichhardt Belt consists of older, exposed basement rocks which accommodated the deformation by working as a buttress during periods of crustal shortening (Drummond et al., 1998).
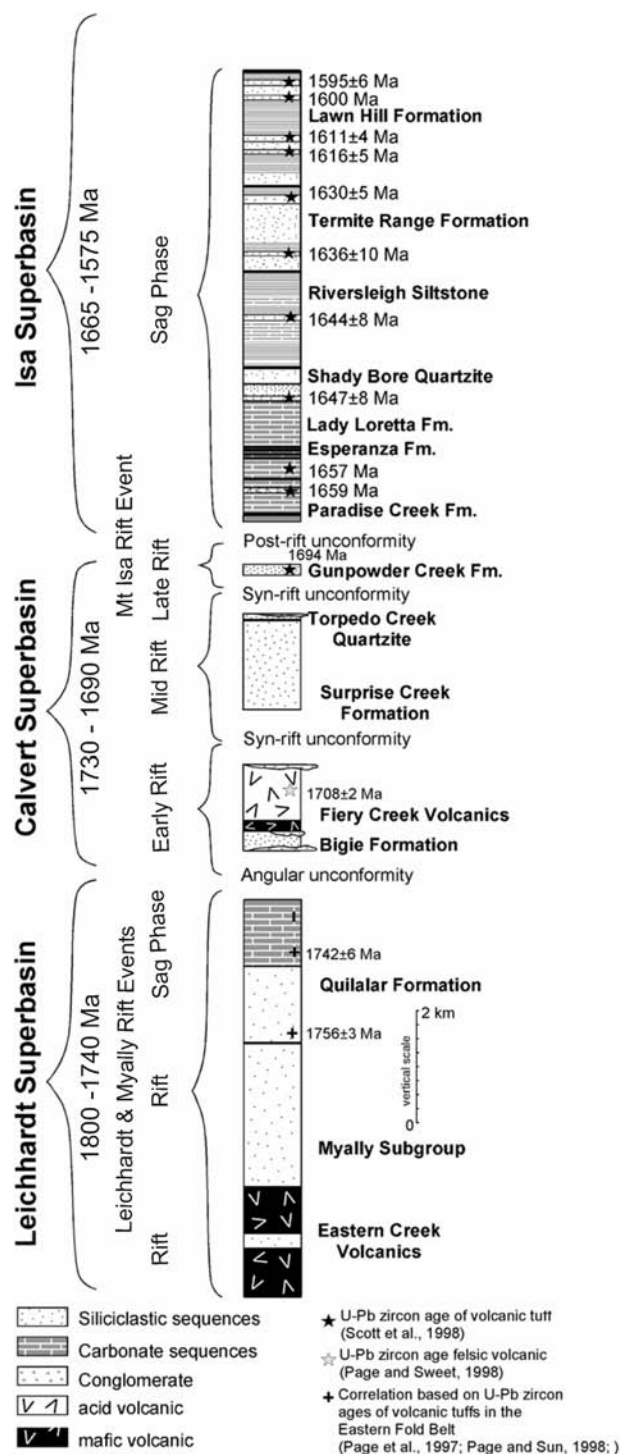
Fig. 4.3 Simplified lithostratigraphic column of the Western Fold Belt displaying the three Superbasins and associated rifting sequences. Geochronological data after Scott et al. (1998), Page and Sun (1998), Page and Sweet (1998) and Page et al. (2000), (modified from Betts et al., 2003).
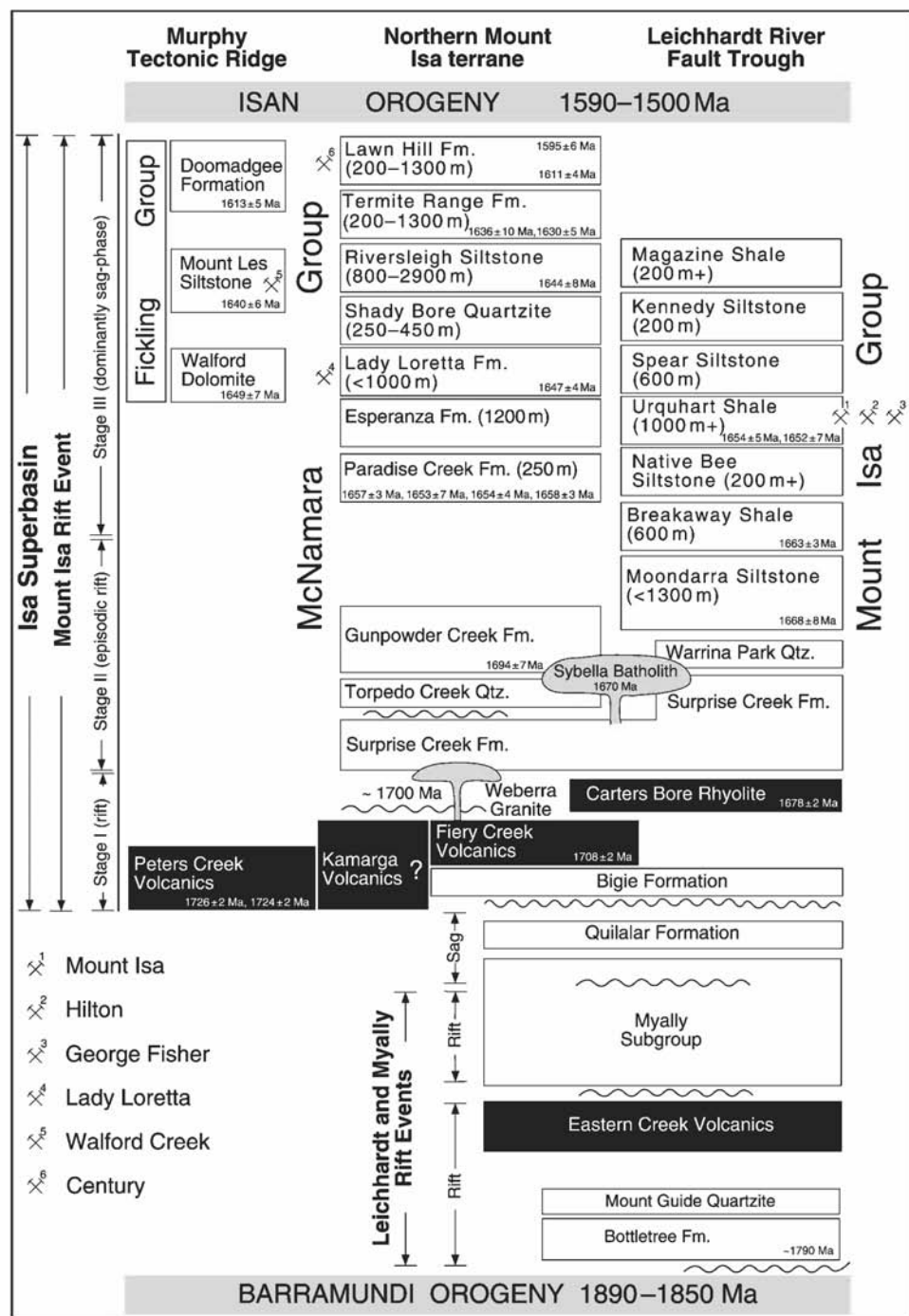
Fig. 4.4 Stratigraphic correlations in the Western Fold Belt displaying the major ore deposits and the age of stratigraphic horizons within the McNamara Group, (after Betts and Lister, 2002).

4.2.3.   Stratigraphy of the Lawn Hill Formation

The Lawn Hill Platform (Plumb and Derrick, 1975) represents the northern part of the Western Fold Belt (Fig. 4.1). Here, Zn-Pb mineralisation (e.g. Century zinc deposit) occurs preferentially in a number of stratigraphic layers hosted in the McNamara Group (Fig. 4.5).
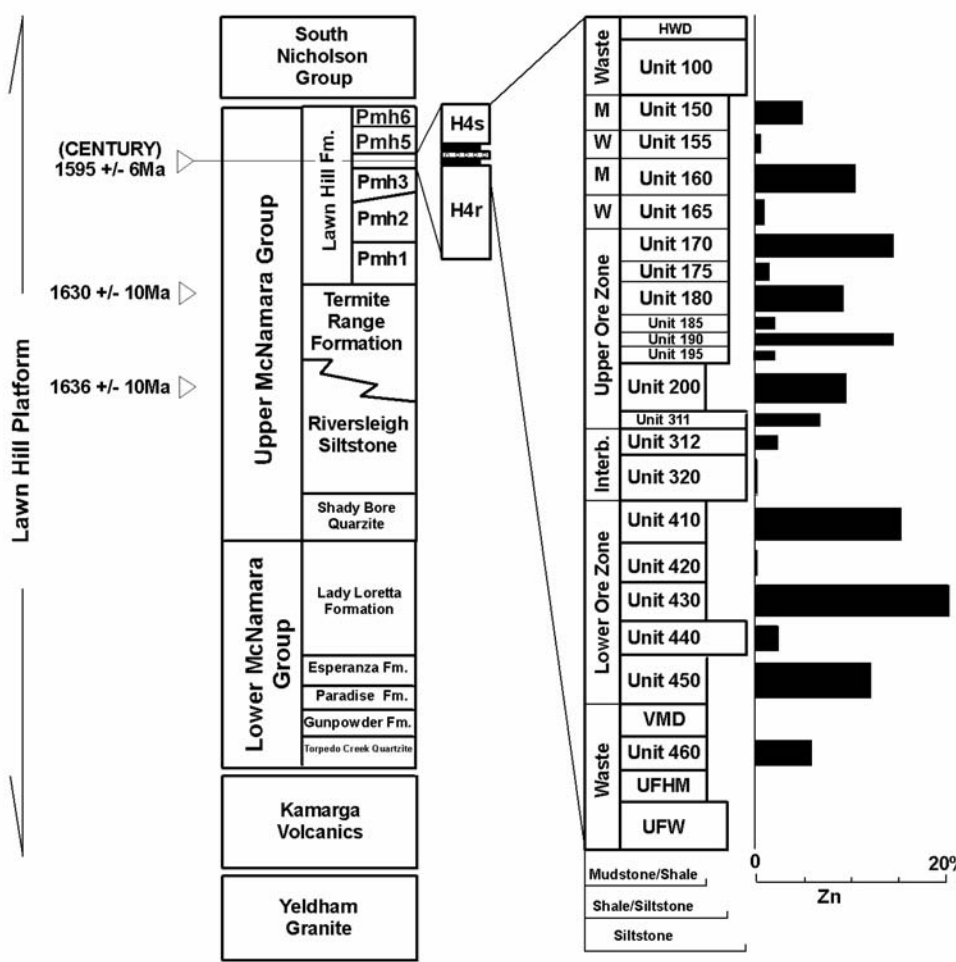
Fig. 4.5 Stratigraphy of the Lawn Hill Platform indicating the relative location of the Century Deposit and stratigraphic ages. On the right is a detailed stratigraphy of Member Pmh4 with the Century Ore Zone linked to grade distribution of %Zn.

Previous interpretations of O'Dea et al. (1997) and O'Dea and Lister (1995) view this thick package of sediments as being deposited during alternative phases of rift and sag episodes, with no significant tectonic activity (Betts, et al., 1998). Scott et al., (1998) and Krassay (2000b) reinterpreted the seismic stratigraphy of this package of sediments, suggesting that several tectonic events occurred during and after sedimentation. Syn-sedimentary deformation is documented by the identification of syn-sedimentary growth faults across the Elisabeth Creek zone. The most obvious structural feature in the region is the northwest striking Termite Range Fault (Andrews, 1998; Betts et al., 1998; Broadbent, 1999) which has been considered the major fluid pathway for mineralisation (Broadbent et al., 1998). The Termite Range Fault (TRF) has been described as a long-lived transverse fault (Betts, et al., 1999; Ord et al., 2002) and was most likely active for > 140 million years. The TRF has had a major influence in the deposition of sediments throughout the upper McNamara Group and has localised sedimentary depocentres (Andrews, 1998). Lateral variations in sedimentation can be found in and around the Century deposit suggesting local thickening, which Broadbent et al. (1998) describes as a result of parasitic faults emanating from the TRF. However, other east-northeast and northeast striking, steep, reactivated faults represent an important characteristic of this region, and were probably also important in transferring brines and controlling deposit locations across the Lawn Hill Mineral Field (see below).

The McNamara Group rocks in the Lawn Hill Platform form the youngest cover successions of the Mount Isa Block, correlative with the Fickling Group (Sweet et al., 1981; Blake, 1987; Blake and Stewart, 1992; Andrews, 1998; Krassay, 2000a) (see Fig. 4.4). The upper McNamara Group comprises up to 7500 m of deep marine, paralic and

terrestrial, siliciclastic-dominated facies of the Shady Bore Quartzite, Riversleigh Siltstone, Termite Range Formation, and Lawn Hill Formation. The Century orebody and surrounding vein-hosted mineralisation is stratigraphically constrained within the upper part of the McNamara Group in the Termite Range Formation and Lawn Hill Formation. This was subdivided by Sweet and Hutton (1982) into six members, Pmh1-Pmh6 (Fig. 4.5). Andrews (1998) distinguished two additional members: H1s within Pmh1 and H4s (host to Century Zn-Pb-Ag mineralisation) at the top of member Pmh4 (Fig. 4.5). Members Pmh1, Pmh2, Pmh4 and Pmh6 are dominantly fine grained and carbonaceous and represent a low energy, deep subaqueous environment. Pmh3 is a sandy interval and represents a shallower, higher energy marine setting. Member Pmh5 comprises thick lithic and feldspathic sandstone interpreted either as high-energy marine shelf deposits (Sweet and Hutton 1982) or sandy turbidites (Andrews 1998). More recently, after the accomplishment of the North Australian Basin Resource Evaluation (NABRE) project, the lithostratigraphy has been reorganised in light of new concepts of sequence stratigraphy (refer to Southgate et al., 2000; Neumann et al., 2006). Outcomes of the NABRE project resulted in an updated stratigraphy that is based on erosional and maximum flooding surface boundaries, new geochronology results (Page et al., 2000), and also palaeomagnetic data sets to constrain the depositional conditions (Idnurm, 2000; Southgate et al., 2000).

In sequence-stratigraphic terms the Lawn Hill Formation comprises the upper part of the Term Supersequence and the Lawn, Wide and Doom Supersequences (Krassay et al., 2000b) (see Fig. 4.6). The Century zinc deposit is hosted in the Wide supersequence (Wide 1), representing a third order maximum flooding surface,

suggesting low energy conditions. As relative sea level reached this maximum flooding

surface, basins became starved of sediment deposition, resulting in a condensed section,

which may have favoured the concentration of sulphides, particularly in shale units

(Ruffell, et al., 1998).
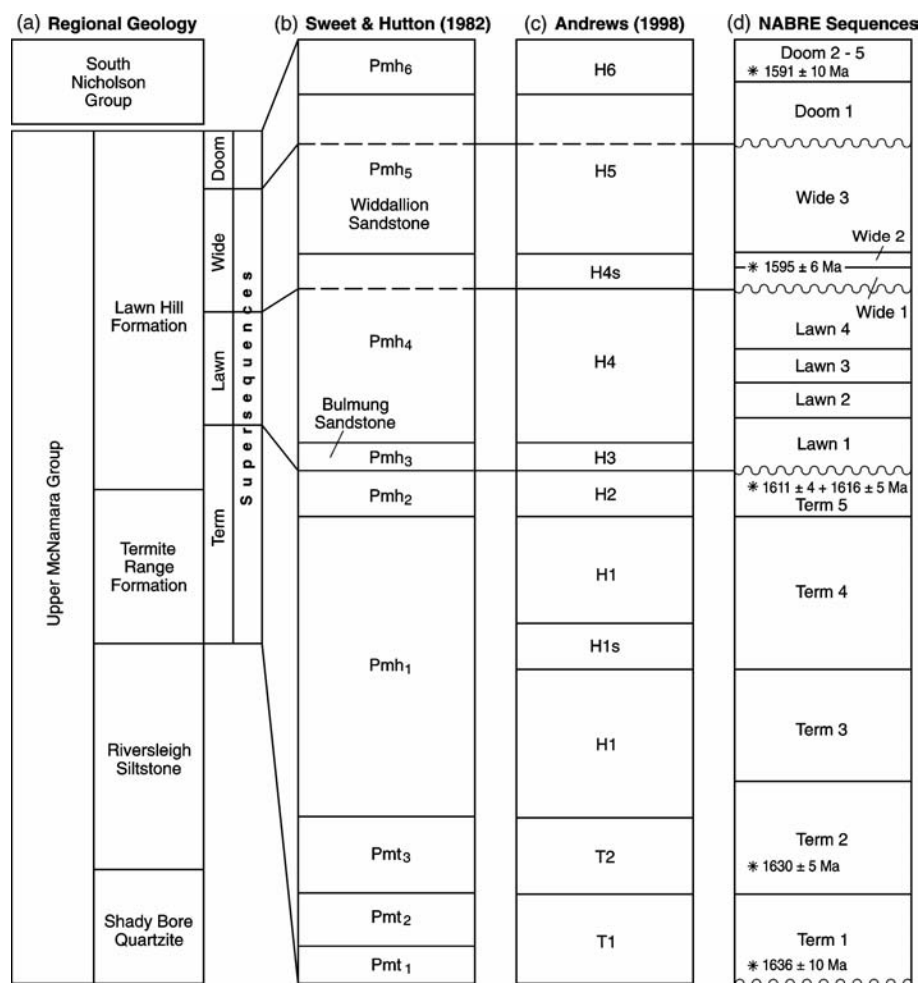
Fig. 4.6 Stratigraphic columns comparing the various classification schemes for rocks of the upper McNamara Group. (a) Regional geology for entire McNamara Group. (b) Upper McNamara Group formally defined lithostratigraphic units after Sweet and Hutton (1982). (c) Upper McNamara Group informal lithostratigraphic units by Andrews (1998). (d) North Australian Basin Resource Evaluation (NABRE) sequence-stratigraphic terminology and SHRIMP depositional zircon ages from the central Lawn Hill Platform. After Krassay et al. (2000a, b).

The Lawn Hill Formation contains tuffs and reworked tuffs at a number of stratigraphic levels. Page and Sweet (1998) dated a population of zircons (1595 ± 6 Ma) in the mineralised member Pmh4 (from Century drill core). Page et al., (2000) also presents consistent results from four new samples, two from member Pmh2 (Lawn Supersequence, 1616 ± 5 Ma; 1611 ± 4 Ma) one from member Pmh4 (Lawn Supersequence, 1595 ± 6 Ma) and one most likely derived from member Pmh6 (Doom Supersequence, 1591 ± 10). The ages derived from Pmh2 (1616 ± 5 Ma and 1611 ± 4 Ma) are stratigraphically in accordance with the age of 1595 ± 6 Ma for Pmh4. Well established geochronological constraints, coupled with sedimentary evidence presented by Krassay et al., (2000a), argue strongly for a tectonic control of the major (2nd-order) supersequences, and most 3rd-order accommodation cycles (sequences) across all of the Isa Superbasin. Evidence of a tectonic influence includes facies changes and thickness trends related directly to active faults, partitioning of depocentres by these faults, abrupt provenance switching, tilting and erosion of older sedimentary sequences. Furthermore, Krassay et al., (2000a) suggests that the Isan Orogeny may have commenced during deposition of Doom 4 and Doom 5. These final considerations suggest that the D1 phase of the Isan Orogeny probably post-dated the depositional age of sediments hosting the Century mineralisation.

4.3.   Century deposit

The Century deposit is one of the largest Zn-Pb-Ag accumulations in the world with a mineral resource of 138 Mt at 8.23% Zn, 1.16% Pb, and 29 g/t Ag (Clifford and

Kelso, 2003). This stratiform mineralisation has not been as extensively studied as other Zn-Pb metal occurrences in the Isa and McArthur Superbasins e.g., Mount Isa, McArthur River (HYC), Lady Loretta etc., as it is one of the more recent discoveries (1990 CRAE exploration Ltd.).

4.3.1. Sulphide textures

The main stratiform mineralised units are a finely laminated shale unit consisting of essentially fine grained sphalerite and siderite with minor galena and pyrite. The presence of hydrocarbons or pyrobitumen with porous sphalerite has been discussed in detail by Broadbent (1999). However, the non-porous sphalerite has no clear relationship to pyrobitumen; it also has the highest grade and volume within the mineralised sequence. The subdivision Pmh5, which is comprised of a thick (~150 m) cemented chlorite rich sandstone lies directly above the 'ore zone'. Broadbent (1999) and Ord et al., (2002) have interpreted this unit as a potential seal in the system due to its characteristics and early cementation (Andrews, 1998). Discordant mineralisation (at meso-scales) is relatively minor, and comprises veins and irregular patches, typically galena-dominant (Broadbent et al., 1998). Vein-style mineralisation which is completely discordant to bedding is common in an area of about a 30 km radius around Century (e.g. Silver King, Waltho and Andrews, 1993).

4.3.2.   Ore zone stratigraphy

The mine stratigraphy is contained in the subdivision Pmh4, which is comprised of over 500 m of interbedded siltstone and shale units with minor mudstone, is summarised in Figure 4.5. Logging of ore zone units has suffered from inconsistent unit definitions in the past. With the completion of re-logging in the Solid Geology project the ore zone units are now much more consistently constrained (Fig. 4.7).

The upper ore zone generally consists of interbedded siltstone and shale bands (Fig. 4.7), and varies from very well laminated to stylolitic layers, with evidence of layer parallel shearing in several units. Unit 200 (3-5 m) is the first major ore unit but has quite a different appearance in Stages 1 and 2 (the southern part of the mine) to the majority of the north block. In Stages 1 and 2 this unit was commonly a massive mudstone interval which was frequently brecciated and deformed by bedding parallel shear, coincident with high lead grades. In the north block the unit occasionally suffers bedding parallel shear within laminated shale (similar to Unit 160), mudstone intervals are rarer. Unit 310 is a transitional unit from the shales of Unit 200 to the siltstones of Unit 320. As the upper part of the unit can contain some very high-grade mineralisation it has been split into Units 311 and 312 on the basis of assay information (Unit 311 is > 6.5% Zn).

THIS TABLE HAS BEEN REMOVED DUE TO
COPYRIGHT RESTRICTIONS
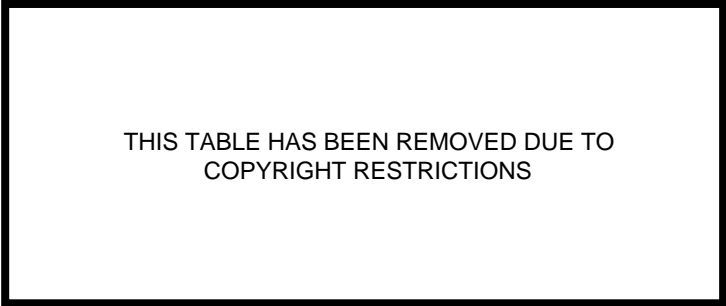
Fig. 4.7 Stratigraphic summary and description of the Century Deposit (courtesy of Century mine & I. Kelso)

The relative thickness of these units is variable and either can comprise the entire interval. If there is no assay information or the unit is affected by hematite alteration it is logged as Unit 310. Unit 311 is the lowest unit in the Upper Zone ore and Unit 312 is the first unit of Internal Waste. Interburden within the ore zone relates to Unit 320 (2.5-3.5 m) and was called the Cappuccino zone by CRA due to the sideritic buff coloured stylolitic siltstones, which comprise the entire interval and the majority of the Internal Waste. The lower ore zone generally consists of high-grade well-laminated black shale with interbedded mudstone.

4.4.   Introduction to the 3D structural modelling

The primary objective of almost every geological characterisation is concerned with predicting the spatial variation of one or more geological variables (Houlding, 1994). A conventional approach that is commonly used to define a geological entity is a 2D representation of the geology using a map or a cross-section, as our ability to deal with geometrical problems in 3D is limited and it is difficult to represent it visually. However, since the advent of computerised methods, defined as CAD (computer aided design), most of these difficulties have been overcome, enhancing our understanding and providing new ways of dealing with complex geometrical problems in 3D space. In computer aided design, a geological scenario requires a mathematical description of the components. This process happens when we adopt algorithms that use discretization and qualification of irregular geological space into irregular volumes, with similar

distinguishing characteristics. Some of the most common characters used to define geological space are lithological subdivisions or physical properties such as density, permeability and mineralisation content, amongst others.

Several types of investigative sources are available and are commonly used to gather the information necessary to construct a generic model, which comprises a set of well constrained geological spaces. The implemented data, when we consider the representation of a mineral deposit, are generally of two types a) a direct sampling of a discrete and representative quantity of rock, soil or unconsolidated sediment; or b) an indirect quantification of a property of the geological space using i.e. topographical, geochemical, or geophysical investigations. This information is made up of a range of observations that must be weighted. For example, we might have data that is collected in outcrops with 99% confidence on its location and geological characteristics, or a geophysical survey that can be regarded as fuzzy in terms of location and geological characterisation. Thus, there is a need to quantify the quality of the information available considering its source, before we integrate it within a generic 3D model. Creating geologically relevant 3D models from low relief, poorly exposed and geologically complex regions is a daunting if not impossible task (de Kemp, 2000). As a consequence, it is also important to have a clear understanding of the spatial density distribution of data used during the interpretative construction of the geology.

Once the representative geometries are defined, the evaluation of the results of a geological characterisation typically involves spatial analysis of the variation of one or more variables. This can be done using modern visualisation tools that allow not only a rapid correlation analysis, but also an interactive query of the database that creates the

3D model. This consents to quantifying the information displayed, facilitating its understanding.

4.4.1. GoCAD a 3D geologically optimised CAD package

GoCAD is a software that allows the reconstruction of geological objects in 3D (see Chapter 2) and was used to construct the model of the Century deposit. An important advantage of this software is that it consents the definition of several types of constraints (Chapter 2), some of them may be imposed to respect the data inserted within the model, others can be used to fit the structural interpretation when the data are incomplete. Constraints are useful for example when modelling stratigraphic layers and faults. The final 3D model represents therefore a combination of data interpolation, and geological interpretation imposed by the user during the modelling process.

4.4.2. Initial steps to construct a 3D model

The basic requirements and procedures adopted to construct the 3D model of the Century Zn-Pb-Ag deposit can be summarised as a sequence of clearly defined steps:

- *Management, Correlation and Integration* of the various information sources available from site investigation. The most important, and potentially most time consuming, aspect of this step is spatial correlation of the available data sources.

- *Review and Analysis* of the information sources in terms of their quality, sufficiency, scale and spatial variability. This provides an initial appreciation of the complexity and magnitude of the conditions we have to deal with. It also allows us to identify the geological characters that influence the spatial variation of the variables of interest.

- *Interpretation* of geological stratigraphy, structure and other relevant factors, based largely on observation of characteristics. The result is a discretization of the subsurface continuum by controlling geological characteristics. The operative term here is *interpretation,* because we are commonly forced to apply our geological intuition and experience to compensate for limited primary data.

- *Prediction* of the spatial variation of relevant variables based on sample information, geological interpretation and appropriate prediction techniques. The operative term in this case is *prediction*, the true conditions are seldom determinate from limited information and our predictions are always subject to some degree of uncertainty.

- *Spatial Analysis* of the interpreted and predicted information, generally in terms of volumetrics and visualisation procedures, and/or transfer of the characterisation results to the relevant end process, such as mine planning or fluid flow modelling.

4.4.3. Data acquired to construct the 3D model

To construct the 3D model of Century and the Lawn Hill mine lease area we have initially developed a mine scale model that uses most of the data collected during exploration and resource evaluation carried out initially by Rio Tinto, Pasminco, and subsequently by Zinifex Pty Ltd, and also a range of data gathered during recent exploitation activities, which involved the design and development of several open-cut stages. In a second, more advanced phase of this project, we have integrated the deposit model with selected data at regional scale. The main sources of data were: (a) the Pasminco Century mine database; (b) Solid Geology reports; and (c) aerial photography.

4.4.4. 3D model components

The Century model in its final stage includes a highly detailed 3D reconstruction of the faults at the deposit and regional scale, a set of horizons representing the topology of some of the highly mineralised intervals, and a Digital Terrain Model (DTM) representing a 3D reconstruction of the mine lease. Interesting results were obtained when comparing the data at different scales, and projecting some of the drilling database information over the mineralised Unit 200 (see Fig. 4.7) with the intent of visually evaluating the relationship between fault distribution versus thickness and grade variation across the Century deposit. Unit 200 was utilised as it was the reference based unit for mine geologists at Century, being the easiest to log.

4.4.5. 3D Modelling results

As mentioned in the initial introduction of this chapter we have attempted to use the 3D model to gain insights into ore genetic processes. After this initial consideration we have defined three research questions as follows:

(1) What was the link between the fault architecture and the mineralisation within the Lawn Hill Mineral Field?

(2) What were the faults that may have contributed to ore transport and deposition other than the Termite Range Fault?

(3) Which structures were the primary growth faults within the Century system, and did they play an important role for mineralisation?

To answer these questions we have tried to identify if regional scale faults mapped in 3D using the DTM (Fig. 4.8a) (in combination with aerial photography), intersect the mineralisation at depth. We also used the model to define what the important faults for mineralisation were, and we attempted to evaluate the relative timing of faulting events.

The rapid visualisation of all the structural data using GoCAD, reveals continuity between NE trending regional scale structures and faults within the Century deposit (Fig. 4.8a, b). We recognise that the regional Silver King Fault (SKF) most likely intersects Century. This link is supported further by a range of data that includes thickness variations and grade distributions at the Century scale (see below), and the topology of the Hangingwall Sandstone (see Fig. 4.7) surface in the hangingwall of the ore zones. Within the deposit we also recognise that the evolved geometry of the

Termite Range Fault (TRF) is surely the result of significant reactivation. Moreover, it is important to remark that NE striking faults were coevally active with the Termite Range Fault from early stages of sedimentary deposition. Evidence of NE structures, intersecting older sediments of the Termite Range Formation, indicates a similar history of reactivation. However, several faults mapped in the pit area are relatively young parasitic branches (e.g. Gecko and Prosperity system faults) of TRF, and most likely developed during the later phase of wrench style deformation (Fig. 4.9). These faults seem to have only partially influenced the present distribution of ore. Superimposed on these events is a final extensional stage that has contributed to the present half graben structures and has subdivided the Century deposit in three independent fault blocks separated by E-W striking structures (e.g. Pandora's Fault). The NE structures can be interpreted as reactivated as some of them displace the E-W faults. The trace of the SKF corresponds well to a significant zone of thickness variations observed within the deposit, (Fig. 4.10a, b) and most likely represents a reactivated growth fault; however some of the thickening could be due to later localised thrusting, especially within the shale 200 interval. The topology of Unit 200 is not influenced by significant deformation along the SKF, possibly supporting the growth fault model. However, this might be due to a different response of the shales (less competent units) to subsequent deformation. In addition, the shales show some evidence of parallel bedding shear.
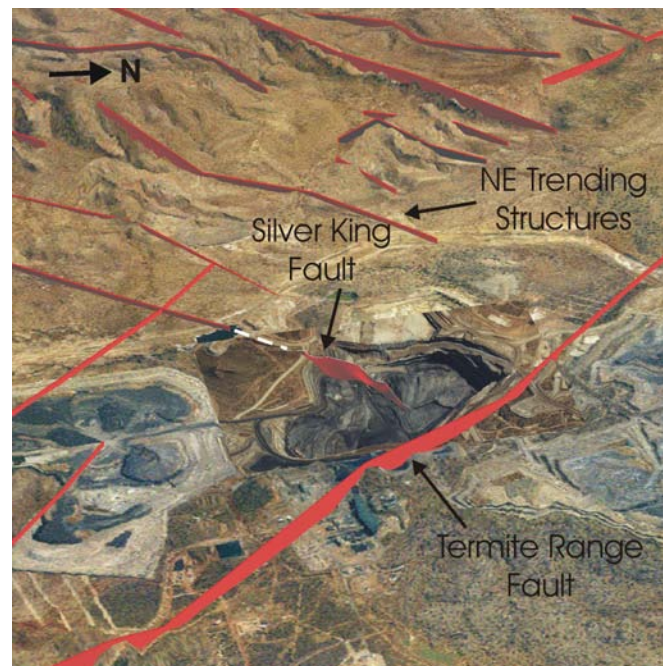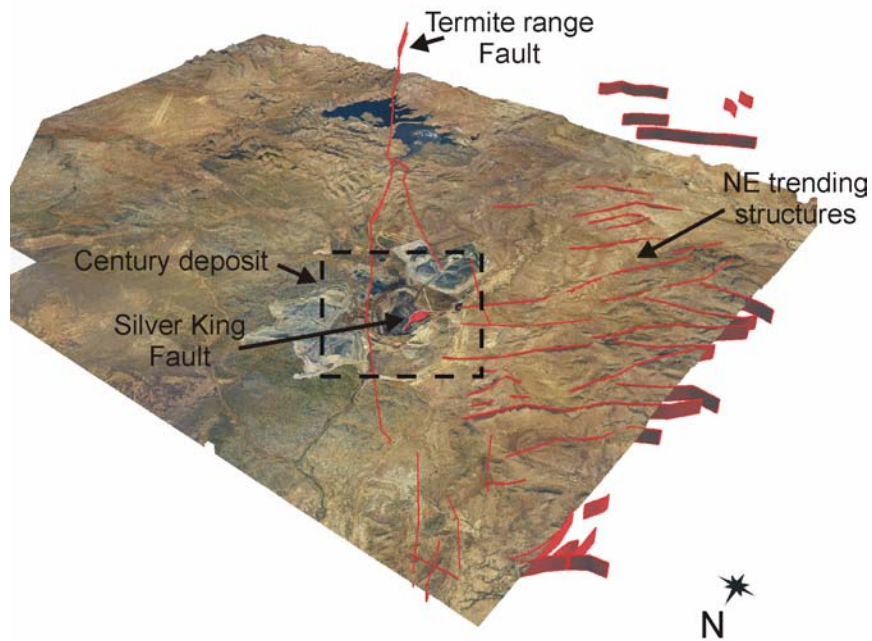
Fig. 4.8 Digital Terrain Model (DTM) of the Century deposit and surrounding region. (a) Century deposit and NE trending structures. (b) Digital terrain Model (DTM) of the Termite Range fault intersecting the Century deposit, and highlighting the potential link between NE trending regional structures and the Silver King Fault.
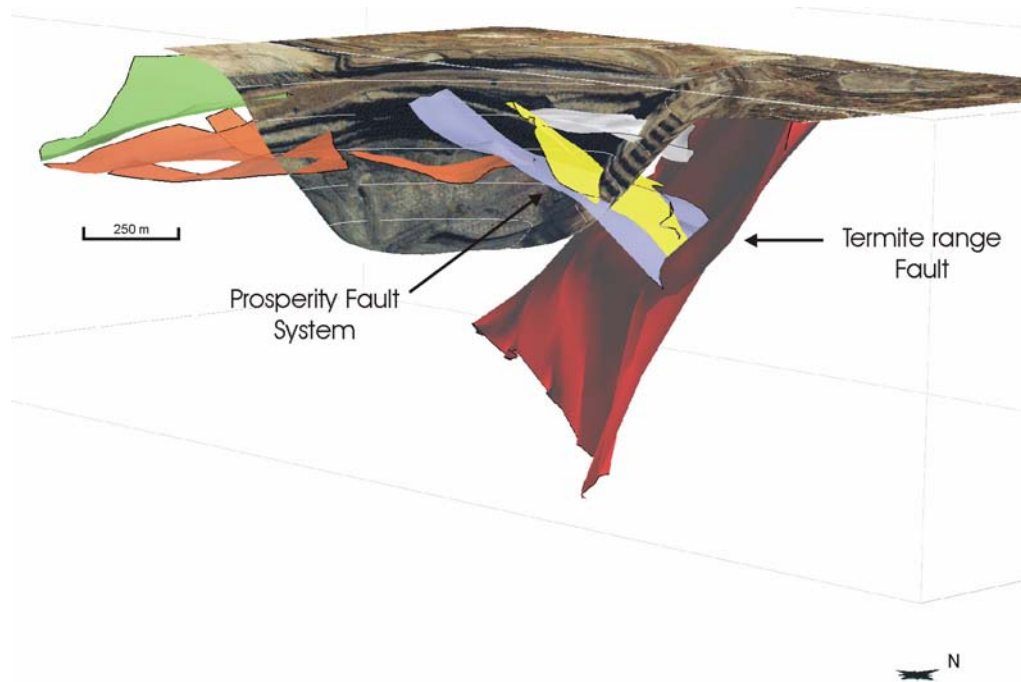
Fig. 4.9 Digital Terrain Model (DTM) integrated with 3D structural data, highlighting the Termite Range Fault and the parasitic Prosperity Fault system.

Grade distributions of both Zn and Pb correlate well with NE trending structures and Pb distribution in Unit 200 displays higher grades closer to the TRF (Fig. 4.11a, b) also associated with NE trends. The distribution of Zn in Unit 200 displays isolines with similar NE trends; and the high grade Zn zone overall is distal relative to the TRF (Fig. 4.12a, b). The isopach map of Unit 200 indicates that major sedimentary thickening occurs in the south eastern corner of the deposit and also within channelled domains in the northern block. In both cases the thickening seems to be associated with NE trending structures if we consider the distribution of isolines. These NE trends of thickness are parallel to trends observed in the Pb and Zn grades.
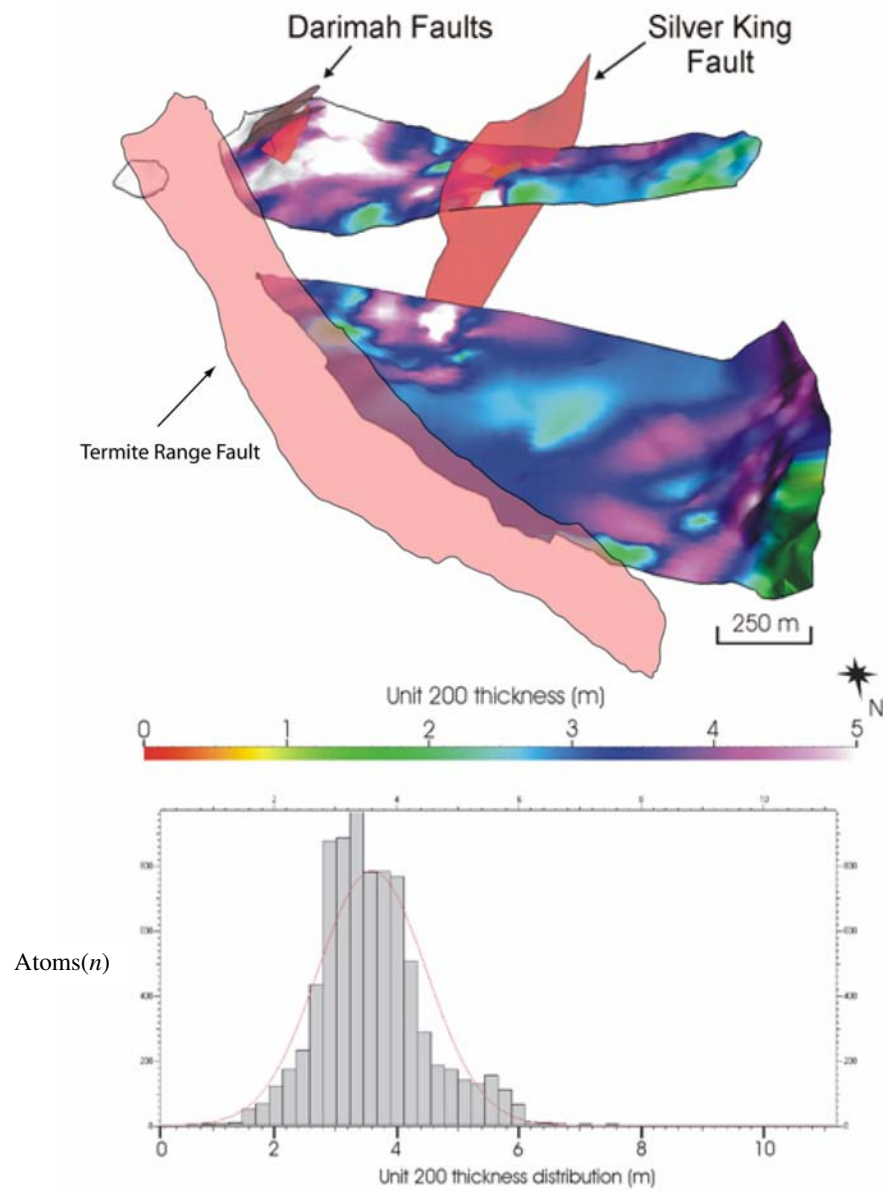
Fig. 4.10a. 3D representation of the thickness variation in Unit 200 of the Century deposit looking south. Note the correlation of thickness increase with NE trending faults. Below: Histogram displaying the thickness distribution of Unit 200.
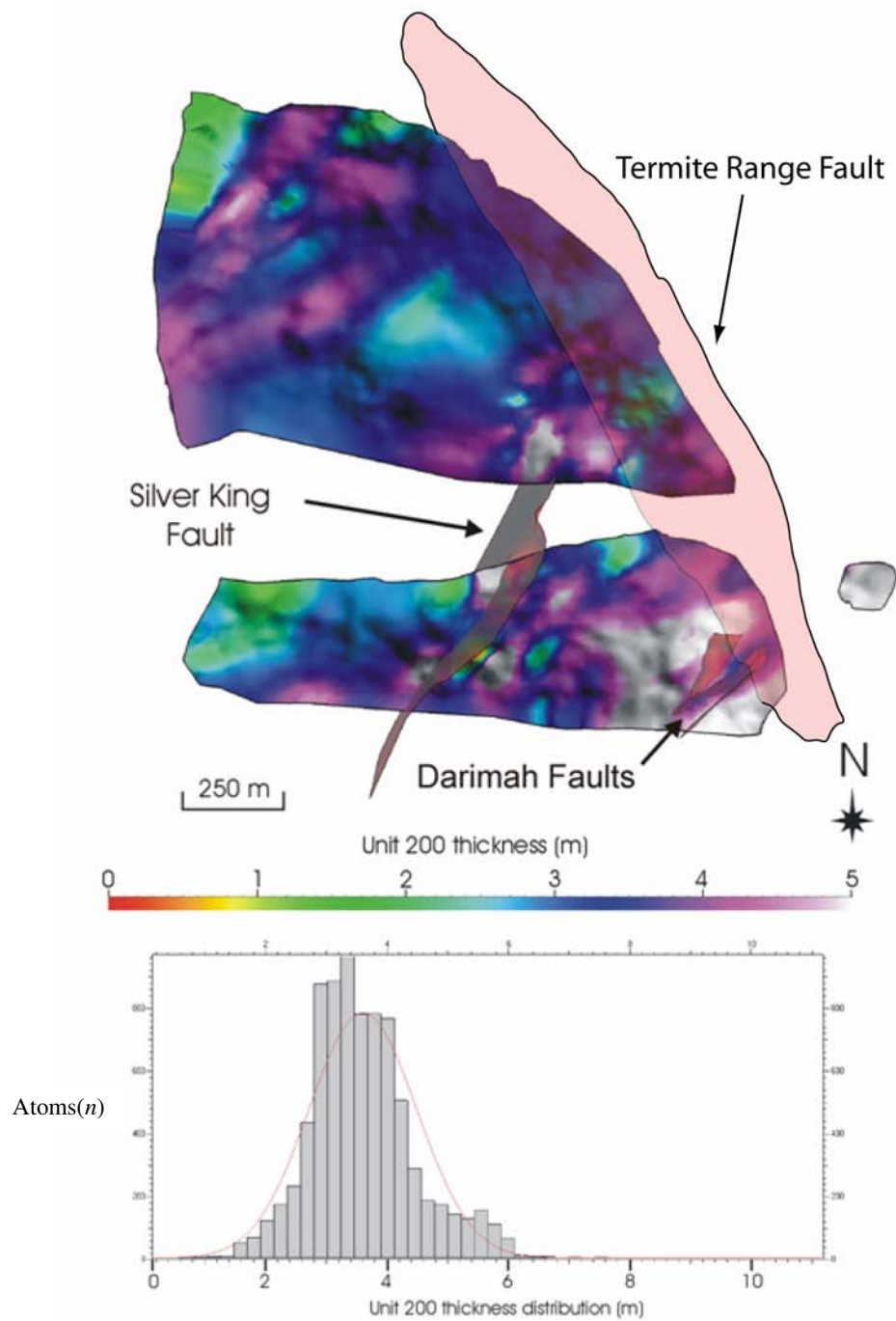
Fig. 4.10b 3D representation of the thickness variation in Unit 200 of the Century deposit looking north. Note the correlation of thickness increase with NE trending faults. Below: Histogram displaying the thickness distribution of Unit 200.

In summary the main conclusions made in relation to this study are:

- The 3D model shows that not only the TRF was active, and played a significant role in ore deposition processes, but other active faults in the system display correlations with thickness and mineralisation. The intersection of NW and NE structures could have been particularly important in focussing fluids

- The geometry of the TRF is the result of significant reactivation; however, several faults that have similar strike to the TRF, but dip towards NE, were interpreted to be relatively young parasitic branches of the TRF and were developed more likely during wrench style deformation occurring post-basin inversion, during the later stages of the Isan Orogeny.

- Bedding parallel shear is a characteristic of the shale's response to the brittle deformation. Much of this deformation may be younger than the main movement on the TRF as it does not seem to have a major influence on the mineralisation. Some localised redistribution of galena, that we interpret as a product of internal remobilisation of laminated ore, occurs exclusively in bands included within specific mine stratigraphic units (e.g. Unit 180) with higher Pb weight % contents.

- Metal distributions for Zn and Pb within Unit 200, which is one of the better constrained units in the upper ore zone, have pointed out the importance of NE trending structures as active faults that controlled ore emplacement.

4.5.   *Century ore genesis*

Two ore genesis models have been proposed for Century, based largely on paragenetic and geochemical work. The first model proposes an early-diagenetic timing of mineralisation (Waltho and Andrews, 1993). Following this work, Broadbent et al. (1998) has reinterpreted some of the textural arguments proposed as evidence of syngenesis to early-diagenesis and using new available lead, sulphur and carbon-oxygen data constrained using his detailed paragenesis, argues that a late-diagenetic to syn-tectonic timing for the mineralisation was more likely at Century. The main geological constraints and evidence for the Century late-diagenetic ore genesis following Broadbent et al. (1998) were:

(1) Overall zoning of ore and gangue mineral assemblages.

(2) The lack of any complex silicate- or barite-bearing assemblage indicative of exhalite facies anywhere within the (preserved) deposit stratigraphy.

(3) The consistent stratigraphic thickness of shale horizons which host ore, regardless of total sulphide content or grade of mineralisation.

(4) The transgressive nature of mineralisation at the overall scale of the deposit.

(5) The intimate associations of siderite, sulphides, and pyrobitumen at microscopic scale.

(6) Progressive timing relationships of silica mobility, siderite deposition, and sulphide deposition relative to compaction and dissolution fabrics of the host sequence.
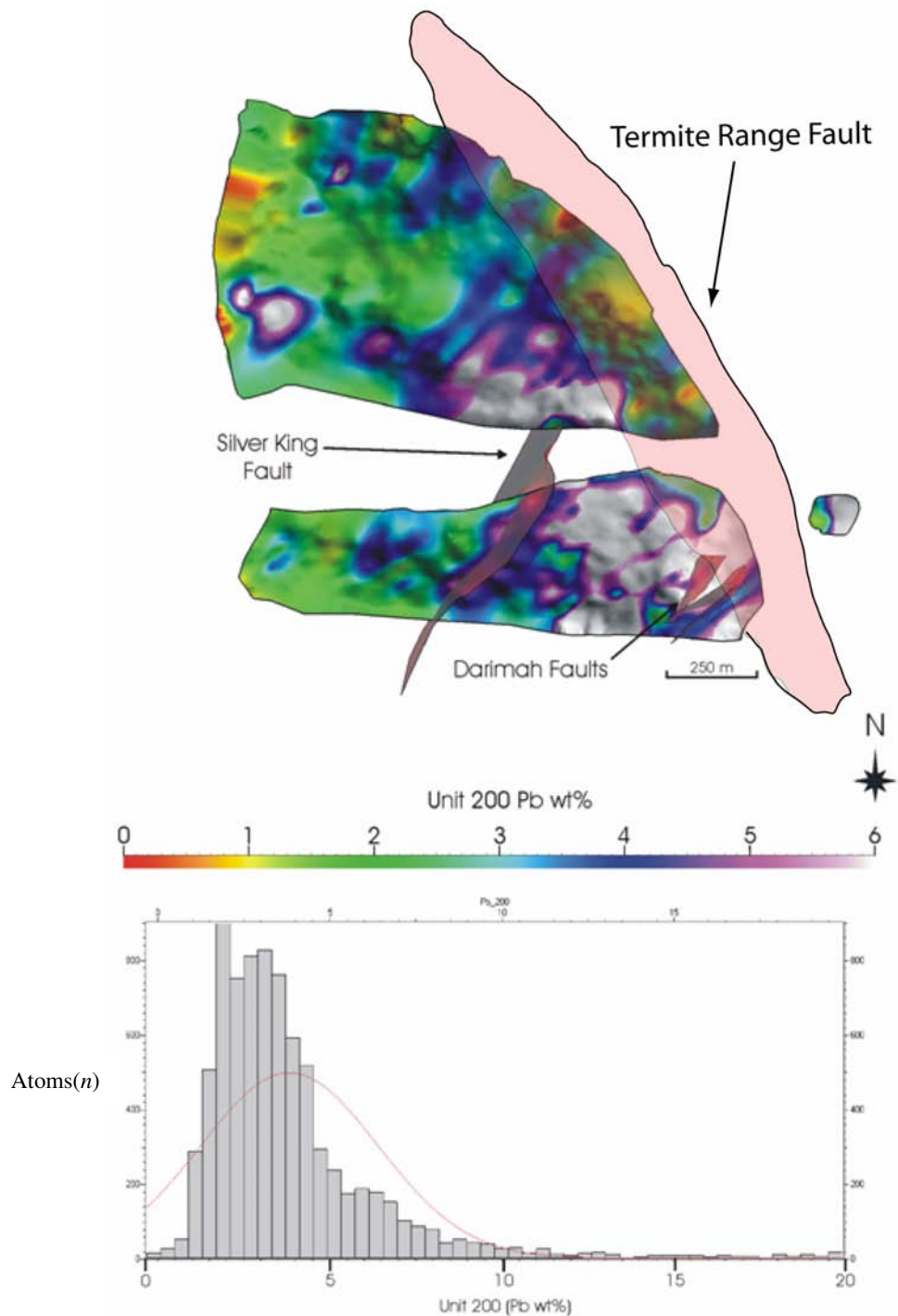
Fig. 4.11a 3D representation of the Pb distribution in Unit 200 of the Century deposit looking north. Note the correlation of higher grades with NE trending faults, and the spatial association of higher grade in the east (closer proximity to the Termite Range Fault). Below: Histogram displaying the Pb grade distribution of Unit 200.
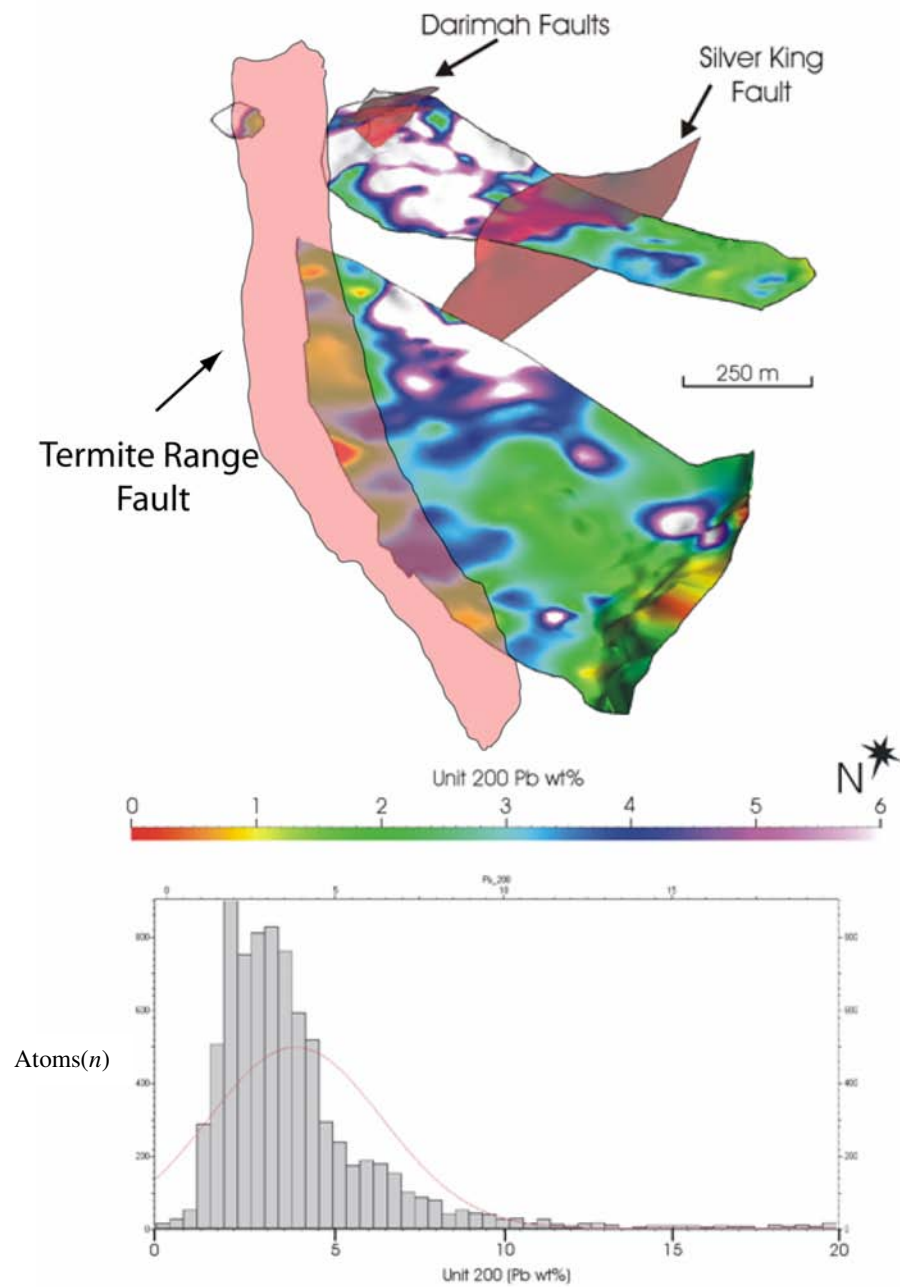
Fig. 4.11b. 3D representation of the Pb distribution in Unit 200 of the Century deposit looking south. Note the correlation of higher grades with NE trending faults, and the spatial association of higher grade in the east (closer proximity to the Termite Range Fault). Below: Histogram displaying the Pb grade distribution of Unit 200.
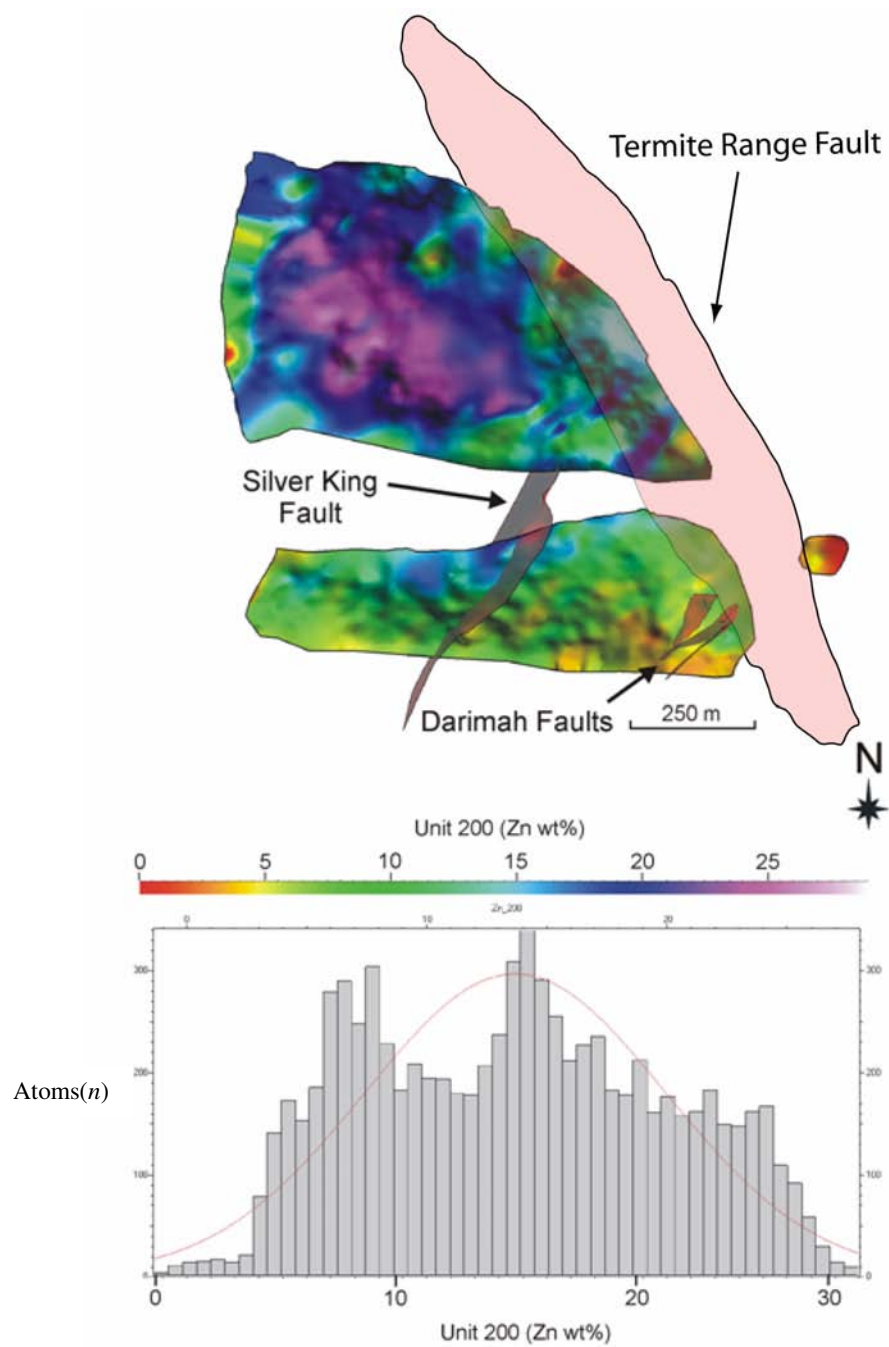
Fig. 4.12a. 3D representation of the Zn distribution in Unit 200 of the Century deposit looking north. Note the correlation of higher grades of Zn projecting along a NE trend, and the spatial distribution of higher grade in the west (distal to the Termite Range Fault). Below: Histogram displaying the Zn grade distribution of Unit 200.
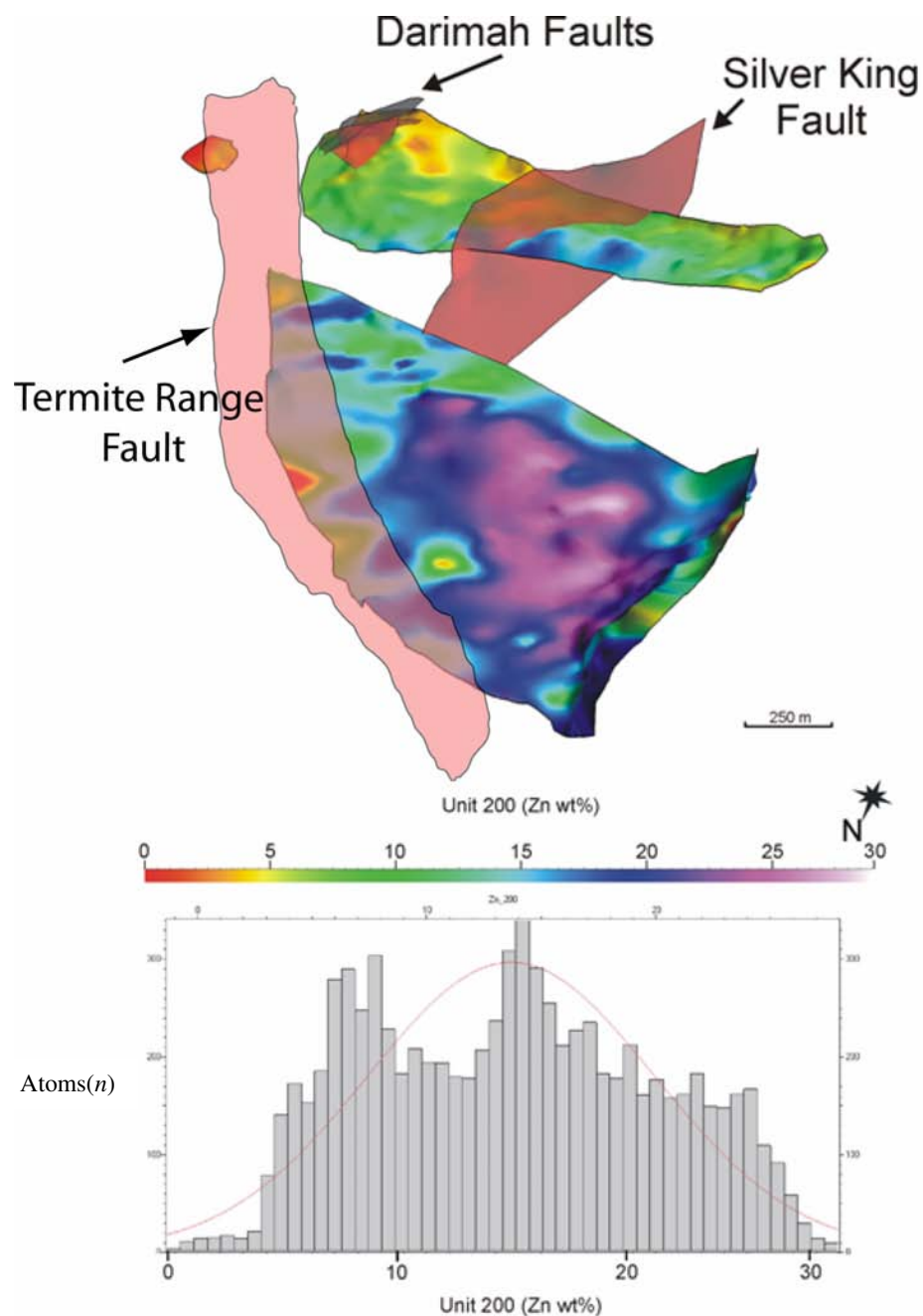
Fig. 4.12b 3D representation of the Zn distribution in Unit 200 of the Century deposit looking south. Note the correlation of higher grades of Zn projecting a NE trend, and the spatial association of higher grade in the west (distal to the Termite Range Fault). Below: Histogram displaying the Zn grade distribution of Unit 200.

To support his interpretation Broadbent (1999) describes a distinct relationship of sphalerite with pyrobitumen and further divides this relationship into upper and lower units within the mineralisation to underline the influence of the hydrocarbon reservoir phases, on textural aspects of the mineralisation. The lower part of the mineralised sequence contains 'porous sphalerite' (see Broadbent, 1999 for definition) which has a fine grained steel-grey appearance and a close association with pyrobitumen. In contrast, the upper part of the mineralised sequence is predominantly non-porous sphalerite consisting of almost pure sphalerite bands ranging from 0.2 to 5 mm in thickness. He concluded that a hydrocarbon source/reservoir represented a chemical trap for the mineralisation and contained an oil/gas interface that produced the different sphalerite textures. Cooke et al. (2003) noted however that both porous and non-porous sphalerite were interbedded throughout the deposit, although the proportions changed according to the gross zonation of Broadbent (1999). Broadbent et al. (1998), Broadbent, (1999) and Ord et al., (2002) also suggest that the hydrocarbon reservoir was overpressured at the time of mineralisation with consequent hydrofracturing and brecciation considered as main processes involved in fluid migration, metal leaching and deposition. Suggested metal sourcing for the Century system was related to clay transformation reactions from deeper units in the Lawn Hill Formation, and the conversion of sulphate to sulphide for metal precipitation as a result of thermochemical sulphate reduction (TSR) as the units passed through the 'oil window'.

4.6.   *Deformation and Fluid Flow*

Relationships between tectonic or geological settings and fluid flow are important in understanding potential sources and fluid pathways responsible for the formation of ore deposits. Common drivers for fluid migration include 1) topographic relief 2) 'squeegee' effects during thrusting and 3) deformation induced flow. The important effect of topographic relief and hydraulic head gradients has been well documented (e.g. Toth, 1962, 1963; Garven and Freeze, 1984a,b, Nesbitt and Muehlenbachs, 1989) and has been proposed as a significant hydrodynamic process with implications for long distance lateral fluid flow (e.g. Garven, 1985 – Mississippi Valley Type deposits). Oliver (1986) described the role of thrusting as a significant process in driving fluid flow in continental margins (the "squeegee" model), and in particular enabling lateral flow and the potential mixing of deep seated and surficial fluids in a contractional setting. Several authors have discussed at length the importance of deformation induced fluid flow (e.g. Etheridge et al., 1983, 1984; Cox, 1999; Ord and Oliver, 1997), which has a major influence over direction and rates of flow.

Compressional environments and inversion of compacted sedimentary basins typically lead to overpressurisation of pore fluids and upward fluid flow (e.g. Bethke, 1985; Upton, 1998) and Sibson (1987) has also linked upward flow and overpressurisation to fault valve activity. In extensional environments however, downward migration of fluids has been linked to the development of underpressure or where interconnectivity of fractures allows deep penetration of surface derived fluids (e.g. Nesbitt and Muehlenbachs, 1989; McLellan et al., 2004), and also in convection

cells (Simms and Garven, 2004). Broadbent (1999) considers overpressurisation as a primary mechanism for layer parallel fracturing, which allowed fluids to infiltrate the shale units and hence resulting in mineralisation. The majority of petroleum literature considers shale units to act as seals or caps, thus trapping fluids in aquifers such as sandstone. Broadbent (1999), however, concludes that the chlorite rich sandstone unit has acted as a seal and enabled overpressure in the shale unit below. He suggested that mechanically induced permeability of an otherwise low permeability unit, enabled lateral infiltration of metal rich fluids, which may have been transported up fault structures such as the TRF. Ord et al. (2002) presented coupled mechanical fluid flow and chemical models for the formation of the Century deposit, based primarily on Broadbent's (1999) interpretation. The main argument for these models, in a mechanical sense, is the preferential permeability assigned to the shale units, which reach a higher permeability than the faults transporting the mineralising fluids. In the context of the Century deposit, this leads to two potential scenarios for migration of fluids in relation to the genetic models presented previously, a syn-sedimentary/early diagenetic model and a syn-tectonic model; however lateral flow from major fluid pathways remains an issue. Here we aim to test possible scenarios for infiltration of fluids responsible for mineralisation by coupled deformation and fluid flow numerical simulations, by examining the potential types of faulting (growth faults and fault reactivation) present during the two most likely periods for mineralisation of the Century Zn-Pb-Ag deposit. The models within this study examine the potential for lateral flow within the shale units during extension and compression, and also the

permeability contrasts required to achieve this. The relationship between upward or downward migrating fluids and lateral fluid migration is also tested.

4.7.   Numerical modelling

The numerical models presented here are based on a coupled deformation and fluid flow approach, where mechanical deformation is the main driving force for fluid migration. To gain a better understanding and useful results, questions regarding the system under investigation must be posed. The main questions asked in this study are:

(1) What pathways controlled the location of favourable sites for mineralisation?

(2) What geological conditions were favourable for lateral fluid flow?

(3) What tectonic regimes were active and suitable for lateral flow?

(4) What role does overpressurisation have in controlling fluid flow and mineralisation?

4.7.1. FLAC (Fast Lagrangian Analysis of Continua)

FLAC is a two-dimensional explicit finite difference modelling program, suitable for simulating the behaviour of geological materials that undergo plastic flow during yield (see Chapter 2). FLAC has been applied to many geological problems in Australia (e.g. Ord, 1991a,b; Ord and Oliver, 1997; Oliver et al., 2001, 2006; Upton et al., 1995, 1998; Upton, 1998; Zhang et al., 1996a,b, 2002; McLellan, 2000; McLellan et

al., 2004; Schaubs and Zhao, 2002). Materials are represented by zones that form a grid, which can be adjusted by the user to fit the geometry of the problem to be solved. Each zone within the grid can be prescribed properties (both elastic and plastic) and the zones behave according to a prescribed linear or non-linear stress/strain law as a response to applied forces. The material is allowed to yield and flow and deform whilst run in large-strain mode, and when in a coupled scenario, fluid allows interaction with and influence over this deformation. For a full description of FLAC see Chapter 2 and Appendix A.

4.7.2.   Sensitivity of Strain Rates

As a result of rigorous sensitivity testing, strain rates within the FLAC models were found to be a critical parameter in determining not only pore pressure and hydraulic head distribution but also plasticity failure and ultimately fluid flow. Simulating deformation in FLAC can be done by either applying a boundary stress or a boundary velocity. In a Mohr-Coulomb constitutive relationship in FLAC there is no inherent time dependence associated with the mechanical steps, hence velocity boundary conditions are prescribed as a length per time step relationship, with real time only being associated with fluid steps in a coupled model. The unbalanced force in FLAC is a measure of equilibrium within the model grid and can represent a condition where we have steady state plastic flow. If the ratio of unbalanced force to internal forces within the model is large e.g. >1% then the boundary velocities are considered to be too great. In extensional deformation for example, we can check the effects of boundary velocities by examining the bulk extension rates of the model. This is done by

extracting information at specific grid points within the mesh and calculating the distance of movement and dividing this by the constitutive time of the model at this point. Typical values for geologically acceptable strain rates range from 1.00e-13 to 1.00e-17 sec^{-1} (e.g. Tadakazu et al., 2001; Pietrantonio and Riguzzi, 2004) and laboratory studies have shown strain rates as high as 1.00e-9 sec^{-1} (Turcotte and Schubbert, 2002). If strain rates are too slow then we have no plastic flow within the model, and if they are too great we have inertia effects and increased rates of deformation and fluctuating velocity histories. All models presented here have been tested for acceptable limits of bulk extension/shortening rates where applicable.

4.7.3. Conceptual models

Prior to any numerical modelling, an important step is to define the conceptual models and address the main questions posed in relation to the system under investigation. In this study two conceptual models are introduced in relation to the two possible fluid flow scenarios previously discussed, and linked to the tectonic setting that controls them. The conceptual models (Fig. 4.13a, b) consist of a 400 m by 400 m cross section representing a simplification of the mine stratigraphic intervals and the main geological components comprising the Century system (Fig. 4.14). The main aim of the constructed conceptual models is to explore the difference between a) extension and compression b) poorly consolidated materials and lithified materials (i.e. at depth) and c) permeability contrasts and hydrofracturing that may provide the potential for fluid to infiltrate the shale units in the Century system. Both models (extension and contraction)

are fully saturated with fluids, and pore pressure is initialised in Model 1 at hydrostatic, which represents conditions commensurate with early basin formation, and an overpressured zone is initialised in Model 2, which represents conditions commensurate with a later stage contraction. All physical properties are given in Table. 4.2.

Attempts were made to numerically model a syngenetic scenario, by prescribing all materials low values of elastic properties and in particular low cohesion values. However, unconsolidated sediments may not behave in a Mohr-Coulomb sense in reality (i.e. they may be poro-elastic, not elastic-plastic or poro-plastic). Not only might the constitutive properties be inappropriate, FLAC cannot simulate the effect of ongoing sedimentation. Finally, lowering the cohesion values produced extreme grid failure at low strains, confirming that FLAC was inappropriate for modelling this scenario. Thus, we consider only two subsurface genetic models, extension during basin evolution (diagenesis) and contraction during orogeny (epigenesis).
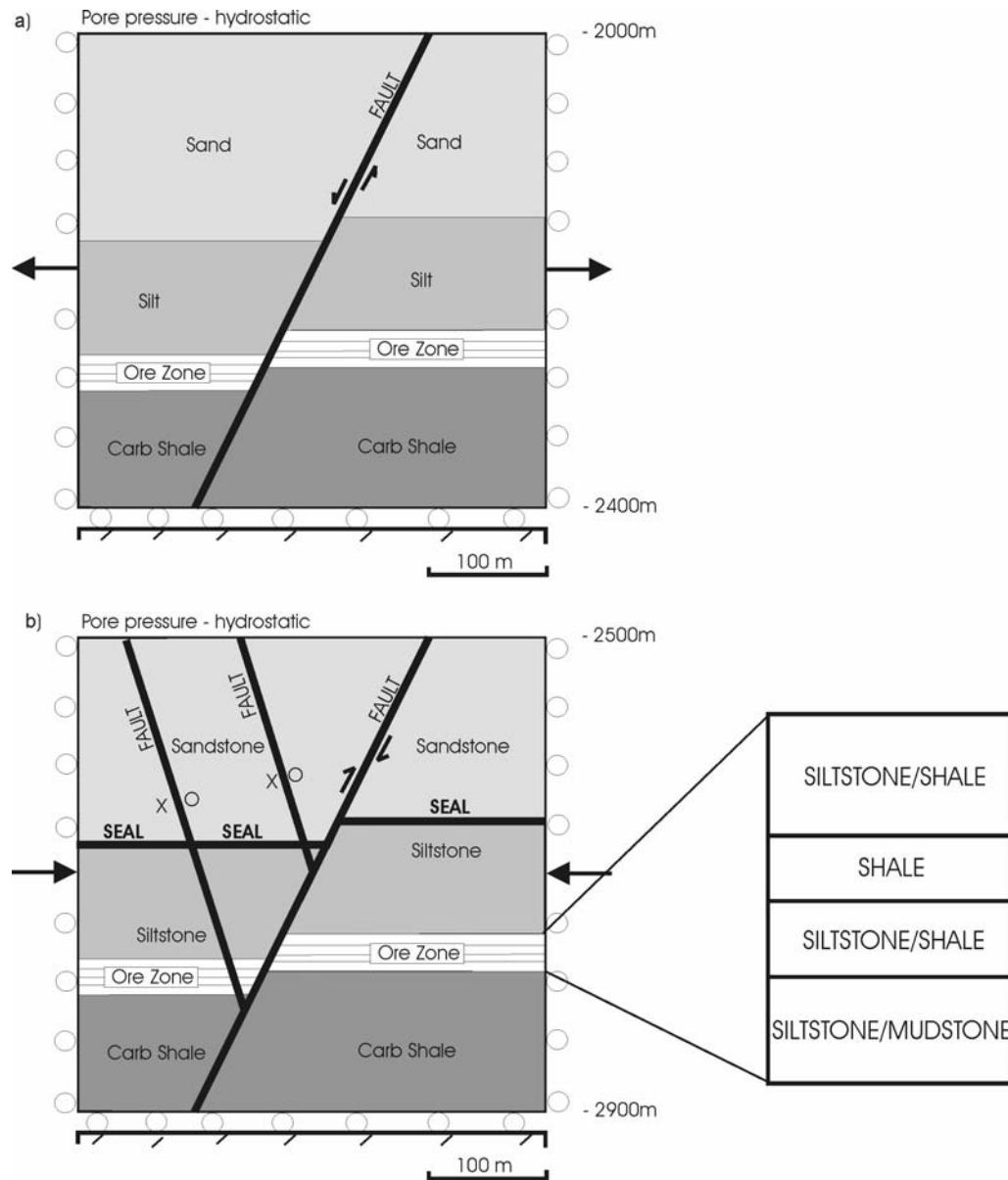
Fig. 4.13 Conceptual models for, a) Model 1 representing soft sediments and extensional deformation and b) Model 2 representing lithified sediments and later stage basin evolution. Ore Zone stratigraphy indicated. Model 2 has an overpressured zone applied in models 2b-d below the sandstone-siltstone interface at lithostatic pressures with the sandstone unit acting as a seal.
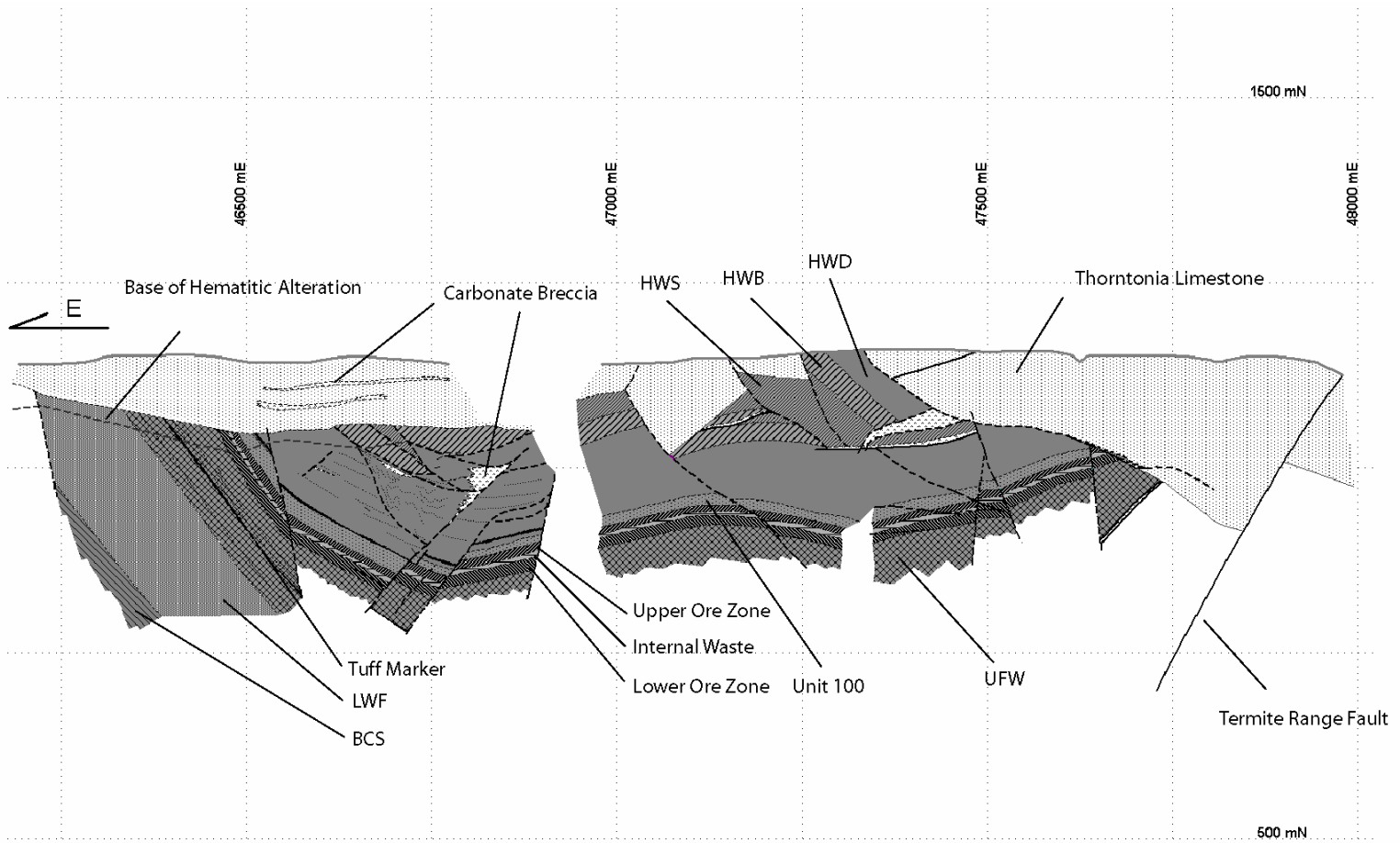
Fig. 4.14 Cross section of the Century deposit looking south, displaying the main structural features and stratigraphic elements. Note the Termite range Fault and its spatial relationship to parasitic faults to the east.

4.7.4. Conceptual Model 1

Conceptual model 1 (Fig. 4.13a) displays a simplified version of the mine stratigraphic units subdivision adopted after Kelso and Edge (unpublished report) (see Fig 4.7), and is cut by a normal fault, which represents the Termite Range Fault during and soon after sedimentation. Extensional deformation is applied to the model. The conceptual model represents an early diagenetic scenario in which sediments are considered to be semi-lithified, and here we are testing the effects of deformation and permeability contrasts on fluid flow.

To understand what permeability conditions are required to allow fluids to migrate through rock hosting the mineralisation, we tested two extensional models:

- **Model 1a** represents semi-lithified sediments and shale units (the most favourable host rock for Zn-Pb ore) with a low permeability value.

- **Model 1b** represents the same stratigraphy but the shales have higher permeability values to evaluate the permeability contrasts required to obtain significant fluid flow through them, and hence potential mineralisation.

Table 4.2 Physical properties for materials, Models 1 and 2.

Model	Density	Bulk modulus	Shear modulus	Cohesion	Friction angle	Dilation angle	Permeability
	(kg/m^3)	(Pa)	(Pa)	(Pa)	(°)	(°)	(m^2)
Model 1a							
Sand	1600	8.33e6	1.88e7	3.0e3	30	5	1.00e-12
Silt	1700	3.0e6	7.5e6	3.0e3	25	5	1.00e-13
All Shale	1800	3.33e5	5.01e6	1.0e3	20	2	1.00e-14
Silt / Shale	1750	8.0e5	7.0e6	2.0e3	22	3	5.00e-13
Silt / Mud	1750	8.0e5	9.5e5	2.0e3	22	3	2.00e-14
Fault	1600	3.33e5	7.0e4	1.0e3	20	5	1.00e-12

Model	Density	Bulk modulus	Shear modulus	Cohesion	Friction angle	Dilation angle	Permeability
	(kg/m^3)	(Pa)	(Pa)	(Pa)	(°)	(°)	(m^2)
Model 1b							
Sand	1600	8.33e6	1.88e7	3.0e3	30	5	1.00e-12
Silt	1700	3.0e6	7.5e6	3.0e3	25	5	1.00e-13
Carbonaceous Shale	1800	3.33e5	5.01e6	1.0e3	20	2	1.00e-14
Ore Shale	1800	3.33e5	5.01e6	1.0e3	20	2	1.00e-12
Silt / Shale	1750	8.0e5	7.0e6	2.0e3	22	3	5.00e-13
Silt / Mud	1750	8.0e5	9.5e5	2.0e3	22	3	2.00e-14
Fault	1600	3.33e5	7.0e4	1.0e3	20	5	1.00e-12

Model	Density	Bulk modulus	Shear modulus	Cohesion	Friction angle	Dilation angle	Permeability
	(kg/m^3)	(Pa)	(Pa)	(Pa)	(°)	(°)	(m^2)
Models 2a-b							
Sandstone	2400	2.68e10	7.0e9	2.7e7	27	4	1e-15 to 1e-19
Siltstone	2450	1.56e10	1.08e10	3.47e7	25	4	1.00e-16
Ore Shale	2500	8.8e9	4.3e9	3.84e7	14	2	1.00e-19
Carbonaceous Shale	2500	8.8e9	4.3e9	3.84e7	14	1	1.00e-19
Siltstone / Shale	2500	1.0e10	7.5e9	3.6e7	23	2	5.00e-16
Siltstone / Mudstone	2600	1.0e10	7.5e9	3.6e7	23	2	1.00e-18
Fault	2300	4.70e9	4.30e9	8.00e5	30	5	1.00e-14

note: Model 2b decreases permeability of Sandstone to 1.00e-19 and overpressure is applied

Model	Density	Bulk modulus	Shear modulus	Cohesion	Friction angle	Dilation angle	Permeability
	(kg/m^3)	(Pa)	(Pa)	(Pa)	(°)	(°)	(m^2)
Models 2c-d							
Sandstone	2400	2.68e10	7.0e9	2.7e7	27	4	1e-15 to 1e-19
Siltstone	2450	1.56e10	1.08e10	3.47e7	25	4	1.00e-16
Ore Shale	2500	8.8e9	4.3e9	3.84e7	14	2	1.00e-15
Carbonaceous Shale	2500	8.8e9	4.3e9	3.84e7	14	1	1.00e-19
Siltstone / Shale	2500	1.0e10	7.5e9	3.6e7	23	2	5.00e-16
Siltstone / Mudstone	2600	1.0e10	7.5e9	3.6e7	23	2	1.00e-18
Fault	2300	4.70e9	4.30e9	8.00e5	30	5	1.00e-14

note: Model 2b has an additional yield function applied

4.7.5. Conceptual Model 2

The second conceptual model (Fig. 4.13b) is similar to Model 1; however two additional parasitic faults have been added to reflect the evolution of the Termite Range Fault, which appears to have been reactivated during syn- to post-tectonic deformation. The stress applied to this second conceptual model is consistent with compression. In this case it is intended to represent a later stage of evolution of the Century system in which fluids are more tectonically driven with major topographic and deformation induced flow. Within this compressional model we test four alternative scenarios:

- **Model 2a** has regular rehological properties assigned for the appropriate rock types;

- **Model 2b** then assigns a low permeability to the sandstone unit (as described earlier) with a decrease in permeability from 1e-15 to 1e-19 m2, and the role of overpressure is investigated following the hypothesis proposed by Broadbent et al. (1998);

- **Model 2c** is also initialised with an overpressured area at the siltstone/sandstone boundary in correspondence with the interpretation of Broadbent (1999), and has an increase in permeability of the shale units from 1e-19 to 1e-15 m2; and

- **Model 2d** introduces an additional function that increases permeability by 10% within the model when materials are at yield and returning to or retaining their original permeability when not at yield. This function

allows deformation induced permeability to be investigated in the shale units and other rocks and faults.

4.8.   Results

Initial models (Model 1a and 1b) were constructed with assigned material properties conducive to semi-lithified sediments (i.e. relatively low cohesion), and as a consequence, the model grid fails shortly following 2% extension. However, initial results during early periods of extension in these models are presented. Models 2a-d represent lithified rocks (higher cohesion) and are deformed to around 12% shortening. The results of all models are presented below.

4.8.1.   Model 1a (extension, semi-lithified sediments, low permeability shale)

At very early stages of extension (1%) fluid flow is primarily focussed within the fault, sandstone and silt layers, due to higher permeability of these units (Fig. 4.15a). Local pore pressure gradients intensify fluid flow with maximum flow velocities of 1.44e-8 m/s^{-1} (0.45 m/yr^{-1}). On closer inspection fluid can be seen to be drawn from the fault into the siltstone layers with an overall flow direction from left to right, however little to no flow is evident within the shale as a result of the low permeability values assigned to these units (Fig. 4.15b). At around 2% extension pore pressure has decayed slightly, displaying supra-hydrostatic pore pressures and a sub-hydrostatic

gradient (Fig. 4.16a). Fluid flow is more evident within the more permeable units of sandstone, siltstone and within the fault, with increased flow velocities of 1.704e-8 m/s^{-1} (0.54 m/yr^{-1}) (Fig. 4.16b).

As a result of the low values in elastic properties of the sediments, the model grid fails soon after 2% deformation. If ore deposition occurred in zones of high fluid flux, it would have been most concentrated in the faults and coarser grained sediments, according to this model.

4.8.2. Model 1b (extension, semi-lithified sediments, high permeability shale)

As with Model 1a, initial extension causes perturbations in fluid flow which is primarily driven by pore pressure gradients (Fig. 4.17a). Unlike Model 1a however, strong lateral flow can be seen in the shale units due to the assigned permeability being similar to the fault and greater than the surrounding sediments (Fig. 4.17b). As pore pressure decays as a result of extension similar patterns to Model 1a are evident, with downward migrating fluid primarily within the more permeable fault and lateral flow within the stratigraphic units (Fig. 4.18). Comparative increases in fluid flow velocities to Model 1a are seen as a result of continuing deformation from 1 to 2% extension (1.475e-8 m/s^{-1} to 1.788e-8 m/s^{-1} – 0.47 m/yr^{-1} to 0.56 m/yr^{-1}). According to this model, substantial fluid flow may have caused mineralisation in shales and faults. Inflow towards the fault or outflow away, along the shale layers, is dependent on detail of the geometry chosen.
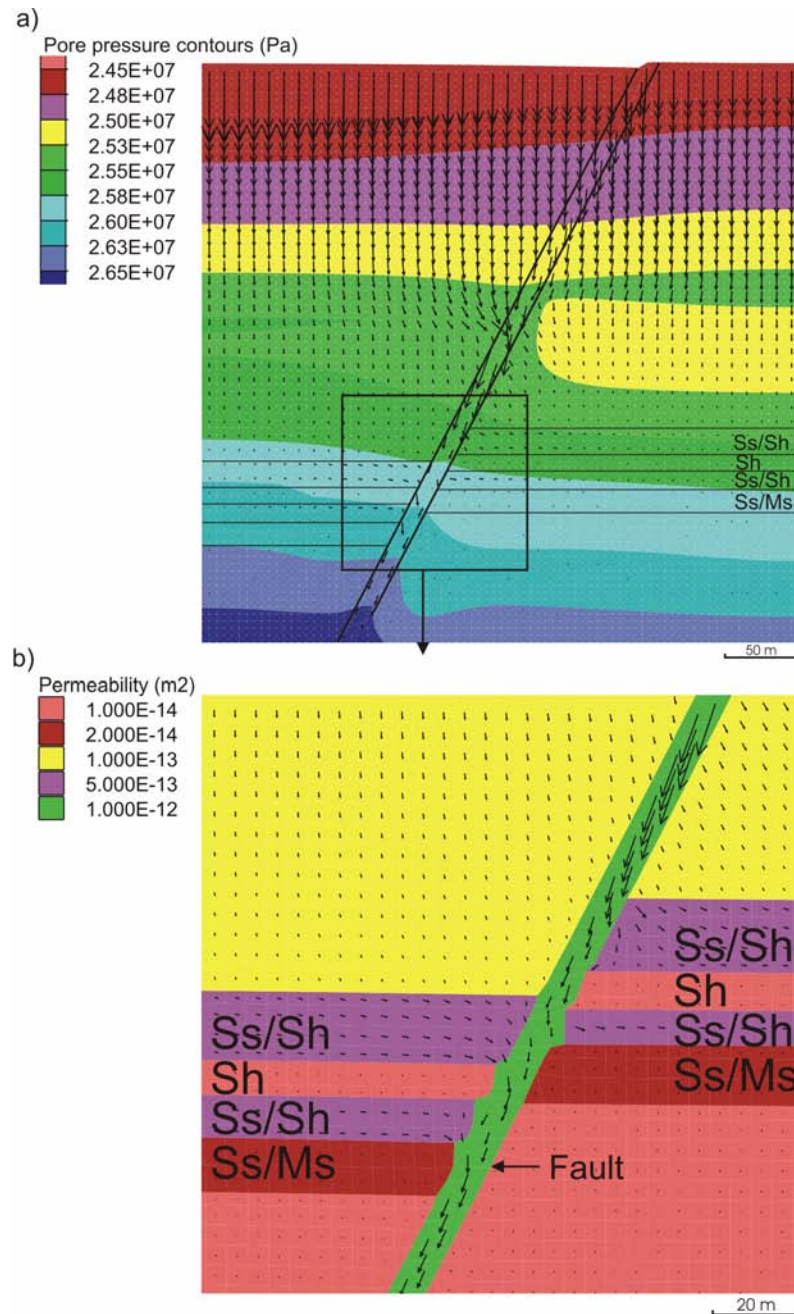
Fig. 4. 15 Model 1a showing plots of a) pore pressure contours and Darcy fluid flow vectors for Model 1a at 1% extension, displaying predominant downward migration of fluids within the more permeable fault and sediments, b) magnified plot of the ore zone displaying permeability values and flow vectors. Note the lack of fluid flow within the shale units.

a)

b)
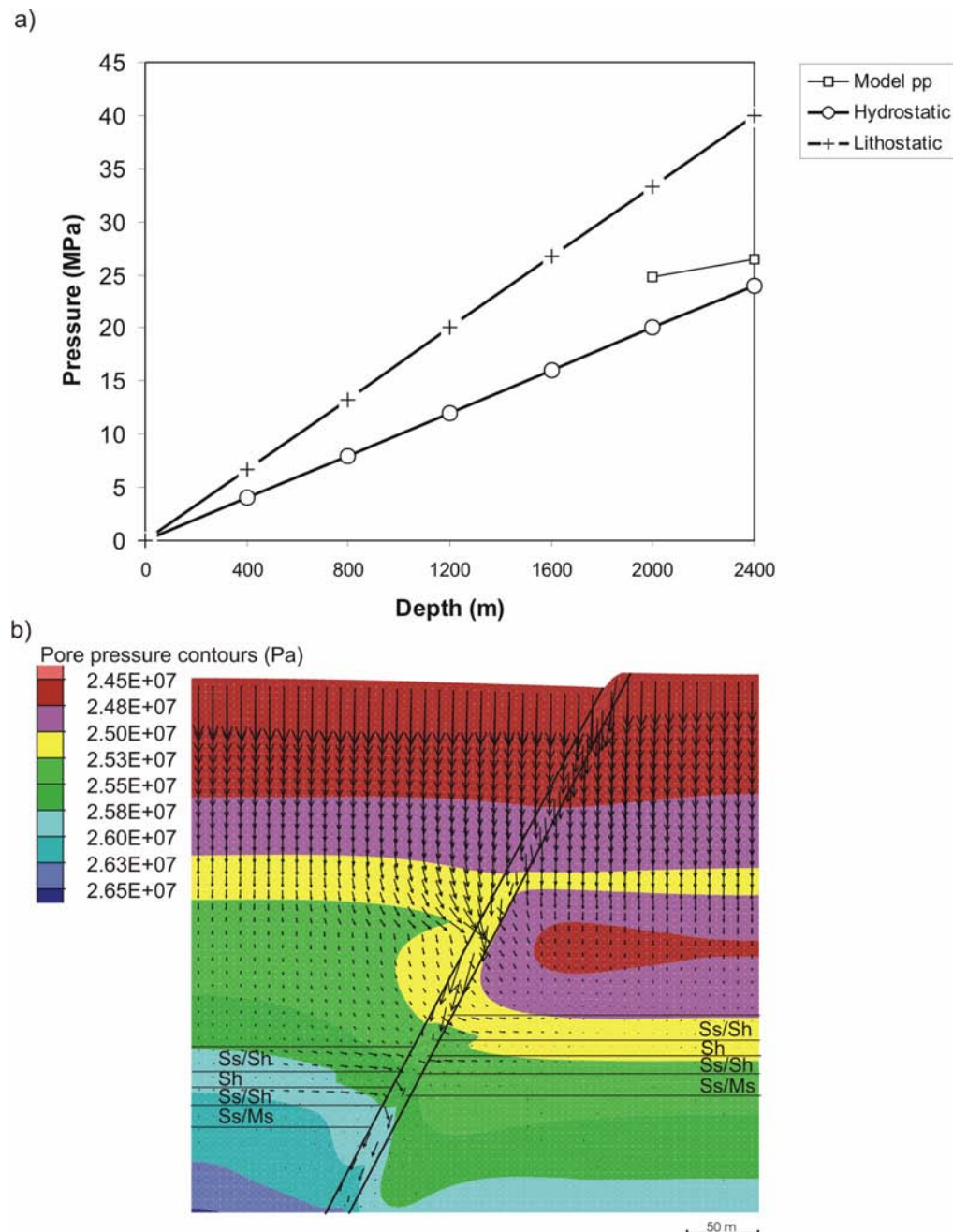
Fig. 4. 16 Model 1a at around 2% extension, a) depth v pressure graph illustrating pore pressure decay due to extension, displaying supra-hydrostatic pore pressures and a sub-hydrostatic gradient, b) plot of pore pressure and Darcy fluid flow vectors indicating an overall downward trend of fluid flow within the fault and lateral flow in the more permeable siltstone layers.
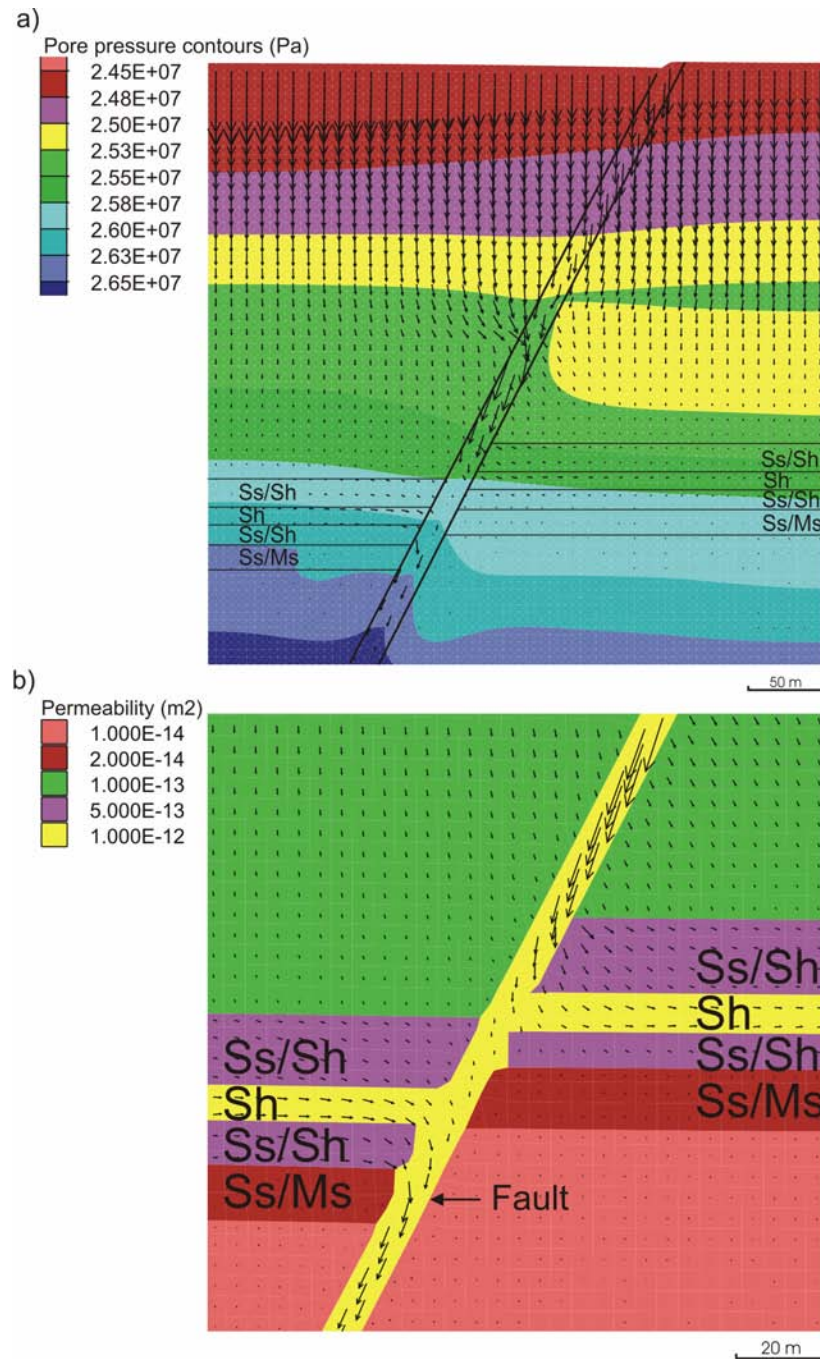
Fig. 4.17 Plot of a) pore pressure contours and Darcy fluid flow vectors for Model 1b at 1% extension, displaying predominant downward migration of fluids within the more permeable fault and sediments, b) magnified plot of the ore zone displaying permeability values and flow vectors. Note the strong fluid flow within the shale units (yellow).
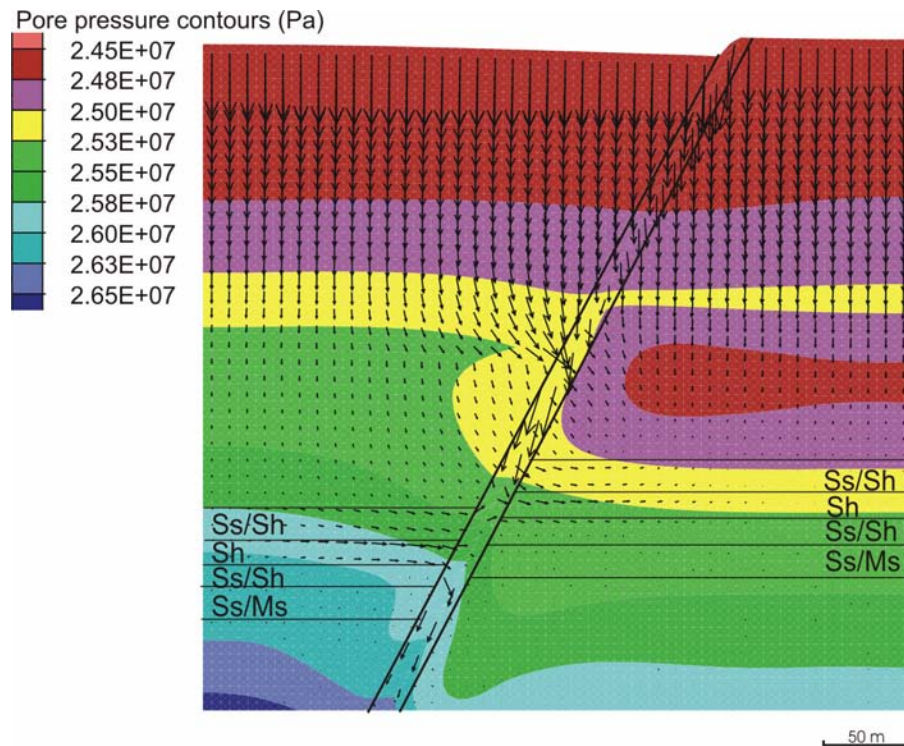
Fig. 4.18 Plot of pore pressure contours and Darcy fluid flow vectors for Model 1b at 2% extension, displaying predominant downward migration of fluids within the more permeable fault and sediments, and strong lateral fluid flow within the shale units.

In summary, the results from the simulation of semi-lithified sediments and poorly consolidated material indicate that FLAC has difficulty in modelling material of this type, due to inadequate constitutive models and grid failure. However, useful results for some models are indicated in very early stages of extension, where fluid flow is focussed within more permeable material and driven by initial changes in pore pressure gradients and permeability contrasts. When the shale unit within the 'ore zone' has permeability values as high as to less than one order of magnitude lower than that of the fault, notable fluid flow is evident in shales, which may indicate the potential for a

diagenetic replacement in a subsurface condition. The permeability is one of the primary factors that control fluid flow, during early stages of diagenesis.

4.8.3. Model 2a (contraction, low permeability shale)

A significant difference from the previous models discussed is that within this model fluid is focussed within the fault in an overall upward migration path (Fig. 4.19a). This was achieved by an initial compression, resulting in an increase in pore pressure (up to 75 MPa) within the model that forces fluid up the more permeable fault. Pore pressure cycles due to deformation and the system responds (Fig. 4.19b). The shale unit contains isolated areas of high pore pressure in comparison to other units as a result of the shale's low permeability and low dilation angle (Fig. 4.20a). Areas of dilation are observed within the model as deformation progresses (10% shortening), in particular to the left of the main fault, although focussing of fluids remains concentrated within the more permeable faults (Fig. 4.20b). The faults, however, show local contractional behaviour and limit fluid flow nearer the top of the model. Due to the limited permeability and lack of dilation in the shale units, no significant fluid flow is noted within them (Fig. 4.21).
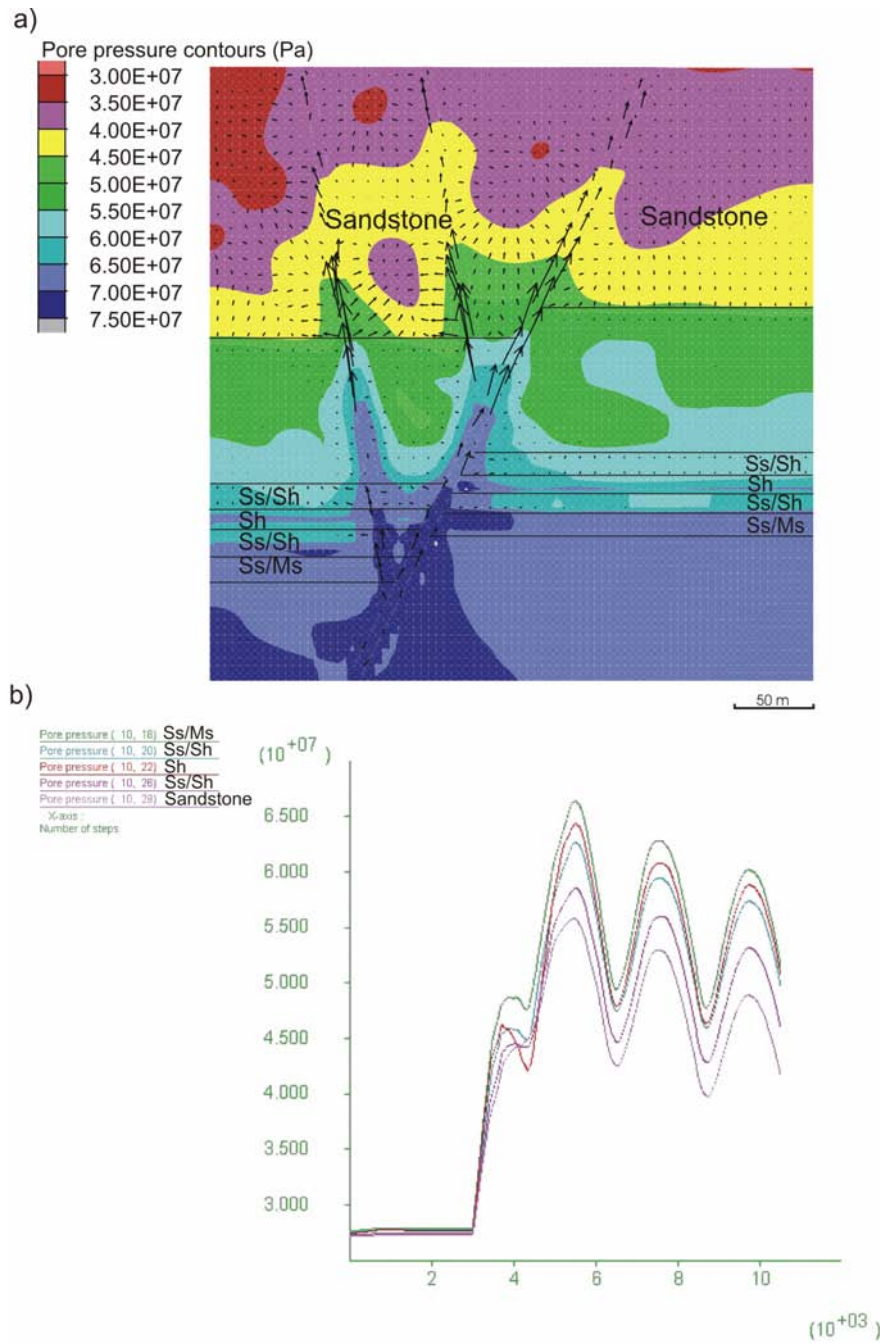
Fig. 4.19 Early stages of compression for Model 2a, a) plot of pore pressure and Darcy fluid flow vectors indicating an overall upward trend of fluid flow within the fault and very limited lateral flow in the permeable siltstone layers b) graph of pore pressure v time, illustrating pore pressures in all units from the over zone to the sandstone. Note the cyclic behaviour of pore pressure due to deformation.
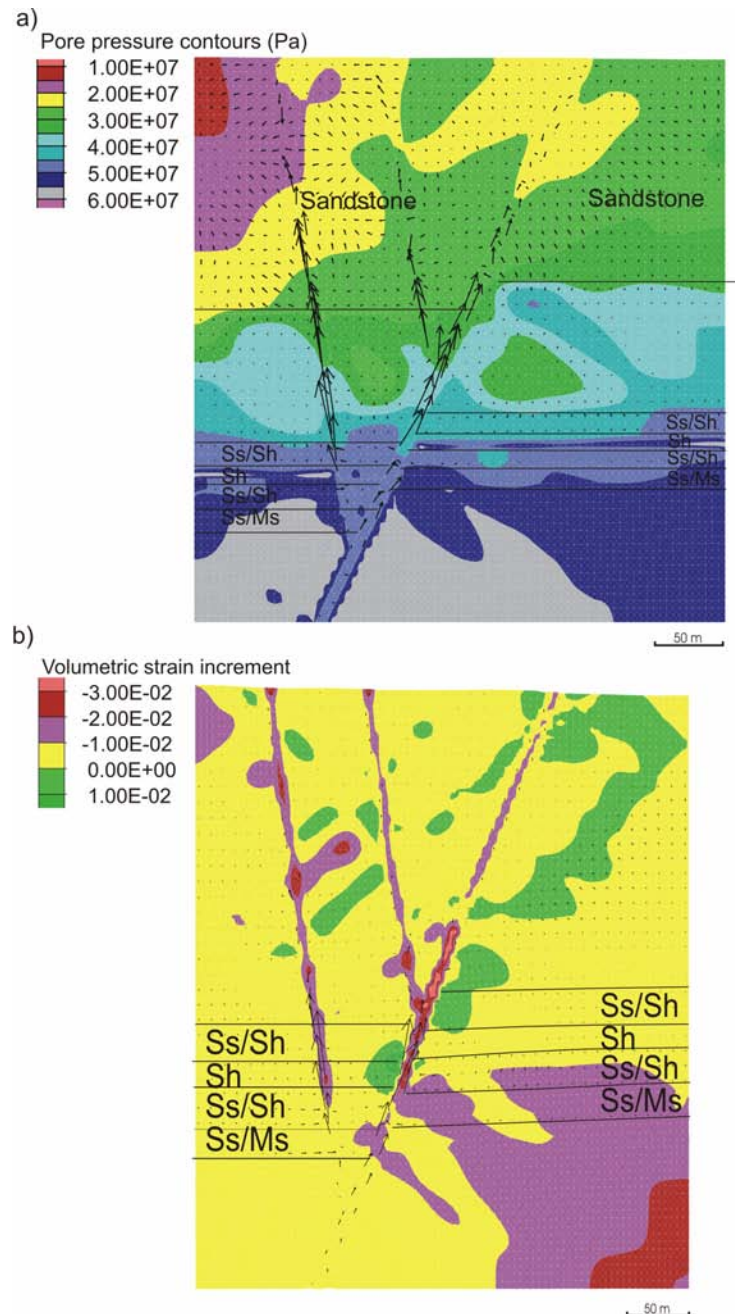
Fig. 4.20 Early to late stages of compression for Model 2a, a) 3% compression, plot of pore pressure and Darcy fluid flow vectors indicating an overall upward trend of fluid flow within the fault and very limited lateral flow in the permeable siltstone layers b) 9% compression, plot of volumetric strain (dilation) and Darcy fluid flow vectors indicating an overall upward trend of fluid flow within the fault and limited lateral flow in the permeable siltstone layers. Most dilation is occurring close to the fault structures.
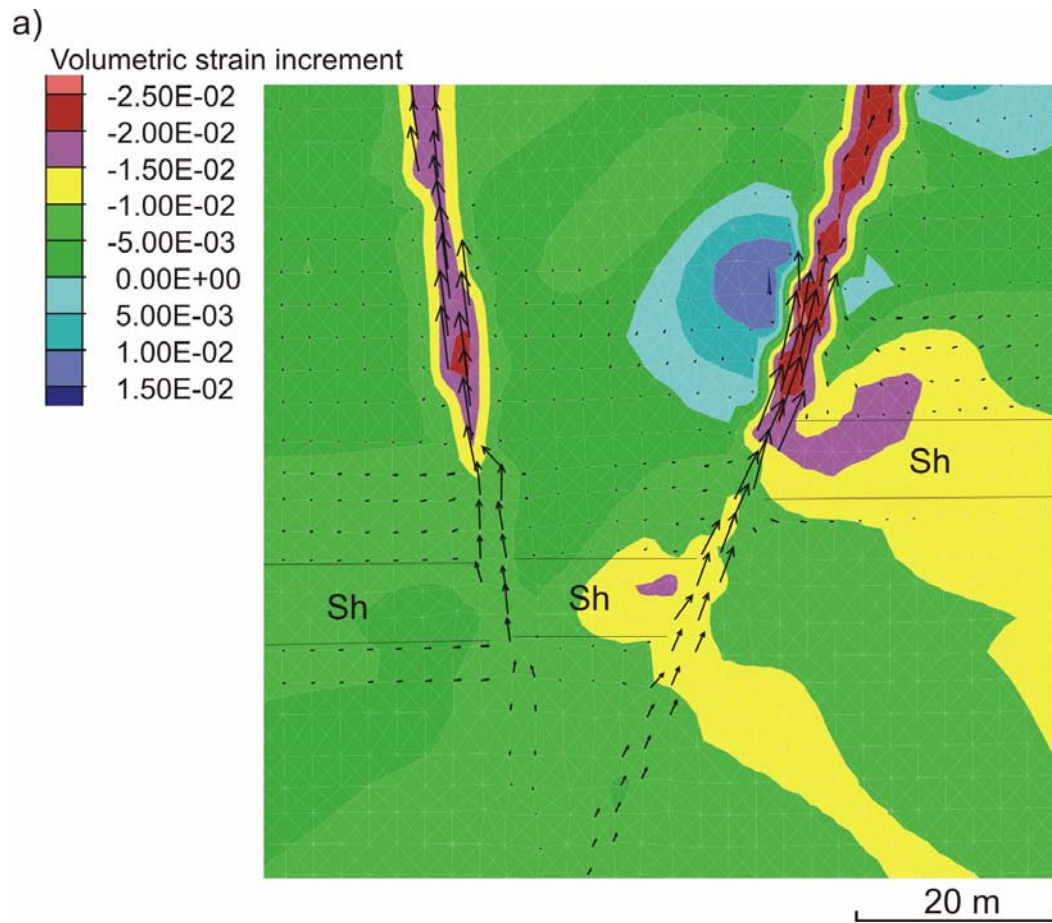
Fig. 4.21 Late stage of compression (9%) for Model 2a, plot of volumetric strain (dilation) and Darcy fluid flow vectors indicating an overall upward trend of fluid flow within the fault and insignificant flow within the shale layers.

4.8.4. Model 2b (contraction, low permeability shale and

sandstone, with overpressure)

In simulating the sandstone unit at the top of the model as a 'cap' or 'seal' to the system, the permeability of this unit is reduced. An overpressure is applied at the base of the sandstone unit and over the ore zone in agreement with the model proposed by Broadbent (1998) and Ord et al. (2002), as the chlorite rich sandstone has been interpreted as a seal in the system. As deformation commences, fluid is forced through the seal and into the faults penetrating above the sandstone (Fig. 4.22a-d). As compression progresses (3% shortening) strong upward flow driven by pore pressure gradients is seen within the fault structures (Fig. 4.23a). At around 5% shortening, dilational zones are prominent within the middle regions of the model and appear to be closely related to areas bounding faults (Fig. 4.23b). As deformation continues fluid flow continues upwards within the more permeable faults, with lesser flow noted within the siltstone layers and no flow in the shale layers (Fig. 4.24). Dilation is prominent as a band within the centre of the model; however this has no major influence on focussed fluid flow.
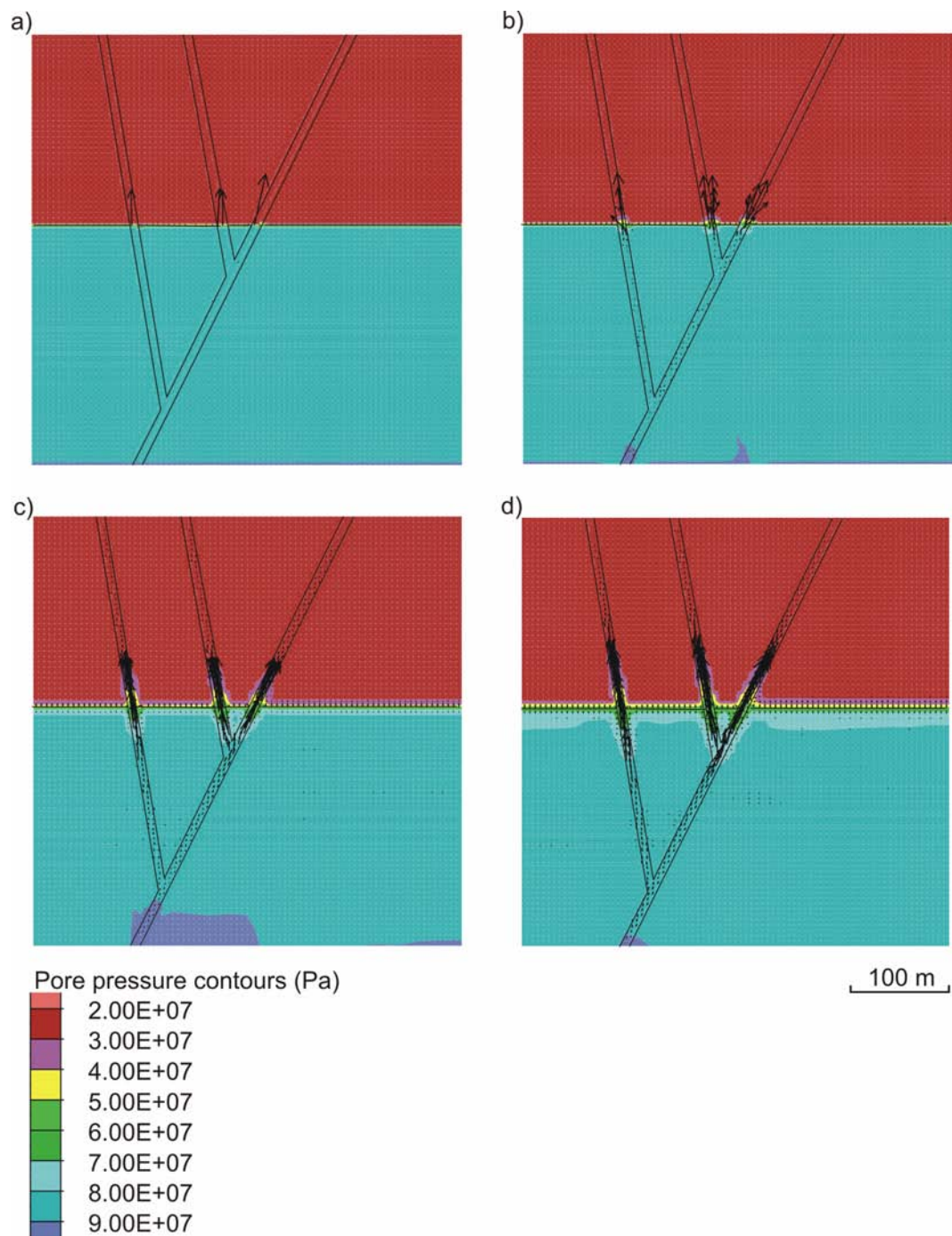
Fig. 4.22 Model 2b at commencement of deformation and release of overpressure, a) to d) representing stages of this process showing pore pressure contours forcing fluid upwards through the fault system with no lateral fluid flow evident.
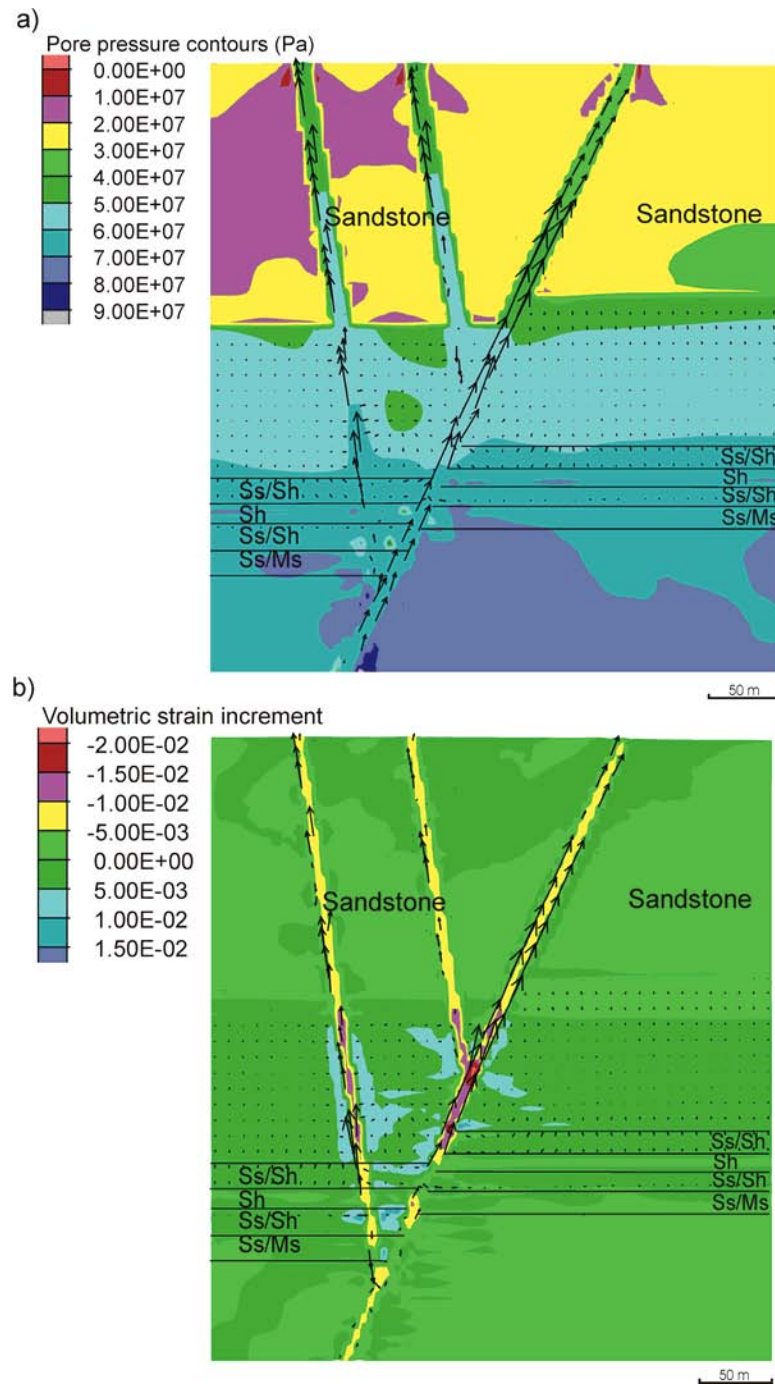
Fig. 4.23 Model 2b at a) 3% deformation, displaying pore pressure contours and a strong Darcy fluid flow focussing within the fault zones and b) 5% deformation, plot of volumetric strain (dilation) and Darcy fluid flow vectors, displaying strong flow within the faults and minor lateral flow in the siltstone layers.
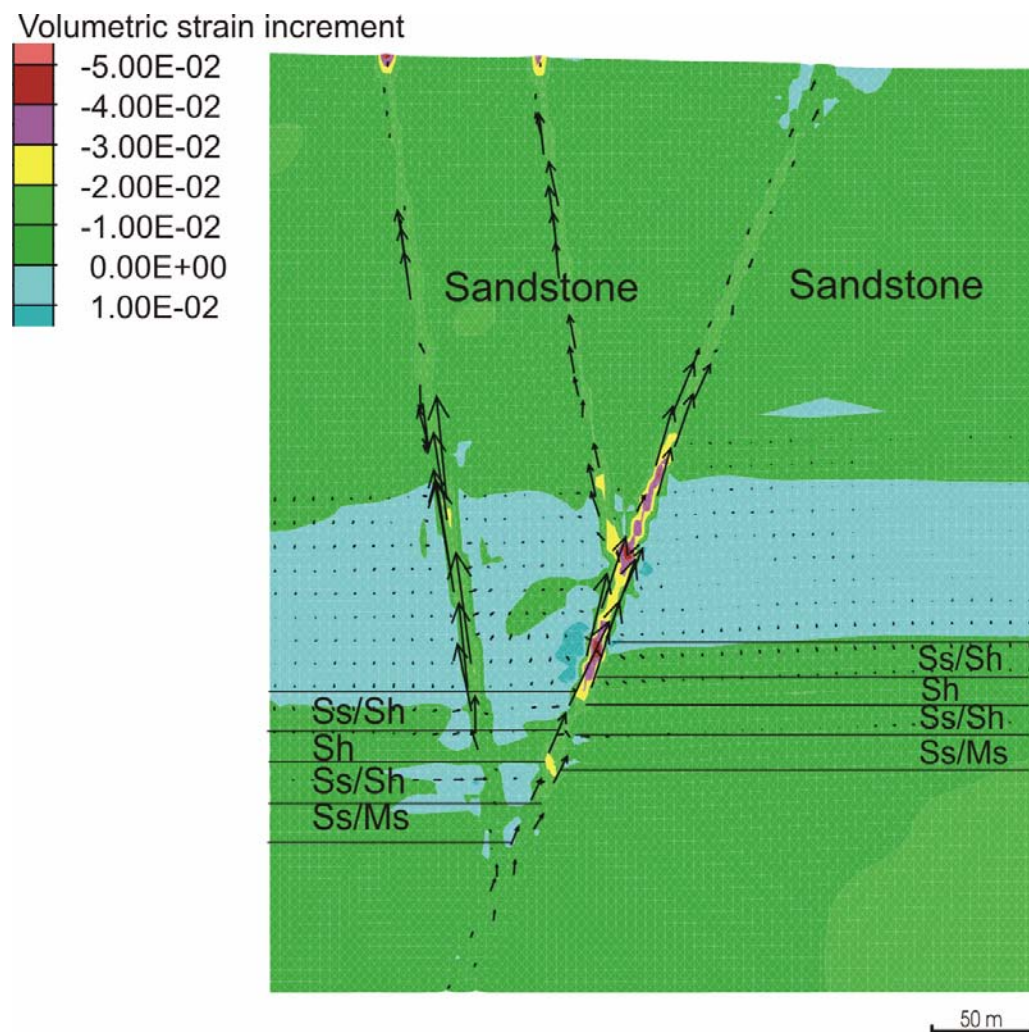
Fig. 4.24 Model 2b at 9% compression displaying volumetric strain (dilation) and Darcy fluid flow vectors. Dilation is primarily associated with a band in the centre region of the model and around fault structures.

4.8.5.   Model 2c (contraction, high permeability shale, low permeability sandstone, with overpressure)

Increasing the permeability of the shale units within the 'ore zone' has a major effect on fluid flow within this unit. At early stages of deformation (1% shortening) fluid flow is focussed in an upward direction within the more permeable faults, and lateral flow is evident from the fault into the shale units (Fig. 4.25a). Areas of high pore pressures are apparent from the base of the main fault (Fig. 4.25b) which is forcing fluid up the fault structures. Corresponding dilational zones are evident in close proximity to fault structures below the sandstone and siltstone interface, and in particular are found between the lower branching fault and the main fault (Fig. 4.26a). As deformation progresses, focussed flow within the shale unit is more apparent, with fluid being drawn from the shale units towards the faults. As deformation continues (5% shortening), fluid flow is preferentially focussed along the shale units and is also driven upwards through the permeable faults (Fig. 4.26b). Very limited fluid flow or dilation is seen within the sandstone, and it maintains overpressure in the units below, allowing only the fault structures to dissipate pressure up the faults. Within this model overall, pore pressure decays towards an equilibrium state following the release of the overpressure, and it is primarily driven by deformation and dilatancy. According to this model, if ore grades were related primarily to large fluid fluxes, shale units between the feeder faults would show high grades.
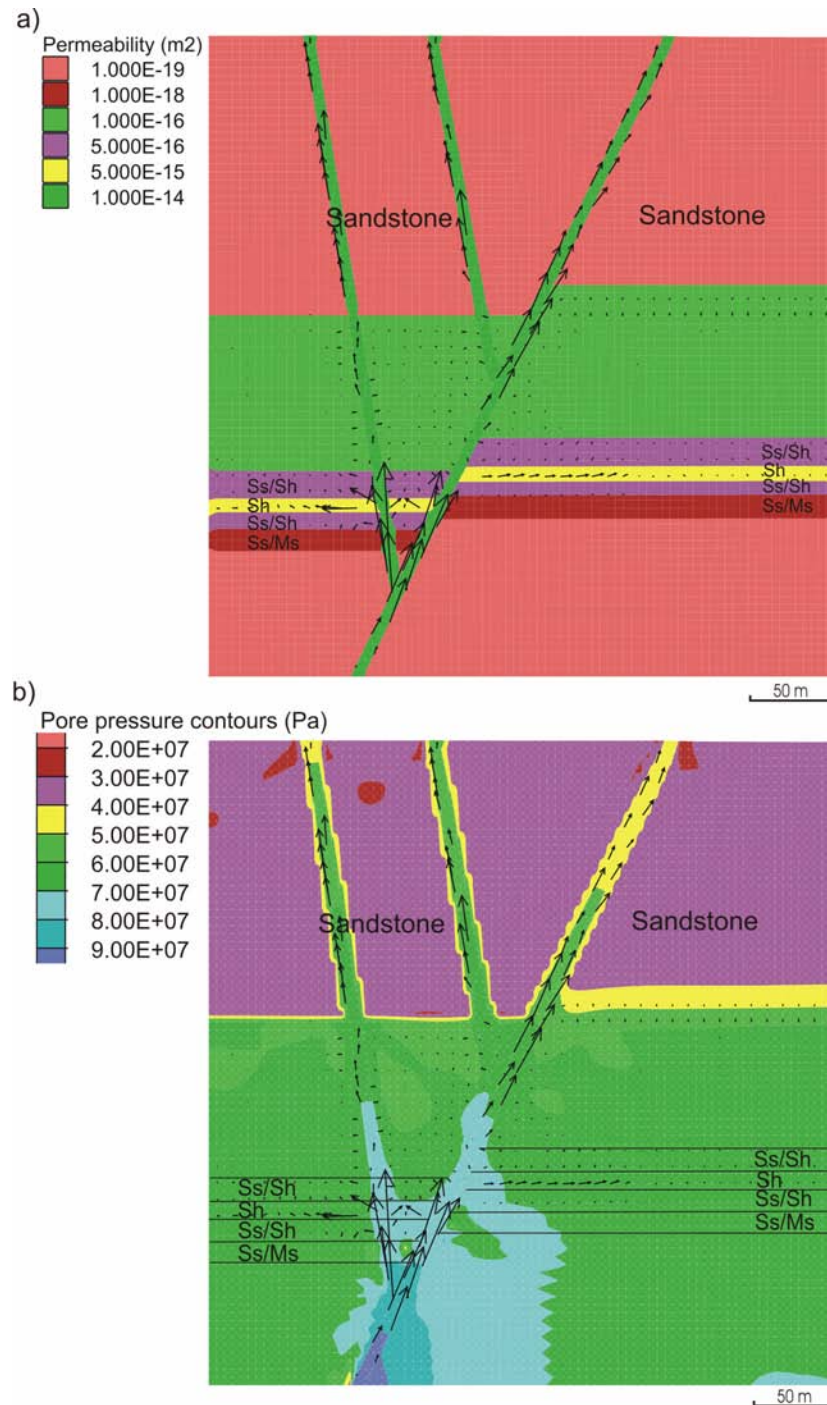
Fig. 4. 25 Model 2c at 1% deformation **a**) displaying permeability values and a strong Darcy fluid flow focussing within the fault zones. Lateral flow is evident within the shale layers, and **b**) plot of pore pressure contours and Darcy fluid flow vectors, displaying strong flow within the faults and minor lateral flow in the shale layers.
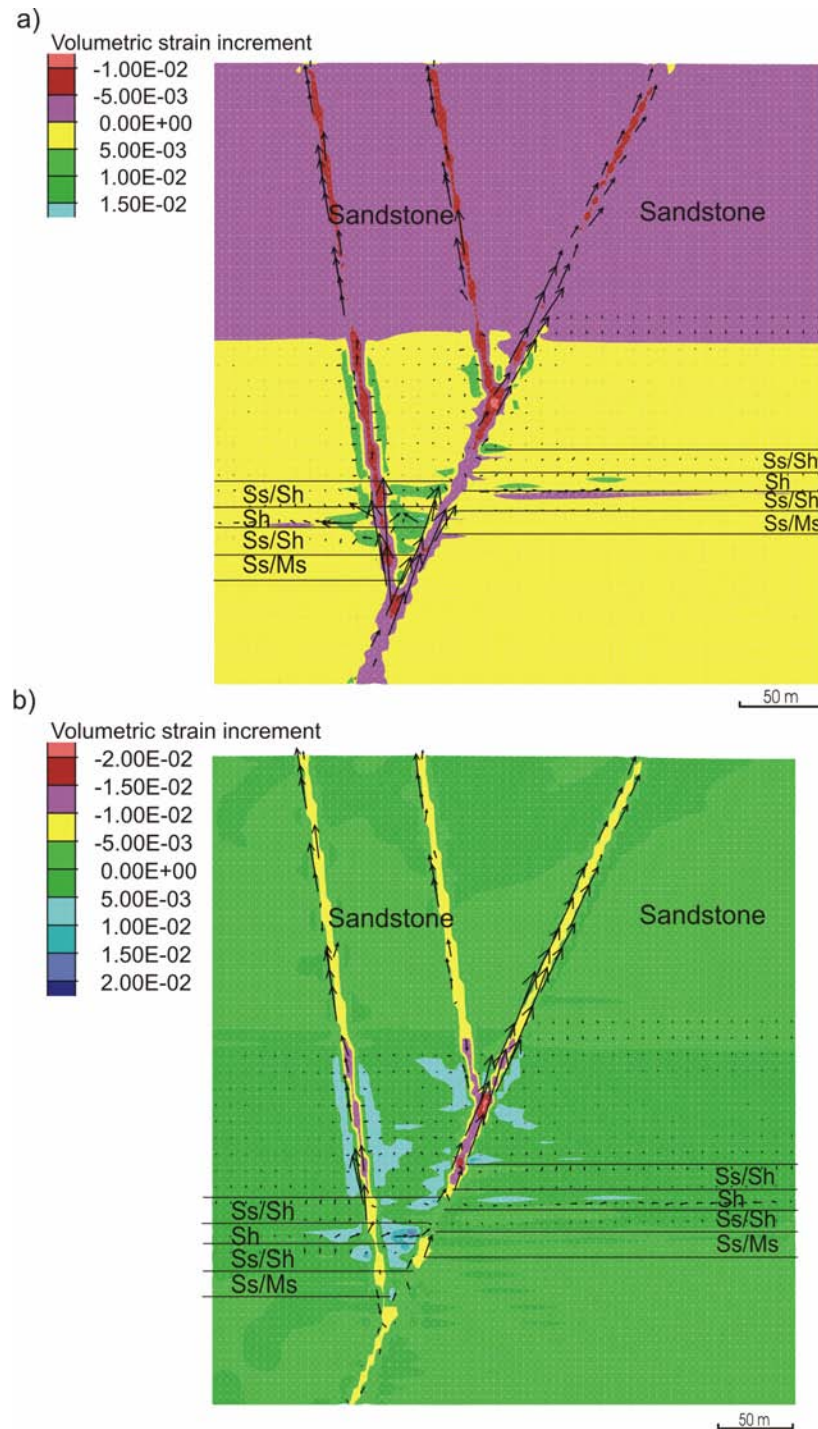
Fig. 4.26 Model 2c at **a**) 1% deformation, displaying volumetric strain (dilation) and a strong Darcy fluid flow focussing within the fault zones and towards dilatant areas in particular near fault intersections **b**) 5% deformation, plot of volumetric strain (dilation) and Darcy fluid flow vectors, displaying strong flow within the faults and lateral flow into the shale layers.

4.8.6. Model 2d (contraction, high permeability shale, low permeability sandstone, with overpressure and yield permeability)

In an attempt to simulate hydrofracturing and resultant permeability increase in the shale units, an additional function was applied to this model which increased the permeability as a function of the plastic state of the material (i.e. as material reaches a yield state, shear or tensile failure, the permeability of the material at that point is increased by 10% from its original value, and returning or retaining its original value when not at yield). This function was to simulate the process of failure and increased permeability due to hydrofracturing, as proposed by Broadbent (1999). In early stages of compression (3% shortening) fluid flow is mainly driven upwards from the base of the more permeable fault structures, however downward migration of fluids is noted around the mid region of the model and within the faults (Fig. 4.27a), and this appears to be primarily driven by a localised decrease in pore pressure and dilatant effects (Fig. 4.27b). Fluid flow is focussed towards areas of dilation in the shale unit near the intersection of the main fault and the left branching fault, and these areas correspond to an increase in permeability due to failure (Fig. 4.28a). These areas display tensile failure, and due to the increase in permeability have focused much of the fluid flow within the model. As deformation progresses (5% shortening) fluid flow intensifies in this region as a result of pore pressure decreases and dilatant effects (Fig. 4.28b). Fluid flow within the shale layer is limited outside this region, and as a result of the yield function applied, the permeability of the shale unit remains one order of magnitude less

than that of the fault, hence, fluid remains focussed mainly within the fault zones. At later stages of contraction (7% shortening) similar results are apparent, with further dilatant effects driving fluid towards areas of failure and some localised contraction due to increasing shear strain (Fig. 4.29). Similar to Model 2c, the results of this model permit interpretations of focussed mineralisation in the shale units close to the faults.

In summary, results from Model 2 indicate that overpressure aids in upward migration of fluids within the more permeable faults, and potentially stimulates hydrofracturing within the shale units. To have any significant fluid flow within the shales, they must have permeabilities close to or the same as the faults. Addition of a 'yield function' to increase permeability within the model allows tensile failure and increased permeability within the shale unit, however, fluid is primarily drawn from the shale units towards the faults in most cases. This scenario also limits upward migrating fluids from deeper basinal horizons or basement material from entering the shale units, so ore genesis models using this scenario would have to source metals and sulphur from above. However, local areas between branching faults that display strong dilational characteristics may provide limited access to shales for deep seated mineralising fluids. Raised issues on permeability paths, their geometry, and their influence on grade distributions will be further addressed with 3D numerical models in the next chapter.
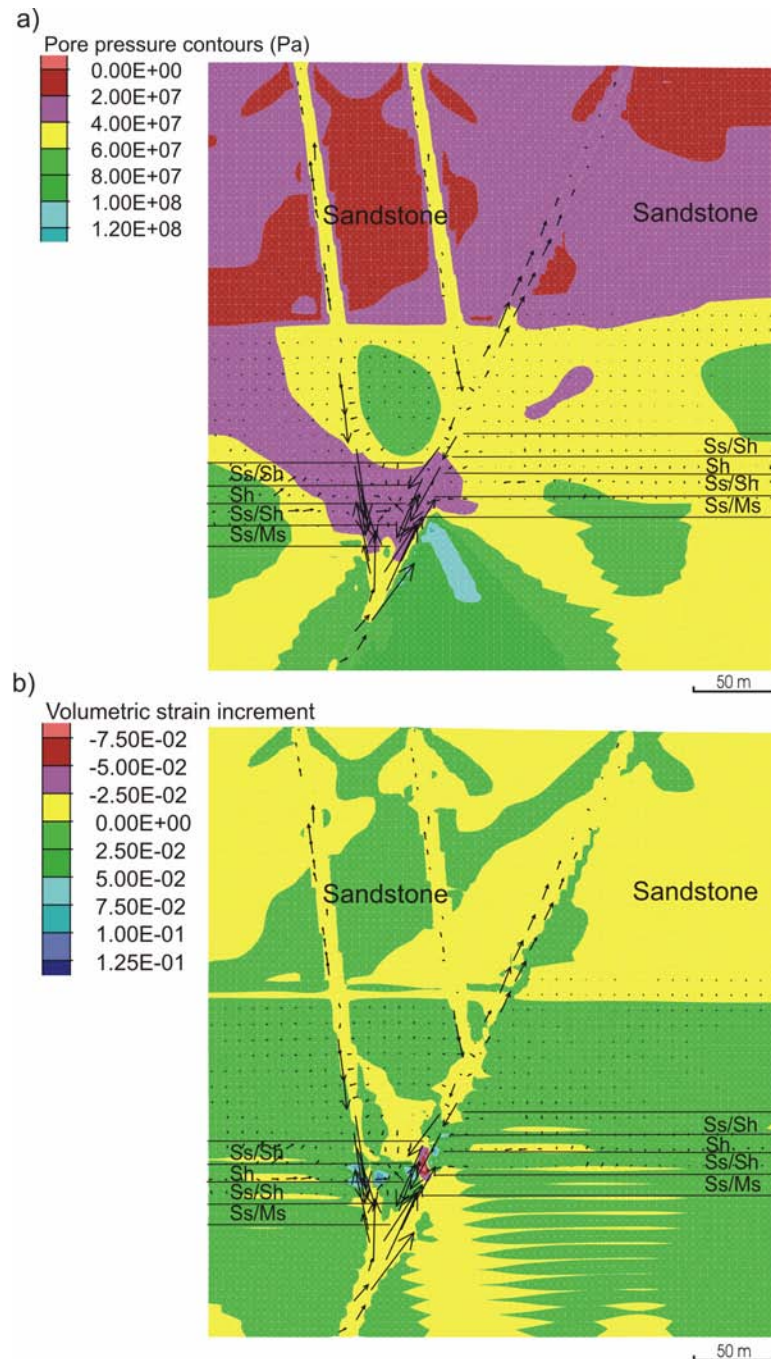
Fig. 4.27 Model 2d at 3% deformation a) displaying pore pressure contours and a strong Darcy fluid flow focussing within the fault zones and towards localised areas of pore pressure decrease b) plot of volumetric strain (dilation) and Darcy fluid flow vectors, displaying strong flow within the faults and focussing towards dilatant areas near fault and stratigraphic intersections of the ore zone.
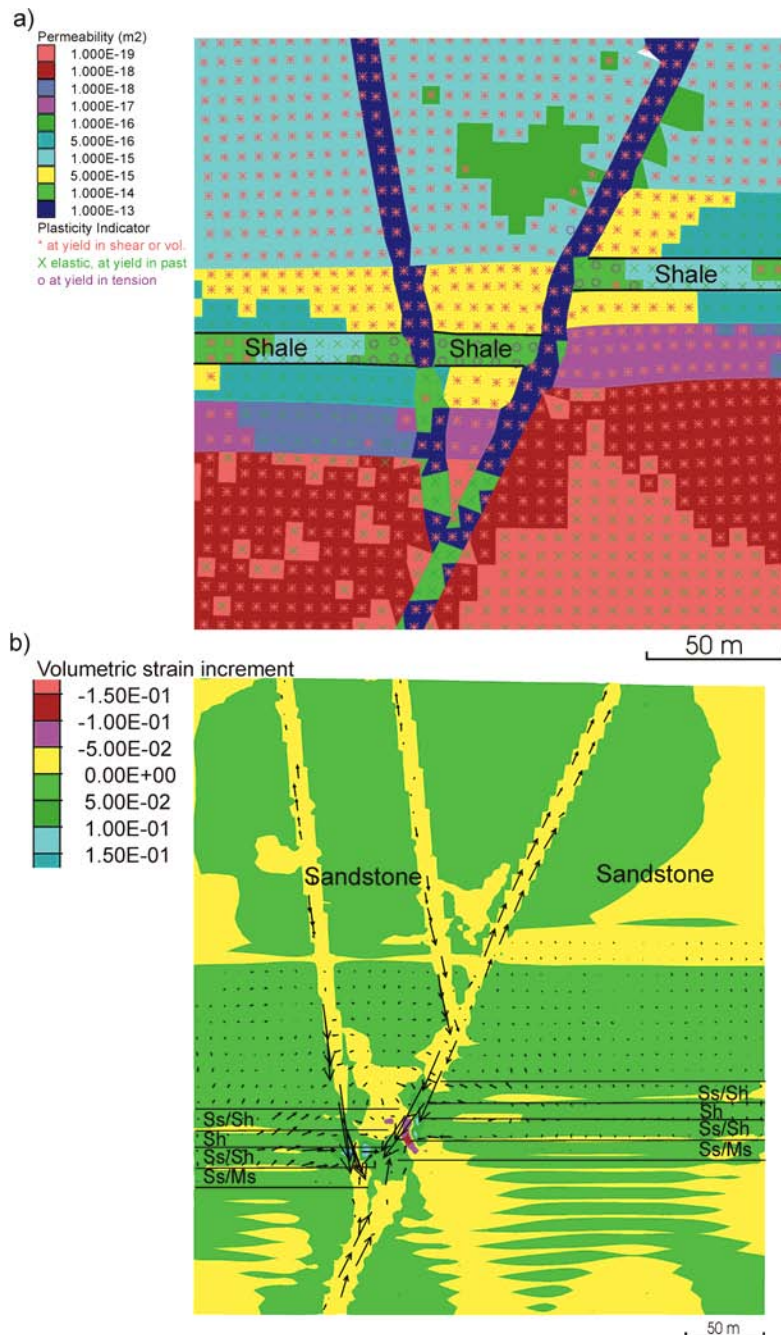
Fig. 4.28 Model 2d at a) 3% deformation, displaying permeability values and yield status or plasticity indicators. As a result of the applied yield function tensile failure is predominantly found in the shale layers (indicated by purple circles) and displaying high permeability values b) 5% deformation, plot of volumetric strain (dilation) and Darcy fluid flow vectors, displaying strong flow within the faults and focussing towards dilatant areas near fault and stratigraphic intersections of the ore zone, with strong fluid flow towards the fault notable within the shale layers.
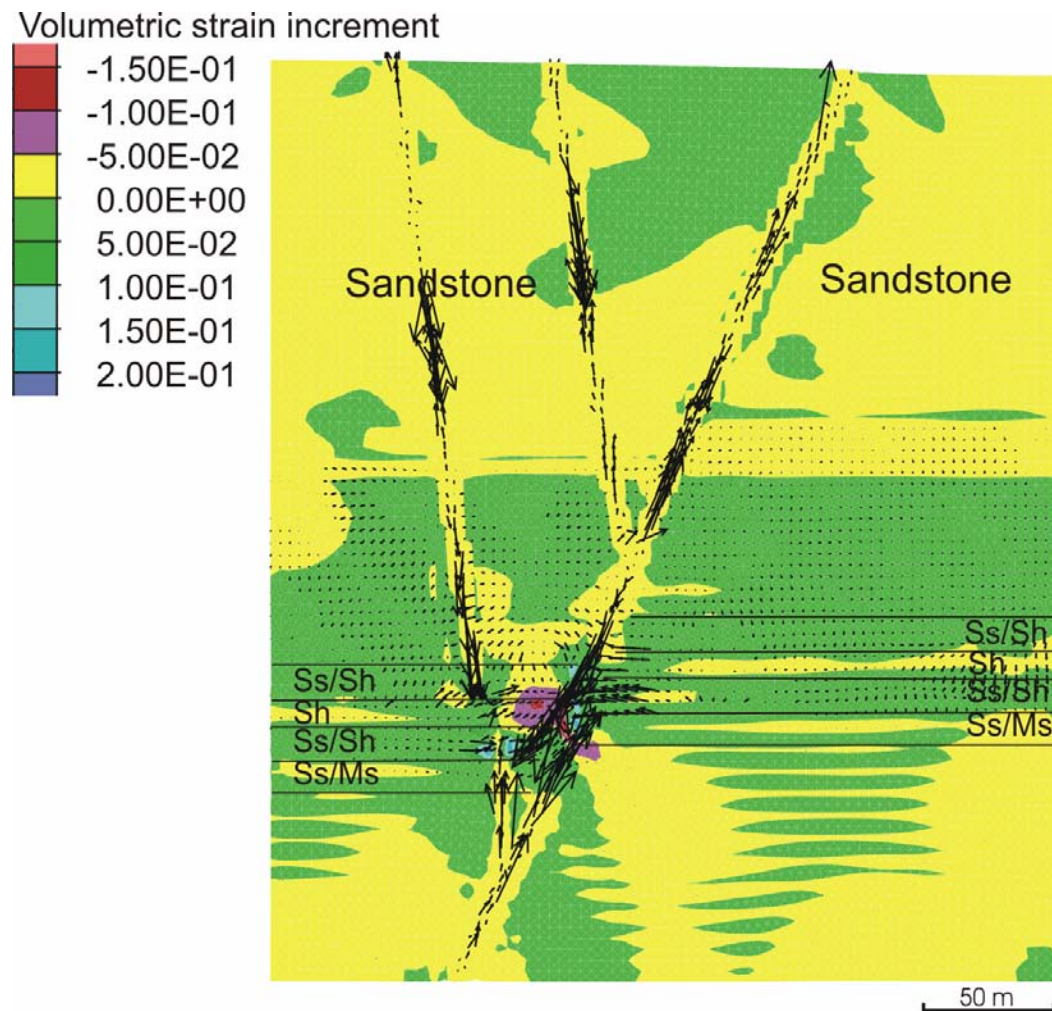
Fig. 4.29 Model 2d at 7% deformation displaying volumetric strain (dilation) and Darcy fluid flow vectors. Strong flow is evident within the faults and focussing towards dilatant areas near fault and stratigraphic intersections of the ore zone.

4.9.   Discussion and conclusions

Interpretation of the 3D structural model for Century suggests that there is a link between the regional and local scale NE trending structures, which relates to mineralisation. In particular, the regional faults contain vein type deposits (e.g. Silver King deposit) that preserve syn-tectonic breccia hosted mineralisation. Hence, proving that some of these structures intersect the Century deposit supports models for syn-tectonic mineralisation or models of remobilisation of earlier ores during the Isan Orogeny. However, these faults also show relationships to both sedimentary thickness variations and ore grades in Century, raising the possibility that they were active early and contributed to syn-sedimentary mineralisation. Interpretation of the TRF as a conduit for mineralisation (Broadbent, et al., 1998) was largely based on grade distribution data. We cannot discount the contribution of TRF fault to the ore system; however, this structure may have been more significant after basin inversion at Century, and as a consequence the general trends of Pb and Zn might be the final product of a more complex hydrothermal history in which the reactivation of faults within the deposit may have changed the original configuration of metal distributions. Zn grades and also thickness variation within Unit 200 have not been influenced by NW faults. Thus, NW faults branching from the TRF may have played only a minor role in ore genetic processes and more likely, if they contributed to the metal budget, they did so during later stages of Isan deformation as Broadbent (1999) suggests. This would explain why within Unit 200 the Zn grades do not seem to be influenced by these potentially later structures. Pb grades seem to be correlated with NE structures, but

overall the distribution is pointing to at least some influence of later NW structures. The consequence of these findings enhances our understanding of possible genetic relationships of the Century deposit and the Lawn Hill mineral field. We favour a model that envisages the emplacement of Zn and Pb early (syngenetic) as NE structures have been demonstrated to control thickness variation and grade distributions across the deposit, in agreement with the structural interpretation and available seismic profiles drawn in the northern part of the Lawn Hill Platform, which demonstrates that NE growth faults are regionally distributed. A model that additional syntectonic Pb or/and remobilisation of early Zn-Pb is also feasible. Late diagenetic to syntectonic emplacement models do not represent a single solution that fully explains our interpretation the results of the 3D model.

To test our remaining uncertainties, numerical simulations of the subsurface models (diagenetic, syntectonic) were undertaken. In normal circumstances sedimentary sequences have a reasonably well-defined variation in permeability, and shale is considered one of the least permeable units (e.g. Dullien, 1979). Our model results indicate that for fluid to permeate into shale sequences we require permeability values of the shale unit to be close to that of in-situ faults and much greater than surrounding sedimentary packages. Therefore, permeability is the primary factor controlling fluid flow and potential sites of ore deposition. The main observation from the extension models is that during extension, fluid from the surrounding sediments and the fault display extensive lateral migration into the shale units if the shale units are assigned high permeabilities. It is thus possible that migration of fluids along subsurface shale

units is mechanically feasible during extensional deformation and may provide the fluid pathways for stratiform diagenetic mineralisation.

Results from the models using fully compacted sediments indicate that overpressure is an additional process that aids in upward migration of fluids within the more permeable faults, and acts as a precursor to hydrofracturing within the shale units. However, the permeability of the shale must be at least $1/10^{th}$ that of the faults to provide any significant fluid flow through shale. Addition of a 'yield function' to increase permeability within the model allows tensile failure and increased permeability within the shale unit; however, fluid is primarily drawn from the shale units towards the fault in most cases. Overpressurisation may provide a process that induces hydrofracturing within the shale units; hence increasing permeability. This deformation induced permeability has the potential to focus fluids into these units; however, as shown by the modelling results these areas would be preferentially located close to the faults, therefore limiting any significant lateral fluid flow. Most of the fluids will then be preferentially driven in and through the fault domain. Thus, even with shale permeability set at unrealistically high values, this scenario works best for mineralisation proximal to faults, and might not be so useful to explain the lateral extent of primary Century mineralisation.

Revisiting the four modelling questions posed earlier, the pathways that controlled the location of favourable sites for mineralisation appear to be two-fold. In an extensional regime, normal reactivation of faults may provide localisation of fluids that have the potential to migrate laterally along more permeable sedimentary units, and during a compressional regime faults appear to be the main fluid conduits, with less

lateral migration of mineralising brines. It appears that both tectonic regimes are suitable for forms of mineralisation styles, however lateral flow is primarily favoured by extension. During compression, overpressurisation appears to have a strong influence over upward fluid flow and particularly tensile failure within the shale units, although this is spatially associated with faults, hence limiting lateral flow.

To conclude, it is apparent that we require either extremely permeable shale units in comparison to sandstones during early sedimentation, to contribute towards a subsurface replacive origin for mineralisation. More likely is the potential for significant failure within the shale units as a driving force for dilation and fluid flow focussing, as secondary porosity has less of an influence on transferring fluids laterally within the mineralised units of the Century deposit. We therefore conclude that a subsurface replacive origin for all the mineralisation is less likely than a syngenetic model with subsequent syntectonic remobilisation.

Chapter 5

Modelling the giant, Zn-Pb-Ag Century deposit,

Queensland, Australia

Acknowledgement of Contributions

Contributions made to this chapter involved:

L. Feltrin – 3D Structural and Property Modelling

J. G. McLellan – Geomechanical Modelling

L. Feltrin – 95% (p. 1-38), 10% (p.38-45), 95% (p. 45-54)

J. G. McLellan – 5% (p. 1-38), 90% (p. 38-45), 5% (p. 45-54)

N.H.S. Oliver – normal supervisory contributions

Abstract

This chapter presents a combination of geometric reconstructions of the Century Zn-Pb-Ag deposit, and finite difference modelling of coupled deformation and fluid flow. Our intention is to demonstrate that these computer based applications represent a new approach in testing ore genesis models. We use a "visiometric" approach, utilising GoCAD 3D structural and property modelling. Computer visualisation is applied to reveal metal zonations, fault distributions and timing, stratigraphic influence on zoning, and the nature and extent of metal redistribution during basin evolution and deformation. We also examine possible links between fluid flow, deformation and mass transfer using the numerical code FLAC3D. Numerical modelling results suggest that subsurface fluid flow during basin inversion is compartmentalised, being focused within more permeable fault zones, thus accounting for the secondary redistribution of base metals identified using the 3D reconstructions. However, the results do not explain the broad metal zonation observed. Both the spatial and numerical models suggest that Century is syngenetic, with further diagenesis and deformation producing metre to 100 m scale (re)mobilisation.

Keywords: 3D structural model; Remobilisation; Fluid flow; Numerical modelling; Basin evolution

5.1.   Introduction

Sediment hosted Zn-Pb-Ag deposits of northern Australia have been proposed to be synsedimentary-(exhalative), early to late diagenetic, and syntectonic in origin by many different researchers (e.g. Perkins, 1997; Broadbent et al., 1998; Large et al., 1998; Cooke et al., 2003; Chapman, 2004; Davis, 2004). Whether base metals are introduced into a body of sedimentary rock after its deposition, or whether they belong to the system, being emplaced during the formation of its host, remains controversial (Amstutz et al., 1982). With the advance of computer science in the fields of 3D modelling and finite element modelling, this classical controversy can now be assessed from a new perspective. The case study presented outlines the benefits of these new computational tools for ore geology, as already remarked by several previous authors (e.g. de Kemp, 2000; Witten, 2004; Xue et al., 2004), and builds the largely 2D-approach used in Chapter 4 into a 3D model.

The conventional explanation for the genesis of Zn-Pb-Ag deposits is an exhalative syngenetic origin from reaction of Pb-Zn brines with anoxic, sulphur-laden seawater, followed by sulphide deposition in (usually) fine grained mud layers (Large et al., 1998). However, observations of discordant mineralisation features (veins, reaction fronts, sulphides in fold hinges or foliations) have been interpreted in several different ways. Conventionally, these features would be regarded as representing short- to medium distance (mm to 10's of m scales) remobilisation of a pre-existing syngenetic deposit during diagenesis or metamorphism (Marshall and Gilligan, 1987). Alternative models propose that such features are feeder structures for subsurface replacement of

shale, or carbonate bearing layers by diagenetic or syntectonic ore fluids (e.g. Perkins, 1997; Broadbent et al., 1998; Chapman, 2004; Davis, 2004). However, models that focus on paragenetic and textural relationships, as the main or sole tool of investigation of these issues, generally remain unconvincing for most geoscientists, because the same sets of textures can be interpretively accepted within any of the above genetic models (Chapter 4). We use here the term "(re)mobilisation" to refer to features that may be a product of either an original introduction of metals (mobilisation), or subsequent remobilisation of earlier metals. The distinction between original mobilisation and subsequent remobilisation is specifically addressed in the discussion, but in the general sense, we use it here to describe discordant mineralisation of uncertain metal source.

The key to understanding the genetic issues is to gain a clear impression of the scale(s) over which metal has been originally derived or subsequently modified. To do this, it is usually necessary to consider combinations of several of the following techniques (e.g. Cartwright and Oliver, 2000; Marshall et al., 2000; Vokes et al., 2000):

- Geochronology and other radiogenic isotope geochemistry to attempt to correlate and distinguish metal introduction, sedimentation and deformation.
- Stable isotope and other radiogenic isotope geochemistry to ascertain the nature of ore-stages and other fluids.
- The distribution of sulphides relative to stratigraphy at micro, meso- and macro-scales.
- Orebody-scale metal zonation relative to both stratigraphy and structure.
- Geochemical and/or fluid flow simulations of a range of possible ore-forming scenarios designed to test alternative models using objective input data.

In this chapter, we focus attention on the power of a well-constrained 3D model to address ore genesis issues (points 3, 4, 5 above). Newly developed interpolation algorithms allow reconstruction of ore deposit meso- and macro-scale attributes at high resolution, such that the 3D model becomes not just a resource definition tool, but also a scientific tool for examining ore genetic aspects. 3D models are forced to respect predefined constraints (Mallet, 2002) to obtain the required accuracy and allow detailed integration of datasets. Moreover, they permit rapid multi-scale structural analysis of data (de Kemp, 2000). The virtual reconstruction of an ore deposit also enables faster visualisation of geometrical characters and intensive spatial analysis of large databases (Houlding, 1994). The geological interpretation remains an essential skill; however, geologists have to respect the "rigidity" of accurate models, which leads to better interpretations, but requires substantial time devoted to model construction and its understanding.

Finite difference modelling, based on simplifications of the 3D geometric models, was also utilised to examine aspects of subsurface fluid flow (point 5 above). Such numerical simulations provide a better understanding of the roles of compaction and deformation on fluid flow. The FLAC3D numerical modelling application (Fast Lagrangian Analysis of Continua – Itasca, 2003) represents a powerful tool to investigate the coupling of mechanical and hydraulic properties. Running multiple model scenarios it is possible to evaluate the influence of variables such as cohesion, tensile strength, shear strength, overpressurisation and pore pressure on fluid flow paths. Interpretation of numerical simulations can lead to the characterisation of possible fluid flow scenarios within specific time frames of basin evolution.

5.2.   *Geological setting*

The Century deposit is one of the largest Zn-Pb-Ag accumulations in the world with a total mineral resource of 122 Mt at 12.6% Zn, 1.9% Pb, and 48 g/t Ag (Mansell, 2005). It is located in the Burketown Mineral Field, in the Lawn Hill Platform, and lies 250 km northwest of Mt. Isa, in the Western Fold Belt, Queensland (Fig. 5.1a).
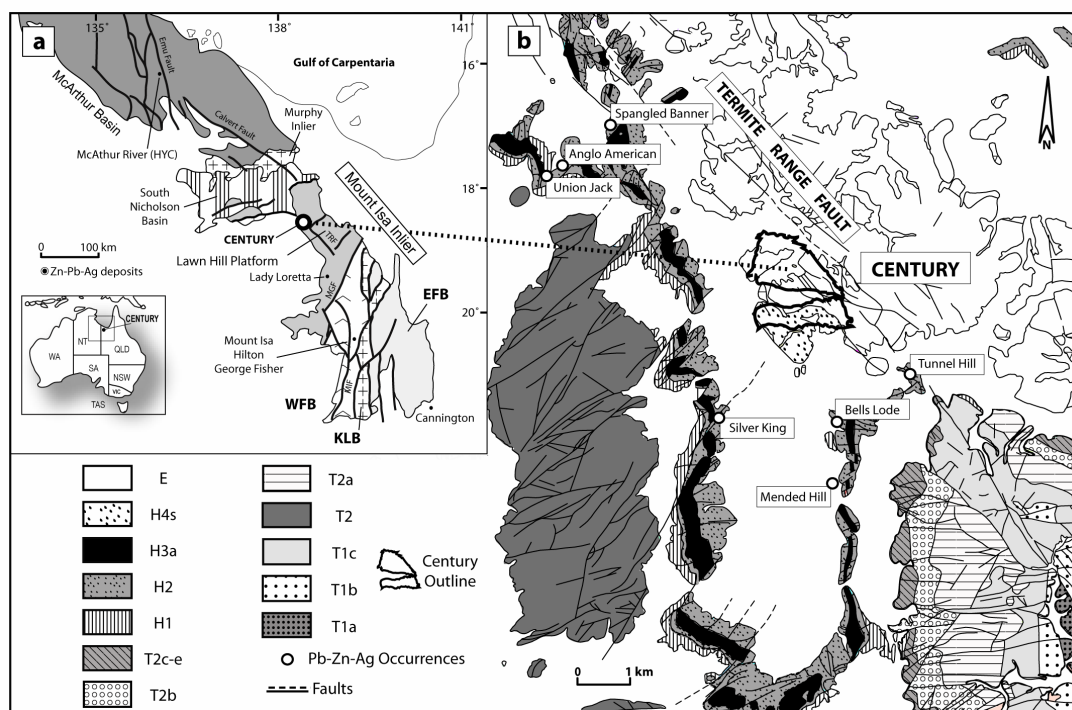
Fig. 5.1 (a) Main tectonostratigraphic subdivisions of the Mount Isa Inlier, and location of major sediment-hosted Zn-Pb-Ag deposits (after Southgate et al., 2000). (b) Geology of the Lawn Hill Mineral Field in proximity of Century (modified from Andrews, 1998) and location of local vein- lode-hosted Pb-Zn-Ag ores. E - Thorntonia limestone; H4s - Laminated siltstone; H3a - Sandstone H2 - Tuffite, H1 – Tuffaceous laminated shale, T2 (a, b, c, d, e) - Turbiditic sandstone, T1 (a, b, c) - Turbiditic sandstone (each sub-unit refers to a facies variation, see Andrews, 1998).

Numerous Pb and Ag prospects and old workings, exploited since 1887, are also found in this region (Fig. 5.1b), and are associated with structurally controlled veins and

lodes. In 1987, the Century deposit was uncovered after the discovery of a zinc soil anomaly during drilling by CRA Exploration. The deposit is currently mined by Zinifex Ltd.

The Mesoproterozoic rocks hosting Century (age approx. 1595 +/- 6 Ma, Page et al., 2000) and surrounding lodes, are part of the Lawn Hill (units H1, H2, H3a, H4s), and Termite Range Formations (units T1, T2, T2b, T2c-e) within the Upper McNamara Group (see Fig. 5.1b). They are composed by a sequence of unmetamorphosed to low-grade metapelitic rocks, mainly sandstones, siltstones, shales, mudstones, and minor tuffaceous layers. In particular, the member H4s (Andrews, 1998), hosting the Century mineralisation, represents a sequence of interlaminated siltstones and shales (Fig. 5.2 a-f) shows their textural appearance and relationship to mineralisation in hand-specimen. The deposit stratigraphy gradually shifts to more sandy intervals in the overlying H5 member (Sweet and Hutton, 1982; Andrews, 1998). This upward coarsening trend is interpreted by Andrews (1998) as evidence of a progradational system of rapidly deposited turbidites in an outer shelfal setting although Krassay et al. (2000) has proposed a deeper-marine origin for this facies.

A representation of the mine stratigraphy is presented in Fig. 5.3 (Clifford and Kelso, 2003). Mineralised intervals display variations in the shale/siltstone ratio (Waltho and Andrews, 1993), generally characterised as 1 to 10 m alternating beds. Sulphide rich layers occur prevalently as laminated bands within shale intervals, enriched in organic content. These are separated by silty layers, only weakly mineralised or barren, and particularly enriched in sideritic cements. Siltstones are also characterised by an abundance of stylolites. We interpret these features as direct

product of compaction induced pressure solution (e.g. McBride, 1989; Dewers and Ortoleva, 1990a), as they are broadly concordant with the stratigraphic layers, and also preserve organic seams, which were most likely accumulated as insoluble material during basin dewatering (Fig. 5.2e).
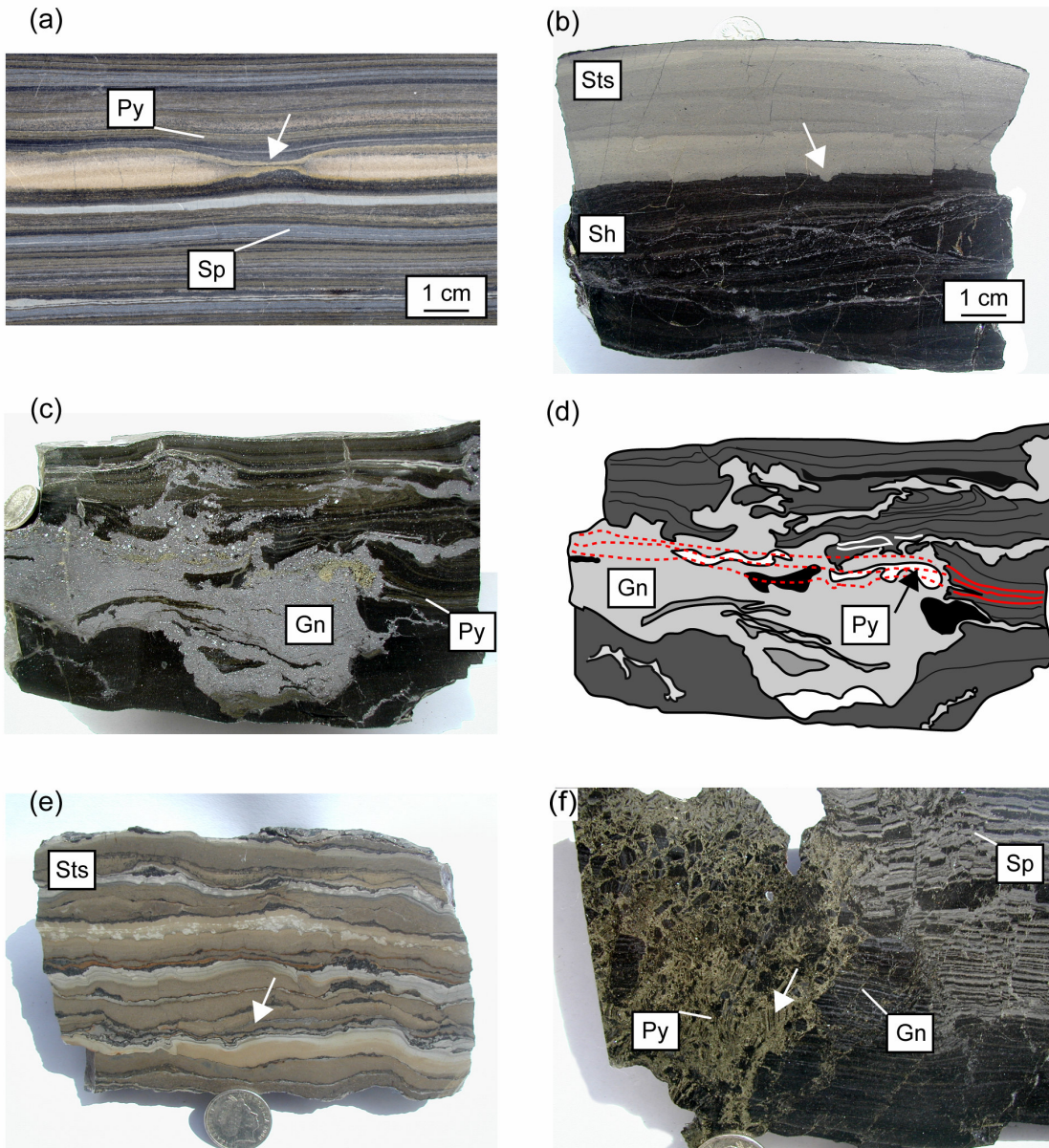
Fig. 5.2 Mineralised and barren host rocks from the Century sequence illustrate characteristic relationships between mineralisation and deformation related fabrics; all samples are shown younging upwards. (a) Example of hand specimen from mine stratigraphic unit 150 (Upper Ore Zone) showing the most common aspect of the mineralisation, with fine grained laminae of sphalerite (Sp), and pyrite (Py), including boudinage of a mudstone layer with localised parallel bedding dissolution seam (arrow), inferred to be a dewatering structure. (b) Example of contact interface between siltstone (Sts) and shale-rich layer (Sh), unit 165; mineralised Sp laminae are developed exclusively in the shale-rich layer. Post-sedimentary, low-angle, discordant galena veins intersect the shale layer. (c) Massive galena veins interpreted as local remobilisation of ore, unit 180. Pyrite is fine grained and occurs mostly in stratiform laminae. (d) Sketch of sample c illustrating the geometrical relationship existing between Py laminae (dashed lines) and recrystallised, coarse grained anhedral crystals of Py (arrow). This relationship is interpreted as evidence of cm-scale remobilisation, whereby the original pyrite layer is preserved, albeit modified, and the galena is introduced from a source outside the scale of the specimen. (e) Sample of stylolitic siltstone, unit 440; stylolites have a low degree of convolution and preserve carbon- and sulphide- rich seams, implying at least some carbon and sulphides predated compaction associated with these stylolites. Most layers display differential compaction (arrow). (f) Breccia in laminated ore displaying replacement of Sp by Gn (galena) and Py, unit 410. Breccia clasts are supported within a matrix of Py that in some cases replaced mm-scale layers, preserved within the floating clasts (arrow). Pyrite replacement is interpreted as postdating the Sp and Gn laminae (Appendix D for specimens spatial location).

The Century zinc deposit lies close to a major structure, the Termite Range Fault (Fig. 5.1). The proximity to faults is a common accepted feature of other world class Pb-Zn massive sulphide deposits, often invoked in genetic models (e.g. Mt. Isa, Australia; Howards Pass, Canada; Navan, Ireland; Meggen and Rammelsberg, Germany; Gamsberg, South Africa; see Gustafson and Williams, 1981). However, at Century the influence of this major fault can be only inferred, as mineralisation results terminated by an erosional unconformity on its eastern side. The Termite Range Fault is the major strike-slip discontinuity in the region, it is orientated northwest - southeast, and together with other northeast, steep-dipping faults, characterises the structural grain of the Lawn Hill Platform. This structural setting was probably important in controlling brine migration, and fluid flow focussing across the region. A protracted reactivation history is documented . The Termite Range fault was apparently active during several episodes of rifting related extension, subsequent compression, and basin inversion

during the Isan Orogeny (Broadbent et al., 1998; Betts et al., 2004). The complex overprinting of brittle and ductile deformational events, in and around the fault, parallels the complex history of mineralisation found in the Lawn Hill Platform and elsewhere in the Mount Isa Inlier. Generally, macroscopic folding recognised in the Western Fold Belt can be attributed to a major orogenic episode, the Isan Orogeny. The Isan Orogeny was considered to comprise three main deformation stages, D_1, D_2 and D_3 (O'Dea et al., 1997). Recently, several authors (e.g. Gauthier et al., 2001; Giles and Nutman, 2002, 2003; Hand and Rubatto, 2002) have reported metamorphic ages of 1585 Ma for rocks of greenschist to amphibolite facies 250 km south of Century. The first folding event in the Lawn Hill Platform (D_2) may have been synchronous with this metamorphic age, but there is no direct geochronological constraint on deformation.

Carr et al. (1996) provides a galena Pb-Pb age of 1575 (a refined age of 1570 ± 5 is referred by Ord et al. 2002 quoted as refined work of Carr (pers. comm. 2000)). These ages are apparently 35 to 15 Ma younger than the Century host sediments age of 1595 ± 6 Ma (Page et al., 2000). However, the galena Pb-Pb ratios may have been influenced by later, more radiogenic fluids introduced during regional metamorphism (e.g. Marcoux and Moelo, 1991). This consideration is supported by available data on galena Pb-Pb ratios on samples from both Century and regional veins/lodes deposits (Pb^{206}/Pb^{204} = 16.294-16.390; 16.436-16.503), (Richards, 1975; Bresser, 1992; Broadbent, 1999), which delineate two distinct populations of radiogenic lead (Bresser, 1992). Therefore, a younger age for the Century mineralisation could be the result of mixing with a later infiltrating Pb-bearing fluid. An alternative explanation might also be that it was due to a syngenetic to early diagenetic enrichment of U^{238} (see Holk et al.,

2003), which may have progressively contributed to the addition of Pb^{206} to the total system (orebody and host rocks). Radiometric airborne data for the Lawn Hill platform show a correspondence between elevated content in U^{238} and the spatial distribution of more reduced packages (e.g. carbonaceous shales and siltstones of the Pmh4 interval hosting Century). Farquharson and Richards (1975) have suggested that a re-equilibration of isotopic signatures may explain the close isotopic association recorded for Mount Isa tuff beds and galena – this implies possible isotopic exchange between host rock and mineralisation after sediment deposition. Therefore, anomalous radiogenic signatures may occur since early stages of basin formation, even without a direct additional supply of Pb^{206}.

Century Stratigraphic Column
& Mineral Content
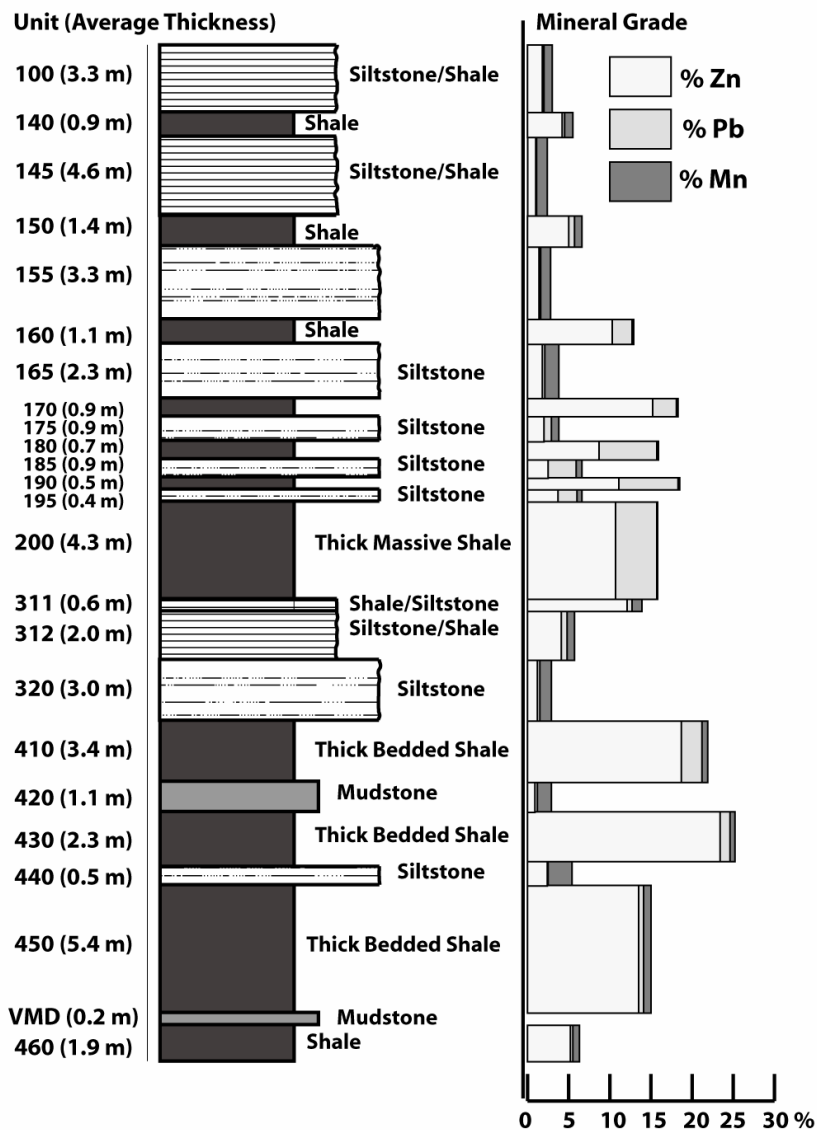
Fig. 5.3 Mine stratigraphic column (Clifford and Kelso, 2003), showing alternating shale, siltstone intervals and relative total deposit, averaged, concentrations in weight % for Zn-Pb-Mn. Note higher Mn contents of siltstones between the Pb-Zn-rich shales.

5.3.   Century 3D structural model and property modelling

5.3.1.   GoCAD and the DSI algorithm

To reconstruct the geometrical aspects of the Century deposit we have used the GoCAD suite (Earth Decision Sciences, http://www.GoCAD.com), which offers a high degree of flexibility in handling complex geological geometries (e.g. Galera et al., 2003). GoCAD allows the user to develop different classes of objects (e.g. point-sets, lines, surfaces, voxets, S-grids). Data are commonly imported as point-sets, well-based information (e.g. geology, logs of properties), or grid based 2D-3D information (geological cross-sections, geochemical and geophysical data).

The core of the GoCAD application is the Discrete Smooth Interpolation Method or DSI (e.g. Mallet, 1989, 2002). The interpolation of a complex geological dataset is solved with this algorithm by reducing a global problem (e.g. fitting a triangulated surface to a cluster of fuzzy control points) to a discrete number of smaller linear problems. Subsequently a finite difference approximation is used to find a spline function that locally fits the geological dataset. DSI is then used to obtain, smooth, interpolated objects, though still respecting predefined linear constraints imposed by the integrated geological information. Conventional CAD packages tend to smooth modelled surfaces, using parametric fitting algorithms (e.g. Bézier curves, parametric

spline curves, rational curves, Bohm et al., 1984). However, they do not respect constraints during interpolation, limiting their application to geological problems.

5.3.2.   Modelling approach

To resolve the complexity of the fault network intersecting the Century deposit and visualise the stratigraphy hosting the ore, we have used a surface based modelling approach. The topology of key horizons has been modelled using optimised triangulated irregular networks (TIN) that connect all known data points (x, y, z) representing drill-hole intersections of logged geological boundaries (geological markers). The horizons were beautified and fitted to these well markers (drill-hole intersections), which were imposed as control points constraints. Border constraints were also implemented, to straighten and smooth each horizon's outline, and to model existing and interpreted relationships between horizons and the main fault contacts. More than 100 fault surfaces were reconstructed in GoCAD from 3D data collected by mine geologists using a remote laser station and a Trimble® RTK (Real Time Kinematic) system (Kelso et al., 2000), and 73 cross-sections intersecting the deposit with 50 m spacing (King, 2002). The surfaces were generated by converting the imported data into a set of separated point-sets that were subsequently used as a control point constraint. GoCAD implements properties for different object types (e.g. different properties can be assigned to a vertex of a triangulated surface). Properties can be interpolated using the DSI and the result is displayable using 8 bit, 256 colour gradients. Fig. 5.4 illustrates an example of interpolation of thickness variability for the mine stratigraphic unit 200. In

addition to the structural aspects, selected datasets from the Zinifex mine database were used to obtain a 3D model that combined 3D geometries (fault systems, horizons) with 2D and 3D property datasets. Six isopach maps were projected on pre-constructed horizons and compared with other maps representing the distribution of base metals and major elements. We also developed and implemented a Visual Basic application to increase the quality of the datasets utilised to construct the isopach maps. This simple tool enabled the estimation of bedding orientations where this information was lacking at a number of data-points. Subsequently, the true thickness values were calculated considering the correction from these interpolated orientations. The steps followed were:

- An initial SQL (*Structured Query Language*) query combined down-hole survey data, consisting of bedding orientations at specific depths, with the appropriate geological markers (e.g. unit 200, 320, 430 etc.). This was achieved by linking an Access database, containing geological information, with a table that records the structural information in dip azimuth format. However, this set of SQL queries retrieved a limited number of oriented markers (due to limitations derived from the poor quality of collected measurements), requiring the introduction of an interpolation algorithm.

- A program was then designed to locate the data points that were lacking down-hole survey information. Within a cluster of data points (P_n), carrying the following properties {x, y, z, dip, azimuth, and t}, the point-set with unknown dip and azimuth was separated and grouped.

- On each grouped point, lacking an orientation, an interpolated bedding was estimated using an inverse distance algorithm (Ware et al., 1991; Bartier and Keller, 1996), by considering a spherical neighbourhood of points (located in other drill-holes) within a radius of 100m, and averaging the collected orientations using their square distances as a weighting coefficient.

- An Excel application finally calculated true thickness values and stored them within a new ASCII file that was used to import the interpolated point-set $P(x, y, z, t)$ in GoCAD (Fig. 5.4).

Assays for six major elements (Zn, Pb, Ag, Mn, Fe, S), were imported in GoCAD in well-object format. After grid based upscaling and subsequent conversion to point-sets, the data were used to paint the reconstructed horizons and to construct an S-grid based block model. A final stage of the reconstruction involved the volumetric representation of base metal distributions using Iso-surfaces. We upscaled the database creating a block model using a GoCAD S-grid object. The result is a stratigraphic grid, composed of voxels that can be adapted to bounding and intersecting surfaces (see Fig. 5.5). A major problem was the selection of an appropriate way to display the spatial variability of base metal contents. Parameters such as the strong stratigraphic control and the extremely sharp vertical variation in grades occurring between shale rich intervals and barren siltstones had to be considered as important geological constraints.
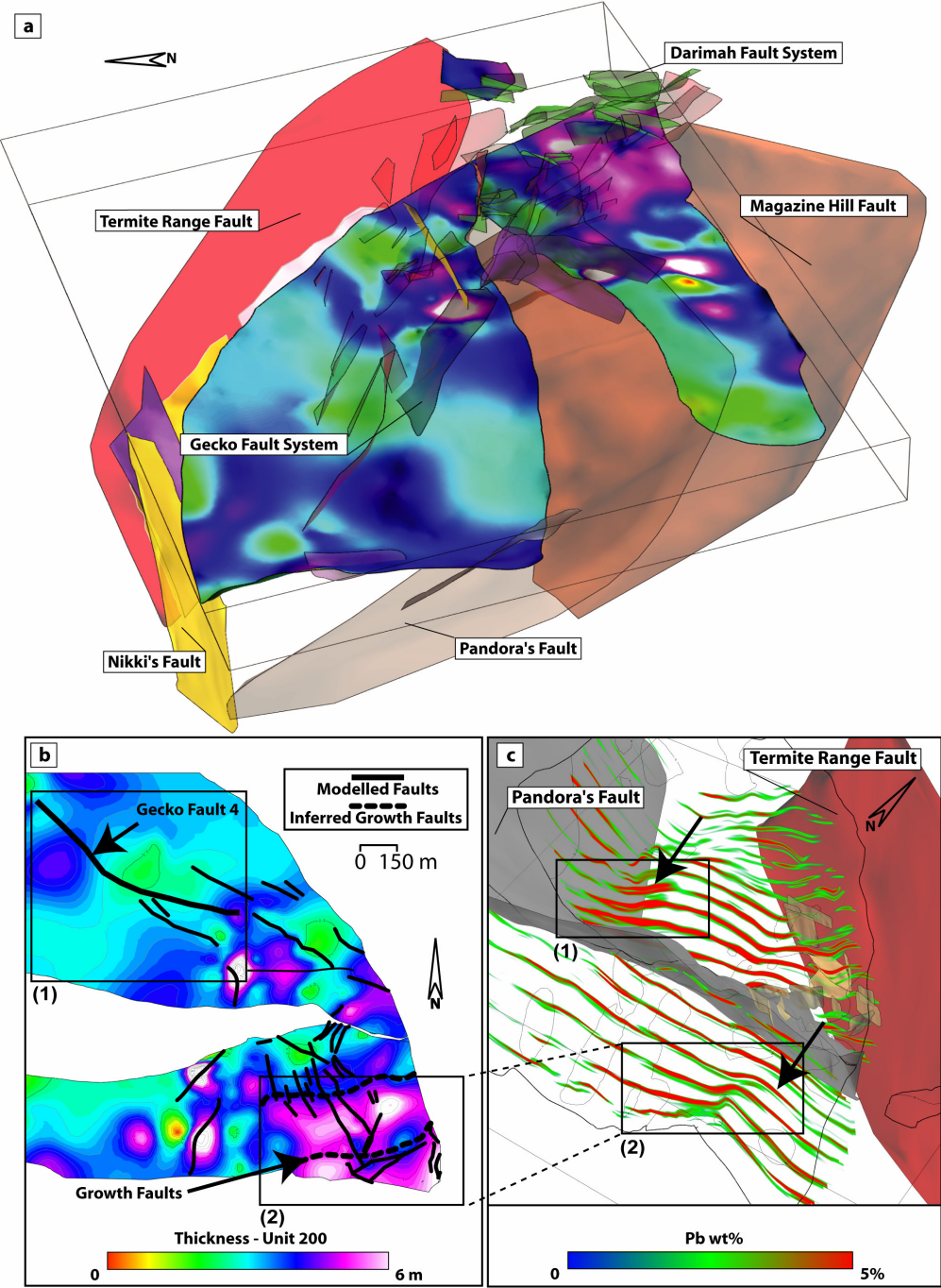
Fig. 5.4 3D structural and property model of the Century deposit. (a) Perspective view of the model illustrating some of the major faults bounding and intersecting the deposit. Also shown is the stratigraphic horizon 200 with a projected isopach, thickness map (refer to thickness scale in (b)). (b) Top view of surface 200 showing the different extent of thicker domains; dashed lines indicate interpreted growth faults on the southeastern corner of Century (the deposit is separated in two major halves,

southern and northern block). Detail b (1), northwest oriented faults (includes Gecko Fault 4) mapped on the northern block. Faults appear unrelated to thickening across this portion of Century. Detail b (2), inferred northeast oriented depocentre, note incompatible orientation with mapped northwest oriented steep dipping faults. (c) Serial cross-sections displaying the spatial variability of interpolated Pb grades. Detail c (1) north-south syncline with interpreted thrusted strata indicated by doubling of Pb-rich units and discontinuity of mineralisation (arrow). Detail c (2) is compared with detail b (2) and shows another perspective of the north-south anticline on the southeastern corner of Century. Pb-rich layers (e.g. 180, 200) appear continuous with no major thrusting (arrow).

GoCAD was particularly useful, as we deformed the S-grid using top and bottom horizons (hanging-wall and footwall of the mineralisation) to constrain the overall geometry of the S-grid. Selection of appropriate size of the voxels (approximately 0.9 m) was sufficient to reach the required resolution and to distinguish, after DSI interpolation, major barren horizons from highly mineralised intervals with a thickness greater than 3 metres. GoCAD is capable of performing the DSI with different initialisations of the properties; hence, we constructed several models trialling different degrees of property propagation. We performed isotropic and anisotropic interpolations varying the fitting factor, which is used to define the importance of weighting coefficients related to control point constraints versus smoothing of properties (see Mallet, 2002). Optimal results were achieved with values of a vertical jump of two, and horizontal jump of four, and a fitting factor of ten (which gives more weighting on the imposed constraints rather than a smoothed result).

a S-Grid Object

150 m

N

b

0   100 m

F₂

F₂

27550-N

0   Zn   30 %

0   100 m

F₂

F₂

27550-N

0   Pb   6 %

0   100 m

F₂

F₂

27550-N

0   Mn   5 %

Interpreted Faults
Fold Axial Planes

E   W

c

27900-N

Unit 200

E   W

0   25 m

Top
Bottom

Geological-Marker

0   Pb   6 %

d

Upper Ore Zone

Lower Ore Zone

N

0   Zn   30 %
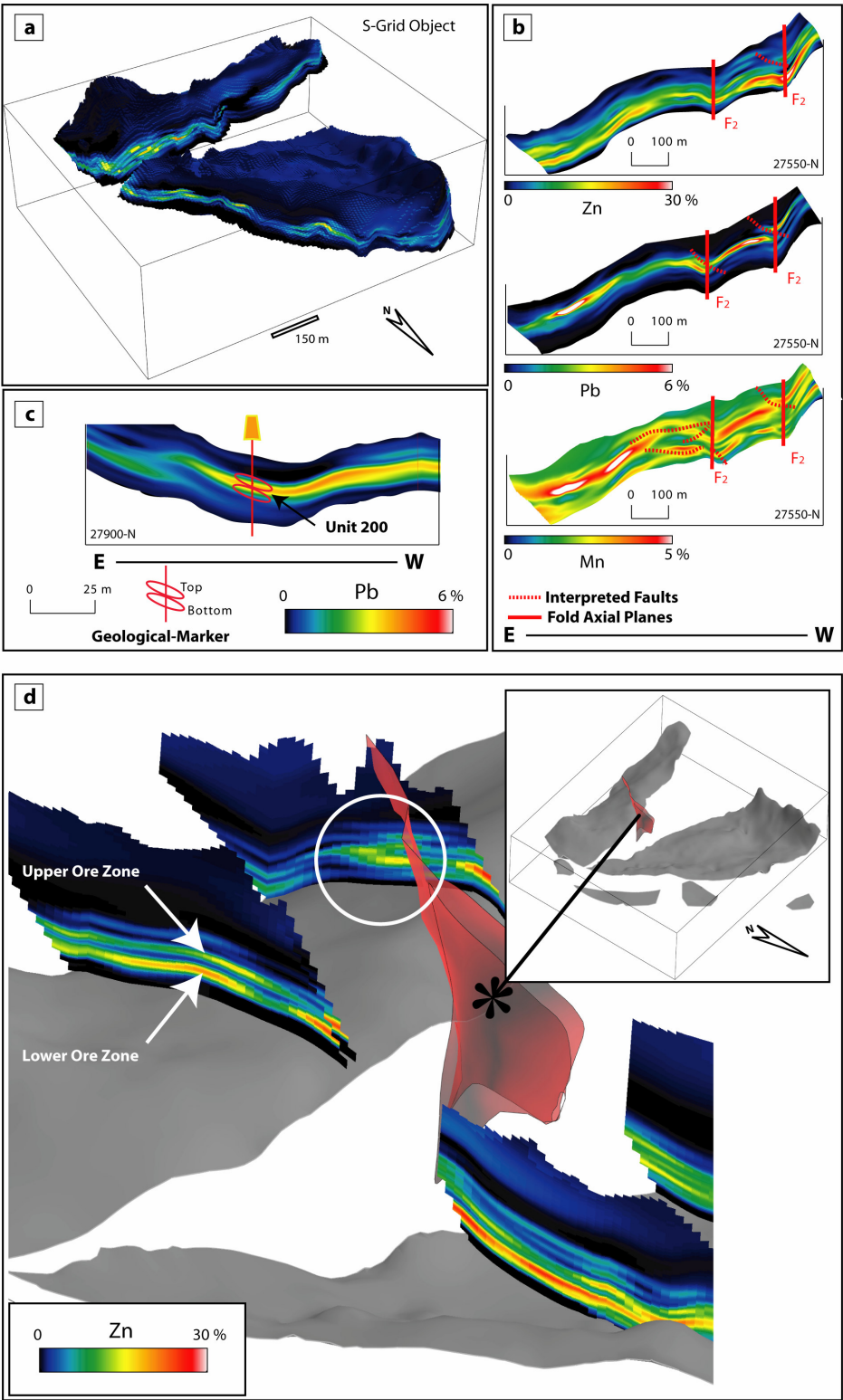
Fig. 5.5 S-Grid model conformed to the stratigraphic layers bounding the ore deposit. The model includes (as cell centred properties) base metal grades and alteration. (a) Solid visualisation of voxels representing the spatial distribution of Zn grade. Voxels have a tile shape (10 m by 10 m by 0.9 m) to account for the stratigraphic control on mineralisation. 0.9 m has been chosen because of the minimum 0.9 assay interval. (b) Examples of interpolated cross-sections for Zn-Pb-Mn portraying evidence of F2 folding and associated local thrusting developed on fold hinges during interpreted E-W shortening. (c) Cross-section showing the preferential localisation of mineralisation at Century, which appears stratiform in several cases, and focused in massive shale-rich intervals (e.g. unit 200). (d) S-grid perspective view of two north-south sections across Century's southern block. Note the distinct upper and lower ore zones (white arrows) that become fuzzy in proximity to the Silver King Fault (steeply dipping surface). Fuzzy overlap of Zn grades across this fault (white circle) suggests that deformation has changed the original configuration of mineral grades.

5.3.3.   3D Model visualisation and spatial analysis

Once different model components were completed, the statistical and spatial analysis was performed by comparative visualisation of GoCAD objects (Houlding, 1994). We follow a "visiometric" approach similar to that of Silver and Zabusky (1993), in three steps:

- *Identify* the features of interest, in particular those that may help to understand ore genesis,

- *Classify and quantify* detected features, defining groups of correlations, and

- Interpretation.

    An additional step beyond the visiometric approach is *Numerically Testing* the interpretation(s). Below we present some examples, developed by using the 3D models as a basis for 3D numerical testing of ore forming or other fluid flow scenarios.

5.3.4.   Results

A summary of the different 3D model components is shown in Fig. 5.6. Throughout the integration of the reconstructed fault network with 2D-3D models of grades and thickness, we evaluated whether faults were syn- to post- sedimentation. We then examined aspects of metal zoning at Century and the possible linkage with the faults.
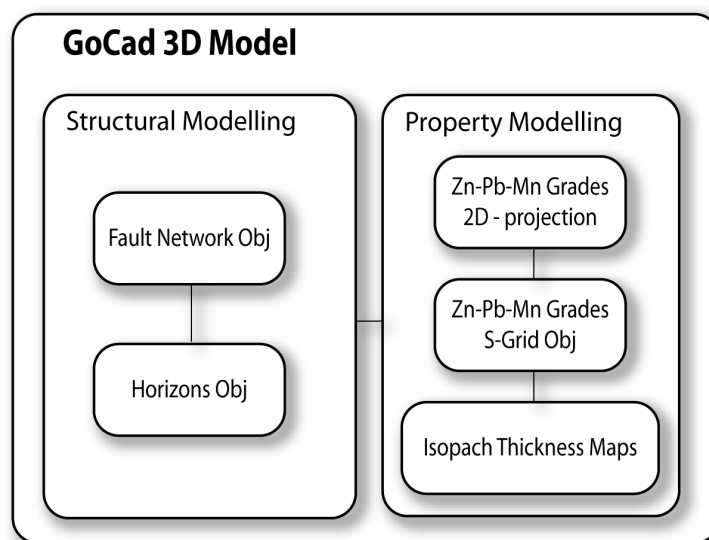
Fig. 5.6 Summary of the GoCAD model components, comprising a surface based structural framework where modelled properties were applied, and an S-grid model representing the 3D spatial distribution of base metals.

5.3.4.1.   Fault discrimination

Comparing the *Fault network object group* with the *Isopach maps object group* (e.g. Fig. 5.4a), we evaluated the potential relationships between different fault generations and sediment thickness. The objective was the identification of potential growth faults (see Hobbs et al., 1976 for growth fault definition). In particular, we investigated if faults had any significant influence on the thickness variability across a highly mineralised stratigraphic interval (unit 200). Limitations exist, as a number of variables control the thickness variability across a basin (e.g. Guidish et al., 1985), including thickening by folding or thrusting and base metals supply (Goodfellow et al., 1993). This has hampered a clear identification of synsedimentary structures. However, significant constraints can be put on structures that do not influence thickening as they likely post-date sedimentation. Fig. 5.4b illustrates a plot of thickness variability across mine stratigraphic interval 200, with fault traces marked on the top of this horizon (black polylines). If we compare thickness variation with the *Gecko Fault 4* (Fig. 5.4b, detail 1) we observe that on both sides of the fault, horizon 200 preserves a constant thickness, except near its southern termination. The thickening around this southern part of the fault could be interpreted as post-sedimentary rupturing, because it is restricted to a small area (approximately 7 m2, conf. with scale of growth faults in Rouby et al., 2002). In contrast, a thick apparent depocentre, at the southeastern corner of Century, extends for approximately 400 m with maximum thickness values ranging between 6 and 8 m. These values contrast with 3 m thickness distal from the depocentre (Fig. 5.4b, detail 2).

By integrating the S-grid model object, visualising the spatial distributions of Zn and Pb (Pb example shown in Fig. 5.4c), and being aware of the stratigraphic detail, we were able to determine if this thickening was associated with any major thrust repetitions within the sequence. Significant thrusting or duplexing makes layers lose their continuity (e.g. Couzens-Schultz et al., 2003), causing repetitions that can be traced using the S-grid based visualisation approach. For example, Fig. 5.4c, detail 1 represents an example of an interpreted thrust in which the upper ore zone appears doubled (arrow on detail 1). On the other hand, the broad thickening illustrated in Fig. 5.4b, detail 2, compared with the Pb spatial distribution (Fig. 5.4c, detail 2), suggests that this part of the Century ore was deformed to form a gentle D_2 north-south trending anticline. However, mineralised horizons appear to be continuous (without major repetitions) on the limbs and crest of this anticline, suggesting that post-sedimentary thickening (e.g. thrusting) did not increase the thickness of these units. Growth faulting is thus proposed as a cause of thickening, and growth faults position, and orientation were inferred by evaluating the sense of thickening, and the known occurrence of northeast oriented structures, in this part of the deposit (sees dashed lines in Fig. 5.4b, detail 2). Known northeast trending faults may either be the product of reactivated syn-depositional structures or newly formed post-depositional ruptures. These interpretations outline that multiple generations of faults may have been acting during basin evolution (Scott et al., 1998; Betts and Lister, 2002). Some of the faults were most likely synsedimentary growth faults (see interpretation of depocentres in Andrews, 1998), prevalently northeast to east-west striking. However, we cannot discount that depocentres may have formed in response to a switch in the provenance of sediments

distal to our inferred growth faults. Other post-depositional factors may also have influenced thickness variation (e.g. differential compaction). In contrast, northwest trending faults (e.g. Gecko Fault System) are interpreted as new branches of reactivated structures (prevalently northwest oriented) developed during post-sedimentary strike-slip deformation. The latter influenced the Pb-Zn distributions; however, they have orientations incompatible with the sense of thickening described for the unit 200 and intersect portions of the deposit that do not display any apparent synsedimentary thickening, for example for the Gecko Fault 4 (Fig. 5.4b, detail 1). This evidence suggests that northwest oriented faults were active during post-sedimentary deformation, more likely causing (re)mobilisation.

5.3.4.2.   Continuity of mineralisation

Previous workers at Century and elsewhere in the Mount Isa district (e.g. Broadbent et al., 1996; Perkins, 1997; Davis, 2004) used apparently discordant geometrical relationships between ore and host to propose that mineralisation formed after sediment deposition, at depths ranging from several hundred meters to several kilometres. However, (re)mobilisation may partly or totally transform an ore system (e.g. see Fig. 5.2c and d). Furthermore, discordant mineralisation may also occur during sedimentation, as "Sedex" models require a proximal feeder and distal, barren host-rocks (Goodfellow et al., 1993), together in which facies variations should be discordant at some scale. Cases of synsedimentary replacement (discordant

disseminated ore) are also presented in the literature (see Zierenberg et al., 1998; Doyle and Allen, 2003).

The visualisation of iso-surfaces computed to enclose the high-grade portions of Century (cut-off of 15% for Zn, and 5% for Pb), was used in conjunction with sectional views of the reconstructed S-grid model (Fig. 5.5a and b) to locate discordant Zn and Pb ore (e.g. Fig. 5.2f). Anisotropic interpolation aided its identification (vertical connectivity was favoured using higher values of jump on S-grid initialisation of properties). Subsequently interpreted areas of discordant ore were compared with modelled fault surfaces. It appears that the ore body, in its present state, is separated in fault blocks with deformed portions that contain discordant mineralisation, and other "stratiform" portions where faulting is negligible (Fig. 5.5b, c and d). The spatial relationship between the boundaries of specific stratigraphic units (e.g. top and bottom of unit 200) has also been compared along vertical S-grid sections with the base metal content. Highest concentrations of Zn and Pb are frequently focused within shale-rich intervals (Fig. 5.5c). The 3D model though did not allow distinction between primary (synsedimentary), discordant mineralisation and later (re)mobilisation along more permeable fault domains. However, it can be considered a useful tool to understand the potential degree of (re)mobilisation and to establish the approximate proportion and scale of this process. Zones where faulting is more intense and the mineralisation loses stratigraphic continuity more likely experienced a higher degree of (re)mobilisation (Fig. 5.5d).

Base metal zoning was also characterised using 2D projections of base metal contents on specific horizons (Fig. 5.7, maps 1 to 24), as follows:

- There is a broad 100 m- to km-scale zonation of Pb-Zn in each metre- to 10 m-thick shaly ore layer (Fig. 5.7a, maps 7-8-9). This broad zonation does not appear to be systematically related to any of the internal faults within the orebody. In addition, there is a zonation of total cumulative sulphide content over similar scales.

- The broad transition zone from Pb-rich to Zn-rich in the ore shales changes its focus depending on stratigraphic position (Fig. 5.7a, maps 2-5-8). This discordant nature was interpreted by Broadbent et al. (1998) as evidence for a replacive origin of the sulphides.

- The interbedded siltstone and mudstones layers show a broad Pb-Zn zonation at similar scales to the shales, but at much lower concentrations, again with a different horizontal focus to the Pb-Zn transition zone in different layers (compare Fig. 5.7a with 5.7b). Mn grades appear to be more broadly distributed across the deposit in siltstones and mudstones (Fig. 5.7b, maps 10-13-16). In Fig. 5.7b, maps 11-12, we note an overlap among maximum concentrations in Pb-Zn along a linear east-west trend.

- For all mine rocks, there is an additional lateral variation of grade acting at 10 m to 100 m scales, which is distinct from the broad zoning within each layer. In terms of grade versus lateral distance, this is manifest as a gentle oscillation relative to the broader zonation (Fig. 5.7b, maps 11-14-17).

- For the latter gentle oscillations in Pb/Zn, there appears to be a systematic spatial relationship to certain generations and orientations of faults (Fig. 5.8a, b and c). For several parts of the orebody, there is a very interesting correlation between 10 m to 100 m scale depletion of Zn in a shale layer adjacent to a fault zone, and enrichment in the same metal in the immediately overlying siltstone layer (Fig. 5.9 and 5.10).

Comparing the spatial variation of mineral grades against the thickness variability across the deposit it is possible to test the hypothesis of Goodfellow et al. (1993). This worker proposed that base metal supply is one of the parametres that controls the thickness variation across a mineral deposit, if the ore deposit formed by exhalation of hydrothermal brines (see Fig. 5.7a and b, maps 19 to 24). We interpret the results of the comparison highlighted in Fig. 5.7 as follows:

- Not only do base metal grades control the thickness variability; apparently, also Mn concentrations contribute (e.g. units 200, 410, 430). Additional supply of carbonates may increase the volume of manganiferous sediment deposited, similarly to base metals.

- We also observed that the Mn control is more pronounced in siltstone/mudstone dominated intervals, consistent with abundance of Mn-siderite in those units (compare plots for units 320, 420, 440).

- Small-scale inconsistencies occur in the broad correlations observed. However, their scale and spatial proximity to major mapped faults suggest that later faulting has contributed to the present spatial variation of thickness across the orebody.
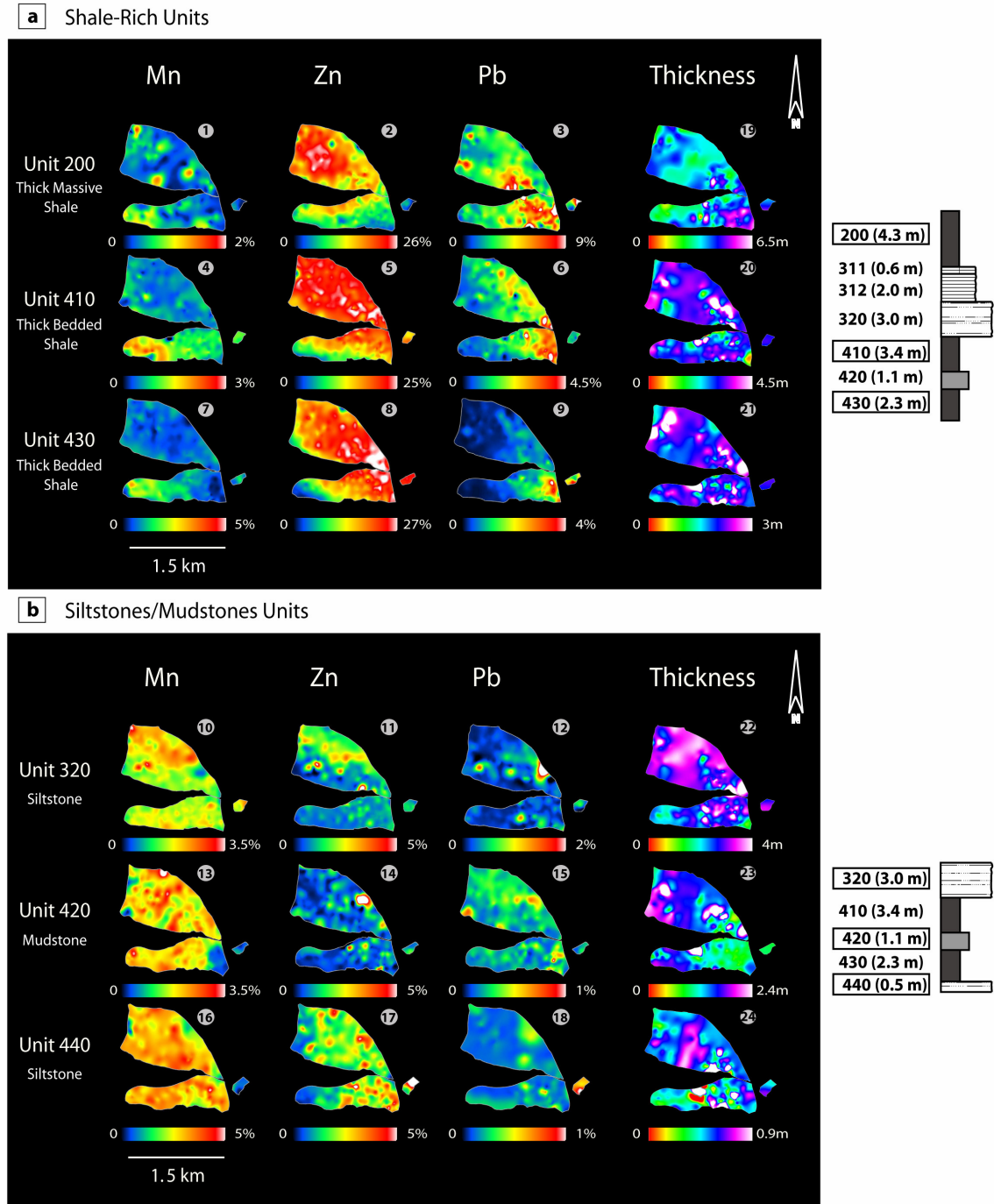
Fig. 5.7 2D map views of base metal concentrations, Mn and thickness distributions over reconstructed surfaces representing mine stratigraphic intervals (200,320,410,420,430 and 440). Maps are based on DSI interpolation of assayed diamond drill-hole data that represent unit confined average of several measurements (multiple assay values taken from each mine stratigraphic interval). (a) Ore bearing shale-rich layers. (b) Intercalated siltstone layers (see also enlarged figure - Appendix E).

5.3.4.3.   Evidence of remobilisation

The comparative spatial analysis of grade variation in different horizons indicates that faulting appears to have modified the broader km-scale metal zonation at 10 m to 100 m scales. This implies faults were involved in external introduction of ore (mobilisation) or remobilisation of pre-existing mineralisation. More likely, both processes occurred in different proportions across the deposit. The evidence of post-sedimentary redistribution (remobilisation) of sulphides is inferred on the basis of the relationship existing between post-sedimentary structures (northwest oriented faults, e.g. Gecko Fault System, Fig. 5.4a) and Pb zoning (Fig. 5.8a, b and c). Identified geochemical anomalies have trends that resemble the orientation of several reconstructed fault surfaces (e.g. distribution of Pb in unit 200, Fig. 5.8c). Nevertheless, comparison of Pb distributions across the stratigraphy (Fig. 5.7a, maps 3-6-9) indicates that in some cases, the higher concentrations of Pb within shale-rich layers, at m- to 100m scale, are not spatially correlated with the same structures (Fig. 5.7a, maps 3-6-9; Fig. 5.8a). If a mineralising fluid infiltrates, using a fault as main conduit, and then moves laterally through the stratigraphic sequence, we should expect to identify consistent spatial correlation in Pb-highs within shale-rich layers moving away from the fault. Therefore, northwest trending faults are interpreted as conduits that partly contributed to the redistribution of Pb. Moreover, localised depletion zones, of Pb and Zn, in high grade, shale-rich intervals, appear to be spatially close to zones of increased grade in overlying siltstone units.
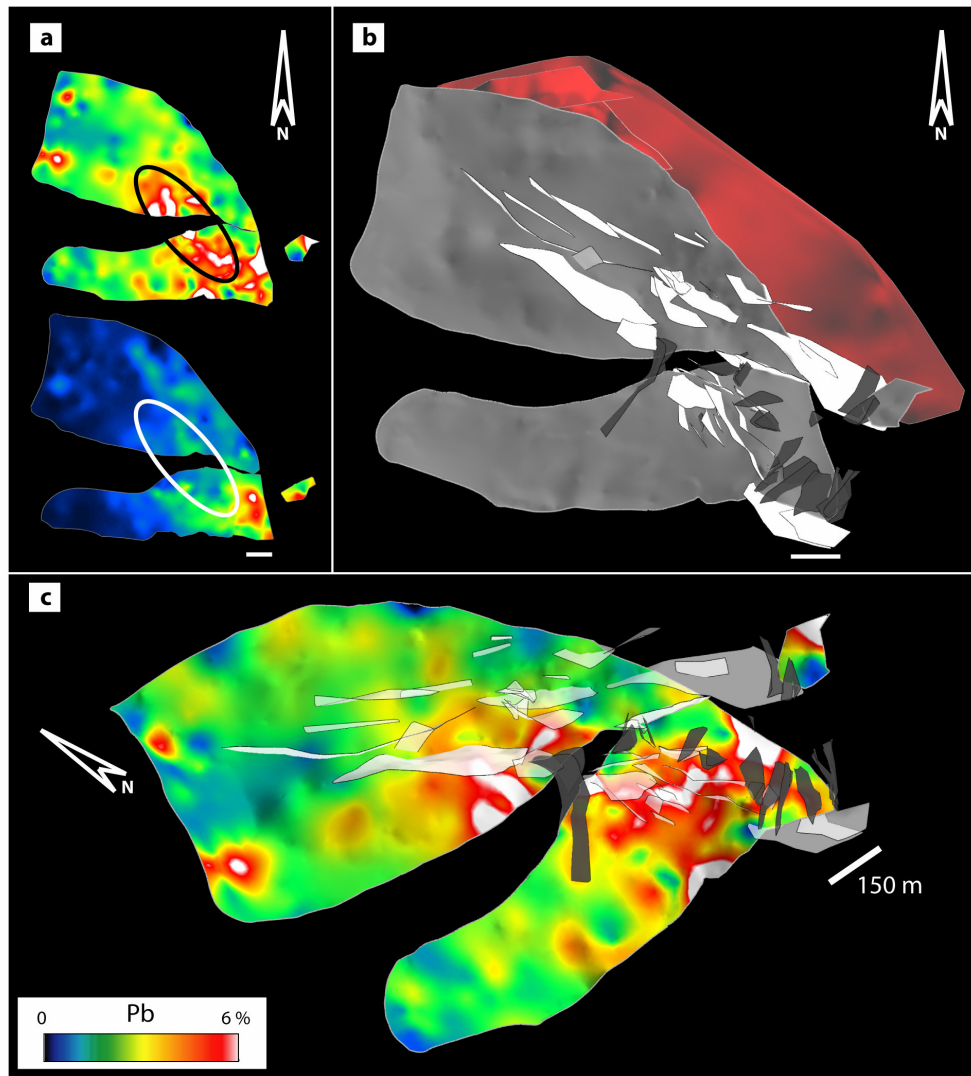
Fig. 5.8 Summary of figures illustrating the relationship between faulting and mineralisation. (a) Spatial distribution of Pb grades (unit 200, 0 to 8% and unit 430, 0 to 4%). Note that linear trends in the distribution of grades in unit 200 are interpreted as indicative of fault control (black oval). These trends are consistent with the orientation of modelled fault surfaces. (b) Map view of the Gecko Fault System (white surfaces) and Darimah Fault System (dark grey surfaces). The Gecko Fault System exerts limited control on the spatial variation of mineral grades in unit 430 (white oval) suggesting that structural control operated differently in each stratigraphic unit. (c) Example of visualisation of fault systems against mineral grades. This approach was used to perform visual correlation analysis. Both NW and NE trending faults seem to influence Pb distribution in unit 200.

This suggests upwards mass redistribution (remobilisation) acted at a high angle to the broad horizontal zonation within each layer (Fig. 5.9 and 5.10). Therefore, shale-shale and shale-siltstone correlations of Pb-Zn grades both support redistribution of base metals. What cannot be easily quantified is the proportion of remobilisation versus mobilisation. However, the systematic relationship of Pb-Zn concentrations shown in Fig. 5.10 suggests that a major syntectonic introduction of ore was unlikely; otherwise, this would have probably obliterated any sign of depletion.

	Pb $f(x,y)_{max}$	Pb $f(x,y)_{min}$	Zn $f(x,y)_{max}$	Zn $f(x,y)_{min}$
UNIT 320	> 0.5 %	−	> 2 %	−
UNIT 410	> 3 %	< 2 %	> 23.5 %	< 22 %
UNIT 420	> 0.3 %	−	> 0.8 %	−
UNIT 430	> 0.8 %	< 0.7 %	> 22 %	< 22 %
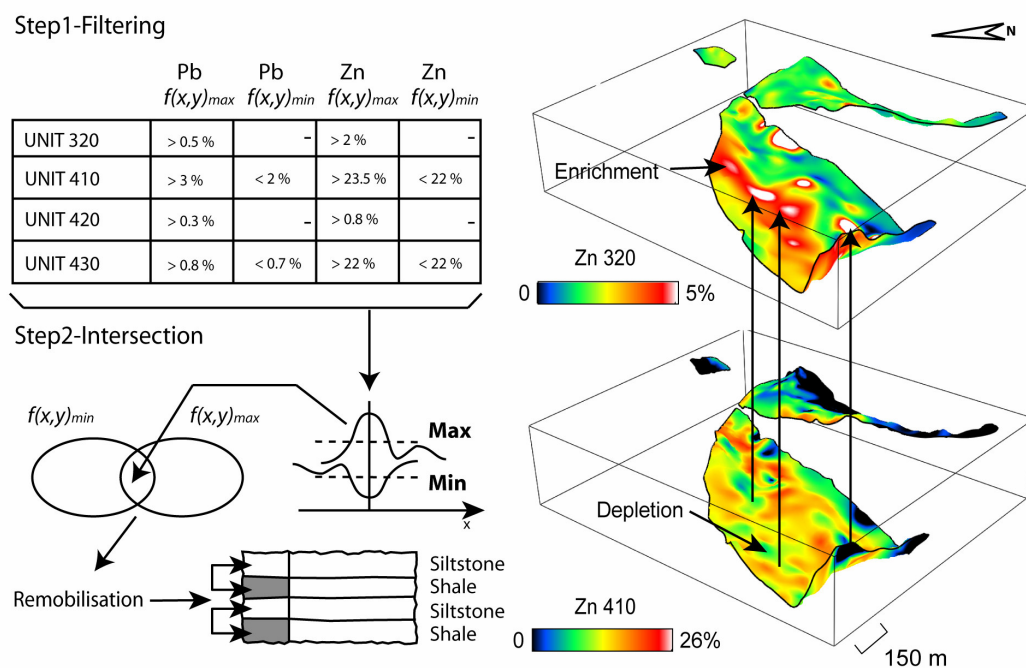
Fig. 5.9 Diagram portraying examples of GoCAD spatial analysis of adjacent shale and siltstone layers (320-410, 420-430), used to estimate the degree of vertical redistribution of Pb and Zn. We applied two steps: (step1) filtering of highs and lows, extracting regions from interpolated data using the GoCad region analysis tool; (step 2) Intersection between filtered maximum-minimum f(x,y) functions to obtain 3D spatial correlograms representing the localisation of sites of local redistribution of base metals. Depletions in Zn-Pb in shales show good correlation with enrichments in the overlying siltstones.

5.3.4.4.   Alteration zoning

The spatial analysis of 3D features was also used to explore aspects of the hydrothermal alteration of the Century deposit. Siderite occurs in sedimentary sequences crystallising either at shallow or deep depths, during burial of sediments and diagenesis (e.g. Pye, 1984; Choi et al., 2003). Previous studies on Australian Pb-Zn deposits (see Carr, 1984; Broadbent et al., 1998; Large et al., 2000) reported also examples of siderite interpreted as a product of alteration related to Pb-Zn mineralisation. These interpretations were constrained using the chemical compositions of siderites, which were anomalous in Mn and Zn (Mn^{2+} up to 20% and Zn^{2+} exceeding 4%) compared to the average compositions for siderites of sedimentary origin. Therefore, at Century, zincian siderites either formed from recrystallisation of diagenetic siderites, or addition to the sequence hosting the mineralisation during hydrothermal alteration, very near the seafloor (Cooke et al., 2000). In any case, the anomalous siderites are linked to Pb-Zn mineralisation.

The spatial distribution of siderite at Century is controlled by the lithological character of the host sediments. Siderite is more abundant in siltstone layers, and the siltstones are more Mn-rich than ore-rich shales (Fig. 5.3). Mn distributions and Mn-highs usually show an inverse correlation with Zn- Pb-highs, for all layers (Fig. 5.7b). Thus, we consider the Mn variation across the deposit to be a good indicator of where the sideritic alteration is distributed.
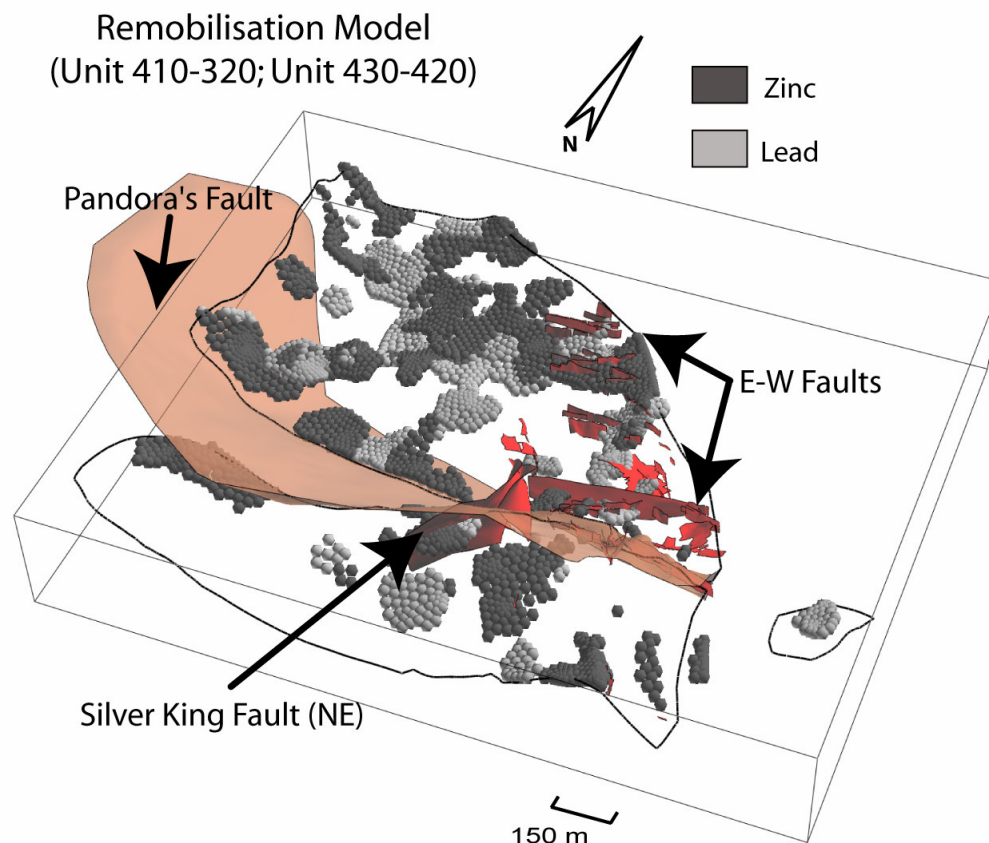
Fig. 5.10 Results from Fig. 5.9 obtained from correlation analysis, showing the areas where Zn-Pb redistribution occurred (depletion in shale is correlated with enrichment in overlying siltstone). Note the correlation of these zones with late east-west faulting (e.g. Pandora's fault).

Using constructed iso-surfaces, we visualised the Mn distribution of the mineralised shales and the interbedded siltstones and mudstones, and compared them with the Pb-Zn distributions (Fig. 5.11a and b). A striking spatial correlation became apparent for Mn anomalies in shale layers found in the southwestern corner of Century, suggesting that an alteration halo is present similar to those found at Lady Loretta (Carr, 1984), or at the HYC deposit (Large et al., 1998). A chemical vector, striking

southwest, can be drawn orthogonally to the isolines that represent the enveloping surfaces of equal Pb and Zn grade variation, along which there is also an inversely proportional relationship between base metals and Mn content. However, the location of highest concentrations of Mn in shales does not always correlate spatially with local Mn-highs within siltstone layers suggesting possible redistribution of siderite contemporaneous with Pb and Zn (re)mobilisation (Fig. 5.7a and 5.7b). Moreover, in unit 320 (Fig. 5.7b), a documented positive correlation between Mn-Zn-Pb defines a linear east-west pattern in contrast to the overall trends (shown also in Fig. 5.11a, trend labelled Pb >5%). East-west oriented faults intersect this portion of Century, further supporting secondary fault related (re)mobilisation.

The primary permeability of the host does not seem to have played a major role in the control of secondary redistribution of base metals and alteration as mudstones have similar zoning compared to siltstones (Fig. 5.7b, unit 320, 420). Therefore, the origin of such localised anomalies most likely relates to secondary induced permeability during later faulting that favoured local connectivity between mineralised shale, siltstones and mudstones. Fig. 5.12 portrays a schematic of the type of behaviour interpreted on the basis of the 3D model, and numerical results presented in the next section. In particular, it shows the different permeability response to fluid flow in case of overpressured conditions at burial depths. Shale intervals, stylolitic siltstones (more permeable units) and fault boundaries reflect different permeability zones. Their spatial distribution and the degree of overpressuring affect the possible redistribution of sulphide species and alteration. The scale of the anomalies and the relative overlap existing between sideritic alteration and Pb-Zn ore suggests that a different process may

have produced such patterns. Primary feeders in exhalative systems generally show a

systematic variation, with base metals separated from the siderite alteration. Such

zonation is apparent at Century for the broad scale zoning, but not for the small-scale

variations observed.
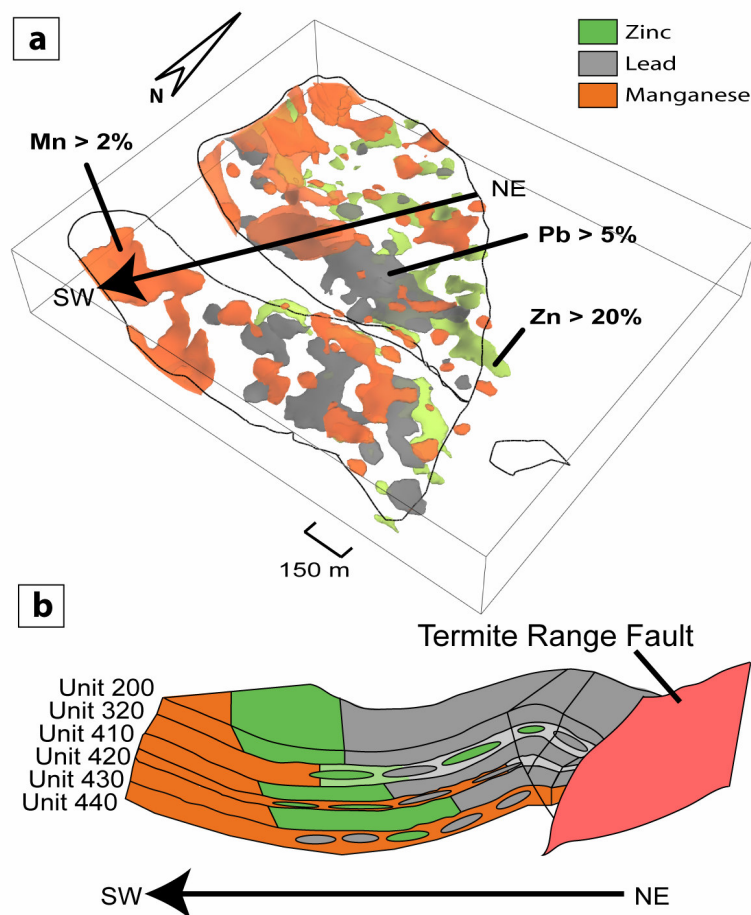
Fig. 5.11 Spatial distribution of Zn-Pb-Mn at Century, (a) showing how the bulk of the mineralisation (Zn-Pb) appears to be more focused on the eastern side of the deposit, with Mn, above 2 %, concentrated on the southwestern corner. The localisation of Pb, more focused in the southeastern corner of Century, is interpreted as (re)mobilisation of Pb in unit 180 - 200. (b) 3D schematic diagram of the ore sequence with representation of the two scales of zoning identified at Century. 10-100 m scale patchy zonation is superposed on broad Zn-Pb-Mn zonation (see text).

5.4.   *Century numerical fluid flow simulations*

This section further examines the influence of the permeability and the hydraulic gradient on fluid flow localisation, and direction, during post-sedimentary deformation, to see to what extent syntectonic, fluid flow may have influenced or controlled mineralisation or (re)mobilisation. We use the results of the GoCAD modelling as a basis for numerical modelling. This can also be regarded as another test of the Broadbent et al. (1998) late diagenetic to syntectonic model for mineralisation (see also Ord et al., 2002).

5.4.1.   Introduction

The numerical models were developed using the FLAC3D code, in which deformation of elastic-plastic material and consequent volume changes, as a result of dilation, are the main driving forces for fluid migration. FLAC is a three-dimensional explicit finite difference-modelling program, suitable for simulating the behaviour of geological materials that undergo plastic flow during yield. FLAC has been applied to several geological problems in Australia, New Zealand and China (e.g. Ord, 1991a, b; Upton et al., 1995; Zhang et al., 1996a; 1996b; Ord and Oliver, 1997; Upton, 1998; McLellan, 2000; Oliver et al., 2001; Schaubs and Zhao C., 2002; McLellan et al., 2004). Simulated materials are represented by zones that form a grid, which can be adjusted by the user to fit the geometry of the problem to be solved. Each zone within the grid holds prescribed properties (both elastic and plastic) and behaves according to a

linear or non-linear stress/strain law as a response to applied forces. The material is allowed to yield and flow and deform, and when in a coupled scenario, fluid allows interaction with and influence over this deformation. Fluid flows according to Darcy's Law. Variations in hydraulic head are induced by volume changes due to rock dilation. Rocks with high dilation angles have a greater propensity to dilate for a given shear stress. Changes in pore pressure influence the effective stress acting on the rock so that feedback occurs between deformation and fluid flow in a coupled manner. Ord and Oliver (1997) and McLellan et al. (2004) provide a more comprehensive description of FLAC.
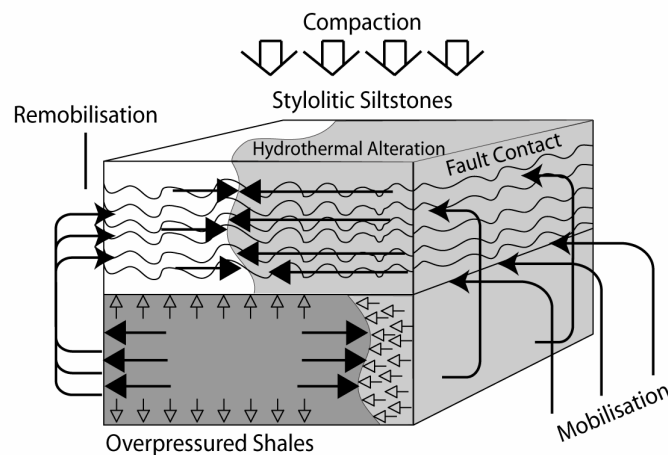
Fig. 5.12 Diagram illustrating the likely effect of faulting and fluid flow in controlling the localisation of remobilisation and mobilisation of base metals during post-sedimentary deformation. Shales are considered overpressured, whereas stylolitic siltstones have a higher permeability partly allowing lateral flow. In particular, base metals within this fluid flow scenario would be more likely transferred from overpressured shale into permeable siltstones. Similarly, fluid in fault zones would possibly permeate into siltstones for limited distances as these intervals have a higher permeability compared to shales although the lateral infiltration is limited by overpressuring.

5.4.2.   Conceptual model

In this study we consider the conceptual model of a possible fluid flow scenario linked to epigenetic mineralisation in a subsurface, compressional tectonic setting (e.g. Broadbent et al., 1998; 2002). The models consist of a 400 m by 400 m by 400 m grid representing a simplification of the mine stratigraphy (Fig. 5.3 and 5.13, Clifford and Kelso, 2003).
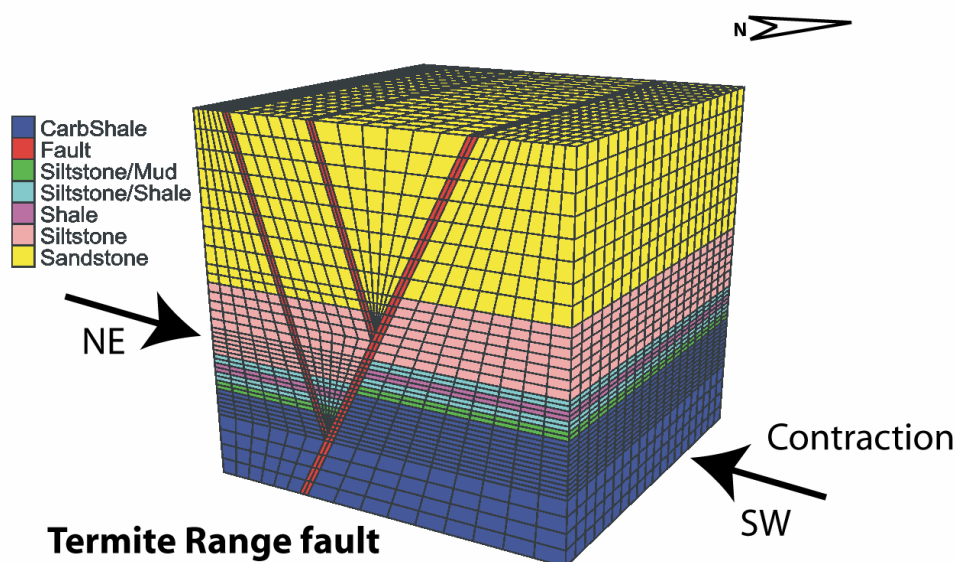
Fig. 5.13 Conceptual model for syntectonic mineralization of the Century deposit. The model consists of a 400 m x 400 m x 400 m volume of rock, incorporating the major stratigraphic units as shown. The fault structures within the model represent the northwest striking, southwest dipping Termite Range Fault, and associated parasitic branching faults. The model is buried to a depth of 2500 m, consistent with estimated geological conditions at this time. Pore pressure is initially set at hydrostatic values and contractional deformation is applied normal to the fault strikes (σ1 approximately NE/SW). The model is deformed to around 5% strain.

The following considerations were based on field evidence and provided constraints for the conceptual model:

- Pit exposures show only restricted zones of apparent hydrofracturing, suggesting this process was not the main fluid focussing mechanism for the shale-rich intervals (e.g. less then 5 m showing fracturing over 100 m lateral intervals).

- The hand-specimen of Fig. 5.2a documents laminated ore enclosed in a volume of siltstone/shale. No secondary fractures or shears affecting ore distribution are noted, which is typical of most of the mineralised shales.

Therefore, the conceptual model incorporates the primary lithological characteristics recognised in the field, without the need for requiring penetrative hydrofracturing (unlike the model of Ord et al., 2002) as a mechanism for fluid flow and ore genesis.

The main aim of the constructed conceptual model (Fig. 5.13) was to explore the difference between permeability contrasts between adjacent layers e.g. shale and siltstone, and to examine the hydraulic gradients induced by overpressurisation and faults, and their control on fluid flow directions. Initial model conditions included full fluid saturation, and pore pressure was initialised to approximately hydrostatic values before compressional deformation was applied. All physical properties are given in Table. 5.1. The model grid is cut by a normal fault, representing the Termite Range Fault (initial syn- to post-rift sagging phase of basin deformation), which is subsequently reactivated in a reverse sense during basin inversion and compressional

deformation (condition tested in the FLAC models). Two additional parasitic faults have been added that correspond with faults believed to have been active during contraction (Fig. 5.13). The geological units within the model represent the interbedded siltstone/shale sequence of the main ore horizon, sandstone and mudstone. The numerical model was deformed to around 5% bulk shortening, with the maximum principal stress (σ_1) orientated approximately NE-SW, consistent with the regionally inferred kinematics during the Isan Orogeny.

Table 5.1. Material properties for the geological units used in the numerical models.

Model	Density	Bulk modulus	Shear modulus	Cohesion	Friction angle	Dilation angle	Permeability
	(kg/m^3)	(Pa)	(Pa)	(Pa)	(°)	(°)	(m^2)
Geological units							
Sandstone	2400	2.68e10	7.0e9	2.7e7	27	4	1.00e-15
Siltstone	2450	1.56e10	1.08e10	3.47e7	25	4	1.00e-16
Ore Shale	2500	8.8e9	4.3e9	3.84e7	14	2	1.00e-19
Carbonaceous Shale	2500	8.8e9	4.3e9	3.84e7	14	2	1.00e-19
Siltstone / Shale	2500	1.0e10	7.5e9	3.6e7	23	2	1.00e-17
Siltstone / Mudstone	2600	1.0e10	7.5e9	3.6e7	23	2	1.00e-18
Fault	2300	4.70e9	4.30e9	8.00e6	30	5	1.00e-14

5.4.3.   Numerical results

Initial model compression results in an increase in pore pressure that forces fluid up the more permeable Termite Range Fault and parasitic faults. This fluid flow within the faults is a result of the higher permeability and dilation within the fault planes (Fig. 5.14a). As deformation continues shear strain is closely associated with faults, and volumetric strain or dilation is broadly coincident with areas of increased shear strain. Areas of dilation are observed within the model as deformation progresses, in particular

west of the main Termite Range Fault, with no significant dilation noted within the shale units. Focussing of fluids remains concentrated within the more permeable faults (Fig. 5.14b). During compressional deformation, there is no evidence of fluids entering the shale units from the fault network, as a result of pressure gradients and low volume change. The shale unit shows isolated areas of high pore pressure in comparison to other units because of the low permeability and low dilation angle (Fig. 5.15). Fluid flow is primarily driven or expelled from the shale units (Fig. 5.16a), and on closer inspection fluids are mainly driven out towards the more permeable faults, and to a lesser extent, the siltstone layers (Fig. 5.16b), preventing lateral infiltration into the overpressured compartments.
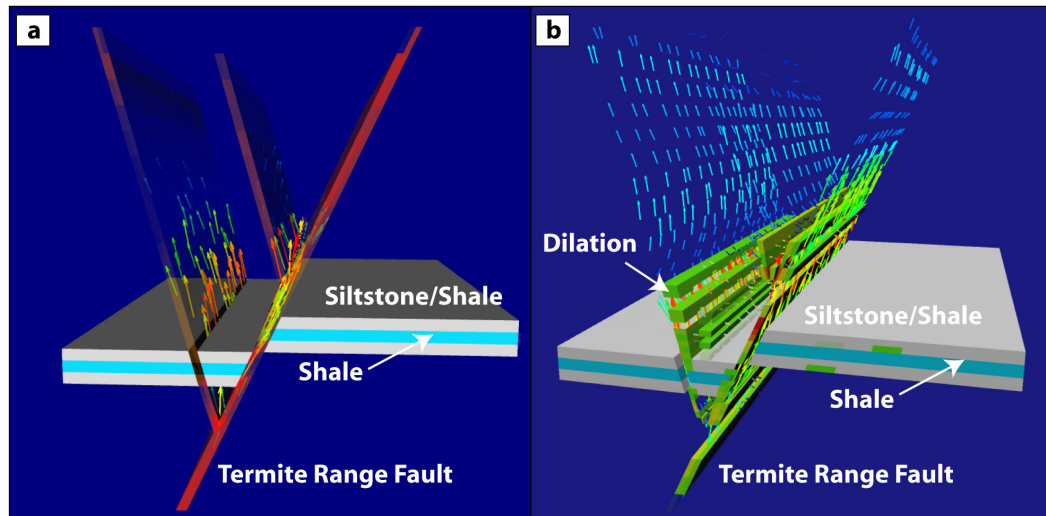
Fig. 5.14 Numerical results for the Century deposit incorporating the main features of the system (Fig. 5.13) such as the Termite Range Fault, parasitic faults, the siltstone/shale layers (grey), and the main ore horizon shale layer (blue). Both plots display volumetric strain increments (dilation) and Darcy fluid flow vectors (red – highest velocity, blue – lowest velocity), with (a) at 2% bulk shortening, showing greatest dilation (red) within the fault planes and fluid flow is focused within the faults, (b) at 5% bulk shortening, showing highest areas of dilation both within and proximal to the faults. Dilation is noted within the siltstone/shale layers but not the shale ore horizon.
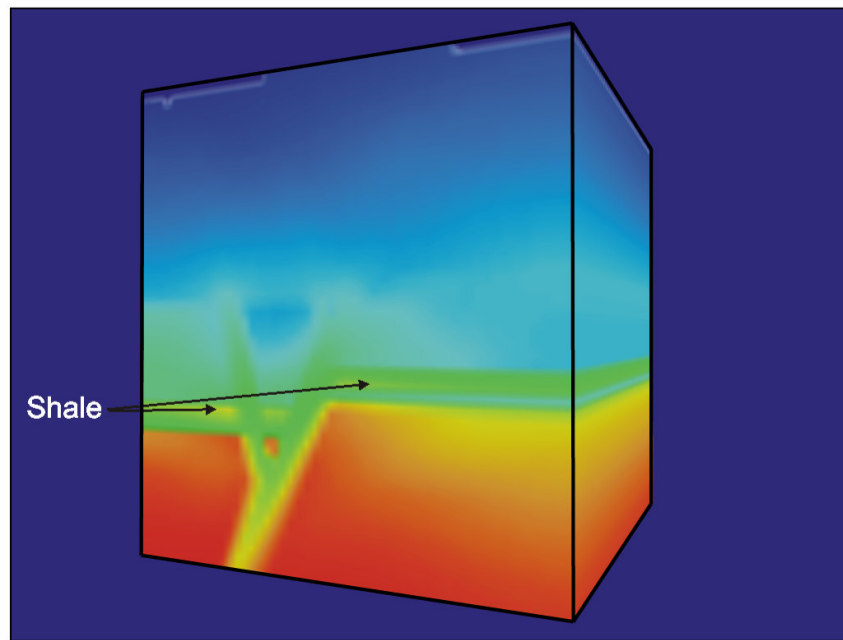
Fig. 5.15 Plot of pore pressure (warm colours – high values, cool colours – low values) at around 3% bulk shortening. Note the increased pore pressure within the shale units relative to the other layers, as indicated by the black arrows. The increased pore pressure prevents lateral fluid migration from the faults or siltstones into the shales. Overpressure in the less permeable units has not caused penetrative hydrofracturing at Century (see text).

5.4.4.   Control of permeability and hydraulic gradient on fluid flow direction

During sensitivity analysis of the numerical model, we tested initial fluid pressure variations, permeability variations, and rock dilation angles. Initial fluid pressure greater than hydrostatic aids in upward migration of fluid flow within the faults, with no major change in fluid flow or dilational patterns observed. Permeability

variations were also tested, and results indicate that the permeability of the shale units would need to be about one-half of the fault permeability, and greater than siltstone, to allow any possible fluid infiltration within the shale layers. It is unreasonable to consider that the shales would have dilation angles greater than siltstone, because shear on fine grained shale would most likely result in little dilation in comparison to coarser grained sediments.

Overpressurisation within the shale units could potentially have stimulated hydrofracturing. However, to have any significant fluid flow within the shales, they must have permeabilities of similar magnitude to faults, and furthermore little hydrofracturing is actually observed at Century in the shales. Local areas between branching faults in the models display strong dilational characteristics, which are mainly focussed around the faults and siltstone contacts; however, these areas only provide limited access to shales for deep-seated mineralising fluids.

Dewers and Ortoleva (1994) model the compartmentalisation of a sedimentary basin as a result of overpressuring. They describe the coupling between permeability enhancement and hydrofracturing, focussing on how the consequent variation of the hydraulic gradient can reduce major lateral infiltration during overpressuring cycles. Our FLAC results provide similar insights. If the shales underwent hydrofracturing during epigenetic conditions, overpressured volumes of rock would have formed isolated cells surrounded by fault zones with channelled flow (Fig. 5.12). Flow was mostly outward directed into and along the faults, preventing lateral infiltration into the overpressured compartments.
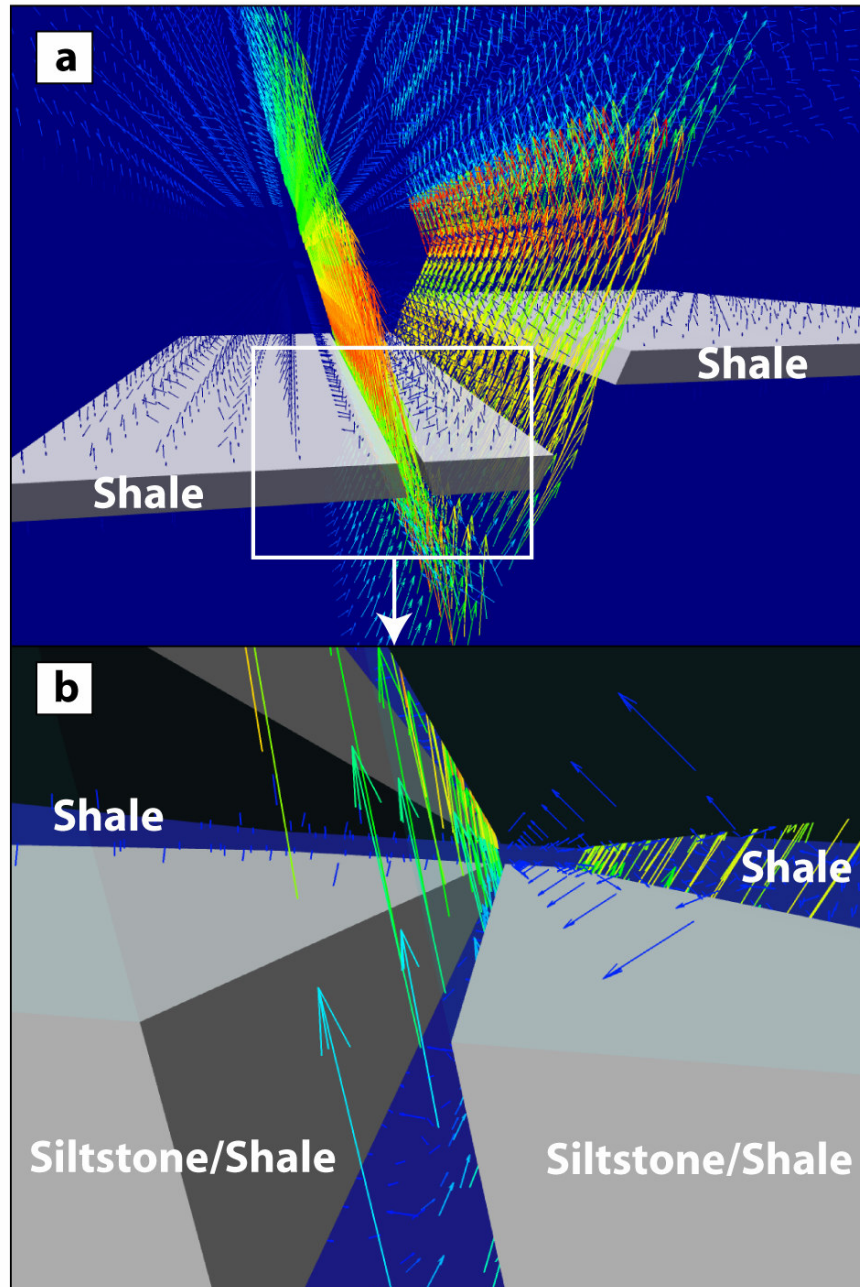
Fig. 5.16 Detail of part of Fig. 5.14b, showing fluid flow vectors (red-high velocity, blue-low velocity) in and around shales; a) plot displaying the relationship between the main shale ore horizon and fluid flow direction and velocity. Note that fluid flow is focused within the more permeable faults and fluid is generally expelled from the shale units (grey) into the surrounding units or nearby faults, b) further magnification displaying the relationship between the shale units (transparent), siltstone/shale units (grey), faults (transparent) and fluid flow. Fluid is expelled from the shale units as previously described.

5.5.   *Discussion*

The results of this study suggest that (re)mobilisation during the late diagenetic to syntectonic phase preferentially occurred along the fault zones. The potential for metal introduction or remobilisation is proportional to the fluid flux pervading the rock matrix adjacent to fault zones (Hobbs, 1987; Phillips, 1991). The 100m-scale irregular metal zonation found at Century is associated with fault zones and most likely occurred as a response to channelised fluid flow adjacent to the faults, as also predicted in the FLAC models. However, comparing the 3D modelling results with the FLAC results we cannot easily explain the origin of the km-scale zoning, which appears unrelated to the later faulting events at Century. Therefore, we consider some theoretical aspects of basin evolution to allow a better understanding of this broad scale zoning.

5.5.1.   Permeability evolution

Compaction and diagenesis generally cause an overall reduction of the primary porosity and permeability of sediments. However, some layers tend to show enhanced permeability, causing horizontal compartmentalization of the flow (refer to Fig. 5.17, a-b-c). The localisation of intense flow depends on the grain size, which controls the rate between advective flow and molecular diffusion of species (Phillips, 1991). Moreover, horizontal, secondary enhancement of permeability may result in response to coupling of mechanical forces with chemical reaction and transport, due to the dependence of mineral free energy on surrounding rock texture (Dewers and Ortoleva, 1990b). The

formation of stylolites represents an example of such process. Secondary permeable pathways, as seen at Century, also form in response to faulting, commonly favouring vertical connectivity. Hence, progressive horizontal and vertical compartmentalisation leads to higher contrasts in permeability of different layers within a basin, favouring development of abnormal pressure gradients. The fluid flux is controlled by the evolution of permeability and, in turn, the rate at which the sulphides are precipitated in favourable sites is proportional to the fluid flux (Phillips, 1991). Therefore, compartmentalisation influences the spatial distribution of base metals (see Fig. 5.17, d-e-f).

5.5.2.   Timing of broad scale zoning

We consider three possible models for the formation of the km-scale zoning at Century (Fig. 5.17, g-h-i):

- Exhalative formation in a brine pool at the sediment/water interface.
- Sub-seafloor genesis associated with early diagenetic replacement.
- Late diagenetic to syntectonic replacement involving (re)mobilisation.

The lack of a relationship between later faulting and the km-scale zoning observed, in conjunction with an inferred spatial correlation of thickness with the distribution of base metals and alteration, suggests that ore genesis occurred very early. The evidence of a km-scale zoning preserved in shales and siltstones indicates that the

broad zonation formed before horizontal and vertical compartmentalisation. Furthermore, an absence of overpressuring is required to allow fluid flow in shale-rich intervals, and we cannot foresee the development of high permeabilities in the shales without extensive hydrofracturing, which was not observed, nor modelled, across the entire shale packages. Moreover, a sub-seafloor replacement model under diagenetic conditions would have to consider at least the effect of horizontal compartmentalisation, which would have controlled the localisation of replacement fronts. The majority of the flow would be focused in permeable siltstones units, with expected reaction fronts localised at the interface between shales and siltstones (Fig. 5.17e), or within siltstones, if the ore forming reactions involved gaseous methane (Cooke et al., 2003). These lithologic boundaries would be the most favourable locations where metalliferous brines would firstly react with organic-rich shales or methane. However, the vertical zoning explored using the S-grid model (Fig. 5.5c) does not support this interpretation, because highest grades are found in shale-rich units. Base metal concentrations in several cases decrease progressively from the centre of shale-rich units towards the siltstone/shale interfaces. Moreover, field observations (e.g. Fig. 5.2b) document the lack of reaction fronts at siltstone/shale interfaces. Therefore, we consider a later replacement model improbable to explain the broad zonation.

An early diagenetic model (sub-seafloor replacement before overpressuring) cannot be completely discounted, although for similar reasons it was probably not the major ore forming mechanism at Century. If replacement is considered the primary mechanism of ore emplacement, we should see a systematic relationship between more permeable siltstone units (the pathways), abundance of organic carbon (the reductant),

and the spatial distribution of ore (the product). A local spatial relationship between organic carbon and sulphides has been demonstrated at Century in some veins (Broadbent et al., 1998). However, widespread ore laminae occur independently of permeable layers in hand-specimen, and at microscopic-scale. They are often localised in the impermeable domains rather than associated with permeable pathways (sub-mm silty layers).

We favour an exhalative model in which the broad scale zoning was caused by temperature and chemical gradients established between the source of metalliferous brines and the site of ore deposition. A syntectonic model is finally considered unreasonable to explain the broad zoning observed although the redistribution of metals around post-sedimentary faults may be linked to the Isan Orogeny or a younger event.
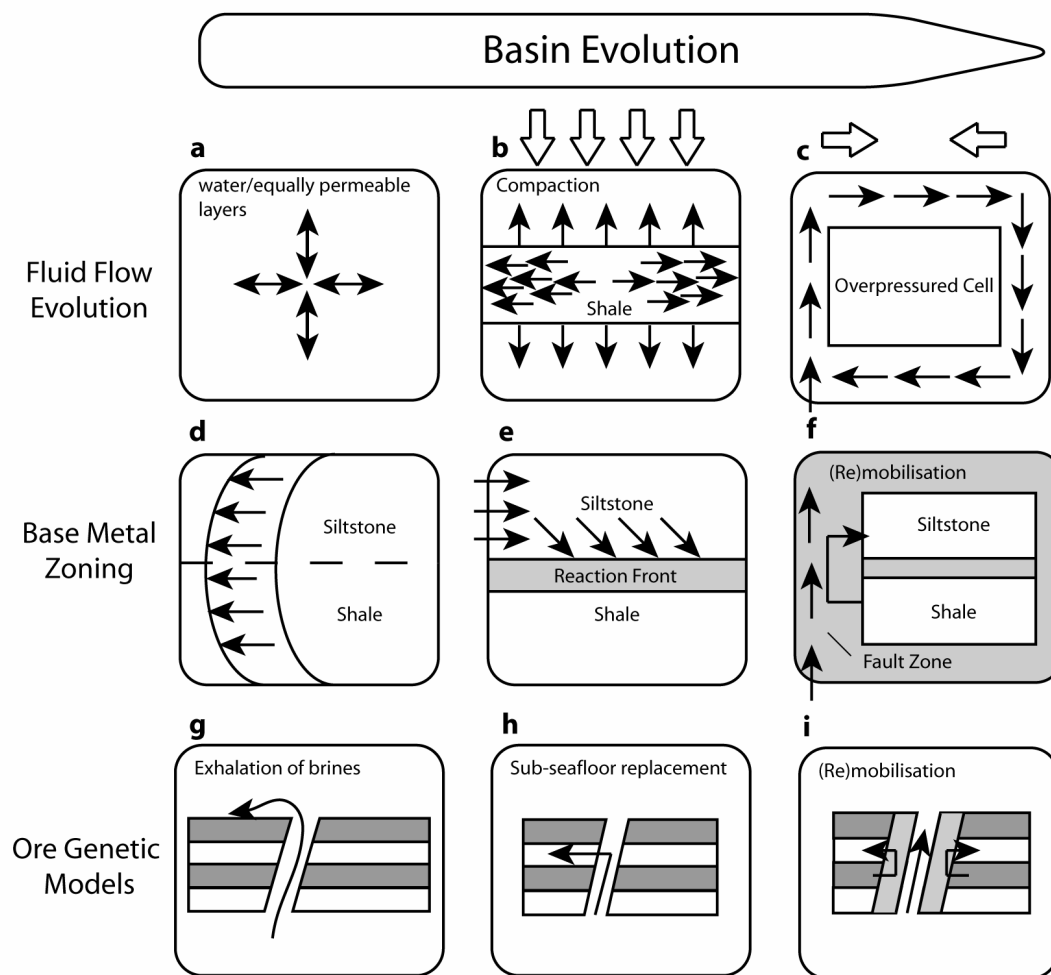
Fig. 5.17 Schematic diagram illustrating the fluid flow variation during basin evolution, and its influence on the type of metal zoning, which represents a constraint for the different ore genetic models. (a) Hydrostatic flow in equally permeable units or seawater (with surficial flow). (b) Overpressuring example during compaction with flow outward directed from shales towards siltstones and faults. (c) Horizontal and vertical compartmentalisation. (d) Reaction front propagating through shale and siltstone before compartmentalisation. (e) Localisation of a reaction front at the shale/siltstone interface in overpressured conditions. (f) Vertical compartmentalisation associated with faulting and (re)mobilisation. (g) Exhalative model involving surficial flow and sulphide deposition at the sediment/water interface. (h) Early-late diagenetic replacement model involving lateral infiltration of metalliferous brines. (i) Syntectonic fault controlled (re)mobilisation model.

5.6.   Conclusions

The integration of geometric models with numerical modelling and theoretical considerations on the timing of metal zonation support the following conclusions:

- Century experienced remobilisation during diagenesis and deformation. Field observations and modelling results document widespread remobilisation of sulphides.

- Systematic patterns in 100 m-scale zonation between siltstones and shales suggests that late diagenetic to syntectonic remobilisation of pre-existing sulphides was more important than introduction of new sulphides to the total system during deformation. If the syntectonic (re)mobilisation involved a significant component of additional introduction of ore, we cannot easily explain why we have patchy depletion of Pb-Zn in the shales.

- The secondary redistribution of sulphides is a result of later reactivation of northeast, northwest and east-west oriented faults, probably during the Isan Orogeny.

- The timing of the primary km-scale zoning is constrained by 3D observations, geomechanical modelling, theoretical permeability considerations, and field constraints. We suggest that the km-scale zoning at Century predates compaction and overpressuring.

- Spatial, numerical and theoretical modelling suggest that Century is syngenetic, with further diagenesis and deformation producing metre to 100 m scale

(re)mobilisation. The timing of the broad scale zoning best matches an exhalative origin with hydrothermal venting and brine pool formation, in conjunction with sub-seafloor replacement that was a minor contributing factor to ore genesis.

Chapter 6

Catastrophic mass failure of a Middle Cambrian platform margin, the Lawn Hill Megabreccia, Queensland, Australia

Acknowledgement of Contributions

N.H.S. Oliver – normal supervisory contributions

Abstract

Megabreccia and related folds are two of the most spectacular features of the Lawn Hill Outlier, a small carbonate platform of Middle Cambrian age, situated in the northeastern part of the Georgina Basin, Australia. The megabreccia is a thick unit (over 200 m) composed of chaotic structures and containing matrix-supported clasts up to 260 m across. The breccia also influenced a Mesoproterozoic basement, which hosts the world class Zn-Pb-Ag Century Deposit. Field-studies (undertaken in the mine area), structural 3D modelling and stable isotopic data were used to assess the origin and timing of the megabreccia, and its relationship to the tectonic framework. Previous workers proposed the possible linkage of the structural disruption to an asteroid impact, to justify the extremely large clasts and the conspicuous basement interaction. However, the megabreccia has comparable clast size to some of the largest examples of sedimentary breccias and synsedimentary dyke intrusions in the world.

Together with our field and isotope data, the reconstruction of the sequence of events that led to the cratonization of the Centralian Superbasin supports a synsedimentary origin for the Lawn Hill Megabreccia. However, later brittle faulting and veining accompanying strain localisation within the Thorntonia Limestones may represent post-sedimentary, syntectonic deformation, possibly linked to the late Devonian Alice Springs Orogeny. An origin linked to an asteroid impact cannot be completely discounted, but the coupling of intrabasinal processes involving destabilization along the platform margin associated with diagenetic karstification and

tectonic dip-slip reactivation of basement faults, explain adequately the documented features.

Keywords: Lawn Hill Outlier, Megabreccia, Century, Dykes, Debris-Flow, Slumps

6.1 Introduction

Understanding the origin and timing of catastrophic events is of primary importance for earth scientists and modern urban society. Modern technologies have the potential to allow identification of early signs of massive failure (e.g. aseismic fault slip on the flank of volcanoes, Cervelli et al., 2002), but the multivariate nature of geological systems still requires the acquisition of data across different geological terrains and time periods, to understand the interplay of variables (such as faulting, lithostratigraphy, climatic conditions, etc.) leading to these "rare" events. Catastrophic sedimentary processes may occur either in continental or marine settings, as a result of intrabasinal evolution or extra-basinal forcing mechanisms (Rossetti et al., 2003), reflecting the nonlinear behaviour of the earth crust (see Nicolis, 1995). Important external causative factors are seismogenic events, either earthquakes or tsunami, but also aseismic events such as meteorite impacts, or hurricanes (Albertao et al., 1996; Shiki et al., 2000). Here we present a case study of a "catastrophic" event that led to the formation of one of the largest breccia accumulations in the world, the Lawn Hill Megabreccia.

Defining the timing and origin of catastrophic events is valuable also for tecnostratigraphic reconstructions, because these deformations can be potentially caused by tectonic movements. For instance, the Lawn Hill Outlier may have been deformed by the Late Devonian, Alice Springs Orogeny (ca. 410-390 Ma), which influenced other Palaeozoic basins in central and northern Australia (e.g. Haines et al., 2001). Therefore, a detailed structural and stratigraphic analysis was undertaken to assess the possible influence of such an orogenic event. A review of the tectonic framework and stratigraphic evolution of the Georgina Basin is presented below and the timing and origin of folding, brecciation and dyke intrusions into the underlying Mesoproterozoic basement is discussed.

The megabreccia is hosted in the Lawn Hill Outlier (originally named as Dentalium Plateaux, Carter and Opik, 1961), located approximately 250 km north northwest of Mount Isa in Queensland (Fig. 6.1a-c). The Outlier has a circular shape, with diameter of 18 km, and unconformably overlays Mesoproterozoic weakly metamorphosed rocks of the Mount Isa Inlier (mainly siltstones and shales of the McNamara Group, Andrews, 1998). The Outlier was firstly mapped by Opik (1957) who used biostratigraphic correlations to define its Middle Cambrian age, and included the carbonate rocks as part of the Thorntonia Limestone, Beetle Creek and Border Waterhole Formations of the Georgina Basin. The Lawn Hill Outlier overlies, on its southwestern margin, one of the largest Zn-Pb-Ag mineral deposits in the world, the Century zinc deposit. This mineral resource is currently mined in open cut by Zinifex Pty Ltd. offering a unique chance of studying large exposures (approx. 250 m high) that represent sections throughout the sedimentary sequence of the Thorntonia Limestone.

The open cut also exposes an erosional unconformity that separates the Mesoproterozoic strata of the Lawn Hill Formation (e.g. Andrews, 1998) from the carbonate cover sediments of the Georgina Basin.

The anomalous folding and brecciation of the Lawn Hill Outlier have been interpreted in diverse ways. De Keyser (1969) invoked dip-slip reactivation of Mesoproterozoic basement faults as the mechanism controlling the formation of the megabreccia. Other workers suggested an early Middle Cambrian asteroid impact as a possible explanation for the complex brecciation and folding observed, and the circular outcrop pattern (Ferguson, 1992). In contrast to De Keyser (1969), Hutton (1992) explained the deformation by solution collapse in limestones elsewhere in the basin. Hutton (1992) also discounted the possibility of a connection between deformational features and an extraterrestrial impact, suggesting that occurrence of cone in cone structures in the central part of the outlier could be also derived by simple volcanic, explosive activity. In summary, several processes operated independently or interactively to cause the observed deformational features and these include: (1) tectonic control with possible reactivation of basement structures; (2) asteroid impact; (3) solution collapse due to karstic activity.
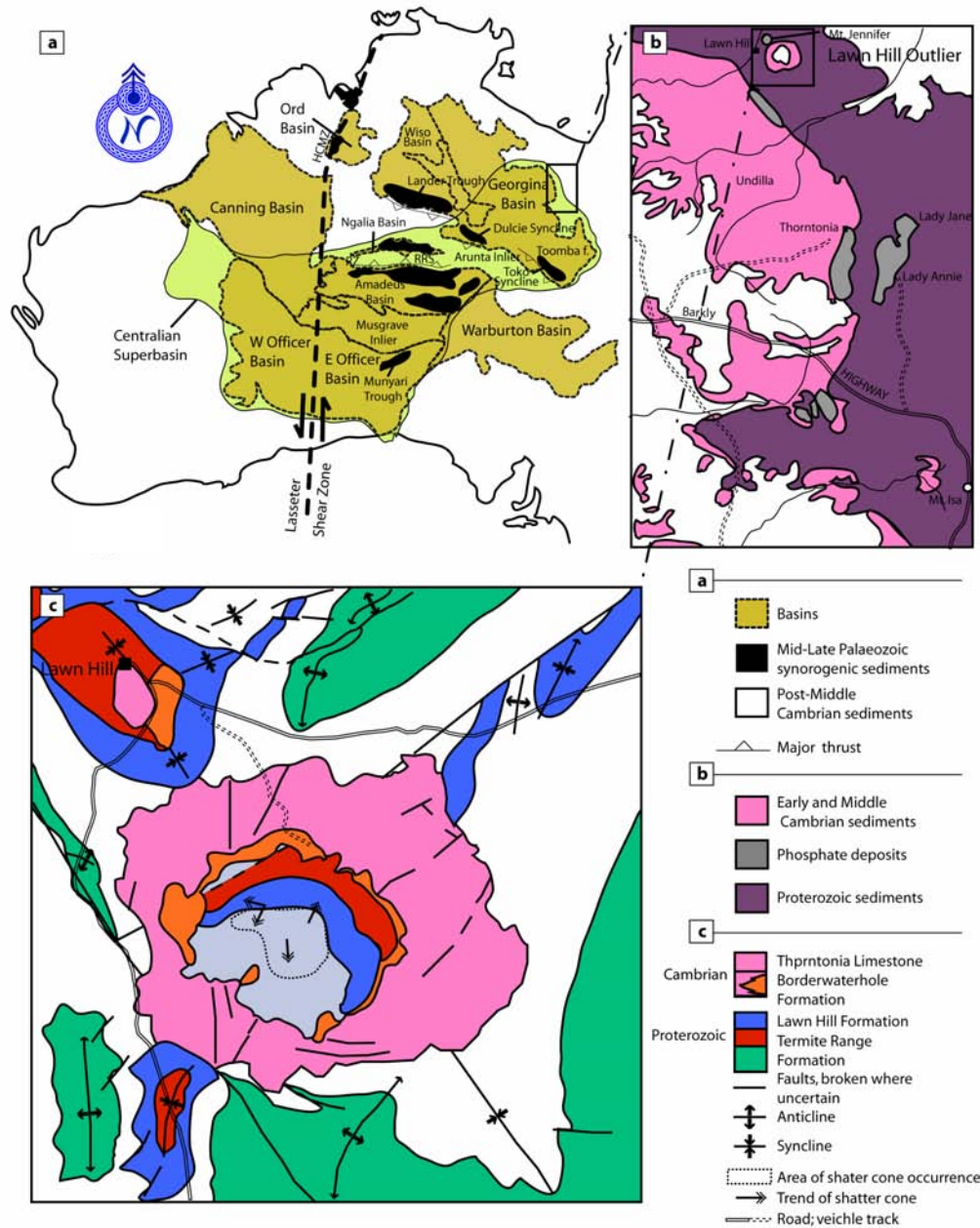
Fig. 6.1 Map view of the study area: (a) locality map (after, Haines et al., 2001) showing main basins (Amadeus, Ngalia, Georgina, Officer, and Savory) and inliers discussed in the text. Delimitation of the Centralian Superbasin and location of Dulcie and Toko synclines. (b) Locality map showing the northeastern margin of the Georgina Basin (Undilla sub-Basin) and location of the Lawn Hill Outlier. (c) Enlarged map-view of the Lawn Hill Outlier illustrating the lithofacies variation in the study area, and the distribution and trends of shatter cones (after Stewart and Mitchell, 1987).

6.2 Regional geotectonic framework

The tectonostratigraphic evolution of the Centralian Superbasin provides elements at cratonic/regional scale that can be used to spatially and temporally define the Lawn Hill Megabreccia event, relative to major tectonic events.

6.2.1 From intracratonic to orogenic times

The Lawn Hill Outlier is formally correlated with the northeastern margin of the Georgina Basin (Undilla sub-Basin) based on lithostratigraphic and biostratigraphic correlations (Szulc, 1992). The Georgina Basin is one of five sedimentary compartments (e.g. Walter et al., 1995) that resulted from the Neoproterozoic separation of an extensive (approx. 2 million km^2) intracratonic basin, termed the Centralian Superbasin (Gorter, 1992; Walter et al., 1992; Walter et al., 1995) (Fig. 6.1a). This Superbasin underwent an initial phase of intracratonic rifting that culminated with Early Cambrian seafloor spreading accompanied by subsidence and crustal thinning at around 800 Ma (Shaw et al., 1991; Zhao et al., 1994). Sub-basins were apparently preserved where little Neoproterozoic and Palaeozoic orogenic deformation occurred (Walter et al., 1995; Sandiford and Hand, 1998). However, the history of sedimentation of basin compartments may have been influenced by these major tectonic events. Understanding how the deformation evolved at cratonic to regional scale, and when such phases developed is essential when attempting to define the origin and timing of brittle and ductile deformation observed at the local scale.

Two orogenies have contributed to the separation of the Centralian Superbasin, with consequent uplifting and exposure of two high-grade metamorphic complexes, the Arunta and Musgrave Inliers (Fig. 6.1a). The oldest event is the Petermann Orogeny (Early Cambrian, ca. 540-600 Ma) is linked to the exhumation of the Musgrave Inlier involving northward-directed thrusting over the southern margin of the Amadeus basin. The younger Alice Springs Orogeny (ca. 410-390 Ma) was involved with the Arunta Inlier uplift causing southward-directed thrusting, thereby separating the Amadeus Basin, on its southern margin, from the northern Georgina Basin (e.g. Walter et al., 1995; Sandiford and Hand, 1998). Although the Petermann and Alice Springs Orogenies are separated by a minimum of 150 Ma they share similar characters. For instance, the shear zones that acted within the metamorphic core generally trend E-W, dipping toward the hinterland. Throughout the evolution of the Centralian Superbasin, depocentres shifted producing localised, sedimentary compartments with thick piles of sediments. Hand and Sandiford (1999) proposed that early sedimentary thickening, accompanied by thermal weakening and synsedimentary faulting, represents the required precursor to orogenesis, causing its localisation. This mechanism was also inferred to be responsible for the reactivation of Proterozoic basement faults (Glickson et al., 1995; Glickson et al., 1996; Hand and Sandiford, 1999) during basin inversion (e.g. within the Redbank Thrust Zone, Korsch et al., 1998). In this context, the thick accumulations (3 - 10 km of maximum stratigraphic thickness) of sedimentary fill observed in the southern margin of the Georgian Basin (Dulcie and Toko Synclines, see Fig. 6.1a), may have been part of pre-orogenic thick domains responsible for the subsequent localisation of the Late Devonian (ca. 410-390 Ma) Alice Springs Orogeny.

The orogenic overprint seems then to be fairly restricted to the southern margin of the Georgina Basin. Sedimentation here started earlier than the Petermann Orogeny and continued till post-Alice Springs Orogeny time (Fig. 6.2). Orogenic deformation acted upon the Georgina Basin in a twofold manner, influencing either its sedimentation or subdividing and folding the strata. In the southern margin of the basin the Toko and Dulcie synclines record this tectonic overprint. These structures are northwest – southeast trending folds with their steep limbs in contact with the metamorphic rocks of the Arunta Inlier. Haines et al. (2001) remark that sedimentary deposition, within the synclines, is locally coarser and conglomeratic (e.g. Cravens Peak beds and Dulcie Sandstone) (Fig. 6.2), providing possible indication of a non-marine setting due to orogenic uplift. The workers also suggest that local folding may have originated during sedimentation, but a synorogenic component may have contributed to its formation. There is finally evidence within the synclines of faults that have close connection with the thrusting observed in the Arunta Inlier (Haines et al., 2001).

South   North

Age	Amadeus	Georgina	Wiso	Daily	Supersequences	Ma
Devonian	Brewer Park Mereenie	Dulcie/ Cravens Peak			6 Alice Springs Orogeny	410-355
Silurian						443-410
Ordovician	Carmichael Stokes Stairway Horn Valley Paccota	Ethabuka Mithaka Carlo Nora Coolibah Kelly Creek		Oolloo Jinduckin	Pertnjara & Rodingan Movement 5 Delamerian Orogeny	490-443 Volcanism
Cambrian	Goyder Shannon/ Jay Ck/ Hugh River Giles Creek Todd River upper Arumbers	Tomahawk Arrinthrunga Arthur Ck **Thorntonia/** Gum Ridge Red Heart	Lothari Hill Hooker Creek Montejinnii	Tindall	4	Volcanism 545-490
Ediacaran	lower Arumbera	Central Mt. Stuart/			3	580-545
Ediacaran	Julie Pertatataka Olympic/Pioneer	Elkera Grant Bluff Elyuah Oorabra			Petermann Orogeny Souths Ra Movement 2b	Marinoan Glaciation 620-580
						660-620
Cryogenian	Aralka Areyonga	Mt. Cornish/Yardida			Rinkabeena Movement 2a Areyonga Movement	700-660 Sturtian Glaciation
						750-700
Cryogenian	Bitter Springs Heavitree	Amesbury/ Yackah			1 Sag Basin	Volcanism 780-750

Fig. 6.2 Simplified stratigraphy from south to north through the Amadeus, Georgina, Wiso and Daly Basins (redrawn from Lindsay et al., 2005).

Although the Lawn Hill Region was relatively far from these sites of intense deformation, Sandiford and Hand (1998) remark that the Alice Springs Orogeny acted on an extensive part of the Amadeus basin (see Fig. 6.1a) to the south, causing overprinting of Petermann Orogeny folds that were tightened by coaxial N-S shortening. The effect of contractional deformation during the orogen extended for more than 200 km outward from the metamorphic core (Fig. 6.3a, b). Perhaps a similar

extent of orogenic overprinting occurred above the northern margin the Arunta Inlier and contributed to faulting and folding of Middle Cambrian sediments in the Georgina Basin. Hand and Sandiford (1999) report that north of the Arunta Block the basement was thrust northward over Neoproterozoic and early Palaeozoic cover sequences of the Georgina and Wiso Basins (Fig. 6.3a, b). These authors also suggest that the thrusts developed on pre-existing syn-rift faults, contributed to their reactivation. N-S verging orogens had the ability to reactivate predominantly E-W trending basement faults, a case that could be valid also for the E-W basement structures occurring in the study area.
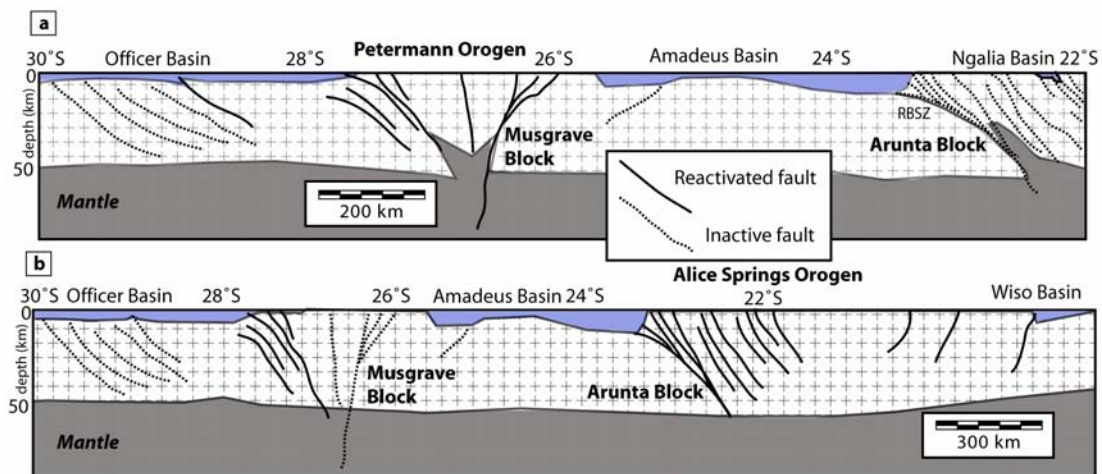
Fig. 6.3 Crustal transect (after Korsch et al., 1998) showing the locus of reactivation during the Petermann and Alice Springs Orogenies. Note the reactivation of basement, south dipping faults during Alice Springs Orogeny proximal to the Wiso Basin. Other structures at similar distance from the core of the orogen may have been reactivated in a similar way within the adjacent Georgina Basin (adapted from Hand and Sandiford, 1999). RBSZ = Redbank Shear Zone.

Scattered examples of possible tectonic related deformation have been reported for the northern part of the Georgina Basin. However, local examples of folding and

faulting may have an origin that is unrelated to the Alice Springs Orogeny and could be for example due to gravity driven deformation – this would be justifying their fairly localised occurrence. For instance, Smith (1972) reports the existence of a structural belt on the southeastern margin of the Georgina Basin in Queensland. Evidence of asymmetric folds is reported also in the Neoproterozoic and Cambrian Outliers found in the Mount Isa and McArthur Basins, such as the one considered in this study (Lawn Hill Outlier) or in the Abner Range of the McArthur Basin, where the late Neoproterozoic to Cambrian Bukalara sandstone appears to be folded with northwest orientation (Jackson et al., 1987; Pietsch et al., 1991; Haines et al., 2001). A preliminary conclusion could be then that the Alice Springs orogenic overprint might have been sufficient in the Lawn Hill Region to cause reactivation of faults and folding of Middle Cambrian sediments although a careful assessment of the style of deformation is required, because anorogenic deformation may produce similar patterns (e.g. van Loon, 2003).

6.2.2 Stratigraphic evolution of the Centralian Superbasin

A brief examination of the sedimentary evolution of the Centralian Superbasin is reviewed here, to place the Georgina Basin into its tectonostratigraphic context. The time interval between 800 and 355 Ma can be formally subdivided into six main supersequences (Fig. 6.2) (Walter et al., 1995; Lindsay et al., 2005). Supersequence 1, (lower Cryogenian) initiated with massive deposition of sandy intervals that are thicker

to the west in the Savory Basin (Bitter Springs, Heavitree Formations - Amadeus Basin) and Yackah beds and Amesbury Formation - Georgina Basin). A sharp variation in the lithofacies sealed the top of Supersequence 1 and is characterised by more marine to lacustrine sequences, predominantly carbonates, evaporates and fine siliciclastics. Supersequence 2 (upper Cryogenian-lower Ediacaran) has a similar succession on its top part, with carbonates and shales, but it is distinct for its basal (Sturtian, ca. 660-650 Ma) glacigene sediments. Supersequence 3 also has glacial sediments at its base (Marinoan, ca. 600-610 Ma), followed by a widespread transgression with deposition of turbiditic sandstones and shales. Carbonates and evaporates cap the sequence. The Phanerozoic sedimentation starts with extensive deposition of sandstones and silts (Supersequence 4 - Lower Cambrian), accompanied by eruption of continental flood basalts that terminated with the final stages of the Petermann Ranges Orogeny (ca. 540 Ma ago). The younger, transitional part of the sequence (lower part of Supersequence 4) is dominated by initial siliciclastic deposition of sandstones and silts characteristic for the presence of "Ediacara fauna" that is however poorly represented within the Centralian Superbasin (Walter et al., 1995). This is then followed by shallower depositional settings with abundant carbonates and evaporites indicative of arid climates (e.g. Thorntonia Limestone in the Georgina Basin, upper part of Supersequence 4). Supersequence 5 (Ordovician) is characterised by an initial marine sedimentation of sandstone and siltstones represented by the Larapinta Group in the Amadeus Basin, which terminates with the Stokes siltstone (Shergold et al., 1991) and is equivalent to the Mithaka Formation and underlying sequences in the Georgina Basin. A permanent change in the style of sedimentation (with a more fluvial

component) occurred then with the incoming of coarse clastic sediments. These form the base of the Carmichael Sandstone in the Amadeus Basin and are correlated to the youngest Ordovician interval in the Georgina Basin, the Ethabuka Sandstone (Shergold et al., 1991; Haines et al., 2001). Supersequence 6 is distinct by the onset of the Alice Springs Orogeny that provides coarser, clastic fills, derived from uplift and erosion, to the surrounding basins. This phase of uplift is contemporaneous with the deposition of the Mereenie Sandstone, derived from aeolian and fluvial environments in the Amadeus Basin; whereas in the Georgina Basin post-Ordovician, non-marine sequences were deposited in the Toko and Dulcie synclines. These are mainly pebbly to boulder conglomerates (Cravens Peak beds) that locally are found also in the Dulcie Sandstones. The effect of the Alice Springs Orogeny is more intense in the late Devonian with coarsening upward deposition of the Pertnjara Group (Haines et al., 2001). The group is preserved locally near the northern margin of the Amadeus Basin and comprises fluvial and aeolian sandstones.

Climatic conditions as seen can contribute significantly to massive failure events. For instance, abundant rainfall may cause instability of land masses or rock falls may occur in response to tidal variation along a platform margin. It is therefore important to establish the climatic context in which a "catastrophic event" has taken place to ascertain its origin. The reviewed stratigraphic evolution provides an indirect way to assess the climatic change, and suggests that an initial phase of relatively cold climates is progressively superseded by wormer sub-tropical conditions that culminated with the Cambrian faunal explosion. Beside the biological implications of seawater temperature

variations these considerations therefore exclude a possible relationship of the Lawn Hill Megabreccia to glacial processes (e.g. Arnaud and Eyles, 2002).

6.3 Georgina Basin

A more focused description of the Georgina Basin is now presented, with further detail of the stratigraphic record relative to the Undilla sub-Basin, to better constrain the location of the Lawn Hill Outlier and its stratigraphic context. The time of deposition of carbonates forming the outlier is also reviewed considering its fossil content, to provide an understanding of the biostratigraphic framework, which is important for later considerations on the origin and timing of deformational features.

6.3.1 Introduction

The Georgina Basin is characterised by variable thicknesses that rarely exceeds 3 km. Mostly flat laying strata extends for approximately 325,000 km^2 across northern Queensland and the eastern part of the Northern Territory (Shergold and Druce, 1980) (Fig. 6.1a, b). Sedimentary rocks of the Georgina Basin cover a predominantly Palaeo- to Mesoproterozoic basement. The sediment fill varies from west to east with a gradual shift from predominantly siliciclastic to more carbonate-rich components (Shergold et al., 1976). On its northeastern margin the basin unconformably overlies the Mesoproterozoic rocks of the Lawn Hill Platform of the Mount Isa Inlier; whereas in its southern and western part it terminates against Palaeo- to Mesoproterozoic rocks of the

Arunta and Tennant Creek Inliers (Compston, 1995; Haines et al., 2001). The Lawn

Hill Outlier is situated along the northeastern margin of the Georgina Basin (Undilla

sub-Basin, see Fig. 6.1b), and is characterised by Middle Cambrian sediments,

predominantly carbonate and dolomites, locally evaporitic and rich in phosphorites –

the latter being an important mineral resource of northern Queensland (De Keyser and

Cook, 1972). Several parts of the basin were also unsuccessfully explored for petroleum

reservoirs, because the fossil shales and siltstones contain significant traces of

hydrocarbons (see Glikson et al., 1985). The sequence of depositional facies supports

interpretations for the palaeogeographic setting that varied from marine slope, ramp

dominated facies to sabhka-type, supratidal depositional settings. The palaeogeographic

scenario was likely a Cambrian epeiric sea surrounded by islands formed by uplifted

metamorphosed blocks and terminated against the Gondwana margin (Shergold et al.,

1976).

6.3.2 Main formations Undilla sub-Basin

The Undilla Basin represents the easternmost part of the Georgina Basin and is

stratigraphically correlated with the Lawn Hill Outlier. The sub-basin rarely exceeds

400 m thickness. It comprises sedimentary rocks of Lower to Middle Cambrian age.

Several classifications based on lithostratigraphic and biostratigraphic subdivisions

have been proposed (e.g. Opik, 1957; De Keyser, 1973; Shergold and Druce, 1980). A

simplified classification using the six lithosomes of De Keyser (1973), was particularly

useful during fieldwork and mapping of pit faces within the Century Mine area, which

is located on the southwestern margin of the Lawn Hill Outlier. More detailed biostratigraphic subdivisions of Opik (1957; 1958; 1970; 1975; 1982) cannot be used so confidently in outcrop. De Keyser (1973) distinguishes the rocks of the Georgina Basin as follow: (1) basal sandstone-conglomerate lithosome (deposited during an initial transgressive littoral-marine phase); (2) chert-siltstone-limestone-phosphate lithosome (deposited in extremely shallow water, on a shelf characterised by shoals and a coastline broken by embayment, estuaries, and lagoons); (3) silt-shale-chert lithosome (deposited under conditions of quiet sedimentation in slightly deeper water); (4) limestone lithosome (deposited some distance off-shore in open marine conditions); (5) dolomite lithosome (deposited in intertital mud flats, saline lagoons, and lakes); and (6) sandstone-siltstone lithosome (deposited during a regressive clastic phase).

Mapped lithosomes in the study area include the formal names of Mount Hendry Formation, Thorntonia Limestone, Beetle Creek, and Border Waterhole Formations. The Mount Hendry Formation consists of conglomerates and ferruginous, sandstone interbeds of littoral-marine and possible fluvial origin of lower Cambrian age (Smith, 1972; De Keyser, 1973). This interval has variable thickness with a maximum of approximately 25 m. The top part of this formation is dolomitic and locally grades into the Thorntonia Limestone (De Keyser, 1973). The early Middle Cambrian 509-506 Ma Thorntonia Limestone, Beetle Creek and Border Waterhole Formations are characterised by abundant transgressive deposition of cherty and dolomitic limestone. Outcrop is usually lumpy and nodular representing the residual cherty part of the cherty-carbonates. Bioclastic layers (silicified microcoquinites) are common. Carbonate strata are interleaved with clastic beds that vary from siltstone to shales. Shales and

siltstones can be distinguished for the persistent lamination and locally for the elevated fossil content. Limestones are predominantly white, cream or grey depending on their alteration and phosphate content. Within the upper part of this lithosome local dolomite-rich laminae can be found intercalated with carbonate biopelsparites (up to 2 mm) (Szulc, 1992).

The fossil content of the Cambrian limestones is diverse. De Keyser and Cook (1972) report the following fauna: trilobites (e.g. Xystridura, Redlichia, Dolichometopid, see Opik, 1958, 1970, 1975, 1982) and also Hyolithus, echinoderms, phosphatic brachiopods, sponge spicules and algal Girvenella structures. Szulc (1992) reports the occurrence of fragments of trilobites in the Lawn Hill Outlier resembling, probably, cranidia of ptychariid trilobites of the Middle Cambrian genus Asthenopsis, and thus the worker proposes a close correlation of the Lawn Hill Outlier with the northeastern margin of the Georgina Basin on the basis of lithostratigraphic correlations and documented fossil record. Biological records also constrain the age of the Thorntonia Limestone and other carbonate formations to within the early Middle Cambrian (Ordian/Templetonian ca. 506-509 Ma, see Lindsay et al., 2005). The fossils suggest relatively shallow water depositional settings (De Keyser, 1973). However, considerable transport may have influenced the present spatial location of certain lithofacies and their relative biostratigraphic record (see below).

6.3.3 Summary

The established tectonostratigraphic framework and timing of the Thorntonia Limestone sedimentation places this event between the Petermann and Alice Springs Orogeny. Approximately 70 m.y. elapsed from the onset of the Petermann Orogeny and the deposition of the limestones. Moreover, the distance of the northeastern Georgina Basin from the core of the Petermann Orogeny exceeds the 600 km. Therefore, the Petermann event probably had a negligible effect during Ordian/Templetonian sedimentation, in the Georgina Basin. In contrast, some of the deformation observed in the basin, as seen, seems to have possible relationship with the Alice Springs Orogeny. This orogeny took place during Devonian time and therefore it may have only acted upon Ordian/Templetonian rocks after their lithification. In other words, the Alice Springs Orogeny did not influence the sedimentary deposition of the Thorntonia Limestone and other coeval formations. It becomes relevant then to characterise the style of deformation in the Lawn Hill Outlier, to ascertain if the deformation occurred during synsedimentary timing (unrelated to Alice Springs Orogeny) or later syntectonic timing.

6.3.4 Folding and brecciation in the Lawn Hill Outlier

Complex overturning of strata and brecciation have been documented by previous workers in the Lawn Hill Outlier and monoclinal folding is reported for several parts of the Georgina Basin (De Keyser and Cook, 1972; Henderson and

Southgate, 1980; Andrews, 1991; Southgate and Shergold, 1991; Szulc, 1992). The following part deals with the characterisation of deformational features observed in the Lawn Hill Outlier. The main objective is to establish the timing of recumbent folding and brecciation. To explain these structural features three different models have been proposed:

- Syn-depositional soft sediment slumping (Andrews, 1991).
- Large scale dissolution of salt forming a collapse breccia (Hutton, 1992).
- Sediment fill and solution breccia inside a crater formed by asteroid impact (Stewart, 1986; Stewart and Mitchell, 1987).

Sediment slumping is only a single aspect of the deformation observed in the region and it may be caused either by failure induced by gravitational instability or in response to instability due to an asteroid impact (point three above). Breccias and folds may also form during orogenic related deformation.

Following Elliott and Williams (1988) we recognise that these styles of deformation may be caused by: (1) local shear; (2) local density gradients; (3) gravity acting on a slope (4) glacio-tectonic processes and (5) the convergence of lithospheric plates. (6) The impact of an asteroid is also considered (extraterrestrial, external to earth processes). These mechanical forces may operate either in a synsedimentary stage or after complete lithification of the sequence, post-burial and diagenesis. These are important distinctions to make because they allow the definition of the timing of deformation. However, earlier gravitational collapse could be overprinted by faulting

and fracturing related to later tectonic deformation. The examination of the style of deformation must therefore consider several time periods as well as multiple scales in order to determine the nature and scale of overprinting.

6.4 Deformational and fluidisation related features

Observed deformational features are here classified using a twofold subdivision that considers (a) ductile, (plastic) deformational features, and (b) more brittle style deformation. The former includes: (1) recumbent and nappe-style folds; (2) injection dykes (mud lime dykes), and (3) monoclinal, gentle, dome-shaped folds. Brittle fractures include: (1) megabreccia with clasts of limestone and basement strata, and (2) post-sedimentary faults and fractures, often accompanied by veins. Notice that this subdivision does not refer to a specific timeframe of the basin history.

Maltman (1984) suggests that certain features, commonly interpreted as post-sedimentary, may form earlier. This is because consolidation does not necessarily imply a completed lithification of the rock. Prior to and during early diagenesis the pore pressure variation largely controls the apparent cohesion of a certain rock-type, because the apparent cohesion is function of the % water content. This causes temporal and spatial fluctuations of the degree of material consolidation. Therefore, during a synsedimentary or diagenetic phase certain portions of the rock-mass may behave as a brittle or brittle-ductile material and undergo consequent intra-crystalline deformation (deformation bands, lamellae, twins and pressure solution), whereas others may respond plastically with intergranular movement or elastically by pore pressure movement

(poro-elasticity) (Oliver et al., 2006). Nonetheless, in the following section we attempt to make a distinction between soft-sediment and hard-rock deformation to constrain its age. This approach can be improved using multiple datasets rather than focussing on a single distinctive element. The discussion aims to integrate the detailed observations and structural analyses and determine the timing these features.

6.4.1 Folding

6.4.1.1 General description of folds:

Pit exposures display a range of fold patterns. Overturned folds range in scale from a few centimetres to hundreds of metres (Figs. 6.4a, b and 6.5a-d). Several folds are tight, and some are isoclinal, and are either cylindrical or non-cylindrical. Notably there is a rapid spatial variation from relatively chaotic breccias through to more complexly folded areas (Fig. 6.4b). On the eastern and northern walls sub-horizontal to low-angle dipping erosional/depositional scars are present (Figs. 6.4a, b and 6.6a). Locally injected marl dykes are observed proximal to and along the scar discontinuities (Fig. 6.6b, c).

6.4.1.2   Folding patterns

Folding patterns have been often discussed at length in the literature trying to address their timing and origin (e.g. Williams et al., 1969; Helwig, 1970; Blatt et al., 1980; Elliott and Williams, 1988; Smith, 2000). However, it has been demonstrated that geometries typical of unlithified rocks develop also in lithified sediments (Elliott and Williams, 1988).
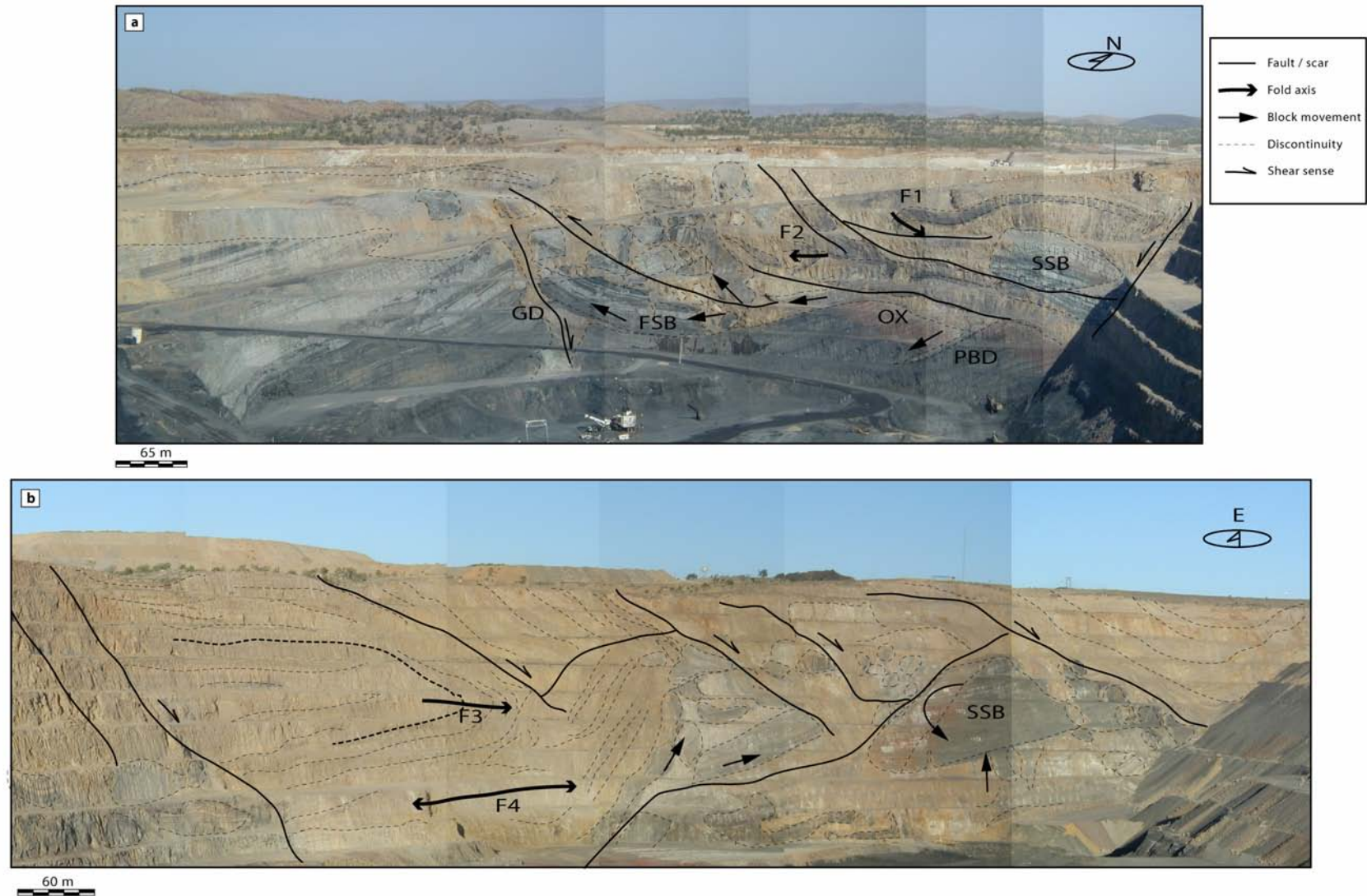
Fig. 6.4 Photographic view and relative structural interpretation of the northern and eastern walls of the Century Mine. (a) Northern side of the Century Mine exposing a sectional view of the Lawn Hill Megabreccia deposited on top of Mesoproterozoic basement composed of black shales, siltstones and chloritic sandstones. The complexity of mechanical interaction with the basement is outlined by several Proterozoic blocks of sandstones/siltstones entrained in the carbonate, breccia matrix (e.g. SSB). A large flat-shaped block (FSB) has been displaced for more than 50 metres in a westerly direction and is bound on its western side by the largest carbonate intrusion in basement (GD), which formed synchronously with apparent dip-slip movement of a steep dipping basement fault. Another indication of apparent extensional deformation is derived from normal displacement of the basement visible on the eastern part of (a) where the oxidised basement (OX) accommodates the deformation with bedding parallel slip accompanied by injection of carbonate slurry (PBD) along the fault boundary. Folding is represented at this scale by recumbent structures (e.g. F1 – 20/120, F2 – 5/304); note the unfolded basement below, which suggests a localisation of ductile deformation in the cover. The basement being more competent is only fractured by post-Middle Cambrian faults. (b) The eastern wall of Century mine displays the biggest recumbent fold within the mine, approximately 200m vertically (F3 – 10/208). The fold is truncated on its northern and southern margin by a set of faults and breccias with mega-clasts composed of bedded limestone. Another recumbent fold lies underneath F3 (F4 – 10/115), but displays orthogonal orientation. Variation of fold axes may have been due to local tilting during accommodation of slumps. Often folds sharply abut against floating breccia blocks.

Therefore, features such as distorted and overturned strata, thickening and thinning, striated folds or fragments, rolled up fragments, detached fold beds, curvilinear fold hinges, folded boudins and chaotic structures (not cut by open fractures or vein filling), can be used only to corroborate the hypothesis of an early (soft-sediment) deformation, if other diagnostic features are well documented. The first examples recognised in the Century area that could be interpreted as indicating soft sediment folding are intrastratal, piled up, recumbent, or nappe-like folds. According to Elliot and Williams (1988) these can be considered a diagnostic criteria only if they are confined within certain stratigraphic intervals – they have to be intrastratal (see also van Loon, 2003). This feature is documented in the North wall of the Century pit (stages 4-5, see Figs. 6.5d, 6.6a), which shows an example of intrastratal folding and brecciation overlain by flat, undeformed layers. The feature is considered diagnostic by Williams et

al. (1969) because undeformed layers on top of a complexly folded intrastratal unit would be explained easily if the top part of the sequence was sedimented after the deformational event that caused slumping and overturning.
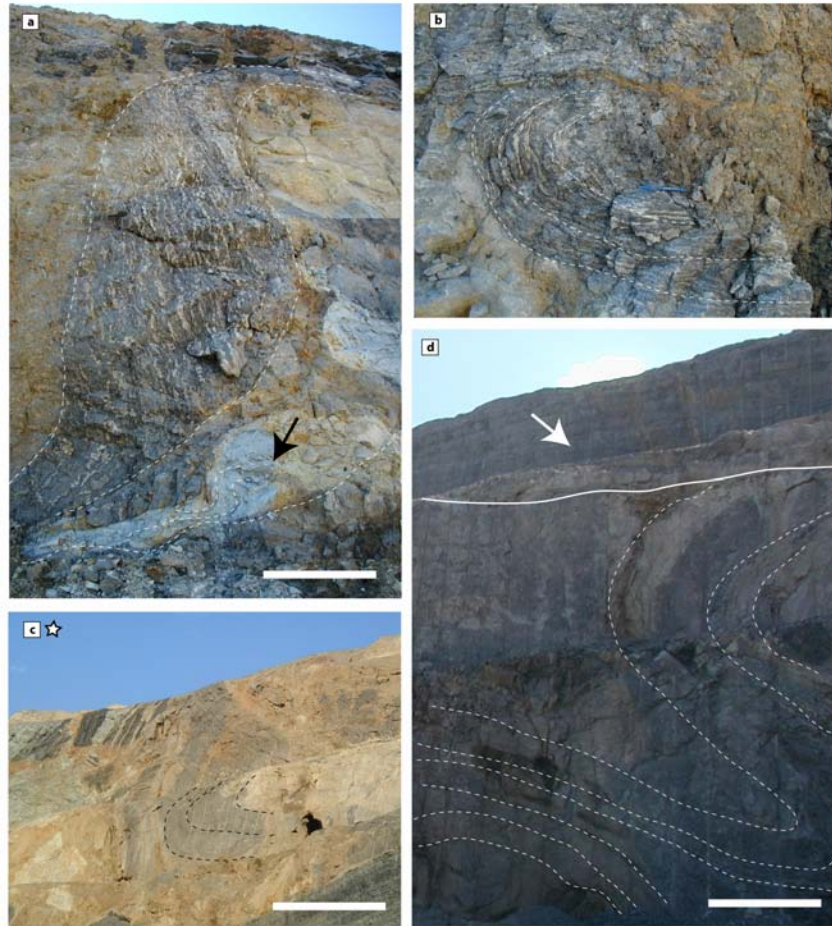
Fig. 6.5 Examples of folding patterns observed in the Thorntonia Limestone. (a) Sigmoidal folding occurring along sub-horizontal shear planes that induced reorientation of mottled, cherty limestone with characteristic parallel bedding siliceous concretions (scale bar 1.5 m). A Marl dyke (black arrow) that resulted was deformed by the same shearing event and also cross-cut by a later intrusion of CBX – the ductile response of marly layers and cherty limestones could have been contemporaneous. Nonetheless, the different phases of overprint may be derived by progressive phases of deformation. It is however common to see a paragenesis suggesting that folding is earlier than the brecciation. (b) and (c) are other examples more typical at various scales of "broken" recumbent folds with sub-horizontal axial planes floating in a carbonate breccia matrix (scale bar in (c) 5 m). Folds are also truncated by sub-horizontal depositional scars (d). In (d) also note the complexity of some folds that can be non cylindrical and be refolded during progressive strain (scale bar 2 m).

A second diagnostic feature of the Century cover is the occurrence of depositional or erosional scars that truncate slumps (e.g. Smith, 2000). The synsedimentary truncation appears to post-date the folding event (Fig. 6.6a) suggesting a syn-depositional age for the folds.
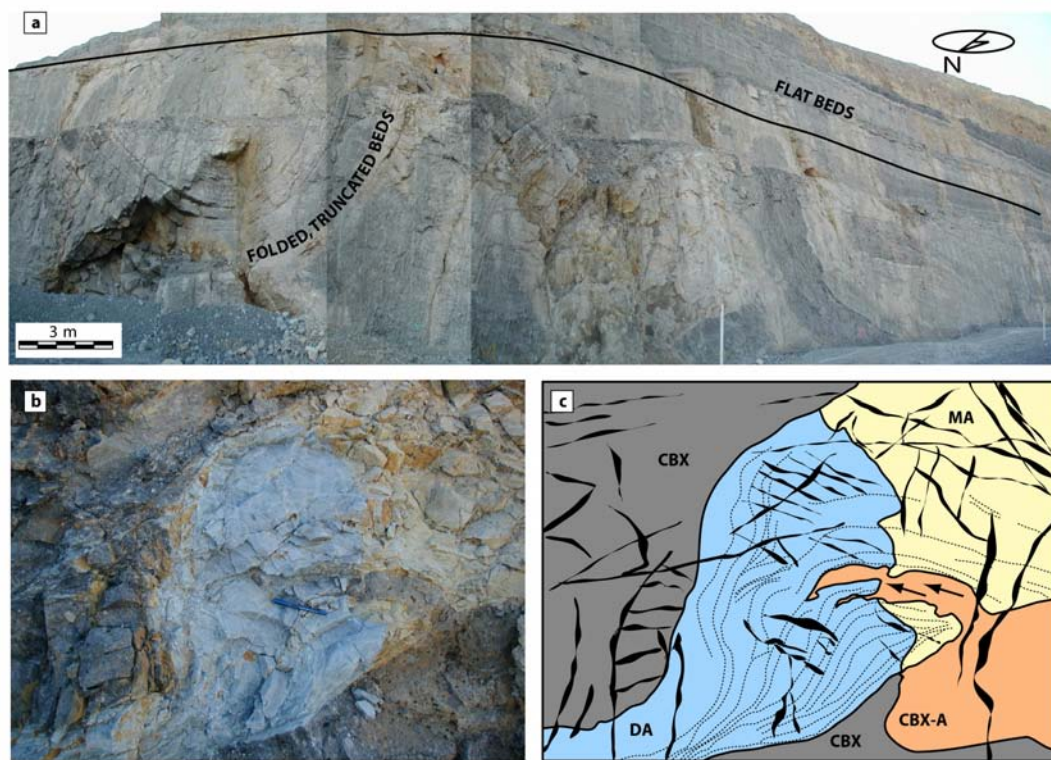
Fig. 6.6 Cross section view of a depositional scar (black line) truncating highly deformed layers of dolomitic grainstone superposed by flat laying undeformed strata. Folds of variable amplitude and interlimb angle abut laterally against broken beds. Often depositional scars are filled with discontinuous pods of marl (b, c) that are locally fractured and folded as shown in the previous figure and in enlarged view here (cf. Fig. 5a with 6b, c). Notice also that a later phase of alteration overprints marl and carbonate breccia injections. Fracturing and jointing postdating hydroplastic deformation represents the latest style of deformation.

6.4.1.3 Slump development

van Loon (2003) remarks that it is possible to reconstruct the original position of a palaeoslope by considering the orientation of overturned strata in sedimentary slumps; however, tectonic overprinting causes anomalous geometrical patterns (Potter and Pettijohn, 1963; Elliott and Williams, 1988). Slumps form in response to palaeoslope instability induced either by gravitational or coseismic activity. The strain distribution is variable along a slump front and commonly produces a curved fold axis. Variation of structural morphology and orientation of folds can be also due to sedimentary influences such as switching of palaeocurrent directions on the palaeoslope, and also flow induced rotation of fold hinges (Allen, 1982; Smith, 2000). It has been demonstrated that in some circumstances slump folds might have a consistent orientation (Kuenen, 1967), but in several other cases (including the study presented here, see Fig. 6.7a-e) they may vary. Following Smith (2000), slump sheets or lobes can be considered to include a central zone C, and a flank zone F (see, Fig. 6.7a). The fold axis is commonly orthogonal to the direction of flow, although along the flanks (F), it may display different orientations compared to the centre (C). This may result from rotational dragging or divergent flow of the slump (Smith, 2000).
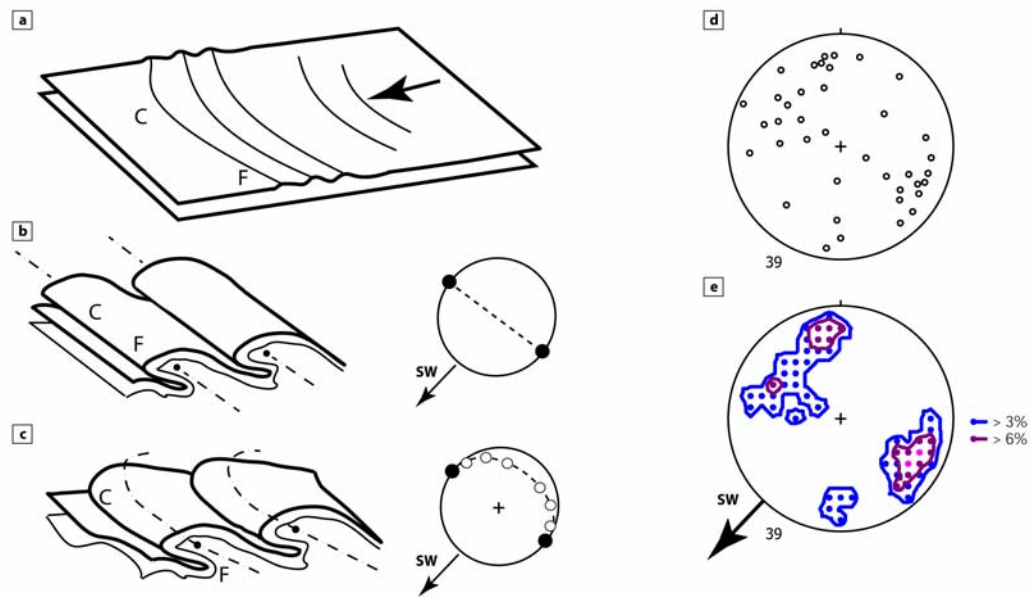
Fig. 6.7 Conceptual models of slump fold development induced by sliding along bedding planes (a, b, c). Comparison of (b) with (c) suggests that one of the causes of misorientation of fold axes is intrinsic to the mechanism of fold development that involves rotational dragging of the flanks (F) in respect to the central front of slump propagation (C). The data collected in the mine area and projected here in (d) as poles of planes in a lower hemisphere projection and in (e) as percent distributions could be interpreted as resembling a girdle distribution considered in (c). However, several other components have conditioned the final orientation of measured structures.

The stereographic projection in Fig. 6.7d displays the orientation of thirty nine fold axes collected along the eastern, northern, and western walls (stages 3, 4, 5) of the Century Mine. Measured fold axes could be interpreted as randomly oriented and this might be partly caused by tectonic titling of strata during faulting and rearrangement of large blocks entrained in the fluidised breccia matrix (e.g. Fig. 6.4a). However, the plot of the density of distribution of fold axes shown in Fig. 6.7e, suggests, alternatively, that recumbent folds might be slumps linked to an extensional stress-field with $\sigma 3$

approximately northeast-southwest striking. Slumps may have been developing along a

basin slope dipping southwest, an orientation compatible with the location of the closest

topographic high in the area (Gum Hole Plain) (see Fig. 6.1c).

6.4.2 Lawn Hill Megabreccia

The most prominent structural character of the Thorntonia Limestones, beside

the large recumbent folds, is the widespread occurrence of breccias. The extensive

brecciation observed in the Century open cut represents an assemblage of various

lithotypes described in Szulc (1992) (Fig. 6.8a, b). Here the different types of breccia

composing the Lawn Hill Megabreccia (this term is used to group all types of breccia

observed in the study area) are described. Their temporal relationships and spatial

distribution is also discussed.

Analysis of spatial associations between faulting and intrusions (CBX) is

another important feature of the Lawn Hill Megabreccia. This character can be used to

evaluate the importance of faulting in the process of redistribution of cover material

during basin evolution. It may be difficult to quantify the spatial distribution of

carbonate dykes where they cut similar lithologies (e.g. dolomite dykes in dolomitic

limestone). However, in the Century area the carbonate dykes/sills penetrate the

underlying, siliciclastic basement. This makes the assessment of their distribution and

orientation relatively easy. Dyke geometry is used to evaluate the possible palaeostress

direction when the dykes were intruded. This is then compared with other structural

indications of the likely palaeostress directions.
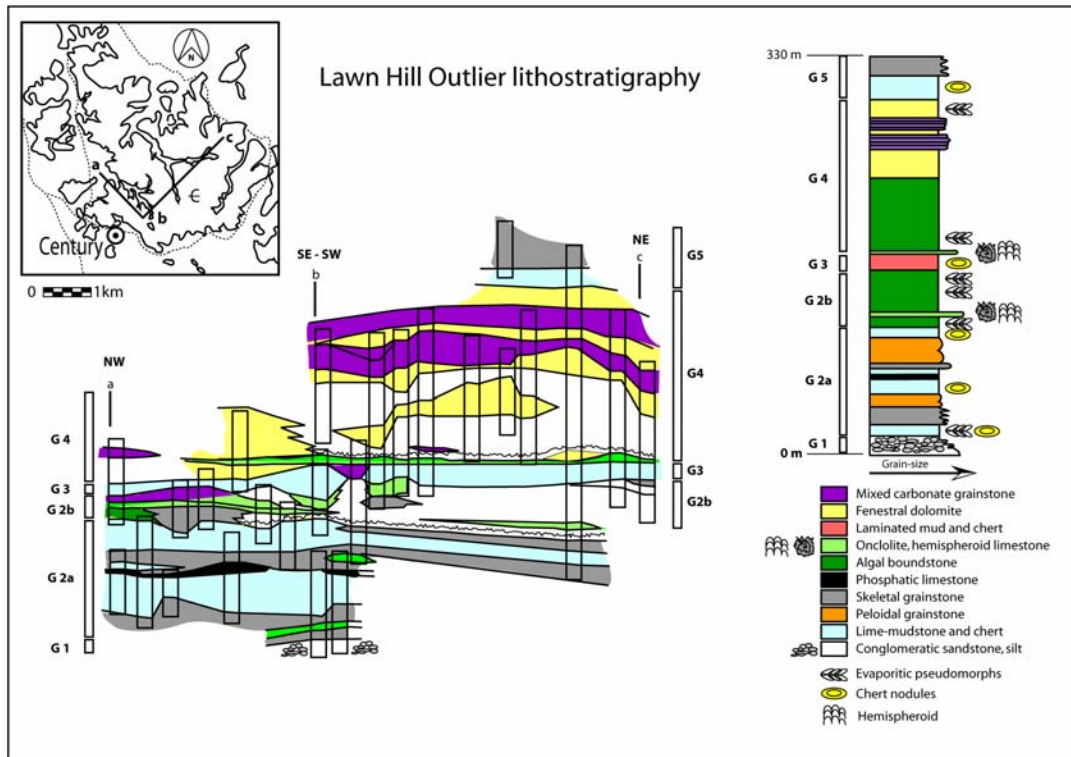
Fig. 6.8 Lithostratigraphic classification, redrawn from Szulc (1992). The stratigraphic section through the annulus offers a perspective of the spatial variation of lithofacies. Notice the shift from deep ramp facies to more inter/supratidal settings inward. The summary of lithostratigraphic variation outlines several marker beds containing allochems such as onkolites and shell-beds (coquina like, e.g. see Loi and Dabard, 2002), often represented by cherty concretions. Also hemispheroids are reported by Szulc (1992).

6.4.2.1   Varieties of breccia

The Lawn Hill Megabreccia displays a various petrographic nature. Several processes contributed to its formation, but also transformed the breccia during basin evolution (e.g. alteration, later deformation etc.). Here we propose a subdivision of the breccia depending upon their textural variety. The term Lawn Hill Megabreccia encompasses all the distinguished end-members, because the megabreccia is considered the final assemblage of multiple phases of breccia developed at different times and from different mechanisms. The distinctions made are then used to infer a possible origin for the different breccias. Notice that diverse breccias may have been coeval, but forming from different genetic processes (e.g. a debris-flow breccia can be formed in a slope setting; whereas contemporaneous sub aerial exposure of shelfal limestones may cause karst-breccia development). Alternatively, multiple types of breccia could be forming also as function of their different time of formation during basin evolution (e.g. debris-flows can be deposited on the seafloor then reworked and redeposited by marine currents, or injected in fractures and faults at later time during diagenesis). Analysis of cross-cutting relationships provides a way to reconstruct a temporal evolution for the different breccias allowing a better understanding of these processes.

The Lawn Hill Megabreccia is more than 200 m thick on the northern side of the Century Mine (stage 4, Fig. 6.4a) and consists of a carbonatic to dolomitic groundmass with huge floating clasts up to hundreds of metres across (Fig. 6.4a, b). The nature of the clasts ranges from monomictic to polymictic. The breccia is composed of

carbonates, marls and cherts with a variable degree of sorting, and also variable rounding of the clasts. The matrix/cement composition varies in a similar manner according to the clast composition, and can be abundant, forming matrix or cement-supported aggregates, to scarce or lacking in clast-supported aggregates.

The geometrical relationship between breccias and host is variable providing additional information on their likely origin. Breccias are distributed both in the Middle Cambrian limestone, and also as sills and dykes in the Mesoproterozoic siliciclastic basement.

In the cover the spatial association of breccia to host is diverse, with the breccia occurring either as dykes (Fig. 6.9a) or sills, but also occurring in limestone cavities, distinct by their irregular outline and by evidence of collapse related fragments detached from their roof (Fig. 6.10a-c). The carbonate breccias also occur as stratiform bodies that extend for several 100's metres. Locally these beds preserve grading and sorted clasts. In the basement, breccia dykes and sills are exclusive - there is no evidence of collapse/solution related cavities or bedded tabular breccias. Sub-vertical dykes are (1 to 30 m) commonly thicker than shallow dipping sills (1 to 5 m), and often sills terminate a few metres away from the connected dykes suggesting, mostly, vertical transport of breccia material (Fig. 6.9b). The biggest example of dyke penetrating the basement is located on the northwestern corner of the pit (stage 4, Century Mine, see Fig 6.4a). The sub-vertical dyke is approximately 30 m wide, its termination into the basement is complex with sills departing laterally and causing jacking of bedding planes in the basal, Mesoproterozoic shales.
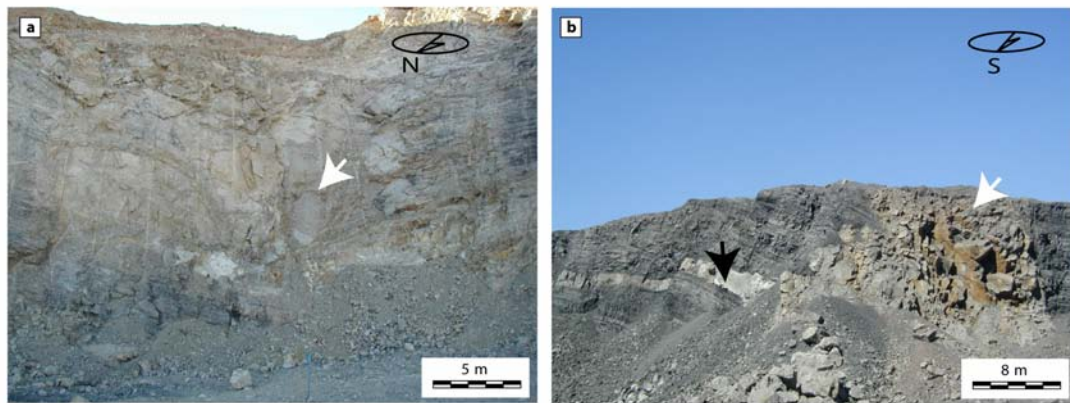
Fig. 6.9 Examples of steep dipping intrusions in Middle Cambrian cover (a) and Mesoproterozoic basement (b) (arrows for dyke/sill location). In (b) the thickness distinction made in the text is outlined. Dykes are generally thicker than sills (black arrow) when penetrating the basement (see also Fig. 4a - GD).

Based on the considerations made, and on textural features described below, we propose a subdivision following the Universal Rudrock Code (Laznicka, 1989; Jebrak, 1997). Four types of breccia were distinct (Fig. 6.11a-f):

1. Flow Breccia (CBX).

2. Flow Breccia (MB).

3. Solution Breccia (SB).

4. Collapse Breccia (CB).

Note however that the some breccias grade into one another (see below).
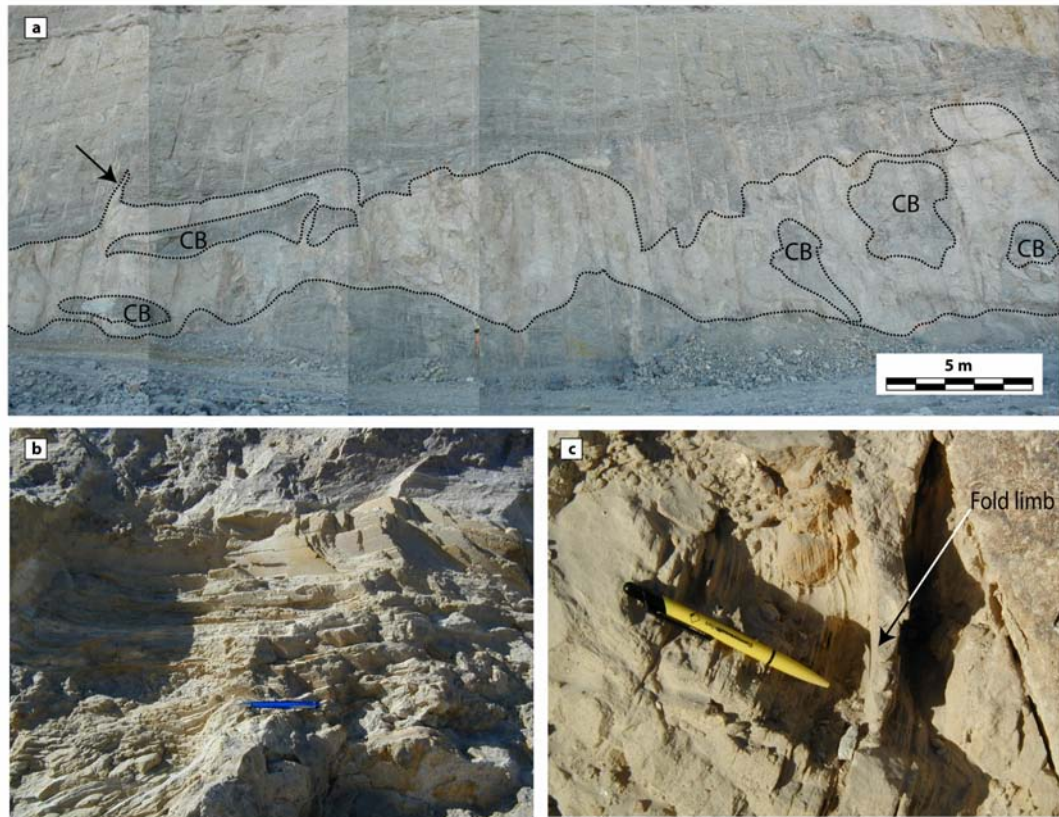
Fig. 6.10 Examples of interpreted solution/collapse cavities in cherty limestone exposed on the western side of the Century Mine (Stage 5). (a) Solution cavity filled by CBX breccia. The breccia has also infiltrated the roof of the cavity that formed in relatively undeformed limestone (see arrow). Note collapsed bedded intervals now floating in the carbonate breccia matrix (CB). Some cavities host bedded sediments such as calcarenites (b and c), beds are flat lying within cavities but may also develop slump folds (c) (pen for scale).
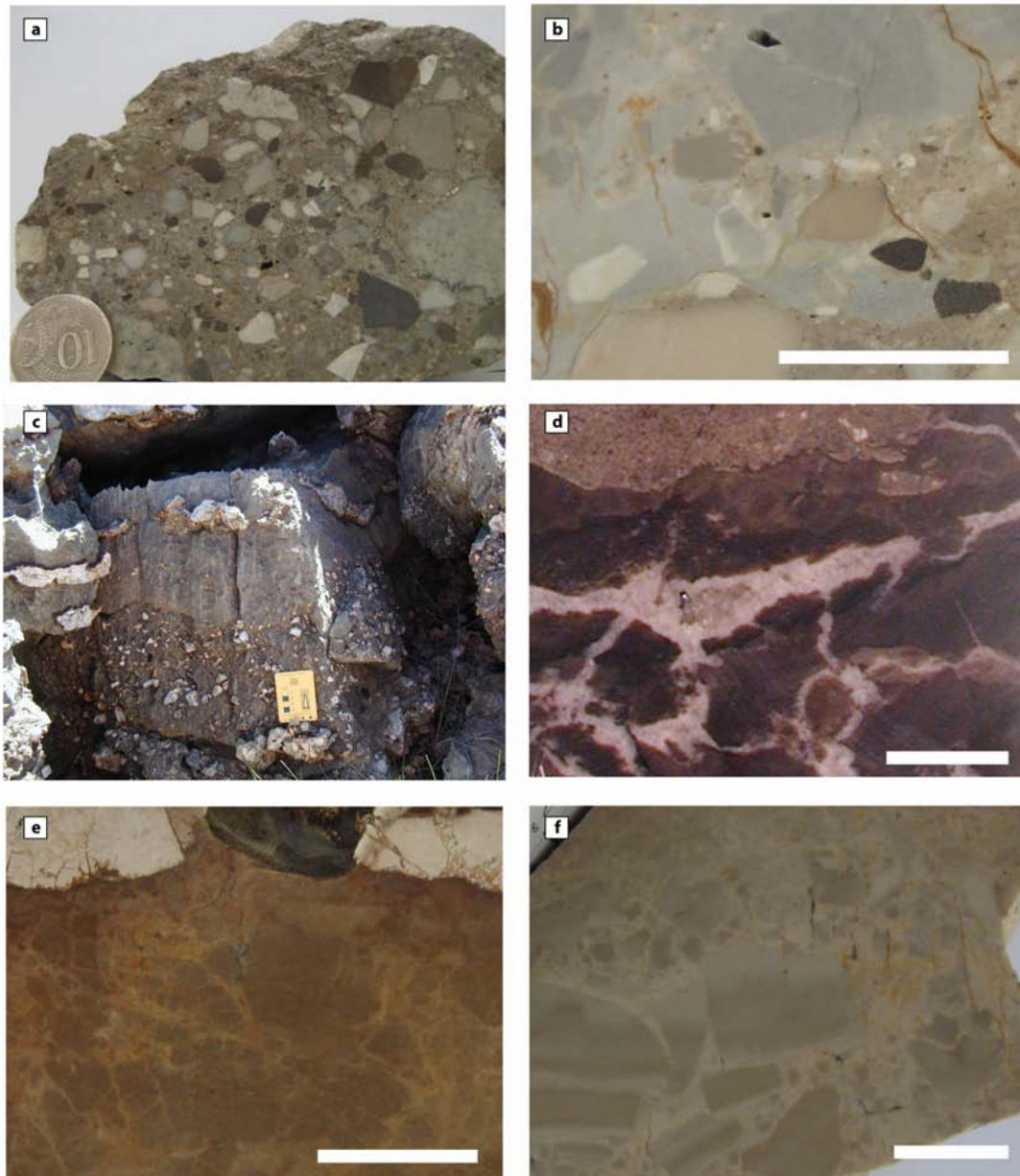
Fig. 6.11 Breccia typologies observed along mine exposures, and also in drill core and outcrop, in the more internal part of the annulus. (a) Polymictic, CBX breccia, the most common variety in the Century mine forming sills and dykes that penetrate cover and basement. (b) Mixing between flow breccia (MB) and a CBX sill (scale bar 0.5 cm). The two end-members mix together gradually and produce an admixture of broken clasts and groundmass representing a composite breccia. This evidence is suggestive of a similar state of consolidation of marl and CBX indicating penecontemporaneous deformation. (c) Stratiform, solution breccia, composed predominantly of chert angular fragments likely derived from siliceous concretions. Grainstone/packstone (d, e) and also oolitic, dolomitic sandstone display corroded

clasts aggregated by calcitic or dolomitic cement(scale bars (d) 1.5 cm and (f) 0.5 cm). (f) Collapse breccia in crystalline dolomitic limestone (scale bar 1 cm). Normal grading and rounding may indicate local transport although the monomictic nature of the clasts is more indicative of local sourcing from adjacent proximal limestones. Local reworking may be explained also with tidal currents that would allow rounding although with limited transport of the clasts that tend to be trapped on the bottom of the cavity (Appendix D for specimens spatial location).

6.4.2.2   Flow breccia CBX

The Flow Breccia (CBX) is the most common variety of breccia across the whole outlier and the only one occurring both in cover and basement (Fig. 6.9a, b). The breccia occurs as dykes and sills and also as infill in irregular cavities (Fig. 6.10a-c). CBX dykes and sills have variable width from a few centimetres to 10's of metres. Sills do not cross-cut dykes and they both have same infill material. CBX dykes locally cross-cut Flow breccia (MB) dykes (another variety of breccia). However, in some cases the two breccias grade into one another and mix together. The clasts include both folded and unfolded fragments derived from the Middle-Cambrian cover, but also from the Proterozoic basement - one of the largest blocks was originally part of the Century orebody (Eastern Block, Fig. 6.4b). Frequently, at larger scale (100's of m) the breccia becomes chaotic with domains filled by groundmass separated by other domains characterised by clast-supported megablocks of carbonate strata. The size of the clasts (excluding the megablocks) is variable from millimetres to metres (typically between 0.5 and 60 cm) (Fig. 6.11a). When the breccia occurs in dykes and sills the clast size is function of the conduit size that causes sorting; therefore, the breccia could be

considered as a coarse, sub-rounded to angular fragmentite that becomes a microfragmentite when infilling narrow fractures and faults. The CBX is polymictic including three varieties of clasts recognised in hand specimen and thin section: (1) lithic clasts of carbonate; (2) cherts and (3) fragments of Mesoproterozoic basement, siltstone/shale. The groundmass composition corresponds to the fragment composition with matrix more abundant than cement. The sandstone/siltstone carbonate matrix supports the clasts of the CBX breccia and is petrographically analoguous to dolomitic limestones occurring predominantly in the upper part of the lithostratigraphic subdivision group G4 of Szulc (1992). The cement is composed of a mixture of calcite, dolomite, quartz, and iron oxides. This type of breccia can be considered transported because of the occurrence of rounded clasts and also because of its polymictic nature. Its occurrence in the basement represents an additional indication of movement exceeding 10's of metres. The close analogy between the CBX matrix and the sandy dolomites of the Thorntonia Limestone, and Border Waterhole Formation may suggest a derivation from these lithofacies. Alternatively, unconsolidated sandstones may have been deposited as debris-flows and turbidites in the present sites before lithification. Local evidence of clast segregation and normal grading may favour this interpretation (see, Fig. 6.12a, b). The breccia appears to have been emplaced in a temporally confined event before matrix consolidation, because apparently there is no evidence of recemented fragments of matrix in CBX, a feature that should be evident if brecciation and emplacement of CBX occurred during a protracted timeframe of basin evolution, involving reactivation and multiple injection events.
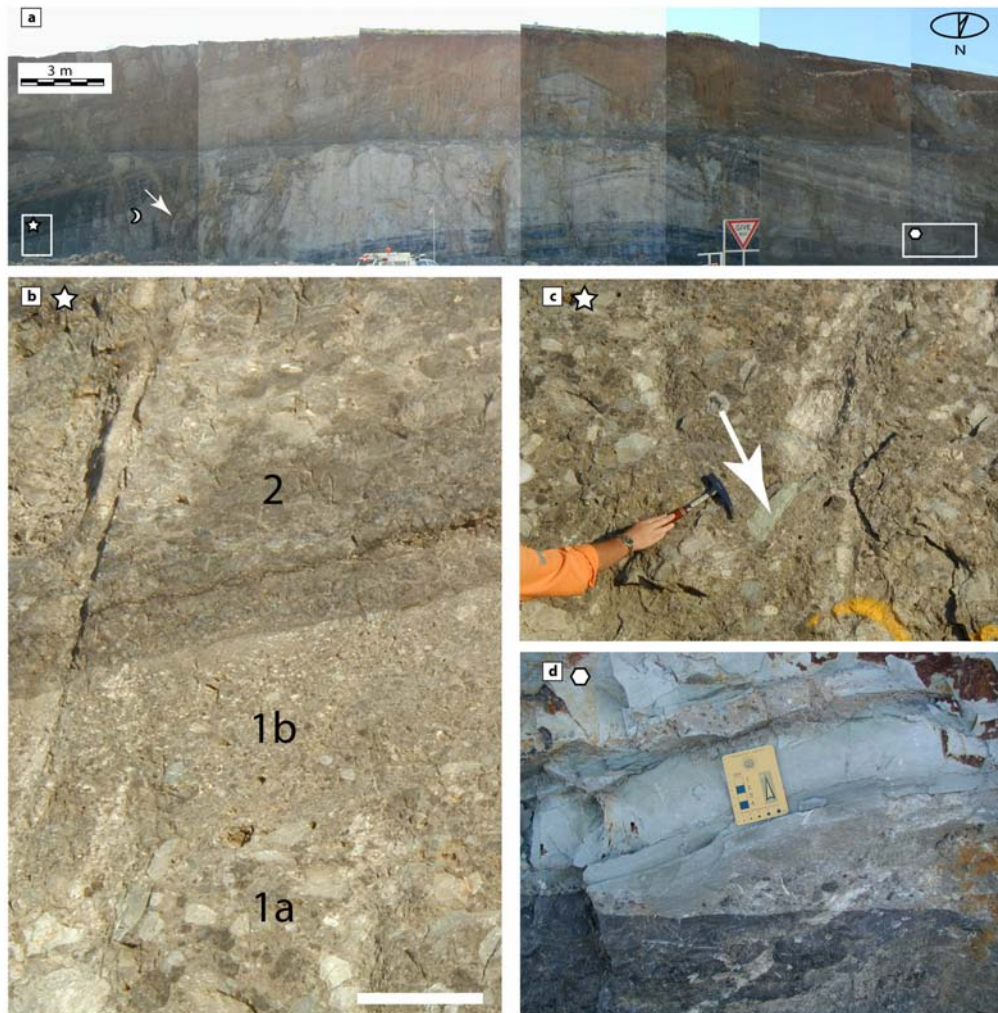
Fig. 6.12 Slumping initiation in relatively undeformed beds of the Thorntonia limestones. (a) Landscape view of a tepee like structure, carbonaceous siltstones and marlstones, distinguished for their dark (carbonaceous colour) and fine grained lamination bound the top and basal part of an intrastratal mass-flow to debris-flow body that has suffered internal reorganisation during slumping. The CBX breccia locally preserves graded beds that formed probably along the slope during debris-flow deposition. (b) Illustrates an example of debris-flow deposit with size segregation of clasts (scale bar 30 cm). A basal unit (1a), of clast supported carbonates, cherts and basement fragments (c) is overlain by matrix-supported and well sorted clasts (1b) of similar provenance. The bimodal admixture is sealed by mud supported carbonate chips (2). As a debris-flow moved basinwards, its sediment concentration and strength progressively decreased due to the entrainment of the ambient seawater. Probably the reduced shear strength and decreased flow viscosity allowed vertical segregation of clasts, resulting in a two-storey debris-flow (e.g. Payros, 1999) (star symbol for sample location, cf. with (a)). (d) On its eastern side (hexagon symbol site) the sedimentary breccia loses its patterning becoming a chaotic assemblage of carbonate sediment indistinct from CBX and partly mixed with coalescent marl.

6.4.2.3   Flow breccia MB

The Flow breccia (MB) was recognised only in two locations within the Century Mine. Its occurrence is limited and stratigraphically constrained to intervals proximal to thin laminated strata of marl (grey-blue in colour). Their occurrence was observed either in the basal part of the megabreccia proximal to the interface with the basement, but also in upper stratigraphic intervals of the Thorntonia Limestone, interbedded with phosphatic limestone and algal boundstones (G2b – G4). Locally the marl beds also form lenticular bodies (Fig. 6.10a). The marls never exceed 5 m thickness and locally, where deformation is more intense, they represent a source for flow breccia dykes that intrude cherty and phosphatic limestones (Figs. 6.6b, c and 6.12c). MB dykes are frequently cross-cut by CBX (Fig. 6.6b, c) or grade into CBX (Fig. 6.12c). MB fragments rarely exceed boulder size (25 cm). The breccia could be defined as angular mesofragmentite. It is also distinct from the CBX for its monomictic nature although it becomes polymictic when mixed with CBX (Figs. 6.11b, 6.12c). The matrix corresponds to the fragments composition, but locally the cement is more abundant and calcite-rich. The fabric is fragment-supported with interfragmental space filled by variable groundmass. This breccia is interpreted as transported, although the distance of transport is considerably less (within 10's metres) than the transport suffered by the CBX. The MB dykes appear to have been emplaced when the marl was partly lithified as they display hydroplastic deformation (e.g. slumps). The gradual mixing of CBX with MB is also indicative of a non lithified condition of both breccias. The rock micro-

fabric indicates a possible mixed component of intergranular movement and cataclastic flow. This may be due to a partial consolidation of the marls or alternatively by multiple phases of deformation. In thin section the MB dykes contain quartz micro-clasts displaying variable undulose extinction, but also apparently preserve undeformed crystals of quartz (homogeneous extinction across the area of the crystal). This textural feature may be the result of a semi-brittle state of the marls during deformation (see Maltman, 1984).

6.4.2.4 Solution breccia

The Solution Breccia (SB) is exclusive to and intrastratal within the Cambrian limestones (Fig. 6.11c) and occurs in horizons frequently associated with halite and gypsum pseudomorphs (see Henderson and Southgate, 1980; Szulc, 1992, groups G2a, G2b and G4). There is no clear cross-cutting relationship among SB and CBX or other breccias. The size of the clasts is variable with a range between 0.5 and 15 cm. The breccia can be classified as an angular mesofragmentite with a single fragment variety composed of chert. The groundmass composition semi-correspond to the fragment composition. The matrix is composed of calcarenitic, lobated micro-clasts, which are floating in dolomitic/calcitic cement. SB is matrix supported and likely formed from solution of its host. This is suggested by the corroded aspect of matrix clasts. Angular monomictic clasts indicate a minimal transport. Notice that the matrix is analogous to the oolitic, dolomitic sandstones of the Thorntonia limestone and Border Waterhole

Formations. The corroded nature of carbonates micro-clasts (Fig. 6.11d, e) is indicative of pressure solution involving mainly calcite and possibly halite and gypsum. Solution breccias may have been precursors of CBX breccias. The two breccias share similar matrix composition, and progressive transport may have been controlling mixing with other carbonatic components, causing selective rounding of clasts and transforming SB into CBX type breccias.

6.4.2.5   Collapse breccia

This type of breccia was recognised in a block of dolomitic limestone (200 m width) occurring at the base of the Lawn Hill Megabreccia, on the eastern side of the Century Mine. The CB has limited extent and is found exclusively in compact thick bedded limestone. Locally CB is crosscut by CBX (which postdates it), and also is found as infill of irregular cavities in limestone. Clasts have variable size ranging from 0.2 to 6.4 cm. The breccia is an angular to sub-rounded mesofragmentite and is monomictic with clasts composed of limestone. The cement is micritic limestone, corresponding to the clast composition. The amount of interfragmental filling is variable, with a fabric variation from clast supported to predominately matrix supported in the top part of the sample (Fig. 6.11f). This textural variation suggests possible gravity or local flow induced sorting during rock fall. CB likely underwent minimal transport (on the order of metres) considering its monomictic nature and the close association to its protolith. A possible explanation of the origin of this breccia would be a collapse of limestones due

to the formation of karstic cavities. Karstic cavities have been identified in the pit and elsewhere in the Lawn Hill Outlier. Alternatively, the fragmentation might be associated with fault movements.

6.4.2.6   Overprinting relationships

CBX, MB, CB, as seen, have distinct temporal relationships among them that can also be useful to further constrain the timing of recumbent folding. A paragenetic chart is proposed in Fig. 6.13. The sequence of cross-cutting relationships could be interpreted as follows: (1) after limestone/marl sedimentation, slope instability caused debris-flow and turbidites leading to the deposition of sorted and segregated clasts forming graded CBX breccia. Further destabilisation of the limestone caused also the development of slumps and redistribution of unconsolidated CBX, followed then by hydroplastic redistribution in dykes and sills of thin marly intervals. The evidence of folded marls (Fig. 6.6b, c) suggests that their hydroplastic deformation and recumbent folding were synchronous at start. Folded marls are cross-cut by CBX breccia that is unfolded. CBX also entrains blocks of limestone containing recumbent folds suggesting that it may be postdating the slumps. However, the gradual mixing observed between CBX and MB supports the alternative interpretation that hydroplastic redistribution of marls and CBX intrusions were synchronous. Therefore, a synchronous emplacement of CBX during penecontemporaneous slump folding cannot be excluded. Finally if the CBX event was relatively early, then also CB formed early because limestone cavities

are filled by CBX. The temporal collocation of SB remains uncertain but likely it shares a common timing with the CB breccia, because cavities initially tend to develop by dissolution followed then by a collapse and CB accumulation in limestones.
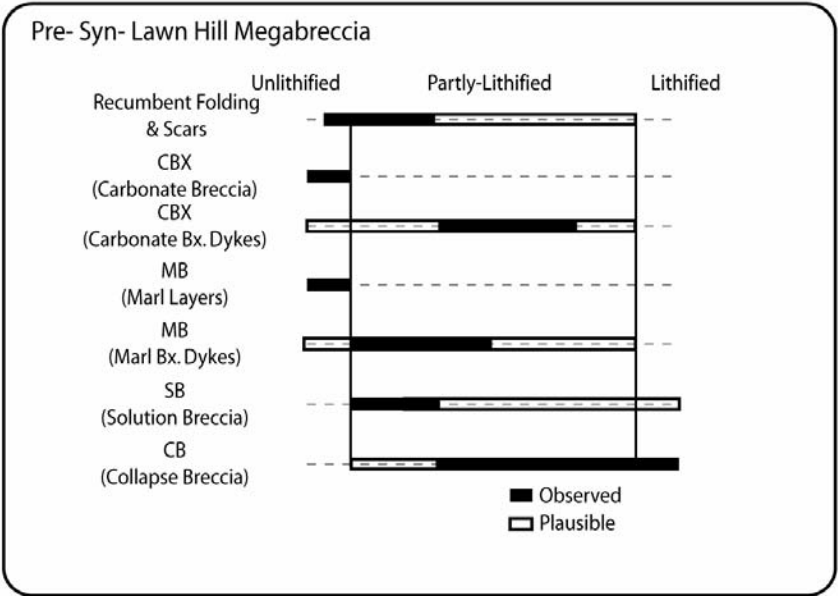
Fig. 6.13 Paragenetic chart illustrating the initial phases of basin evolution involving slump/scar development, the formation of different breccia types, and their evolution (see text for discussion).

Fig. 6.12a shows an interpreted tepee structure with a series of examples of CBX and MB breccias interrelationships. Tepees are expansion polygons with deformed raised edges formed by a volume increase of the associated sediments, accomplished by in situ, near surface, displacive growth of evaporites or carbonates (Gandin et al., 2005). Tepees may be also produced by gravitational collapse and

redistribution of partly lithified sediments, because their injection causes local increases in volume. The whole structure appears as an internal, stratiform body of CBX delimited on top and bottom by massive and deformed limestones. Locally the limestones are folded (e.g. the limbs of a recumbent fold are outlined in proximity of the core of the tepee structure, Fig. 6.12a, see arrow) and also they resemble imbricated stacks. Fig. 6.12b-d illustrates various styles of CBX breccias. Observed textural and structural appearances are in the first case (Fig. 6.12b) suggestive of a sedimentary deposition in a debris-flow deposit (this would be also an indication of slope instability) that evolved in a turbiditic current. In contrast, the chaotic mixing of marl and carbonate breccia (Figs. 6.12c, 6.6a, b) is interpreted as a sign of later injection of MB breccias.

The temporal relationships among CB and CBX are illustrated in Fig. 6.10a which outlines the infill of a limestone's cavity by CBX. Occurrence of bedded and slumped sandstones has been also found in other cavities (Fig. 6.10b, c). These evidences coupled with the textural evidence provided in Fig. 6.11e are suggestive of karstic collapse. Dissolution has contributed to the development of cavities in more massive carbonate strata that were subsequently filled by a groundmass of variable composition (CBX, MB, CB, SB).

A synergy of described genetic processes may have been contributing to the Lawn Hill Megabreccia development. However, considering the relative abundance and distribution of CBX breccia and the scale of slump folding, it is easier to invoke the transport component (1) as the dominant process at least for the Century area.

6.4.3 The control of basement faulting and fracturing on the CBX megabreccia distribution

Statistical correlation analysis was allowed by the available 3D reconstruction of the Century Zinc deposit (Feltrin et al., 2006), which represents a 3D virtual environment where spatial analysis can be undertaken to allow better geological interpretations. The analysis is focused on CBX-type breccia, The most widespread in the Century Mine, but also confined to dykes and sills occurring in basement.

6.4.3.1   Importance of spatial analysis in establishing the palaeostress direction

A structural analysis of the orientation of dykes in basement is proposed as a useful way to infer the direction of the palaeostress field during their emplacement. Palaeostress directions can be compared with the inferred spatial orientation of the palaeoslope, to ascertain if dykes were emplaced in a stress field that would have been favoring the slumping observed. Similarly, the palaeostress direction may be compared with other potentially younger tectonic structures to check on possibilities of reactivation or syntectonic brecciation.

Fractures that host injected materials may have been tensile, in which case they propagated orthogonally to the least compressive stress direction (Delaney et al., 1986; Boehm and Moore, 2002). This may be recognized by swarms of commonly oriented dykes. However, dyke patterns can be controlled by pre-existing structures prone to reactivation during subsequent deformation (Pollard, 1973; Jolly and Sanderson, 1995; Boehm and Moore, 2002), and they may also have intruded at angles oblique to $\sigma 3$ if they were acting as normal faults, i.e. shear failure (Jaeger, 1969 ; Hobbs et al., 1976) (Fig. 6.14a-d).

A 3D structural model representing the Century Mine has been constructed using the software GoCAD (see Fig. 6.15a-e) to obtain a detailed visualisation of breccias and faults in three-dimensional space. Additionally a Visual Basic algorithm was compiled to statistically estimate the trend of carbonate dykes considering their proximity to faults.
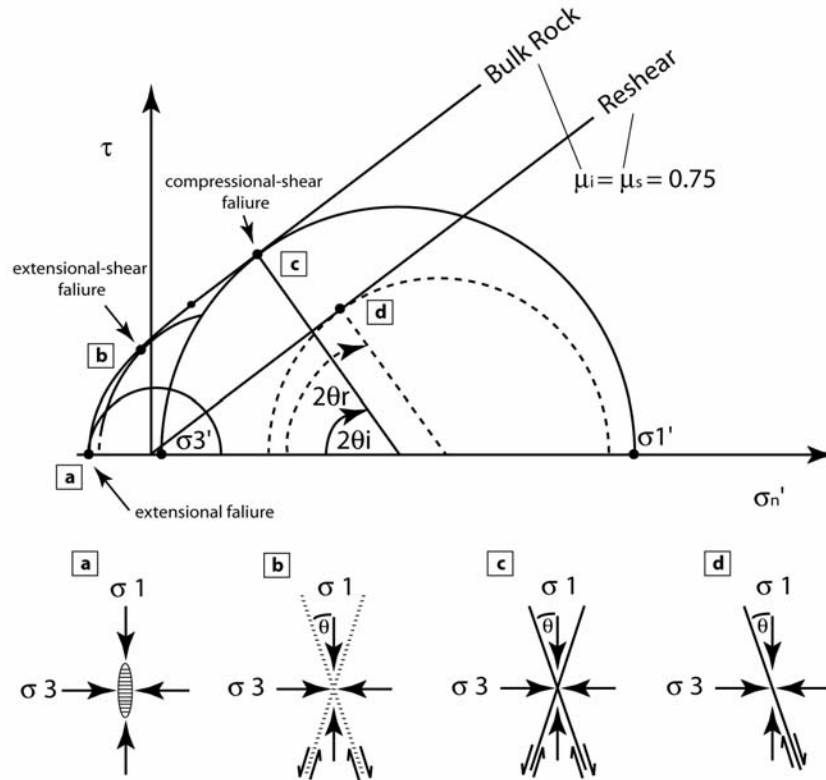
Fig. 6.14 Mohr diagram of shear stress, τ , against effective normal stress, $\sigma_n^{'}$ with a composite Griffith-Coulomb failure envelope for intact rock normalised to tensile strength, T, illustrating the stress conditions for the three different modes of macroscopic brittle failure, plus the reshear condition for an existing cohesionless fault (the internal friction μ_i is assumed for simplicity to be equal to the sliding friction angle and both are averages of experimental determined values) (adapted from Sibson, 2000). The four criteria of brittle failure are also presented with their relative orientation with respect to the stress field assuming a projection plane orthogonal to σ_2: (a) extensional; (b) extensional-shear; (c) compressional-shear and (d) reshear of cohesionless fault.

Comparative visualisation of the spatial distribution of CBX and faults outlines a close correlation between the spatial location of faults and the spatial location of CBX dykes. In addition the orientation and distribution of CBX in several examples matches the fault patterns (see Fig. 6.15e). Therefore, proximity to faults has been used as a likelihood parameter to infer the spatial orientation of CBX breccia dykes and sills. Fig. 6.16 illustrates the various fault orientations that more likely host CBX dikes in the Century Mine. Shallow dipping structures (Fig. 6.15a), and steep dipping faults are present both in cover and basement. The predominant trends of steep dipping structures are NW-SE (Fig. 6.15d, e), an orientation consistent with one of the major Mesoproterozoic faults in the region (Termite Range Fault) (Feltrin et al., 2006). Also prominent are NE to NNE trending faults (Fig. 6.15c), characterised by multiple sets of slickenlines recording multiple directions of movement (either dip-slip or strike-slip). E-W faults are also documented (Fig. 6.15b) and represent a system of lateral splays of the Termite Range Fault forming a half-graben, which hosts the Century deposit. These structures display a large dip-slip component of movement (e.g. Pandora's Fault) that can exceed hundreds of metres. There is consistency between orientations of faults that were mapped in the cover with documented orientations of corresponding structures measured on mine benches in basement, suggesting possible reactivation of basement faults.
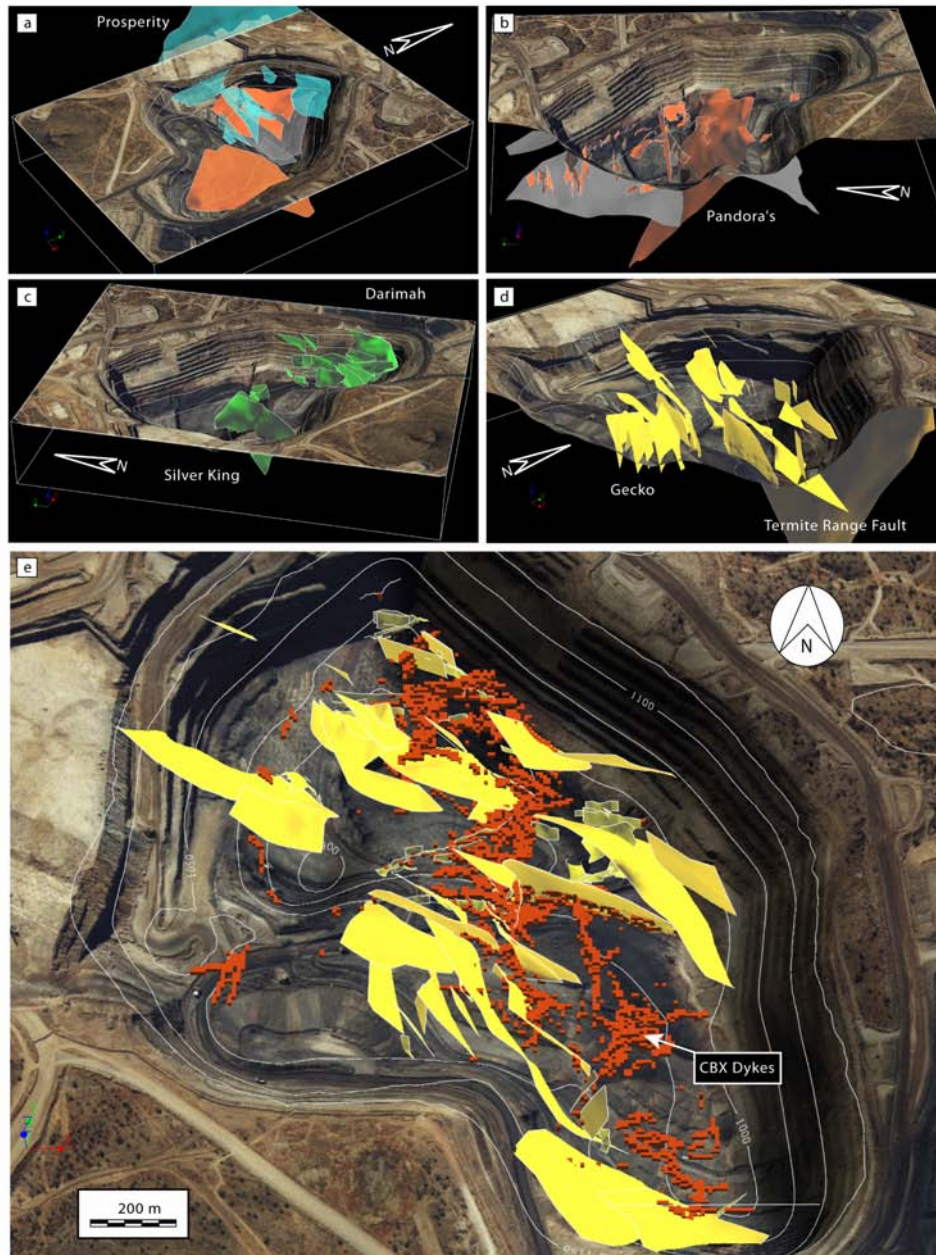
Fig. 6.15 3D structural/CBX breccia model of the Century Mine. (a), (b), (c) and (d) illustrate the modelled fault systems intersecting cover and basement with relative (fault systems are referred into the text using the mine terminology). (e) represents a top view of the pit showing the Gecko System and other faults with similar orientation that in places display a strong association with modelled spatial distribution of dykes (CBX) (hosting the Century Zn-Pb-Ag mineral deposit). Breccia dikes follow mostly WNW trends but also N-S, NE and NW trends are common.

6.4.3.2   Quantitative estimation of the spatial distribution of dykes

The abundance of dykes in the basement decreases from east to west across the mine area. This is a function of the spatial location and continuity of faulting and fracturing throughout the mineral deposit. Frequently, the dykes become more prominent and abundant at fault intersections (Fig. 6.15e). To better describe the variation in concentration and orientation of dykes, sub-sampled distributions of CBX were integrated in a voxet model (Fig. 6.15e). Two main datasets were considered, to statistically estimate the spatial orientation of CBX dykes: (1) fault distributions and orientations reduced to pointset data (X, Y, Z, Dip, Azimuth); and (2) the spatial distribution of dykes (X, Y, Z) occurring in drill core and exposed in the pit. A software program was then used to compute Euclidean distances between these two datasets (see Appendix C), using the following equation:

$$d = \sqrt{(x_i - x)^2 + (y_i - y)^2 + (z_i - z)^2} \qquad\qquad (6.1)$$

Calculated distances (d) were used to find the closest orientation (x, y, z) of a fault to a generic voxel (xi, yi, zi) containing CBX breccia. This provided the most likely orientation of a dyke based on fault data at a maximum of five metres interval (d). Plots for different (d) are presented in Fig. 6.16. The results were also classified depending on the dip of the dykes. Dykes with less than 30 degrees dip were classified as sills, while dykes with a dip angle (D) between 30 and 60 degrees were defined as

oblique. Finally, sub-vertical dykes dip between 60 and 90 degrees. The equal area projections show multiple and either persistent or variable patterns, as a function of interpolation distances. For example the sills appear to be focused in two clusters within all the four plots (<2-5m), suggesting that dips vary gently between 0 and 30 degrees. In contrast, the focussing of normal poles in the first and third quadrant (clockwise notation) is indicative of discrete planes striking from north-south to northwest-southeast. Oblique dykes have poles prominently distributed in the second and third quadrant and small isolated clusters of poles suggesting a minimum of four subsets of faults/dykes orientations. NW- and NE-striking systems are prominent. Sub-vertical dykes have persistent patterns, although extending the interpolation distance causes an increasing spread of the point distribution. However, a noticeable pattern with fairly concentrated point distributions is evidenced in the <2m plots. This suggests that most of the steep dipping dykes have WNW strike and can either dip toward NNE or SSW apparently forming a conjugate dip-slip system. Finally a system of faults/dykes that strikes NNE and dips toward WNW is also prominent.
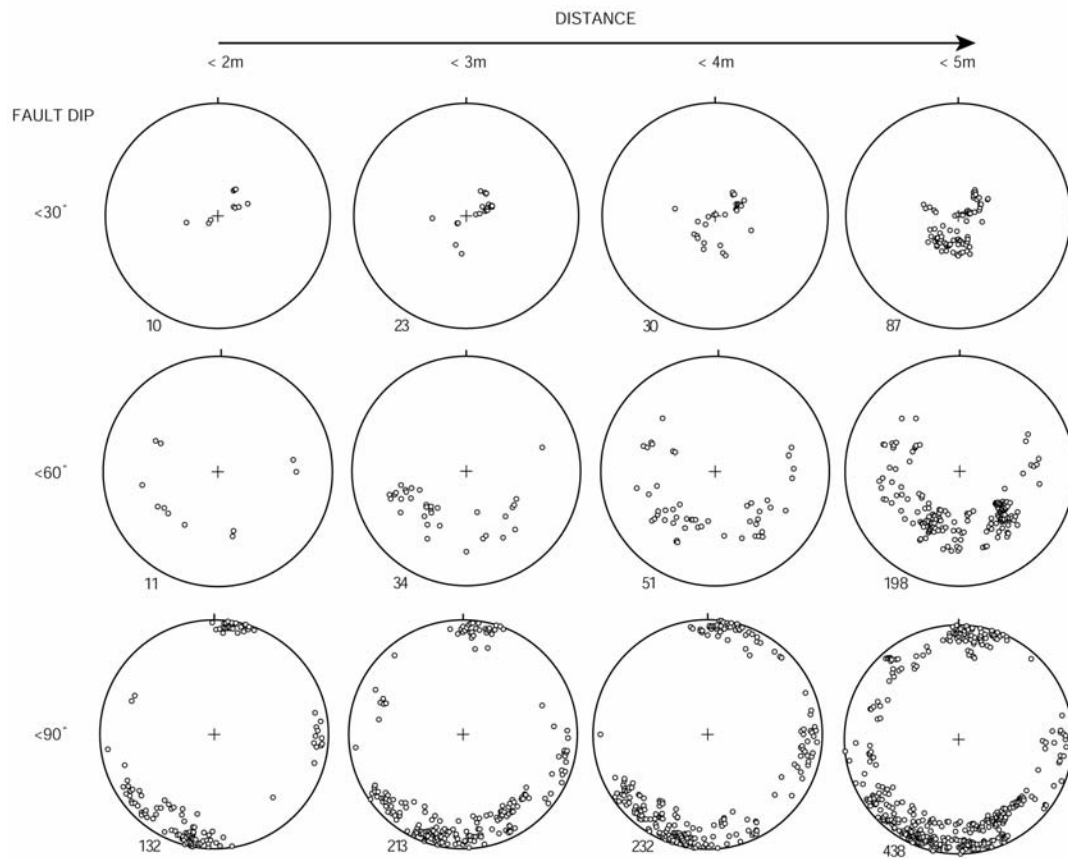
Fig. 6.16 Stereoplots of fault planes proximal to voxels containing CBX breccia, see text for discussion. The distance parameter is the neighbourhood space between spatial location of carbonate breccia and faulting. The number of intersections between CBX breccia and the modelled fault network increases for larger distances although this leads to higher background and consequent girdle distributions. Numbers on the bottom left are the sample totals

In summary the statistical model suggests that more likely the dykes formed mainly within NW and WNW striking structures, and to a lesser extent along NE and NNE directions. This may indicate that all major fault systems of Proterozoic age experienced at least local extension or reactivation to allow the intrusion of dykes

during the Middle Cambrian. Most fault systems are interpreted as initiated during Proterozoic time because they share a similar hydrothermal history (Feltrin et al., 2006). Clearly at least some of the preserved geometries may have been exclusive of the Georgina Basin extensional history.

To further understand the palaeostress history during dyke intrusion, three contour plots for the classes D<30; 30<D<60; 60<D<90 are shown in Fig. 6.17. Each plot contains poles of planes calculated for distances D < 5 m, and was compared with the respective eigenvectors/eigenvalues (see Table 6.1). Eigenvectors/eigenvalues were determined using the software StereoWin (Allmendinger, 2002), which makes use of the Bingham method of Fisher et al. (1987) to compute the scalars and vectorial components of the orientation matrix. Each population of directional data is generally fitted to the Bingham distribution, to test how closely the population's mean (and its dispersion around the mean) fits the distribution for a chosen confidence interval (e.g. Marcotte and Henry, 2002).
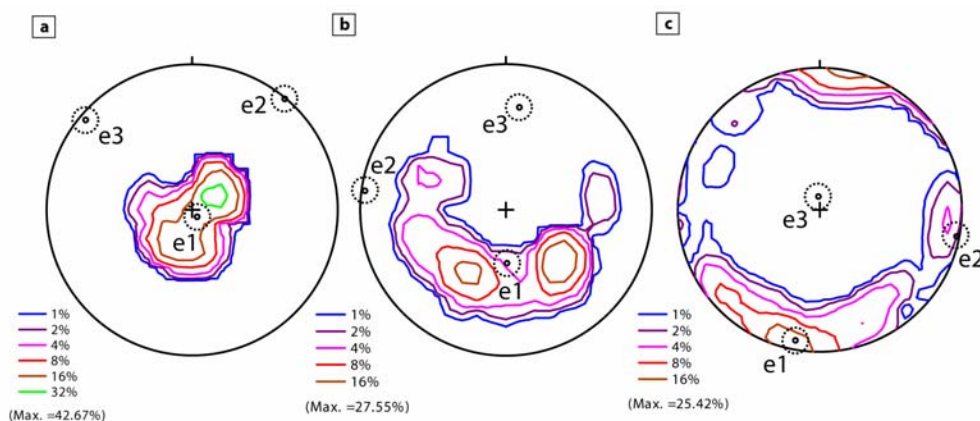
Fig. 6.17 Palaeostress directions (eigenvectors/eigenvalues, e1, e2, e3) for the dip-classes considered in (a) D<30; (b) 30<D<60; (c) D>60 (Fig. 6.16). All plots consider a 5 m correlation interval.

Table 6.1. Bingham axial distributions for sills, oblique dikes, and sub-vertical dikes.

Bingham Axial Distributions								
0° < Planes < 30° dip			30°< Planes < 60° dip			60° < Planes < 90° dip		
Eigenvalues	Eigenvectors		Eigenvalues	Eigenvectors		Eigenvalues	Eigenvectors	
	Trend	Plunge		Trend	Plunge		Trend	Plunge
0.8987	146.5	85.1	0.6558	178.6	55.9	0.7186	190.7	8.2
0.0783	40	1.4	0.2622	274.9	4.3	0.235	100.4	2.4
0.0231	309.9	4.7	0.062	7.7	33.7	0.0464	354.3	81.5

Eigenvalues relate to the basic concept of a deformation matrix (discussed for example in Flinn, 1979). A deformation matrix represents a convenient way to describe the deformation of a rock in three-dimensional space. Three linear equations equivalent to a squared matrix characterised by nine components are sufficient to describe such system. Matrix elements are always real numbers in case of geological deformations. A deformation matrix can always be decomposed to a product of two matrixes, one representing the eigenvalues and another representing the eigenvectors as long as the eigenvector matrix is also square (according to the Eigen theorem Arfken, 1985; Marcus and Minc, 1988). Obtained matrixes provide vectors and scalars that represent the semi-axes on a deformation ellipsoid (eigenvectors) and their relative modulus (eigenvalues) (de Paor, 1983). Considering the relationships between stress and strain, the strain matrix can be thought of as the equivalent of the stress matrix for pure shear conditions. If this is a reasonable assumption, eigenvalues and eigenvectors would reflect respectively magnitude and orientation of orthogonal components of the stress tensor ($\sigma1,\sigma2,\sigma3$) (Flinn, 1979; Boehm and Moore, 2002). Limitations clearly apply in

the case of reactivated systems (Fig. 6.14). Here, statistical analysis provides probability distributions that reflect mixed components derived from multiple palaeostress directions. The plots presented in Fig. 6.17 reflects then the interpreted local variation of σ1,σ2,σ3 in space as a function of the orientation of a dyke/sill dilating during injection of carbonate breccia. Notice that calculated eigenvectors/eigenvalues reflect the datasets considered; therefore, they represent a local stress field (voxel based) not necessarily matching a mine-scale palaeostress direction. Nonetheless, measure of the frequency of orientation of dykes (number of voxels containing breccia with a specific orientation) can be used as a weighting parameter in the interpretation of the possible overall trend. Fig. 17c shows the highest amount of data (greatest breccia volume) suggesting that most of the breccia dykes were accommodated by NNE – SSW directed sub-horizontal extension. This consideration is in agreement with evidence of thick sub-vertical dykes at least an order of magnitude larger than sills (Figs. 6.4a and 6.9b).

6.4.4 Post intrusion deformational history

6.4.4.1 Assessing later deformation and fluid flow

To further constrain the timing of emplacement of carbonate dykes, a series of structural features were examined that developed during the syn- to post-burial history

of the Georgina Basin. These features include: (1) sub-horizontal stylolites identified in drill-core (Fig. 6.18a); (2) low-angle to high-angle faults and fractures and sub-vertical joints (Fig. 6.18b, c); and (3) veins (Fig. 6.18d). These structural features are demonstrated to postdate the Lawn Hill Megabreccia event. Carbon and oxygen isotopic analyses on whole rock samples and carbonate veins were also used to understand the possible involvement of fluids during a later tectonic overprint.

6.4.4.2   Timing constraints: stylolites, fractures, joints and veins

A prominent feature observed in carbonate breccia dykes are sub-horizontal macro-stylolites (Fig. 6.18a). Stylolites form during burial and loading in a sedimentary basin typically being oriented approximately orthogonal to $\sigma 1$(Andrews and Railsback, 1997). Dewers and Ortoleva (1990) proposed, on the basis of mathematical modelling and numerical simulations, that stylolites are a product of self-organisation by mechano-chemical feedback. Essentially the host-rock reorganises itself during sedimentary compaction and diagenesis, involving dissolution during stylolitization and simultaneous precipitation elsewhere. Organised networks of fractures and joints may similarly reflect mechanical self-organisation (Zhang and Sanderson, 2002). Reed and Wallace (2004) proposed a minimum depth of formation of macro-stylolites of 800 m. Elevated pore pressure values may inhibit the development of these features even at several kilometres of depth, so timing information derived from these features is approximate. However, because these sub-horizontal stylolites occur in carbonate dykes

(Fig. 6.18a), the dykes must have been emplaced prior to diagenesis at these depths, i.e.,

Middle to Late Cambrian age at the latest.

Widely distributed and complex fracturing and jointing in the breccia dykes also

postdate the emplacement of the breccia. As Price (1966) concluded, it is unlikely that

complex fracturing and jointing observed in a geological system could be the result of a

single deformational event. In this context, the discrimination of the possible timing of

joints and fault reactivation is attempted. Joints can be classified using the approach of

Engelder (1985), because they represent particular types of fractures (mode 1,

dilational) that typically form orthogonal to $\sigma3$ (e.g. Pollard and Segall, 1987; Peacock,

2001). Within the Century Mine they are fairly continuous and are found in Proterozoic

shales/siltstones, Mesozoic breccia dykes/sills that infiltrate the Proterozoic rocks (Fig.

6.18b), and limestones in the main body of Cambrian rocks (Fig 6.4a, b).
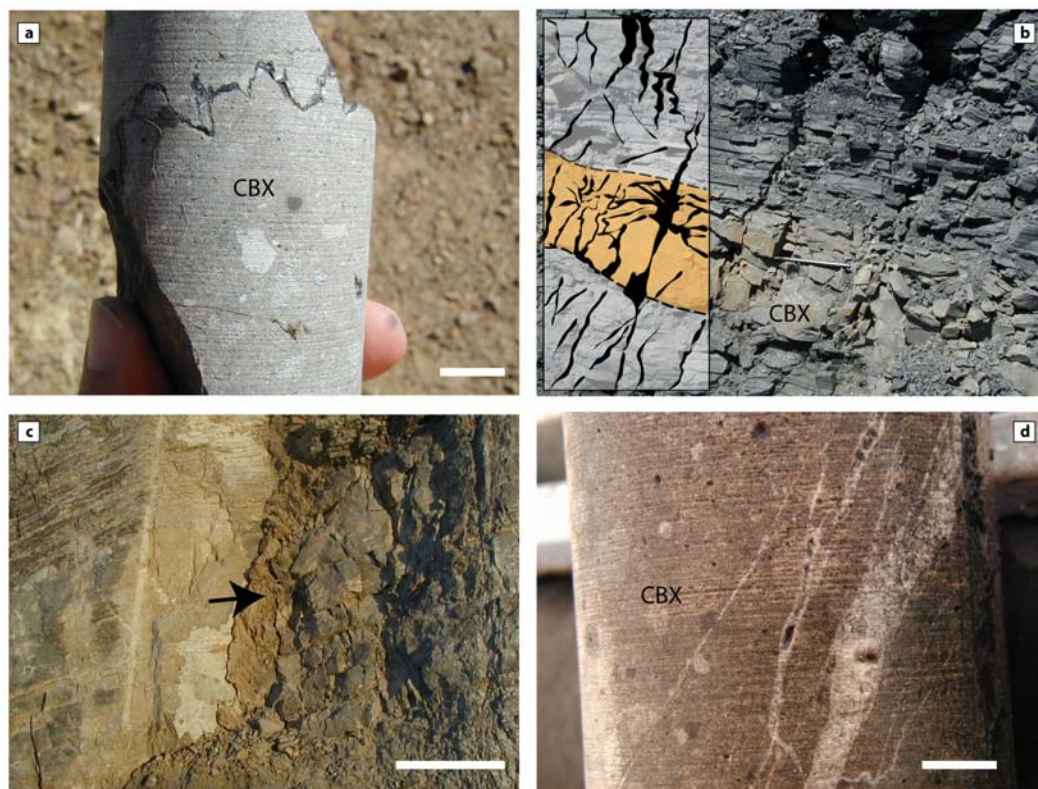
Fig. 6.18 Examples of post-intrusion structural features: (a) compaction related, sub-horizontal, macrostylolite with cuspate, sinusoidal profile (scale bar 1.5 cm). Organic (graphite) solution seams accumulated along the stylolite's margin. The stylolite cuts carbonate breccia (CBX) postdating its emplacement. (b) Image portraying field relationships among joint distribution, a CBX sill, and basement shales/siltstones. Sketch outlines evidence of jointing/fracturing developed across the different lithotypes (pen for scale). (c) Example of joint Type 2 (length >10 m) containing fault gouge material (arrow, scale bar 1.5 m). Fault gouge differs from carbonate breccia infill as it is composed of soft, friable micaceous claystone entraining chips and cm-scale clasts of carbonate limestone. Type 2 joints cross-cut carbonate breccia postdating breccia emplacement, see Fig. 6.12a (moon symbol for location). (d) Example of network of calcite veins cross-cutting CBX breccia (scale bar 1cm).

Two distinct generations of joints were identified in the Century Mine (Type 1 and Type 2). An array of sub-parallel joints intersects both carbonate breccia and shale/siltstone layers in the basement (Fig. 6.18b) and is also widespread across the whole mine, occurring in Cambrian cover. These joints frequently occur in complicated

networks, forming numerous dihedral intersections that originate by combination of steep dipping joints with reactivation of weak, cohesionless bedding planes (Fig. 6.18b). Other joints are distinct because of their more consistent orientation (NW-NNW) and infill (Type 2, see Fig. 6.18c), and because of their scale (exceeding 10's of metres). Specifically, they contain a clay-carbonate rich fault gouge that is interpreted as possible tectonic comminution associated with later post-Cambrian shearing. Type 2 joints have also wider spacing, becoming isolated fractures/faults.

Field observations were complemented with structural mapping of fractures and joints along three transects (eastern wall of the Century Mine, stage 4 – transect 1, RL 1120 m and transect 3, RL 1088 m; western wall of Century Mine, stage 5 – transect 2, RL 1104 m). The fieldwork aimed to outline the influence of pre-existing faulting on the joint/fracture distribution. Two approaches were implemented: (1) stereonet based plotting of structural data; (2) scanlines to quantitatively analyse fracture density variation relative to fault proximity. Three plots summarise the orientations of the data collected (Fig. 6.19a-c). In particular, two rose diagrams are presented showing the orientation of steep dipping joints/fracture sets (dip $\geq$ 60°) measured in cover and basement (Fig. 6.19a, b). Three trends (NNE-SSW, E-W, and NW-SE) occur in cover rocks and similarly in basement. NNE-SSW and NW-SE joints persist with similar abundance although there is a slight variation in abundance of E-W joints in spite of more ENE-WSW joints in the basement. NW-SE joints are less abundant compared to the other trends both in cover and basement.
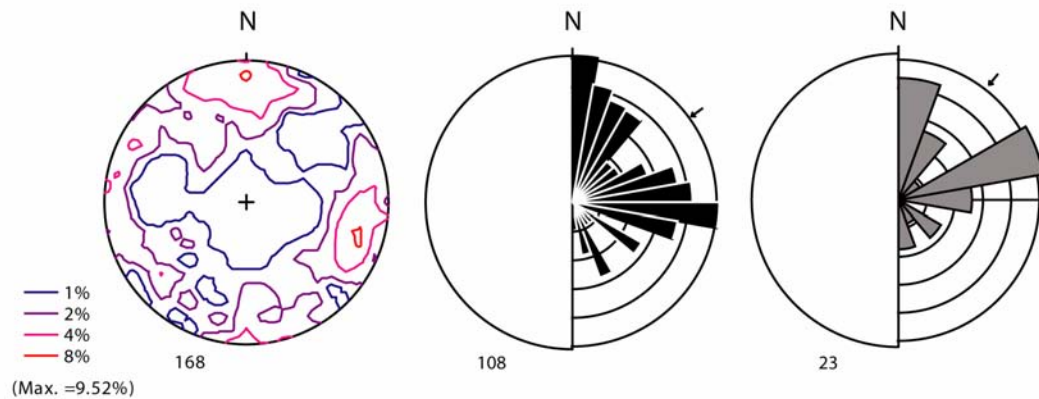
Fig. 6.19 Stereoplots representing the preferential trend of distribution expressed in % area for the whole joint dataset and rose diagrams of joints measurements in Middle Cambrian limestone (black, 15º sector) and Mesoproterozoic shales/siltstones (grey, 20º sector). For comparison see discussion in the text.

Joints in cover were compared with joints in basement to differentiate between structures exclusive of Proterozoic rocks from structures that likely formed both in cover and basement during Palaeozoic time. NNE and NW and E-W striking joint sets have close orientation in basement and cover. Therefore, they formed in a similar stress-field during post-Cambrian tensile failure. The joint set striking ENE is more prominent in the basement, however this may be a) real, b) due to the variation in orientation of selected transects, or c) bias induced by the sample size considering that partitioning of deformation and local influence of pre-existing faults causes inhomogeneous distribution of joints (Hancock, 1985).

To evaluate a possible relationship between joints and older faults, poles to joints are compared with the previous plots of faults and dykes orientations. In general Hancock (1985) remarks that joints tend to be rarely parallel both in strike and dip to

the main plane of dip-slip faults or thrusts. This would favour a more common situation that sees a time gap between faulting and jointing. In the Century Mine a good correlation between the two datasets exists. However, Type 1 joints cut CBX suggesting a time separation between these sets and faulting related to the intrusion of the CBX breccia. Type 1 Joints propagated as planar tensile fractures cross-cutting different rocktypes, suggesting that variation of mechanical properties of the host played minor control on their development (see Engelder, 1985). Therefore, their origin is possibly due to unloading or release, during uplift and erosion (Engelder, 1985). A shallow depth of formation seams a more reasonable solution to explain also the local occurrence of iron oxides-hydroxides (hematite, limonite, goethite) as matrix infill in these joints (e.g. Perez and Boles, 2005). It is likely that some joints formed by reactivation of older faults (Type 2), but others formed later, independently (Type 1). Rather than necessarily requiring reactivation, older basement faults may have only acted passively, because pre-existing anisotropies tend to control the orientation of later tensile fractures/joints (Zhang and Sanderson, 2002).

To further address this issue, image processing of four scanlines was undertaken (along transect 2) to measure the density variation of fractures/joints as a function of distance from a major E-W fault that records Palaeozoic movement. The selected fault (Pandora's Fault, Fig. 6.20) is also intruded by carbonate breccia. In a recent contribution, Peacock (2001) remarks that a possible key distinguishing factor for joints and fractures that form contemporaneously with dip-slip faulting could be their increasing number towards a fault zone (see also Hammond and Evans, 2003).
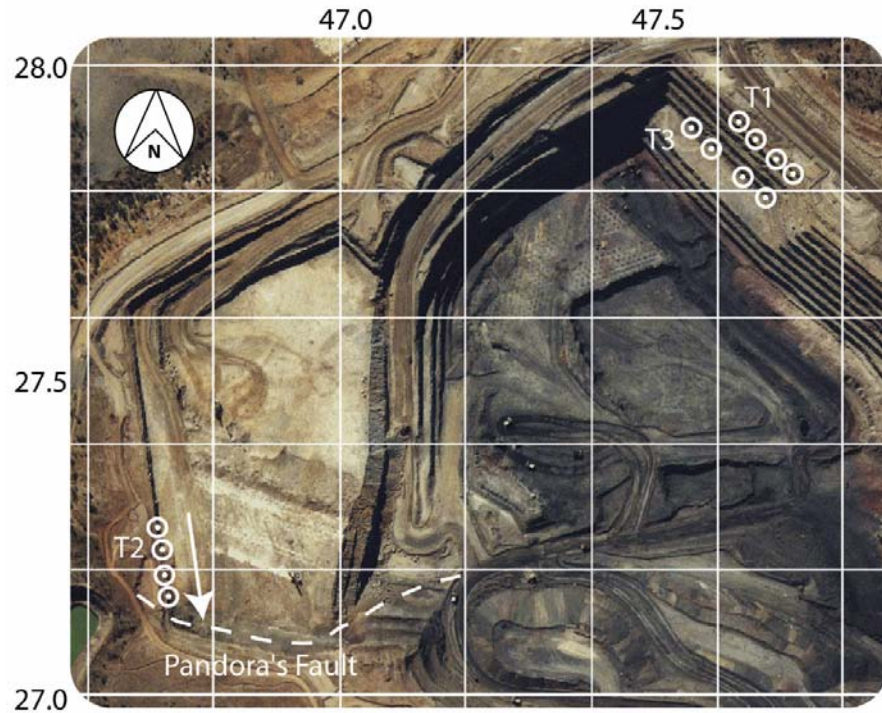
Fig. 6.20 Map-view of the northwestern corner of the Century Mine illustrating transects where structural data were collected (T1-T3). Along T2, photographic sampling of fractures were collected in four locations within a 140 m interval, dashed line indicates approximate location of the Pandora's Fault.

Four scanlines of one metre each were sampled with spacing of approximately 35 metres along the western wall of the Century Mine. This section represented an optimal condition where only joints and fractures were observed along the photographed transect. The scanlines were photographed at equal distance from the limestone exposure (3 m) orthogonal to the pit face to respect the scale dependency factor which conditions the fracture density estimation. Collected images were processed using the MATLAB ® Image Processing Toolbox, which allows: (1) image contrasting, (2) edge detection of linear features (e.g. fractures etc.), and (3) pixel

profiling and counting after threshold and subsequent binary conversion. Fig. 6.21 illustrates four plots representing the density distribution of fractures/joints across each (1 m) scanline and the relative density of edges per column of pixel data. A final plot also considers a comparison of the local (area based) density of fracturing/jointing every 35 m interval.

The density variation measured along the 140 m transect does not appear to be related to the major fault, at least within the constraints of our sample spacing. In contrast with the general observations of some orientational relationships between faults and joints, these data suggest that earlier syn-sedimentary Cambrian faults where not substantially reactivated to produce the later joints. It is therefore more likely that the majority of the joints (Type 1) formed unrelated to faults although in a tectonically preconditioned scenario in which rock's anisotropies contributed to their trends.

The investigation of the timing of fracturing and jointing thus provides only limited constraint on the age of the Lawn Hill Megabreccia. Some of the brittle structures (Type 2) indicate possible tectonic reactivation of the system during post-Cambrian deformation that however was unrelated to the megabreccia event. More likely both types of joints formed during unroofing linked to late-Devonian Alice Springs Orogeny (ca. 410-390 Ma). Twinning fabrics and subgrains development in CBX clasts may be the result of this later tectonic movement, as well as some of the hydrothermal calcite veins observed on the eastern wall of the mine. Alternatively, the hydrothermal calcite-veining and pressure solution seams could be linked to dewatering

and basin compaction at relatively shallow depths, 10's to 100's of metres, soon after

formation of the megabreccia (Feltrin et al., 2003; Oliver et al., 2006).
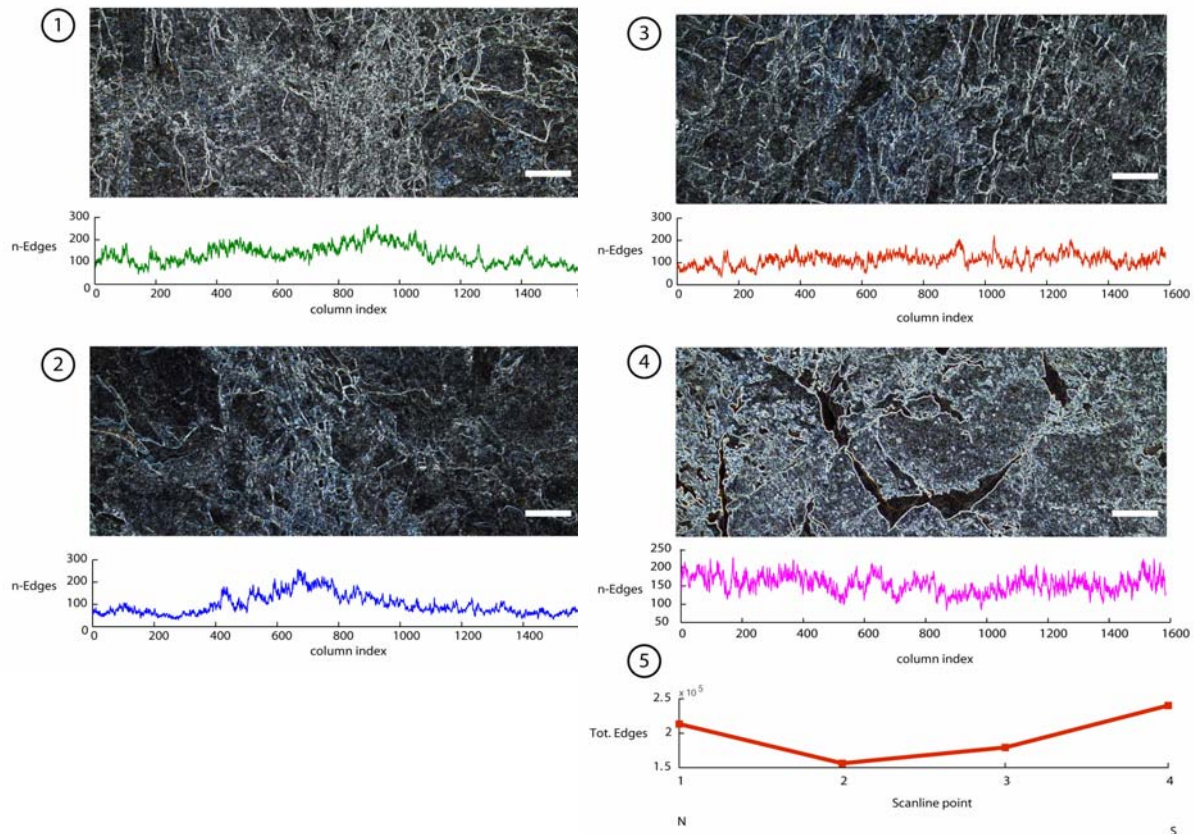
Fig. 6.21 Scanlines along transect 2 ordered from north to south. The density of fracturing has been computed as the number of pixels/edges derived from image processing (edge detection). This approach was utilised to produce binary files used then to plot cumulative slopes representing the total number of edges for each column of the scanline – a parameter that gives a quantitative estimation of the horizontal variation of fracture density across a single scanline (1 to 4). Scanline results were also summed up to get a total number of edges for the whole area and they were compared to obtain an evaluation of the density of fractures/joints variation at larger scale (5).

6.4.4.3   Carbon and oxygen isotope analyses of hydrothermal phases

To allow the characterisation of these hydrothermal events, stable isotope analyses were performed on whole rock and veins (Table 6.2). These include host rock, cements and veins from cover, basement rocks, and also calcite veins intersecting carbonate breccia and basement. Fig. 6.22 schematically shows the spatial relationship of isotopic data to field locations, and also a schematic representation of the rock-types. Petrography was used to refine the otherwise ambiguous interpretation of isotopic data.

Results are presented in the conventional terminology with $\delta^{13}C$ referenced to PDB and $\delta^{18}O$ relative to SMOW. Analyses were performed on powdered carbonate with phosphoric acid (McCrea, 1950; Swart et al., 1991), and using the mass spectrometer of the Central Science Laboratory of the University of Tasmania.

The results were (1) thirteen analyses comprising whole rock (carbonate) and calcite-veins of Mesozoic age (Thorntonia Limestones) with $\delta^{13}C_{carb}$ ranging from -14.8 to 0.8 $^0/_{00}$ with average -3.1 $^0/_{00}$, and $\delta^{18}O_{carb}$ 9.9 to 23.9 $^0/_{00}$ with average 20.9 $^0/_{00}$ in average; (2) four carbon isotopic values on organic matter (pyrobitumen) found in stylolites occurring in mottled limestone in the cover (CLS55), and shales from the basement (SH75, SH23, SH12), with values within the interval -27.8 to -33.5 $^0/_{00}$ $\delta^{13}C_{graph}$, mean -30.1 $^0/_{00}$; and (3) three siderite veins in Proterozoic basement ranging from -5.2 to -4.3 $^0/_{00}$ $\delta^{13}C_{carb}$ averaging -4.8 $^0/_{00}$, and 15.8 to 16.8 $^0/_{00}$ $\delta^{18}O_{carb}$ averaging 16.6 $^0/_{00}$. All data are reported for convenience in Table 6.2 and separated in groups (whole rocks, veins, etc., see also Fig. 6.22), according to the following discussion.

Table 6.2. Carbon and oxygen isotope analyses of whole rock and veins on the Thorntonia Limestone and Mesoproterozoic basement hosting carbonate breccia dikes (Century area).

Sample Name	Transducer	Delta 13C	Precision	Delta 18O	Precision	Delta 18O	Description
(alternate)	(mBar)	wrt PDB	Delta 13C	wrt PDB	Delta 18O	wrt SMOW	
C-63-R	30.2	0.5	0.011	-6.7	0.009	23.9	Marl
C-69	16	0.1	0.012	-7.8	0.007	22.8	Carbonate breccia
C-65	20.4	0.2	0.007	-6.7	0.013	23.9	Nodular phosphatic bedded limestone
C-62	27.4	0.7	0.011	-8.9	0.015	21.7	Mottled cherty limestone (siliceous nodules)
C-64	22.2	0.6	0.01	-8.9	0.015	21.7	Fenestral dolomite
C-6	0	0.4	0.012	-8.8	0.009	21.8	Stylolitic limestone
C-7	22.2	0.4	0.01	-8.9	0.008	21.7	Dolomitic limestone
C-43-V-BCS	15.5	-8.3	0.008	-9.1	0.013	21.5	Calcite vein in Mesoproterozoic (shale)
C-74-V	15	-10.4	0.014	-9.3	0.016	21.3	Calcite vein in Mesoproterozoic (siltstone)
C-9-V	20.7	-1.4	0.014	-10.5	0.012	20.1	Calcite vein in dark, grey, stylolitic and phosphatic limestone
C-54-V	0	-14.8	0.006	-20.3	0.01	9.9	Calcite vein in mottled limestone
C-63-V	15	0.8	0.009	-10.9	0.006	19.6	Calcite vein in marl
C-43-V-CBX	19.2	-9.0	0.013	-9.4	0.016	21.2	Calcite vein in dolomitic breccia
SH75	0	-33.4	0.013				Nodule of siderite in shale Mesoprot. (sample C-291 G. Broadbent collection)
CLS55	0	-29.6	0.005				Organic-rich stylolites in mottled Cambrian limestone
SH23	0	-29.7	0.019				Hydrocarbon in fractures - Mesoproterozoic siltstones
SH12	0	-27.8	0.008				Mesoproterozoic shale
C-41-V	0	-4.3	0.015	-13.6	0.007	16.8	Siderite vein - Mesoproterozoic
C-46-S	0	-5.2	0.008	-14.6	0.005	15.8	Siderite vein - Mesoproterozoic
C-46-H	0	-5.0	0.005	-14.5	0.012	15.9	Siderite vein - Mesoproterozoic

Whole rock isotopic signatures from Century Cambrian limestones are in general agreement with global Lower/Middle Cambrian boundary data (Brasier and Sukhov, 1998; Veizer et al., 1999; 2000) obtained from brachiopods from the Amgan Stage, northern Siberia. The Century data obtained for Middle-Cambrian limestone also have isotopic signatures similar to the ones reported by Lindsay et al. (2005) in Thorntonia Limestone outcropping within the O'Shannassy River, 9 Km south of Riversleigh Homestead, in the northeastern part of the Georgina Basin. These workers report slight depletions in $\delta^{13}C_{carb}$ and $\delta^{18}O_{carb}$ relative to normal Cambrian marine seawater signatures, probably due to diagenetic recrystallisation and fluid flow in the more permeable grainstone units of the Thorntonia Limestones. Results from whole rocks at Century reflect a similar trend with approximately a 2 $^0/_{00}$ $\delta^{18}O_{carb}$ difference between fresh and isotopically lighter, dolomitised limestones.

The carbonate breccia has values indistinguishable form the limestones. Analysed veins show similar $\delta^{18}O_{carb}$ isotopic trends, but oscillations are shown for $\delta^{13}C_{carb}$ and $\delta^{18}O_{carb}$ in veins sampled in limestones, suggesting some degree of open system behaviour during veining (Bons, 2001; Oliver, 2001), possibly linked to meteoric input (Faure, 1991; Aranburu et al., 2002) or diagenesis, because $\delta^{18}O_{carb}$ values are comparable with dolomites and diagenetically altered limestones. Slight depletion in $\delta^{13}C_{carb}$ for some veins may suggest that the system interacted with other carbon rich reservoirs (organic-rich basement shales or petroleum reservoirs hosted in limestones) that are strongly depleted in $\delta^{13}C_{carb}$ (mean of -30.1 $^0/_{00}$ $\delta^{13}C_{graph}$). A marked depletion in $\delta^{13}C_{carb}$ observed in a calcite vein cross-cutting carbonate breccia and basement shale along a fault contact is indicative of a possible basement interaction.

Similar trends are observed for veins crosscutting the breccia and basement, which are also strongly depleted in ^{13}C (mean, -9.3 $^{0}/_{00}$ $\delta^{13}C_{carb}$). A single sub-horizontal vein in mottled limestone, which was part of a pressure solution related network of veins, shows even more marked depletion in $\delta^{13}C_{carb}$ and $\delta^{18}O_{carb}$ (see, Table 6.2). This "anomalous value" may be linked to proximal petroleum sources hosted in cover rocks in the Middle-Cambrian limestones. Bitumen was observed in stylolite seams and cavities in porous sandy-limestone on the northern exposure of the Century Mine.

Siderite veins sampled on the northeastern corner of the Century deposit, where the basement abuts against cover, revealed signatures comparable to the data reported by Broadbent et al. (1998) suggesting an earlier origin linked to the Proterozoic mineral deposit and other smaller regional occurrences; therefore, they are considered unrelated to the Mesozoic calcite veining event.

In summary, the similarity of data for breccia and limestone suggests that lithification of both rocks occurred at similar depths (temperatures) from similar sources, and similar fluid involvement. These all suggest that the breccias lithified at shallow depths. $\delta^{18}O_{carb}$ values in veins likely represent the mixing of seawater carbonate dominated signatures with a meteoric component, or reflect late diagenetic recrystallisation in response to pressure solution at slightly elevated temperatures. The evidence of calcite veins with characteristic depletion in ^{13}C along breccia/fault boundaries across basement contacts suggests that faults were involved with fluid flow across the cover/basement interface during the burial history.
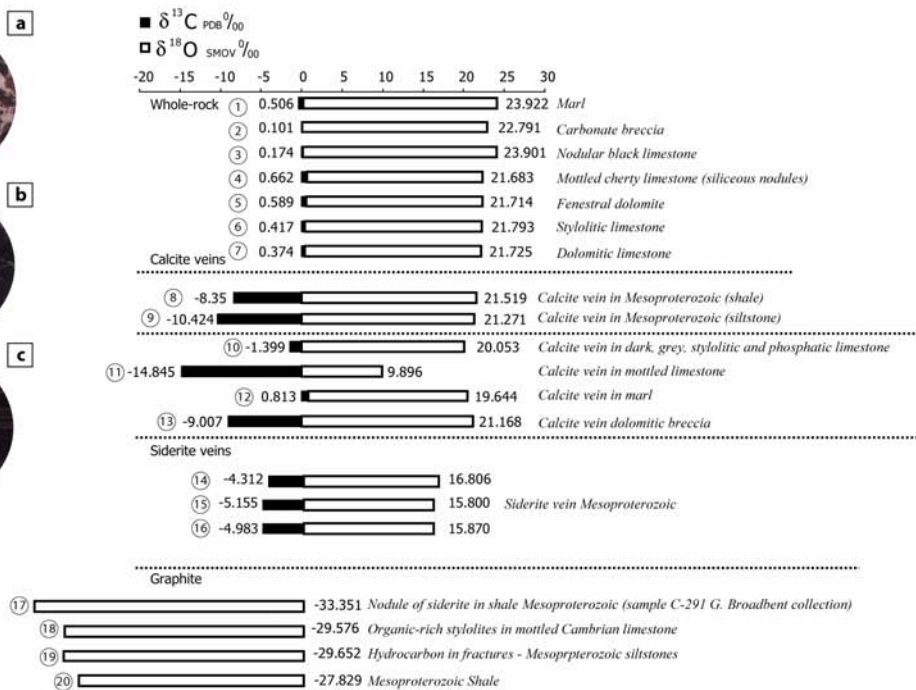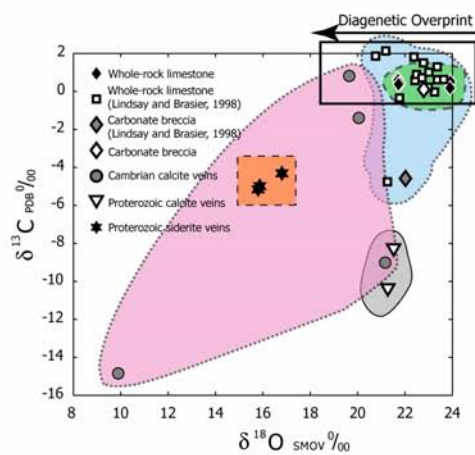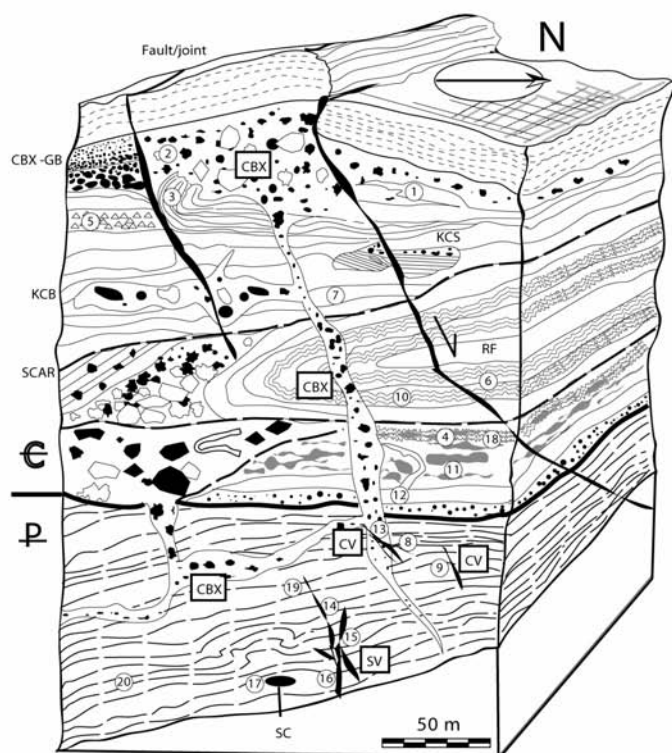
Fig. 6.22 3D Block diagram representing a summary of the field relationships discussed in the text and presented in previous plates. (GB) graded breccia, (KCS) karst cavity containing sandstone fill; (KCB) Karst cavity with breccia fill; (CBX) carbonate breccia dyke; (CBX-GB) carbonate breccia with normal grading; (CV) calcite vein; (SV) siderite vein; (SC) siderite concretion. Location of specimens where carbon and oxygen isotopic ratios were measured is given within the portrayed spatial context (see numbering 1-20) and relative reference to the histogram and scatter plot. Three examples of photographed veins are also documented representing, calcite veins in cover, calcite veins cross-cutting cover and basement, and siderite veins in basement (a, b, c).

6.5 Discussion and conclusions

A summary of the documented spatial and temporal constraints is presented to ascertain the timing of failure and consequent megabreccia development in the Lawn Hill Outlier. Finally, the geological, causative agents are assessed – seawater eustatic variations, earthquake or meteorite impact?

6.5.1 Timing of the megabreccia

6.5.1.1   Importance of the tectonostratigraphic reconstruction

There is a ~100 m.y. gap between Middle-Cambrian sedimentation and later orogenic inversion of the Georgina Basin (Alice Springs Orogeny). Bedded limestones, outcropping in the Lawn Hill Outlier, were thus sedimented during subsidence in an overall extensional setting. This orogen has likely controlled the later Devonian sedimentary evolution, and at least part of the deformational features occurring in the

whole stratigraphic sequence. However, the style of folding of the Thorntonia Limestone supports its early synsedimentary origin. More likely, the folds developed on a palaeoslope dipping toward SE, and were driven by extensional deformation unrelated to the Alice Springs Orogeny. This latter interpretation is corroborated by the 3D reconstruction and quantitative estimation of dyke trends in basement. The dikes formed preferentially along NW to WNW faults suggesting that they may have developed contemporaneously with the slumping. The deformation likely caused reactivation of NW and WNW structures because they were more prone to dip-slip reactivation (Sibson, 1985). These scenarios could be explained by a steepened ramp/slope and fault induced destabilisation contributing to the Lawn Hill Megabreccia formation.

6.5.1.2   Paragenesis of deformational features

The structural style of folding is only one of several features suggesting an early origin for the megabreccia. The paragenetic reconstruction based on cross-cutting relationships (Fig. 6.23) suggests that a component of the Lawn Hill Megabreccia (CBX) formed initially as sedimentary breccia (derived from mass-flow and also debris and turbidites), but then the destabilisation of the platform caused reorganisation of this breccia-type causing the formation of chaotic structures including dykes that infiltrated the basement. MB is similarly derived from such destabilisation process that however involved the marl lithofacies rather than the CBX. In this context, the relationship among CBX and MB indicates that recumbent folding was at least initially synchronous

with CBX and MB formation. Superposed on these deformational phases the action of fluids penetrating the ramp margin may have favoured destabilisation, because the meteoric and/or seawater flows were able to dissolve the limestone forming SB and relative cavities that resulted in local collapse filled by CBX and in situ breccias CB. This process was contemporaneous with CBX redistribution but may also have predated the CBX phase. The occurrence of stylolites in CBX dykes is a plausible indication that the breccia was intruded earlier than the Alice Springs Orogeny that more likely was responsible for the two generations of joints observed. The veins observed in a faulted CBX dyke indicates that a calcite-precipitating hydrothermal phase occurred at a depth ranging from few 100's of metres to a few kilometres and that fluid flow occurred between basement and cover. The constraints obtained from Carbon and Oxygen isotope results are insufficient to attribute with certainty these veins to the Alice Springs related reactivation. However, the stable isotopic results confirm the conclusions derived from the style of deformation and cross-cutting relationships, indicating that cementation of CBX dikes occurred early in a relatively seawater-dominated setting (relatively low-temperatures). In summary paragenetic relationships and stable isotopic data suggest an early timing for the Lawn Hill Megabreccia.
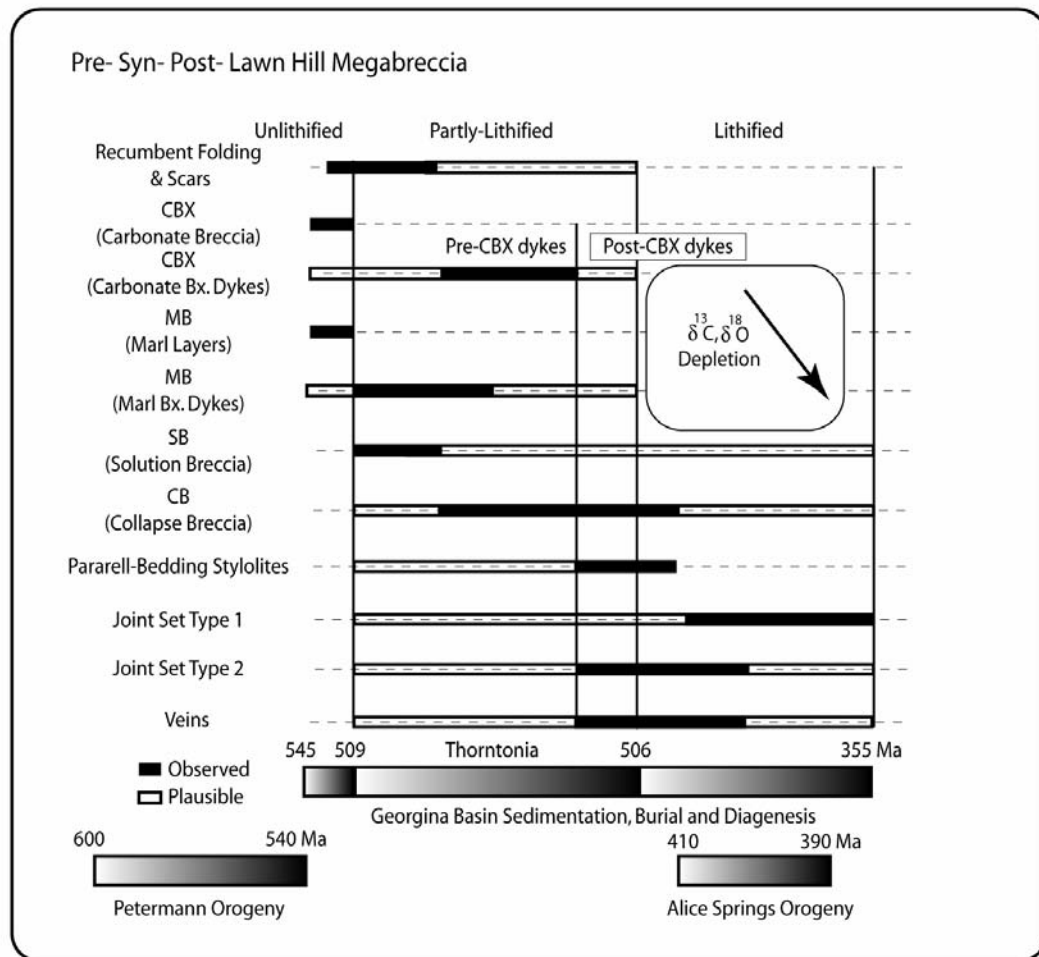
Fig. 6.23 Paragenetic reconstruction of the cross-cutting relationships used to reconstruct the temporal evolution of the sedimentary and tectonic events that contributed to the formation of the Lawn Hill Megabreccia. The diagram includes the early phases of breccia development followed by post-breccia events. The basin evolution led to a gradual depletion in both $\delta^{18}O$ and $\delta^{13}C$ (see text for discussion).

6.5.1.3   Palaeogeographic scenario

A reasonable palaeogeographic scenario is one in which the Thorntonia limestones formed in a shallow epicontinental sea around a topographic high, centred approximately 10 km northeast of the Century Mine. The occurrence of an internal ring of phosphatic limestones in the central part of the small circular platform, could be linked to possible ocean upwelling during sedimentation, governed by this palaeogeographic setting (De Keyser and Cook, 1972; De Keyser, 1973). For instance, Hallock et al. (1988) and Pomar et al. (2002) propose that topography-induced upwelling brings nutrient-rich cold waters to the shelf edge and produces an area of high organic production. This could explain the elevated phosphatic contents in these limestones.

The lithofacies assemblage forming the Lawn Hill Megabreccia more likely formed in a slope setting located seaward of a ramp environment (Fig. 6.24). Mass-flows, debris-flows and turbidites occurring in the Century Mine represent assemblages of these various sedimentary components. The lithofacies variation was a function of the ramp location and comprised barrier-bank complexes of skeletal carbonate, lagoonal carbonates, tidal flats, and supratidal sequences (Fig. 6.24). Lithofacies distinctive of barrier-bank complexes are evaporites, cherts and fenestral dolomites. Notice that these types of ramp have relatively low-angles (usually 1° to 15°) and most likely would be relatively stable. However, sedimentary ramps can evolve to steeper angles in case of fault movement along their margin, as discussed in Payros et al. (1999).
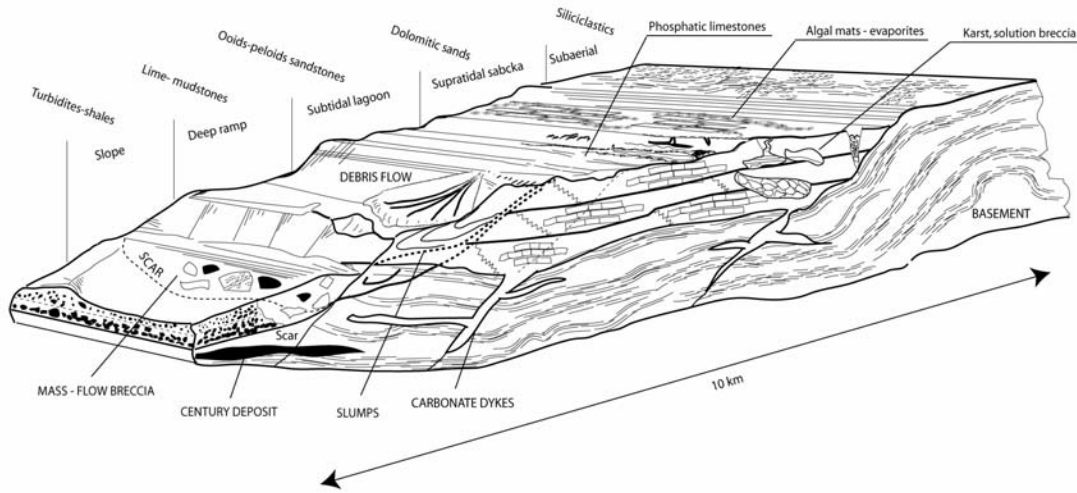
Fig. 6.24 3D Block diagram illustrating the variation of depositional environments across the Lawn Hill Outlier. The reconstruction is based on documented field relationships and lithostratigraphic interpretations of Szulc (1992) and palaeogeographic models proposed by Read (1985). Limestone exposure in the area proximal to the Century Mine is interpreted as part of a slope setting during Middle Cambrian times adjoined to a ramp of barrier-bank type. Recognised styles of brecciation find a logical collocation within this paleoenviromental setting. The 3D diagram illustrates also a possible influence of reactivation of basement structures controlling local steepening of the basinal slope. Superposition of a carbonate platform on a basement high produced by an asteroid impact may have also conditioned the ramp inclination allowing slumping within intertital and subtidal settings.

A contributing component to basal slip along the slope could have been also the localised, intrastratal occurrence of evaporites and dolomites (Fig. 6.8) that may have lubricated and weakened the marginal part of the ramp. For example, Aranburu et al. (2002) describe a close link between dissolution/precipitation processes (karstification) and the Valnero-Ruahermosa fault in the Jorrios Platform of the Basque-Cantabrian Basin, suggesting that a close interrelationship between meteoric circulation of fluids and limestone dissolution along the fault zone were likely to have occurred. As seen the variety of breccias identified in this study emphasise, in conjunction with observed

cavity fills, that karstic dissolution was also prominent in proximity of the Termite Range Fault zone.

6.5.2 Origin of the Lawn Hill Megabreccia - is it the result of an astobleme impact?

As discussed above, the timing of the Lawn Hill Megabreccia and dykes formation appears to be fairly constrained in an early synsedimentary phase, and as seen the synergy of several processes contributed to its formation. However, the data collected and relative interpretations allow only a partial discrimination of the causative agents. In this section three factors are considered: (1) the effect of eustatic variations; (2) the tectonic control; and (3) a meteorite impact.

Eustatic variations can be a prominent destabilising factor along a platform margin. Abrupt pore pressure decreases associated with the fall of eustatic sea-level may lead to drastic increase of differential stresses (Secor, 1965). However, steep inclination of the ramp is a requirement for such model, and therefore other mechanisms have to be invoked to explain the Lawn Hill event. The relative palaeogeographic location in respect to the Georgina Basin and the occurrence of CBX dykes in basement with trends suggesting reactivation of pre-existing basement faults is indicative of a possible extensional, tectonic component. However, another external process may have been contributing to the Lawn Hill Megabreccia formation - an asteroid impact.

Stewart and Mitchell (1987) define some important points regarding the Lawn Hill circular structure (firstly reported by Stewart, 1986) and its possible derivation from a Proterozoic cryptoexplosion - here briefly reviewed: (1) Shock deformation induced mosaic structures observed in quartz grains from shattered fragments (the existence of cone in cone structures is confirmed in this study, Fig. 6.25). Multiple intersecting sets of lamellae indicates impact pressures higher than 10 GPa for the central part of the Lawn Hill Outlier (Officer and Carter, 1991). However, at this location the Mesoproterozoic basement of the Upper Lawn Hill Formation is outcropping (see map in Fig. 6.1c). In fact, no shock deformation microstructures are visible in thin sections of chert breccia sampled in limestone. Additionally, the chert breccia is also found in other localities of the Georgina Basin suggesting that as mentioned previously part of the brecciation formed by solution collapse (Wilson and Hutton, 1980) and debris-flows. (2) "pahoehoe-like" melted rocks were observed at the centre of the inferred crater. (3) The broken folds in the breccia hardly resemble a syn- to post-Middle Cambrian impact. (4) The haphazard nature of the bedding in limestone further supports the hypothesis of a solution collapse.

These arguments were used to suggest that an asteroid impact took place before limestone sedimentation - which is in agreement with the above mentioned phosphate ring formed around the central basement high (Gum Hole Plain). Stewart and Mitchell (1987) remark also that the absence of signs of impact in the surrounding limestones might be the due to their relative distance from the impact site. Moreover a possible explanation for the absence of shatter cones in the Thorntonia Limestone would be a Middle-Cambrian synsedimentary impact - the lack of impact signs could be

consequence of the state of consolidation of the sediments. Shoemaker (1992) pointed out that the size and height of the central uplift are anomalously low compared to other impact structures. However, the topography may have been remodelled by later erosional processes soon after impact and Dypvik and Jansa (2003) suggest that in a submarine impact the crater morphology is generally devoid of well developed rims and also sedimentary processes inside and outside the crater can be variable, causing its reshaping.
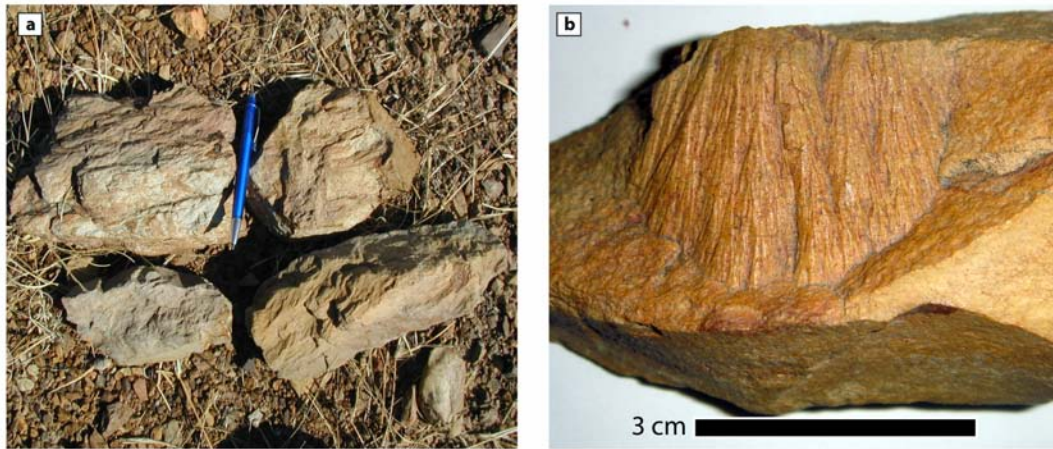
Fig. 6.25 Examples of shatter cones collected in the Gum Hole Plain. (a) Samples of shatter cones found in oxidised siltstones of the Upper Lawn Hill Formation. (b) Enlargement illustrating typical horsetail structure in quartz sandstone (Termite Range Formation). Shatter cones can be formed also in dyke intrusions and volcanic explosions, however if quartz grains display crossed lamellae (in thin section) due to impact they indicate pressure ranges that can be produced only by cryptoexplosion (Stewart and Mitchell, 1987; Shoemaker and Shoemaker, 1996).

A synsedimentary impact represents an attractive alternative to catastrophic gravity driven deposits associated with earthquakes (or tsunami). Dypvik and Jansa (2003) remark that admixtures of melted particles in these deposits (possibly

anomalously enriched in Iridium) would be a distinctive parameter. In this regard Shoemaker (1992) reports limited Iridium contents for suevite sampled in the Lawn Hill crater although this author suggests that the degree of contamination of melted materials can be variable and therefore a cryptoexplosion derivation is often hard to ascertain on this ground. A more recent contribution of Lindsay and Brasier (1998), which adds new carbon oxygen isotopic data on Middle-Cambrian limestones (see Fig. 6.22) led these workers to conclude that the impact predated the limestones deposition, as suggested by Stewart and Mitchell (1987), and Shoemaker and Shoemaker (1996).

Isotopic signatures reported by Lindsay and Brasier (1998) are similar to those presented here on carbonate breccia. The carbonate breccia sampled by Lindsay and Brasier (1998) in the northern part of the annular structure also revealed values similar to the sedimentary limestones confirming that these rocks and the breccia lithified after the meteorite impact and are normal marine carbonates. Lindsay and Brasier (1998) consider seawater derived, isotopic signatures a distinctive parameter as markedly lighter values would result from melting of carbonates after an impact. However, the lack of anomalous isotopic signatures may have been a function of distance from the main site of impact. Also in the case of sub-marine impact the isotopic signature would be more likely seawater dominated if the sediments were not yet lithified.

Further investigations, on the Iridium content in limestones might be a possible way to ascertain a Middle Cambrian impact provided that evidence of melted fragments can be ascertained. However, the evidence of shock induced, intersecting micro-lamellae in quartz crystals represents a strong indication that a cryptoexplosion did occur in the Lawn Hill Outlier. What remains uncertain is the timing of this event and

therefore its possible connection to the Lawn Hill Megabreccia. Multiple depositional/erosional scars provide an indication that the megabreccia, more likely, originated from a sedimentary process (multiple debris-flows and turbidites). The data are however insufficient to completely discount the direct involvement of a sub-marine impact.

Chapter 7

Complexity and self-organisation

Acknowledgement of Contributions

N.H.S. Oliver – normal supervisory contributions

7.1.   Introduction

Most of this thesis concerned the study and interpretation of the dynamical evolution of different geological systems. Research questions were focused on the mineral potential of the Lawn Hill Region and on the origin and timing of rare geological events such as the genesis of Century and the Lawn Hill Megabreccia event. Answers to these questions were all derived from recognised patterns, explored qualitatively and quantitatively with the aid of computational tools.

In this conclusive chapter, new theoretical models (chaos, complexity, fractals, attractors, self-organisation, etc.) are combined with information derived from previous sections, to better define the origin of some of these "exclusive patterns". Introduced theoretical concepts are then used to propose a theoretical discussion on the genesis of Pb-Zn mineral deposits.

7.2.   Complexity and self-organisation

Earlier chapters focused on different scales and perspectives of the Lawn Hill Region, allowing the identification of several interrelationships within, and among, presented models. Each "universe" (e.g. a geological terrain, a mineral deposit, a deformed structure, a textural style) contains in fact other sub-universes that are often characterised by complex interrelationships different from the larger scale counterpart and with their own *emergent* properties (Flake, 1998). A system also contains both

stochastic and deterministic components, and can display similar organisation among different scales (self-similarity). In this regard, Flake (1998) distinguishes three main groups of rules that are useful to consider when dealing with complex systems: (1) Collection, Multiplicity and Parallelism; (2) Iteration, Recursion, and Feedback; (3) Adaptation, Learning and Evolution.

7.2.1.   Collection, Multiplicity and Parallelism

Complex systems with emergent properties are often highly *Parallel Collections* of similar units. A natural example could be a colony of bees or ants that are numerous groups of equivalent individuals (agents) although they accomplish specialised tasks. *Multiplicity* considered as system duplication in space can be also seen in geological systems. A mineral deposit often comprises intricate, irregular networks of veins that formed ideally following the same ore genetic process. The spatial distribution of mineral grades could be seen as an example of specialisation, because the same type of brine (e.g. within a Pb-Zn system) can interact differently, via feedback relationships with the environment producing different paragenetic styles (e.g. Sedex, MVT and others).

7.2.2.   Iteration, Feedback, and Recursion

Iteration is similar to multiplicity except that it develops in time rather than in space. A SEDEX-type deposit (e.g. Large et al., 1998; Schardt et al., 2006) is composed of numerous laminae and bands derived from sequential deposition of mixtures of sediment and sulphides. Also the periodicity of hydrothermal pulses can be thought as an example of iteration. In this context, a *Feedback* relationship controls the system evolution in time. The feedback is represented by the interaction of a system with its environment. For instance, if the system is a brine precipitating mineralisation the outcome of this process will be strongly controlled by the environment parameters and by how they evolve in time, because the system can also actively modify the environment. The morphology of a reaction front created by brines diffusing in a host rock will be then strongly dependent on the type of the occurring feedback relationship (e.g. Ciobanu and Cook, 2004). *Recursion* represents more the path that arises from the combination of iteration and feedback relationships. The recursion of systems produces energetically convenient structures (self-similar) or fractal objects in nature. The term *fractal* was firstly introduced by Benoit Mandelbrot (Mandelbrot, 1983; Flake, 1998; Barnett et al., 2005) who used it to describe the geometry of non-Euclidean objects. Fractals are self-similar on multiple scales (e.g. a fern leaf looks like a fern tree) and their dimension is fractional, Fig. 7.1.
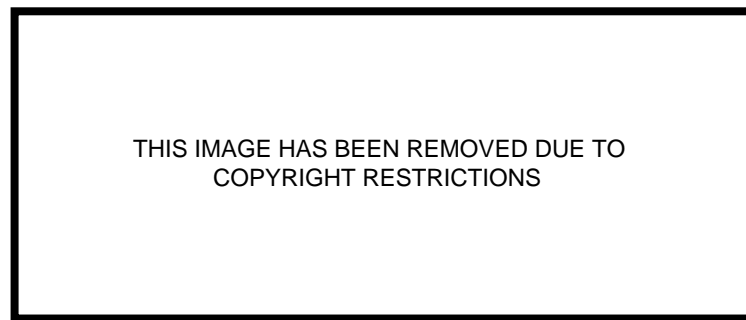
Fig. 7.1 Mandelbrot-set and relative enlargement views of smaller details on the edge of the Cardioid. Each enlargement contains more detail and is composed of self-similar patterns that are slightly rotated copies of their neighbourhood. From Mandelbrot (1983).

7.2.3.   Adaptation, Learning and Evolution

Adaptation can be seen as the combination of *Multiplicity* and *Iteration*. This can be considered equivalent to natural selection in a biological system, in which only the fittest individuals survive within multiple groups of agents and they reproduce (iteration) leading to adaptation of the whole collection. However, the concept can be extended to a geological context using adaptation to qualify how a mineral deposit evolves in response to changes in pressure and temperature or other thermodynamic variables. Reciprocal feedback type relationships in space (multiplicity) and time (recursion) control these modifications. In summary, a system is usually governed by simple rules repeated in time and space and its evolution is strongly influenced by feedback type relationships. These simple rules are, for instance, represented by fractals.

7.2.4.   Fractals, attractors and self-organisation

Recent theories, derived from experimental mathematics (e.g. the Mandelbrot-set in the 80s), offer a description of this latter concept defined symbolically by a power law relationship of the following type:

$$N_i \approx r_i^{-D} \tag{7.1},$$

where N_i is the number of objects of size r_i and D is the fractal dimension, a scaling exponent introduced by Mandelbrot (1967; 1983). The equation (7.1) known as fractal scaling relation seems to hold for many natural systems (Turcotte and Rundle, 2002), providing a mathematical explanation for at least some of the patterning observed in nature. Probably the most striking geological example of a complex system reducible to a fractal object is the spatial distribution of faults in the lithosphere (e.g. Sornette, 1991;1999). Fractals and self-similarity are related to the concept of self-organisation. The idea of an Earth's crust self-organised to minimise the energy in response to plate tectonic motion could be well explained by classic thermodynamics, but the use of self-organised-criticality links this re-equilibration process to the formation of observable and non-observable (e.g. chemical) patterns (e.g. Grasso and Sornette, 1998). In other words, natural systems in certain conditions tend to reorder "spontaneously" forming fractals. This system behaviour was firstly recognised in classical experiments in chemistry such as the Belousov-Zhabotinski reaction or the Bénard cell. In the latter an external constraint is imposed to the system causing its reorganisation in convective cells (Nicolis, 1995; Haken, 2004). These experiments led to the idea that in a certain limiting condition a system breaks its symmetry spontaneously (*Bifurcation,* Fig. 7.2), and demonstrated intuitively that disorder can be chaotic (deterministic). The deterministic component can potentially be mapped also when dealing with more complex cases (e.g. it might hold also for the patterning of faults in the crust). For example, there is interest in constructing more refined models based on self-organisation that could predict the future location of earthquakes (e.g. Sornette, 1999).

However, the validity of these models has not yet been demonstrated convincingly, probably because of the incompleteness of information in the geological applications, The problem is also apparent in other fields such as Economics, where a significant wealth of data exists (e.g. the variability of time series for the stock market), and the application of chaos and self-organisation seems to be predictive only for a limited extent (on a short-time scale).
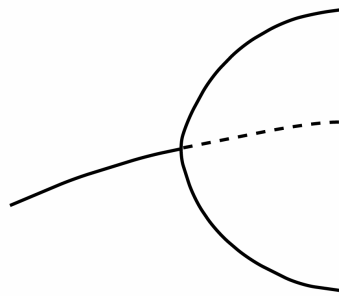
Fig. 7. 2 Bifurcation diagram representing a change from a single state of equilibrium to two stable phases. Continuous line represents stable conditions, dashed line represents an unstable condition.

The initial considerations made regarding deterministic and stochastic processes (Chapter 2) helped their distinction, but here chaos and self-organisation provide more richness to this "binary" subdivision. This makes it difficult to define the proportion of a stochastic component in a system. In other words, measuring the randomness of a system does not provide indications relative to its statistical nature, because a deterministic process can generate indistinguishable random distributions as well. In this regard this concept is explained referring to the example of the *Logistic map* (a univariate system):

$$x_{t+1} = 4rx_t \left(1 - x_t\right) \tag{7.2},$$

where r is a parameter that can be set to reflect the reproduction rate in time (t) of a generic population, and four is a numeric constant used to constrain the interval of variation of x_t between [0, 1]. Flake (1998) illustrates several examples of how the logistic function behaves for specific values of r (Fig. 7.3). The interesting point is that this deterministic relationship assumes a chaotic (nonlinear) variation for a value ($r = 1$) that approximates a random statistical distribution although yet fully deterministic. Other examples include in higher dimensional space the *Henan map* (a bivariate system) or the *Lorenz attractor* (a multivariate systems). These mathematical experiments based on iterative mapping provide the formal demonstration of how a simple linear process can evolve into nonlinear chaos. A good approach to handle the more complex cases (in multivariate examples) is to represent their variation in a *phase space*, which is a representation of the evolution of the considered system variables in time, as illustrated in Fig. 7.4, for the Lorenz attractor. An attractor is a representation of the whole time trajectory of the system in phase space (Nicolis, 1995). Usually natural systems are dissipative therefore they can be approximated to quasi periodic motion (Barnett et al., 2005). In such cases the attractor often has an irregular shape and is therefore defined as a *Strange Attractor*. Phase space representations are useful because the attractor may have a fractal dimension suggesting that the system evolves following specific iterative rules. Problem envisioning in phase space allows then to

identify at least the possible deterministic component of a system outlining the existence of a chaotic motion. However, pattern formation and consequent ordering of a certain structure can arise from either a stochastic or a deterministic process (i.e. existence of stochastic and deterministic fractals). The interpretation of the significance of an attractor in the more complex examples is also aggravated by a remaining component of random noise (Chatterjee and Yilmaz, 1992). Identification and iterative mapping of patterns or bifurcation is possible, but the system selection of relative states of equilibrium remains governed by chance (e.g. coin tossing in Chapter 2; Haken, 2004). Despite the limitations, if a component of order is recognised in a system and a deterministic model is suitable to map its evolution, then prediction is possible in the simplest cases (few variables) or at least in a short-timeframe (e.g. the successful prediction of the path of hurricanes on the order of days; Flake, 1998). Beside predictability the identification of a fractal component in a system can be used to better understand the origin of certain patterns, and how the system converges to, or diverges from a certain condition.
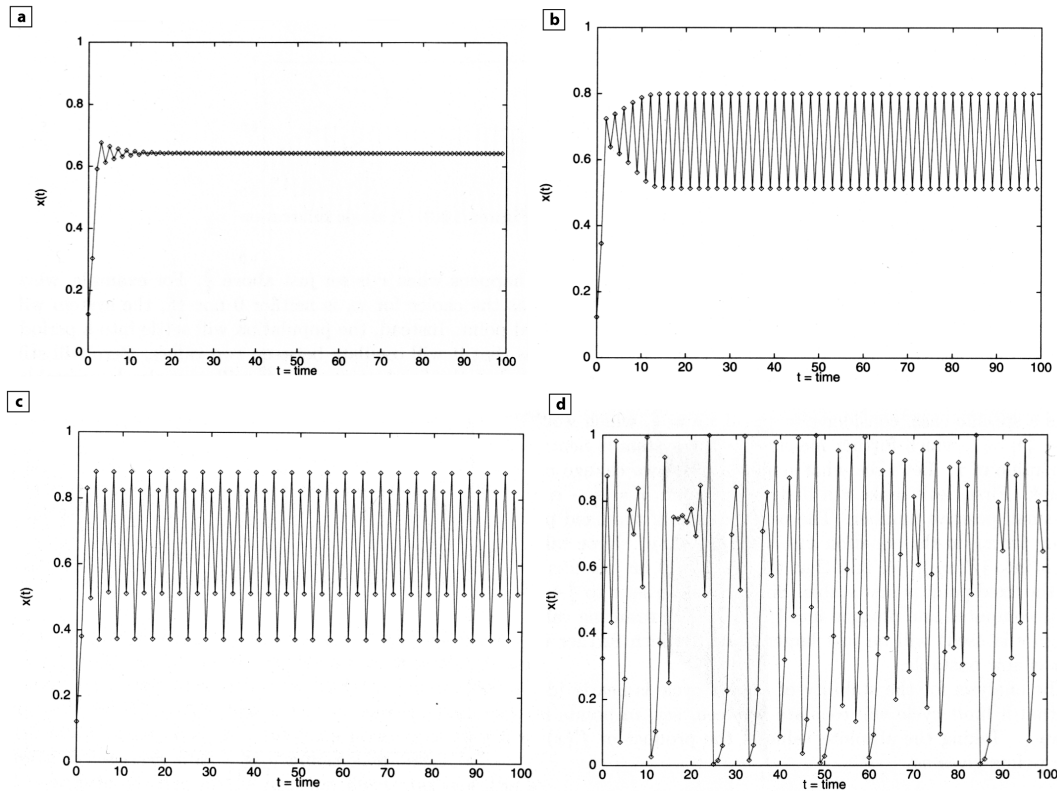
Fig. 7.3 Plots of logistic function for different values of (*r*). (a) Logistic map with *r*=7/10. The time series stabilised to a constant value *x*(t). (b) Logistic map with *r*= 8/10. The time series evolves into a periodic two limits cycle. (c) Case similar to b, with *r*=88/10, except that the period has four limits per cycle. (d) Logistic map with *r*=1. This latter example has a chaotic time series approximating noise (adapted from Flake, 1998).

7.3.   Practical applications to the Lawn Hill Region

In this final section we discuss the application of introduced concepts on self-organisation and chaos in complex systems. The objective is to use some of the results obtained in previous chapters to propose a theoretical discussion that focuses on the genesis of Pb-Zn mineral deposits.
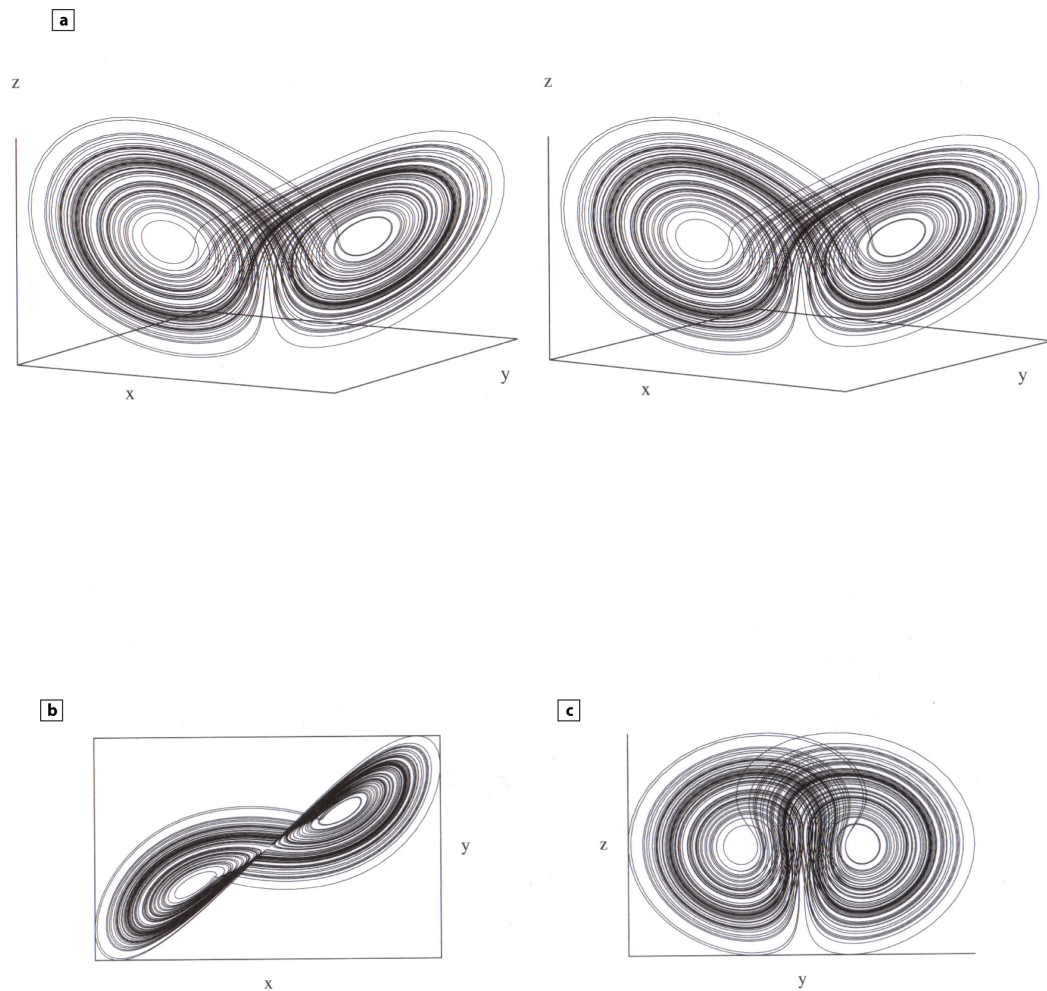
Fig. 7.4 Perspective views of the Lorenz attractor in phase space. (a) Stereoscopic diagram of the strange attractor. To view simply cross your eyes until the image overlaps then refocus.(b) Sectional view in *XY*-plane. (c) Sectional view in *YZ*-plane (adapted from Flake, 1998).

7.3.1.   The fractal nature of faulting and mineralisation

Assuming that self-organisation criticality is a valid model to describe the deformation of the crust (Grasso and Sornette, 1998), by analogy it could be extended to the fault patterns observed in the Lawn Hill Region. The multi-scale analysis (Chapters 3, 4, 5) has outlined a component of self-similarity among structures that would favour this interpretation (i.e. observed self-similarity in the fault patterns at regional to deposit scale). The advantage of working with a geological system is that often system transformations are partial allowing evaluation of multiple states of evolution. The information gained is sufficient to understand the variables that effectively lead to macroscopic fractal geometries. Other techniques can also be helpful in defining non-morphological fractal properties of the system, because self-organised patterns can also form during chemical reactions (Ciobanu and Cook, 2004). In the Lawn Hill case a component of structural self-similarity among faults has been documented at different spatial and temporal scales (Chapter 3 and Chapter 6). Self-similar ordering is also evident in the base metals that have close spatial association to faults as demonstrated in Chapter 3 (correlation between prospects/deposits and faults), but is also valid for a component of base metals at Century (as illustrated by the 3D reconstructions of Chapter 4 and 5). These patterns suggest that similar fractal functions controlled the spatial and temporal organisation of faulting and fracturing and vein-style mineralisation at Century as well as in veins/lodes and prospects surrounding the giant

ore deposit. The following equations could be defined to describe the spatial association between faulting and mineralisation:

$$\nabla M = \nabla P_s \qquad\qquad (7.3),$$

for a system in equilibrium. The (7.3) becomes in a time series equal to

$$\nabla \dot{M} = \nabla \dot{P}_s \qquad\qquad (7.4).$$

In equation 7.3 ∇M is the spatial distribution of mineralisation (M) and ∇P_s is the permeability structure (P). In equation 7.4 the quantities expressed are the respective rate of variation in space and time of M and P. The fractal component in space of epigenetic mineralisation can be also inferred simply considering the geometrical branching of Pb-Zn mineralised veins because their morphology mimics the bifurcation diagrams of (Fig. 7.2 Nicolis, 1995; Flake, 1998) and approximate a power law size distribution (Mandelbrot, 1967). ∇P_s is not only controlled by mechanical processes such as brittle faulting and fracturing of rocks. There is also a chemical reaction and transport component that regulates both ∇P_s and ∇M. Further complication is also introduced by an "alternative" component of ∇M which is independent of ∇P_s. Notice that it may be ordered as well, but its degree of ordering is governed by a different iterative (stochastic or deterministic) process. For example, in an exhalative

Pb-Zn system a purely exhalative component which forms at seawater/sediment
interface would be defined by a relationship of this type:

$$\bigtriangledown M \not\equiv \bigtriangledown P_s \qquad\qquad\qquad (7.5),$$

involving possible self-organisation of mineralisation during early deposition of
sulphides (e.g. the chemical oscillatory behaviour induced by pycocline fluctuations,
Chapter 3). The periodicity and patterning is however unrelated to $\bigtriangledown P_s$. However, for
a stringer zone where replacement fronts form in response to lateral diffusion of Pb-Zn
brines, $\bigtriangledown P_s$ will be controlling the spatial distribution of mineralisation (eq.7.3).

7.3.2.   The mineral system attractor

The dynamic evolution of a mineral system (eq. 7.4) could be envisaged using a
strange attractor, which reflects the quasi periodic nature of this dissipative system,
meaning that each modification will contribute to a loss of energy or matter (Chatterjee
and Yilmaz, 1992). In a Pb-Zn mineral deposit, sulphides can be (re)mobilised or
dispersed (Chapter 5, Fig. 7.5a). There is then the possibility to deplete or enrich
(upgrade) the initial base metal reservoir introducing epigenetic mineralisation.
However, from the definition of a dissipative system a loss of matter/energy is required.
The process is invariant working for any scale of transformation (small or large sub-
systems, Fig. 7.5b). Each transformation causes a loss of matter or energy within the

considered sub-system. The process is then self-similar. A practical example that fits a Pb-Zn scenario could be the evolution of a sedimentary basin during compaction and diagenesis. To compact a basin, the expulsion of basinal fluids is required, and also dissolution of certain mineralogical species (e.g. quartz, carbonates etc.) occurs involving the transfer of solutes in relatively empty domains such as pores, cavities, fractures or faults. In this regard, the chemical and physical transformations reflect the general tendency of energy to equally distribute within all available states (Chapter 2). A small scale transformation will cause a local redistribution of matter/energy in its proximal neighbourhood, for example, a fracture filled by hydrothermal minerals. Following this consideration rather than an internal process generating local permeability enhancement, perhaps an external process involving large scale solution/precipitation reactions would be more appropriate to incorporate base metals in a dissipative system (Fig. 7.5c, d). For example, if a local transformation produces a loss of volume (e.g. hydrocarbon maturation producing low-pH solvents may dissolve silica in shales creating secondary porosity) the neighbourhood will react to equilibrate such permeability imbalance. Therefore, to introduce epigenetic mineralisation, a replacive process would be energetically convenient, because it does not require a large change of volume to introduce base metals within the system.

a   Mobility of base metals

Remobilisation (R)

Syngenetic →(R)→ Diagenetic →(R)→ Syntectonic

Depletion-
Dispersion   External
(D)   introduction
                 (M)

(D)   (M)   (D)   (M)

b   Scaling and self-similarity   c   Dissipative behavior

T   Vi

T

T   T   (R)   Vf

T   (M)

d   Neighborhood Re-equilibration   Seal   Vs

T2   T1-T2

T1

∮ T < > 0
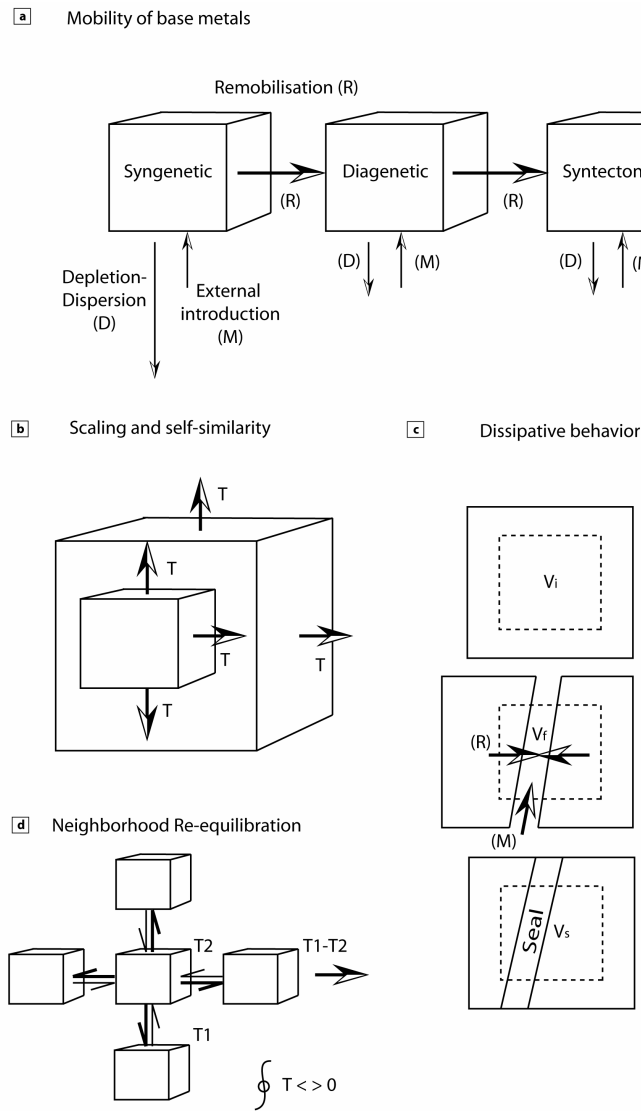
Fig. 7.5 Schematic diagrams representing the basic rules that constrain the mineral system evolution. (a) Possible transformations in a mineral deposit involving chemical and mechanical redistribution of sulphides. The processes are mainly Remobilisation (R), Dispersion (*D*) and Mobilisation (*M*). (b) Example of transfer of energy/matter from a small- into a larger-scale system (environment) containing the dissipative sub-system. (c) Similar case applied to a vein sealed by hydrothermal minerals. (d) Same dissipative behaviour although in space. Arrows outline the imbalance corresponding with dissipative behaviour and relative non-conservativity, expressed by the integration in a closed cycle.

The mineral system attractor converges toward a specific condition leading the spatial distribution of mineralisation to gain a fractal component that is similar to the fractal component present in the evolving permeability structure (e.g. newly developed fractures tend to be spontaneously filled by mineralised veins). Clearly a number of exceptions apply to this example (i.e. a hydrothermal mineralising fluid must be present, veins may be barren). However, any transformation involving mineralisation either remobilised or externally introduced will work according to the following:

$$\left(\triangledown M_{syn} + \triangledown M_{epi} \right) \mapsto \triangledown P_s \tag{7.6}$$

Subscripts (*syn, epi*) refer respectively to syngenetic and epigenetic mineralisation. Notice that equation 7.6 represents (in case of Pb-Zn deposits) either a SEDEX or an MVT deposit. Overprinting affects the syngenetic component of the mineralisation where the permeability variation is more intense such as portions of the mineral deposit intersected by faults and subject to new hydrothermal pulses.

Two considerations are thus made using the theoretical models on self-organisation and accepting a fractal component for the mineral system, i.e. replacive processes are favoured, and the system tends during its evolution to converge to an epigenetic style. These have implications for the understanding of the genesis of Pb-Zn mineralisation. In a SEDEX-type ore there should be evidence of both styles of

mineralisation (dependent   and independent from $\triangledown P_s$ equations 7.3 and 7.5).
Exclusively syntectonic or late-diagenetic ores represent the epigenetic end-member
that would be equivalent to the final stages of the trajectory in phase space of an
attractor representing the evolution of a SEDEX system (eq. 7.4), because mineralising
brines get access to the host as a direct function of $\triangledown P_s$. In agreement with intuitive
interpretations provided in Chapter 5, I conclude that the genesis of shale-hosted and
relatively low-grade metamorphosed or unmetamorphosed Pb-Zn deposits found in the
Mount Isa Inlier might be assessed by evaluating the proportion of mineralisation
associated to the permeability structure $\triangledown P_s$ and throughout the identification of the
type of self-similar ordering occurring (Fig. 7.6). Understanding and mapping the
exclusive fractal distributions in a mineral deposit may provide a chance to understand
how and when the mineralisation formed. In this context, mathematical models of
reaction fronts that evaluate nonlinear instabilities represent the most direct application
of self-organisation in porous media flow (e.g. Chadam et al., 1986; Xin et al., 1993).
However, a close understanding (e.g. depending on the mineral system considered) of
the parameters controlling the stability of reaction surfaces is required to establish the
condition in which instability occurs (i.e. in the form of morphological fingering,
scalloping etc., Fig. 7.6).
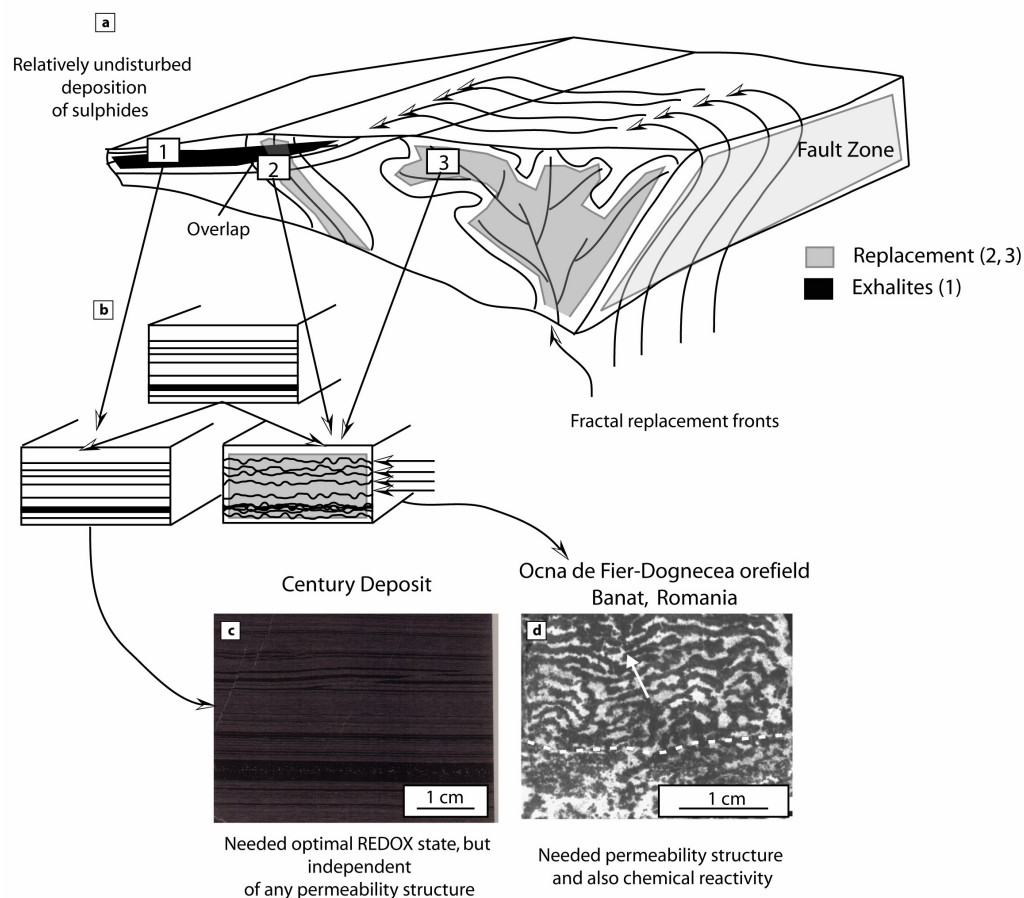
Fig. 7. 6 Diagram summarising distinctive patterns as a function of spatial location within an exhalative system. (a) Schematic illustration showing the spatial location of different styles of mineralisation as direct function of their distance from the source of hydrothermal Pb-Zn brines. (1) Zone where the mineralisation occurs in laminae deposited with sediment at the seawater/sediment boundary. Mineralisation in this case is unrelated to the permeability structure. (2) Overlapping zone in which either syngenetic or epigenetic mineralisation is present. (3) Feeder where predominantly the sulphides are hosted in veins. (b) Evolution of exhalites as a function of their spatial location and consequent interaction with later hydrothermal fluids that can either add, remove or simply transform the base metals. (c) Relatively undisturbed laminae of sphalerite at Century. (d) Intense modification of sedimentary bedding (arrow) in a reaction front in the Ocna de Fier-Dognecea Orefield, Romania. The latter comparison is a clear example that in certain cases it is possible to use the spatial organisation of minerals and their relative morphological character to infer the timing of mineralisation.

Chapter 8

Conclusions

Acknowledgement of Contributions

N.H.S. Oliver – normal supervisory contributions

8.1   *Summary of the thesis conclusions*

A summary of the conclusions is presented for each chapter of the thesis that concerned the three geological studies presented. The general research question and main purpose of the thesis, was an evaluation of how modern computational techniques and quantitative geology can substantially improve our understanding of a geological system. The thesis results have confirmed the benefit obtained by utilisation of modern computational tools in solving classical geological problems. WofE Modeller, GoCAD and FLAC have extended my interpretation of the various features and geological patterns observed leading to better, multi-scale classification. This has been demonstrated by the following results concerning the predictive modelling undertaken in (Chapter 3): (1) Favourability KD models produced for SEDEX mineralisation and VS ores suggests that most of the known mineral deposits and prospects occur in areas that are more favourable to the formation of SEDEX style ore; (2) KD models indicate favourable stratigraphic intervals based upon expert driven scores assigned; (3) the DD-modelling showed that fault intersections appear to be more favourable sites for the deposition of Pb-Zn mineralisation of any style. However, fault intersections were also among the most troubling patterns when assessing conditional independence; (4) the data driven model suggests that new Pb-Zn prospects may be localised in proximity of the Termite Range Fault; (5) moreover the DD model indicates new areas that were not previously considered prospective (e.g. north of the Edith cluster and in the northern part of the Kamarga Dome area); (6) the integration of KD-models with DD-models

allowed definition of degree of favourability for SEDEX and VS mineralisation in areas proximal to the Termite Range Fault. Potential for SEDEX has been outlined by the favourability map north of the Edith cluster of vein style deposits/prospects.

Favourability and probabilistic models offer the advantage of integrating the information and synthesising it in map format to facilitate exploration. Favourability KD models can be also used to assess the relationship between characters typical of certain styles of mineralisation and their relative association to known mineral occurrences.

In Chapters 4 and 5, the problem of ore genesis at Century was investigated and tested using 3D geometrical and 2D numerical techniques providing insights on how the ore deposit might have been evolving in time. Results from structural modelling developed at camp- to deposit-scale have outlined the possible interaction between regional structures and local structures modelled inside the mineral deposit. This suggests that some of the regional vein style mineralisation may have been the product of remobilisation of metals. This may explain the relatively high tonnage observed at Silver King (proximal to Century) compared to other lodes that could be linked to regional scale redistribution of base metals from Century. However, this could not be proved. Locally (at the deposit-scale) internal faults were classified broadly in three sets NE to ENE, NW and E-W. NE and ENE faults were possibly active since early stages of deposition according to the thickening observed form reconstructed isopach-maps. Regional scale thickening interpreted from seismic profiles north of Century in the

Elizabeth Creek Fault Zone is consistent with the role of ENE faults as growth faults that controlled sedimentary patterns in the Lawn Hill Region.

Two dimensional fluid flow modelling indicated that local extension may allow lateral infiltration of fluids. However, the models encountered significant problems after several steps of extensional deformation due to the limitation of the Mohr-Coulomb constitutive model in the simulation of relatively unconsolidated materials (e.g. unlithified argillaceous sediments). On the other hand, the models run for the compressional scenario (Broadbent, 1999) have clearly illustrated how fluid flow tends to be focused in more permeable domains – the faults, and is distributed vertically rather than the horizontal, lateral flow required for the replacement model. This led to the conclusion that a replacement model could not readily be applied to the Century case, at least during compression.

Results from Chapter 5 represent an extension of the results obtained in Chapter 4. In Chapter 5 all datasets become fully three-dimensional both in the structural property model and also in the numerical simulations. From the analysis of 2D projection maps of grade and thickness variability we step into a multi-layer model coupled with a 3D deformed S-grid that was used as a base for DSI 3D interpolation of mineral grades. A better understanding of how remobilisation could work after lithification of relatively impermeable layers lead to the following interpretations: (1) the deposit was locally influenced by later hydrothermal fluids that (re)mobilised Pb-Zn ores at least at the metre scale along some fault/fractured domains; however, the extent of remobilisation processes is difficult to ascertain for the larger scale; (2) the deposit

zoning varies depending upon the scale of observation considered. At small scale below a diameter of 100 m there is a rapid variation of mineral grades (either sharp increase or decrease of mineral grades depending upon the stratigraphic interval and base metal pattern considered). In particular, across adjacent horizons the vertical correlation of depletion and enrichment in shale/siltstone layers of Pb-Zn ore supports the role of faults as (re)mobilising agents; (3) (re)mobilisation therefore was interpreted as a restricted process - permeability driven, and also a function of the hydraulic gradients established between the bedded sulphides, the feeder/fault zone and other barren, and ideally more permeable horizons, within the mineral deposit; (4) If the (re)mobilisation is governed by permeability patterns, then when the permeability structure changes during basin evolution also (re)mobilisation would change accordingly; (5) moreover, base metals would be more likely remobilised early when the host rock is not yet lithified, because permeability is higher; (6) this consideration also provided a model for the different zoning observed. The broad zoning of Pb-Zn-Mn, which is a typical character of SEDEX deposits, more likely would form during early stages and therefore can be considered of an exhalative nature; (7) In a later stage after compartmentalisation the permeability structure of a mineral deposit is better defined and therefore any modification is confined to areas that have sufficient permeability to allow fluid percolation and therefore facilitate fluid assisted chemical (re)mobilisation. Also mechanical remobilisation is a possible alternative although limited in scale and to softer sulphides, such as galena; (8) on the basis of all considerations made I concluded that Century is more likely an exhalative system. However, the mineral deposit may

have experienced additional input of base metals, for example during inversion or when later vein style ore was emplaced. Although the veins themselves may represent a remobilised product of early synsedimentary stockworks, Pb-Pb ages on galena support a model in which at least some additional Pb was introduced well after diagenesis and lithification of the host.

3D FLAC models displayed negligible variations in the pore pressure distributions if compared with 2D models, confirming the results obtained in the initial simulations. 3D numerical modelling results showed that fluid flow could not laterally move through the shale intervals, unless significant secondary permeability enhancement (developed by hydro-fracturing) would allow these units to reach the same order of magnitude of permeability assigned to the faults – a case not observed in the available exposures of the mineral deposit, which displays scarce abundance of mineralised veins. When shortening is applied to the models, also relatively impermeable units (shales), tend to become overpressured causing expulsion of fluids, which might explain the presence of localised sub-vertical cracks sealed by sulphide and carbonate/quartz precipitates. Numerical models were integrated with the results obtained from the 3D geometrical and property modelling to illustrate also that fluid flow changes accordingly to the permeability structure evolution.

In Chapter 6 a third geological problem concerning the timing and genesis of the Lawn Hill Megabreccia was addressed. The observations collected in the field coupled with spatial analysis led to the following conclusions. The timing of the Lawn Hill Megabreccia is constrained to be synchronous with the depositional age of the

Thorntonia Limestone. The structural features (slumps, truncated folds etc.) coupled with the paragenetic study of the distribution of flow breccia dikes (CBX) paragenetic relationships with the flow breccia (MB), and isotopic data, support a model in which the source of the breccias were originally part of the sedimentary sequence and were subsequently reworked and redeposited or injected in reactivated faults. These processes may be explained easily by simple gravity driven failure of the platform, assisted by tectonic destabilisation of the margin, in the eastern part of the Georgina Basin. However, a sub-marine meteoritic impact is also a plausible alternative. (4) The integration of qualitative and computational/quantitative models provides invaluable feedback regarding validation of modelling results. In other words, the two approaches should be combined to avoid oversimplification and misinterpretations.

In Chapter 7 we considered the complexity of a geological system from an alternative perspective: fractals and self-organisation are viable non-linear models of geological complexity. The chapter reflects a purely theoretical approach to geological complexity. Complex systems or chaotic systems can ideally be reduced to simple laws repeated in time and space (e.g. fractals, attractors). I concluded the thesis suggesting future directions using these approaches, which hitherto have not been applied by geologists because of the high-level mathematical background required. However, new software tools such as Matlab can substantially assist in the usage of non-linear approaches such as Neural-Net learning and classification of geological complexity. The advantage of these techniques is essentially their capability of exploring the deterministic component of a chaotic system. To conclude, these methods may provide

better prediction in mineral potential mapping and also help understanding ore genesis, and other complex geological scenarios such as the Lawn Hill Megabreccia.

8.2   General concluding remarks

A general conclusion can be made concerning computational modelling and quantitative geology. They certainly extend our capability of analysis, however I believe that understanding of geological objects is still largely based on the geologist's intuitions. Models must be then validated using either additional quantitative methodologies, but also integrating geological observations.

References

Adshead-Bell, N.S., 1998. Evolution of the Starra and Selwyn High-Strain Zones, Eastern Fold Belt, Mount Isa Inlier: Implications for Au-Cu Mineralization. Economic Geology, 93, 1450-1462.

Agterberg, F. P., 1967. Computer techniques in geology. Earth-Science Reviews, 3, 47-77.

Agterberg, F. P., 1974. Geomathematics. Elsevier, Amsterdam, 596 p.

Agterberg, F. P., 1989. Systematic approach to dealing with uncertainty of geoscience information in mineral exploration. In: A. Weiss (Ed.), Application of Computers and Operations in the Mineral Industry: Proc. 21st APCOM Symposium. Colorado Society of Mining Engineers, Littleton, pp. 165-178.

Agterberg, F. P., 1992. Estimating the probability of occurrence of mineral deposits from multiple map patterns. In: D. F. Merriam and H. Kurzl (Eds.), The Use of Microcomputers in Geology. Plenum Press, New York, pp. 73-92.

Agterberg, F. P., 2001. Appreciation of Contributions by Georges Matheron and John Tukey to a Mineral-Resources Research Project. Natural Resources Research, 10, (4), 287-295.

Agterberg, F. P., Bonham-Carter, G. F., 2005. Measuring the Performance of Mineral-Potential Maps. Natural Resources Research, 14, (1), 1-17.

Agterberg, F. P., Bonham-Carter, G. F., Cheng, Q. M., Wright, D. F., 1993. Weights of evidence modeling and weighted logistic regression for mineral potential mapping. In: J. C. Davis and U. C. Herzfeld (Eds.), Computers in Geology-25 Years of Progress. Oxford University Press, New York, pp. 13-32.

Agterberg, F. P., Bonham-Carter, G. F., Wright, D. F., 1990. Statistical pattern integration for mineral exploration. In: G. Gaál and D. F. Merriam (Eds.), Computer Applications in Resource Estimation. Pergamon Press, Oxford, pp. 1-21.

Agterberg, F. P., Cheng, Q., 2002. Conditional Independence Test for Weights-of-Evidence Modeling. Natural Resources Research, 11, (4), 249-255.

Agterberg, F. P., Robinson, S. C., 1972. Mathematical problems in geology [with discussion]. International Statistical Institute Bulletin, 44, 567-595.

Akande, S.O., Horn, E.E., Reutel, C., 1988. Mineralogy, fluid inclusion and genesis of the Arafu and Akwana Pb-Zn-F mineralisation, middle Benue Trough, Nigeria. J.Afr. Earth Science, 7, 167-180.

Albertao, G. A., Martins, J., Paulo P., 1996. A possible tsunami deposit at the Cretaceous-Tertiary boundary in Pernambuco, northeastern Brazil. Sedimentary Geology, 104, (1-4), 189-201.

Algeo, T. J., Maynard, J. B., 2004. Trace-element behavior and redox facies in core shales of Upper Pennsylvanian Kansas-type cyclothems. Chemical Geology, 206, (3-4), 289-318.

Allen, J. R. L., 1982. Sedimentary Structures - Their Character and Physical Basis. Elsevier, Amsterdam, Vol. 1, 593 p.

Allmendinger, R. W., 2002. StereoWin. http://www.geo.cornell.edu/geology/faculty/RWA/RWA.html.

Amstutz, G. C., El-Goresy, A., Frenzel, G., Kluth, C., Moh, G. H., Wauschkuhn, A., Zimmermann, R. A. (Eds.), 1982. Ore genesis; the state of the art. Berlin, Springer-Verlag, Federal Republic of Germany, pp. 804.

Anderson, G. M., Macqueen, R. W., 1982. Ore deposit models; 6, Mississippi valley type lead-zinc deposits Geoscience Canada 9, (2), 108-117.

Andrews, L. M., Railsback, L. B., 1997. Controls on stylolite development: morphologic, lithologic, and temporal evidence from bedding-parallel and transverse stylolites from the U.S. Appalachians. Journal of Geology, 105, (1), 59-73.

Andrews, S. J., 1991. Surface mapping of Cambrian limestone at the Century deposit north west Queensland: a summary of findings (unpublished). CRAE report number 17730, 6 p.

Andrews, S. J., 1998. Stratigraphy and depositional setting of the upper McNamara Group, Lawn Hills region, Northwest Queensland. Metallogeny of the McArthur River-Mount Isa-Cloncurry minerals province Economic Geology and the Bulletin of the Society of Economic Geologists, 93, (8), 1132-1152.

Andrews, S., Baker, T., Rotherham, J. F., Richmond, J. M., Mark, G., Williams, P. J. (Eds.), 1996. Stratigraphy and depositional setting of the upper McNamara Group, Lawn Hill region. James Cook University of North Queensland, Geology Department, [Townsville, Qld.], Australia, pp. 5-9.

Aranburu, A., Fernandez-Mendiola, P. A., Lopez-Horgue, M. A., Garcia-Mondejar, J., 2002. Syntectonic hydrothermal calcite in a faulted carbonate platform margin (Albian of Jorrios, northern Spain). Sedimentology, 49, (4), 875-890.

Arfken, G., 1985. Mathematical Methods for Physicists, 6th ed. Academic Press, 1200 p.

Arnaud, E., Eyles, C. H., 2002. Catastrophic mass failure of a Neoproterozoic glacially influenced continental margin, the Great Breccia, Port Askaig. Sedimentary Geology, 151, (3), 313-333.

Asadi, H. H., Hale, M., 2001. A predictive GIS model for mapping potential gold and base metal mineralization in Takab area, Iran. Computers & Geosciences, 27, (8), 901-912.

Barnett, W., Serletis, A., Serletis, D., 2005. Nonlinear and complex dynamics in real systems. International Journal of Nonlinear Sciences and Numerical Simulation, 1-6.

Barr, A. H., 2001. The Einstein summation notation, introduction to Cartesian tensors and extensions to the notation. Available on http://www.gg.caltech.edu/~cs174ta/1998–1999/Fall/index.html.

Bartier, P. M., Keller, C. P., 1996. Multivariate interpolation to incorporate thematic surface data using inverse distance weighting (IDW). Computers & Geosciences, 22, (7), 795-799.

Beardsmore, T.J., Newberry, S.P., Laing, W.P., 1988. The Maronan Supergroup: an inferred early volcano-sedimentary rift sequence in the Mount Isa Inlier and its implications for ensialic rifting in the Middle Proterozoic of northwest Queensland. Precambrian Research, 40, 487-507.

Bell, T. H., 1983. Thrusting and duplex formation at Mount Isa, Queensland, Australia. 304, (5926), 493-497.

Bell, T. H. and Hickey, K.A., 1998. Multiple Deformations with Successive Subvertical and Subhorizontal Axial Planes in the Mount Isa Region: Their Impact on Geometric Development and Significance for Mineralization and Exploration. Economic Geology, 93, 1269-1289.

Bernoulli, D., 1954. Exposition of a New Theory on the Measurement of Risk.
        Econometrica, 22, (1), 23-36.

Bertolin, A., Frizzo, P., Rampazzo, G., 1995. Sulphide speciation in surface sediments
        of the Lagoon of Venice: A geochemical and mineralogical study. Marine
        Geology, 123, (1-2), 73-86.

Bethke, C. M., 1985. A numerical model of compaction-driven groundwater flow and
        heat transfer and its Application to the paleohydrology of intracratonic
        sedimentary basins. Journal of Geophysical Research, 90, (8), 6817-6828.

Bethke, C. M., Harrison, W. J., Upson, C., Altaner, S. P., 1988. Supercomputer analysis
        of sedimentary basins. Science, 239, (4837), 261-267.

Bethke, C.M., 1985. A numerical model of compaction-driven groundwater flow and
        heat transfer and its Application to the palaeohydrology of intracratonic
        sedimentary basins. Journal of Geophysical Research, 90b, 6817-6828.

Betts, P. G., 1999. Palaeoproterozoic mid-basin inversion in the northern Mt Isa terrane,
        Queensland. Australian Journal of Earth Sciences, 46, (5), 735-748.

Betts, P. G., 2001. Three-dimensional structure along the inverted Palaeoproterozoic
        Fiery Creek Fault System, Mount Isa terrane, Australia. Journal of Structural
        Geology, 23, (12), 1953-1969.

Betts, P. G., Giles, D., 2006. The 1800-1100 Ma tectonic evolution of Australia.
        Precambrian Research, 144, (1-2), 92-125.

Betts, P. G., Giles, D., Lister, G. S., 2003. Tectonic environment of shale-hosted
        massive sulfide Pb-Zn-Ag deposits of Proterozoic northeastern Australia.
        Economic Geology and the Bulletin of the Society of Economic Geologists, 98,
        (3), 557-576.
Betts, P. G., Giles, D., Lister, G. S., 2004. Aeromagnetic patterns of half-graben and
        basin inversion: implications for sediment-hosted massive sulfide Pb-Zn-Ag
        exploration. Journal of Structural Geology, 26, (6-7), 1137-1156.

Betts, P. G., Lister, G. S., 2001. Comparison of the 'strike-slip' versus the 'episodic rift-
        sag' models for the origin of the Isa Superbasin. Australian Journal of Earth
        Sciences, 48, (2), 265-280.

Betts, P. G., Lister, G. S., 2002. Geodynamically indicated targeting strategy for shale-
        hosted massive sulfide Pb-Zn-Ag mineralisation in the Western Fold Belt, Mt
        Isa terrane. Australian Journal of Earth Sciences, 49, (6), 985-1010.

Betts, P. G., Lister, G. S., O'Dea, M. G., 1998. Asymmetric extension of the middle Proterozoic lithosphere, Mount Isa Terrane, Queensland, Australia. Tectonophysics, 296, (3-4), 293-316.

Betts, P. G., Lister, G. S., Pound, K. S., 1999. Architecture of a Palaeoproterozoic Rift System: evidence from the Fiery Creek Dome region, Mt Isa terrane. Australian Journal of Earth Sciences, 46, (4), 533-554.

Betts, P.G., 2001. Three-dimensional structure along the inverted Palaeoproterozoic Fiery Creek Fault system, Mt Isa terrane, Australia. Journal of Structural Geology, 23, 1953–1969.

Betts, P.G., Giles, D., Lister, G.S., 2003. Tectonic Environment of Shale-Hosted Massive Sulfide Pb-Zn-Ag Deposits of Proterozoic Northeastern Australia. Economic Geology, 98, 557-576.

Betts, P.G., Lister, G.S. 2002. Geodynamically indicated targeting strategy for shale-hosted massive sulfide Pb-Zn-Ag mineralisation in the Western Fold Belt, Mt Isa terrane. Australian Journal of Earth Sciences, 49, 985–1010.

Bishop, M. M., Feinberg, S. E., Holland, P. W., 1975. Discrete Multivariate Analysis: Theory and Practice. MIT Press, Cambridge, Massachusetts, 587 p.

Blake, D. H., 1987. Geology of the Mount Isa Inlier and environs, Queensland and Northern Territory. Bureau of Mineral Resources Bulletin, 225, 83 p.

Blake, D. H., Stewart, A. J., 1992. Stratigraphic and tectonic fremework, Mount Isa Inlier. In: A. J. Stewart and D. H. Blake (Eds.), Detailed Studies of the Mount Isa Inlier. Australian Geological Survey Organisation Bulletin, 243, pp. 1-11.

Blatt, H., Middleton, G., Murray, R., 1980. Origin of Sedimentary Rocks. Prentice-Hall, 643 p.

Blenkinsop, T. G., Mustard, R., Bierlein, F. P., 2004. Fault Roughness, Length and Mineral Endowment. PmdCRC final unpublished project I2+I3 report, James Cook University,Townsville, 11 p.

Boehm, A., Moore, J. C., 2002. Fluidized sandstone intrusions as an indicator of paleostress orientation, Santa Cruz, California. Geofluids, 2, 147-161.

Bohm, W., Farin, G., Kahmann, J., 1984. A survey of curve and surface methods in CAGD. Computer Aided Geometric Design, 1, (1), 1-60.

Bonham-Carter, G. F., 1994. Geographic Information Systems for Geoscientists: Modelling with GIS. Pergamon Press, New York, 398 p.

Bonham-Carter, G. F., Agterberg, F. P., Wright, D. F., 1989. Weights of evidence modelling: new approach to mapping mineral potential. In: F. P. Agterberg, Bonham-Carter and C. M. G. Fanning (Eds.), Statistical Applications in the Earth Science. Geological Survey Canada, 89-9, pp. 171-183.

Bons, P. D., 2001. The formation of large quartz veins by rapid ascent of fluids in mobile hydrofractures. Tectonophysics, 336, (1-4), 1-17.

Bradley, D.C., Leach, D.L., 2003. Tectonic controls of Mississippi Valley-type lead–zinc mineralization in orogenic forelands. Mineralium Deposita, 38, 6, 652 – 667.

Brasier, M. D., Sukhov, S., 1998. The falling amplitude of carbon isotopic oscillations through the Lower to Middle Cambrian; northern Siberia data. Canadian Journal of Earth Sciences, 35, 353-373.

Bresser, H. A., 1992. Origin of base metal vein mineralisation in the Lawn Hill mineral field, North-Western Queensland. James Cook University of North Queensland. Key Centre in Economic Geology, unpublished honour thesis, 115 p.

Briggs, L. I., Pollack, H. N., 1967. "Digital model of evaporite sedimentation". Science, 155, 453-456.

Broadbent, G. C., 1999. Geology and Origin of the Century Zinc Deposit. James Cook University, PhD thesis (Unpublished), 216 p.

Broadbent, G. C., Andrews, S. J., Kelso, I. J., 2002. A decade of new ideas: Geology and exploration history of the Century Zn-Pb-Ag deposit, Northwestern Queensland, Australia. In: R. J. Goldfarb and R. L. Nielsen (Eds.), Integrated Methods for Discovery: Global Exploration in the Twenty-First Century. Society of Economic Geologists Special Publication, 9, pp. 119-140.

Broadbent, G. C., Myers, R. E., Wright, J. V., 1996. Geology and origin of shale-hosted Zn-Pb-Ag mineralisation at the Century Mine, Northwest Queensland. In: T. Baker, J. F. Rotherham, J. M. Richmond, G. Mark and P. J. Williams (Eds.), James Cook University of North Queensland, Geology Department, [Townsville, Qld.], Australia, 55, pp. 24-27.

Broadbent, G. C., Myers, R. E., Wright, J. V., 1998. Geology and origin of shale-hosted Zn-Pb-Ag mineralization at the Century Deposit, Northwest Queensland, Australia. Metallogeny of the McArthur River-Mount Isa-Cloncurry minerals province Economic Geology and the Bulletin of the Society of Economic Geologists, 93, (8), 1264-1294.

Broadbent, G. C., Waltho, A. E., Berkman, D. A., Mackenzie, D. H. (Eds.), 1998.
    Century zinc-lead-silver deposit. Australasian Institute of Mining and
    Metallurgy, Melbourne, Victoria, Australia, pp. 729-735.

Brown, W. M., Gedeon, T. D., Groves, D. I., Barnes, R. G., 2000. Mineral prospectivity
    mapping; a comparison of MLP neural network, fuzzy logic and weights of
    evidence methods. Proceedings Understanding planet Earth; searching for a
    sustainable future; on the starting blocks of the third millennium; abstracts.
    Sydney, N.S.W., Geological Society of Australia, pp. 63.

Carr, G. R., 1984. Primary geochemical and mineralogical dispersion in the vicinity of
    the Lady Loretta Zn-Pb-Ag deposit, Northwest Queensland. Journal of
    Geochemical Exploration, 22, (1-3), 217-238.

Carr, G. R., Sun, S., Page, R. W., Hinman, M., 1996. Recent developments in the use of
    lead isotope model ages in Proterozoic terrains [abs.]. In: T. Baker, J. F.
    Rotherham, J. M. Richmond, G. Mark and P. J. Williams (Eds.), Economic
    Geology Research Unit Contribution. James Cook University, 55, pp. 33-35.

Carranza, E. J. M., 2002. Geologically-Constrained Mineral Potential Mapping
    (Examples from the Philippines). PhD thesis, ITC Delft, Philippines, 474 p.

Carranza, E. J. M., 2004. Weights of Evidence Modeling of Mineral Potential: A Case
    Study Using Small Number of Prospects, Abra, Philippines. Natural Resources
    Research, 13, (3), 173-187.

Carranza, E. J. M., Hale, M., 2000. Geologically Constrained Probabilistic Mapping of
    Gold Potential, Baguio District, Philippines. Natural Resources Research, 9, (3),
    237-253.

Carranza, E. J. M., Hale, M., 2003. Evidential belief functions for data-driven
    geologically constrained mapping of gold potential, Baguio district, Philippines.
    Ore Geology Reviews, 22, (1-2), 117-132.

Carranza, E. J. M., Woldai, T., Chikambwe, E. M., 2005. Application of Data-Driven
    Evidential Belief Functions to Prospectivity Mapping for Aquamarine Bearing
    Pegmatites, Lundazi District, Zambia. Natural Resources Research, 14, (1), 47-
    63.

Carter, E. K., Brooks, J. H., Walker, K. R., 1961. The Precambrian mineral belt of
    north-western Queensland. Australian Bureau of Mineral Resources Bulletin,
    61, 344 p.

Carter, E. K., Opik, A. A., 1961. Lawn Hill, first edition. Queensland 1:250 000 Geological Series - Explanatory Notes. Bureau of Mineral Resources, Geology and Geophysics, Australia, n. 21.

Cartwright, I., Oliver, N. H. S., 2000. Metamorphic fluids and their relationship to the formation of metamorphosed and metamorphogenic ore deposits. In: P. G. Spry, B. Marshall and F. M. Vokes (Eds.), Metamorphosed and Metamorphogenic Ore Deposits. Society of Economic Geologists, Socorro, NM, 11, pp. 81-96.

Cervelli, P., Segall, P., Johnson, K., Lisowski, M., Miklius, A., 2002. Sudden aseismic fault slip on the south flank of Kilauea volcano. 415, (6875), 1014-1018.

Chadam, J., Hoff, D., Merino, E., Ortoleva, P., Sen, A., 1986. Reactive Infiltration Instabilities. IMA Journal of Applied Mathematics, 36, 207-221.

Chapman, L. H., 2004. Geology and mineralization styles of the George Fisher Zn-Pb-Ag deposit, Mount Isa, Australia. Economic Geology and the Bulletin of the Society of Economic Geologists, 99, (2), 233-255.

Chatterjee, S., Yilmaz, M. R., 1992. Chaos, Fractals and Statistics. Statistical Science, 7, (1), 49-68.

Chen, J., Walter, M. R., Logan, G. A., Hinman, M. C., Summons, R. E., 2003. The Paleoproterozoic McArthur River (HYC) Pb/Zn/Ag deposit of northern Australia: organic geochemistry and ore genesis. Earth and Planetary Science Letters, 210, (3-4), 467-479.

Choi, K. S., Khim, B. K., Woo, K. S., 2003. Spherulitic siderites in the Holocene coastal deposits of Korea (eastern Yellow Sea): elemental and isotopic composition and depositional environment. Marine Geology, 202, (1-2), 17-31.

Ciobanu, C. L., Cook, N. J., 2004. Skarn textures and a case study: the Ocna de Fier-Dognecea orefield, Banat, Romania. Ore Geology Reviews Metamorphic processes in ore formation and transformation: A thematic series of papers, 24, (3-4), 315-370.

Clifford, M., Kelso, I. J., 2003. Pasminco Century Mine mineral resource statement. Annual Report, Garbutt, Queensland, Australia, 25 p.

Coley, D. A., 1999. An Introduction to Genetic Alghorithms for Scientists and Engineers. World Scientific, Singapore, 227 p.

Collins, W. J., Shaw, R. D., 1995. Geochronological constraints on orogenic events in the Arunta Inlier: a review. Precambrian Research, 71, (1-4), 315-346.

Coman, D. C., 2004. Finite Element Methods for PDE's.
        http://www.maths.gla.ac.uk/~cdc/F_ELEMENTS/info.html.

Compston, D. M., 1995. Time constraints on the evolution of the Tennant Creek Block,
        northern Australia. Precambrian Research, 71, (1-4), 107-129.

Connors, K. A., Page, R. W., 1995. Relations between magmatism, metamorphism and
        deformation in the western Mt Isa Inlier, Australia. Precambrian Research, 71,
        131–153.

Connors, K.A., Lister, G.S., 1995. Polyphase deformation in the western Mount Isa
        Inlier, Australia: episodic or continuous deformation? Journal of Structural
        Geology, 17, 3, 305-328.

Cooke, D. R., Bull, S. W., Large, R. R., 2003. Processes of ore formation in the
        stratiform sediment-hosted Zn-Pb deposits of Northern Australia: testing the
        Century model. Proceedings Journal of Geochemical Exploration. pp. 519-524.

Cooke, D. R., Bull, S. W., Large, R. R., McGoldrick, P. J., 2000. The importance of
        oxidized brines for the formation of Australian Proterozoic stratiform sediment-
        hosted Pb-Zn (sedex) deposits. Economic Geology and the Bulletin of the
        Society of Economic Geologists, 95, (1), 1-17.

Cooke, D.R., Bull, S., Large, R.R., 2003. Processes of ore formation in the stratiform
        sediment-hosted Zn–Pb deposits of Northern Australia: testing the Century
        model. Journal of Geochemical Exploration, 78-79, 519-524.

Couzens-Schultz, B. A., Vendeville, B. C., Wiltschko, D. V., 2003. Duplex style and
        triangle zone formation: insights from physical modeling. Journal of Structural
        Geology, 25, (10), 1623-1644.

Coveney, J., Raymond M., Pasava, J., 2004. Diverse connections between ores and
        organic matter. Ore Geology Reviews, 24, (1-2), 1-5.

Coveney, R. M., 2000. Metalliferous shales and the role of organic matter with
        examples from China, Poland, and the United States Ore genesis and
        exploration; the roles of organic matter 9, 251-280.

Cox, S. F., Etheridge, M. A., Wall, V. J., 1987. The role of fluids in syntectonic mass
        transport, and the localization of metamorphic vein-type ore deposists. Ore
        Geology Reviews, 2, (1-3), 65-86.

Cox, S.F., 1999. Deformation controls on the dynamics of fluid flow in mesothermal
        gold systems. In: McCaffery, K.J.W., Lonergan, L., Wilkinson, J.J. (Eds.),

Fractures, Fluid Flow and Mineralization Geological Society Special Publication 155, 123-140.

Dadet, P., Marchesseau, J., Millon, R., Motti, E., 1970. Mineral occurrences related to stratigraphy and tectonics in Tertiary sediments near Umm Lajj, eastern Red Sea, Saudi Arabia, Philos Trans. R. Soc. London Series A, 267, 99-106.

Davis, T. P., 2004. Mine-scale structural controls on the Mount Isa Zn-Pb-Ag and Cu orebodies. Economic Geology and the Bulletin of the Society of Economic Geologists, 99, (3), 543-559.

de Kemp, E. A., 2000. 3-D visualization of structural field data: examples from the Archean Caopatina Formation, Abitibi greenstone belt, Quebec, Canada. Computers & Geosciences, 26, (5), 509-530.

De Keyser, F., 1969. The phosphate-bearing Cambrian formations in the Lawn Hill and Lady Annie districts, northwestern Queensland (unpublished). Australia, Bureau of Mineral Resources, Geology and Geophysics, Record 1969/147.

De Keyser, F., 1973. A review of the middle Cambrian stratigraphy in the Queensland portion of the Georgina Basin. In: Geological Papers 1970-71. Australia, Bureau of Mineral Resources, Geology and Geophysics, Bulletin, 139, pp. 13-27.

De Keyser, F., Cook, P. J., 1972. Geology of the Middle Cambrian Phosphorites and Associated Sediments of Northwestern Queensland. Australia, Bureau of Mineral Resources, Geology and Geophysics, Bulletin, 138, 79 p.

de Paor, D. G., 1983. Orthographic analysis of geological structures--I. Deformation theory. Journal of Structural Geology, 5, (3-4), 255-277.

Deep seismic profiling of the continents, II: A global survey, 288, (1-4), 57-69.

Degens, E.T., Ross, D.A., 1969. Hot brines and recent heavy metal deposits in the Red Sea: a geophysical and geochemical account. Springer, New York.

Delaney, P. T., Pollard, D. D., Ziony, J. I., McKee, E. H., 1986. Field relations between dikes and joints: emplacement processes and paleostress analysis. Journal of Geological Research, 91, 4920-4938.

Derrick, G. M., 1982. A Proterozoic rift zone at Mount Isa, Queensland, and implications for mineralisation. BMR Journal of Australian Geology & Geophysics, (7), 81-92.

Derrick, G. M., Wilson, I. H., Sweet, I. P., 1980. The Quilalar and Surprise Creek Formations—new Proterozoic units from the Mt Isa Inlier: their regional sedimentology and application to regional correlation. BMR Journal of Australian Geology & Geophysics, (5), 215-223.

Desai, C. S., Christian, J. T., 1977. Numerical Methods in Geomechanics. McGraw-Hill, New York.

Dewers, T., Ortoleva, P., 1990a. A coupled reaction/transport/mechanical model for intergranular pressure solution, stylolites, and differential compaction and cementation in clean sandstones. Geochimica et Cosmochimica Acta, 54, (6), 1609-1625.

Dewers, T., Ortoleva, P., 1990b. Differentiated structures arising from mechano-chemical feedback in stressed rocks. Earth-Science Reviews, 29, (1-4), 283-298.

Dewers, T., Ortoleva, P., 1994. Nonlinear dynamical aspects of deep basin hydrology; fluid compartment formation and episodic fluid release. American Journal of Science, 294, (6), 713-755.

Doyle, M. G., Allen, R. L., 2003. Subsea-floor replacement in volcanic-hosted massive sulfide deposits. Ore Geology Reviews, 23, (3-4), 183-222.

Drummond, B.J., Goleby, B.R., Goncharov, A.G., Wyborn, L.A.I., Collins, C.D.N., MaCready, T., 1998. Crustal-scale structures in the Proterozoic Mount Isa Inlier of north Australia: their seismic response and influence on mineralisation. Tectonophysics, 288, 43-56.

Duanne, M.J., de Wit, M.J., 1988. Pb-Zn ore deposits of the northern Caledonides – products of continental scale fluid mixing and tectonic expulsion during continental collision. Geology, 16, 999-1002.

Duda, R. O., Hart, P. E., Barrett, P., Gaschnig, J. C., Konolige, K., Reboh, R., Slocum, J., 1978. Development of the PROSPECTOR consultation system for mineral exploration. Stanford Research Institute International, SRI International, Artificial Intelligence Centre, Menlo Park, California, 193 p.

Dullien, F.A.L., 1979. Porous Media Fluid Transport and Pore Structure. Academic Press Inc., New York.

Dypvik, H., Jansa, L. F., 2003. Sedimentary signatures and processes during marine bolide impacts: a review. Sedimentary Geology, 161, (3), 309-337.

Eastman, J. R., 1999. IDRISI 32:Guide to GIS and Image Processing. Clark Lab, Clark University, Worcestar, MA, USA.

Eastman, J. R., and Jiang, H., 1996. Fuzzy Measures in Multi-Criteria Evaluation, Proceedings, Second International Symposium on Spatial Accuracy Assessment in Natural Resources and Environmental Studies, May 21-23, Fort Collins, Colorado, 527-534.

Einstein, A., 1934. On the method of theoretical physics. Philosophy of Science, 1, (2), 163-169.

El Arif, M.M., 1984. Strat-bound and stratiform iron sulfides, sulfur and galena in the Miocene evaporates, Ranga, Red Sea, Egypt (with special emphasis on their diagenetic crystallization rhythmites). In: Wauschkuhn, A., Kluth, C., Zimmermann, R.A. (Eds.) Syngenesis and epigenesis in the formation of mineral deposits. Springer, New York, 457-467.

Elliott, C. G., Williams, P. F., 1988. Sediment slump structures: a review of diagnostic criteria and application to an example from Newfoundland. Journal of Structural Geology, 10, (2), 171-182.

Engelder, T., 1985. Loading paths to joint propagation during a tectonic cycle: an example from the Appalachian Plateau, U.S.A. Journal of Structural Geology, 7, (3), 459-476.

Etheridge, M. A., Wall, V. J., Cox, S. F., 1984. High fluid pressure during regional metamorphism and deformation: implications for mass transport and deformation mechanisms. Journal of Geophysical Research, 89, (6), 4344-4358.

Etheridge, M. A., Wall, V. J., Vernon, R. H., 1983. The role of the fluid phase during regional metamorphism and deformation. Journal of Metamorphic Geology, 1, (3), 205-226.

Etheridge, M.A., Rutland, R.W.D., Wyborn, L.A.I., 1987. Orogenesis and Tectonic Process in the Early to Middle Proterozoic of Northern Australia. American Geophysical Union, Geodynamic Series 17, 131-147.

Farquharson, R. B., Richards, J. R., 1975. Isotopic remobilization in the Mount Isa tuff beds. Chemical Geology, 16, (2), 73-88.

Farrington, J.L., 1952. A preliminary description of the Nigerian lead-zinc field. Economic Geology, 47, 583-608.

Faure, G., 1991. Principles and Applications of Inorganic Geochemistry. Prentice-Hall, New Jersey, 626 p.

Feltrin, L., McLellan, J. G., Oliver, N. H. S., 2006. Modelling the giant, Zn-Pb-Ag Century deposit, Queensland, Australia. Computers & Geosciences, in review.

Feltrin, L., Oliver, n. H. S., 2004. Evidence of Multi-stage Ore Genesis at the Century Zinc Deposit Northwestern Queensland, Australia. Proceedings Pmd*CRC Barossa Conference (Extended Abs.). Adelaide, Record 2004/09, pp. 49-52.

Feltrin, L., Oliver, N. H. S., Kelso, I. J., King, S., 2003. Basement metal scavenging during basin evolution; Cambrian and Proterozoic interaction at the Century Zn-Pb-Ag deposit, Northern Australia. Proceedings Geofluids IV. Utrecht, Netherlands, Elsevier, Journal of Geochemical Exploration, pp. 159-162.

Feltrin, L., Oliver, N., Chapman, L., Kelso, I., McPhie, J., McGoldrick, P., 2004. Evolution of mineralised breccias at the Century zinc deposit, northwestern Queensland, Australia. Proceedings 17th Australian geological convention. Geological Society of Australia, Sydney, N.S.W., Australia, pp. 75.

Ferguson, J., 1992. Lawn Hill Circular Structure. (unpublished report) Bungendore, NSW, 17 p.

Fisher, N. I., Lewis, T. L., Embleton, B. J., 1987. Statistical analysis of spherical data. Cambridge University Press, 329 p.

Fisher, R. A., 1925. The application of "Student's" distribution. Metron, 5, (3), 90-104.

Flake, G. W., 1998. The computational beauty of nature. A Bradford Book, The MIT Press, London, 493 p.

Flinn, D., 1979. The deformation matrix and the deformation ellipsoid. Journal of Structural Geology, 1, (4), 299-307.

Foster, D.R.W., 2003. Proterozoic low-pressure metamorphism in the Mount Isa Inlier, northwest Queensland, Australia, with particular emphasis on the use of calcic amphibole chemistry as temperature-pressure indicators. Unpublished PhD thesis, James Cook University, Australia.

Galera, C., Bennis, C., Moretti, I., Mallet, J. L., 2003. Construction of coherent 3D geological blocks. Computers & Geosciences, 29, (8), 971-984.

Gandin, A., Wright, D. T., Melezhik, V., 2005. Vanished evaporites and carbonate formation in the Neoarchaean Kogelbeen and Gamohaan formations of the Campbellrand Subgroup, South Africa. Journal of African Earth Sciences, 41, (1), 1-23.

Garven, G., 1985. The role of regional fluid flow in the genesis of the Pine Point deposit, western Canada Sedimentary Basin. Economic Geology, 80, (2), 307-324.

Garven, G., Bull, S.W., Large, R.R., 2001. Hydrothermal fluid flow models of stratiform ore genesis in the McArthur Basin, Northern Territory, Australia. Geofluids, 1, (4), 289-313.

Garven, G., Freeze, R.A., 1984a. Theoretical analysis of the role of groundwater flow in the genesis of stratabound ore deposits. Mathematical and numerical model. American Journal of Science, 284, 1085 1124.

Garven, G., Freeze, R.A., 1984b. Theoretical analysis of the role of groundwater flow in the genesis of stratabound ore deposits. Quantitative results. American Journal of Science, 284, 1125-1174.

Gauss, C. F., Weber, W., 1839. Resultate aus den Beobachtungen des magnetishen Vereins im Jahre 1838. Weidmann, Leipzig, Dieterich, Göttingen, 151 p.

Gauthier, L., Hall, G., Stein, H., Schaltegger, U., 2001. The Osborne deposit, Cloncurry district: a 1595 Ma Cu–Au skarn deposit. In: P. J. Williams (Ed.), A Hydrothermal Odyssey, Extended Abstracts. 58, pp. 58–59.

Giles, D., Betts, P. G., Lister, G. S., 2004. 1.8-1.5-Ga links between the North and South Australian Cratons and the Early-Middle Proterozoic configuration of Australia. Tectonophysics, 380, (1-2), 27-41.

Giles, D., Nutman, A. P., 2002. SHRIMP U-Pb monazite dating of 1600-1580 Ma amphibolite facies metamorphism in the southeastern Mt Isa Block, Australia. Australian Journal of Earth Sciences, 49, (3), 455-465.

Giles, D., Nutman, A. P., 2003. SHRIMP U-Pb zircon dating of the host rocks of the Cannington Ag-Pb-Zn deposit, southeastern Mt. Isa Block, Australia. Australian Journal of Earth Sciences, 50, (3), 295-309.

Glasby, G. P., Notsu, K., 2003. Submarine hydrothermal mineralization in the Okinawa Trough, SW of Japan: an overview. Ore Geology Reviews, 23, (3-4), 299-339.

Glickson, A. Y., Ballhaus, C. J., Clarke, G. L., Sheraton, J. W., Stewart, A. J., Sun, S.-s., 1995. Geological framework and crustal evolution of the Giles Complex, western Musgrave Block, Western Australia. Australian Geological Survey Organisation, Journal of Geolgy and Geophysics, 16, 41-68.

Glickson, A. Y., Stewart, A. J., Ballhaus, C. J., Feeken, E. J. H., Leven, J. H., Sheraton, J. W., Sun, S.-s., 1996. Geology of the western Musgrave Block, central Australia with particular reference to the mafic–ultramafic Giles Complex. Australian Geological Survey Organisation Bulletin, 239, 177 p.

Glikson, M., Gibson, D. L., Philp, R. P., 1985. Organic matter in Australian Cambrian oil shales and other Iower Palaeozoic shales. Chemical Geology, 51, (3), 175-191.

Goodfellow, W. D., 1987. Anoxic stratified oceans as a source of sulphur in sediment-hosted stratiform Zn---Pb deposits (Selwyn Basin, Yukon, Canada). Chemical Geology: Isotope Geoscience section, 65, (3-4), 359-382.

Goodfellow, W. D., Lydon, J. W., Turner, R. J. W., 1993. Geology and genesis of stratiform sediment-hosted (SEDEX) zinc-lead-silver sulphide deposits. In: R. V. Kirkham, W. D. Sinclair, R. I. Thorpe and J. M. Duke (Eds.), Geological Association of Canada, Toronto, ON, Canada, 40, pp. 201-251.

Gorter, J. D., 1992. Cambro-Ordovician petroleum in the Centralian Superbasin: relationships with sea-level changes. American Association of Petroleum Geologists, 76, (7), 1103.

Grant, F., 1957. A problem in the analysis of geophysical data. Geophysics, 22, (2), 309-344.

Grant, N.K., 1971. South Atlantic, Benue trough, and the Gulf of Guinea Cretaceous triple junction. Bulletin Geol. Society America, 82, 2295-2298.

Grasso, J. R., Sornette, D., 1998. Testing self-organized criticality by induced seismicity. Journal of geophysical research, 103, (B12), 29965-29987.

Griffin, W. R., 1949. Residual gravity in theory and practice. Geophysics, 14, (1), 39-56.

Guidish, T. M., Kendall, C. G. S. C., Lerche, I., Toth, D. J., Yarzab, R. F., 1985. Basin evaluation using burial history calculations; an overview. AAPG Bulletin, 69, (1), 92-105.

Gustafson, L. B., Williams, N., 1981. Sediment-hosted stratiform deposits of copper, lead, and zinc. In: B. J. Skinner (Ed.), Econ. Geol. Publ. Co., pp. 139-178.

Hackett, J.P., Bischoff, J.L., 1973. New data on the stratigraphy, extent and geological history of the Red Sea geothermal deposits. Economic Geology, 68, 533-564.

Haines, P. W., Hand, M., Sandiford, M., 2001. Palaeozoic synorogenic sedimentation in central and northern Australia: a review of distribution and timing with implications for the evolution of intracontinental orogens. Australian Journal of Earth Sciences, 48, (6), 911-928.

Haken, H., 2004. Synergetics introduction and advanced topics. Springer-Verlag Berlin Heidelberg, Germany, 758 p.

Hallock, P., Hine, A. C., Vargo, G. A., Elrod, J. A., Jaap, W. C., 1988. Platforms of the Nicaraguan Rise; examples of the sensitivity of carbonate sedimentation to excess trophic resources. Geology, 16, (12), 1104-1107.

Hammond, K. J., Evans, J. P., 2003. Geochemistry, mineralization, structure, and permeability of a normal-fault zone, Casino mine, Alligator Ridge district, north central Nevada. Journal of Structural Geology, 25, (5), 717-736.

Hancock, P. L., 1985. Brittle microtectonics: principles and practice. Journal of Structural Geology, 7, (3), 437-457.

Hand, M., Rubatto, D., 2002. The Scale of the Thermal Problem in the Mt Isa Inlier. In: Preiss, V.P. (Ed.), Geoscience 2002: Expanding Horizons. Abstracts of the 16th Australian Geological Convention, Adelaide, July 2002, 67, pp.173.

Hand, M., Sandiford, M., 1999. Intraplate deformation in central Australia, the link between subsidence and fault reactivation. Tectonophysics, 305, (1-3), 121-140.

Harbaugh, J. W., Bonham-Carter, G. F., 1970. Computer simulation in geology. Wiley, New York, 575 p.

Harris, D. P., Pan, G., 1999. Mineral favorability mapping: A comparison of artificial neural networks, logistic regression, and discriminant analysis. Natural Resources Research, 8, (2), 93-109.

Hayes, B., 2002. Terabyte territory. American Scientist, 90, (3), 212-216.

Heinrich, C. A., Walshe, J. L., Harrold, B. P., 1996. Chemical mass transfer modelling of ore-forming hydrothermal systems: current practise and problems. Ore Geology Reviews, 10, (3-6), 319-338.

Helwig, J., 1970. Slump folds and early structures, Northeastern Newfoundland Appalachians. Journal of Geology, 78, 172-187.

Henderson, R. A., Southgate, P. N., 1980. Cambrian evaporitic sequences from the georgina basin. Search, 11, (7-8), 247-249.

Hobbs, B. E., 1987. Principles involved in mobilization and remobilization. Ore
        Geology Reviews, 2, (1-3), 37-45.
Hobbs, B. E., Means, W. D., Williams, P. F., 1976. An outline of structural geology.
        Wiley, xviii, 571 p.

Holk, G. J., Kyser, T. K., Chipley, D., Hiatt, E. E., Marlatt, J., 2003. Mobile Pb-isotopes
        in Proterozoic sedimentary basins as guides for exploration of uranium deposits.
        Journal of Geochemical Exploration, 80, (2-3), 297-320.

Houlding, S.W., 1994. 3D Geoscience Modeling, Computer techniques for geological
        characterization. Springer-Verlag, New York, pp. 304.

Howarth, R. J., 2001. A History of Regression and Related Model-Fitting in the Earth
        Sciences (1636?-2000). Natural Resources Research, 10, (4), 241-286.

Hutton, L. J., 1992. Report on the investigation of postulated astrobleme (unpublished).
        Geological Survey Division, Department of Minerals and Energy, Queensland, 6
        p.
Hutton, L. J., Sweet, I. P., 1982. Geological evolution, tectonic style, & economic
        potential of the Lawn Hill Platform cover, Northwest Queensland. BMR Journal
        of Australian Geology and Geophysics, 7, (2), 125-134.

Idnurm, M., 2000. Towards a high resolution Late Palaeoproterozoic-earliest
        Mesoproterozoic apparent polar wander path for northern Australia. Australian
        Journal of Earth Sciences, 47, 405-429.

Ireland, T., Bull, S.W., large, R.R., 2003. Mass flow sedimentology within the HYC
        Zn–Pb–Ag deposit, Northern Territory, Australia: evidence for syn-sedimentary
        ore genesis. Mineralium Deposita, 39, 2, 143 – 158.

Isaaks, E. H., Srivastava, R. M., 1989. An introduction to applied geostatistics. Oxford
        University Press, New York, 561 p.

Itasca, 2003. FLAC, Fast Lagrangian Analysis of Continua Command Reference, 2nd
        Edition. Itasca Consulting Group Inc., Minnesota, USA, 362 p.

Jackson, M. J., Muir, M. D., Plumb, K. A., 1987. Geology of the southern McArthur
        Basin. Bureau of Mineral Resources Bulletin, 220 p.

Jackson, M. J., Scott, D.L., Rawlings, D.J., 2000. Stratigraphic framework for the
        Leichhardt and Calvert Superbasins: review and correlations of the pre-1700 Ma
        successions between Mt Isa and McArthur River. Australian Journal of Earth
        Sciences 47, 381–404.

Jackson, S. A., Beales, F. W., 1967. An aspect of sedimentary basin evolution: the concentration of Mississippi Valley Type ores during the late stages of diagenesis. Canadian Society of Petroleum Geologists, Bulletin, 15, 393-433.

Jaeger, J. C., 1969 In: Elasticity, fracture and flow, with engineering and geological applications Methuen & Co. , 3, pp.

Jaques, A. L., Blake D. H., Donchak, P. J. T., 1982. Regional metamorphism in the Selwyn Range area, Northwest Queensland. BMR Journal of Australian Geology and Geophysics, 7, 3, 181-196.

Jebrak, M., 1997. Hydrothermal breccias in vein-type ore deposits: A review of mechanisms, morphology and size distribution. Ore Geology Reviews, 12, (3), 111-134.

Johnson, L. C., 2000. Sedimentological Controls on Ore Genesis, Century Zinc Deposit, Northwest Queensland. Queensland University of Technology, Unpublished Honour thesis, 89 p.

Jolly, R. J. H., Sanderson, D. J., 1995. Variation in the form and distribution of dykes in the Mull swarm, Scotland. Journal of Structural Geology, 17, (11), 1543-1557.

Kelso, I., Briggs, T., Basford, P., 2000. The Century zinc deposit; a geological update. Northern Queensland exploration and mining 2000; extended abstracts Bulletin - Australian Institute of Geoscientists, 31, 79-81.

Kesler, S. E., 1997. Metallogenic evolution of convergent margins: Selected ore deposit models. Ore Geology Reviews, 12, (3), 153-171.

Khain, V. Y., 1992. The role of rifting in the evolution of the Earth's crust. Tectonophysics, 215, (1-2), 1-7.

King, S., 2002. Cross section construction and fault modelling of the northern block, Century zinc mine NW Queensland. Solid Geology Report, Brisbane, Australia, 54 p.

Korsch, R. J., Goleby, B. R., Leven, J. H., Drummond, B. J., 1998. Crustal architecture of central Australia based on deep seismic reflection profiling. Tectonophysics Deep seismic profiling of the continents, II: A global survey, 288, (1-4), 57-69.

Krassay, A.A., Bradshaw, B.E., Domagala, J., Jackson, M.J., 2000a. Siliclastic shoreline to growth-faulted, turbiditic sub-basins: the Proterozoic River Supersequence of the upper McNamara Group on the Lawn Hill Platform, northern Australia. Australian Journal of Earth Sciences, 47, 533-562.

Krassay, A. A., Domagala, J., Bradshaw, B. E., Southgate, P. N., 2000b. Lowstand ramps, fans and deep-water Palaeoproterozoic and Mesoproterozoic facies of the Lawn Hill Platform; the Term, Lawn, Wide and Doom supersequences of the Isa Superbasin, northern Australia. Carpentaria-Mt. Isa Belt; basement framework, chronostratigraphy and geodynamic evolution of Proterozoic successions Australian Journal of Earth Sciences, 47, (3), 563-597.

Krige, D. G., 1951. A statistical approach to some mine valuation problems on the Witwatersrand. Journal of the Chemical Mining and Metallurgical Society of South Africa, 52, 119-139.

Krige, D. G., 1960. On the departure of ore value distributions from the lognormal model in South African Gold Mines. Journal of the South African Institute of Mining and Metallurgy, 64, (4), 231-244.

Krige, D. G., 1966. Two-dimensional weighted moving average trend surfaces for ore valuation [with discussion]. Journal of the South African Institute of Mining and Metallurgy, (Special Symposium Issue), 379-380.

Krige, D. G., Ueckermann, H. J., 1963. Value contours and improved regression techniques for ore reserve valuations. Journal of the South African Institute of Mining and Metallurgy, 63, (10), 429-452.

Krumbein, W. C., 1959. Trend surface analysis of contour-type maps with irregular control-point spacing. Journal of Geophysical Research, 64, (7), 823-834.

Krumbein, W. C., 1962. The computer in geology. Science, 136, (3522), 1087-1092.

Krumbein, W. C., 1969. The computer in geological perspective. In: D. F. Merriam (Ed.), Computer Applications in the Earth Sciences. Plenum, New York, pp. 251-275.

Krumbein, W. C., Pettijohn, F. J., 1938. Manual of sedimentary petrography. Appleton-Century, New York, 549 p.

Kuenen, P. H., 1967. Emplacement of flysch-type sand beds. Sedimentology, 9, 203-244.

Large, D., 1988. The evaluation of sedimentary basins for massive sulfide mineralization Base metal sulfide deposits in sedimentary and volcanic environments; proceedings of Deutsche Mineralogische Gesellschaft, Gesellschaft Deutscher Metallhuetten- und Bergleute, Society of Geology Applied to Mineral Deposits joint meeting on ore deposits 5, 3-11.

Large, D.E., 1980. Geological parameters associated with sediment-hosted, submarine exhalative Pb-Zn deposits: an empirical model for mineral exploration. Geologisches Jahrbuch, 40, 59-129.

Large, R. R., Bull, S. W., Cooke, D. R., McGoldrick, P. J., 1998. A genetic model for the H.Y.C. Deposit, Australia; based on regional sedimentology, geochemistry, and sulfide-sediment relationships. Metallogeny of the McArthur River-Mount Isa-Cloncurry minerals province Economic Geology and the Bulletin of the Society of Economic Geologists, 93, (8), 1345-1368.

Large, R. R., Bull, S. W., McGoldrick, P. J., 2000. Lithogeochemical halos and geochemical vectors to stratiform sediment hosted Zn-Pb-Ag deposits; Part 2, HYC Deposit, McArthur River, Northern Territory. Journal of Geochemical Exploration, 68, (1-2), 105-126.

Large, R. R., McGoldrick, P. J., 1998. Lithogeochemical halos and geochemical vectors to stratiform sediment hosted Zn-Pb-Ag deposits, 1. Lady Loretta Deposit, Queensland. Journal of Geochemical Exploration, 63, (1), 37-56.

Laznicka, P., 1989. Breccias and ores. Part 1: History, organization and petrography of breccias. Ore Geology Reviews, 4, (4), 315-344.

Leach, D. L., Sangster, D. F., 1993. Mississippi valley-type lead-zinc deposits. In: R. V. Kirkham, W. D. Sinclair, R. I. Thorpe and J. M. Duke (Eds.), Mineral deposit modeling. Geological Association of Canada, 40, pp. 289-314.

Leach, D. L., Marsh, E., Emsbo, P., Rombach, C. S., Kelley, K. D., Anthony, M., 2004. Nature of Hydrothermal Fluids at the Shale-Hosted Red Dog Zn-Pb-Ag Deposits, Brooks Range, Alaska. Economic Geology, 99, (7), 1449-1480.

Lindsay, J. F., Brasier, M. D., 1998. The Nature and Origin of the Lawn Hill Structure a Report to Pasminco Exploration. AGSO, Canberra ACT, 13 p.

Lindsay, J. F., Kruse, P. D., Green, O. R., Hawkins, E., Brasier, M. D., Cartlidge, J., Corfield, R. M., 2005. The Neoproterozoic-Cambrian record in Australia: A stable isotope study. Precambrian Research, 143, (1), 113-133.

Lister, G. S., O'dea, M. G., Somaia, I., 1999. A tale of two synclines: rifting, inversion and transpressional popouts at Lake Julius, northwestern Mt Isa terrane, Queensland. Australian Journal of Earth Sciences, 46, (2), 233-250.

Mair, J. L., Ojala, V. J., Salier, B. P., Groves, D. I., Brown, S. M., 2000. Application of stress mapping in cross-section to understanding ore geometry, predicting ore zones and development of drilling strategies. In: D. I. Groves and J. M. Dunphy (Eds.), Applications of geochronology, geochemistry and GIS to mineral exploration. Geological Society of Australia, 47, pp. 895-912.

Mallet, J. L., 1989. Discrete smooth interpolation. ACM. Transactions on Graphics, 8, (2), 121-144.

Mallet, J. L., 2000. Geomodeling with gOcad. Proceedings 31st international geological congress. Brazil 2000.

Mallet, J. L., 2002. Geomodeling. Oxford University Press, New York, 593 p.

Maltman, A., 1984. On the term "soft-sediment deformation". Journal of Structural Geology, 6, (5), 589-592.

Mandelbrot, B. B., 1967. How Long Is the Coast of Britain? Statistical Self-Similarity and Fractional Dimension. Science, 156, (3775), 636-638.

Mandelbrot, B. B., 1983. The fractal geometry of nature. W. H. Freeman, New York, 488 p.

Mansell, P., 2005. Zinifex Ltd, Annual Report, Melbourne, Australia, 93 p.

Marcotte, D., Henry, E., 2002. Automatic joint set clustering using a mixture of bivariate normal distributions. International Journal of Rock Mechanics and Mining Sciences, 39, (3), 323-334.

Marcoux, E., Moelo, Y., 1991. Lead isotope geochemistry and paragenetic study of inheritance phenomena in metallogenesis; examples from base metal sulfide deposits in France. Economic Geology and the Bulletin of the Society of Economic Geologists, 86, (1), 106-120.

Marcus, M., Minc, H., 1988. Introduction to Linear Algebra. 145 p.

Marshall, B., Gilligan, L. B., 1987. An introduction to remobilization: Information from ore-body geometry and experimental considerations. Ore Geology Reviews, 2, (1-3), 87-131.

Marshall, B., Vokes, F. M., Larocque, A. C. L., 2000. Regional metamorphic remobilization; upgrading and formation of ore deposits. In: P. G. Spry, B. Marshall and F. M. Vokes (Eds.), Metamorphosed and Metamorphogenic Ore Deposits. Society of Economic Geologists, Socorro, NM, 11, pp. 19-38.

Matheron, G., 1965. Les variables régionalisées et leur estimation. Masson, 212 p.

Matheron, G., 1970. Random functions and their application in geology. In: D. F. Merriam (Ed.), Geostatistics. Plenum, New York, pp. 79-88.

Maynard, J. B., 1991. Shale-hosted deposits of Pb, Zn, and Ba; syngenetic deposition from exhaled brines in deep marine basins Sedimentary and diagenetic mineral deposits; a basin analysis approach to exploration 5, 177-185.

McBride, E. F., 1989. Quartz cement in sandstones; a review. Earth-Science Reviews, 26, (2), 69-112.

McCrea, J. M., 1950. On the isotopic chemistry of carbonates and a palaeotemperature scale. Journal of Chemical Physics, 18, 849-857.

McLellan, J. G., 2000. Structural controls and numerical modelling of mineralisation at the Osborne Cu-Au deposit, Mount Isa Block, N.W. Queensland. James Cook University, Honour Thesis, 153 p.

McLellan, J. G., 2004. Numerical Modelling of Deformation and Fluid Flow in Hydrothermal Systems. James Cook University, PhD thesis (Unpublished), 307 p.

McLellan, J.G., 2000. Structural Controls and Numerical Modelling of Mineralisation at the Osborne Cu-Au Deposit, Mount Isa Block, N.W. Queensland. Hons. Thesis. James Cook University.

Merriam, D. F., 1981. A forecast for use of computers by geologists in the coming decade of the 80s. Computer Applications in the Earth Sciences. An Update of the 70's. Proceedings of the 8th Geochautauqua, 369-380.

Merriam, D. F., 1999. Reminiscences of the editor of the Kansas Geological Survey Computer Contributions, 1966-1970 and a byte. Computers and Geosciences, 25, (4), 321-334.

Merriam, D. F., 2004. The quantification of geology: from abacus to Pentium: A chronicle of people, places, and phenomena. Earth-Science Reviews, 67, (1-2), 55-89.

Metamorphic processes in ore formation and transformation: A thematic series of papers, 24, (3-4), 315-370.

Miller, J. M., Wilson, C. J. L., 2004. Stress Controls on Intrusion-Related Gold Lodes: Wonga Gold Mine, Stawell, Western Lachlan Fold Belt, Southeastern Australia. Economic Geology, 99, (5), 941-963.

Miller, R. L., 1956. Trend surfaces: their application to analysis and description of environments of sedimentation. I. The relation of sediment-size parameters to current-wave systems and physiography. Journal of Geology, 64, (5), 425-446.

Morganti, J. M., 1981. Ore deposit models; 4, Sedimentary-type stratiform ore deposits; some models and a new classification Geoscience Canada 8, (2), 65-75.

Nesbitt, B. E., Muehlenbachs, K., 1989. Origins and movement of fluids during deformation and metamorphism in the Canadian Cordillera. Science, 245, (4919), 733-736.

Neudert, M. K., McGeough, M., 1996. A new tectonostratigraphic framework for the deposition of the upper McArthur Group, N.T. In: T. Baker, J. F. Rotherham, J. M. Richmond, G. Mark and P. J. Williams (Eds.), James Cook University of North Queensland, Geology Department, [Townsville, Qld.], Australia, 55, pp. 90-94.

Nicolis, G., 1995. Introduction to Nonlinear Science. Cambridge University Press, New York, 254 p.

O'Dea, M.G., Lister, G.S., 1995. The role of ductility contrast and basement architecture in the structural evolution of the Crystal Creek block, Mount Isa Inlier, NW Queensland, Australia. Journal of Structural Geology, 17, 7, 949-960.

O'Dea, M.G., Lister, G.S., Betts, P.G., Pound, K.S., 1997. A shortened intraplate rift system in the Proterozoic Mt Isa terrain, NW Queensland, Australia. Tectonics 16, 425-441.

O'Dea, M. G., Lister, G. S., Kennard, J. M., 1996. Extensional geometries within the Leichhardt River Fault Trough of the Mount Isa Terrain, NW Queensland, Australia. Proceedings 13th Australian geological convention. Geological Society of Australia, Sydney, N.S.W., Australia, pp. 322.

O'Dea, M. G., Lister, G., MacCready, T., Betts, P. G., Oliver, N. H. S., Pound, K. S., Huang, W., Valenta, R. K., 1997. Geodynamic evolution of the Proterozoic Mount Isa terrain. In: J.-P. Burg and M. Ford (Eds.), Orogeny Through Time. Geological Society of London, London, United Kingdom, 121, pp. 99-122.

Officer, C. B., Carter, N. L., 1991. A review of the structure, petrology, and dynamic deformation characteristics of some enigmatic terrestrial structures. Earth-Science Reviews, 30, (1-2), 1-49.

Oldham, C. H. G., Sutherland, D. B., 1955. Orthogonal polynomials: their use in estimating the regional effect. Geophysics, 20, (2), 295-306.

Oliver, J., 1986. Fluids expelled tectonically from orogenic belts; their role in hydrocarbon migration and other geologic phenomena. Geology (Boulder), 14, (2), 99-102.

Oliver, N. H. S., 2001. Linking of regional and local hydrothermal systems in the mid-crust by shearing and faulting. Tectonophysics, 335, (1-2), 147-161.

Oliver, N. H. S., Holcombe, R. J., Hill, E. J., Pearson, P. J., 1991. Tectono-metamorphic evolution of the Mary Kathleen fold belt, Northwest Queensland; a reflection of mantle plume processes? . Australian Journal of Earth Sciences 38, (4), 425-455.

Oliver, N. H. S., McLellan, J. G., Hobbs, B. E., Cleverley, J. S., Ord A., Feltrin, L., 2006. Numerical Models of Extensional Deformation, Heat Transfer, and Fluid Flow across Basement-Cover Interfaces during Basin-Related Mineralization. Economic Geology, 101, 1-31.

Oliver, N. H. S., Ord, A., Valenta, R. K., Upton, P., 2001. Deformation, Fluid Flow, and Ore Genesis in Heterogeneous Rocks, with Examples and Numerical Models from the Mount Isa District, Australia. Society of Economic Geologists, Reviews, 14, 51-74.

Oliver, N. H. S., Pearson, P. J., Holcombe, R. J., Ord, A., 1999. Mary Kathleen metamorphic-hydrothermal uranium-rare-earth element deposit; ore genesis and numerical model of coupled deformation and fluid flow. Australian Journal of Earth Sciences, 46, (3), 467-484.

Oliver, N.H.S., 1995. Hydrothermal history of the Mary Kathleen Fold Belt, Mount Isa Block, Queensland. Australian Journal of Earth Sciences, 42, 267-279.

Oliver, N.H.S., Ord, A., Valenta, R.K., Upton, P., 2001a. Deformation, Fluid Flow, and Ore Genesis in Heterogeneous Rocks, with Examples and Numerical Models from the Mount Isa District, Australia. Society of Economic Geologists, Reviews, 14, 51-74.

Opik, A. A., 1957. The Cambrian Geology of Australia. Australia, Bureau of Mineral Resources, Geology and Geophysics, Bulletin, 49, 284 p.

Opik, A. A., 1958. The Cambrian Trilobite Redlichia: organisation and generic concept. Australia, Bureau of Mineral Resources, Geology and Geophysics, Bulletin, 42, 50 p.

Opik, A. A., 1970. Redlichia of the Ordian (Cambrian) of northern Australia and New South Wales. Australia, Bureau of Mineral Resources, Geology and Geophysics, Bulletin, 114, 67 p.

Opik, A. A., 1975. Templetonian and Ordian xystridurid trilobites of Australia. Australia, Bureau of Mineral Resources, Geology and Geophysics, Bulletin, 121, 84 p.

Opik, A. A., 1982. Dolichometopid trilobites of Queensland, Northern Territory, and New South Wales. Australia, Bureau of Mineral Resources, Geology and Geophysics, Bulletin, 175, 85 p.

Ord A., Hobbs B.E., Zhang Y., Broadbent G.C., Brown, M., Willetts G., Sorjonen-Ward P., Walshe J.L., Zhao C., 2002. Geodynamic modelling of the Century deposit, Mt Isa Province, Queensland. Australian Journal of Earth Sciences, 49, 6, 1011-1039.

Ord, A., 1991a. Deformation of Rock: A Pressure-Sensitive, Dilatant Material. Pure and Applied Geophysics, 137, (4), 337-366.

Ord, A., 1991b. Fluid flow through patterned shear zones. Computer Methods and Advances in Geomechanics. Beer, G., Booker, J. R., Carter, J. P. (Eds). Rotterdam, Balkema, 393-398.

Ord, A., Hobbs, B. E., Zhang, Y., Broadbent, G. C., Brown, M., Willetts, G., Sorjonen-Ward, P., Walshe, J. L., Zhao, C., 2002. Geodynamic modelling of the Century deposit, Mt Isa Province, Queensland. Australian Journal of Earth Sciences, 49, (6), 1011-1039.

Ord, A., Oliver, N. H. S., 1997. Mechanical controls on fluid flow during regional metamorphism: some numerical models. Journal Metamorphic Geology, 15, (3), 345-359.

Ortoleva, P. J., Parrish, J. T., Coleman, M. R., 1993. Self-organization and nonlinear dynamics in sedimentary basins. Philosophical Transaction Royal Society of London. A, 344, 171-179.

Paganelli, F., Richards, J. P., C., G. E., 2002. Integration of Structural, Gravity, and Magnetic Data Using the Weights of Evidence Method as a Tool for Kimberlite Exploration in the Buffalo Head Hills, Northern Central Alberta, Canada. Natural Resources Research, 11, (3), 219-236.

Page, R. W., 1988. Geochronology of early to middle Proterozoic fold belts in northern Australia: a review. Precambrian Research, 40-41, 1–19.

Page, R. W., Bell, T.H., 1986. Isotopic and structural responses of granite to successive deformation and metamorphism. Journal of Geology, 94, 365-379.

Page, R. W., Jackson, M. J., Krassay, A. A., 2000. Constraining sequence stratigraphy in North Australian basins; SHRIMP U-Pb zircon geochronology between Mt Isa and McArthur River. Carpentaria-Mt. Isa Belt; basement framework, chronostratigraphy and geodynamic evolution of Proterozoic successions Australian Journal of Earth Sciences, 47, (3), 431-459.

Page, R. W., Sweet, I. P., 1998. Geochronology of basin phases in the western Mt Isa Inlier, and correlation with the McArthur Basin. Australian Journal of Earth Sciences, 45, 219–232.

Page, R.W., Sun, S.S., 1998. Aspects of geochronology and crustal evolution in the Eastern Fold Belt, Mt Isa Inlier. Australian Journal of Earth Sciences, 45, 343-363.

Park, A. J., Ortoleva, P. J., 2003. WRIS.TEQ; multi-mineralic water-rock interaction, mass-transfer and textural dynamics simulator Reactive transport modeling in the geosciences 29, (3), 277-290.

Payros, A., Pujalte, V., Orue-Etxebarria, X., 1999. The South Pyrenean Eocene carbonate megabreccias revisited: new interpretation based on evidence from the Pamplona Basin. Sedimentary Geology, 125, (3), 165-194.

Peacock, D. C. P., 2001. The temporal relationship between joints and faults. Journal of Structural Geology, 23, (2), 329-341.

Perez, R. J., Boles, J. R., 2005. Interpreting fracture development from diagenetic mineralogy and thermoelastic contraction modeling. Tectonophysics, 400, (1), 179-207.

Perkins, C., Wyborn, L.A.I., 1998. Age of Cu-Au mineralisation, Cloncurry District, eastern Mt. Isa Inlier, Queensland, as determined by Ar/Ar dating. Australian Journal of Earth Sciences, 45, 233-246.

Perkins, W. G., 1997. Mount Isa lead-zinc orebodies: Replacement lodes in a zoned syndeformational copper-lead-zinc system? Ore Geology Reviews, 12, (2), 61-110.

Phillips, O. M., 1991. Flow and reactions in permeable rocks. Cambridge, Cambridge Univ. Press, United Kingdom, 285 p.

Pietrantonio, G., Riguzzi, F., 2004. Three-dimensional strain tensor estimation by GPS observations: methodological aspects and geophysical applications. Journal of Geodynamics, 38, 1-18.

Pietsch, B. A., Rawlings, D. J., Creaser, P. M., Kruse, P. D., Ahmad, M., Ferenczi, P. A., Findhammer, T. L. R., 1991. Bauhinia Downs 1:250 000 geological map series. Northern Territory Geological Survey Explanatory Notes SE 53–3.

Plumb, K. A., Derrick, G. M., 1975. Geology of the Proterozoic rocks of the Kimberley to Mount Isa Region. In: Economic Geology of Australia and Papua New Guinea, pp. 217–252. Australian Institute of Mining and Metallurgy Monograph Series 5.

Plumb, K. A., Derrick, G. M., Wilson, I.H., 1980. Precambrian geology of the McArthur River Mount Isa Region, northern Australia. In: Henderson, R.A., Stephenson, P.J. (Eds.) The Geology and Geophysics of Northeastern Australia. Geological Society of Australia, Queensland Division, 77-88.

Pollard, D. D., 1973. Derivation and evaluation of a mechanical model for sheet intrusions. Tectonophysics, 19, (3), 233-269.

Pollard, D. D., Segall, P., 1987. Theoretical displacements and stresses near fractures in rock: with applications to faults, joints, veins, dikes, and pressure solution surfaces. In: B. K. Atkinson (Ed.), Fracture Mechanics of Rock. Academic Press, London, pp. 277-349.

Pomar, L, Obrador, A., Westphal, H., 2002. Sub-wavebase cross-bedded grainstones on a distally steepened carbonate ramp, Upper Miocene, Menorca, Spain. Sedimentology, 49, (1), 139-169.

Porwal, A., Carranza, E. J. M., Hale, M., 2006. Bayesian network classifiers for mineral potential mapping. Computers & Geosciences, 32, (1), 1-16.

Potter, P. E., Pettijohn, F. J., 1963. Paleocurrents and Basin Analysis. Springer-Verlag, New York, 296 p.

Price, N. J., 1966. Fault and Joint Development in Brittle and Semibrittle Rock. Pergamon Press, London, 176 p.

Pye, K., 1984. SEM analysis of siderite cements in intertidal marsh sediments, Norfolk, England. Marine Geology, 56, (1-4), 1-12.

Raines, G. L., 1999. Evaluation of Weights of Evidence to Predict Epithermal-Gold Deposits in the Great Basin of the Western United States. Natural Resources Research, 8, (4), 257-276.

Reed, C., Wallace, M., 2004. Zn-Pb mineralisation in the Silvermines district, Ireland: a product of burial diagenesis. Mineralium Deposita, 39, (1), 87-102.

Richards, J. R., 1975. Lead isotope data on three North Australian galena localities. Mineralium Deposita, 10, (4), 287-301.

Rona, P. A., 1984. Hydrothermal mineralization at seafloor spreading centers. Earth-Science Reviews, 20, (1), 1-104.

Rossetti, D. F., Santos, J., Antonio E., 2003. Events of sediment deformation and mass failure in Upper Cretaceous estuarine deposits (Cameta Basin, northern Brazil) as evidence for seismic activity. Sedimentary Geology, 161, (1-2), 107-130.

Rouby, D., Raillard, S., Guillocheau, F., Bouroullec, R., Nalpas, T., 2002. Kinematics of a growth fault/raft system on the West African margin using 3-D restoration. Journal of Structural Geology, 24, (4), 783-796.

Rubenach, M. J., 1992. Proterozoic low-pressure/high-temperature metamorphism and an anticlockwise P–T–t path for the Hazeldene area, Mt Isa Inlier, Queensland, Australia. Journal Metamorphic Geology, 10, 333-346.

Rubenach, M., Adshead, N., Oliver, N.H.S., Tullemans, F., Esser, D., Stein, H., 2001. The Osborne Cu-Au Deposit: Geochronology, and Genesis of Mineralisation in Relation to Host Albitites and Ironstones. In: Williams, P.J. (Ed) A Hydrothermal Odyssey, Extended Conference Abstracts, JCU, Economic geology Research Unit Contribution 59, 172-173.

Ruffell, A. H., Moles, N. R., Parnell, J., 1998. Characterisation and prediction of sediment-hosted ore deposits using sequence stratigraphy. Ore Geology Reviews, 12, (4), 207-223.

Russell, M.J., 1978. Downward-excavating hydrothermal cells and Irish-type ore deposits: importance of an underlying thick Caledonian prism. Trans. Inst. Min. Metal., 87b, 168-171.

Saaty, T.L., 1977. A Scaling Method for Priorities in Hierarchical Structures. J. Math. Psychology, 15, 234-281.

Sahoo, N. R., Pandalai, H. S., 1999. Integration of Sparse Geologic Information in Gold Targeting Using Logistic Regression Analysis in the Hutti-Maski Schist Belt, Raichur, Karnataka, India-A Case Study. Natural Resources Research, 8, (3), 233-250.

Sandiford, M., Hand, M., 1998. Controls on the locus of intraplate deformation in central Australia. Earth and Planetary Science Letters, 162, (1), 97-110.

Sangster, D.F., 1983. Sediment-hosted stratiform lead-zinc deposits. Min. Assoc. Canada Short Course Handbook, 8, pp.309.

Sawkins, F.J., 1990. Metal Deposits in Relation to Plate Tectonics. Springer-Verlag, New York, pp. 388.

Schardt, C., Large, R. R., Yang, J., 2006. Controls on heat flow, fluid migration, and massive sulfide formation of an off-axis hydrothermal system-the Lau Basin perspective. American Journal of Science, 306, (2), 103-134.

Schaubs, P. M., Zhao C., 2002. Numerical models of gold-deposit formation in the Bendigo-Ballarat Zone, Victoria. Australian Journal of Earth Sciences, 49, (6), 1077-1096.

Scott, D. L., Bradshaw, B. E., Tarlowski, C. Z., 1998. The tectonostratigraphic history of the Proterozoic Northern Lawn Hill Platform, Australia: an integrated intracontinental basin analysis. Tectonophysics, 300, (1-4), 329-358.

Scott, D. L., Rawlings, D. J., Page, R. W., Tarlowski, C. Z., Idnurm, M., Jackson, M. J., Southgate, P. N., 2000. Basement framework and geodynamic evolution of the Palaeoproterozoic superbasins of north-central Australia: an integrated review of geochemical, geochronological and geophysical data. Australian Journal of Earth Sciences, 47, (3), 341-380.

Scott, D., Tarlowski, C., Page, R., Idnurm, M., Jackson, M. J., Mackenzie, D., Rawlings, D., 1998a. Basement studies in basin analysis; new insights into the evolution of the Lawn Hill Platform. AGSO Research Newsletter, 28, 29-32.

Secor, D. T., 1965. Role of fuid pressure in jointing. American Journal of Science, 263, 633-646.

Shafer, G., 1976. A Mathematical Theory of Evidence. Princeton Univ. Press, Princeton, NJ., 297 p.

Shaw, R. D., Etheridge, M. A., Lambeck, K., 1991. Development of the late Proterozoic to mid-Paleozoic, intracratonic Amadeus Basin in central Australia: a key to understanding tectonic forces in plate interiors. Tectonics, 10, (4), 688-721.

Shergold, J. H., Druce, E. C., 1980. Upper Proterozoic and Lower Palaeozoic rocks of the Georgina Basin. In: R. A. Henderson and P. J. Stephenson (Eds.), The

Geology and Geophysics of Northeastern Australia. Geological Society of Australia, Queensland Division, pp. 149-174.

Shergold, J. H., Druce, E. C., Radke, B. M., Draper, J. J., 1976. Cambrian and Ordovician stratigraphy of the eastern portion of the Georgina Basin, Queensland and eastern Northern Territory (Guidebook - International Geological Congress). 25, Excursion 4C, 54 p.

Shergold, J. H., Elphinstone, R., Laurie, J. R., Nicoll, R. S., Walter, M. R., Young, G. C., Zang, W., 1991. Late Proterozoic and early Palaeozoic palaeontology and biostratigraphy of the Amadeus Basin. In: Bureau of Mineral Resources Bulletin, 236, pp. 97-111.

Shiki, T., Cita, M. B., Gorsline, D. S., 2000. Sedimentary features of seismites, seismo-turbidites and tsunamiites-an introduction. Sedimentary Geology, 135, (1), vii-vix.

Shoemaker, E. M., 1992. Letter to the Australian Heritage Commission on the Lawn Hill Structure, Queensland.

Shoemaker, E. M., Shoemaker, C. S., 1996. The Proterozoic impact record of Australia. AGSO Journal of Geology and Geophysics, 16, 379-398.

Sibson, R. H., 1985a. A note on fault reactivation. Journal of Structural Geology, 7, (6), 751-754.

Sibson, R. H., 1985b. Stopping of earthquake ruptures at dilational fault jogs. Nature 316, (6025), 248-251.

Sibson, R. H., 1987. Earthquake rupturing as a hydrothermal mineralising agent. Geology, 15, (8), 701-704.

Sibson, R. H., Scott, J., 1998. Stress/fault controls on the containment and release of overpressured fluids: Examples from gold-quartz vein systems in Juneau, Alaska; Victoria, Australia and Otago, New Zealand. Ore Geology Reviews, 13, (1-5), 293-306.

Silver, D., Zabusky, N. J., 1993. Quantifying Visualizations for Reduced Modeling in Nonlinear Science: Extracting Structures from Data Sets. Journal of Visual Communication and Image Representation, 4, (1), 46-61.

Simms, M. A., Garven, G., 2004. Thermal convection in faulted extensional sedimentary basins: theoretical results from finite-element modelling. Geofluids, 4, (2), 109-130.

Simoneit, B. R. T., Lonsdale, P. F., 1982. Hydrothermal petroleum in mineralized mounds at the seabed of Guaymas Basin. 295, (5846), 198-202.

Singer, D. A., Kouda, R., 1996. Application of a feedforward neural network in the search for kuroko deposits in the Hokuroku District, Japan. Mathematical Geology, 28, (8), 1017-1023.

Smets, P., 1990. The combination of evidence in the transferable belief model. Pattern Analysis and Machine Intelligence, IEEE Transactions, 12, (5), 447-458.

Smith, J. V., 2000. Flow pattern within a Permian submarine slump recorded by oblique folds and deformed fossils, Ulladulla, south-eastern Australia. Sedimentology, 47, (2), 357-366.

Smith, K. G., 1972. Stratigraphy of the Georgina Basin. Bureau of Mineral Resources Bulletin, 111, p.

Smith, W.D., 1969. Penecontemporaneous faulting and its likely significance in relation to Mount Isa ore deposition. Special Publications of the Geological Society of Australia, 2, 225-235.

Snedecor, G. W., Cochran, W. G., 1967. Statistical Methods: 6th Edition. 593 p.

Solomon, M., Groves, D. I., 1994. The geology and origin of Australia's mineral deposits. Oxford University Press, New York, 951 p.

Sornette, D., 1991. Self-organized criticality in plate tectonics. Proceedings NATO ASI "Spontaneous Formation of Space-time Structures and Criticality". Geilo, Norway, 2-12 April 1991, Kluwer Academic Press, Dordrecht, pp. 57-106.

Sornette, D., 1999. Earthquakes: from chemical alteration to mechanical rupture. Physics Reports, 313, (5), 237-292.

Southgate, P. N., 2000. Carpentaria - Mt Isa Zinc Belt: basement framework, chronostratigraphy and geodynamic evolution of Proterozoic successions. Australian Journal of Earth Sciences, 47, (3), 337-340.

Southgate, P. N., Bradshaw, B. E., Domagala, J., Jackson, M. J., Idnurm, M., Krassay, A. A., Page, R. W., Sami, T. T., Scott, D. L., Lindsay, J. F., and others, 2000. Chronostratigraphic basin framework for Palaeoproterozoic rocks (1730-1575 Ma) in northern Australia and implications for base-metal mineralisation. Aust J Earth Sci, 47, (3), 461-483.

Southgate, P. N., Shergold, J. H., 1991. Application of sequence stratigraphic concepts to Middle Cambrian phosphogenesis, Georgina Basin, Australia BMR Journal of Australian Geology and Geophysics 12, (2), 119-144.

Spiegelhalter, D. J., 1986. Uncertainty in expert systems. In: W. A. Gale (Ed.), Artificial intelligence and statistics. Addison-Wesley, Reading, Massachusetts, pp. 17-55.

Stanton, R. L., 1972. Ore Petrology. McGraw-Hill, New York, N. Y., 713 p.

Stewart, A., 1986. Proof of explosive origin for the Lawn Hill circular structure. Bureau of Mineral Resources, Geology and Geophysics, Australia, Research Newsletter 4, 10-11.

Stewart, A., Mitchell, K., 1987. Shatter cones at the Lawn Hill circular structure, northwestern Queensland; presumed astrobleme Australian Journal of Earth Sciences 34, (4), 477-485.

Stewart, A.J., Blake, D.H., 1992. Detailed studies of the Mount Isa Inlier: Australian Bureau of Mineral Research Bulletin, 243, pp. 374.

Stuart, J. T., Tabor, M., 1990. The Lagrangian Picture of Fluid Motion. Philosophical Transaction: Physical Sciences and Engineering, 333, (1631), 263-271.

Sun, S.S., Page, R.W., Carr, G., 1994. Lead-isotope-based stratigraphic correlations and ages of Proterozoic sediment-hosted Pb-Zn deposits in the Mount Isa Inlier. AGSO Bulletin, 20, 1-2.

Swart, P. K., Burns, S. J., Leder, J. J., 1991. Fractionation of the stable isotopes of oxygen and carbon in carbon dioxide during the reaction of calcite with phosphoric acid as a function of temperature and technique. Chemical Geology: Isotope Geoscience section, 86, (2), 89-96.

Sweet, I. P., Hutton, L. J., 1982a. Geology of the Lawn Hill region, Queensland. Aust. Gov. Publ. Serv., Canberra, Australia, 1 sheet, 36 p.

Sweet, I. P., Hutton, L. J., 1982b. Lawn Hill Region 1: 100 000 geological map commentary. Bureau of Mineral Resources, Canberra.

Sweet, I. P., Mock, C. M., Mitchell, J. E., 1981. Seigal (Northern Territory) and Hedleys Creek (Queensland) 1:100 000 Geological Map Commentary. Bureau of Mineral Resources, Canberra.

Szulc, S. A., 1992. The stratigraphic reconstruction of a mega-breccia: a sedimentological study of the south western corner of the Lawn Hill Outlier (unpublished). James Cook University, B.Sc.(Hons.), 97 p.

Tadakazu, U., Akira, I., Yu, Y., 2001. Horizontal Strain Rate in Relation to Vein Formation of the Hishikari Gold Deposits, Southern Kyushu, Japan. Resource Geology, 51, 1, 7-18.

Taylor, H. P., Jr., 1971. Oxygen Isotope Evidence for Large-scale Interaction between Meteoric Ground Waters and Tertiary Granodiorite Intrusions, Western Cascade Range, Oregon. Journal of Geophysical Research, 76, (32), 7855-7874.

Terzaghi, K., 1945. Stress conditions for the failure of saturated concrete and rock. Proceedings American Society for Testing and Materials, 45, 777-801.

Thiart, C., Bonham-Carter, G. F., Agterberg, F. P., 2003. Conditional independence in weights-of-evidence: application of an improved test. Proceedings IAMG 2003 Ann. Conf. Portsmouth, England, CD-ROM.

Toth, D. J., 1962. A Theory of Groundwater Motion in Small Drainage basins in Central Alberta, Canada. Journal of Geophysical Research, 68, (16), 4795-4812.

Tukey, J. W., 1972. Discussion of "Mathematical Problems in Geology". In: F. P. Agterberg and S. C. Robinson (Eds.), Proceedings of the 38th session. International Statistical Institute Bulletin, Book 1, pp. 596.

Turcotte, D. L., Rundle, J. B., 2002. Self-Organized Complexity in the Physical, Biological and Social Sciences. Proceedings of the National Academy of Sciences of the United States of America, 99, (3), 2463-2465.

Turcotte, D.L., Schubert, G., 2002. Geodynamics, 2nd Edition, Cambridge University Press, U.K.

Turner, R. J. W., 1992. Formation of Phanerozoic stratiform sediment-hosted zinc-lead deposits: Evidence for the critical role of ocean anoxia. Chemical Geology, 99, (1-3), 165-188.

Upton, P., 1998. Localization of deformation and Fluid Flow in a Compressional Orogen: Implications for the Southern Alps of New Zealand. American Journal of Science, 298, 296-323.

Upton, P., Baxter, K., O'Brien, G.W., 1998. Coupled Mechanical / Fluid Flow Models of Trap Integrity and Fault Reactivation: Application to the North West Shelf of Australia. Australian Petroleum Production and Exploration Association Journal 1998, 488-499.

Upton, P., Koons, P. O., Chamberlain, C. P., 1995. Penetration of deformation-driven meteoric water into ductile rocks: isotopic and model observations from the

Southern Alps, New Zealand. Journal of Geology and Geophysics, 38, (4), 535-543.

van Loon, A. J., 2003. How 'hard' are hard-rock deformations? Earth-Science Reviews, 61, (1), 181-188.

Veizer, J., Ala, D., Azmy, K., Bruckschen, P., Buhl, D., Bruhn, F., Carden, G. A. F., Diener, A., Ebneth, S., Godderis, Y., 1999. 87Sr/86Sr, [delta]13C and [delta]18O evolution of Phanerozoic seawater. Chemical Geology, 161, (1-3), 59-88.

Veizer, J., Godderis, Y., Francois, L. M., 2000. Evidence for decoupling of atmospheric CO_2 and global climate during the Phanerozoic eon. Nature, 408, (6813), 698-701.

Vermeer, P. A., de Borst, R., 1984. Non-associated plasticity for soils, concrete and rock. Heron, 29, 1-62.

Vokes, F. M., Spry, P. G., Marshall, B., 2000. Ores and metamorphism; introduction and historical perspectives. In: P. G. Spry, B. Marshall and F. M. Vokes (Eds.), Metamorphosed and Metamorphogenic Ore Deposits. Society of Economic Geologists, Socorro, NM, 11, pp. 1-18.

Walker, P. A., Lev, J., 1953. Statistical Inference. Holt, Rinehart and Winstone, New York, 510 p.

Walter, M. R., Veevers, J. J., Calver, C. R., Grey, K., 1995. Neoproterozoic stratigraphy of the Centralian Superbasin, Australia. Precambrian Research, 73, (1), 173-195.

Walter, M. R., Veevers, J. J., Calver, C. R., Grey, K., Hilyard, D., 1992. The Proterozoic Centralian Superbasin: a frontier petroleum province. Proceedings 1992 AAPG Int. Conf. Exhib. pp. 77.

Waltho, A. E., Andrews, S. J., 1993. The Century zinc-lead deposit, Northwest Queensland. Proceedings The Australasian Institute of Mining and Metallurgy; centenary conference. Publisher Australas. Inst. Min. and Metall., Parkville, Vict., Australia, pp. 41-61.

Ware, C., Knight, W., Wells, D., 1991. Memory intensive statistical algorithms for multibeam bathymetric data. Computers & Geosciences, 17, (7), 985-993.

Wellman, P., 1992. Structure of the Mount Isa region inferred from gravity and magnetic anomalies. In: A. J. Stewart and D. H. Blake (Eds.), Detailed Studies of the Mount Isa Inlier. Australian Geological Survey Organisation Bulletin, 243, pp. 15-27.

Williams, P. F., Collins, A. R., Wiltshire, R. G., 1969. Cleavage and penecontemporaneous deformation structures in sedimentary rocks. Journal of Geology, 77, 415-425.

Wilson, I. H., Hutton, L. J., 1980. Geological field work in Mount Isa district - Aug. Sept., 1980. Geological Survey of Queensland Record, 34, 12-18.

Witten, A., 2004. A MATLAB-based three-dimensional viewer. Computers & Geosciences, 30, (7), 693-703.

Wolf, K. H., 1994. Artificial Intelligence (AI) and Expert Systems (ES). Ore Geology Reviews, 9, (3), 241-243.

Wyborn, L. A. I., Page, R. W., McCulloch, M. T., 1988. Petrology, geochronology and isotope geochemistry of the post-1820 Ma granites of the Mount Isa Inlier: mechanisms for the generation of Proterozoic anorogenic granites. Precambrian Research, 40-41, 509-541.

Xin, J., Peirce, A., Chadam, J., Ortoleva, P., 1993. Reactive flows in layered porous media II. The shape stability of the reaction interface. SIAM Journal of applied mathematics, 53, (2), 319-339.

Xue, Y., Sun, M., Ma, A., 2004. On the reconstruction of three-dimensional complex geological objects using Delaunay triangulation. Future Generation Computer Systems, 20, (7), 1227-1234.

Yager, R. R., 1988. On ordered weighted averaging aggregation operators in multicriteria decisionmaking. IEEE Trans. Syst. Man Cybern., 18, (1), 183-190.

Voogd, H., 1983. Multicriteria Evaluation for Urban and Regional Planning. Pion, Ltd., London.

Zhang, X., Sanderson, D. J., 2002. Numerical Modelling and Analysis of Fluid Flow and Deformation of Fractured Rock Masses. Pergamon Press, London, 288 p.

Zhang, Y., Hobbs, B. E., Ord, A., Muhlhaus, H.-B., 1996a. Computer simulation of single-layer buckling. Journal of Structural Geology, 18, (5), 643-655.

Zhang, Y., Scheibner, E., Ord, A., Hobbs, B. E., 1996b. Numerical modelling of crustal stresses in the eastern Australian passive margin. Australian Journal of Earth Sciences, 43, (2), 161-175.

Zhao, J.-x., McCulloch, M. T., 1995. Geochemical and Nd isotopic systematics of granites from the Arunta Inlier, central Australia: implications for Proterozoic crustal evolution. Precambrian Research, 71, (1-4), 265-299.

Zhao, J.-X., McCulloch, M. T., Korsch, R. J., 1994. Characterisation of a plume-related
~ 800 Ma magmatic event and its implications for basin formation in central-
southern Australia. Earth and Planetary Science Letters, 121, (3-4), 349-367.

Zierenberg, R. A., Fouquet, Y., Miller, D. J., Bahr, J. M., Baker, P. A., Bjerkgård, T.,
Brunner, C. A., Duckworth, R. C., Gable, R., Gieskes, J., and others, 1998. The
deep structure of a sea-floor hydrothermal deposit. Nature, 392, 485-488.

APPENDIX A

A.1. Nodal formulation

Even though the mathematical approach based on the solution of stress/strain relationships, equations of motion and equilibrium, and constitutive laws was set in Chapter 2; it is necessary to reduce the equations from an integral or differential form to a finite-difference form as illustrated in earlier examples on exponential growth. In other words the FLAC models will be discretised in a nodal formulation. Therefore finite-difference approximation is needed both in time and space to allow computer simulation in FLAC. The time is commonly discretised by subdivision in small constant calculation steps, whereas the use of discretised grids of nodes represents an approximation of the spatial continuum. A final important constraint imposed in FLAC is that the material derivation of the nodal velocities has to be reduced to zero to obtain a condition of static equilibrium. This is reasonable if it is imagined a natural example such as an earthquake. Earth motion in this case is due to accumulation of stresses due to plate tectonics abruptly released and converted into strain energy until an equilibrium state is reached. FLAC aims at equilibrium to simulate such natural tendency to minimise energy.

Reduction to a nodal form of classes of equations introduced (e.g. translational (ξ_{ij}) and rotational (ω_{ij}) strain-rates) is firstly obtained reducing the laws at the tetrahedron scale. A deforming tetrahedron can be thought as a velocity field. In analogy to other conservative fields using the Gauss or divergence theorem:

$$\iiint_V v_{i,j}\, dV = \oiint_S v_i\, n_j\, dS \tag{A.1}$$

it can be demonstrated that the flux escaping from an element of volume (*V*) containing a source of constant intensity (e.g. a stationary fluid) is equivalent to the sum of the fluxes exiting from a closed surface surrounding the volume independent of the surface area interested by the flux. The symmetry of the problem lead then to a reduction to a finite summation of fluxes escaping from multiple surfaces of the FLAC tetrahedron, allowing a linear approximation of the nodal velocity as follows:

$$v_{ij} = -\frac{1}{3V}\sum_{l=1}^{4} v_i^l\, n_j^{(l)}\, S^{(l)} \tag{A.2}$$

The (A.2) is essentially a finite summation over the indexes (*l*) that represent the four nodes of each tetrahedron. The superscript (*l*) indicates a nodal property that is considering the sum of the contributions of all adjacent tetrahedrons acting on a certain node. (*S*) is the area of each face.

 Substitution into (2.66 – Chapter2) and (2.67) leads to a nodal formulation of translational and rotational strain rates (σ_{ij}, ξ_{ij}):

$$\xi_{ij} = -\frac{1}{6V}\sum_{l=1}^{4}\left(v_i^l\,n_j^{(l)} + v_j^l\,n_i^{(l)}\right)S^{(l)}$$ (A.3)

$$\omega_{ij} = -\frac{1}{6V}\sum_{l=1}^{4}\left(v_i^l\,n_j^{(l)} - v_j^l\,n_i^{(l)}\right)S^{(l)}$$ (A.4)

The (A.3) and (A.4) shows that nodal velocities can be used to represent forces applied to the whole tetrahedral grid and the relative strains and their rates resulting from the application of such stresses in time. In this regard seems to be clearer the meaning of a Lagrangian representation that look at the kinematic behaviour of individual nodes. In contrast, the required generalisation is brought by the nodal formulation of the laws of motion.

A.2. Theorem of the virtual work

The principle of *virtual work* is a convenient way to treat the laws of motion and it is used here to derive a nodal formulation for the Cauchy's equations. It is based on the concept of kinetic energy in the form of thermodynamic work internal and external (W_i, W_e) although unnecessary as the two represent the same measurement of strain in the considered model, the separation is however instructive. Taking the Gauss theorem as an analogy: the *work* performed on a generic surface would be equivalent to a flux of energy transferred from the environment into the system incrementing its energy

although such energy rather than be stored is taken up by deformation and released internally producing work that corresponds to the rearrangement of the nodes of the tetrahedrons. The two are therefore the same quantity although described from a different frame of reference:

$$W_i = \int\int\int_V v_{i,j}\, dV \tag{A.5}$$

$$W_e = \oiint_S v_i\, n_j\, dS \tag{A.6}$$

Comparing with the (A.1) it can be defined:

$$W_i = W_e \tag{A.7}$$

After these considerations the (2.68) can be expressed as representing W_e in the form:

$$W_e = \sum_{n=1}^{4} \delta v_i^n\, f_i^n + \int_V \delta v_i\, B_i\, dV \tag{A.8}$$

the two terms on the left side of (A.8) represent respectively the contribution of contact forces (f_i) and body forces here considered coupled with the material derivative of the velocity (B_i), in this case note that rather than calculating the work for a tetrahedron in term of virtual displacement, it is considered the nodal virtual velocity (δv_i^n) representing therefore a rate of external virtual work (W_e). On the other hand, the Cauchy's relationships for the theorem of virtual work (A.7) have to be equated to the nodal formulation of the internal rate of displacement (W_i). It is in this case convenient to recall the (A.72) replacing strain with internal stresses as follows:

$$W_i = -\frac{1}{6}\sum_{l=1}^{4}\left(\delta v_i^l\, \sigma_{ij}\, n_j^{(l)} + \delta v_j^l\, \sigma_{ij}\, n_i^{(l)}\right) S^{(l)} \qquad (A.9)$$

Such relationship can be further simplified in light of the symmetrical character of the stress tensor regrouping in the (A.10), where (T_i) is the stress vector:

$$T_i^l = \sigma_{ij}\, n_j^{(l)}\, S^{(l)} \qquad (A.10)$$

W_i becomes:

$$W_i = -\frac{1}{3}\sum_{n=1}^{4}\delta v_i^l\, T_i^l \qquad (A.11)$$

With further rearranging and combining the (A.8) with the (A.11) a relationship that provides a value for the nodal force (f_i):

$$-f_i^n = \frac{T_i^n}{3} + \frac{\rho b_i\, V}{4} - m^n\left(\frac{dv_i}{dt}\right)^n \qquad (A.12)$$

where the first term on the right side represents the internal work component whereas the other two terms account respectively for the body forces here considered function of the material derivative of the nodal velocity:

$$b_i = \left(\frac{B_i}{\rho} + \frac{dv_i}{dt} \right) \qquad\qquad (A.13)$$

and the contact forces obtained considering fictitious nodal masses (m) that are adjusted in FLAC to stabilise the solution. The (A.12) can be further generalised to the whole body considering the sum of the contributions of all nodes (n_n) and relative inertial terms (P_i):

$$F_i^{<l>} = M^{<l>} \left(\frac{T_i}{3} + \frac{\rho b_i V}{4} \right)^{<l>} + P_i^{<l>} \qquad\qquad <l> = 1, \dots n_n \qquad\qquad (A.14)$$

To reach a static condition, after a perturbation has been imposed to the body, as seen from definition (A.7) the sum of all forces should progressively tend to zero. $F_i^{<l>} \to 0$ during reorganisation resulting in stress accumulation and release of strain in time.

From the outlined relationships it is concluded that the spatial approximation is soundly based on the concepts of discretization and minimization of energy of the modelled body. Similarly to the forme discretization is adopted in FLAC to reduce the continuity of time to finite intervals. FLAC computes nodal velocities on the basis of a central finite difference approximation in which each time step is half of the Δt used to compute the forces and displacements of the nodes. The approach can be demonstrated to give a second order approximation error of time derivatives the velocity

approximation is given as an example; it can be expressed in finite difference form after integration of the second law of Newton as follows:

$$v_i^{<l>}\left(t+\frac{\Delta t}{2}\right)=v_i^{<l>}\left(t-\frac{\Delta t}{2}\right)+\frac{\Delta t}{M^{<l>}}F^{<l>} \qquad\qquad (A.15)$$

here the term M refers to the sum of all the contributions (m) of the tetrahedrons surrounding the node of interest $<l>$.

A.3. The Mohr-Coulomb constitutive model and its relationship to the motion equations

The constitutive models work conceptually in a similar way, they try to differentiate between the plastic and the elastic component of the strain tensor. The distinction is possible thanks to the experimental mechanics models available. The simulated materials will be deforming in a variable manner for an applied stress accordingly to their relative properties (e.g. cohesion, the friction angle, the elastic/shear modulus, etc.). The objective is to describe the co-rotational stress increments in time (co-rotational is a convention in which the stress rates are measured by an observer rotating at the same angular velocity of the particle considered – here the suffix on top of the co-rotational stress ($\breve{\sigma}$) is omitted because all stresses are co-rotational). Note that in a plastic deformation the co-rotational stress increments represent only the elastic part of

the deformation. To make a distinction between a plastic and elastic response of a material, a yield function is therefore assigned to the model (e.g. Fig. A.1):

$$f\left(\sigma_{ij}\right) = 0 \tag{A.16}$$

The (A.16) is equal to zero when the material fails for a certain combination of compressive or tensile stresses. For the Mohr-Coulomb material the (A.16) is represented by two functions (Fig. A.2) becoming:

$$f^{s} = \sigma_{1} - \sigma_{3} N_{\Phi} + 2c \sqrt{N_{\Phi}} \tag{A.17}$$

which is the Mohr-Coulomb criteria, and also for a tensile failure the criteria becomes:

$$f^{t} = \sigma_{3} - \sigma^{t} \tag{A.18}$$

in such examples of yield functions it is outlined the dependency of the point of yield from mechanical terms other than confining stresses, i.e., the cohesion (c), a function of the friction angle (N_{Φ}) (A.17), and the tensile strength (σ^{t}) in the (A.18). Usually a generic Mohr-Coulomb material subject to an applied stress reacts firstly in an elastic manner until it yields and subsequently deform plastically.

a)

b)
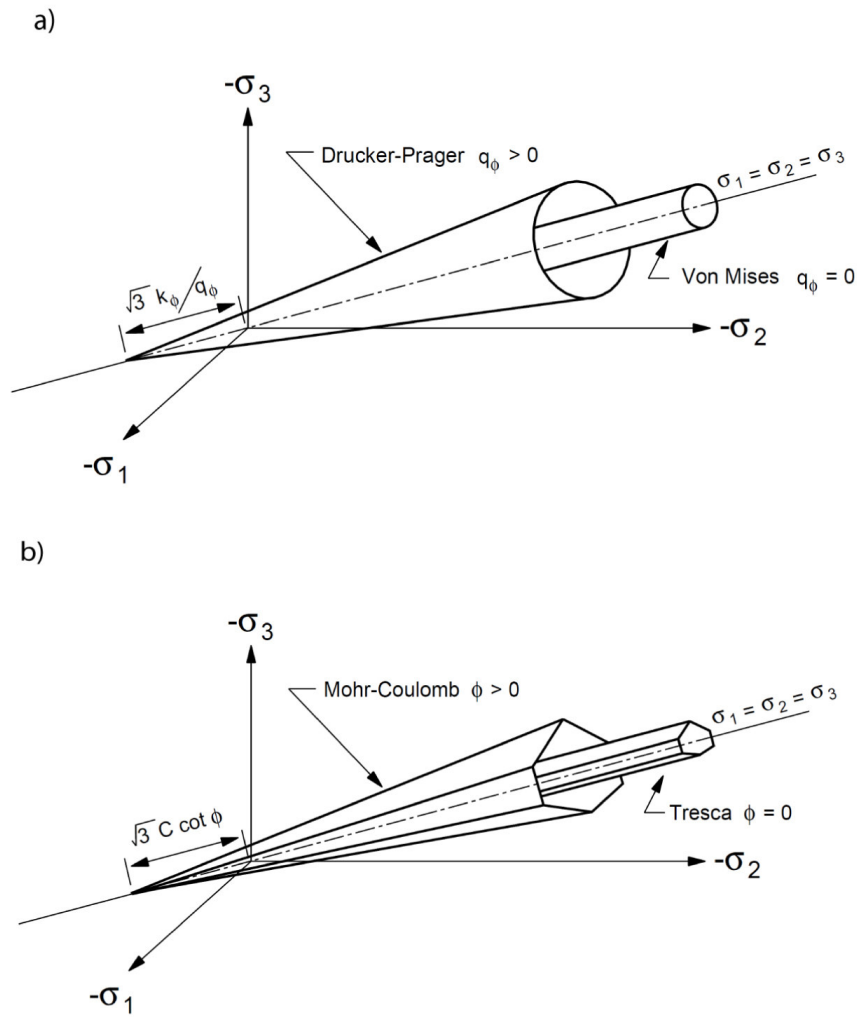
Fig. A. 1 Example of yield surface function in stress space respectively for: (a) Drucker-Prager and Von Mises yield (conical) surfaces in principal stress space; (b) Mohr-Coulomb and Tresca failure envelops (irregular hexagonal). Adapted from (Itasca, 2003).
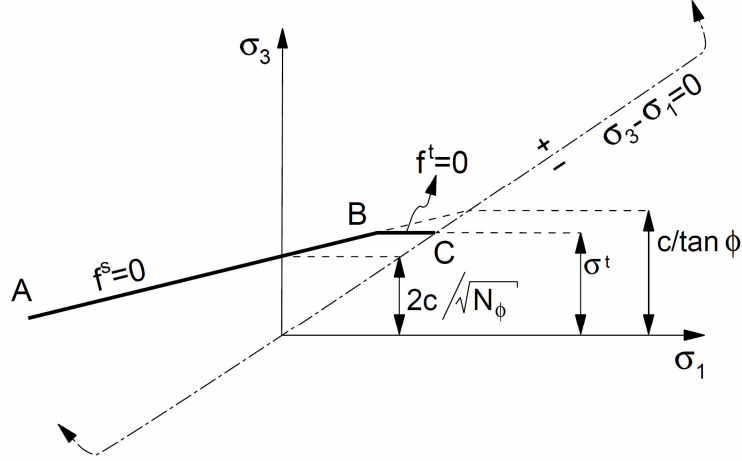
Fig. A. 2 Composite Mohr-Coulomb criterion with tension cut-off. represented in planar space (σ_1, σ_3). Compressive stress considered negative with $\sigma_1 \leq \sigma_2 \leq \sigma_3$. The failure envelope $f(\sigma_1, \sigma_3) = 0$ is defined within the interval A-B following Mohr-Coulomb type behaviour, whereas the curve in section B-C is characterised by a tensile failure criterion in which $\sigma_3 \leq \dfrac{c}{\tan(\Phi)}$ with cohesion (c) and friction angle (Φ). The yield function for shear/tensile failure (f_s, f_t) are violated where (σ_1, σ_3) fall above the lines corresponding to higher deviatoric stresses (σ_1, σ_3) or when the tensile strength (σ_t) is exceeded (Itasca, 2003).

The total strain increment ($\Delta\varepsilon_i$) is therefore defined by:

$$\Delta\varepsilon_{ij} = \Delta\varepsilon_{ij}^e + \Delta\varepsilon_{ij}^p \tag{A.19}$$

both strain increments can be used to calculate the stress increments that generated them. Usually the elastic component responds to a linear law such as Hook's law whereas non-linearity may result from the plastic component of strain that is represented by:

$$\Delta\varepsilon_{ij}^{p} = \lambda \left(\frac{\partial g}{\partial \sigma_{ij}} \right) \qquad\qquad\qquad (A.20)$$

This relationship based on the flow rule outlines that the direction of the plastic strain increment vector is normal to the potential surfaces of (g) with λ representing a constant. When the function (g) is equal to the yield function (f) the material is considered associative. The spatial association of the two tensorial fields (stress-rate and strain rate) is linear as in the elastic case. Non-associative materials however are the most common in natural examples as they commonly dilate during deformation (e.g. Vermeer and de Borst, 1984; Ord, 1991; McLellan, 2004). Non-associative materials have $f\left(\sigma_{ij}\right) \neq g\left(\varepsilon_{ij}^{p}\right)$; therefore, there are conditions in which the material may deform plastically before reaching a yield condition based for instance on the Mohr-Coulomb criterion.

An iterative approach is used to guess a possible value for the state of stress after a certain stress increment has occurred; the new stress (N) would be defined by:

$$\sigma_{ij}^{N} = \sigma_{ij} + \Delta\sigma_{ij} \qquad\qquad\qquad (A.21)$$

If it is considered that the stress increment, as seen, is reduced by the plastic component of the strain rate tensor then a possible way to make a definitive distinction between the two components of deformation is to formulate what is defined as an *elastic guess* in which it is assumed that the material is non-plastic or perfectly elastic and then using an iterative method the stress increment values are recomputed until they meet the yield function for the chosen constitutive relationship. It is then given the following:

$$\sigma_{ij}^{N} = \sigma_{ij}^{I} - \lambda S_{i}\left(\frac{\partial g}{\partial \sigma_{ij}}\right) \qquad\qquad (A.22)$$

in which the new stress state is obtained, as discussed, subtracting the linear term $S_i(.)$ from the elastic guess (σ_{ij}^{I}). Once the co-rotational stress increment is defined it can be used in conjunction with the equations of motion to derive more realistic nodal velocities in the FLAC models.

A.4. Effect of fluid flow in a deforming porous media

One of the advantages of FLAC is the availability of a fluid flow module that can be coupled to the deformation module. This is represented by a set of equations with a general organisation similar to the mechanical module. In this regard the equations of motion are replaced by the Biot and Darcy's laws that defines the variation

of fluid flow, a quantity that can be characterised with a fluid intensity field such as the one described by fluid discharge vectors (q_i) in 3D, or in alternative a scalar function that is represented by the spatial variation of pore pressure (*p*) to understand the distribution of equipotentials in the fluid flow field. This latter representation is particularly useful as seen in chapter 4 and chapter 5 to evaluate possible fluid pathways during deformation. In this context FLAC has the advantage that it can capture the effect of deformation on fluid flow or alternatively the effect of fluid pressure in dissipating the confining pressure (Terzaghi, 1945). In particular, FLAC makes use of the Biot coefficient (α) to couple mechanical calculations with transient fluid flow. In addition to this the software allows also to consider the effect on temperature on the volume variation of modelled materials using a linear thermal expansion coefficient (α_t), and in undrained conditions adopting a thermal coefficient (β).

Here it is given a brief description of the fluid-flow equations and their interaction with the constitutive functions introduced in the mechanical part of this review. The linear quasi-static theory of Biot is used in this context to couple deformation and diffusion processes in Darcy's type flow. It is considered a porous material as a media that can transfer and store fluids. However, such properties can vary accordingly to a series of parameters that can be defined internal if they depend upon the system subjected to flow (e.g. permeability) or external if they are controlled by the environment. An example is given providing the equation that serves to calculate the coefficient of diffusivity (*c*):

$$c = \frac{k}{\frac{1}{M} + \frac{\alpha^2}{\alpha_1}} \qquad\qquad\qquad (A.23)$$

where k is the permeability, M represents the Biot modulus, α is the Biot coefficient, α_1 is a function of the bulk and shear modulus. An external parameter could be for instance exemplified by temperature variations or the control of hydraulic gradient. To mathematically constrain these components a mass-balance equation is formulated below. This relationship opportunely combined with the fluid constitutive relation provides a differential equation in terms of pore pressure that can be solvable for certain conditions providing a means for the fluid flow. For small deformations the equation is given by:

$$-q_{i,i} + q_v = \frac{\partial \zeta}{\partial t} \qquad\qquad\qquad (A.24)$$

the (A.23) can be interpreted similarly to the divergence theorem presented above in the (A.1) because it uses the same principle of conservation of mass. In other words the intensity of the flow is a measure of the divergence of the flow field, which is here in (A.24) represented by the partial derivative in time on the right side. On the left side of the same equation $q_{i,i}$ is the spatial variation of the discharging vectors (outflow) whereas q_v represents the volumetric fluid source intensity. The shape of potential surfaces is then controlled by fluid sources, leaks or other morphological boundaries

that directly defines the fluid flow directions within a confined reservoir. However, other more intrinsic parameters need to be considered, as seen, to fully describe the problem of modelling fluid migration within saturated porous media. According to this the fluid flow intensity gradients are also governed directly by the storage capacity of a reservoir. Volumetric variation is the prominent controlling factor, but this in turn is function of strain distributions, temperature and pore pressure variations. This lead to a different formulation of the (A.24) that incorporates these variables:

$$\frac{\partial \zeta}{\partial t} = \left(\frac{1}{M} \frac{\partial p}{\partial t} \right) + \alpha \frac{\partial \varepsilon}{\partial t} - \beta \frac{\partial T}{\partial t} \qquad\qquad (A.25)$$

here pore pressure gradients (p), strain-rate (ε) and temperature gradients (T) are all linearly related to the variation of fluid content per unit volume of porous material (ζ). Combining the (A.24) with the (A.25) and rearranging it follows:

$$-q_{i,i} + q_v^{\times} = \frac{1}{M} \left(\frac{\partial p}{\partial t} \right) \qquad\qquad (A.26)$$

where

$$q_v^{\times} = q_v - \alpha \frac{\partial \varepsilon}{\partial t} + \beta \frac{\partial T}{\partial t} \qquad\qquad (A.27)$$

the (A.26) is used to calculate the pore pressure (p) variation in time knowing the parameters condensed in (A.27) and also calculating q_i using the Darcy's law that for an homogeneous isotropic solid is given by:

$$q_i = -\frac{k}{\eta} \, p_{,i} \tag{A.28}.$$

This equation, by definition, relates the discharge vector intensity (flow velocity) to the intrinsic permeability coefficient (k), and the gradient of the pore pressure (p) in space. If the velocity of the fluids percolating a porous media is controlled by the spatial variability of the scalar field of pore pressure distributions; in turn, the pore pressure itself may vary accordingly to the (A.26) and (A.27), depending on the parameters (e.g. material properties). Mechanical constitutive laws in this regard are accordingly modified to account for such variations. Recalling the general form of the constitutive equations (2.69) an updated incremental expression of the co-rotational stress increment is given by:

$$\Delta\left[\breve{\sigma}\right]_{ij} + \alpha \, \Delta p \delta_{ij} = H_{ij}^{\times}\left(\sigma_{ij}, \Delta\varepsilon_{i,j} - \Delta\varepsilon_{i,j}^{T}\right) \tag{A.29}$$

the thermal-mechanical coupling is defined as:

$$\Delta\varepsilon_{ij}^{T} = \alpha_{t}\,\Delta T\delta_{ij} \qquad\qquad\qquad (A.30)$$

fluid flow correction terms are present on both sides of the constitutive equation (A.29). In particular, the additional term on the left side outlines the influence of the pore pressure increment in reducing (similarly to the effective stress concept) the co-rotational stress component. The stress correction term comprehend also the Biot coefficient (α) and the Kronecker Delta (unitary tensor (δ_{ij}), used to convert to tensorial form the scalar field of pore pressure). On the right side of (A.29) as also in (A.30) the strain increment is influenced by the effect of temperature increments that may for instance increase the volume of the porous media expanding its matrix. The (A.29) also shows the interconnection existing among the mechanical and fluid flow modules. Correction terms in the constitutive equation, for example, could lower the co-rotational stress increment causing a reduction of nodal velocities.

 Outlined equations are solved in FLAC using a finite different approach. The numerical scheme rests on a nodal formulation of the mass balance equation. This approach is not reviewed here because it is equivalent to the mechanical formulation presented above, which leads to the nodal form of the Newton's law. This simply involves the substitution of pore pressure, specific discharge vector and pore pressure gradient for velocity vector, stress and the strain-rate tensors, respectively. Nonetheless the solution of ordinary differential equation is obtained using two distinct discretization models in time (implicit/explicit formulation) in the fluid flow module.

However, the scope of this section on FLAC was primarily focused on the understanding of the concept of discretization and the general organisation of the software, for a deeper understanding the reader is referred to the FLAC documentation (Itasca, 2003).

APPENDIX B

B.1. Weights of Evidence formulation

The Weights of Evidence method and relative algorithms are briefly discussed here (adapted from Bonham-Carter, 1994 and Carranza, 2004).

The Weights of Evidence method is a way to express the likelihood of finding a mineral deposit based on a certain representation of knowledge, which is a conditional probability function $P(x)$. The knowledge itself is mathematically expressed as Weights of Evidence, numerical scores derived from a measure of the spatial association between known deposits (D) and a considered pattern (B_n) . The spatial association represents a conditional probability expressed as follows:

$$P\left(D \mid B_n\right) = P\left(D \cap B_n\right) / P\left(B_n\right)$$
(B.1)

where $P\left(D \colon B_n\right)$ is the conditional probability of finding D overlapping with a pattern B_n which is proportional to the area of D and B_n and inversely proportional to $N(T)$ as $P(B_n) = N(B_n)/N(T)$. It is also possible to express the conditional probability of finding a pattern (B_n) overlapping with (D). $P(D \cap B_n)$ is equal to $P(B_n \cap D)$; however the conditional probability is different because the same area of intersection is divided by diverse prior probabilities as follows:

$$P\left(B_n \mid D\right) = P\left(B_n \cap D\right) / P\left(D\right)$$
(B.2).

Equations (10 and 11) can be combined to obtain the following representation of posterior probability (equivalent to conditional probability):

$$P\left(D \mid B_n\right) = P\left(B_n \mid D\right) P\left(D\right) / P\left(B_n\right)$$
(B.3)

A similar expression can be derived as a measure of correlation of D with the absence of a pattern (B_n) from known deposits (D):

$$P\left(D \mid \overline{B_n}\right) = P\left(\overline{B_n} \mid D\right) P\left(D\right) / P\left(\overline{B_n}\right)$$
(B.4)

These conditional probabilities are expressed for convenience as odds and also are converted in a logarithmic form to obtain the Weights of Evidence values. Odds can be defined as:

$$O = \frac{P}{1 - P} = \frac{P}{\overline{P}} = P\left(D \mid B_n\right) / P\left(\overline{D} \mid B_n\right)$$
(B.5)

From equations (B.3, B.4) conditional probabilities can be substituted to obtain, for instance, the conditional odd of deposits given the presence of B_n:

$$O\left(D\mid B_n\right)=O\left(D\right)\cdot P\left(B_n\mid D\right)/P\left(B_n\mid \overline{D}\right) \tag{B.6}$$

In logarithmic form, both the presence or absence of B_n are expressed for convenience as follows, where W_n is the weight depending on the pixel considered, as this may fall within either an area where B_n occurs or is missing:

$$postlogit\left(D\mid B_n\right)=prilogit\left(D\right)+W_n^+ \tag{B.7}$$

$$postlogit\left(D\mid \overline{B_n}\right)=prilogit\left(D\right)+W_n^- \tag{B.8}$$

Rearranging these equations (B.7, B.8) the Weights of Evidence can be calculated as follows:

$$W_n^+=\ln\left[P\left(B_n\mid D\right)/P\left(B_n\mid \overline{D}\right)\right] \tag{B.9}$$

$$W_n^-=\ln\left[P\left(\overline{B_n}\mid D\right)/P\left(\overline{B_n}\mid \overline{D}\right)\right] \tag{B.10}$$

Equations (B.7, B.8, B.9, B.10) can be combined in a single algorithm, representing the Bayes rule of combination, where the k coefficient defines if the pattern is present or absent as a function of the pixel (n) considered:

$$postlogit\left(D \mid B_n^{k(n)}\right) = prilogit\left(D\right) + \sum_{n=1}^{n} W_n^{k(n)} \tag{B.11}$$

A posterior probability value that represents the sum of all the evidential layers is computed from equation (B.11) back-calculating its value as follows:

$$P_{Post} = \left(\frac{e^{\sum_{n=1}^{n} W_n^{k(n)} + lnO(D)}}{1 + \left(e^{\sum_{n=1}^{n} W_n^{k(n)} + lnO(D)}\right)}\right) \tag{B.12}$$

An estimate of the error involved with the calculation of the Weights of Evidence can be expressed using the asymptotic assumption of Bishop et al. (1975). These represent the variances of the Weights of Evidence as a function of the total area of study expressed as total number of pixels (unit cells) $N(T)$. The mathematical relationships are also function of the area of known occurrences $N(D)$. The equations are:

$$s^2\left(W_n^+\right) = \left(\frac{1}{N\left(B \cap D\right)}\right) + \left(\frac{1}{N\left(B \cap \overline{D}\right)}\right) \tag{B.13}$$

$$s^2\left(W_n^+\right) = \left(\frac{1}{N\left(\overline{B} \cap D\right)}\right) + \left(\frac{1}{N\left(\overline{B} \cap \overline{D}\right)}\right) \tag{B.14}$$

These values were used to compute either the studentised value of the Contrast (*C*) and also for the calculation of the error involved in the estimation of posterior probabilities (P_{post}). This is derived from a multiple combination of layers that form multiple classes (*k*) of pixel column combinations:

$$s^2\left(P_{Post}\right)=\left[\frac{1}{N(D)}+\sum_{n=1}^{n}\left(s^2\left(W_n^{k(n)}\right)\right)\right]\cdot P_{Post}^2 \qquad\qquad (B.15)$$

The available estimate of the variance of the posterior probability is used to compute the error involved in the estimation of the number of predicted mineral deposits in a certain region:

$$s\left(N(D)_{Pred}\right)=\sqrt{\sum_{n=1}^{n}\left[\left(N(k)\right)^2\times s^2\left(P_{Post}\right)\right]} \qquad\qquad (B.16)$$

This latter equation can be used to increase the statistical robustness of the NOT test (Chapter 3).

APPENDIX C

C.1. Wofe Modeler

Compiled in VB 2005 (Express Edition)

```vb
Software used to compute Byesian probability in WofE (Chapter 3)


Region " Software developed by Feltrin Leonardo – James Cook
University"

Imports System.IO
Imports System.Text
Imports System
Imports System.Drawing
Imports System.Drawing.Printing
Imports System.Collections
Imports System.ComponentModel
Imports System.Windows.Forms
Imports System.Data
Imports Rebuild_wofe.Form5

'these instructions are initialising "libraries" to open and write txt
files- see line and drawing
Public Class Form1

    Inherits System.Windows.Forms.Form
    'variable used in case of multi selection of bool geology
    Dim BoolM() As String



    'variables inserted to allow bitmap functionalities
    Private bmpImage As System.Drawing.Bitmap
    Private bayesmap As System.Drawing.Bitmap
    Private curZoom As Double = 1.0
    Private curRect As Rectangle
    Private originalSize As New Size(0, 0)
    Private mouseDownPt As New Point(0, 0)
    Private mouseUpPt As New Point(0, 0)
    Private zoomMode As Boolean = False
    Private imagesize As System.Drawing.Bitmap
    Private myfile() As Byte
    Private cellsz As Double

    'Variables that are used by missing evidence functionalities
    Dim d() As Byte
    Dim PkD() As Single
    Dim PDx() As Single
    ' Dim Px() As Single
    Dim SigmaSQm() As Double
    Dim s2Pk() As Double
    Dim s2Pkf As Double
    Dim s2Pkf_miss As Double
```

```vbnet
    Dim Dep As Integer
    Dim SigmaSQ_missingev() As Double




    Public Property Image_size()
        Get
            Return imagesize
        End Get
        Set(ByVal value)
            imagesize = value
        End Set
    End Property



    'variables for wofe
    Dim FileNames() As String
    Private Shared bmpsizepub As Integer
    Private Shared AD_w, AI_w, AG_w, AT_w As Double 'shared variables
expressing areas as cell numbers; they work in all sub routines
    Private Shared SumArray() As Byte
    Private Shared SumArray2() As Byte
    Private Shared WplusARR(), WminusARR(), ContrastARR(),
Stud_CwARR(), sqvar_WplusARR(), sqvar_WminusARR(), _
    stdv_ContrastARR(), stdv_WplusARR(), stdv_WminusARR() As Double
    Private Shared ar() As String


    'it is left to test 2bmp under process might be some inconsistency
of overlap of data as
    'exporting we lose precision
    Private Sub Button1_Click(ByVal sender As System.Object, ByVal e
As System.EventArgs) Handles Button1.Click
        Dim cellsz = TextBox9.Text
        If TextBox9.Text = Nothing Then
            MsgBox("Please insert the required cell size in square
kilometres")
            Exit Sub
        End If

        'we delete all files with old data

        If RadioButton2.Checked = True Then

            Try
```

```vb
My.Computer.FileSystem.DeleteFile("c:\wofe\weights_calc_output\Wplus.t
xt")

My.Computer.FileSystem.DeleteFile("c:\wofe\weights_calc_output\Wminus.
txt")

My.Computer.FileSystem.DeleteFile("c:\wofe\weights_calc_output\Contras
t.txt")

My.Computer.FileSystem.DeleteFile("c:\wofe\weights_calc_output\sqvar_W
plus.txt")

My.Computer.FileSystem.DeleteFile("c:\wofe\weights_calc_output\stdv_Wp
lus.txt")

My.Computer.FileSystem.DeleteFile("c:\wofe\weights_calc_output\sqvar_W
minus.txt")

My.Computer.FileSystem.DeleteFile("c:\wofe\weights_calc_output\stdv_Wm
inus.txt")

My.Computer.FileSystem.DeleteFile("c:\wofe\weights_calc_output\stdv_Co
ntrast.txt")

My.Computer.FileSystem.DeleteFile("c:\wofe\weights_calc_output\Stud_Cw
.txt")

My.Computer.FileSystem.DeleteFile("c:\wofe\weights_calc_output\ArrayCu
mAI.txt")

My.Computer.FileSystem.DeleteFile("c:\wofe\weights_calc_output\ArrayCu
mAG.txt")

            Catch : MsgBox("no files to delete")
            End Try

            Dim myarray2() As Byte

            'we have to import the string header of multilayer info
(multiple binari files 1 0 maps)
            'to do that we need a list with the names of the files we
need to load and then we use for to create

            'Dim header As String = Nothing

            Dim a As String
            a = TextBox1.Text

            'header = My.Computer.FileSystem.ReadAllText(a)
            'MsgBox(header & "Check and delete any final space
character")
            'MsgBox("Check and delete any final space character")
```

```vb
            Dim myarray() As String = BoolM

            'Dim c As Integer
            'For c = 0 To myarray.Length – 1
            '    myarray(c) = "c:\wofe\bmp_geol\" & myarray(c)
            'Next

            'now we need a for loop to load the files if multiple
layers are chosen
            Dim s As Integer
            For s = 0 To myarray.Length – 1

                myarray2 =
My.Computer.FileSystem.ReadAllBytes(myarray(s).ToString)

                'this convert one file.bmp to a myarray
                ' Dim binary(myarray2.Length – 1) As Byte



                'we jump on the cleaning algo each time to clean up
the bitmap


                Dim r As Integer
                'Here we need some code that cleans up the bitmaps for
us, we declare 2 new myarrays that will be locally storing
                'the original BMP in binary format. Then we get the
data out of them and feed SumArray and SumArray2
                Dim OriginalAD() As Byte =
My.Computer.FileSystem.ReadAllBytes(TextBox8.Text) 'we use the deposit
layer
                Dim OriginalAG(myarray2.Length – 1) As Byte

                OriginalAG = myarray2

                Try
                    r = (ComboBox3.Text * ComboBox4.Text) ' the number
of cells needed to get the number of good data pixels
                Catch : MsgBox("provide rows and columns numbers")
                    Exit Sub
                End Try

                'MsgBox("Numeber of Cells " & r)
                'Dim po As New Integer
                'Dim ps As Integer
                'Dim pq As Integer
                Dim SumArray(r – 1) As Byte
                Dim SumArray2(r – 1) As Byte
                'tronca arrays con remove command
```

```
                Array.Reverse(OriginalAD)
                Array.Resize(OriginalAD, r)
                Array.Reverse(OriginalAD)

                SumArray = OriginalAD

                Array.Reverse(OriginalAG)
                Array.Resize(OriginalAG, r)
                Array.Reverse(OriginalAG)

                SumArray2 = OriginalAG


                ''For cycles to load arrays (SumArray...
                'For po = (OriginalAD.Length) - r To OriginalAD.Length
- 1
                '    ps = (po - ((OriginalAD.Length) - r))
                '    SumArray.SetValue(OriginalAD(po), ps) ' SumArray
-> AD
                ''Next
                'For po = (OriginalAG.Length) - r To OriginalAG.Length
- 1
                '    pq = (po - ((OriginalAG.Length) - r))
                '    SumArray2.SetValue(OriginalAG(po), pq) '
SumArray2 -> AG
                'Next

                'MsgBox(SumArray2.GetValue(r - 1))
                'MsgBox(OriginalAG(OriginalAG.Length - 1))

                Dim b As Integer = 0
                Dim Sum As Double = 0
                Dim Sum2 As Double = 0
                'Dim SumCounter As Integer
                'Dim Counter(255) As Integer
                'Dim CounterTwo(255) As Integer

                'These following are two constants AD and AT Area of
deposits and Total Study area

                ' algebric sum of array (AD) we get just 1s not 0
counted, therfore the area of deposits cells
                For b = 0 To SumArray.Length - 1
                    Sum = Sum + SumArray(b) '-1 is inserted as the
array starts from 0
                Next b
                Label9.Text = Sum.ToString() 'Output AD
                Dim AD As Double = Sum
                'assign shared variable for w calc
                AD_w = Sum * cellsz
```

```vbnet
''''''''''''''''''''''''''''''''''''''''''''''''''''
'here we add the conversion to deposit number
Label35.Text = Sum * cellsz & "pixels"
''''''''''''''''''''''''''''''''''''''''''''''''''''
'Sum of all cells to get total area expressed as cell
units (AT)
Dim AT As Double = SumArray.Length
Label8.Text = AT.ToString() 'Output AT
AT_w = r * cellsz

'This part is inserted to calculate the weights


Dim a2 As Integer = SumArray2.Length 'array limit for
cycle
Dim b2 As Integer

'The following code has to be run in case of binary 0
1 classes of files
' algebric sum of array (AG) we get just 1's not 0
counted, therfore the area of geology or other things
For b2 = 0 To SumArray2.Length – 1

    Sum2 = Sum2 + SumArray2(b2) '-1 is inserted as the
array starts from 0
Next
Label10.Text = Sum2.ToString() 'Output AG

Dim AG As Double = Sum2
AG_w = AG * cellsz ' see above


'we want to add each element of an array with an
element of a second array with same index
'firstly we declare the 2 arrays, first geo second
deposit
'If geo is multiclass this code cannot handle it
therefore it has to run only in case of 0,1 image
'To make it work with the multiclass it has to cycle
with AG variation, we need a new array {AI}
'we want also store the result in a third array
'define the lenght as Array have specific lenght

'we declare the boolean array
Dim third(SumArray.Length – 1) As Byte
Dim q As Integer
'here we create the for loop, which makes a
multiplication of pixels ( = to boolean intersection)
For q = 0 To SumArray.Length – 1
    'third is an array that stores the value AI for
each pixel
    third(q) = (SumArray(q) * SumArray2(q))
Next
```

```vb
                Dim AI As Double
                For q = 0 To SumArray.Length – 1
                    AI = AI + third(q)
                Next

'My.Computer.FileSystem.WriteAllBytes("c:\wofe\pmh_final.rst", third,
False)
                Label11.Text = AI.ToString 'Output AI
                AI_w = AI * cellsz ' see above


                'Here we get the weight using previous variables
WEIGHT MODULE

                Dim Wplus As Double
                Dim Wminus As Double
                Dim Contrast As Double
                Dim Stud_Cw As Double
                Dim sqvar_Wplus As Double
                Dim sqvar_Wminus As Double
                Dim stdv_Contrast As Double
                Dim stdv_Wplus As Double
                Dim stdv_Wminus As Double

                Try


My.Computer.FileSystem.WriteAllText("c:\wofe\weights_calc_output\Array
CumAI.txt", AI_w.ToString & " ", True)
                Catch ex As Exception

My.Computer.FileSystem.CreateDirectory("c:\wofe\weights_calc_output\")

My.Computer.FileSystem.WriteAllText("c:\wofe\weights_calc_output\Array
CumAI.txt", AI_w.ToString & " ", True)

                End Try

My.Computer.FileSystem.WriteAllText("c:\wofe\weights_calc_output\Array
CumAG.txt", AG_w.ToString & " ", True)


                'Equation for W+

                Wplus = Math.Log(((AI_w / AD_w) * ((AT_w – AD_w) /
(AG_w – AI_w))))
                Label19.Text = Wplus.ToString


My.Computer.FileSystem.WriteAllText("c:\wofe\weights_calc_output\Wplus
.txt", Wplus.ToString & " ", True)
```

```vbnet
                'Equation for W-

                Wminus = Math.Log(((AD_w - AI_w) / AD_w) * ((AT_w -
AD_w) / (AT_w - AD_w - AG_w + AI_w)))
                Label20.Text = Wminus.ToString


My.Computer.FileSystem.WriteAllText("c:\wofe\weights_calc_output\Wminu
s.txt", Wminus.ToString & " ", True)


                'Equation for Cw

                Contrast = Wplus - Wminus '21
                Label21.Text = Contrast.ToString


My.Computer.FileSystem.WriteAllText("c:\wofe\weights_calc_output\Contr
ast.txt", Contrast.ToString & " ", True)

                'Equation for v(W+)

                sqvar_Wplus = (1 / AI_w) + (1 / (AG_w - AI_w))


My.Computer.FileSystem.WriteAllText("c:\wofe\weights_calc_output\sqvar
_Wplus.txt", sqvar_Wplus.ToString & " ", True)

                'Equation for s(W+)
                stdv_Wplus = Math.Sqrt(sqvar_Wplus) '23
                Label23.Text = stdv_Wplus.ToString


My.Computer.FileSystem.WriteAllText("c:\wofe\weights_calc_output\stdv_
Wplus.txt", stdv_Wplus.ToString & " ", True)

                'Equation for v(W-)

                sqvar_Wminus = (1 / (AD_w - AI_w)) + (1 / (AT_w - AG_w
- AD_w + AI_w))


My.Computer.FileSystem.WriteAllText("c:\wofe\weights_calc_output\sqvar
_Wminus.txt", sqvar_Wminus.ToString & " ", True)

                'Equation for s(W-)
                stdv_Wminus = Math.Sqrt(sqvar_Wminus) '24
                Label24.Text = stdv_Wminus.ToString


My.Computer.FileSystem.WriteAllText("c:\wofe\weights_calc_output\stdv_
Wminus.txt", stdv_Wminus.ToString & " ", True)
```

```vb
                'Equation for s(Cw)
                stdv_Contrast = Math.Sqrt(sqvar_Wplus + sqvar_Wminus)
'25
                Label25.Text = stdv_Contrast.ToString


My.Computer.FileSystem.WriteAllText("c:\wofe\weights_calc_output\stdv_
Contrast.txt", stdv_Contrast.ToString & " ", True)

                'Equation for the studentized value of Cw '22
                Dim Stud_CwARR(255) As Double
                Stud_Cw = Contrast / stdv_Contrast
                Label22.Text = Stud_Cw.ToString


My.Computer.FileSystem.WriteAllText("c:\wofe\weights_calc_output\Stud_
Cw.txt", Stud_Cw.ToString & " ", True)

                'output lines relative to each value we get a number
of array


                AI = Nothing
                AG = Nothing
                AI_w = Nothing
                AG_w = Nothing
                Wplus = Nothing
                Wminus = Nothing
                Contrast = Nothing
                Stud_Cw = Nothing
                sqvar_Wplus = Nothing
                sqvar_Wminus = Nothing
                stdv_Contrast = Nothing
                stdv_Wplus = Nothing
                stdv_Wminus = Nothing
                'WplusARR(255) = Nothing
                'WminusARR(255) = Nothing
                'sqvar_WplusARR(255) = Nothing
                'stdv_WplusARR(255) = Nothing
                'sqvar_WminusARR(255) = Nothing
                'stdv_WminusARR(255) = Nothing
                'stdv_ContrastARR(255) = Nothing
                'ContrastARR(255) = Nothing
                SumArray = Nothing
                SumArray2 = Nothing


            Next
            MsgBox("Well done leo!")
            Exit Sub


        Else
```

```vb
            Try
My.Computer.FileSystem.DeleteFile("c:\wofe\weights_calc_output\Wplus.t
xt")

My.Computer.FileSystem.DeleteFile("c:\wofe\weights_calc_output\Wminus.
txt")

My.Computer.FileSystem.DeleteFile("c:\wofe\weights_calc_output\Contras
t.txt")

My.Computer.FileSystem.DeleteFile("c:\wofe\weights_calc_output\sqvar_W
plus.txt")

My.Computer.FileSystem.DeleteFile("c:\wofe\weights_calc_output\stdv_Wp
lus.txt")

My.Computer.FileSystem.DeleteFile("c:\wofe\weights_calc_output\sqvar_W
minus.txt")

My.Computer.FileSystem.DeleteFile("c:\wofe\weights_calc_output\stdv_Wm
inus.txt")

My.Computer.FileSystem.DeleteFile("c:\wofe\weights_calc_output\stdv_Co
ntrast.txt")

My.Computer.FileSystem.DeleteFile("c:\wofe\weights_calc_output\Stud_Cw
.txt")

My.Computer.FileSystem.DeleteFile("c:\wofe\weights_calc_output\ArrayCu
mAI.txt")

My.Computer.FileSystem.DeleteFile("c:\wofe\weights_calc_output\AIhisto
.txt")

My.Computer.FileSystem.DeleteFile("c:\wofe\weights_calc_output\AGhisto
.txt")

My.Computer.FileSystem.DeleteFile("c:\wofe\weights_calc_output\ArrayCu
mAG.txt")
            Catch : MsgBox("no files to delete")
            End Try


            'Here we need some code that cleans up the bitmaps for us,
we declare 2 new arrays that will be locally storing
            'the original BMP in binary format. Then we get the data
out of them and feed SumArray and SumArray2
            Dim OriginalAD() As Byte =
My.Computer.FileSystem.ReadAllBytes(TextBox8.Text) 'we use the deposit
layer
```

```vbnet
            Dim OriginalAG() As Byte =
My.Computer.FileSystem.ReadAllBytes(TextBox7.Text) 'we use the geo

            Dim r As Integer = (ComboBox3.Text * ComboBox4.Text)
            'MsgBox("Numeber of Cells " & r)
            Dim po As Integer
            Dim ps As Integer
            Dim pq As Integer
            Dim SumArray(r - 1) As Byte
            Dim SumArray2(r - 1) As Byte

            'For cycles to load arrays (SumArray...
            For po = (OriginalAD.Length) - r To OriginalAD.Length - 1
                ps = (po - ((OriginalAD.Length) - r))
                SumArray.SetValue(OriginalAD(po), ps)
            Next
            po = 0
            For po = (OriginalAG.Length) - r To OriginalAG.Length - 1
                pq = (po - ((OriginalAG.Length) - r))
                SumArray2.SetValue(OriginalAG(po), pq)
            Next

            'MsgBox(SumArray2.GetValue(r - 1))
            'MsgBox(OriginalAG(OriginalAG.Length - 1))

            Dim b As Integer = 0
            Dim Sum As Double = 0
            Dim Sum2 As Double = 0
            Dim SumCounter As Integer
            Dim Counter(255) As Integer
            Dim CounterTwo(255) As Integer

            'These following are two constants AD and AT Area of
deposits and Total Study area

            ' algebric sum of array (AD) we get just 1s not 0 counted,
therfore the area of deposits cells
            Dim a As Integer = SumArray.Length - 1
            For b = 1 To a
                Sum = Sum + SumArray(b - 1) '-1 is inserted as the
array starts from 0
            Next b
            Label9.Text = Sum.ToString() 'Output AD
            Dim AD As Double = Sum
            'assign shared variable for w calc
            AD_w = Sum * cellsz
            ''''''''''''''''''''''''''''''''''''''''''''''''''''''''
            'here we add the conversion to deposit number
            Label35.Text = Sum * cellsz & " km^2"
            ''''''''''''''''''''''''''''''''''''''''''''''''''''''''
            'Sum of all cells to get total area expressed as cell
units (AT)
            Dim AT As Double = SumArray.Length
```

```vb
            Label8.Text = AT.ToString() 'Output AT
            AT_w = r * cellsz ' input by user



            'This code creates an histogram array (counter)used to
detect the type of evidence image used
            'works anlysing the third element of Counter() if the sum
of all the values except the first two of Counter() is equal to
            '0, then we deal with a binary 0 1 file
            'Compute the sum of all elements of Counter() except the
first two (0,1) why?
            'Counter for a 0 1 type file will give a final sum = to 0.
This is true as we
            'we are using cleaned arrays (SumArray see up stripping)
            'Conter refers to AG array
            For a = 0 To SumArray2.Length – 1 'histo for AG class

                Counter(SumArray2(a)) += 1
                ' MsgBox(Counter(a))

            Next a
            Try


                For b = 0 To Counter.Length – 1

My.Computer.FileSystem.WriteAllText("c:\wofe\weights_calc_output\AGhis
to.txt", Counter(b).ToString & " ", True)
                Next

            Catch ex As Exception

My.Computer.FileSystem.CreateDirectory("c:\wofe\weights_calc_output\")

                For b = 0 To Counter.Length – 1

My.Computer.FileSystem.WriteAllText("c:\wofe\weights_calc_output\AGhis
to.txt", Counter(b).ToString & " ", True)
                Next


            End Try


            'Checking the type of data....
            For a = 2 To Counter.Length – 1
                SumCounter = SumCounter + Counter(a)
            Next a

            'we need a second histo for AI not sure if I have to
insert it below
```

```vbnet
            'now we write on a file txt or compile a database.....


            'Dim objStreamWriter As StreamWriter


            ''Open the file. The software runs and save each time on
hist, therefore we might need to solve the issue of
            ''copying above the same file (problem can be solved with
user imput or using a delete opion instruction)
            'objStreamWriter = New StreamWriter("c:\wofe\histoAG.txt",
True, _
            '   Encoding.Unicode)

            ''Write out the numbers on the same line.

            'Dim c As Integer
            'For c = 0 To 255
            '     objStreamWriter.Write(Counter(c) & " ")
            'Next c
            ''Closes the file.
            'objStreamWriter.Close()



            'If the sum is 0 then the image is binary therefore use
the following code to caculate AG
            If SumCounter = 0 Then
                MsgBox("Binary file [0,1]")

                Dim a2 As Integer = SumArray2.Length 'array limit for
cycle
                Dim b2 As Integer
                'The following code has to be run in case of binary 0
1 classes of files
                ' algebric sum of array (AG) we get just 1's not 0
counted, therfore the area of geology or other things
                For b2 = 1 To a2

                    Sum2 = Sum2 + SumArray2(b2 – 1) '-1 is inserted as
the array starts from 0
                Next b2
                Label10.Text = Sum2.ToString() 'Output AG
                Dim AG As Double = Sum2
                AG_w = AG * cellsz ' see above


                'we want to add each element of an array with an
element of a second array with same index
                'firstly we declare the 2 arrays, first geo second
deposit
                'If geo is multiclass this code cannot handle it
therefore it has to run only in case of 0,1 image
```

Leonardo Feltrin   C-14

```vb
                    'To make it work with the multiclass it has to cycle
with AG variation, we need a new array {AI}
                    'we want also store the result in a third array

                    'define the lenght as Array have specific lenght
                    b = SumArray.Length
                    Dim third(b) As Byte

                    'here we create the for cycle, which makes a
multiplication of pixels ( = to boolean intersection)
                    For a = 1 To b
                        'third is an array that stores the value AI for
each pixel
                        third.SetValue(SumArray(a – 1) * SumArray2(a – 1),
a – 1)
                    Next a
                    Dim AI As Double = 0
                    For a = 1 To b
                        AI = AI + third(a – 1)
                    Next a

'My.Computer.FileSystem.WriteAllBytes("c:\wofe\pmh_final.rst", third,
False)
                    Label11.Text = AI.ToString 'Output AI
                    AI_w = AI * cellsz ' see above


                    'Here we get the weight using previous variables
WEIGHT MODULE

                    Dim Wplus As Double
                    Dim Wminus As Double
                    Dim Contrast As Double
                    Dim Stud_Cw As Double
                    Dim sqvar_Wplus As Double
                    Dim sqvar_Wminus As Double
                    Dim stdv_Contrast As Double
                    Dim stdv_Wplus As Double
                    Dim stdv_Wminus As Double

                    'Equation for W+
                    Wplus = Math.Log(((AI_w / AD_w) * ((AT_w – AD_w) /
(AG_w – AI_w))))
                    Label19.Text = Wplus.ToString
                    'Equation for W-
                    Wminus = Math.Log(((AD_w – AI_w) / AD_w) * ((AT_w –
AD_w) / (AT_w – AD_w – AG_w + AI_w)))
                    Label20.Text = Wminus.ToString
                    'Equation for Cw
                    Contrast = Wplus – Wminus '21
                    Label21.Text = Contrast.ToString
                    'Equation for v(W+)
                    sqvar_Wplus = (1 / AI_w) + (1 / (AG_w – AI_w))
```

```vb
                'Equation for s(W+)
                stdv_Wplus = Math.Sqrt(sqvar_Wplus) '23
                Label23.Text = stdv_Wplus.ToString
                'Equation for v(W-)
                sqvar_Wminus = (1 / (AD_w - AI_w)) + (1 / (AT_w - AG_w
- AD_w + AI_w))

                'Equation for s(W-)
                stdv_Wminus = Math.Sqrt(sqvar_Wminus) '24
                Label24.Text = stdv_Wminus.ToString
                'Equation for s(Cw)
                stdv_Contrast = Math.Sqrt(sqvar_Wplus + sqvar_Wminus)
'25
                Label25.Text = stdv_Contrast.ToString
                'Equation for the studentized value of Cw '22
                Stud_Cw = Contrast / stdv_Contrast
                Label22.Text = Stud_Cw.ToString


                AI = Nothing
                AG = Nothing
                AI_w = Nothing
                AG_w = Nothing
                Wplus = Nothing
                Wminus = Nothing
                Contrast = Nothing
                Stud_Cw = Nothing
                sqvar_Wplus = Nothing
                sqvar_Wminus = Nothing
                stdv_Contrast = Nothing
                stdv_Wplus = Nothing
                stdv_Wminus = Nothing
                WplusARR(255) = Nothing
                WminusARR(255) = Nothing
                sqvar_WplusARR(255) = Nothing
                stdv_WplusARR(255) = Nothing
                sqvar_WminusARR(255) = Nothing
                stdv_WminusARR(255) = Nothing
                stdv_ContrastARR(255) = Nothing
                ContrastARR(255) = Nothing

                SumArray = Nothing
                SumArray2 = Nothing



                '----------------------------------------------------
----------------------------------------------------------------------
--------------
            Else
```

```vbnet
                    'we want to add each element of an array with an
element of a second array with same index
                    'firstly we declare the 2 arrays, first geo second
deposit
                    'If geo is multiclass this code cannot handle it
therefore it has to run only in case of 0,1 image
                    'To make it work with the multiclass it has to cycle
with AG variation, we need a new array {AI}
                    'we want also store the result in a third array
                    'Counter() is a list of all AG in order from 0 to 255,
we need to feed the AG to produce the AI array
                    'Looping through Counter we pick each value and
perform the computation of AI and W


                    'this code works for a single AG array calculation

                    'define the lenght as Array have specific lenght

                    Dim third(SumArray.Length – 1) As Byte


                    'here we create the for cycle, which makes a
multiplication of pixels ( = to boolean intersection)
                    For a = 1 To SumArray.Length
                        'third is an array that stores the value AI for
each pixel
                        third.SetValue(SumArray(a – 1) * SumArray2(a – 1),
a – 1) 'SumArray2 is a single array of AG
                    Next a
                    'We get third() which represents the array
intersection
                    'Now we run HISTO on third()
                    'CounterTwo refers to AD array
                    For a = 0 To third.Length – 1 'histo for AG class

                        CounterTwo(third(a)) += 1
                    Next a
                    For b = 0 To Counter.Length – 1

My.Computer.FileSystem.WriteAllText("c:\wofe\weights_calc_output\AIhis
to.txt", CounterTwo(b).ToString & " ", True)
                    Next
                    ' MsgBox(Counter(a))


                    'In both cases AG and AI has to be estimated as
cumulative proportions, therefore we need to progressively sum up
                    ' the different elements of the two arrays to obtain 2
new arrays with cumulative growth of areas
```

```vb
                Dim n As Integer
                'Dim s As Integer
                'Dim p As Integer
                Dim ArrayCumAG(Counter.Length – 1) As Double
                ArrayCumAG(0) = Counter(0)
                For n = 1 To Counter.Length – 1
                    ArrayCumAG(n) = ((Counter(n)) + ArrayCumAG(n – 1))

My.Computer.FileSystem.WriteAllText("c:\wofe\weights_calc_output\Array
CumAG.txt", ArrayCumAG(n).ToString & " ", True)


                'This code requires too much resources
                'For n = 0 To SumArray2.Length – 1

'       For s = 0 To n
'            p = p + SumArray2(s)
'       Next s
'       ArrayCumAG(n) = p
'       p = 0

                'ArrayCum is the array that contains cumulative AI
proportions
                Next n
                'we correct the first value for (0) derived by non
intersection during bool
                CounterTwo(0) = (CounterTwo(0) – (r – Sum))
                'AI cumulative prop...Changed we keep same values as
CounterTWO

                Dim ArrayCumAI(CounterTwo.Length – 1) As Double
                'For b = 0 To 255
'       ArrayCumAI(b) = CounterTwo(b)

                'Next


                'cumulative of AI increasing with distance analysis
                ArrayCumAI(0) = CounterTwo(0)
                For n = 1 To CounterTwo.Length – 1
                    ArrayCumAI(n) = ((CounterTwo(n)) + ArrayCumAI(n –
1))

My.Computer.FileSystem.WriteAllText("c:\wofe\weights_calc_output\Array
CumAI.txt", ArrayCumAI(n).ToString & " ", True)
                Next n

                'After evaluation of multiclass layers we obtain two
final arrays (ArrayCumAI(); ArrayCumAG())

                'In this case the module WEIGHT is integrated and
modified to run with two arrays of AG and AI values that run in
parallel
```

```vb
                        'Here we get the weight using previous variables
WEIGHT MODULE



                Dim Wplus As Double
                Dim Wminus As Double
                Dim Contrast As Double
                Dim Stud_Cw As Double
                Dim sqvar_Wplus As Double
                Dim sqvar_Wminus As Double
                Dim stdv_Contrast As Double
                Dim stdv_Wplus As Double
                Dim stdv_Wminus As Double
                Dim WplusARR(255) As Double
                Dim WminusARR(255) As Double
                Dim sqvar_WplusARR(255) As Double
                Dim stdv_WplusARR(255) As Double
                Dim sqvar_WminusARR(255) As Double
                Dim stdv_WminusARR(255) As Double
                Dim stdv_ContrastARR(255) As Double
                Dim ContrastARR(255) As Double
                'delete all files in data folder




                For a = 0 To Counter.Length – 1
                    'Equation for W+
                    AI_w = ArrayCumAI(a) * cellsz  'we convert in area
of deposits km2

                    AG_w = ArrayCumAG(a) * cellsz 'we convert the area
in km^2 from cells

                    Wplus = Math.Log(((AI_w / AD_w) * ((AT_w – AD_w) /
(AG_w – AI_w))))
                    Label19.Text = Wplus.ToString
                    WplusARR.SetValue(Wplus, a)

My.Computer.FileSystem.WriteAllText("c:\wofe\weights_calc_output\Wplus
.txt", WplusARR(a).ToString & " ", True)

                    'Equation for W–

                    Wminus = Math.Log(((AD_w – AI_w) / AD_w) * ((AT_w
– AD_w) / (AT_w – AD_w – AG_w + AI_w)))
                    Label20.Text = Wminus.ToString
                    WminusARR.SetValue(Wminus, a)

My.Computer.FileSystem.WriteAllText("c:\wofe\weights_calc_output\Wminu
s.txt", WminusARR(a).ToString & " ", True)
```

```vb
                'Equation for Cw

                Contrast = WplusARR(a) - WminusARR(a) '21
                Label21.Text = Contrast.ToString
                ContrastARR.SetValue(Contrast, a)

My.Computer.FileSystem.WriteAllText("c:\wofe\weights_calc_output\Contr
ast.txt", ContrastARR(a).ToString & " ", True)

                'Equation for v(W+)

                sqvar_Wplus = (1 / AI_w) + (1 / (AG_w - AI_w))
                sqvar_WplusARR.SetValue(sqvar_Wplus, a)

My.Computer.FileSystem.WriteAllText("c:\wofe\weights_calc_output\sqvar
_Wplus.txt", sqvar_WplusARR(a).ToString & " ", True)


                'Equation for s(W+)
                stdv_Wplus = Math.Sqrt(sqvar_WplusARR(a)) '23
                Label23.Text = stdv_Wplus.ToString
                stdv_WplusARR.SetValue(stdv_Wplus, a)

My.Computer.FileSystem.WriteAllText("c:\wofe\weights_calc_output\stdv_
Wplus.txt", stdv_WplusARR(a).ToString & " ", True)


                'Equation for v(W-)

                sqvar_Wminus = (1 / (AD_w - AI_w)) + (1 / (AT_w -
AG_w - AD_w + AI_w))
                sqvar_WminusARR.SetValue(sqvar_Wminus, a)

My.Computer.FileSystem.WriteAllText("c:\wofe\weights_calc_output\sqvar
_Wminus.txt", sqvar_WminusARR(a).ToString & " ", True)

                'Equation for s(W-)
                stdv_Wminus = Math.Sqrt(sqvar_WminusARR(a)) '24
                Label24.Text = stdv_Wminus.ToString
                stdv_WminusARR.SetValue(stdv_Wminus, a)


My.Computer.FileSystem.WriteAllText("c:\wofe\weights_calc_output\stdv_
Wminus.txt", stdv_WminusARR(a).ToString & " ", True)
                'Equation for s(Cw)
                stdv_Contrast = Math.Sqrt(sqvar_WplusARR(a) +
sqvar_WminusARR(a)) '25
                Label25.Text = stdv_Contrast.ToString
                stdv_ContrastARR.SetValue(stdv_Contrast, a)

My.Computer.FileSystem.WriteAllText("c:\wofe\weights_calc_output\stdv_
Contrast.txt", stdv_ContrastARR(a).ToString & " ", True)
```

```vb
                    'Equation for the studentized value of Cw '22
                    Dim Stud_CwARR(255) As Double
                    Stud_Cw = ContrastARR(a) / stdv_ContrastARR(a)
                    Label22.Text = Stud_Cw.ToString
                    Stud_CwARR.SetValue(Stud_Cw, a)

My.Computer.FileSystem.WriteAllText("c:\wofe\weights_calc_output\Stud_
Cw.txt", Stud_CwARR(a).ToString & " ", True)



                Next a


                'output lines relative to each value we get a number
of arrays

                'AI = Nothing
                'AG = Nothing
                AI_w = Nothing
                AG_w = Nothing
                Wplus = Nothing
                Wminus = Nothing
                Contrast = Nothing
                Stud_Cw = Nothing
                sqvar_Wplus = Nothing
                sqvar_Wminus = Nothing
                stdv_Contrast = Nothing
                stdv_Wplus = Nothing
                stdv_Wminus = Nothing
                WplusARR(255) = Nothing
                WminusARR(255) = Nothing
                sqvar_WplusARR(255) = Nothing
                stdv_WplusARR(255) = Nothing
                sqvar_WminusARR(255) = Nothing
                stdv_WminusARR(255) = Nothing
                stdv_ContrastARR(255) = Nothing
                ContrastARR(255) = Nothing
                SumArray = Nothing
                SumArray2 = Nothing

                MsgBox("Weighting Completed!")



            End If

            'Make sure the 2 images have same size and resolution
before u start intersecting and weighting

        End If
```

```vbnet
    End Sub


    Private Sub Button2_Click(ByVal sender As System.Object, ByVal e _
As System.EventArgs) Handles Button2.Click
        My.Forms.Form2.Show()
    End Sub

    Private Sub Button3_Click(ByVal sender As System.Object, ByVal e _
As System.EventArgs) Handles Button3.Click
        'Dim myStream As Stream
        Dim selectFileDialog1 As New OpenFileDialog()

        selectFileDialog1.InitialDirectory = "c:\"
        selectFileDialog1.Filter = "bmp files (*.bmp)|*.bmp|All files
(*.*)|*.*"
        selectFileDialog1.FilterIndex = 2
        selectFileDialog1.RestoreDirectory = True

        If selectFileDialog1.ShowDialog() = DialogResult.OK Then

            TextBox7.Text = selectFileDialog1.FileName

            'myStream = selectFileDialog1.OpenFile()
            'If Not (myStream Is Nothing) Then
            ' Insert code to read the stream here.
            'myStream.Close()
            'End If
        End If
    End Sub

    Private Sub Button4_Click(ByVal sender As System.Object, ByVal e _
As System.EventArgs) Handles Button4.Click
        'Dim myStream As Stream
        Dim selectFileDialog1 As New OpenFileDialog()

        selectFileDialog1.InitialDirectory = "c:\"
        selectFileDialog1.Filter = "bmp files (*.bmp)|*.bmp|All files
(*.*)|*.*"
        selectFileDialog1.FilterIndex = 2
        selectFileDialog1.RestoreDirectory = True

        If selectFileDialog1.ShowDialog() = DialogResult.OK Then


            TextBox8.Text = selectFileDialog1.FileName

            'myStream = selectFileDialog1.OpenFile()
            'If Not (myStream Is Nothing) Then
            ' Insert code to read the stream here.
            'myStream.Close()
```

```vbnet
            'End If
        End If
    End Sub

    Private Sub Button5_Click(ByVal sender As System.Object, ByVal e
As System.EventArgs) Handles Button5.Click
        'multiselect option
        'Dim myStream As Stream
        Dim selectFileDialog1 As New OpenFileDialog()

        selectFileDialog1.InitialDirectory = "c:\"
        selectFileDialog1.Filter = "bitmap file (*.bmp)| *.bmp"
        selectFileDialog1.FilterIndex = 1
        selectFileDialog1.RestoreDirectory = True
        selectFileDialog1.Multiselect = True

        If selectFileDialog1.ShowDialog() = DialogResult.OK Then
            'ar() can be used to process the data for calculation of
weights
            Dim ar() As String = selectFileDialog1.FileNames
            Dim a As String = Join(ar, "")
            TextBox1.Text = a

            'myStream = selectFileDialog1.OpenFile()
            'If Not (myStream Is Nothing) Then
            ' Insert code to read the stream here.
            'myStream.Close()
            'End If
            BoolM = ar
        End If
    End Sub


    Public Function BinaryConv(ByVal bound As Byte, ByVal myarray() As
Byte, ByVal bmpSize As Integer, ByVal FileName As String) As Double

        'we need to strip the header and store it somewhere
        Dim headerLength As Integer
        headerLength = (myarray.Length) - bmpSize
        'Dim ab As Integer
        Dim stripArray() As Byte
        stripArray = myarray
        Array.Resize(stripArray, headerLength)
        Array.Reverse(myarray)
        Array.Resize(myarray, bmpSize)
        Array.Reverse(myarray)

        'For ab = 0 To headerLength
        '    stripArray(ab) = myarray(ab)
        'Next
        'My.Computer.FileSystem.WriteAllBytes("c:\wofe\hearer.bmp",
stripArray, False)
```

```vb
        'we need to perform a bit conversion to get a 0,1 binary type
        Dim a As Integer
        Dim value As Byte
        For a = 0 To myarray.Length - 1

            value = myarray(a)


            If value >= bound Then
                myarray(a) = 0
            Else
                If value < bound Then
                    myarray(a) = 255
                End If

            End If


        Next


        'problem is that final...(2) give an array with length 3, with
3 elements not 2, therefore use -1
        Dim finalarray((stripArray.Length + myarray.Length) - 1) As
Byte
        Dim ac As Integer
        For ac = 0 To stripArray.Length - 1
            finalarray(ac) = stripArray(ac)
        Next
        For ac = stripArray.Length To finalarray.Length - 1
            finalarray(ac) = myarray(ac - stripArray.Length)
        Next
        'we need to create a folder where we can store the evidential
boolean layers

        My.Computer.FileSystem.WriteAllBytes("c:\wofe\image.bmp",
finalarray, False)
        Form4.Show()

    End Function

    Private Sub Button6_Click(ByVal sender As System.Object, ByVal e
As System.EventArgs) Handles Button6.Click
        'Dim myStream As Stream
        Dim selectFileDialog1 As New OpenFileDialog()

        selectFileDialog1.InitialDirectory = "c:\wofe\"
        selectFileDialog1.Filter = "bmp files (*.bmp)|*.bmp|All files
(*.*)|*.*"
        selectFileDialog1.FilterIndex = 2
        selectFileDialog1.RestoreDirectory = True

        If selectFileDialog1.ShowDialog() = DialogResult.OK Then
```

```vb
            TextBox2.Text = selectFileDialog1.FileName

            'myStream = selectFileDialog1.OpenFile()
            'If Not (myStream Is Nothing) Then
            ' Insert code to read the stream here.
            'myStream.Close()
            'End If
        End If
    End Sub

    Private Sub Button7_Click(ByVal sender As System.Object, ByVal e
As System.EventArgs) Handles Button7.Click

        Dim myarray() As Byte =
My.Computer.FileSystem.ReadAllBytes(TextBox2.Text)
        Dim bound As Integer
        Dim bmpsize As Integer
        bound = Byte.Parse(TextBox3.Text)
        bmpsize = Integer.Parse(TextBox4.Text)
        bmpsizepub = bmpsize
        Me.BinaryConv(bound, myarray, bmpsize, TextBox2.Text)


    End Sub


    Private Sub Button9_Click(ByVal sender As System.Object, ByVal e
As System.EventArgs) Handles Button9.Click
        Dim a As Integer
        'Dim b As Integer

        Dim FileName(Bayes_Data_Source_ModelDataGridView.Rows.Count)
As String
        Dim Wplus(Bayes_Data_Source_ModelDataGridView.Rows.Count) As
Single
        Dim Wminus(Bayes_Data_Source_ModelDataGridView.Rows.Count) As
Single


        For a = 0 To Bayes_Data_Source_ModelDataGridView.Rows.Count
            Try

                FileName(a) =
Bayes_Data_Source_ModelDataGridView.Rows(a).Cells(6).Value
                Wplus(a) =
Bayes_Data_Source_ModelDataGridView.Rows(a).Cells(1).Value
                Wminus(a) =
Bayes_Data_Source_ModelDataGridView.Rows(a).Cells(2).Value

            Catch : Exit For
```

```vbnet
            End Try
        Next

        Bayes(FileName, Wplus, Wminus)


    End Sub


    Public Function Bayes(ByVal FileName() As String, ByVal Wplus() As
Single, ByVal Wminus() As Single) As Byte

        ' I need to firslty select the bitmaps created with convert,
then store the strings in the first column
        'manually we type in the weights and ask for that with a msg
box
        'all is set and ready for the calculation
        'we need to select each row and use the loop to convert the
pixels to an array of weights
        'we need to sum up the images to the prior probability image
        Dim Form5Inst As New Form5
        Dim Dep As Integer
        Dep = Form5Inst.AD(TextBox8.Text)

        imagesize = Bitmap.FromFile("imagesize.bmp")


        Dim postlogit((imagesize.Height * imagesize.Width) – 1) As
Single 'four
        Dim weightedArray((imagesize.Height * imagesize.Width) – 1) As
Single 'six necessary to weight step
        Dim rescale((imagesize.Height * imagesize.Width) – 1) As
Single 'seven

        Dim ab As Integer
        For ab = 0 To FileName.Length – 1



            ' imagesize = Bitmap.FromFile(FileName(ab))
            If FileName(ab) = Nothing Then
                Exit For
            End If
            Dim evidence As Bitmap =
Bitmap.FromFile(FileName(ab).ToString)

            Dim myfile((evidence.Width * evidence.Height) – 1) As Byte
            Dim color As System.Drawing.Color
            Dim county As Integer
            Dim countx As Integer
            Dim s As Integer
            For county = 0 To evidence.Height – 1
```

```
                For countx = 0 To evidence.Width – 1
                    color = evidence.GetPixel(countx, county)

                    If CInt(color.B) <> 0 And CInt(color.G) <> 0 And
CInt(color.R) <> 0 Then
                        myfile(s) = 1
                    Else
                        myfile(s) = 0
                    End If

                    s = s + 1
                Next
            Next
            s = 0
            Dim value As Byte
            Dim ard As Integer

            If FileName(ab) Is Nothing Then
                Exit For
            Else


                'here we convert the image in evdence layer using the
weights
                For ard = 0 To myfile.Length – 1

                    value = myfile(ard)

                    If value = 0 Then
                        weightedArray(ard) = Wminus(ab)
                    Else
                        weightedArray(ard) = Wplus(ab)
                    End If
                Next

            End If


            'modified'''''''''''''''''''to exclude textbox6
input''''''''''''''''''''''''''''''''''''''''''''''''''''''''''''''''''''
''''''''''''
            'now we need to add the evidence layer created to the
prior probability
            'prilogit should be calculated as the ratio D/T the
conversion in ODDS and
            'ln function gives prilogit value
            'I need the deposit layer and the tot number of pixels

            ' Dim Dep_conv As Single = Dep * 0.000269
            Dim priprob As Single = (Dep / (imagesize.Height *
imagesize.Width))
            Dim priOdd As Single = priprob / (1 – priprob)
            Dim con As Single
```

```vb
            con = Math.Log(priOdd)


            Dim ac As Integer
            Dim priorlogit((imagesize.Height * imagesize.Width) - 1)
As Single 'five

            ' con = Single.Parse(TextBox6.Text)
            For ac = 0 To ((imagesize.Height * imagesize.Width) - 1)
                priorlogit(ac) = con
            Next


            For ac = 0 To postlogit.Length - 1
                If ab = 0 Then
                    postlogit(ac) = postlogit(ac) + priorlogit(ac) +
weightedArray(ac)
                Else
                    postlogit(ac) = postlogit(ac) + weightedArray(ac)
                End If
            Next



        Next


        'now we need to rescale the double in a way that we can
generate a byte array

        Dim ad As Integer
        Dim aq As Integer
        Dim postodds(postlogit.Length - 1) As Single
        Dim postprob(postlogit.Length - 1) As Single
        Dim postprobByte(postlogit.Length - 1) As Byte
        For aq = 0 To postlogit.Length - 1
            'we convert to probability


            postodds(aq) = Math.Exp(postlogit(aq))

            postprob(aq) = postodds(aq) / (1 + postodds(aq))

        Next
        Array.Copy(postprob, rescale, postlogit.Length)
        Array.Sort(rescale)

        Dim min As Single = rescale(0)
        Dim max As Single = rescale(rescale.Length - 1)
        My.Computer.FileSystem.WriteAllText("c:\wofe\scale.txt",
min.ToString, False)
        My.Computer.FileSystem.WriteAllText("c:\wofe\scale.txt",
max.ToString, True)
```

```vb
        For ad = 0 To postprob.Length - 1

            ' we shift or translate the scale to get a minimum of 0
            'min must become firslty equal to 1 so if min*x=1
            Try
                Dim alfa As Single = (1 / min)
                postprob(ad) = postprob(ad) * alfa
                postprob(ad) = (postprob(ad) - (min * alfa))
                postprob(ad) = (postprob(ad) * 255) / ((max * alfa) -
(min * alfa))
                postprobByte(ad) = CByte((postprob(ad)))
                postprob(ad) = (postprob(ad) * ((max * alfa) - (min *
alfa))) / 255
                postprob(ad) = (postprob(ad) + (min * alfa))
                postprob(ad) = postprob(ad) / alfa

            Catch ex As Exception
                MsgBox("something wrong with the input?")
                Exit Function
            End Try

        Next

My.Computer.FileSystem.WriteAllBytes("c:\wofe\postprobebyte.bin",
postprobByte, False)

        MsgBox("Pprob Completed!")

    End Function


    Private Sub Button8_Click(ByVal sender As System.Object, ByVal e
As System.EventArgs) Handles Button8.Click

        'Dim myStream As Stream
        Dim selectFileDialog1 As New OpenFileDialog()

        selectFileDialog1.InitialDirectory = "c:\"
        selectFileDialog1.Filter = "bitmap file (*.bmp)| *.bmp"
        selectFileDialog1.FilterIndex = 1
        selectFileDialog1.RestoreDirectory = True
        selectFileDialog1.Multiselect = True

        If selectFileDialog1.ShowDialog() = DialogResult.OK Then


            bindingNavigatorAddNewItem.PerformClick()
            Dim ar() As String = selectFileDialog1.FileNames

            ' Dim a As String = Join(ar, " ")
```

```vbnet
            Dim a As Integer
            Dim b As String
            Dim c As String
            FileNames = ar
            For a = 0 To ar.Length - 1

                b = ar(a)
                c = ar(a)
                b = b.Substring(b.LastIndexOf("\") + 1)

                Try

Bayes_Data_Source_ModelDataGridView.Rows(a).Cells(0).Value = b

Bayes_Data_Source_ModelDataGridView.Rows(a).Cells(6).Value = c
                Catch ex As Exception

                    bindingNavigatorAddNewItem.PerformClick()

Bayes_Data_Source_ModelDataGridView.Rows(a).Cells(0).Value = b

Bayes_Data_Source_ModelDataGridView.Rows(a).Cells(6).Value = c

                End Try


            Next
            '  bindingNavigatorDeleteItem.PerformClick()
            ' MsgBox("Insert relative weights")

            'myStream = selectFileDialog1.OpenFile()
            'If Not (myStream Is Nothing) Then
            ' Insert code to read the stream here.
            'myStream.Close()
            'End If

        End If
    End Sub


    'Public Function ArrayMax(ByVal math() As Double) As Double

    '    Dim a As Integer
    '    Dim av As Double
    '    Dim b As Double
    '    Dim c As Integer
    '    Dim d As Integer
    '    For a = 0 To math.Length - 1

    '        b = b + math(a)

    '    Next
    '    av = b / math.Length
```

```vb
'     Dim newmath(math.Length - 1) As Double
'     For c = 0 To math.Length - 1
'         If math(c) >= av Then
'             newmath(c) = math(c)
'         End If

'     Next


'End Function

    Public Function ArrayAn(ByVal ar() As Single) As Integer

        Dim a As Integer

        Dim c As Integer

        Dim counter(10) As Single

        c = 0
        Try
            For a = 0 To ar.Length - 1
                If ar(a) <> ar(a + 1) Then
                    counter(c) = ar(a)
                    counter(c + 1) = ar(a + 1)
                    c = c + 2
                End If
            Next
        Catch : Exit Try
        End Try
        Dim d As Integer
        For d = 0 To counter.Length - 1

My.Computer.FileSystem.WriteAllText("c:\wofe\arrayanalysis.txt",
counter(d), True, System.Text.Encoding.Unicode)

        Next
        ' Return MsgBox("ok")

    End Function

    Private Sub Button10_Click(ByVal sender As System.Object, ByVal e
As System.EventArgs) Handles Button10.Click
        If TextBox9.Text = "" Then
            MsgBox("Please insert a valid cell size value")
            Exit Sub
        End If
        My.Forms.Form5.Show()
    End Sub

    Public Function imagesizefunc() As Integer

        Dim a As Integer
```

```vb
        imagesize = Bitmap.FromFile("imagesize.bmp")

        a = (imagesize.Width * imagesize.Height)
        Return a
    End Function



    Private Sub Button13_Click(ByVal sender As System.Object, ByVal e
As System.EventArgs) Handles Button13.Click
        'start new ot ot

        Try
            cell = Me.TextBox9.Text
        Catch ex As Exception
            MsgBox("Please provide cell size")
            Exit Sub
        End Try

        d = Nothing
        PkD = Nothing
        PDx = Nothing

        SigmaSQm = Nothing
        s2Pk = Nothing
        s2Pkf = Nothing
        s2Pkf_miss = Nothing
        Dep = Nothing
        bmpsizepub = Nothing
        AD_w = Nothing
        AI_w = Nothing
        AG_w = Nothing
        AT_w = Nothing 'shared variables expressing areas as cell
numbers; they work in all sub routines


        Dim a As Integer
        'Dim b As Integer

        Dim FileName(Bayes_Data_Source_ModelDataGridView.Rows.Count)
As String
        Dim Wplus(Bayes_Data_Source_ModelDataGridView.Rows.Count) As
Single
        Dim Wminus(Bayes_Data_Source_ModelDataGridView.Rows.Count) As
Single
        Dim sWplus(Bayes_Data_Source_ModelDataGridView.Rows.Count) As
Single
        Dim sWminus(Bayes_Data_Source_ModelDataGridView.Rows.Count) As
Single

        For a = 0 To Bayes_Data_Source_ModelDataGridView.Rows.Count
            Try
```

```
                FileName(a) =
Bayes_Data_Source_ModelDataGridView.Rows(a).Cells(6).Value
                Wplus(a) =
Bayes_Data_Source_ModelDataGridView.Rows(a).Cells(1).Value
                Wminus(a) =
Bayes_Data_Source_ModelDataGridView.Rows(a).Cells(2).Value
                sWplus(a) =
Bayes_Data_Source_ModelDataGridView.Rows(a).Cells(4).Value
                sWminus(a) =
Bayes_Data_Source_ModelDataGridView.Rows(a).Cells(5).Value
            Catch : Exit For
            End Try
        Next

        missing_evidence_Pk(FileName, Wplus, Wminus)
        'missing_evidence_PDx(FileName, Wplus, Wminus)
        'SigmaSQ_missing_evidence()
        SigmaSQ(FileName, sWplus, sWminus)
        OminbusTest_NewOminibus()

    End Sub

    Private Function missing_evidence_Pk(ByVal FileName() As String,
ByVal Wplus() As Single, ByVal Wminus() As Single) As Integer

        'looks fine
        'here we use the first part of bayes to get the value of
posterior probability
        'we have to use the postlogit array as prior probability when
we calculate P(d:x)
        'and P(d)
        'weights are automatically picked from the data grid view, but
the arrays with final summation of weights
        'has to be stripped of values that are not included within
deposits and missing evidence ???
        'we need to input a layer representing the area of missing
evidence = bmp indexed image then perform a boolean with
        'deposit and this layer to get only values useful for the
calculation, we consider only missing evidence as we are
        'using it to calculate the posterior probability resulting
when missing evidence is intersected
        'therefore a cumulative area obtained combining all the
missing evidence on a single layer positively defines
        'the pixel where this calculation is meaningfull
        'in any case we cannot calculate sigma^2(p) for missing
eveidence if there is no missing evidence
        Dim Form5Inst As New Form5

        Dep = Form5Inst.AD(TextBox8.Text)
        imagesize = Bitmap.FromFile(FileName(0))

        'Static header() As Byte 'on
```

```vb
        Dim postlogit((imagesize.Height * imagesize.Width) – 1) As
Single
        Dim postlogit_miss((imagesize.Height * imagesize.Width) – 1)
As Single
        'four
        Dim weightedArray((imagesize.Height * imagesize.Width) – 1) As
Single 'six necessary to weight step
        ' Static rescale((imagesize.Height * imagesize.Width) – 1) As
Single 'seven

        Dim ab As Integer
        For ab = 0 To FileName.Length – 1

            If FileName(ab) = Nothing Then
                Exit For
            End If
            Dim evidence As Bitmap =
Bitmap.FromFile(FileName(ab).ToString)

            Dim myfile((evidence.Width * evidence.Height) – 1) As Byte
            Dim color As System.Drawing.Color
            Dim county As Integer
            Dim countx As Integer
            Dim s As Integer
            For county = 0 To evidence.Height – 1
                For countx = 0 To evidence.Width – 1
                    color = evidence.GetPixel(countx, county)

                    If CInt(color.B) <> 0 And CInt(color.G) <> 0 And
CInt(color.R) <> 0 Then
                        myfile(s) = 1
                    Else
                        myfile(s) = 0
                    End If

                    s = s + 1
                Next
            Next
            s = 0
            Dim value As Byte
            Dim ard As Integer

            If FileName(ab) Is Nothing Then 'solves issue of final (0)
                Exit For
            Else


                'here we convert the image in evdence layer using the
weights
                For ard = 0 To myfile.Length – 1

                    value = myfile(ard)
```

```vb
                            If value = 0 Then
                                weightedArray(ard) = Wminus(ab)
                            Else
                                weightedArray(ard) = Wplus(ab)
                            End If
                    Next



                    'For y = 0 To imagesize.Height – 1
                    '    For x = 0 To imagesize.Width – 1
                    '          'value = imagesize(a)


                    '          If imagesize.GetPixel(x, y) =
Color.FromArgb(0, 0, 0) Then
                    '              weightedArray(x * y) = Wminus(ab)
                    '          Else
                    '              weightedArray(x * y) = Wplus(ab)
                    '          End If

                    '    Next
                    'Next


            End If

            'now we need to add the evidence layer created to the
prior probability
            'prilogit should be calculated as the ratio D/T the
conversion in ODDS and
            'ln function gives prilogit value
            'I need the deposit layer and the tot number of pixels


            ' Dep = Form5Inst.AD(TextBox8.Text)
            ' Dim Dep_conv As Single = Dep * 0.000269
            Dim priprob As Single = (Dep / (imagesize.Height *
imagesize.Width))
            Dim priOdd As Single = priprob / (1 – priprob)
            Dim con As Single
            con = Math.Log(Double.Parse(priOdd))


            Dim ac As Integer
            Dim priorlogit((imagesize.Height * imagesize.Width) – 1)
As Single 'five

            ' con = Single.Parse(TextBox6.Text)
            For ac = 0 To ((imagesize.Height * imagesize.Width) – 1)
                priorlogit(ac) = con
            Next
```

```vb
            For ac = 0 To postlogit.Length - 1
                If ab = 0 Then
                    postlogit(ac) = postlogit(ac) + priorlogit(ac) +
weightedArray(ac)
                Else
                    postlogit(ac) = postlogit(ac) + weightedArray(ac)
                End If
                'we get a postlogit value that is the sum of all
images- as postlogit is declared
                'outside the For "ab" loop, each cycle updates its
value

            Next


'''''''''''''''''''''''''''''''''''''''''''''''''''''''''''''''''''''''''
''''''''''''''''''''''''''''''''''''''''''''
            'From this point we introduce new code that considers the
missing eveidence
            'the code loads the missing eveidence layer a boolean
image
            'where pixel columns contain missing information the
weights are turned to (0)

            Dim MissingEv As String
            Dim MEArray() As Byte
            Dim test As String =
Bayes_Data_Source_ModelDataGridView.Rows(ab).Cells(3).Value.ToString

            If Not
Bayes_Data_Source_ModelDataGridView.Rows(ab).Cells(3).Value.ToString =
"" Then

                MissingEv =
Bayes_Data_Source_ModelDataGridView.Rows(ab).Cells(3).Value
                MEArray =
My.Computer.FileSystem.ReadAllBytes(MissingEv)
                Array.Reverse(MEArray)
                Array.Resize(MEArray, imagesize.Height *
imagesize.Width)
                'Array.Reverse(MEArray) changed as all others were not
reversed to original like bayes to display purpose

                Dim a As Integer
                For a = 0 To MEArray.Length - 1
                    If Not MEArray(a) = 0 Then
                        'seems that here we turn to 0 all the pixels
that has at least one layer with missing evidence in it
                        'the weightedArray is computed multiple times
for each j layer so we put 0 in each layer with missing
                        'evidence
                        weightedArray(a) = 0
```

```vbnet
                        End If
                    Next

                End If

'''''''''''''''''''''''''''''''''''''''''''''''''''''''''''''''''''''
''''''''''''''''''''''''''''''''''''''''''
                For ac = 0 To postlogit.Length – 1
                    If ab = 0 Then
                        postlogit_miss(ac) = postlogit_miss(ac) +
priorlogit(ac) + weightedArray(ac)
                    Else
                        postlogit_miss(ac) = postlogit_miss(ac) +
weightedArray(ac)
                    End If
                    'we get a postlogit value that is the sum of all
images– as postlogit is declared
                    'outside the For "ab" loop, each cycle updates its
value

                Next
            Next

        ' I think that here we can insert some code to filter out the
postlogit that are needed for the missing ev.
        ' postlogit will be used as p(d:x)




        'MsgBox(postlogit(postlogit.Length – 1).ToString)
        'Dim am As Integer
        'For am = 0 To postlogit.Length – 1

        '     'we need to convert to integer
        '     'Dim MyDouble As Double = 42.72
        '     'Dim MyInt As Integer = CType(MyDouble, Integer)
        '     '' MyInt has the value of 43.



        'Next

        'For am = 0 To postlogit.Length – 1
        '     My.Computer.FileSystem.WriteAllText("c:\wofe\test",
postlogit(am), True)
        'Next
```

```
        'now we need to rescale the double in a way that we can
generate a byte array

        'Dim ad As Integer
        Dim aq As Integer

        Dim postprob(postlogit.Length – 1) As Single
        Dim postprob_miss(postlogit.Length – 1) As Single
        '  Dim postprobByte(postlogit.Length – 1) As Byte
        For aq = 0 To postlogit.Length – 1
            'we convert to probability
            'postodds= exp(postlogit)
            'postprob= postodds/(1+postodds)


            'this post prob is Pk of Carranza 2004
            postprob(aq) = Math.Exp(postlogit(aq)) / (1 +
Math.Exp(postlogit(aq)))
            postprob_miss(aq) = Math.Exp(postlogit_miss(aq)) / (1 +
Math.Exp(postlogit_miss(aq)))


            'we recover the alghorithm need to be modified the input
as we have to filter out the areas without the
            'missing evidence
            'note that we need just the pixels intersecting a deposit
            'therefore we have to perform the summation of weights
only overlapping with pixel 1 of deposit layer
            'an if statement should work
            'we consider only the weights of layers holding the
missing evidence as the other weights were previously
            'updated, therfore we introduce an updated prior
probability that already considers the weight of layers
            'without missing evidence
        Next

        'These below are two arrays with values of Posterior prob in
case of non-missing or missing evidence
        'We can save these arrays as binary files but this will need
to convert them in a scale of 255 bytes
        PkD = postprob_miss
        PDx = postprob

        If CheckBox1.Checked Then

            BinArcon(PkD)
```

```vb
            Try

My.Computer.FileSystem.RenameFile("c:\wofe\arraybin.bin",
"PkD_miss.bin")
            Catch ex As Exception
                File.Delete("c:\wofe\PkD_miss.bin")

My.Computer.FileSystem.RenameFile("c:\wofe\arraybin.bin",
"PkD_miss.bin")
            End Try
        Else
            PkD = PDx
            File.Delete("c:\wofe\PkD_miss.bin")
        End If

        BinArcon(PDx)
        Try
            My.Computer.FileSystem.RenameFile("c:\wofe\arraybin.bin",
"PDx.bin")
        Catch ex As Exception
            File.Delete("c:\wofe\PDx.bin")
            My.Computer.FileSystem.RenameFile("c:\wofe\arraybin.bin",
"PDx.bin")
        End Try




        'Dim acd As Integer
        'Dim counter As Integer
        'Dim d() As Byte =
My.Computer.FileSystem.ReadAllBytes("d.bin")
        'For acd = 0 To postprob.Length - 1
        '    If d(acd) > 0 Then
        '        PkD(counter) = postprob(acd)
        '        counter = counter + 1
        '    End If
        'Next



        'My.Computer.FileSystem.OpenTextFileWriter("Pk.txt", False,
System.Text.Encoding.Unicode)
    End Function



    Private Sub Button12_Click(ByVal sender As System.Object, ByVal e
As System.EventArgs) Handles Button12.Click
        My.Forms.Form6WofeViewer.Close()
        My.Forms.Form6WofeViewer.Show()
    End Sub
```

```vbnet
    Private Function SigmaSQ(ByVal FileName() As String, ByVal
sWplus() As Single, ByVal sWminus() As Single) As Integer

        ' I need to firslty select the bitmaps created with convert,
then store the strings in the first column
        'manually we type in the weights and ask for that with a msg
box
        'all is set and ready for the calculation
        'we need to select each row and use the loop to convert the
pixels to an array of weights
        'we need to sum up the images to the prior probability image


        Dim s2SumWeights((imagesize.Height * imagesize.Width) - 1) As
Single

        Dim s2SumWeights_miss((imagesize.Height * imagesize.Width) -
1) As Single

        Dim ab As Integer

        For ab = 0 To FileName.Length - 1
            Dim weightedArray((imagesize.Height * imagesize.Width) -
1) As Single 'six necessary to weight step
            ''''''new code from here
            If FileName(ab) = Nothing Then
                Exit For
            End If
            Dim evidence As Bitmap =
Bitmap.FromFile(FileName(ab).ToString)

            Dim myfile((evidence.Width * evidence.Height) - 1) As Byte
            Dim color As System.Drawing.Color
            Dim county As Integer
            Dim countx As Integer
            Dim s As Integer
            For county = 0 To evidence.Height - 1
                For countx = 0 To evidence.Width - 1
                    color = evidence.GetPixel(countx, county)

                    If CInt(color.B) <> 0 And CInt(color.G) <> 0 And
CInt(color.R) <> 0 Then
                            myfile(s) = 1
                        Else
                            myfile(s) = 0
                        End If

                        s = s + 1
```

```
                Next
            Next
            s = 0
            '''''''''''''to here
            'here we start looping the different layers
            Dim value As Byte
            Dim ard As Integer

            If FileName(ab) Is Nothing Then
                Exit For
            Else

                'here we convert the image in evdence layer using the
weights
                For ard = 0 To myfile.Length - 1

                    value = myfile(ard)

                    If value = 0 Then
                        weightedArray(ard) = Math.Pow(sWminus(ab), 2)
' here we get the variance from the previously calculated standard dev
                    Else
                        weightedArray(ard) = Math.Pow(sWplus(ab), 2)
                    End If
                Next


            End If
            Dim ac As Integer

            'progressively the weights grow
            For ac = 0 To s2SumWeights.Length - 1
                'this result works if no missing evidence is
considered
                s2SumWeights(ac) = s2SumWeights(ac) +
weightedArray(ac)

            Next



            'From this point we introduce new code that considers the
missing eveidence
            'the code loads the missing eveidence layer a boolean
image
            'where pixel columns contain missing information the
weights are turned to (0)

            Dim MissingEv As String
            Dim MEArray() As Byte
            Dim test As String =
Bayes_Data_Source_ModelDataGridView.Rows(ab).Cells(3).Value.ToString
```

```vbnet
            If Not
Bayes_Data_Source_ModelDataGridView.Rows(ab).Cells(3).Value.ToString =
"" Then

                MissingEv =
Bayes_Data_Source_ModelDataGridView.Rows(ab).Cells(3).Value
                MEArray =
My.Computer.FileSystem.ReadAllBytes(MissingEv)
                Array.Reverse(MEArray)
                Array.Resize(MEArray, imagesize.Height *
imagesize.Width)
                'Array.Reverse(MEArray) changed as all others were not
reversed to original like bayes to display purpose

                Dim a As Integer
                For a = 0 To MEArray.Length – 1
                    If Not MEArray(a) = 0 Then
                        weightedArray(a) = 0
                    End If
                Next

            End If

            'progressively the weights grow
            For ac = 0 To s2SumWeights.Length – 1
                'this result works if missing evidence is considered
                'note that s2SumWeights_miss is different
                s2SumWeights_miss(ac) = s2SumWeights_miss(ac) +
weightedArray(ac)

            Next
        Next


        Dim cellsz = TextBox9.Text
        Dim s2Pk(PkD.Length – 1) As Single
        Dim arl As Integer
        Dim s2Pk_tot(PkD.Length – 1) As Single
        Dim s2PDx(PDx.Length – 1) As Single
        For arl = 0 To s2SumWeights.Length – 1

            'here we consider missing evidence as not really missing
so we use either positive or negative s2(weights)
            s2PDx(arl) = (((1 / (Dep * cellsz)) + s2SumWeights(arl)) *
Math.Pow(PDx(arl), 2))

            'here we consider the missing evidence as 0 so the s(W)
become 0 when the evidence is missing, this is equivalent to
            'summing up only patterns that have weights on them
            If CheckBox1.Checked Then
                s2Pk(arl) = (((1 / (Dep * cellsz)) +
s2SumWeights_miss(arl)) * Math.Pow(PkD(arl), 2))
```

```
            End If
            'here we get the total s(Pk) adding the re-estimated
influence of missing evidence due to its uncertainty
            'this should improve our error estimate
            'here I want a message box that split the calculation

            If CheckBox1.Checked Then
                s2Pk_tot(arl) = s2Pk(arl) + SigmaSQ_missingev(arl)
            End If

        Next
        'out of this we get 2 matrix one is s2pk and the other is
s2Pk_tot, we have already created the function that
        'converts probability arrays to maps so we just need to
provide the files to that function
        'For uncertainty maps we just then want s2pk and s2Pk_tot
        If CheckBox1.Checked Then
            s2Pkf_miss = Spk_sum(s2Pk_tot)
            BinArcon(s2Pk_tot)
            Try

My.Computer.FileSystem.RenameFile("c:\wofe\arraybin.bin",
"s2Pk_tot_miss.bin")
            Catch ex As Exception
                File.Delete("c:\wofe\s2Pk_tot_miss.bin")

My.Computer.FileSystem.RenameFile("c:\wofe\arraybin.bin",
"s2Pk_tot_miss.bin")
            End Try

        End If
        s2Pkf = Spk_sum(s2PDx)
        BinArcon(s2PDx)
        Try
            My.Computer.FileSystem.RenameFile("c:\wofe\arraybin.bin",
"s2PDx.bin")
        Catch ex As Exception
            File.Delete("c:\wofe\s2PDx.bin")
            My.Computer.FileSystem.RenameFile("c:\wofe\arraybin.bin",
"s2PDx.bin")

        End Try
        'This function provides the final s^2(Pk)results considering
the two cases of missing or non missing evidence,
        ' these also represent the s^2(N{D}pred)
        'remains to estimate the values of N{D} and N{Dpred}, we have
to be careful
        ' as there is a change of variables also during the estimation
of N{D}pred
        'if we consider the missing evidence

    End Function
```

```vbnet
'Public Sub SigmaSQ_missing_evidence()

'     Dim a As Integer
'     Dim b(PkD.Length - 1) As Double

'     For a = 0 To PkD.Length - 1
'          If PDx(a) - PkD(a) = 0 Then
'               b(a) = 0
'          Else
'               b(a) = Math.Pow((PDx(a) - PkD(a)), 2) '* 'frequency
of occurrence for class deltaPpost(k)(1 / (imagesize.Width *
imagesize.Height) * cellsz)
'          End If
'     Next
'     SigmaSQm = b
'End Sub


    Private Function Spk_sum(ByVal Input() As Single) As Single
        cellsz = TextBox9.Text

        Dim arr1(Input.Length - 1) As Single
        Input.CopyTo(arr1, 0) 'e.g. s2Pk
        Dim arr2(arr1.Length - 1) As Single
        Dim arr3(arr2.Length - 1) As Single

        Dim b As Integer = 0
        Dim spk As Double = 0
        Array.Sort(arr1)
        Dim a As Integer = Nothing
        'This cycle loop through the array s2Pk and define its classes
that are summarised in arr2
        For a = 0 To arr1.Length - 2
            If Not arr1(a) = arr1(a + 1) Then
                Array.ConstrainedCopy(arr1, a, arr2, b, 1)
                b = b + 1
                arr2(b) = arr1(a + 1) 'classes

            End If
        Next

        Array.Resize(arr2, Array.IndexOf(arr2, Nothing))
        'This cycle counts the number of elements within s2Pk for each
defined class
        For a = 0 To arr2.Length - 1
            For b = 0 To arr1.Length - 1
                If arr2(a) = arr1(b) Then
                    arr3(a) = arr3(a) + 1 'counter
                End If
            Next
        Next
        Array.Resize(arr3, Array.IndexOf(arr3, Nothing))
        Dim arr4(arr2.Length - 1) As Single
```

```vbnet
        'This cycle creates an array that computes the square value of
the area of each class mutiplied for its value then finally
        'all the cumulative classes of spk are summed up to get the
total value (this number when is big it means that there might be
overestimation)
        For a = 0 To arr2.Length - 1
            arr4(a) = Math.Pow((arr3(a) * cellsz), 2) * arr2(a)
            spk = spk + arr4(a)
        Next
        'MsgBox((spk), MsgBoxStyle.OKOnly)
        Return spk

    End Function
    Private Sub OminbusTest_NewOminibus()

        'we need to compute the summation of Pk or PDx depending if we
consider missing evidence or not
        'Carranza uses PDx instead of Pk to verify the influence of
missing evidence layers

        Dim cellsz = TextBox9.Text
        Dim a As Integer
        Dim NDpred As Double = 0
        Dim NDpred_m As Double = 0
        For a = 0 To PkD.Length - 1

            NDpred_m = NDpred_m + PkD(a) 'these are not standard
deviations

            NDpred = NDpred + PDx(a)

        Next
        PkD = Nothing
        PDx = Nothing
        Dim OT As Single = 0
        Dim OT_m As Single = 0
        OT = Dep / NDpred
        Label39.Text = OT
        OT_m = Dep / NDpred_m
        Label41.Text = OT_m
        ' MsgBox("OT should be higher than 0.85<< " & "OT   " &
OT.ToString & "OT_m  " & OT_m.ToString)

        Dim NewOT As Single = 0
        Dim NewOT_m As Single = 0

        NewOT_m = ((NDpred_m * cellsz) - (Dep * cellsz)) /
Math.Sqrt(s2Pkf_miss)
        Label45.Text = NewOT_m
        NewOT = ((NDpred * cellsz) - (Dep * cellsz)) /
Math.Sqrt(s2Pkf)
        Label43.Text = NewOT
```

```vb
        ' MsgBox("NewOT should be lower than 0.7>> " & "NewOT  " &
NewOT.ToString & "NewOT_m  " & NewOT_m.ToString)

        Dim file As System.IO.StreamWriter
        file =
My.Computer.FileSystem.OpenTextFileWriter("c:\wofe\NOT&OT.txt", False)

        file.WriteLine("OT   OT_m")
        file.WriteLine(OT & "   " & OT_m)
        file.WriteLine("NewOT    NewOT_m")
        file.WriteLine(NewOT & "   " & NewOT_m)
        file.Close()


    End Sub

    Public Sub open_dep()
        'Dim myStream As Stream

        Dim selectFileDialog1 As New OpenFileDialog()

        selectFileDialog1.InitialDirectory = "c:\wofe\"
        selectFileDialog1.Filter = "bmp files (*.bmp)|*.bmp|All files
(*.*)|*.*"
        selectFileDialog1.FilterIndex = 2
        selectFileDialog1.RestoreDirectory = True

        If selectFileDialog1.ShowDialog() = DialogResult.OK Then

            Me.TextBox8.Text = selectFileDialog1.FileName


            'myStream = selectFileDialog1.OpenFile()
            'If Not (myStream Is Nothing) Then
            ' Insert code to read the stream here.
            'myStream.Close()
            'End If
        End If



    End Sub


    Private Sub saveToolStripMenuItem_Click(ByVal sender As
System.Object, ByVal e As System.EventArgs) Handles
saveToolStripMenuItem.Click
        If Me.Validate Then
            Me.Bayes_Data_Source_ModelBindingSource.EndEdit()

Me.Bayes_Data_Source_ModelTableAdapter.Update(Me.BayesDataSet.Bayes_Da
ta_Source_Model)
        Else
```

```vb
            System.Windows.Forms.MessageBox.Show(Me, "Validation
errors occurred.", "Save", System.Windows.Forms.MessageBoxButtons.OK,
System.Windows.Forms.MessageBoxIcon.Warning)
        End If

        Try
            My.Computer.FileSystem.CopyFile("Bayes.mdb",
"c:\wofe\DataBase\Bayes.mdb")
        Catch ex As Exception

My.Computer.FileSystem.DeleteFile("c:\wofe\DataBase\Bayes.mdb")
            My.Computer.FileSystem.CopyFile("Bayes.mdb",
"c:\wofe\DataBase\Bayes.mdb")
        End Try
    End Sub

    Private Sub exitToolStripMenuItem_Click(ByVal sender As
System.Object, ByVal e As System.EventArgs) Handles
exitToolStripMenuItem.Click
        Me.Close()
    End Sub

    Private Sub openToolStripMenuItem_Click(ByVal sender As
System.Object, ByVal e As System.EventArgs) Handles
openToolStripMenuItem.Click
        Try
            My.Computer.FileSystem.CopyFile("Bayes.mdb",
"c:\wofe\DataBase\Bayes.mdb")
        Catch ex As Exception
            Exit Try
        End Try




        'this is to open bmp files and display or manipulate them
        Dim openFileDialog As New OpenFileDialog
        openFileDialog.Filter = "Data Files(*.MDB)" + "|*.MDB;|All
files (*.*)|*.*"
        openFileDialog.FilterIndex = 2
        openFileDialog.RestoreDirectory = True



        If DialogResult.OK = openFileDialog.ShowDialog() Then


            Dim a As String = openFileDialog.FileName
            Try
                My.Computer.FileSystem.RenameFile("Bayes.mdb",
"Bayes_saved.mdb")
            Catch ex As Exception
                My.Computer.FileSystem.DeleteFile("Bayes_saved.mdb")
```

```vb
                My.Computer.FileSystem.RenameFile("Bayes.mdb",
"Bayes_saved.mdb")
            End Try

            My.Computer.FileSystem.CopyFile(a, "Bayes.mdb")

        ElseIf DialogResult.Cancel Then
            Exit Sub


        End If


        'TODO: This line of code loads data into the
'FirstDatabaseDataSet.sysdiagrams' table. You can move, or remove it,
as needed.

Me.Bayes_Data_Source_ModelTableAdapter.Fill(Me.BayesDataSet.Bayes_Data
_Source_Model)



        '    bmpImage = CType(Bitmap.FromFile(openFileDialog.FileName,
False), Bitmap)
        '    Me.AutoScroll = False
        '    ' Me.AutoScrollMinSize = New Size(CInt(bmpImage.Width *
curZoom), CInt(bmpImage.Height * curZoom))
        '    ' Me.Invalidate()
        '    ' zoomMode = True
        'End If
        '' curRect = New Rectangle(0, 0, bmpImage.Width,
bmpImage.Height)
        ''originalSize.Width = bmpImage.Width
        ''originalSize.Height = bmpImage.Height
    End Sub

    Private Sub Form1_Load(ByVal sender As System.Object, ByVal e As
System.EventArgs) Handles MyBase.Load
        'TODO: This line of code loads data into the
'BayesDataSet.Bayes_Data_Source_Model' table. You can move, or remove
it, as needed.

Me.Bayes_Data_Source_ModelTableAdapter.Fill(Me.BayesDataSet.Bayes_Data
_Source_Model)
    End Sub

    Private Sub bindingNavigatorSaveItem_Click_1(ByVal sender As
System.Object, ByVal e As System.EventArgs) Handles
bindingNavigatorSaveItem.Click
        If Me.Validate Then
            Me.Bayes_Data_Source_ModelBindingSource.EndEdit()
```

```
Me.Bayes_Data_Source_ModelTableAdapter.Update(Me.BayesDataSet.Bayes_Da
ta_Source_Model)
        Else
            System.Windows.Forms.MessageBox.Show(Me, "Validation
errors occurred.", "Save", System.Windows.Forms.MessageBoxButtons.OK,
System.Windows.Forms.MessageBoxIcon.Warning)
        End If
        Try
            My.Computer.FileSystem.CopyFile("Bayes.mdb",
"c:\wofe\DataBase\Bayes.mdb")
        Catch ex As Exception

My.Computer.FileSystem.DeleteFile("c:\wofe\DataBase\Bayes.mdb")
            My.Computer.FileSystem.CopyFile("Bayes.mdb",
"c:\wofe\DataBase\Bayes.mdb")
        End Try
    End Sub

    Private Sub Bayes_Data_Source_ModelDataGridView_MouseWheel(ByVal
sender As Object, ByVal e As System.Windows.Forms.MouseEventArgs)
Handles Bayes_Data_Source_ModelDataGridView.MouseWheel
        Dim selectFileDialog1 As New OpenFileDialog()

        selectFileDialog1.InitialDirectory = "c:\"
        selectFileDialog1.Filter = "bmp files (*.bmp)|*.bmp|All files
(*.*)|*.*"
        selectFileDialog1.FilterIndex = 2
        selectFileDialog1.RestoreDirectory = True

        'If selectFileDialog1.ShowDialog() = DialogResult.Cancel Then
        '    Exit Sub
        If selectFileDialog1.ShowDialog() = DialogResult.OK Then

            Me.Bayes_Data_Source_ModelDataGridView.CurrentCell.Value =
selectFileDialog1.FileName

            '    'myStream = selectFileDialog1.OpenFile()
            '    'If Not (myStream Is Nothing) Then
            '    ' Insert code to read the stream here.
            '    'myStream.Close()
        End If
    End Sub


    Private Function BinArcon(ByVal input() As Single) As Byte

        'This function is a generalisation of the second part of the
Bayes alghorithm, it is designed to solve a problem of
        'compatibility between arrays and bmp files, basically we need
a conversion from single to byte
        'The main difficulty is that this conversion has to represent
probability in a scale of 255 colors.
```

```vb
        'Casting of single withought rescaling will likely reduce all
the array values to 0. Therfore it is useful to
        'firstly define the minimum value of the array then multiply
for an appropriate scaling factor to
        'obtain a range of values large than delta255
        'We need a string to save the name of each output file


        Dim ad As Integer


        Dim postprobByte(input.Length – 1) As Byte
        Dim rescale(input.Length – 1) As Single

        Array.Copy(input, rescale, input.Length)
        Array.Sort(rescale)

        Dim min As Single = rescale(0)
        Dim max As Single = rescale(rescale.Length – 1)

        My.Computer.FileSystem.WriteAllText("c:\wofe\scale_M.txt",
"min = " & min.ToString & "max = " & max.ToString, False)

        For ad = 0 To input.Length – 1

            ' we shift or translate the scale to get a minimum of 0
            'min must become firslty equal to 1 so if min*x=1
            Dim alfa As Single = (1 / min)
            input(ad) = input(ad) * alfa
            input(ad) = (input(ad) – (min * alfa))
            input(ad) = (input(ad) * 255) / ((max * alfa) – (min *
alfa))
            postprobByte(ad) = CByte((input(ad)))
            input(ad) = (input(ad) * ((max * alfa) – (min * alfa))) /
255
            input(ad) = (input(ad) + (min * alfa))
            input(ad) = input(ad) / alfa
        Next


        Dim response As MsgBoxResult = MsgBox("Binary conversion
completed, would you like to save the file?", MsgBoxStyle.YesNo)

        If response = MsgBoxResult.Yes Then

            Dim saveFileDialog1 As New SaveFileDialog()

            saveFileDialog1.InitialDirectory = "c:\wofe\"
            saveFileDialog1.Filter = "bin files (*.bin)|*.bin|All
files (*.*)|*.*"
            saveFileDialog1.FilterIndex = 2
            saveFileDialog1.RestoreDirectory = True
```

```vb
            If saveFileDialog1.ShowDialog() = DialogResult.OK Then

My.Computer.FileSystem.WriteAllBytes((saveFileDialog1.FileName),
postprobByte, False)
            End If
        Else

My.Computer.FileSystem.WriteAllBytes("c:\wofe\arraybin.bin",
postprobByte, False)
        End If

    End Function

    Private Sub Button11_Click(ByVal sender As System.Object, ByVal e
As System.EventArgs) Handles Button11.Click

        'This function save a bmp file of an array of posteriror
probability
        'Dim myStream As Stream
        Dim selectFileDialog1 As New OpenFileDialog()

        selectFileDialog1.InitialDirectory = "c:\wofe\"
        selectFileDialog1.Filter = "bin files (*.bin)|*.bin|All files
(*.*)|*.*"
        selectFileDialog1.FilterIndex = 2
        selectFileDialog1.RestoreDirectory = True
        'first dialog fpr selection of binary array to map
        If selectFileDialog1.ShowDialog() = DialogResult.OK Then

            Dim name As String = selectFileDialog1.FileName


            Dim postprobByte() As Byte =
My.Computer.FileSystem.ReadAllBytes(name)
            MsgBox("Please select reference (rows*column bmp file)",
MsgBoxStyle.OKOnly)
            'Array.Reverse(postprobByte)

            'second dialogue box for selection of a bmp as reference
            Dim selectFileDialog2 As New OpenFileDialog()

            selectFileDialog2.InitialDirectory = "c:\wofe\"
            selectFileDialog2.Filter = "bmp files (*.bmp)|*.bmp|All
files (*.*)|*.*"
            selectFileDialog2.FilterIndex = 2
            selectFileDialog2.RestoreDirectory = True

            If selectFileDialog2.ShowDialog() = DialogResult.OK Then

                'There might be a problem with loading this binary
file in term of header
                bayesmap = Bitmap.FromFile(selectFileDialog2.FileName)
                Dim x As Integer
```

```vbnet
                Dim y As Integer
                Dim count As Integer = 0

                '(bayesmap.Width – 1) – inverted also y with x

                For y = 0 To bayesmap.Height – 1
                    For x = 0 To bayesmap.Width – 1
                        bayesmap.SetPixel(x, y,
Color.FromArgb(postprobByte(count), postprobByte(count),
postprobByte(count)))
                        count = count + 1
                    Next
                Next

                File.Delete(name & ".bmp")
                bayesmap.Save(name & ".bmp")

                MsgBox("Map completed and saved in " & name & ".bmp")
            End If
        End If
    End Sub

    Private Sub Button14_Click(ByVal sender As System.Object, ByVal e
As System.EventArgs) Handles Button14.Click
        'This routine is compiled to solve the problem of calculating
the additional error seen as variance of the posterior
        'probability. The objective is to create a function that input
info from the datagrid view
        'in particular the weights and the relative missing patterns,
in term of number and area

        'Here we select the patterns with missing evidence
        'start new ot ot

        Try
            cell = Me.TextBox9.Text
        Catch ex As Exception
            MsgBox("Please provide cell size")
            Exit Sub
        End Try

        d = Nothing
        PkD = Nothing
        PDx = Nothing

        SigmaSQm = Nothing
        s2Pk = Nothing
        s2Pkf = Nothing
        s2Pkf_miss = Nothing
        Dep = Nothing
        bmpsizepub = Nothing
        AD_w = Nothing
```

```vb
        AI_w = Nothing
        AG_w = Nothing
        AT_w = Nothing 'shared variables expressing areas as cell
numbers; they work in all sub routines


        Dim a As Integer
        'Dim b As Integer

        Dim FileName(Bayes_Data_Source_ModelDataGridView.Rows.Count)
As String
        Dim Wplus(Bayes_Data_Source_ModelDataGridView.Rows.Count) As
Single
        Dim Wminus(Bayes_Data_Source_ModelDataGridView.Rows.Count) As
Single
        Dim sWplus(Bayes_Data_Source_ModelDataGridView.Rows.Count) As
Single
        Dim sWminus(Bayes_Data_Source_ModelDataGridView.Rows.Count) As
Single
        Dim MissEv(Bayes_Data_Source_ModelDataGridView.Rows.Count) As
String

        Dim FileName_r(Bayes_Data_Source_ModelDataGridView.Rows.Count)
As String
        Dim Wplus_r(Bayes_Data_Source_ModelDataGridView.Rows.Count) As
Single
        Dim Wminus_r(Bayes_Data_Source_ModelDataGridView.Rows.Count)
As Single
        Dim sWplus_r(Bayes_Data_Source_ModelDataGridView.Rows.Count)
As Single
        Dim sWminus_r(Bayes_Data_Source_ModelDataGridView.Rows.Count)
As Single
        Dim MissEv_r(Bayes_Data_Source_ModelDataGridView.Rows.Count)
As String



        For a = 0 To Bayes_Data_Source_ModelDataGridView.Rows.Count
            'DBnull
            Try
                If
Bayes_Data_Source_ModelDataGridView.Rows(a).Cells(3).Value Is
System.DBNull.Value Then
                    Exit Try
                End If
                FileName(a) =
Bayes_Data_Source_ModelDataGridView.Rows(a).Cells(6).Value
                Wplus(a) =
Bayes_Data_Source_ModelDataGridView.Rows(a).Cells(1).Value
                Wminus(a) =
Bayes_Data_Source_ModelDataGridView.Rows(a).Cells(2).Value
                sWplus(a) =
Bayes_Data_Source_ModelDataGridView.Rows(a).Cells(4).Value
```

```vbnet
                sWminus(a) =
Bayes_Data_Source_ModelDataGridView.Rows(a).Cells(5).Value
                MissEv(a) =
Bayes_Data_Source_ModelDataGridView.Rows(a).Cells(3).Value

            Catch : Exit For

            End Try

        Next

        Dim b As Integer
        For a = 0 To FileName.Length - 1
            If FileName(a) <> Nothing Then
                FileName_r(b) = FileName(a)
                Wplus_r(b) = Wplus(a)
                Wminus_r(b) = Wminus(a)
                sWplus_r(b) = sWplus(a)
                sWminus_r(b) = sWminus(a)
                MissEv_r(b) = MissEv(a)

                b = b + 1
            Else


            End If
        Next
        ' we need to reduce FileName to just the layer with missing
evidence in it
        missing_evidence(FileName_r, Wplus_r, Wminus_r, MissEv_r)


    End Sub

    Private Function missing_evidence(ByVal FileName_r() As String,
ByVal Wplus_r() As Single, ByVal Wminus_r() As Single, ByVal
MissEv_r() As String) As Integer

        'looks fine
        'here we use the first part of bayes to get the value of
posterior probability
        'we have to use the postlogit array as prior probability when
we calculate P(d:x)
        'and P(d)
        'weights are automatically picked from the data grid view, but
the arrays with final summation of weights
        'has to be stripped of values that are not included within
deposits and missing evidence ???
        'we need to input a layer representing the area of missing
evidence = bmp indexed image then perform a boolean with
        'deposit and this layer to get only values useful for the
calculation, we consider only missing evidence as we are
```

```vbnet
        'using it to calculate the posterior probability resulting
when missing evidence is intersected
        'therefore a cumulative area obtained combining all the
missing evidence on a single layer positively defines
        'the pixel where this calculation is meaningfull
        'in any case we cannot calculate sigma^2(p) for missing
eveidence if there is no missing evidence
        Dim Form5Inst As New Form5
        Dim SigmaSQ2(imagesize.Height * imagesize.Width – 1) As Double
        Dep = Form5Inst.AD(TextBox8.Text)
        imagesize = Bitmap.FromFile(FileName_r(0))

        'Static header() As Byte 'on



        'four
        'six necessary to weight step
        ' Static rescale((imagesize.Height * imagesize.Width) – 1) As
Single 'seven

        Dim ab As Integer
        For ab = 0 To FileName_r.Length – 1
            Dim weightedArray((imagesize.Height * imagesize.Width) –
1) As Single
            Dim postlogit((imagesize.Height * imagesize.Width) – 1) As
Single
            Dim postlogit_miss((imagesize.Height * imagesize.Width) –
1) As Single
            Dim postlogit_wplus((imagesize.Height * imagesize.Width) –
1) As Single
            Dim postlogit_wminus((imagesize.Height * imagesize.Width)
– 1) As Single


            Try
                ' imagesize = Bitmap.FromFile(FileName(ab))
                myfile =
My.Computer.FileSystem.ReadAllBytes(FileName_r(ab)) 'may need to
string –– 'three
            Catch : Exit Try
            End Try

            'need to strip the header
            ' Dim headerfile() As Byte =
My.Computer.FileSystem.ReadAllBytes("c:\wofe\imageheader.bmp")
            'header = headerfile
            'Array.Resize(header, (headerfile.Length –
(imagesize.Height * imagesize.Width)))
            Array.Reverse(myfile)
            Array.Resize(myfile, (imagesize.Height * imagesize.Width))
            'Array.Reverse(myfile)
```

```vbnet
              'here we start looping the different layers

              'Dim x As Integer
              'Dim y As Integer
              Dim value As Byte
              Dim ard As Integer

              If FileName_r(ab) Is Nothing Then 'solves issue of final
(0)
                  Exit For
              Else


              'here we convert the image in evdence layer using the
weights
                  For ard = 0 To myfile.Length - 1

                      value = myfile(ard)

                      If value = 0 Then
                          weightedArray(ard) = Wminus_r(ab)
                      Else
                          weightedArray(ard) = Wplus_r(ab)
                      End If
                  Next


                  'For y = 0 To imagesize.Height - 1
                  '    For x = 0 To imagesize.Width - 1
                  '            'value = imagesize(a)

                  '            If imagesize.GetPixel(x, y) =
Color.FromArgb(0, 0, 0) Then
                  '                    weightedArray(x * y) = Wminus(ab)
                  '            Else
                  '                    weightedArray(x * y) = Wplus(ab)
                  '            End If

                  '    Next
                  'Next

              End If

              'now we need to add the evidence layer created to the
prior probability
              'prilogit should be calculated as the ratio D/T the
conversion in ODDS and
```

```vbnet
            'ln function gives prilogit value
            'I need the deposit layer and the tot number of pixels


            ' Dep = Form5Inst.AD(TextBox8.Text)
            ' Dim Dep_conv As Single = Dep * 0.000269
            Dim priprob As Single = (Dep / (imagesize.Height *
imagesize.Width))
            Dim priOdd As Single = priprob / (1 - priprob)
            Dim con As Single
            con = Math.Log(Double.Parse(priOdd))


            Dim ac As Integer
            Dim priorlogit((imagesize.Height * imagesize.Width) - 1)
As Single 'five

            ' con = Single.Parse(TextBox6.Text)
            For ac = 0 To ((imagesize.Height * imagesize.Width) - 1)
                priorlogit(ac) = con
            Next

            'For ac = 0 To postlogit.Length - 1
            '     If ab = 0 Then
            '          postlogit(ac) = postlogit(ac) + priorlogit(ac) +
weightedArray(ac)
            '      Else
            '          postlogit(ac) = postlogit(ac) + weightedArray(ac)
            '      End If
            '     'we get a postlogit value that is the sum of all
images- as postlogit is declared
            '      'outside the For "ab" loop, each cycle updates its
value

            'Next



'''''''''''''''''''''''''''''''''''''''''''''''''''''''''''''''''''''''''''''''''
''''''''''''''''''''''''''''''''''''''''''''''
            'From this point we introduce new code that considers the
missing eveidence
            'the code loads the missing eveidence layer a boolean
image
            'where pixel columns contain missing information the
weights are turned to (0)

            Dim MissingEv As String
            Dim MEArray() As Byte
            '  Dim test As String =
Bayes_Data_Source_ModelDataGridView.Rows(ab).Cells(3).Value.ToString
```

```
            MissingEv = MissEv_r(ab)
            MEArray = My.Computer.FileSystem.ReadAllBytes(MissingEv)
            Array.Reverse(MEArray)
            Array.Resize(MEArray, imagesize.Height * imagesize.Width)
            'Array.Reverse(MEArray) changed as all others were not
reversed to original like bayes to display purpose

            Dim a As Integer
            For a = 0 To MEArray.Length - 1
                If Not MEArray(a) = 0 Then
                    'seems that here we turn to 0 all the pixels that
has at least one layer with missing evidence in it
                    'the weightedArray is computed multiple times for
each j layer so we put 0 in each layer with missing
                    'evidence
                    weightedArray(a) = 0

                End If
            Next


'''''''''''''''''''''''''''''''''''''''''''''''''''''''''''''''''''''''
''''''''''''''''''''''''''''''''''
            For ac = 0 To postlogit.Length - 1
                If ab = 0 Then
                    postlogit_miss(ac) = postlogit_miss(ac) +
priorlogit(ac) + weightedArray(ac)
                Else
                    postlogit_miss(ac) = postlogit_miss(ac) +
weightedArray(ac)
                End If
                'we get a postlogit value that is the sum of all
images- as postlogit is declared
                'outside the For "ab" loop, each cycle updates its
value

            Next


            'LOOP to change to W+


            For a = 0 To MEArray.Length - 1
                If Not MEArray(a) = 0 Then
                    'seems that here we turn to 0 all the pixels that
has at least one layer with missing evidence in it
                    'the weightedArray is computed multiple times for
each j layer so we put 0 in each layer with missing
                    'evidence
                    weightedArray(a) = Wplus_r(ab)
```

```
                    End If
              Next



''''''''''''''''''''''''''''''''''''''''''''''''''''''''''''''''''''
''''''''''''''''''''''''''''''''''''
              For ac = 0 To postlogit.Length - 1
                    If ab = 0 Then
                        postlogit_wplus(ac) = postlogit_wplus(ac) +
priorlogit(ac) + weightedArray(ac)
                    Else
                        postlogit_wplus(ac) = postlogit_wplus(ac) +
weightedArray(ac)
                    End If
                    'we get a postlogit value that is the sum of all
images- as postlogit is declared
                    'outside the For "ab" loop, each cycle updates its
value

              Next


              'LOOP to change to W-


              For a = 0 To MEArray.Length - 1
                    If Not MEArray(a) = 0 Then
                        'seems that here we turn to 0 all the pixels that
has at least one layer with missing evidence in it
                        'the weightedArray is computed multiple times for
each j layer so we put 0 in each layer with missing
                        'evidence
                        weightedArray(a) = Wminus_r(ab)
                    End If
              Next



''''''''''''''''''''''''''''''''''''''''''''''''''''''''''''''''''''
''''''''''''''''''''''''''''''''''''
              For ac = 0 To postlogit.Length - 1
                    If ab = 0 Then
                        postlogit_wminus(ac) = postlogit_wminus(ac) +
priorlogit(ac) + weightedArray(ac)
                    Else
                        postlogit_wminus(ac) = postlogit_wminus(ac) +
weightedArray(ac)
                    End If
                    'we get a postlogit value that is the sum of all
images- as postlogit is declared
                    'outside the For "ab" loop, each cycle updates its
value
```

```vb
            Next

            'now we have all three Pprob we need for the calculation
the area where the jth layer with Pattern Bj has 1 and the area with 0
value
            'which is negBj

            'Calculation of AreaBj
            'For this we need the file path we call the binary file
and use a bit counter to find out the number of 0 and 1



            Dim r As Integer
            'Here we need some code that cleans up the bitmaps for us,
we declare 2 new myarrays that will be locally storing
            'the original BMP in binary format. Then we get the data
out of them and feed SumArray
            Dim PatternBj() As Byte =
My.Computer.FileSystem.ReadAllBytes(FileName_r(ab)) 'we call the file
with missing evidence




            r = (imagesize.Height * imagesize.Width) ' the number of
cells needed to get the number of good data pixels




            'tronca arrays con remove command

            Array.Reverse(PatternBj)
            Array.Resize(PatternBj, r)
            Array.Reverse(PatternBj)

            Dim b As Integer = 0
            Dim Sum As Single = 0

            ' algebric sum of array (PatternBj) we get just 1s not 0
counted, therfore the area of cells containing the pattern
            For b = 0 To PatternBj.Length – 1
                Sum = Sum + PatternBj(b) '-1 is inserted as the array
starts from 0
            Next b

            Dim AreaPattern As Single = Sum
```

```vbnet
            Dim Area_emptyPattern As Single = (r – AreaPattern)



            'estimation of postbrob for the 3 postlogits

            Dim aq As Integer

            Try

                weightedArray = Nothing

                Dim postprob_wminus(postlogit.Length – 1) As Single
                Dim postprob_miss(postlogit.Length – 1) As Single
                Dim postprob_wplus(postlogit.Length – 1) As Single

                '  Dim postprobByte(postlogit.Length – 1) As Byte
                For aq = 0 To postlogit.Length – 1
                    'we convert to probability
                    'postodds= exp(postlogit)
                    'postprob= postodds/(1+postodds)

                    'this post prob is Pk of Carranza 2004
                    postprob_wplus(aq) = Math.Exp(postlogit_wplus(aq))
/ (1 + Math.Exp(postlogit_wplus(aq)))
                    postprob_wminus(aq) =
Math.Exp(postlogit_wminus(aq)) / (1 + Math.Exp(postlogit_wminus(aq)))
                    postprob_miss(aq) = Math.Exp(postlogit_miss(aq)) /
(1 + Math.Exp(postlogit_miss(aq)))


                Next

                'sigmasq(Pk)= (P(DBj)–Pk)^2 * PBJ + (P(BnegBj)–Pk)^2 *
PnegBj


                cellsz = TextBox9.Text

                For a = 0 To postlogit.Length – 1
                    SigmaSQ2(a) = (Math.Pow((postprob_wplus(a) –
postprob_miss(a)), 2) * ((AreaPattern * cellsz) / (imagesize.Height *
imagesize.Width)) + (Math.Pow((postprob_wminus(a) – postprob_miss(a)),
2) * (Area_emptyPattern * cellsz) / ((imagesize.Height *
imagesize.Width))))
                Next
            Catch ex As Exception
                Exit Function
            End Try
```

```
        Next

        SigmaSQ_missingev = SigmaSQ2
        MsgBox("missing evidence calculated!")
    End Function


End Class
'remember that inside the buttons we have the code that defines the
order of use of such functionalities
#End Region
```

C.2. Spatial Analyser

Compiled in VB 2005 (Express Edition)

```
Software used to compute minimum Euclidean distances (Chapter 6)

Imports System.IO
Imports System.Text
Imports System
Imports System.Drawing
Imports System.Drawing.Printing
Imports System.Collections
Imports System.ComponentModel
Imports System.Windows.Forms

Public Class Form1

    Dim breccia() As Double
    Dim faults() As Double
    Dim deltaMin() As Double

    'Array gen
    Private Sub Button1_Click(ByVal sender As System.Object, ByVal e
As System.EventArgs) Handles Button1.Click
        'the button is used to convert a txt file to an array of data
in double format
        'we need a the initialisation of the butto to get access to
the hard drive and select the file

        Dim selectFileDialog1 As New OpenFileDialog()

        selectFileDialog1.InitialDirectory = "C:\Documents and
Settings\Leonardo\My Documents"
```

```vb
        selectFileDialog1.Filter = "txt files (*.txt)|*.txt|All files
(*.*)|*.*"
        selectFileDialog1.FilterIndex = 2
        selectFileDialog1.RestoreDirectory = True

        If selectFileDialog1.ShowDialog() =
Windows.Forms.DialogResult.OK Then
            TextBox1.Text = selectFileDialog1.FileName

            'we need a call to the file that we host in a string
            Dim mystring As String =
My.Computer.FileSystem.ReadAllText(TextBox1.Text)
            'This command split the string in an array of string
containing xyz separated by space
            Dim mystring2() As String = Split(mystring,
Environment.NewLine)

            Dim a As Integer
            Dim b As Integer
            Dim mystring4((mystring2.Length) * 3) As Double
            'the loop is used to split more all data are charging a
single array
            For a = 0 To ((mystring2.Length – 1) * 3)
                Dim mystring3() As String = Split(mystring2(b), " ")
                mystring4(a) = Double.Parse(mystring3(0))
                mystring4(a + 1) = Double.Parse(mystring3(1))
                mystring4(a + 2) = Double.Parse(mystring3(2))
                a = a + 2
                'as b is always very small compared to a then it is
reasonable the use of b in the same loop
                'the problem would be that the loop is based on a
therefore if a ends earlier than b then
                b = b + 1
                If mystring2(b) = "" Then Exit For
            Next
            breccia = mystring4
            While breccia(breccia.Length – 1) = 0
                Array.Resize(breccia, breccia.Length – 1)
            End While

        End If
    End Sub
    'Array gen
    Private Sub Button2_Click(ByVal sender As System.Object, ByVal e
As System.EventArgs) Handles Button2.Click
        'the button is used to convert a txt file to an array of data
in double format
        'we need a the initialisation of the butto to get access to
the hard drive and select the file

        Dim selectFileDialog1 As New OpenFileDialog()
```

```vb
        selectFileDialog1.InitialDirectory = "C:\Documents and
Settings\Leonardo\My Documents"
        selectFileDialog1.Filter = "txt files (*.txt)|*.txt|All files
(*.*)|*.*"
        selectFileDialog1.FilterIndex = 2
        selectFileDialog1.RestoreDirectory = True

        If selectFileDialog1.ShowDialog() =
Windows.Forms.DialogResult.OK Then
            TextBox2.Text = selectFileDialog1.FileName

            'we need a call to the file that we host in a string
            Dim mystring As String =
My.Computer.FileSystem.ReadAllText(TextBox2.Text)
            Dim mystring2() As String = Split(mystring,
Environment.NewLine)

            Dim a As Integer
            Dim b As Integer
            Dim mystring4(((mystring2.Length) * 5)) As Double
            'the loop is used to split more all data are charging a
single array
            For a = 0 To (mystring2.Length * 5)
                Dim mystring3() As String = Split(mystring2(b), " ")
                mystring4(a) = Double.Parse(mystring3(0))
                mystring4(a + 1) = Double.Parse(mystring3(1))
                mystring4(a + 2) = Double.Parse(mystring3(2))
                mystring4(a + 3) = Double.Parse(mystring3(3))
                mystring4(a + 4) = Double.Parse(mystring3(4))

                a = a + 4
                b = b + 1
                If b > mystring2.Length – 1 Then Exit For
                If mystring2(b) = "" Then Exit For
            Next
            faults = mystring4
            While faults(faults.Length – 1) = 0
                Array.Resize(faults, faults.Length – 1)
            End While


        End If


    End Sub
    'Algorithm to compute minimum distances between the two pointsets
    Private Sub MainAlgho()
        'variables
        Dim a As Integer

        Dim xb As Double
        Dim yb As Double
        Dim zb As Double
```

```vb
        Dim xf As Double
        Dim yf As Double
        Dim zf As Double
        'clear txt file
        Dim file As System.IO.StreamWriter
        file = My.Computer.FileSystem.OpenTextFileWriter("c:\spatial
data\results.txt", False)
        file.WriteLine("")
        file.Close()
        'loops to select the coordinates to compute distance, store
distances on delta

        For a = 0 To breccia.Length – 1
            xb = breccia(a)
            yb = breccia(a + 1)
            zb = breccia(a + 2)

            a = a + 2

            Dim b As Integer = 0
            Dim c As Integer = 0
            Dim delta(faults.Length – 1) As Double 'delta lasts only
inside the b loop
            Dim deltacopy(faults.Length – 1) As Double
            For b = 0 To faults.Length – 1

                xf = faults(b)
                yf = faults(b + 1)
                zf = faults(b + 2)
                b = b + 4
                'delta gets all the distances of a single cbx point
                delta(c) = distance(xb, yb, zb, xf, yf, zf)
                c = c + 1
            Next

            'copy delta for index search
            Array.Copy(delta, deltacopy, delta.Length – 1)
            'sort delta to get a minimum
            Array.Resize(delta, c – 1)
            Array.Sort(delta)

            'compute index and retrive d1 and d2 on faults array
            Dim index As Integer = Array.IndexOf(deltacopy, delta(0))

            Dim d1 As Double = faults((index * 5) + 3)
            Dim d2 As Double = faults((index * 5) + 4)


            'write halt instruction in case of 0 or multiple equal
minimum values
            If delta(0) = 0 Or delta(0) = delta(1) Then
                'export values on a file text that is progressively
updated for each breccia loop in case of 0 or multiple
```

```vbnet
                file =
My.Computer.FileSystem.OpenTextFileWriter("c:\spatial
data\results.txt", True)
                file.WriteLine(xb & "     " & yb & "    " & zb & "     "
& d1 & "     " & d2 & "     " & delta(0) & "   err")
                file.Close()

                'export values on a file text that is progressively
updated for each breccia loop
            Else
                file =
My.Computer.FileSystem.OpenTextFileWriter("c:\spatial
data\results.txt", True)
                file.WriteLine(xb & "     " & yb & "    " & zb & "     "
& d1 & "     " & d2 & "     " & delta(0))
                file.Close()
            End If



        Next
        MsgBox("Computation completed!")
    End Sub

    Function distance(ByVal xb As Double, ByVal yb As Double, ByVal zb
As Double, ByVal xf As Double, ByVal yf As Double, ByVal zf As Double)
        'Euclidean formula
        Dim dist As Double = Math.Sqrt((Math.Pow(xb – xf, 2)) +
(Math.Pow(yb – yf, 2)) + (Math.Pow(zb – zf, 2)))
        Return dist
    End Function

    Private Sub Button3_Click(ByVal sender As System.Object, ByVal e
As System.EventArgs) Handles Button3.Click
        Me.mainAlgho()
    End Sub
End Class
```

APPENDIX D

Table D.1. Summary of rock specimens used in this thesis, illustrating their relative location, age, lithology and stratigraphic collocation.

Specimen ID	Location	Easting*	Northing	Age**	Lithotype	Stratigraphic Unit	Chapter	Figure
CDH 114	PCM 338(171.41 m)	47132.61	27873.7	MP	Siltstone/Shale	Pmh4s	3	5a
CDH83	PCM325(271.17 m)	46849.8	27850.56	MP	Siltstone/Shale	Pmh4s	3	5b
CDH85	PCM325(235.20 m)	46849.8	27850.56	MP	Shale	Pmh4s	3	5c
HSCM103	Century Mine (St4)	47430	27460	MP	Shale	Pmh4s	3	5d
HSCMT	Century Mine (St4)	47400	27550	MP	Mudstone/Siltstone	Pmh4s	3	5e
RLWL01	Watson's Lode	246462	7916970	MP	Qtz/Sid vein	Pmh3	3	6c
RLWL02	Watson's Lode	246301	7916930	MP	Qtz vein	Pmh3	3	6d
RLSK-BC35786	Silver King	245470	7925470	MP	Qtz/Sulph. infill	Pmh2	3	6e
RLWL-BC35780	Watson's Lode	246211	7916340	MP	Siltstone/Qtz vein	Pmh3	3	6f
HSCM32	Century Mine (St4)	47320	27500	MP	Siltstone/Shale	Pmh4s	5	2a
HSCM106	Century Mine (St4)	47410	27590	MP	Siltstone/Shale	Pmh4s	5	2b
HSCM109	Century Mine (St4)	47460	27510	MP	Siltstone/Shale	Pmh4s	5	2c
HSCM111	Century Mine (St4)	47340	25530	MP	Siltstone/Shale	Pmh4s	5	2e
HSCM33	Century Mine (St4)	47560	27313	MP	Siltstone/Shale	Pmh4s	5	2f
HSCML69	Century Mine (St4)	46920	28220	MC	CBX breccia	Thorntonia Limestones	6	11a
HSCML63	Century Mine (St4)	47070	28260	MC	MB Marl breccia	Thorntonia Limestones	6	11b
CDH55	PCM302(168 m)	47070	28250	MC	CLS nodular limestone	Thorntonia Limestones	6	11d
HSLHA67	Lawn Hill Annulus	251460	7928439	MC	Sandstone	Thorntonia Limestones	6	11e
HSCML64	Century Mine (St4)	46980	28240	MC	Karst breccia	Thorntonia Limestones	6	11f
LHCSO1	Lawn Hill Annulus	251049	7933520	MP	Siltstone	Pmh4s	6	25b

* Easting and Northing expressed either as AMG84 coordinates or Mine Grid coordinates.
** MP = Mesoproterozoic, MC = Middle Cambrian.

Basement metal scavenging during basin evolution: Cambrian and Proterozoic interaction at the Century Zn–Pb–Ag Deposit, Northern Australia

L. Feltrin ⸌ , N.H.S. Oliver , I.J. Kelso , S. King

Evidence of multi-stage ore genesis at the Century zinc deposit, Northwestern Queensland, Australia

Leonardo Feltrin and Nicholas H.S. Oliver

A Visual Basic Express tool to perform 3D Weights of Evidence Modelling

Leonardo Feltrin

Numerical Models of Extensional Deformation, Heat Transfer, and Fluid Flow across Basement-Cover Interfaces during Basin-Related Mineralization

NICHOLAS H.S. OLIVER,[†] JOHN G. MCLELLAN,

BRUCE E. HOBBS,

JAMES S. CLEVERLEY,

ALISON ORD,

AND LEONARDO FELTRIN